NEUROPROTEOMICS: INSIGHT INTO BRAIN FUNCTION AND DISEASE

EDITED BY: Tija Carey Jacob, Mark Oliver Collins, Matthew L. MacDonald and Susan T. Weintraub

PUBLISHED IN: Frontiers in Molecular Neuroscience

frontiers Research Topics

frontiers

ISSN 1664-8714
ISBN 978-2-88974-995-9
DOI 10.3389/978-2-88974-995-9

About Frontiers

Frontiers is more than just an open-access publisher of scholarly articles: it is a pioneering approach to the world of academia, radically improving the way scholarly research is managed. The grand vision of Frontiers is a world where all people have an equal opportunity to seek, share and generate knowledge. Frontiers provides immediate and permanent online open access to all its publications, but this alone is not enough to realize our grand goals.

Frontiers Journal Series

The Frontiers Journal Series is a multi-tier and interdisciplinary set of open-access, online journals, promising a paradigm shift from the current review, selection and dissemination processes in academic publishing. All Frontiers journals are driven by researchers for researchers; therefore, they constitute a service to the scholarly community. At the same time, the Frontiers Journal Series operates on a revolutionary invention, the tiered publishing system, initially addressing specific communities of scholars, and gradually climbing up to broader public understanding, thus serving the interests of the lay society, too.

Dedication to Quality

Each Frontiers article is a landmark of the highest quality, thanks to genuinely collaborative interactions between authors and review editors, who include some of the world's best academicians. Research must be certified by peers before entering a stream of knowledge that may eventually reach the public - and shape society; therefore, Frontiers only applies the most rigorous and unbiased reviews.
Frontiers revolutionizes research publishing by freely delivering the most outstanding research, evaluated with no bias from both the academic and social point of view. By applying the most advanced information technologies, Frontiers is catapulting scholarly publishing into a new generation.

What are Frontiers Research Topics?

Frontiers Research Topics are very popular trademarks of the Frontiers Journals Series: they are collections of at least ten articles, all centered on a particular subject. With their unique mix of varied contributions from Original Research to Review Articles, Frontiers Research Topics unify the most influential researchers, the latest key findings and historical advances in a hot research area! Find out more on how to host your own Frontiers Research Topic or contribute to one as an author by contacting the Frontiers Editorial Office: frontiersin.org/about/contact

NEUROPROTEOMICS: INSIGHT INTO BRAIN FUNCTION AND DISEASE

Topic Editors:
Tija Carey Jacob, University of Pittsburgh, United States
Mark Oliver Collins, The University of Sheffield, United Kingdom
Matthew L. MacDonald, University of Pittsburgh, United States
Susan T. Weintraub, The University of Texas Health Science Center at San Antonio, United States

Citation: Jacob, T. C., Collins, M. O., MacDonald, M. L., Weintraub, S. T., eds. (2022). Neuroproteomics: Insight into Brain Function and Disease. Lausanne: Frontiers Media SA. doi: 10.3389/978-2-88974-995-9

Table of Contents

frontiers in Molecular Neuroscience

ORIGINAL RESEARCH
published: 22 October 2020
doi: 10.3389/fnmol.2020.563091

Isolation and Characterization of Multi-Protein Complexes Enriched in the K-Cl Co-transporter 2 From Brain Plasma Membranes

*Joshua L. Smalley[1], Georgina Kontou[1,2], Catherine Choi[1], Qiu Ren[1], David Albrecht[1,2], Krithika Abiraman[1,2], Miguel A. Rodriguez Santos[1], Christopher E. Bope[1], Tarek Z. Deeb[1,2], Paul A. Davies[1], Nicholas J. Brandon[2,3] and Stephen J. Moss[1,4]**

[1] Department of Neuroscience, Tufts University School of Medicine, Boston, MA, United States, [2] AstraZeneca Tufts Lab for Basic and Translational Neuroscience, Boston, MA, United States, [3] Neuroscience, IMED Biotech Unit, AstraZeneca, Boston, MA, United States, [4] Department of Neuroscience, Physiology, and Pharmacology, University College London, London, United Kingdom

Kcc2 plays a critical role in determining the efficacy of synaptic inhibition, however, the cellular mechanisms neurons use to regulate its membrane trafficking, stability and activity are ill-defined. To address these issues, we used affinity purification to isolate stable multi-protein complexes of K-Cl Co-transporter 2 (Kcc2) from the plasma membrane of murine forebrain. We resolved these using blue-native polyacrylamide gel electrophoresis (BN-PAGE) coupled to LC-MS/MS and label-free quantification. Data are available via ProteomeXchange with identifier PXD021368. Purified Kcc2 migrated as distinct molecular species of 300, 600, and 800 kDa following BN-PAGE. In excess of 90% coverage of the soluble N- and C-termini of Kcc2 was obtained. In total we identified 246 proteins significantly associated with Kcc2. The 300 kDa species largely contained Kcc2, which is consistent with a dimeric quaternary structure for this transporter. The 600 and 800 kDa species represented stable multi-protein complexes of Kcc2. We identified a set of novel structural, ion transporting, immune related and signaling protein interactors, that are present at both excitatory and inhibitory synapses, consistent with the proposed localization of Kcc2. These included spectrins, C1qa/b/c and the IP3 receptor. We also identified interactors more directly associated with phosphorylation; Akap5, Akap13, and Lmtk3. Finally, we used LC-MS/MS on the same purified endogenous plasma membrane Kcc2 to detect phosphorylation sites. We detected 11 sites with high confidence, including known and novel sites. Collectively our experiments demonstrate that Kcc2 is associated with components of the neuronal cytoskeleton and signaling molecules that may act to regulate transporter membrane trafficking, stability, and activity.

Keywords: potassium chloride cotransporter 2, proteome, interactome, phosphorylation, protein purification

OPEN ACCESS

Edited by:
Mark Oliver Collins, The University of Sheffield, United Kingdom

Reviewed by:
Marianne Renner, Sorbonne Université, France
Eckart D. Gundelfinger, Leibniz Institute for Neurobiology (LG), Germany
Esperanza Fernandez, Ghent University, Belgium

***Correspondence:**
Stephen J. Moss
Stephen.Moss@Tufts.edu

Received: *17 May 2020*
Accepted: *14 September 2020*
Published: *22 October 2020*

Citation:
Smalley JL, Kontou G, Choi C, Ren Q, Albrecht D, Abiraman K, Santos MAR, Bope CE, Deeb TZ, Davies PA, Brandon NJ and Moss SJ (2020) Isolation and Characterization of Multi-Protein Complexes Enriched in the K-Cl Co-transporter 2 From Brain Plasma Membranes. Front. Mol. Neurosci. 13:563091. doi: 10.3389/fnmol.2020.563091

INTRODUCTION

The K^+/Cl^- co-transporter Kcc2 (encoded by the gene *SLC12A5*) is the principal Cl^--extrusion mechanism employed by mature neurons in the CNS (Moore et al., 2017). Its activity is a pre-requisite for the efficacy of fast synaptic inhibition mediated by Glycine (GLYR) and type A γ-aminobutyric acid receptors ($GABA_AR$), which are Cl^- permeable ligand-gated ion channels.

At prenatal and early postnatal stages in rodents, neurons have elevated intracellular Cl^- levels resulting in depolarizing $GABA_A$-mediated currents (Ben-Ari et al., 2012). The postnatal development of canonical hyperpolarizing $GABA_AR$ currents is a reflection of the progressive decrease of intraneuronal Cl^- levels that is caused by the upregulation of Kcc2 expression and subsequent activity (Payne, 1997; Rivera et al., 1999; Li et al., 2002; Uvarov et al., 2006). These changes in neuronal Cl^--extrusion reflect a sustained increase in the expression levels of Kcc2 after birth, the mRNA levels of which do not reach their maximal levels in humans until 20–25 years of age (Sedmak et al., 2016). In addition to this, the appropriate developmental appearance of hyperpolarizing $GABA_AR$ currents is also in part determined by the phosphorylation status of Kcc2, a process that facilitates its membrane trafficking and activity (Lee et al., 2007, 2011; Rinehart et al., 2009; Titz et al., 2015; Moore et al., 2019; Pisella et al., 2019).

In keeping with its essential role in determining the efficacy of synaptic inhibition, humans with mutations in Kcc2 develop severe epilepsy soon after birth (Stödberg et al., 2015; Saitsu et al., 2016; Saito et al., 2017). Deficits in Kcc2 activity are also believed to contribute to the development of temporal lobe epilepsy (Chen et al., 2017; Kelley et al., 2018), in addition to other traumas including ischemia and neuropathic pain (Jaenisch et al., 2010; Mapplebeck et al., 2019). Given the critical role that Kcc2 plays in determining the maturation of inhibitory neurotransmission, subtle changes in its function are also strongly implicated in autism spectrum disorders (ASD) (Tyzio et al., 2014), Down syndrome (Deidda et al., 2015), fragile X syndrome (He et al., 2014), and Rett syndrome (Duarte et al., 2013; Tang et al., 2016, 2019).

Here, we isolated and resolved stable protein complexes that contain Kcc2 from highly purified plasma membranes from mouse forebrain, and characterized their composition using a quantitative proteomic approach. In this way we were able to detect Kcc2 interactors in rank order of abundance. We subsequently identified several novel Kcc2-associated proteins. We used the same purification strategy and proteomics to measure Kcc2 phosphorylation. In this way we have developed new insights into the potential mechanisms of Kcc2 stabilization and regulation in the plasma membrane along with measuring the phosphorylation status of Kcc2 on the cell surface in parallel.

RESULTS

Isolating Native Stable Protein Complexes Containing Kcc2 From Brain Plasma Membranes

In order to define which proteins are associated with Kcc2 in the neuronal plasma membrane we developed a novel methodology for isolating stable multi-protein complexes enriched in this transporter. To do so, fresh isolated mouse forebrain was homogenized in detergent-free conditions to preserve organelle structure. The resulting homogenate was then subjected to differential gradient-based centrifugation and the plasma membrane fraction was isolated (**Figure 1A**). To confirm effective fractionation, we immunoblotted for established protein markers for each specific organelle (**Figure 1B**); HSP90 (cytosol), HSP60 (mitochondria), calreticulin (ER/Golgi), and n-cadherin (n-Cadh) (plasma membrane). Each organelle fraction showed enrichment for its respective marker protein. Importantly, the plasma membrane fraction was both enriched for n-Cadh and depleted for HSP60 compared to the total lysate, demonstrating efficient separation of plasma membrane and mitochondria, a common contaminant of membranous fractions. Kcc2 was enriched in the ER fraction and highly enriched in the mitochondrial and plasma membrane fractions. The enrichment of Kcc2 in our target fraction, the plasma membrane fraction, was highly encouraging for downstream purification. The presence of Kcc2 in the mitochondrial fraction could be an interesting future area of research, as chloride homeostasis is fundamental for correct mitochondrial function.

Following detergent solubilization, membrane fractions were subjected to immunoprecipitation with a monoclonal antibody directed against the intracellular C-terminus of Kcc2 covalently coupled to protein G-coated ferric beads. Initial optimization experiments revealed that we were able to isolate approximately 65% of the Kcc2 available in the lysate and the lysate preparation produced minimal Kcc2 oligomerization when resolved by SDS-PAGE (**Supplementary Figures S1A,B**). Purified material was eluted under native conditions using a "soft elution buffer" containing 2% Tween-20 (Antrobus and Borner, 2011), and subjected to blue-native-PAGE (BN-PAGE; **Figure 1C**). We observed well-resolved bands by colloidal Coomassie staining at 300, 600, and 800 kDa. These bands were not seen in control experiments performed with non-immune mouse IgG. An immunoblot of the same sample confirmed that these bands contained Kcc2. Immunoblots of plasma membrane lysates separated by BN-PAGE showed that these distinct Kcc2 complex bands exist in the lysate and are not an artifact of or degraded by purification. Despite the high stringency of our method (with high speed centrifugation and low concentration SDS exposure), no monomeric Kcc2 was observed (∼150 kDa when resolved by SDS-PAGE), indicating that Kcc2 was maintained in higher order complexes. This method may disrupt low affinity, or transient protein interactions and favor the detection of higher affinity binding partners.

After we confirmed that these well-resolved bands contained Kcc2, we assessed their composition by LC-MS/MS following trypsin digestion. The proteomic approach we used is summarized in **Figure 1D**. First, we extracted peptide counts for quality control measurements (**Figure 1E**). The 300, 600, and 800 kDa bands contained an average of 443, 159, and 45 total peptides for Kcc2, respectively, which equated to average coverage of 44%, 35%, and 23% of the total Kcc2 protein sequence, respectively. In all three bands, the majority of peptides corresponded to the cytoplasmic and extracellular domains of Kcc2, while peptides corresponding to the transmembrane domains were rarely detected. The failure to detect these regions is consistent with their high hydrophobicity and subsequent low recovery by LC-MS/MS (**Supplementary Figure S2A**). To assess the complexity of each band we compared the average total peptide counts for Kcc2, with the average total peptide

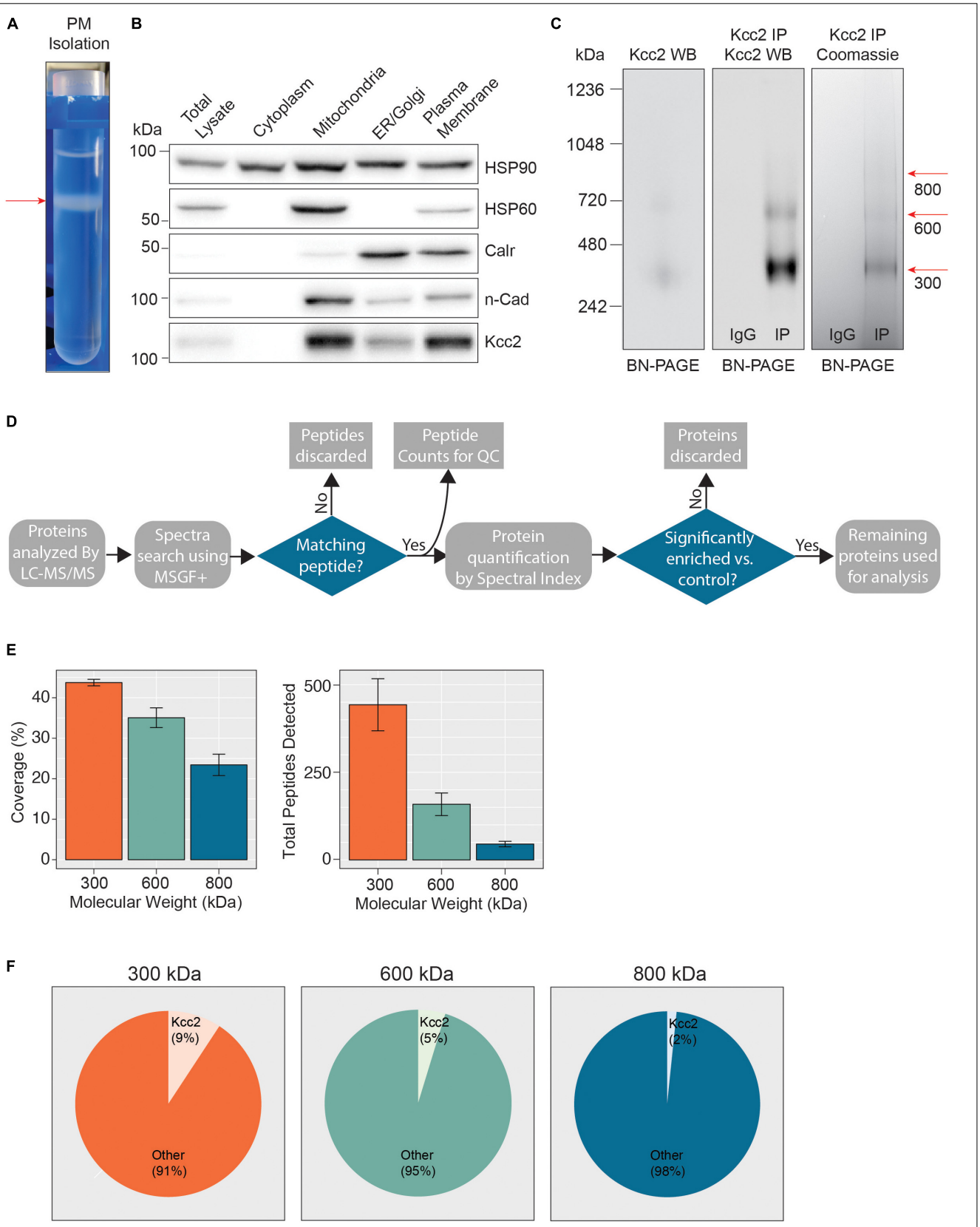

FIGURE 1 | Continued

FIGURE 1 | Highly enriched Kcc2-containing protein complexes were isolated from purified plasma membranes from mouse forebrain. **(A)** Differential centrifugation of homogenized forebrain from 8 to 12-week-old mice was used to fractionate cellular organelle and obtain an enriched plasma membrane fraction, visualized here at the final purification stage on a discontinuous sucrose gradient. **(B)** Western blots of the organelle fractions were used to measure the abundance of organelle markers; HSP90 (cytosol), HSP60 (mitochondria), calreticulin (ER/Golgi), n-Cadherin (n-Cadh) (plasma membrane). Kcc2 abundance was also measured to confirm Kcc2 enrichment in the plasma membrane fraction. **(C)** Blue-native PAGE (BN-PAGE) was carried out on plasma membrane lysates, and immunoprecipitated Kcc2 to resolve the native protein complexes that contain Kcc2. These were correlated with protein bands observed by Coomassie staining. Coomassie-stained bands were excised and used for proteomic analyses. **(D)** Flow diagram of the methodological approach for proteomic data processing. **(E)** Detected peptides were mapped to the Kcc2 reference sequence to determine Kcc2 sequence coverage obtained from LC-MS/MS of BN-PAGE protein bands produced following Kcc2 IP. Bar charts of the Kcc2 sequence coverage expressed as a percentage of the full sequence and by total Kcc2 peptides detected ($n = 4$). **(F)** Pie charts showing the average number of total Kcc2 peptides detected by LC-MS/MS relative to the average number of total peptides detected for all other proteins in each molecular weight complex.

counts for all proteins that were detected in our LC-MS/MS spectra (**Figure 1F**). In the 300, 600, and 800 kDa bands, Kcc2 was the most abundant protein detected, however, the proportion of peptides for Kcc2 relative to peptides for all other detected proteins decreased with increasing complex molecular mass, this is likely due to the increased protein complexity of the high molecular weight complexes. Taken together, these results demonstrate our experimental methodology facilitates the isolation of stable high molecular mass protein complexes enriched in Kcc2.

Analyzing the Composition of Stable Protein Complexes of Kcc2

Having confirmed the veracity of our Kcc2 purifications we investigated the reproducibility of the proteins associated with Kcc2 in each of the bands. First, we extracted the spectral index normalized to global intensity (SI_{GI}), a label-free quantitative measurement for each detected protein, using the MSnbase package in R (**Supplementary Tables S2–S14**). We compiled a data matrix of all the proteins and SI_{GI} values detected by proteomic analysis in each of our samples, including those detected as binding to non-immune IgG control beads. We then performed a Welch *t*-test to identify proteins significantly enriched in the Kcc2 IP compared to the control. This resulted in the identification of 246 proteins in total across all molecular weight complexes.

Next, we evaluated the reproducibility of the significantly detected proteins in each of the 4 biological repeats for each band (**Figure 2A**). The vast majority of proteins detected were present in at least three of the 4 biological replicates, illustrating the reproducibility of our purifications and analyses. Only proteins detected in all 4 repeats were taken forward for further analysis as "significantly enriched proteins" (**Supplementary Table S1**). We then compared these "significantly enriched proteins" between the 300, 600, and 800 kDa complexes (**Figure 2B**). The 300 kDa band contained many unique proteins not identified in the 600 or 800 kDa bands. These may be large proteins that had dissociated from Kcc2 complexes. However, the amounts of these proteins were an order of magnitude lower than Kcc2 itself, indicating that the 300 kDa band is mostly Kcc2 alone. The 600 and 800 kDa bands contained proteins in more comparable quantities to Kcc2 itself, indicating these are likely to be Kcc2-binding proteins.

Finally, we used principal component analysis (PCA) to assess the degree of similarity in binding protein patterns between all 12 of the proteomic samples (**Figure 2C**). PCA identifies variance between samples and expresses the degree of similarity by proximity in a PCA plot. We did this to both assess the reproducibility of the biological replicates and the degree of difference in the binding proteins for each complex. The "significantly enriched proteins" were assembled into a matrix of all repeats and detected proteins along with SI_{GI} values for each. The data were normalized by z-transformation and the PCA plot created using the default settings in the ggfortify package (accessed January 2019) in R (Hilario and Kalousis, 2008). The datasets clearly separated into biological repeats of the different mass bands. PC1, which accounted for 68.78% of the variance, was highly positively correlated with amount of Sptan1, Sptbn1, and C1qa/b/c, and negatively correlated with the amount of Kcc2. This is consistent with the detection of more spectrin and C1q in the higher molecular weight bands, and a concomitant decrease in the amount of detected Kcc2 due to higher sample complexity. PC2, which accounted for 18.53% of the variance was also positively correlated with the detection of more C1qa/b/c. This demonstrates that we have identified a reproducible set of binding proteins for the 300, 600, and 800 kDa bands. While there is a substantial degree of overlap between the interacting proteins from each molecular mass band (**Figure 2B**), their protein content is different enough that they can be clearly differentiated by PCA.

Next, we performed network analysis on the "significantly enriched proteins." We omitted proteins whose SI_{GI} values were lower than 2% of those detected for Kcc2, to remove "trace" binding proteins. Network analysis was carried out using data from STRINGdb for known experimental interactions (Szklarczyk et al., 2019) as previously described (Goldman et al., 2019). We overlaid the highest scoring Gene Ontology (GO) Biological Process term for each protein to provide insight into protein function (Szklarczyk et al., 2019). We also scaled the node size representing each protein to the SI_{GI} values detected for each protein. In this way we were able to visualize quantitative Kcc2 networks and subnetworks along with developing insights into the functional groups of proteins that associate with Kcc2 (**Figures 3A–C**). In the 300 kDa band, Kcc2 (SI_{GI} of 0.184) was detected at more than 10-fold higher abundance than the next most abundant proteins; Slc1a2 (0.0159) and Cntn1 (0.0037). The 600 kDa protein complex contained high levels of Kcc2 (0.0792). A subnetwork

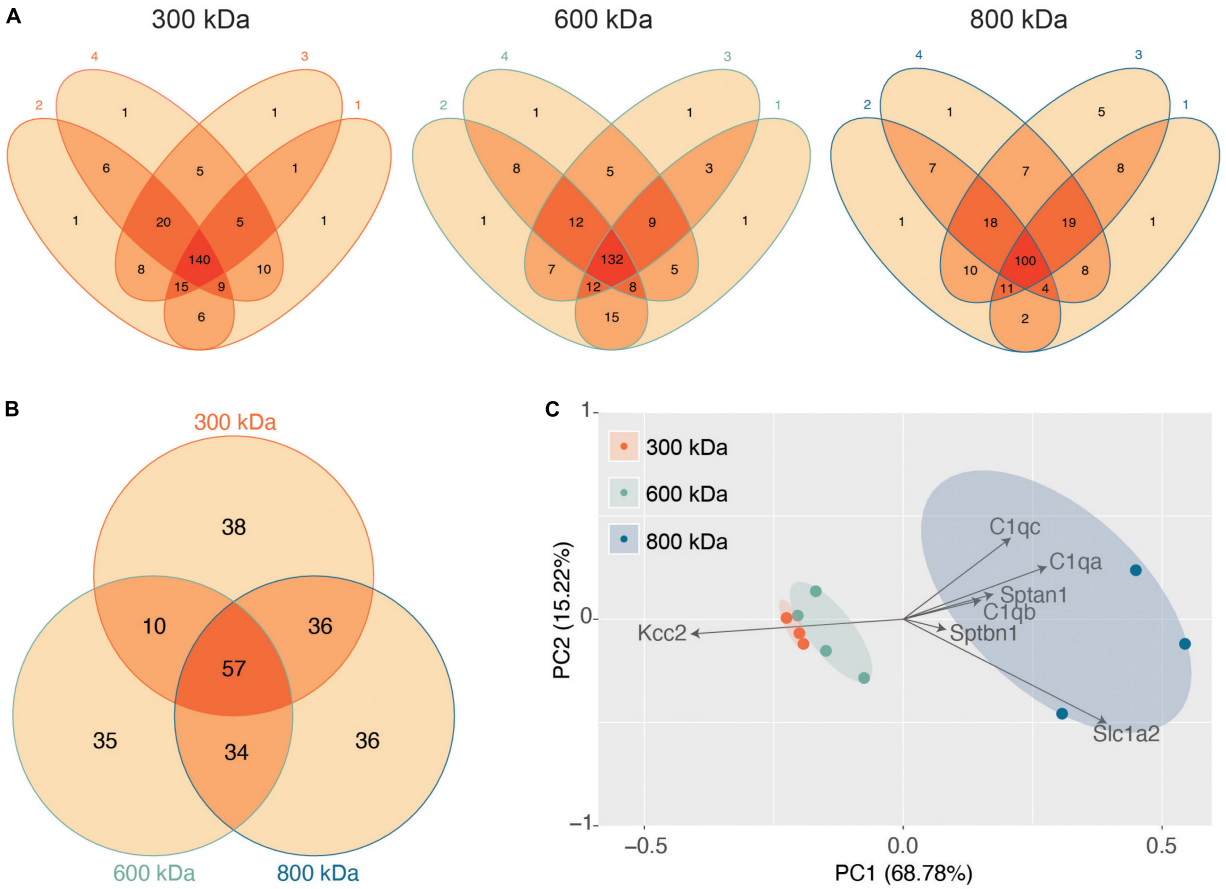

FIGURE 2 | Stable protein complexes contain large amounts of Kcc2 and a robust set of associated proteins, which differ subtly between the different molecular weight bands. **(A)** Venn diagrams showing the number and overlap of significantly enriched Kcc2-associated proteins identified in each of 4 biological replicates in each molecular weight complex. **(B)** Venn diagram showing the overlap in significantly enriched associated proteins detected in all 4 replicates for each molecular weight complex. **(C)** PCA analysis of each biological replicate for each molecular weight complex based on their protein composition. PCA loadings were also included to show the contribution of each protein to the position of sample on the PCA plot.

of Sptan1 (0.0062) and Sptbn1 (0.0044) also emerged, along with Slc4a4 (0.0072). The associated proteins were largely involved in cytoskeleton organization or ion transport according to the top scoring Biological Process Gene Ontology terms. The 800 kDa complex also contained high amounts of Kcc2 (0.0229) along with comparable amounts of Sptan1 (0.0110), Sptbn1 (0.0044), C1qa/b/c (0.0142, 0.0075, 0.0144). There were three main subnetworks containing C1qa/b/c, another containing Sptan1/Sptbn1/Cnp/Map2, and another containing Grm2/3/5/Gabbr1/2). The 800 kDa complex contained more functionally diverse proteins involved in the innate immune response, GPCR signaling, and signal transduction, along with cytoskeleton organization and ion transport as seen in the 600 kDa band.

Confirming the Association of "Robust Binding Proteins" With Kcc2

Next, we set out to confirm the association of a subset of the newly identified interactors with Kcc2. We chose to focus on the spectrin complex as it was highly prominent and contained structural, regulatory, and other ion transporting proteins. We immunoblotted isolated Kcc2 protein complexes resolved by BN-PAGE for Sptan1, Sptbn1, Itpr1, and Scn2a (**Figure 4**). We also included Cntn1 and Scn2a as specificity controls as they were particularly abundant in the low (300 kDa) and high (800 kDa) bands, respectively according to the proteomic analyses. No immunoreactivity was observed in the IgG control lanes. Mirroring the proteomic data Cntn1 showed specificity for the 300 kDa band, whereas Scn2a showed strong specificity for the 800 kDa band. In agreement with the proteomic data, none of the components of the spectrin subnetwork were present in the 300 kDa band. Sptan1 was present in the 600 kDa band and was also present in the 800 kDa band along with Sptbn1 and Itpr1.

Kcc2 Co-localizes With the Spectrin Complex on, or Close to the Neuronal Plasma Membrane

Having established that Kcc2 forms protein complexes with components of the spectrin complex, we used

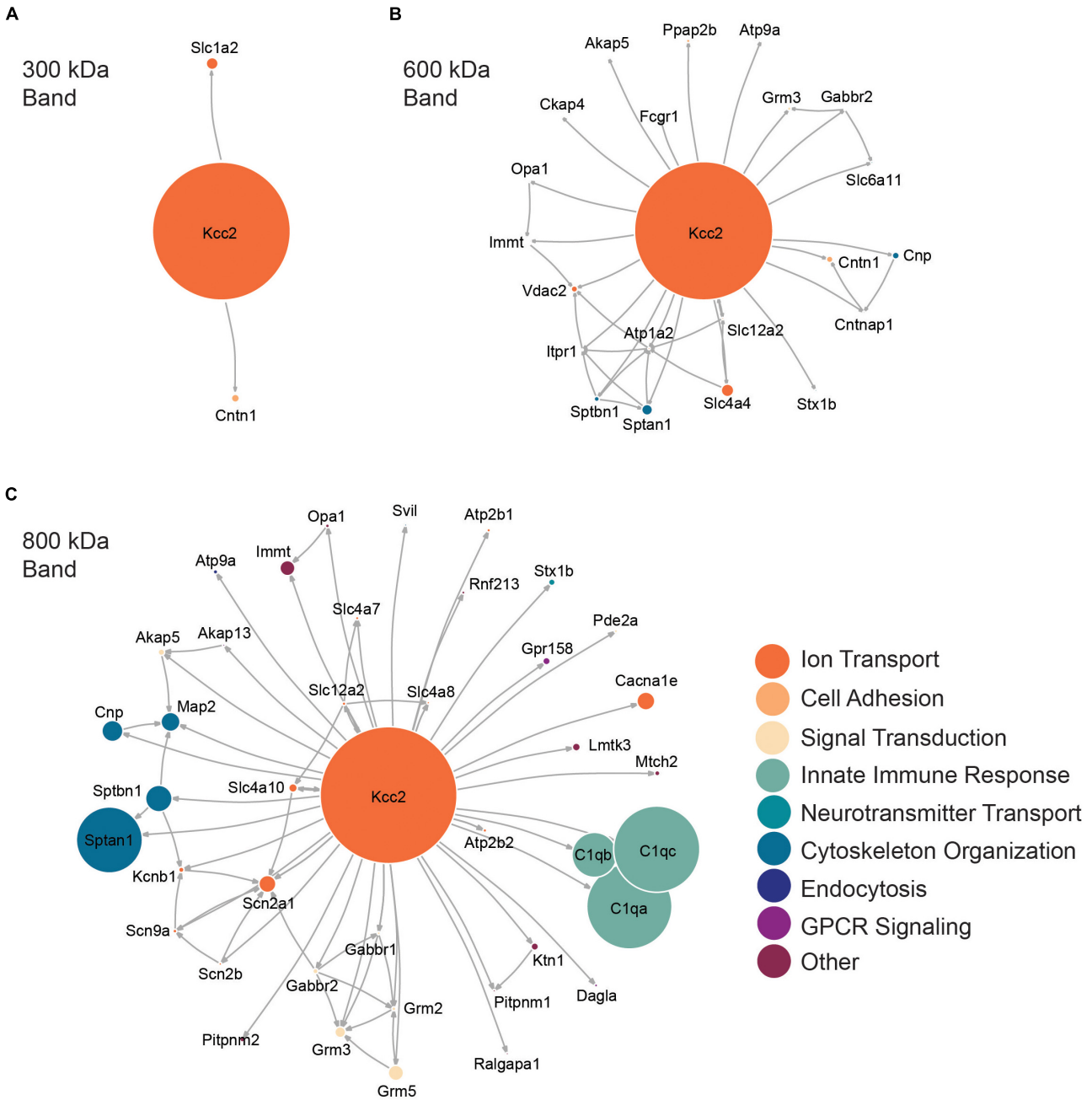

FIGURE 3 | High molecular weight complexes of Kcc2 contain a robust set of proteins from multiple functional classes, with some highly interconnected subnetworks. Protein network diagrams for **(A)** the 300 kDa band, **(B)** the 600 kDa band, and **(C)** the 800 kDa band. Only proteins with >2% of the SI_{GI} values for Kcc2 were included to remove "trace" binding proteins. Known interactions were obtained using stringent high confidence, direct experimental association parameters from STRINGdb. These were used to construct a network diagram of protein nodes and arrows to indicate known interactions. The interactions for each protein with Kcc2 were included as discovered here. The node diameter was scaled relative to the SI_{GI} values detected for each protein. An overlay of Gene Ontology (GO) Biological Process terms was used to provide protein classification information (n = 4).

immunocytochemistry to investigate the proximity of each to Kcc2. We used DIV 21 mouse primary cultured cortical/hippocampal neurons infected with CamKII-AAV-GFP to ensure we imaged excitatory neurons and to visualize the morphology of the cell and identify whether the interaction between Kcc2 and the spectrin complex was restricted to specific cellular compartments (**Figure 5**). Sptan1 exhibited widespread staining along dendrites, which co-localized with puncta of Kcc2. Itpr1 exhibited punctate staining with convincing co-localization with Kcc2 in the dendritic compartment. Sptbn1 was present

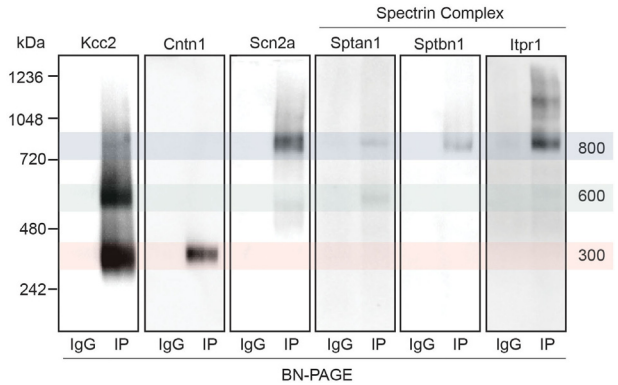

FIGURE 4 | Immunoblots confirm the presence of several interactors in protein complexes that contain Kcc2. Kcc2 protein complexes were isolated from forebrain plasma membrane fractions of 8–12-week-old mice by immunoprecipitation, resolved by BN-PAGE and immunoblotted for components of the spectrin subnetwork. IPs were loaded adjacent to parallel IgG reactions to demonstrate specificity. Cntn1 and Scn2a were included as a further demonstration of band specificity, as proteomic analysis suggested specific enrichment in the 300 kDa and 800 kDa bands, respectively. Transparent overlays mark the location of each Kcc2 complex.

in dendritic clusters with Kcc2 mostly located on the edges. Scn2a, outside of the easily identifiable AIS regions, was also robustly co-localized with Kcc2. These results were also reflected in density plots carried out as previously described (Bolte and Cordelières, 2006; Davenport et al., 2017). Taken together, these data demonstrate that proteins associated in high molecular weight complexes with Kcc2 are also highly co-localized with Kcc2 in neurons.

Kcc2 Is at or in Close Proximity to Inhibitory Synapses

We detected several proteins in complex with Kcc2 that have been proposed to be located at inhibitory synapses. To investigate this further, we used immunocytochemistry to visualize Kcc2 relative to the inhibitory pre- and post-synaptic marker proteins Vgat and $GABA_A$-γ2, respectively (**Figure 6**). Kcc2 puncta appeared to be immediately adjacent to Vgat puncta, and co-localized robustly with $GABA_A$-γ2, suggesting Kcc2 could be in close proximity to the post-synaptic region of inhibitory synapses.

Kcc2 Is Highly Phosphorylated at Multiple Sites in the Murine Plasma Membrane

Kcc2 expression levels, membrane trafficking and activity have been shown to be subject to modulation via multiple phosphorylation sites within the C-terminal cytoplasmic domain. As we had succeeded in obtaining highly purified Kcc2 from murine brain plasma membranes, we also analyzed Kcc2 using phosphoproteomics. To do so, we immunoprecipitated Kcc2 from plasma membrane fractions prepared from WT mice as outlined in **Figure 1**. To limit dephosphorylation purified material was resolved by SDS-PAGE and visualized using Coomassie (**Figure 7A**). Major bands of 125 kDa were seen with material purified on the Kcc2 antibody, but not control IgG. The band was excised, proteins were digested with trypsin, and analyzed by LC-MS/MS. LC-MS/MS confirmed the 125 kDa band was highly enriched for Kcc2 with an average of 884 peptides detected (n = 4), which equates to coverage of 53% (**Supplementary Figure S2**).

We identified 11 high confidence Kcc2 phosphorylation sites based on A-scores either 15–19 or greater than 19, which equates to 90% or 99% confidence in assignment, respectively (**Figure 7B** and **Supplementary Table S15**). One site (S25/26), is located on the N-terminus of Kcc2, whereas the other 10 sites are located on the C-terminus (S896, T902, T906, S913, T932, S940, T1007, T1009, S1022, and S1034) (**Figure 7C**). The number of times a phosphopeptide was detected with an A-score 15–19 or >19 was recorded across 4 biological replicates, to provide a measure of abundance and confidence in each phosphorylation site. We detected the three well characterized sites; T906, S940, and T1007, however, T1007 was only detected once with a qualifying A-score. The two most regularly detected high confidence phosphosites were S932, and S1022 (detected 18 and 16 times, respectively), which are relatively unstudied phosphosites. T906 and S940 were also detected with high confidence several times. Collectively, these results demonstrate that plasma membrane Kcc2 is phosphorylated at multiple sites at the N- and C-termini, at both known and novel sites (**Figure 7C**).

DISCUSSION

Isolation of Stable Multi-Protein Complexes Enriched in Kcc2

The K^+/Cl^- co-transporter, Kcc2, is expressed at the cell surface of mature neurons where it is of fundamental importance for maintaining intracellular chloride levels, and thereby the efficacy of neuronal inhibition. To gain insights into how neurons regulate the plasma membrane accumulation and activity of Kcc2, we applied a method for the isolation of native multi-protein complexes enriched in this transporter from brain plasma membranes (Suski et al., 2014; Agez et al., 2017). Following plasma membrane isolation by differential centrifugation, immuno-affinity purification, BN-PAGE/SDS-PAGE and LC-MS/MS we were able to isolate highly purified preparations of Kcc2. When resolved by SDS-PAGE we obtained a single band at approximately 140 kDa. When resolved by BN-PAGE we observed major molecular mass species of 300, 600, and 800 kDa. This methodology provided very high sequence coverage of Kcc2 (approximately 45% of the total sequence, and 90% of the intra- and extracellular soluble regions), maximizing the probability of detecting associated proteins and post-translational modifications. It could therefore prove to be a beneficial methodology for the isolation of other plasma membrane proteins from brain tissue,

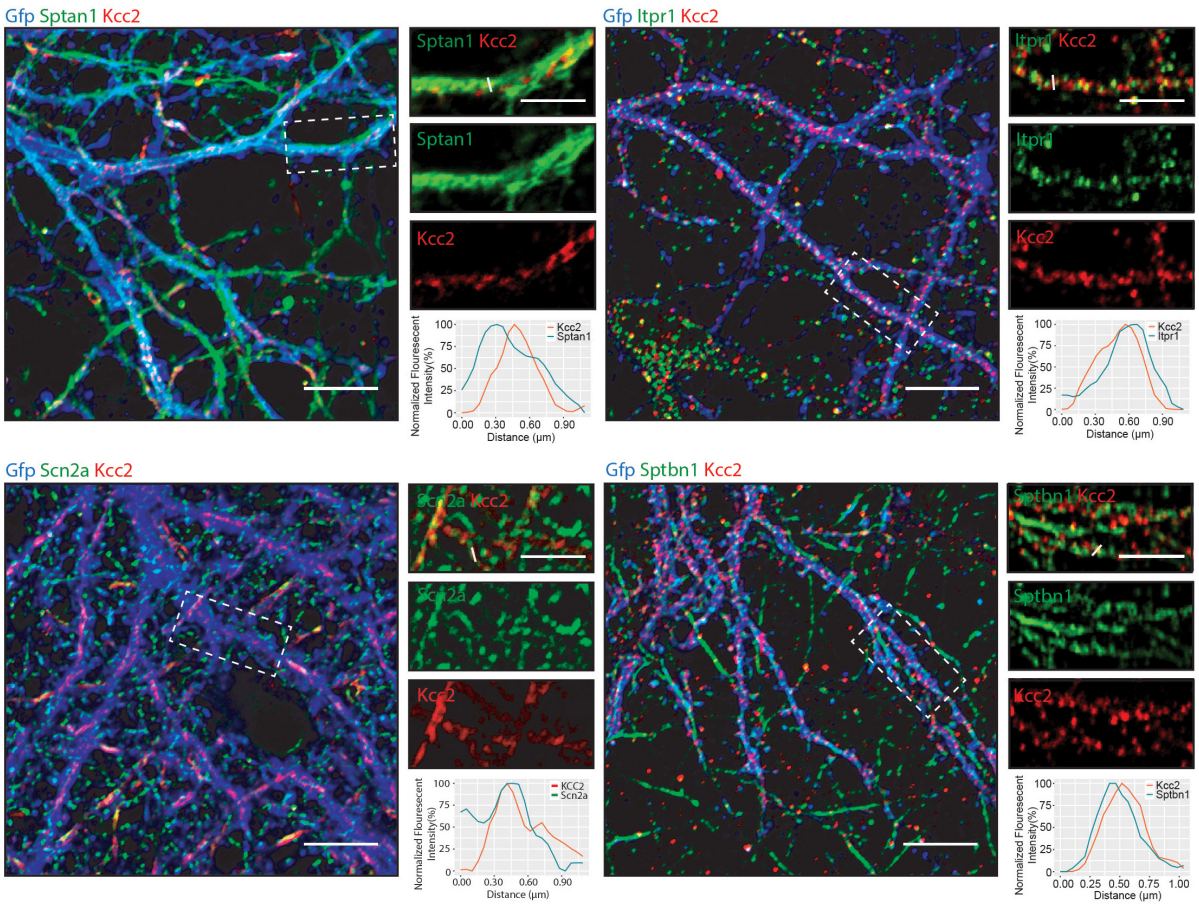

FIGURE 5 | Components of the spectrin subnetwork co-localize with Kcc2 in several neuronal cellular compartments. Primary cultured neurons from P0 pups were infected with CamKII-AAV-GFP at DIV 3 (to visualize cell morphology and to identify excitatory neurons) and fixed at DIV 21. The cells were immunostained for Kcc2 and components of the spectrin subnetwork; Sptan1, Sptbn1, Itpr1, and Scn2a. Co-localization was measured using line scans (white lines) and represent the normalized fluorescent intensity of single pixels (approximately 1 μm) on dendrites (n = 3). Scale bars are 10 μm for large images and 5 μm for cropped images.

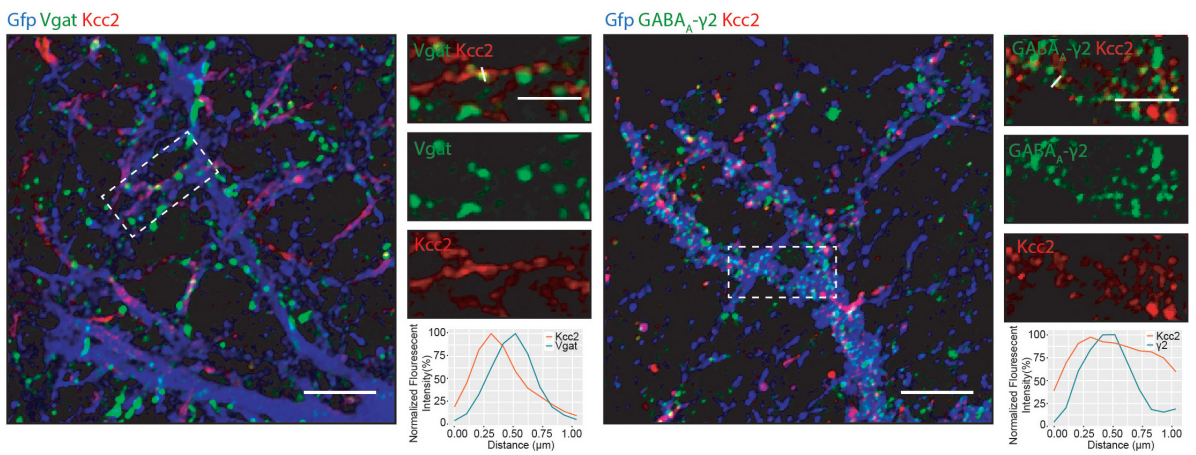

FIGURE 6 | Kcc2 is localized at inhibitory synapses. Primary cultured neurons from P0 pups were infected with CamKII AAV-GFP at DIV 3 and fixed at DIV 21. The cells were immunostained for Kcc2 and the inhibitory pre- and post-synaptic markers Vgat and $GABA_A$-γ2. Co-localization was measured using line scans (white lines) and represent the normalized fluorescent intensity of single pixels (approximately 1 μm) on dendrites (n = 3). Scale bars are 10 μm for large images and 5 μm for cropped images.

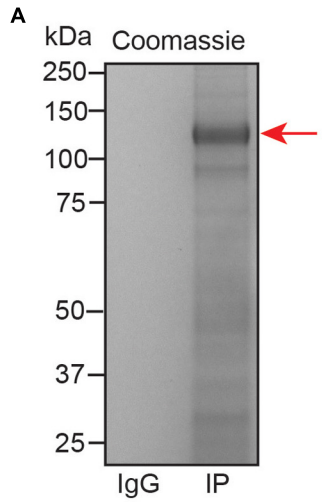

B

Site	Sequence	Number of Detections A-Score 15-19	Number of Detections A-Score >19	Maximum A-Score
S25	NPKES#SPFI	3	0	19.2
S896	MHES#DISA	0	1	30.8
T902	ISAYT#YEKT	1	1	24.2
T906	TYEKT#LVME	3	5	1000.0
S913	MEQRS#QILK	0	2	46.9
S932	REIQS#ITDES	5	12	36.7
S940	ESRGS#IRRK	5	4	31.9
T1007	EVHLT#WTKD	0	1	21.4
T1009	HLTWT#KDKS	2	1	19.5
S1022	NKGPS#PVSS	4	12	72.8
S1034	KDFFS#MKPE	1	1	22.9

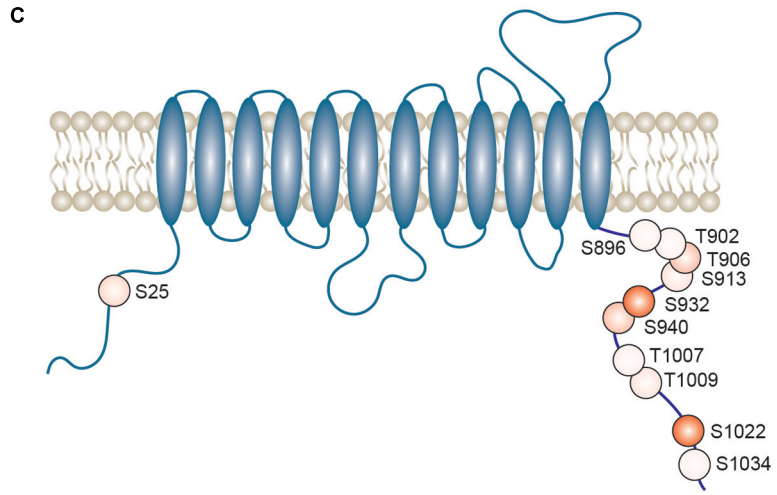

FIGURE 7 | In the neuronal plasma membrane, Kcc2 can be phosphorylated at 11 distinct sites. **(A)** Kcc2 was isolated from plasma membrane fractions of mouse forebrain, resolved by SDS-PAGE and visualized using colloidal Coomassie. **(B)** Table of detected high confidence Kcc2 phosphorylation sites. Site numbering is according to the mature UniProt Kcc2 protein sequence. A-score were determined as previously described (Beausoleil et al., 2006). A score 15–19 and >19 represent a >90% and >99% confidence score, respectively. The number of times a particular phospho-peptide was detected at either A-score range was recorded across 4 individual experiments, along with the maximum recorded A-score (n = 4). Table cells are color coded according to the number of detections. **(C)** Illustrative diagram of high confidence Kcc2 phosphorylation site positions color coded according to the number of detections at an A-score >19. Transmembrane domain positions according to the UniProt database.

that not only maintains protein complexes, but also post-translational modifications.

Kcc2 Exists as Dimers in the Neuronal Plasma Membrane

Kcc2 consists of 1139 amino acids including the signal sequence, which equates to a mass of 126 kDa without post-translational modifications. Kcc2 is, however, subject to extensive post-translational modification including glycosylation at 6 sites so is often observed in a band of around 140 kDa (Agez et al., 2017) when resolved by SDS-PAGE. Previous work has shown extensive aggregation of Kcc2 following SDS-PAGE that results in a band at 250 kDa, however, this depends on whether it is heterologously expressed or the manner in which it is prepared from neuronal tissues (Medina et al., 2014). Indeed, we see no aggregation in our samples following SDS-PAGE, possibly due to the use of low detergent concentrations and samples immediately processed for SDS-PAGE without freeze thaw cycles (**Supplementary Figure S1**). Interestingly, when resolved by BN-PAGE, Kcc2 protein complexes form distinct bands at 300 kDa, 600 kDa, and 800 kDa. The 300 kDa band contains approximately 10-fold more Kcc2 than the next most abundant protein, indicating that this band consists largely of Kcc2. At 300 kDa, this would indicate that in the plasma membrane Kcc2 exists as homodimers, which is consistent with recently published studies on recombinant Kcc2

molecules visualized using cryo-EM (Agez et al., 2017). This, however, is the first demonstration that endogenously expressed Kcc2 is in dimeric form in the murine brain.

Kcc2 Forms Stable Multi-Protein Complexes in the Plasma Membrane

The most abundant protein in the 600 kDa and 800 kDa bands was consistently Kcc2, confirming that these are legitimate Kcc2-containing protein complexes. Significantly the ratio of the associated proteins relative to Kcc2 increased with molecular mass. Given the stringency of our methodology and the use of native conditions these species represent stable-protein complexes that primarily reside in the plasma membrane. The proteins detected by a previous proteomic analysis of Kcc2 complexes (Mahadevan et al., 2017) overlapped with 13% and 16% of the proteins we detected in the 600 kDa and 800 kDa bands, respectively. This low degree of overlap is likely due to the methodological differences between the studies; the previous work extracted Kcc2 complexes from a crude membrane preparation and used on-bead digest prior to LC-MS/MS, rather than complexes purified from a plasma membrane fraction resolved by BN-PAGE, then distinct bands excised for analysis. This difference in biochemical preparation is more likely to detect transient interactions due to less sample processing, but is also far less stringent, and results in a highly complex sample being introduced to the LC-MS/MS, which can significantly impact resolution. However, the method presented here ensured a sample of reduced complexity analyzed by LC-MS/MS, resulting in a higher resolution snapshot of the proteins associated with high affinity with Kcc2 on the neuronal plasma membrane, which were then measured using label-free quantification. Similarly to Mahadevan et al. (2017), we also did not detect Neto2 (Ivakine et al., 2013), Grik2 (Gluk2) (Mahadevan et al., 2014), Epb41l1 (4.1n) (Li et al., 2007), Arhgef7 (Beta-pix) (Chevy et al., 2015), Rcc1 (Garbarini and Delpire, 2008) or the signal transduction molecules; Pkc, Wnk, Spak or Osr (Lee et al., 2007; Friedel et al., 2015). This could be either due the transient or low affinity nature of these interactions, or that these interactors are less abundant in complex with Kcc2 than the interactors presented here, as this quantitative methodology provides information on associated proteins in rank order of abundance. We did, however, detect $GABA_BRs$ which have previously shown to be associated with Kcc2 (Wright et al., 2017), further confirming the veracity of our purification strategy.

Kcc2 Is Associated With Proteins Enriched at Excitatory and Inhibitory Synapses

Previous work has shown that Kcc2 is located at or in close proximity to excitatory synapses (Gulyás et al., 2001; Chamma et al., 2012; Mahadevan et al., 2017). In agreement with this we detected well characterized excitatory synapse proteins such as Cntn1 (Cijsouw et al., 2018), and Grm2/3 (Ting et al., 2016; Spence et al., 2019). Interestingly, we also identified several proteins associated with inhibitory synapses including Cacna1e (Nakamura et al., 2016), and Cyfip1 (**Supplementary Table S1**; Davenport et al., 2019). Grm5 has been detected in high abundance at both excitatory and inhibitory synapses (Nakamura et al., 2016; Spence et al., 2019). Immunostaining of Kcc2 and inhibitory synapse marker proteins presented here, shows that Kcc2 is located in close proximity to inhibitory synapses. Taken together, these data suggest that Kcc2 is not located exclusively at either type of synapse but is likely to be positioned at or in close proximity to both. This is consistent with the suggestion that Kcc2 may play a role in the regulation of excitatory and inhibitory synapses (Awad et al., 2016). It is also of note that many of the proteins we detected are protein products of autism- and epilepsy-risk genes.

Kcc2 Is Associated With the Spectrin Cytoskeleton

The most prominent subnetwork that we identified associated with Kcc2 was the spectrin complex, which consisted of Sptan1, Sptbn1, Itpr1, and Map2 (Shi et al., 2009). Sptan1, the most abundant binding protein in the higher molecular weight complexes, is a structural protein that forms dimers with a β-spectrin isoform such as Sptbn1. These spectrin dimers interact with actin filaments and ankyrins, to regulate the expression of plasma membrane proteins, including calcium channels (including Cacna1e) (Garcia-Caballero et al., 2018), sodium channels (including Scn2a) (Bouzidi et al., 2002), potassium channels, and Itpr1 (El Refaey and Mohler, 2017). Cntn1 is also thought to interact with spectrins either directly or via Caspr1 (Querol et al., 2017). The importance of this complex is reflected in the debilitating diseases associated with spectrin mutations. Sptan1 mutation is associated with epilepsy (Tohyama et al., 2015), and Sptbn1 is implicated in ASDs (Kim H. G. et al., 2008). Both Scn2a and Itpr1 are high risk ASD genes identified by SFARI. Sptan1 cleavage by calpains, as also occurs with Kcc2 (Puskarjov et al., 2012), is an established marker of neuronal damage (Yan and Jeromin, 2012).

Our data suggests that Kcc2 may interact directly with Sptan1, as it is present in the 600 kDa band with Kcc2. In contrast, Sptbn1 and Itpr1 are likely to require the binding of Sptan1 to associate with Kcc2, as they are most highly abundant in the 800 kDa band, and absent in the 600 kDa band (**Figure 4**). This hypothesis is also consistent with the shift in molecular weight observed in the Kcc2 complex. A Kcc2 dimer of approximately 300 kDa would run at approximately 600 kDa with an associated Sptan1 protein (285 kDa). The subsequent association of either Sptbn1 (275 kDa), or Itpr1 (310 kDa) would shift the mass to around 800 kDa. Sptan1 has a variety of binding domains where interactions with Kcc2 could occur, such as SH3 domains (Ackermann and Brieger, 2019). It has previously been proposed that Kcc2 also contains a non-canonical SH3 domain in its C-terminus (Llano et al., 2015).

The association of Kcc2 with the spectrin complex would not only stabilize Kcc2 in the plasma membrane, but also provide a link to signaling processes via Itpr1. Itpr1 is present at PM/ER junctions and following activation by G-protein coupled receptors (GPCR), releases Ca^{2+} from the ER. High Ca^{2+} concentration would lead to localized PKC activation, which has

been shown to phosphorylate Kcc2 at multiple sites (Lee et al., 2007). This may also be consistent with other GPCR signaling proteins detected here, such as GPR158. The presence of Kcc2 and its associated proteins at PM/ER contact sites is a potentially exciting observation that could influence Kcc2 synthesis and regulation and will be the subject of future studies. Finally, we also detected high quantities of C1qa/b/c in high molecular weight complexes with Kcc2. This is a potentially important observation, due to the proximity of Kcc2 to both excitatory and inhibitory synapses and the role of C1q proteins in synaptic elimination during development and in disease (Schafer and Stevens, 2010).

Plasma Membrane Populations of Kcc2 Are Phosphorylated on Up to 11 Residues

We used the same purification techniques to analyze endogenous Kcc2 phosphorylation from the neuronal plasma membrane. Phosphorylation plays a key role in regulating the transporter activity. We detected 11 residues including the well characterized sites; T906, S940, and T1007. These play a critical role in regulating Kcc2 function (Moore et al., 2018; Pisella et al., 2019). Interestingly, T1007 was only detected above the accepted higher A-score threshold once. T1007 phosphorylation is inversely correlated with Kcc2 function (Kahle et al., 2013), and therefore this could suggest that T1007 is largely absent in PM-associated Kcc2, where it is active.

In addition to the well characterized sites we also detected 8 further phosphorylation sites. These included S25/S26 and S1022 consistent with recent publications (Weber et al., 2014; Agez et al., 2017). We also identified 5 further sites of phosphorylation; S896, T902, S913, S932, T1009, and S1034. S932 and S1022 were the most frequently detected phosphosites, indicating that Kcc2 in the PM is highly phosphorylated at these residues. S932 is in close proximity to the well characterized S940 site, which is vital for correct Kcc2 function (Silayeva et al., 2015). S1022 lies adjacent to, or within the isotonic domain of Kcc2, suggesting that its phosphorylation may impact its basal activity (Mercado et al., 2006). We isolated several proteins in stable complexes with Kcc2 that play a direct role in protein phosphorylation; including Lmtk3, Akap5, Akap13. Conversely, the differential phosphorylation of Kcc2 may influence the proteins it associates with, influencing the subcellular localization and turnover of Kcc2. The expanded evidence of associated kinases and novel phosphorylation sites presented here, will be the subject of future investigation.

In conclusion we have demonstrated a highly efficient method for isolating Kcc2 from murine plasma membranes, in a highly phosphorylated form within its native protein complex. This has allowed us to perform quantitative studies on stable Kcc2 protein complexes and phosphorylation in parallel from the same preparation. We confirm that endogenous Kcc2 is in homo-dimeric conformation in murine plasma membranes. These dimers associate with a spectrin subnetwork that is likely to not only stabilize it in the plasma membrane but provide an environment for regulating its phosphorylation at the 11 potential sites.

Experimental Procedures

Unless otherwise stated chemicals were obtained from Sigma-Aldrich, St. Louis, MO, United States.

Animals

Animal studies were performed according to protocols approved by the Institutional Animal Care and Use Committee of Tufts Medical Center. 8–12-week-old male and female mice were kept on a 12 h light/dark cycle with *ad libitum* access to food and water.

Antibodies

The following antibodies were used for immunoprecipitation (IP), immunoblot (IB), or immunocytochemistry (Icc): Cntn1 (rabbit, IB, Abcam Ab66265), Itpr1 (rabbit, IB/Icc, Alomone Acc-019), Kcc2 (mouse, IP/Icc, NeuroMab 75-013), Kcc2 (rabbit, IB/Icc, Millipore 07-432), Scn2a (mouse, Icc, NeuroMab 75-024), Scn2a (rabbit, IB, Alomone ASC-002), Sptan1 (mouse, Icc, Abcam Ab11755), Sptan1 (rabbit, IB, Cell Signaling 21225), Sptbn1 (rabbit, IB/Icc, Abcam Ab72239), α-Tubulin (mouse, IB, Sigma T9026), vGAT (guinea pig, Icc, SYSY 131004), GABA γ2 (mouse, Icc, SYSY 224011), GFP (chicken, Icc, Abcam Ab13970).

Immunoblotting

Sodium dodecyl sulfate polyacrylamide gel electrophoresis (SDS-PAGE) was carried out as previously described (Schiavon et al., 2018). Briefly, proteins were isolated in RIPA lysis buffer (50 mM Tris, 150 mM NaCl, 0.1% SDS, 0.5% sodium deoxycholate, and 1% Triton X-100, pH 7.4) supplemented with mini cOmplete protease inhibitor and PhosSTOP phosphatase inhibitor tablets. Protein concentration was measured using a Bradford assay (Bio-Rad, Hercules, CA, United States). Samples were diluted in 2x sample buffer and 20 μg of protein was loaded onto a 7–15% polyacrylamide gel depending on the molecular mass of the target protein. After separation by SDS-PAGE, proteins were transferred onto nitrocellulose membrane. Membranes were blocked in 5% milk in tris-buffered saline 0.1% Tween-20 (TBS-T) for 1 h, washed with TBS-T, and then probed with primary antibodies diluted in TBS-T (dilution and incubation time dependent on the antibody). The membranes were washed and incubated for 1 h at room temperature with HRP-conjugated secondary antibodies (1:5000 – Jackson ImmunoResearch Laboratories, West Grove, PA, United States). Protein bands were visualized with Pierce ECL (Thermo Fisher Scientific) and imaged using a ChemiDoc MP (Bio-Rad). Band intensity was compared to α-tubulin as a loading control.

BN-PAGE

For blue-native polyacrylamide gel electrophoresis (BN-PAGE), proteins were isolated using Triton lysis buffer (150 mM NaCl, 10 mM Tris, 0.5% Triton X-100, pH 7.5). Samples were diluted in 4x NativePAGE sample buffer and G250 additive. Samples were loaded onto 4–16% NativePAGE gradient gels and run using a mini gel tank (Thermo Fisher Scientific, Waltham, MA, United States). Gels were run for approximately 2 h and then prepared for Coomassie staining

or immunoblotting. For Coomassie staining the gels were fixed in 50% ethanol and 10% acetic acid, washed in 30% ethanol, washed in water, then stained with EZ blue stain. The gels were destained in ultrapure water, imaged using a ChemiDoc MP (Bio-Rad), and bands were excised for liquid chromatography tandem mass spectrometry (LC-MS/MS). For immunoblotting, proteins were transferred to PVDF membrane overnight. The membranes were then fixed in 8% acetic acid, washed with ultrapure water and air-dried before being briefly destained with 100% methanol. The membranes were then blocked, immunoblotted, and imaged as described above.

Plasma Membrane Isolation

Plasma membrane isolation from mouse forebrain was carried out using a modified version of a previously described method (Suski et al., 2014). Briefly, mouse forebrain was rapidly isolated and placed in ice-cold starting buffer [225 mM mannitol, 75 mM sucrose, 30 mM Tris–HCl (pH 7.4)]. The tissue was then transferred to ice-cold isolation buffer (225 mM mannitol, 75 mM sucrose, 0.5% (wt/vol) BSA, 0.5 mM EGTA, 30 mM Tris–HCl, pH 7.4) supplemented with mini cOmplete protease inhibitor and PhosSTOP. Forebrain tissue from 5 to 7 mice was pooled and used for each Kcc2 immunoprecipitation biological replicate. The brains were homogenized in the isolation buffer using 14 strokes of a Dounce homogenizer. The samples were transferred to centrifuge tubes for centrifugation, which was carried out at 4°C throughout. The samples were initially spun at 800 × *g* for 5 min to remove nuclei and non-lysed cells. The pellet was discarded, and the supernatant was spun again at 800 × *g* for 5 min to remove residual nuclei and non-lysed cells. The supernatant was transferred to high speed centrifuge tubes and spun at 10000 × *g* for 10 min to remove mitochondria. The pellet was discarded, and the supernatant spun again at 10000 × *g* for 10 min to remove mitochondrial contamination. The supernatant was then spun at 25000 × *g* for 20 min to pellet plasma membranes. The pellet was resuspended in starting buffer and spun again at 25000 × *g* for 20 min to remove cytosolic and ER/Golgi contamination. Finally, the plasma membrane fraction was purified on a discontinuous sucrose gradient (53%, 43%, 38% sucrose), and spun at 93000 × *g* for 50 min to remove residual contamination from cytosol and other membranous compartments.

Primary Neuron Culture

Mouse cortical and hippocampal mixed cultures were created from P0 mouse pups as previously described (Kelley et al., 2018). Briefly, P0 mice were anesthetized on ice and the brains removed. The brains were dissected in Hank's buffered salt solution (Invitrogen/Thermo Fisher Scientific) with 10 mM HEPES. The cortices and hippocampi were trypsinized and triturated to dissociate the neurons. Cells were counted using a hemocytometer and plated on poly-l-lysine-coated 13 mm coverslips in 24-well plate wells at a density of 2×10^5 cells/ml in Neurobasal media (Invitrogen/Thermo Fisher Scientific). At days *in vitro* (DIV) 3, 10^5 genomic copies per cell of CamKII-AAV9-GFP (Addgene, Watertown, MA, United States) were added to the neuronal media. After 24 h, the media was replaced with new conditioned media. At DIV 21, cells were fixed in 4% paraformaldehyde in PBS for 10 min at room temperature. They were then placed in PBS at 4°C until being processed for immunocytochemistry.

Immunocytochemistry

Fixed primary neurons were permeabilized for 1 h in blocking solution (3% bovine serum albumin (BSA), 10% normal goat serum, 0.2 M glycine in phosphate buffered saline (PBS) with 0.1% Triton-X100). Cells were exposed to primary and then fluorophore-conjugated secondary antibodies (Alexa Fluor 488, 555, and 647; Thermo Fisher Scientific, 405 Dylight; Jackson ImmunoResearch) diluted in blocking solution for 1 h each at room temperature. The coverslips were then washed in PBS, dried, and mounted onto microscope slides with Fluoromount-G (SouthernBiotech, Birmingham, AL, United States). The samples were imaged using a Nikon Eclipse Ti (Nikon Instruments, Melville, NY, United States) or Leica Falcon (Leica Microsystems, Buffalo Grove, IL, United States) confocal microscope using a 60x oil immersion objective lens. Image settings were manually assigned for each fluorescent channel. For image processing, the background was subtracted for each fluorescent channel and the median filter was applied (Radius = 1 pixel) on Fiji Software (Schindelin et al., 2012). The line scans (white lines) used for protein localization were generated using the plotProfile function in Fiji and represent the fluorescent intensity of single pixels against the distance of a manually drawn line (approximately 1 μm) on dendrites as previously described (Bolte and Cordelières, 2006; Davenport et al., 2017).

Densitometry

For Western blot analysis, bands from raw images were analyzed using the Fiji densitometry features. Biological replicates were run on the same gels for comparison, and area under the curve was calculated for each band. Average signal and standard error were calculated for each treatment group and ANOVA carried out using R for statistical comparison of protein expression levels.

Protein Purification

Protein G Dynabeads (Thermo Fisher Scientific) were washed three times with phosphate buffered saline with 0.05% Tween-20 (PBS-Tween). The beads were resuspended in PBS-Tween and incubated overnight at 4°C with antibodies for the target protein at an experimentally predetermined bead:antibody ratio (**Supplementary Figure S1**). The antibody was crosslinked onto the beads by washing twice with 0.2 M triethanolamine (pH 8.2) (TEA), and then incubated for 30 min with 40 mM dimethyl pimelimidate (DMP) in TEA at room temperature. The beads were transferred to 50 mM Tris (pH 7.5) and incubated at room temperature for 15 min. The beads were then washed three times with PBS-Tween and resuspended in solubilized plasma membranes in ice-cold Triton lysis buffer, supplemented with mini cOmplete protease inhibitor and PhosSTOP. The immunoprecipitation reaction was incubated overnight at 4°C. The beads were then washed three times with PBS-Tween and eluted either with 2x sample buffer (for SDS-PAGE) or soft

elution buffer [0.2% (wt/vol) SDS, 0.1% Tween-20, 50 mM Tris–HCl, pH = 8.0] (Antrobus and Borner, 2011) (for BN-PAGE).

Protein Analysis by LC-MS/MS

Excised gel bands were cut into 1 mm^3 pieces and subjected to modified in-gel trypsin digestion, as previously described (Shevchenko et al., 1996). Briefly, gel pieces were washed and dehydrated with acetonitrile for 10 min and then completely dried in a speed-vac. Gel pieces were rehydrated with 50 mM ammonium bicarbonate solution containing 12.5 ng/μl modified sequencing-grade trypsin (Promega, Madison, WI, United States) and incubated for 45 min at 4°C. The excess trypsin solution was removed and replaced with 50 mM ammonium bicarbonate solution. Samples were then incubated at 37°C overnight. Peptides were extracted by washing with 50% acetonitrile and 1% formic acid. The extracts were then dried in a speed-vac (∼1 h). The samples were stored at 4°C until analysis. Before analysis the samples were reconstituted in 5–10 μl of HPLC solvent A (2.5% acetonitrile, 0.1% formic acid). A nano-scale reverse-phase HPLC capillary column was created by packing 2.6 μm C18 spherical silica beads into a fused silica capillary (100 μm inner diameter × ∼30 cm length) with a flame-drawn tip (Peng and Gygi, 2001). After equilibrating the column each sample was loaded via a Famos auto sampler (LC Packings, San Francisco, CA, United States) onto the column. A gradient was formed between solvent A (97.5% water, 2.5% acetonitrile, and 0.1% formic acid), and increasing concentrations of solvent B (97.5% acetonitrile, 2.5% water, and 0.1% formic acid). Acquisition time was 16–79 min. As each peptide was eluted, they were subjected to Nanospray ionization (NSI) and then entered into an LTQ Orbitrap Velos Pro ion-trap mass spectrometer (Thermo Finnigan, San Jose, CA, United States). MS1 was set at 70 k, with a scan range of m/z 85–2000, charge-state screening parameters +2 to +5, using a centroid acquisition mode, with a precursor ion isolation window of 2 m/z and 35% normalized collision energy. Eluting peptides were detected and the most intense were isolated using the Top 10 scan mode and fragmented by Higher-energy C-trap dissociation (HCD). MS2 ions were analyzed by an Orbitrap mass spectrometer with a resolution of 17.5 k and the dynamic exclusion settings; 30 s repeat duration, 60 s exclusion duration, $n = 1$, 10 ppm mass width, to produce a tandem mass spectrum of specific fragment ions for each peptide.

Bioinformatics and Statistics

Peptide/Protein Searches

Peptide sequences (and hence protein identity) were determined by matching protein or translated nucleotide databases with the acquired fragmentation pattern using the MSGF+ (Kim and Pevzner, 2014). Raw mzXML files were used to search the UniProt mouse reference proteome (last modified May 4th 2020, containing 21989 sequences) also containing the Thermo list of common contaminants. The search was carried out using settings for high-resolution Orbitrap mass spectrometers, tryptic digestion, no limit to enzyme missed cleavages, 20 ppm precursor mass tolerance, charge states of +2 to +5, minimum and maximum peptide lengths of 6–40 amino acids in length, respectively, and a fixed modification of standard amino acids with C + 57. For phosphopeptide detection a variable modification of 79.9663 mass units to serine, threonine, and tyrosine was included in the database searches. Phosphorylation assignments were determined by the A score algorithm (Beausoleil et al., 2006). Peptide identification was scored by MSGF+ Q- (PSM-level target-decoy approach) and E- (expected number of peptides in a random database) scores. These were used for quality control in the initial protein screening process for associated proteins, and phospho-modified peptide screening (Kim S. et al., 2008).

Proteomic Data Analysis

The resulting mzID files from the spectral searches were combined with mzXML files using the MSnbase package in R (accessed July 20th 2020), and used to calculate peptide counts and the quantitative measurement; spectral index normalized to global intensity (SI_{GI}). This has previously been shown to be an effective measurement for label-free protein quantification and to normalize replicate data well (Griffin et al., 2010). The mass spectrometry proteomics data have been deposited to the ProteomeXchange Consortium via the PRIDE (Perez-Riverol et al., 2019) partner repository with the dataset identifier PXD021368 and 10.6019/PXD021368.

For initial quality control we assessed protein coverage by aligning detected peptides for Kcc2 to the mouse Kcc2 reference sequence (UniProt ID: Q91V14) using the Multiple Sequence Alignment (MSA) package in R (accessed January 10th, 2019). We also recorded the number of peptides detected for Kcc2 and other detected proteins. Proteins with fewer than two peptides detected were removed for this analysis.

SI_{GI} values for each protein detected by Kcc2 immunoprecipitation were compared to non-immune IgG purifications by Welch *t*-test to identify significantly enriched proteins. Venn diagrams were produced using the Vennerable package in R (accessed January 10th, 2019), and only significantly detected proteins in all repeats were considered for downstream analysis. The SI_{GI} values for proteins contained within each gel band (**Supplementary Table S1**) were normalized by z-transformation (**Supplementary Table S2**) and used for principal Component Analysis (PCA), which was carried out using PCA functions in the ggfortify package in R (accessed January 10th, 2019). The significantly detected protein lists for each band were ordered according to SI_{GI} values and proteins with <50-fold lower SI_{GI} values than those for Kcc2 were removed as they were considered "trace" binding partners. The protein lists were compared against the latest version of the STRINGdb database (Szklarczyk et al., 2019) to establish known interactions and annotations for each protein using only high confidence, experimental evidence. Functional protein information, specifically the highest scoring Biological Process Gene Ontology terms, were extracted for each protein using the "mygene" package in R (accessed July 29th, 2020). The interaction for each protein with Kcc2 was imputed and network diagrams were constructed in R using the igraph package and the nodes were scaled to the SI_{GI} values for each protein (accessed February 1st, 2019).

DATA AVAILABILITY STATEMENT

The datasets presented in this study can be found in online repositories. The names of the repository/repositories and accession number(s) can be found in the article/**Supplementary Material**.

ETHICS STATEMENT

The animal study was reviewed and approved by Tufts University.

AUTHOR CONTRIBUTIONS

JS and SM conceptualized the project, developed and analyzed data, and wrote the manuscript. GK performed immunocytochemistry experiments. CC and QR performed western blot experiments. MS and CB maintained the mouse colony and performed genotyping. PD, TD, NB, KA, and DA edited the manuscript. All authors contributed to the article and approved the submitted version.

FUNDING

SM was supported by the National Institutes of Health (NIH)–National Institute of Neurological Disorders and Stroke Grants NS051195, NS056359, NS081735, R21NS080064, and NS087662; NIH–National Institute of Mental HealthGrant MH097446.

ACKNOWLEDGMENTS

We would like to thank the Taplin Mass Spectrometry Facility at Harvard and the Yale/NIDA Neuroproteomics Center and the Yale/NIDA grant DA018343. GK, DA, and KA were fellows of and funded by the AstraZeneca Postdoctoral Program.

SUPPLEMENTARY MATERIAL

The Supplementary Material for this article can be found online at: https://www.frontiersin.org/articles/10.3389/fnmol.2020.563091/full#supplementary-material

FIGURE S1 | Initial optimization of antibody:bead ratios for optimal Kcc2 enrichment by immunoprecipitation. Immunoblots were carried out on protein resolved by SDS-PAGE. Total lysate (TL) levels of Kcc2 were compared with immunoprecipitated (IP) samples purified with 0–10 μl of Kcc2 antibody crosslinked to 50 μl of Protein G Dynabeads, and the respective flow-through (FT) samples (to detect the amount of Kcc2 extracted from the total pool). **(B)** Densitometry of the immunoblot demonstrating considerable enrichment of Kcc2 by immunoprecipitation, and depletion of approximately 65% of the total Kcc2 available at the highest antibody:bead ratio.

FIGURE S2 | The total Kcc2 peptides detected by LC-MS/MS across all biological repeats were aligned to the Kcc2 reference sequence (UniProt ID: Q91V14) to visualize protein coverage. **(A)** The Kcc2 coverage obtained from the 300, 600, and 800 kDa bands of Kcc2 resolved by BN-PAGE. **(B)** The Kcc2 coverage of wild type (WT) mouse samples from the ∼140 kDa band resolved by SDS-PAGE.

TABLE S1 | A shortened list containing only significantly enriched proteins used for downstream analysis. SI_{GI} scores were used to detect significantly enriched proteins associated with Kcc2 by comparing them with control (IgG) purifications using a Welch *t*-test (Data Table 1).

TABLES S2–S14 | A list of all the proteins detected by proteomic analysis in all samples with accompanying SI_{GI} values for each sample replicate. SI_{GI} scores were calculated from raw spectra data for all proteins detected across all samples. 300 kDa 1 – Data Table 2, 300 kDa 2 – Data Table 3, 300 kDa 3 – Data Table 4, 300 kDa 4 – Data Table 5, 600 kDa 1 – Data Table 6, 600 kDa 2 – Data Table 7, 600 kDa 3 – Data Table 8, 600 kDa 4 – Data Table 9, 800 kDa 1 – Data Table 10, 800 kDa 2 – Data Table 11, 800 kDa 3 – Data Table 12, 800 kDa 4 – Data Table 13, Control 1–4, Data Table 14.

TABLE S15 | A list of the phosphorylated Kcc2 peptides detected. A summary table of the phosphorylated Kcc2 peptides detected. Calculated A-scores are displayed for each repeat as well as the highest MSGF + raw scores (peptide-spectrum match), *de novo* scores (optimal scoring peptide for the spectrum), spectral *E*-values, database *E*-values, and PSM-level and peptide-level *Q*-values (estimate using the target-decoy approach) across all repeats.

REFERENCES

Ackermann, A., and Brieger, A. (2019). The role of nonerythroid spectrin αII in cancer. *J. Oncol.* 2019:7079604. doi: 10.1155/2019/7079604

Agez, M., Schultz, P., Medina, I., Baker, D. J., Burnham, M. P., Cardarelli, R. A., et al. (2017). Molecular architecture of potassium chloride co-transporter KCC2. *Sci. Rep.* 7:16452.

Antrobus, R., and Borner, G. H. H. (2011). Improved elution conditions for native co-immunoprecipitation. *PLoS One* 6:e18218. doi: 10.1371/journal.pone.0018218

Awad, P. N., Sanon, N. T., Chattopadhyaya, B., Carriço, J. N., Ouardouz, M., Gagné, J., et al. (2016). Reducing premature KCC2 expression rescues seizure susceptibility and spine morphology in atypical febrile seizures. *Neurobiol. Dis.* 91, 10–20. doi: 10.1016/j.nbd.2016.02.014

Beausoleil, S. A., Villén, J., Gerber, S. A., Rush, J., and Gygi, S. P. (2006). A probability-based approach for high-throughput protein phosphorylation analysis and site localization. *Nat. Biotechnol.* 24, 1285–1292. doi: 10.1038/nbt1240

Ben-Ari, Y., Khalilov, I., Kahle, K. T., and Cherubini, E. (2012). The GABA excitatory/inhibitory shift in brain maturation and neurological disorders. *Neuroscientist* 18, 467–486. doi: 10.1177/1073858412438697

Bolte, S., and Cordelières, F. P. (2006). A guided tour into subcellular colocalization analysis in light microscopy. *J. Microsc.* 224(Pt 3), 213–232. doi: 10.1111/j.1365-2818.2006.01706.x

Bouzidi, M., Tricaud, N., Giraud, P., Kordeli, E., Caillol, G., Deleuze, C., et al. (2002). Interaction of the Nav1.2a subunit of the voltage-dependent sodium channel with nodal ankyrinG. In vitro mapping of the interacting domains and association in synaptosomes. *J. Biol. Chem.* 277, 28996–29004. doi: 10.1074/jbc.M201760200

Chamma, I., Chevy, Q., Poncer, J. C., and Lévi, S. (2012). Role of the neuronal K-Cl co-transporter KCC2 in inhibitory and excitatory neurotransmission. *Front. Cell. Neurosci.* 6:5. doi: 10.3389/fncel.2012.00005

Chen, L., Wan, L., Wu, Z., Ren, W., Huang, Y., Qian, B., et al. (2017). KCC2 downregulation facilitates epileptic seizures. *Sci. Rep.* 7:156.

Chevy, Q., Heubl, M., Goutierre, M., Backer, S., Moutkine, I., Eugène, E., et al. (2015). KCC2 gates activity-driven AMPA receptor traffic through Cofilin phosphorylation. *J. Neurosci.* 35, 15772–15786. doi: 10.1523/JNEUROSCI.1735-15.2015

Cijsouw, T., Ramsey, A. M., Lam, T. K. T., Carbone, B. E., Blanpied, T. A., and Biederer, T. (2018). Mapping the proteome of the synaptic cleft through proximity labeling reveals new cleft proteins. *Proteomes* 6:48. doi: 10.3390/proteomes6040048

Davenport, E. C., Pendolino, V., Kontou, G., McGee, T. P., Sheehan, D. F., López-Doménech, G., et al. (2017). An essential role for the tetraspanin LHFPL4 in the cell-type-specific targeting and clustering of synaptic GABAA receptors. *Cell Rep.* 21, 70–83. doi: 10.1016/j.celrep.2017.09.025

Davenport, E. C., Szulc, B. R., Drew, J., Taylor, J., Morgan, T., Higgs, N. F., et al. (2019). Autism and schizophrenia-associated CYFIP1 regulates the balance of synaptic excitation and inhibition. *Cell Rep.* 26, 2037–2051.e6. doi: 10.1016/j.celrep.2019.01.092

Deidda, G., Parrini, M., Naskar, S., Bozarth, I. F., Contestabile, A., and Cancedda, L. (2015). Reversing excitatory GABAAR signaling restores synaptic plasticity and memory in a mouse model of Down syndrome. *Nat. Med.* 21, 318–326. doi: 10.1038/nm.3827

Duarte, S. T., Armstrong, J., Roche, A., Ortez, C., Pérez, A., O'Callaghan, M., et al. (2013). Abnormal expression of cerebrospinal fluid cation chloride cotransporters in patients with rett syndrome. *PLoS One* 8:e68851. doi: 10.1371/journal.pone.0068851

El Refaey, M. M., and Mohler, P. J. (2017). Ankyrins and spectrins in cardiovascular biology and disease. *Front. Physiol.* 8:852. doi: 10.3389/fphys.2017.00852

Friedel, P., Kahle, K. T., Zhang, J., Hertz, N., Pisella, L. I., Buhler, E., et al. (2015). WNK1-regulated inhibitory phosphorylation of the KCC2 cotransporter maintains the depolarizing action of GABA in immature neurons. *Sci. Signal.* 8:ra65. doi: 10.1126/scisignal.aaa0354

Garbarini, N., and Delpire, E. (2008). The RCC1 domain of protein associated with Myc (PAM) interacts with and regulates KCC2. *Cell. Physiol. Biochem.* 22, 31–44. doi: 10.1159/000149781

Garcia-Caballero, A., Zhang, F. X., Hodgkinson, V., Huang, J., Chen, L., Souza, I. A., et al. (2018). T-type calcium channels functionally interact with spectrin (α/β) and ankyrin B. *Mol. Brain* 11:24.

Goldman, A., Smalley, J. L., Mistry, M., Krenzlin, H., Zhang, H., Dhawan, A., et al. (2019). A computationally inspired in-vivo approach identifies a link between amygdalar transcriptional heterogeneity, socialization and anxiety. *Transl. Psychiatry* 9:336.

Griffin, N. M., Yu, J., Long, F., Oh, P., Shore, S., Li, Y., et al. (2010). Label-free, normalized quantification of complex mass spectrometry data for proteomic analysis. *Nat. Biotechnol.* 28, 83–89. doi: 10.1038/nbt.1592

Gulyás, A. I., Sík, A., Payne, J. A., Kaila, K., and Freund, T. F. (2001). The KCl cotransporter, KCC2, is highly expressed in the vicinity of excitatory synapses in the rat hippocampus. *Eur. J. Neurosci.* 13, 2205–2217. doi: 10.1046/j.0953-816X.2001.01600.x

He, Q., Nomura, T., Xu, J., and Contractor, A. (2014). The developmental switch in GABA polarity is delayed in fragile X mice. *J. Neurosci.* 34, 446–450. doi: 10.1523/JNEUROSCI.4447-13.2014

Hilario, M., and Kalousis, A. (2008). Approaches to dimensionality reduction in proteomic biomarker studies. *Brief. Bioinform.* 9, 102–118. doi: 10.1093/bib/bbn005

Ivakine, E. A., Acton, B. A., Mahadevan, V., Ormond, J., Tang, M., Pressey, J. C., et al. (2013). Neto2 is a KCC2 interacting protein required for neuronal Cl- regulation in hippocampal neurons. *Proc. Natl. Acad. Sci. U.S.A.* 110, 3561–3566. doi: 10.1073/pnas.1212907110

Jaenisch, N., Witte, O. W., and Frahm, C. (2010). Downregulation of potassium chloride cotransporter KCC2 after transient focal cerebral ischemia. *Stroke* 41, e151–e159. doi: 10.1161/STROKEAHA.109.570424

Kahle, K. T., Deeb, T. Z., Puskarjov, M., Silayeva, L., Liang, B., Kaila, K., et al. (2013). Modulation of neuronal activity by phosphorylation of the K-Cl cotransporter KCC2. *Trends Neurosci.* 36, 726–737. doi: 10.1016/j.tins.2013.08.006

Kelley, M. R., Cardarelli, R. A., Smalley, J. L., Ollerhead, T. A., Andrew, P. M., Brandon, N. J., et al. (2018). Locally reducing KCC2 activity in the hippocampus is sufficient to induce temporal lobe epilepsy. *EBioMedicine* 32, 62–71. doi: 10.1016/J.EBIOM.2018.05.029

Kim, H. G., Kishikawa, S., Higgins, A. W., Seong, I. S., Donovan, D. J., Shen, Y., et al. (2008). Disruption of neurexin 1 associated with autism spectrum disorder. *Am. J. Hum. Genet.* 82, 199–207. doi: 10.1016/j.ajhg.2007.09.011

Kim, S., Gupta, N., and Pevzner, P. A. (2008). Spectral probabilities and generating functions of tandem mass spectra: a strike against decoy databases. *J. Proteome Res.* 7, 3354–3363. doi: 10.1021/pr8001244

Kim, S., and Pevzner, P. A. (2014). MS-GF+ makes progress towards a universal database search tool for proteomics. *Nat. Commun.* 5:5277. doi: 10.1038/ncomms6277

Lee, H. H. C., Deeb, T. Z., Walker, J. A., Davies, P. A., and Moss, S. J. (2011). NMDA receptor activity downregulates KCC2 resulting in depolarizing GABAA receptor-mediated currents. *Nat. Neurosci.* 14, 736–743. doi: 10.1038/nn.2806

Lee, H. H. C., Walker, J. A., Williams, J. R., Goodier, R. J., Payne, J. A., and Moss, S. J. (2007). Direct protein kinase C-dependent phosphorylation regulates the cell surface stability and activity of the potassium chloride cotransporter KCC2. *J. Biol. Chem.* 282, 29777–29784. doi: 10.1074/jbc.M705053200

Li, H., Khirug, S., Cai, C., Ludwig, A., Blaesse, P., Kolikova, J., et al. (2007). KCC2 interacts with the dendritic cytoskeleton to promote spine development. *Neuron* 56, 1019–1033. doi: 10.1016/j.neuron.2007.10.039

Li, H., Tornberg, J., Kaila, K., Airaksinen, M. S., and Rivera, C. (2002). Patterns of cation-chloride cotransporter expression during embryonic rodent CNS development. *Eur. J. Neurosci.* 16, 2358–2370. doi: 10.1046/j.1460-9568.2002.02419.x

Llano, O., Smirnov, S., Soni, S., Golubtsov, A., Guillemin, I., Hotulainen, P., et al. (2015). KCC2 regulates actin dynamics in dendritic spines via interaction with β-PIX. *J. Cell Biol.* 209, 671–686. doi: 10.1083/jcb.201411008

Mahadevan, V., Khademullah, C. S., Dargaei, Z., Chevrier, J., Uvarov, P., Kwan, J., et al. (2017). Native KCC2 interactome reveals PACSIN1 as a critical regulator of synaptic inhibition. *eLife* 6:e28270. doi: 10.7554/eLife.28270.001

Mahadevan, V., Pressey, J. C., Acton, B. A., Uvarov, P., Huang, M. Y., Chevrier, J., et al. (2014). Kainate receptors coexist in a functional complex with KCC2 and regulate chloride homeostasis in hippocampal neurons. *Cell Rep.* 7, 1762–1770. doi: 10.1016/j.celrep.2014.05.022

Mapplebeck, J. C. S., Lorenzo, L. E., Lee, K. Y., Gauthier, C., Muley, M. M., De Koninck, Y., et al. (2019). Chloride dysregulation through downregulation of KCC2 mediates neuropathic pain in both sexes. *Cell Rep.* 28, 590–596.e4. doi: 10.1016/j.celrep.2019.06.059

Medina, I., Friedel, P., Rivera, C., Kahle, K. T., Kourdougli, N., Uvarov, P., et al. (2014). Current view on the functional regulation of the neuronal K+-Cl- cotransporter KCC2. *Front. Cell. Neurosci.* 8:27. doi: 10.3389/fncel.2014.00027

Mercado, A., Broumand, V., Zandi-Nejad, K., Enck, A. H., and Mount, D. B. (2006). A C-terminal domain in KCC2 confers constitutive K+-Cl - cotransport. *J. Biol. Chem.* 281, 1016–1026. doi: 10.1074/jbc.M509972200

Moore, Y. E., Conway, L. C., Wobst, H. J., Brandon, N. J., Deeb, T. Z., and Moss, S. J. (2019). Developmental regulation of KCC2 phosphorylation has long-term impacts on cognitive function. *Front. Mol. Neurosci.* 12:173. doi: 10.3389/fnmol.2019.00173

Moore, Y. E., Deeb, T. Z., Chadchankar, H., Brandon, N. J., and Moss, S. J. (2018). Potentiating KCC2 activity is sufficient to limit the onset and severity of seizures. *Proc. Natl. Acad. Sci. U.S.A.* 115, 10166–10171. doi: 10.1073/pnas.1810134115

Moore, Y. E., Kelley, M. R., Brandon, N. J., Deeb, T. Z., and Moss, S. J. (2017). Seizing control of KCC2: a new therapeutic target for epilepsy. *Trends Neurosci.* 40, 555–571. doi: 10.1016/j.tins.2017.06.008

Nakamura, Y., Morrow, D. H., Modgil, A., Huyghe, D., Deeb, T. Z., Lumb, M. J., et al. (2016). Proteomic characterization of inhibitory synapses using a novel pHluorin-tagged γ-aminobutyric acid receptor, type a (gabaa), α2 subunit knock-in mouse. *J. Biol. Chem.* 291, 12394–12407. doi: 10.1074/jbc.M116.724443

Payne, J. A. (1997). Functional characterization of the neuronal-specific K-Cl cotransporter: implications for [K+]o regulation. *Am. J. Physiol.* 273, C1516–C1525. doi: 10.1152/ajpcell.1997.273.5.c1516

Peng, J., and Gygi, S. P. (2001). Proteomics: the move to mixtures. *J. Mass Spectrom.* 36, 1083–1091. doi: 10.1002/jms.229

Perez-Riverol, Y., Csordas, A., Bai, J., Bernal-Llinares, M., Hewapathirana, S., Kundu, D. J., et al. (2019). The PRIDE database and related tools and resources in 2019: improving support for quantification data. *Nucleic Acids Res.* 47, D442–D450. doi: 10.1093/nar/gky1106

Pisella, L. I., Gaiarsa, J. L., Diabira, D., Zhang, J., Khalilov, I., Duan, J. J., et al. (2019). Impaired regulation of KCC2 phosphorylation leads to neuronal network dysfunction and neurodevelopmental pathology. *Sci. Signal.* 12:eaay0300. doi: 10.1126/scisignal.aay0300

Puskarjov, M., Ahmad, F., Kaila, K., and Blaesse, P. (2012). Activity-dependent cleavage of the K-Cl cotransporter KCC2 mediated by calcium-activated protease calpain. *J. Neurosci.* 32, 11356–11364. doi: 10.1523/JNEUROSCI.6265-11.2012

Querol, L., Devaux, J., Rojas-Garcia, R., and Illa, I. (2017). Autoantibodies in chronic inflammatory neuropathies: diagnostic and therapeutic implications. *Nat. Rev. Neurol.* 13, 533–547. doi: 10.1038/nrneurol.2017.84

Rinehart, J., Maksimova, Y. D., Tanis, J. E., Stone, K. L., Hodson, C. A., Zhang, J., et al. (2009). Sites of regulated phosphorylation that control K-Cl cotransporter activity. *Cell* 138, 525–536. doi: 10.1016/j.cell.2009.05.031

Rivera, C., Voipio, J., Payne, J. A., Ruusuvuori, E., Lahtinen, H., Lamsa, K., et al. (1999). The K+/Cl- co-transporter KCC2 renders GABA hyperpolarizing during neuronal maturation. *Nature* 397, 251–255. doi: 10.1038/16697

Saito, T., Ishii, A., Sugai, K., Sasaki, M., and Hirose, S. (2017). A de novo missense mutation in SLC12A5 found in a compound heterozygote patient with epilepsy of infancy with migrating focal seizures. *Clin. Genet.* 92, 654–658. doi: 10.1111/cge.13049

Saitsu, H., Watanabe, M., Akita, T., Ohba, C., Sugai, K., Ong, W. P., et al. (2016). Impaired neuronal KCC2 function by biallelic *SLC12A5* mutations in migrating focal seizures and severe developmental delay. *Sci. Rep.* 6:30072. doi: 10.1038/srep30072

Schafer, D. P., and Stevens, B. (2010). Synapse elimination during development and disease: immune molecules take centre stage. *Biochem. Soc. Trans.* 38, 476–481. doi: 10.1042/BST0380476

Schiavon, E., Smalley, J. L., Newton, S., Greig, N. H., and Forsythe, I. D. (2018). Neuroinflammation and ER-stress are key mechanisms of acute bilirubin toxicity and hearing loss in a mouse model. *PLoS One* 13:e0201022. doi: 10.1371/journal.pone.0201022

Schindelin, J., Arganda-Carreras, I., Frise, E., Kaynig, V., Longair, M., Pietzsch, T., et al. (2012). Fiji: an open-source platform for biological-image analysis. *Nat. Methods* 9, 676–682. doi: 10.1038/nmeth.2019

Sedmak, G., Jovanov-Miloševiæ, N., Ulamec, M. P. M., Krušlin, B., Kaila, K., and Judaš, M. (2016). Developmental expression patterns of KCC2 and functionally associated molecules in the human brain. *Cereb. Cortex* 26, 4574–4589. doi: 10.1093/cercor/bhv218

Shevchenko, A., Wilm, M., Vorm, O., and Mann, M. (1996). Mass spectrometric sequencing of proteins silver-stained polyacrylamide gels. *Anal. Chem.* 68, 850–858. doi: 10.1021/ac950914h

Shi, X., Yasumoto, S., Nakagawa, E., Fukasawa, T., Uchiya, S., and Hirose, S. (2009). Missense mutation of the sodium channel gene SCN2A causes Dravet syndrome. *Brain Dev.* 31, 758–762. doi: 10.1016/j.braindev.2009.08.009

Silayeva, L., Deeb, T. Z., Hines, R. M., Kelley, M. R., Munoz, M. B., Lee, H. H. C., et al. (2015). KCC2 activity is critical in limiting the onset and severity of status epilepticus. *Proc. Natl. Acad. Sci. U.S.A.* 112, 3523–3528. doi: 10.1073/pnas.1415126112

Spence, E. F., Dube, S., Uezu, A., Locke, M., Soderblom, E. J., and Soderling, S. H. (2019). In vivo proximity proteomics of nascent synapses reveals a novel regulator of cytoskeleton-mediated synaptic maturation. *Nat. Commun.* 10:386. doi: 10.1038/s41467-019-08288-w

Stödberg, T., McTague, A., Ruiz, A. J., Hirata, H., Zhen, J., Long, P., et al. (2015). ARTICLE Mutations in SLC12A5 in epilepsy of infancy with migrating focal seizures. *Nat. Commun.* 6:8038. doi: 10.1038/ncomms9038

Suski, J. M., Lebiedzinska, M., Wojtala, A., Duszynski, J., Giorgi, C., Pinton, P., et al. (2014). Isolation of plasma membrane-associated membranes from rat liver. *Nat. Protoc.* 9, 312–322. doi: 10.1038/nprot.2014.016

Szklarczyk, D., Gable, A. L., Lyon, D., Junge, A., Wyder, S., Huerta-Cepas, J., et al. (2019). STRING v11: protein-protein association networks with increased coverage, supporting functional discovery in genome-wide experimental datasets. *Nucleic Acids Res.* 47, D607–D613. doi: 10.1093/nar/gky1131

Tang, X., Drotar, J., Li, K., Clairmont, C. D., Brumm, A. S., Sullins, A. J., et al. (2019). Pharmacological enhancement of *KCC2* gene expression exerts therapeutic effects on human Rett syndrome neurons and *Mecp2* mutant mice. *Sci. Transl. Med.* 11:eaau0164. doi: 10.1126/scitranslmed.aau0164

Tang, X., Kim, J., Zhou, L., Wengert, E., Zhang, L., Wu, Z., et al. (2016). KCC2 rescues functional deficits in human neurons derived from patients with Rett syndrome. *Proc. Natl. Acad. Sci. U.S.A.* 113, 751–756. doi: 10.1073/pnas.1524013113

Ting, A. Y., Stawski, P. S., Draycott, A. S., Udeshi, N. D., Lehrman, E. K., Wilton, D. K., et al. (2016). Proteomic analysis of unbounded cellular compartments: synaptic clefts. *Cell* 166, 1295–1307.e21. doi: 10.1016/j.cell.2016.07.041

Titz, S., Sammler, E. M., and Hormuzdi, S. G. (2015). Could tuning of the inhibitory tone involve graded changes in neuronal chloride transport? *Neuropharmacology* 95, 321–331. doi: 10.1016/j.neuropharm.2015.03.026

Tohyama, J., Nakashima, M., Nabatame, S., Gaik-Siew, C., Miyata, R., Rener-Primec, Z., et al. (2015). SPTAN1 encephalopathy: distinct phenotypes and genotypes. *J. Hum. Genet.* 60, 167–173. doi: 10.1038/jhg.2015.5

Tyzio, R., Nardou, R., Ferrari, D. C., Tsintsadze, T., Shahrokhi, A., Eftekhari, S., et al. (2014). Oxytocin-mediated GABA inhibition during delivery attenuates autism pathogenesis in rodent offspring. *Science* 343, 675–679. doi: 10.1126/science.1247190

Uvarov, P., Ludwig, A., Markkanen, M., Rivera, C., and Airaksinen, M. S. (2006). Upregulation of the neuron-specific K+/Cl- cotransporter expression by transcription factor early growth response 4. *J. Neurosci.* 26, 13463–13473. doi: 10.1523/JNEUROSCI.4731-06.2006

Weber, M., Hartmann, A. M., Beyer, T., Ripperger, A., and Nothwang, H. G. (2014). A novel regulatory locus of phosphorylation in the C terminus of the potassium chloride cotransporter KCC2 that interferes with n-ethylmaleimide or staurosporine-mediated activation. *J. Biol. Chem.* 289, 18668–18679. doi: 10.1074/jbc.M114.567834

Wright, R., Newey, S. E., Ilie, A., Wefelmeyer, W., Raimondo, J. V., Ginham, R., et al. (2017). Neuronal chloride regulation via KCC2 is modulated through a GABA B receptor protein complex. *J. Neurosci.* 37, 5447–5462. doi: 10.1523/JNEUROSCI.2164-16.2017

Yan, X.-X., and Jeromin, A. (2012). Spectrin breakdown products (SBDPs) as potential biomarkers for neurodegenerative diseases. *Curr. Transl. Geriatr. Exp. Gerontol. Rep.* 1, 85–93. doi: 10.1007/s13670-012-0009-2

Conflict of Interest: SM serves as a consultant for AstraZeneca, and SAGE Therapeutics, relationships that are regulated by the Tufts University. SM holds stock in SAGE Therapeutics.

The remaining authors declare that the research was conducted in the absence of any commercial or financial relationships that could be construed as a potential conflict of interest.

frontiers in Molecular Neuroscience

ORIGINAL RESEARCH
published: 13 November 2020
doi: 10.3389/fnmol.2020.570640

Quantitative Changes in the Mitochondrial Proteome of Cerebellar Synaptosomes From Preclinical Cystatin B-Deficient Mice

*Katarin Gorski[1,2], Albert Spoljaric[3], Tuula A. Nyman[4], Kai Kaila[3], Brendan J. Battersby[5] and Anna-Elina Lehesjoki[1,2]**

[1] Folkhälsan Research Center, Helsinki, Finland, [2] Department of Medical and Clinical Genetics, Medicum, University of Helsinki, Helsinki, Finland, [3] Molecular and Integrative Biosciences, and Neuroscience Center (HiLIFE), Faculty of Biological and Environmental Sciences, University of Helsinki, Helsinki, Finland, [4] Institute of Clinical Medicine, University of Oslo and Oslo University Hospital, Oslo, Norway, [5] Institute of Biotechnology, University of Helsinki, Helsinki, Finland

Progressive myoclonus epilepsy of Unverricht-Lundborg type (EPM1) is a neurodegenerative disorder caused by loss-of-function mutations in the cystatin B (*CSTB*) gene. Progression of the clinical symptoms in EPM1 patients, including stimulus-sensitive myoclonus, tonic-clonic seizures, and ataxia, are well described. However, the cellular dysfunction during the presymptomatic phase that precedes the disease onset is not understood. CSTB deficiency leads to alterations in GABAergic signaling, and causes early neuroinflammation followed by progressive neurodegeneration in brains of a mouse model, manifesting as progressive myoclonus and ataxia. Here, we report the first proteome atlas from cerebellar synaptosomes of presymptomatic *Cstb*-deficient mice, and propose that early mitochondrial dysfunction is important to the pathogenesis of altered synaptic function in EPM1. A decreased sodium- and chloride dependent GABA transporter 1 (GAT-1) abundance was noted in synaptosomes with CSTB deficiency, but no functional difference was seen between the two genotypes in electrophysiological experiments with pharmacological block of GAT-1. Collectively, our findings provide novel insights into the early onset and pathogenesis of CSTB deficiency, and reveal greater complexity to the molecular pathogenesis of EPM1.

Keywords: myoclonus epilepsy, synaptosome, neurodegeneration, cerebella, electrophysiology, mitochondria

OPEN ACCESS

Edited by:
Tija Carey Jacob, University of Pittsburgh, United States

Reviewed by:
Joern R. Steinert, University of Nottingham, United Kingdom
Tiziana Bonifacino, University of Genoa, Italy
Susan T. Weintraub, University of Texas Health Science Center at San Antonio, United States

***Correspondence:**
Anna-Elina Lehesjoki
anna-elina.lehesjoki@helsinki.fi

Received: *08 June 2020*
Accepted: *21 October 2020*
Published: *13 November 2020*

Citation:
Gorski K, Spoljaric A, Nyman TA, Kaila K, Battersby BJ and Lehesjoki A-E (2020) Quantitative Changes in the Mitochondrial Proteome of Cerebellar Synaptosomes From Preclinical Cystatin B-Deficient Mice. Front. Mol. Neurosci. 13:570640. doi: 10.3389/fnmol.2020.570640

INTRODUCTION

Progressive myoclonus epilepsy, EPM1 (Unverricht-Lundborg disease; OMIM 254800) is an autosomal recessive neurodegenerative disorder characterized by disease onset between 6 and 16 years, severe stimulus-sensitive, treatment-resistant and physically disabling myoclonus, tonic-clonic seizures and ataxia, with cognition essentially preserved (Koskiniemi et al., 1974; Kälviäinen et al., 2008). Magnetic resonance imaging (MRI) studies of EPM1 patient brains have shown loss of gray matter volume in the thalamus and motor cortex (Koskenkorva et al., 2009), thinning of the sensorimotor, visual and auditory cortices (Koskenkorva et al., 2012), and widespread degenerative white matter changes (Manninen et al., 2013). The histopathology have revealed widespread non-specific degenerative changes in both the cerebellum and cerebrum (Haltia et al., 1969;

Koskiniemi et al., 1974; Eldridge et al., 1983; Cohen et al., 2011). MRI-navigated transcranial magnetic stimulation studies have shown significant neurophysiological changes in cortical responses, including increased prevailed inhibition in the primary motor cortex (Danner et al., 2009) and impaired intracortical interactions and coherence (Julkunen et al., 2013).

EPM1 is caused by loss-of-function mutations in cystatin B (*CSTB*; OMIM 601145) (Pennacchio et al., 1996; Joensuu et al., 2008). The majority of patients are homozygous for a repeat expansion mutation in the promoter region of *CSTB*, reducing CSTB protein expression to 5–10% of controls (Joensuu et al., 2007). When patients are compound heterozygous for the repeat expansion and a null mutation, a more severe clinical presentation of EPM1 manifests (Koskenkorva et al., 2011; Canafoglia et al., 2012). Patients homozygous for predicted null mutations in *CSTB* manifest a severe neonatal-onset progressive encephalopathy (Mancini et al., 2016; O'Brien et al., 2017), suggesting an important role for CSTB in nervous system development. CSTB is a ubiquitously expressed intracellular inhibitor of cysteine proteases, including cathepsins B, H, S, K, and L (Turk et al., 2008). In addition, it is reported to protect cells against apoptosis (Pennacchio et al., 1998) and oxidative stress (Lehtinen et al., 2009), and play a role in cell cycle regulation (Ceru et al., 2010). Nonetheless, the precise molecular function of CSTB at the cellular level is far from resolved.

A genetically modified mouse model with a complete loss of *CSTB* expression (*Cstb*$^{-/-}$) manifests myoclonus from one month and a progressive ataxia from 6 months of age (Pennacchio et al., 1998). The onset of the clinical symptoms are preceded by early glial activation and inflammation, followed by progressive volume loss in the brain and increased oxidative damage (Lehtinen et al., 2009; Tegelberg et al., 2012; Okuneva et al., 2015). Pathological changes are detected throughout the brain, but are most striking in the cerebellum (Pennacchio et al., 1998; Tegelberg et al., 2012), where progressive atrophy reduces the cerebellar volume by almost 50% at 6 months of age (Tegelberg et al., 2012).

The characteristic symptoms in EPM1 imply alterations in the inhibitory GABAergic circuits of the brain. In older *Cstb*$^{-/-}$ mice, this presents as decreased GABAergic inhibition in the cortex (Buzzi et al., 2012), higher susceptibility to kainate-induced seizures (Franceschetti et al., 2007), and a progressive loss of inhibitory interneurons (Buzzi et al., 2012). However, altered GABAergic signaling was first noted in cerebella of presymptomatic postnatal day (P) 7 aged *Cstb*$^{-/-}$ mice during GABAergic synapse development (Joensuu et al., 2014). This presented as increased expression of the genes encoding for $GABA_A$ receptor ($GABA_AR$) subunits α6 and δ in cerebellar tissue lysates, and as an imbalance between excitatory and inhibitory postsynaptic currents (EPSCs; IPSCs), and a complete absence of synchronous IPSC bursts in cerebellar Purkinje cells. At this early age, the number of interneurons in the cerebellum was not altered. By the early symptomatic stage (P30), the number of GABAergic presynaptic terminals and ligand binding to $GABA_ARs$ were reduced. Together, the data indicate a disruption of GABAergic synapse formation in *Cstb*$^{-/-}$ mice.

To investigate the mechanisms behind the altered GABAergic synapse formation, we used a quantitative mass-spectrometry-based proteomics approach to analyze cerebellar synaptosomes of presymptomatic *Cstb*$^{-/-}$ mice. The data show a robust alteration to the mitochondrial proteome and factors important for intracellular transport and cytosolic ribosomal biogenesis.

MATERIALS AND METHODS

Ethics Statement

The Animal Ethics Committee of the State Provincial Office of Southern Finland approved all animal research protocols (decisions ESAVI/10765/2015 and ESAVI/471/2019).

Mice

Cstb$^{-/-}$ mice were obtained from The Jackson Laboratory (Bar Harbor, ME; 129-Cstb^{tm1Rm}/SvJ; stock #003486) (Pennacchio et al., 1998). Age-matched wild-type (wt) mice of the 129S2/SvHsd background were used as controls. The *Cstb*$^{-/-}$ mouse line was maintained by backcrossing heterozygous *Cstb*$^{-/-}$ males with inbred wt females and expanding the colony from heterozygous littermates.

Proteomics

Synaptosome Isolation

Synaptosomes were isolated from the cerebella of P14-aged *Cstb*$^{-/-}$ and wt mice (n = 5/genotype, males and females) according to the protocol described by Nolt et al. (2011), with slight modifications. Briefly, mice were sacrificed by decapitation and the cerebella dissected into ice-cold PBS. Cerebella were homogenized in 3 ml ice-cold buffer [0.32 M sucrose, 4 mM Hepes pH 7.4, protease- and phosphatase inhibitors (Pierce Protease and Phosphatase Inhibitor Mini Tablets, Thermo Fisher Scientific, Waltham, MA, United States)] and centrifuged twice at 1000 × g for 10 min at +8°C. The resulting supernatant was centrifuged at 10 000 × g for 15 min at +8°C. The resulting pellet was resuspended in 1.5 ml homogenization buffer and re-centrifuged to yield a washed crude synaptosomal fraction. This fraction was resuspended in 2 ml homogenization buffer and layered on top of 10 ml ice-cold 1.2 M sucrose and centrifuged at 230 000 × g (Sw40Ti swinging bucket rotor, Optima L-80 XP ultracentrifuge, Beckman Coulter, CA, United States) for 15 min at +4°C. The gradient interphase was diluted in homogenization buffer, layered on top of 9 ml ice-cold 0.8 M sucrose, and centrifuged at 230 000 × g for 15 min at +4°C. Synaptosomal purity and protein enrichment were analyzed by Western blot (**Supplementary Figure S1**).

Sample Preparation and LC-ESI-MS/MS Analysis

Lipids were removed from synaptosome samples by incubating them overnight at −20°C in five volumes ice-cold (−20°C) acetone. Samples were centrifuged twice at 1000 × g for 10 min at +8°C with an additional acetone wash in between. The pellet was air dried for 5 min and resuspended in freshly prepared 6.0 M urea/25 mM ammonium bicarbonate. Protein concentrations (μg/μl) were determined spectrophotometrically

using the BCA protein assay kit (Pierce, Thermo Fisher Scientific) according to the manufacturer's instructions. For analysis of the proteome, 25 μg of each sample was digested with trypsin (1:30 w/w, enzyme:protein; V5111 Sequencing Grade Modified Trypsin, Promega Corporation, WI, United States), and desalted by C18 cartridges. An additional phospholipid removal step was applied to samples due to impurities that interfered with ionization. Phospholipids were removed by hydrophilic interaction liquid chromatography (HILIC) using HILIC HyperSep Tips (60109-214; Thermo Fisher Scientific). Tips were conditioned by aspirating/expelling 50 μl of binding solution [15 mM ammonium acetate, pH 3.5 in 85% acetonitrile (ACN)] for five times prior to sample binding, and peptides were bound to the HILIC tips by aspirating/expelling the samples (10 μl, diluted in 85% ACN) for 20 times. Samples were washed by aspirating/expelling 20 μl binding solution for ten times, discarding the expelled solution each time. Peptide samples were released by aspirating/expelling 10 μl elution buffer (15 mM ammonium acetate, pH 3.5 in 10% ACN) for ten times, collecting the expelled solution in a 1.5 ml Eppendorf Maximum Recovery Tube (Axygen, Corning, NY, United States). Purified peptide samples were concentrated (SpeedVac, Thermo Fisher Scientific) for 10–15 min and dissolved in 1% formic acid. For liquid chromatography-electrospray ionization-tandem mass spectrometry (LC-ESI-MS/MS), 400 ng peptides/sample were analyzed in random order with several washes and blank runs in between. The analyses were performed on a nanoflow HPLC system (Easy-nLC1000, Thermo Fisher Scientific, Bremen, Germany) coupled to a Q Exactive mass spectrometer (Thermo Fisher Scientific) equipped with a nano-electrospray ionization source. Peptides were loaded on a trapping column and separated inline on a 15 cm C18 column (75 um × 15 cm, ReproSil-Pur 5 um 200 Å C18-AQ, Dr. Maisch HPLC GmbH, Ammerbuch-Entringen, Germany), with the mobile phase consisting of water with 0.1% formic acid (solvent A) and ACN/water [80:20 (v/v)] with 0.1% formic acid (solvent B). Peptides were eluted with a two-step linear gradient at a flow rate of 300 nl/min: from 2 to 20% of solvent B in 85 min, and to 40% of solvent B in 35 min, followed by a 15 min wash with 100% solvent B. MS analysis was performed using the Thermo Xcalibur 3.0 software (Thermo Fisher Scientific). The analyses were performed in a data-dependent acquisition (DDA) mode for 10 most intense peptide ions, consisting of an Orbitrap MS survey scan of mass range 300–2000 m/z, with a resolution of 140 000, mass window for precursor ion selection 2.0 m/z, and intensity threshold for triggering MS2 240, followed by fragmentation of selected peptide ions (MS2) by higher-energy collisional dissociation (HCD), with a mass resolution of 17 500 for MS/MS. Ions with unassigned charges and singly charged ions were excluded for precursor selection. The selected peptide ions were fragmented with a normalized collision energy of 27 in the collision cell. Dynamic exclusion duration was 10 s.

MS Quantification and Protein Identification

Peptides were quantified using the Progenesis LC-MS software (Non-linear Dynamics Limited, Tyne, United Kingdom), and proteins were identified using the Mascot 2.4.1 search engine (Matrix Science, MA, United States) through the Proteome Discoverer 1.4 software (Thermo Fisher Scientific). The Swiss-Prot Mus musculus database, uploaded in January 2016, was used as reference. Error tolerances on peptide and fragment ions were maximum 5 ppm and 0.02 Da, respectively. Database searches were limited to fully tryptic peptides with maximum one missed cleavage, and cysteine carbamidomethylation (+57.021464 Da) and methionine oxidation (+15.994915 Da) were set as fixed and variable modifications, respectively. Peptide-level false discovery rate (FDR) was set to 1%, and minimal peptide length to 7 amino acids. Only proteins with minimum two unique peptides were used for further analyses. The mass spectrometry proteomics data have been deposited to the ProteomeXchange Consortium[1] via the PRIDE partner repository (Vizcaíno et al., 2013) with the dataset identifier PXD019370.

Data Processing and Analysis

The proteomics data was normalized, followed by missing value imputation of proteins with null-intensity in either sample group. Sample relations were examined by Spearman's correlation analysis, hierarchical clustering, and principal component analysis (PCA) using R language and environment for statistical computing [version 3.2.2 (2015-08-14)] (R Core Team, 2016), and the Bioconductor module (version 3.2) (Gentleman et al., 2004). Statistical testing of abundance between sample groups (*Cstb*$^{-/-}$ vs. wt) was performed using the R package ROTS (Reproducibility-Optimized Test Statistic) (Elo et al., 2008). An abundance change with a false discover rate (FDR) -corrected *p*-value (*q*-value) ≤ 0.05 was considered as significant change. Downstream analyses of the results were conducted to proteins with a *q*-value ≤ 0.05 using the following softwares and statistical tests: PANTHER Overrepresentation Test (Released 20200407) using the Gene Ontology (GO) database (Mi et al., 2013) (Released 2020-02-21), using Fisher's exact test followed by Benjamini-Hochberg correction (FDR) for multiple testing, considering FDR < 0.05 statistically significant; the web-tool ClustVis (Metsalu and Vilo, 2015), performed using singular value decomposition; the STRING database (Szklarczyk et al., 2019), using high confidence interaction score (>0.700) as cutoff, and experiments, databases, and co-expression as active interaction sources. The softwares Cytoscape (Shannon et al., 2003) and Inkscape[2] were used for visualization of the results. Function and localization of mitochondrial proteins for **Figure 1C** were manually curated.

Electrophysiological Recordings

Cerebellar Slice Preparation

Mice (P14, $n = 5$ (*Cstb*$^{-/-}$) and 10 (wt); P30, $n = 5$ (*Cstb*$^{-/-}$) and 7 (wt); males and females) were deeply anesthetized with halothane, followed by cervical dislocation. Brains were quickly dissected and placed into ice-cold (+4°C) cutting solution with (in mM): 87 NaCl, 2.5 KCl, 0.5 $CaCl_2$, 25 $NaHCO_3$, 1.25 NaH_2PO_4, 7 $MgCl_2$, 50 sucrose, and 25 D-glucose. Sagittal cerebellar slices (225 μm) were cut using a vibrating microtome

[1] http://proteomecentral.proteomexchange.org

[2] https://inkscape.org

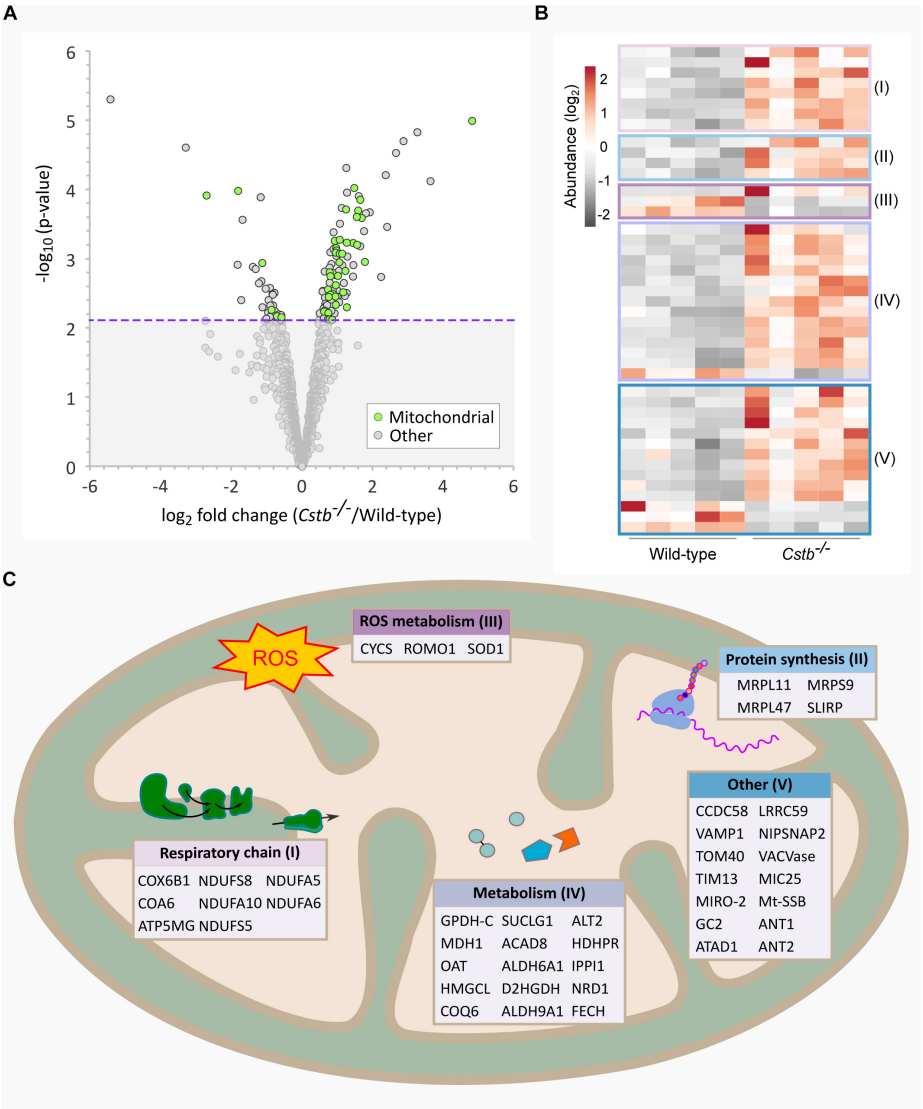

FIGURE 1 | Differentially abundant mitochondrial proteins in *Cstb*$^{-/-}$ synaptosomes. **(A)** Mitochondrial proteins (green) are plotted as $-\log_{10}$-transformed *p*-value vs. $\log_2$-transformed fold change (*Cstb*$^{-/-}$/wild-type) protein abundance. The 128 DAPs significantly differing in abundance (*q*-value $\leq$ 0.05) are plotted above the threshold limit of $-\log_{10}$ (*p*-value) 2.1 (purple dotted line). The remaining identified proteins (1973) with a non-significant *q*-value are plotted below the threshold limit. **(B)** Heatmap of 44 differentially abundant mitochondrial proteins with 36 and 6 proteins having increased and decreased fold changes, respectively. Proteins are grouped by key processes as outlined in C. Each column represents an independent biological sample. See **Supplementary Table S3** for complete list of proteins. **(C)** Differentially abundant mitochondrial proteins detected for key processes compartmentalized within the organelle.

(7000 SMZ-2; Campden Instruments). Slices were incubated for 1 h at +34°C in standard solution containing (in mM): 124 NaCl, 3 KCl, 2 $CaCl_2$, 25 $NaHCO_3$, 1.1 NaH_2PO_4, 2 $MgSO_4$, and 10 D-glucose. The slices were maintained at room temperature until use in electrophysiological recordings. All solutions were equilibrated with carbogen (95% O_2, 5% CO_2, pH 7.4).

Electrophysiological Recordings of Tonic $GABA_AR$ Currents and Effects of Blocking GAT-1

Whole-cell voltage clamp recordings were performed in a genotype-blinded manner from cerebellar granule cells, 1-2 cells per animal. Granule cells were identified based on their morphology and electrophysiological signatures (Silver et al., 1992). Currents were amplified (EPC10, HEKA Elektronik GmbH, Lambrecht, Germany) at a sampling rate of 20–50 kHz. Data were collected using Patchmaster software (HEKA Elektronik GmbH). Recordings were corrected for a liquid junction potential of 3.9 mV. Patch pipettes from borosilicate glass had open-tip resistances of 4–7 MΩ, and they were filled with a solution containing (in mM): 140 CsCl, 10 HEPES, 5 EGTA, 4 NaCl, 1 $CaCl_2$, 2 Mg-ATP, 5 QX-314 bromide, pH 7.3 at +20°C with NaOH; osmolarity 284 mOsm. Recordings were done in a submerged recording chamber at +32 ± 0.5°C, and slices were constantly perfused with standard solution

(3.5 ml/min). GABAergic transmission was pharmacologically isolated by blocking ionotropic AMPA and NMDA receptors using CNQX (10 μM) and D-AP5 (20 μM), respectively. $GABA_AR$ antagonist picrotoxin (100 μM) was used at the end of all experiments to fully block all $GABA_AR$ -mediated currents, including the extrasynaptic tonic current. Picrotoxin and the GAT-1 inhibitor NNC-711 (10 μM) were directly applied to the perfusate.

Cells were voltage clamped at a holding potential of −70 mV. At the beginning of each experiment, current amplitudes were measured for 3 min to obtain a stable baseline.

Analysis of Data

Analysis of the electrophysiological recordings was done using the WinEDR software (Dr. J. Dempster, University of Strathclyde, Glasgow, United Kingdom). The holding currents were analyzed by taking all-point histograms derived from 30-second-windows of the recording periods (baseline; 60 s after NNC-711 application; 100 s after picrotoxin application). A Gaussian curve was fitted on the all-point histograms, and the peak value was used as the holding current value for analysis (Sipilä et al., 2005). The effect of GAT-1 activity and the total tonic $GABA_AR$ -mediated currents were defined as the net change in holding current following application of NNC-711 and picrotoxin, respectively. The change in tonic current in the presence of NNC-711 was read from the baseline of the recording during time intervals in which sIPSCs were absent. This eliminates any influence of synaptic currents on the quantification of the peak change in tonic current (see **Figure 4A**). In order to normalize the amount of the extrasynaptic tonic current with regard to cell size the data is presented as pA/pF.

Statistical analysis was done using GraphPad Prism version 8 for Windows (GraphPad Software, La Jolla, CA, United States)[3]. Testing for statistical outliers was done using the ROUT method (Q = 1%), and significance was evaluated using the two-tailed unpaired t-test and the non-parametric Mann-Whitney U test. Statistical significance was defined as $p < 0.05$.

RESULTS

Cstb$^{-/-}$ Synaptosomes Are Quantitatively and Qualitatively Distinct

To investigate the basis for altered GABAergic signaling in *Cstb*$^{-/-}$ mice, we analyzed the proteome of cerebellar synaptosomes from presymptomatic P14 *Cstb*$^{-/-}$ and wt mice by LC-ESI-MS/MS. Altogether, a total of 2101 proteins were identified and quantified (**Supplementary Table S1**), with Spearman's rank order correlation coefficients varying between 0.973 and 0.986 for *Cstb*$^{-/-}$ and 0.986 and 0.991 for wt samples, indicating strong positive relationships between the biological replicates (n = 5 / genotype) within sample groups. Downstream analyses were carried out for proteins with a q-value ≤ 0.05, narrowing the sample size to 128 differentially abundant proteins (DAPs) (**Supplementary Table S2**). Among these was CSTB, identified solely in synaptosomes of wt preparations, thus providing additional evidence of its location and function in the synapse.

Principal component analysis (PCA, **Supplementary Figure S2A**) revealed the ten replicates falling into two clusters and accounting for 75.5% (PC1) and 7.1% (PC2) of the variance, thus corresponding to the variation between genotypes. Individuals within sample groups did not cluster according to sex (females and males, n = 2 and 3 for *Cstb*$^{-/-}$, and 3 and 2 for wt, respectively). Protein abundance ratios were consistent across biological replicates (**Supplementary Figure S2B**).

Cstb$^{-/-}$ Synaptosomes Are Distinct in Mitochondrial, Ribosomal and Intracellular Transport Proteins

To predict the biological relationships between the 128 DAPs in *Cstb*$^{-/-}$ synaptosomes, we performed Gene Ontology (GO) classification and PANTHER enrichment analyses assessing the current biological knowledge of these proteins (**Supplementary Table S3**).

When examining the predicted cellular components of the DAPs, we observed a striking number of proteins that localize to mitochondria (n = 44) (**Figure 1A**). Most of these proteins were increased in abundance (n = 36) (**Figure 1B**) and the fold changes were among the highest in the dataset. The differentially abundant mitochondrial proteins affect various sub-compartments of the organelle (**Figure 1C**), with the highest function-related fold enrichments associated to the respiratory chain (**Figure 2A** and **Supplementary Table S3**).

Next, we investigated the predicted biological processes of the DAPs. In this category, we observed an enrichment of proteins associated with intracellular transport of organelles, proteins and other cellular substances (n = 40), which were grouped to several overlapping transport-related GO terms (**Figure 2A** and **Supplementary Table S3**). The majority (n = 27) of these proteins were increased in abundance in *Cstb*$^{-/-}$ synaptosomes (**Figure 2B**), and most group to the GO terms protein and peptide, and mitochondrial transport. We also investigated the predicted relations between the intracellular transport proteins by protein-protein interaction network –analysis using the software STRING (**Supplementary Table S4**). Most of these interactions belong to the same network, consisting of the GO terms protein and peptide transport (**Figure 2C**).

Since axonal transport of mRNA transcripts is partly mediated by the same transport mechanisms as organelles (Kennedy and Ehlers, 2006), we asked whether the abundance of proteins involved in synaptic protein synthesis was altered. A substantial number (n = 16) of the DAPs were related to mRNA translation or to the ribonucleoprotein complex, as predicted by GO terms for molecular function and cellular component (**Supplementary Table S3**). Of these, 12 proteins were cytoplasmic and four mitochondrial, however, these two processes are functionally distinct. Nine of the cytosolic proteins were part of the same interaction network (**Figure 3A** and **Supplementary Table S4**) with the majority (n = 7) being structural components

[3]www.graphpad.com

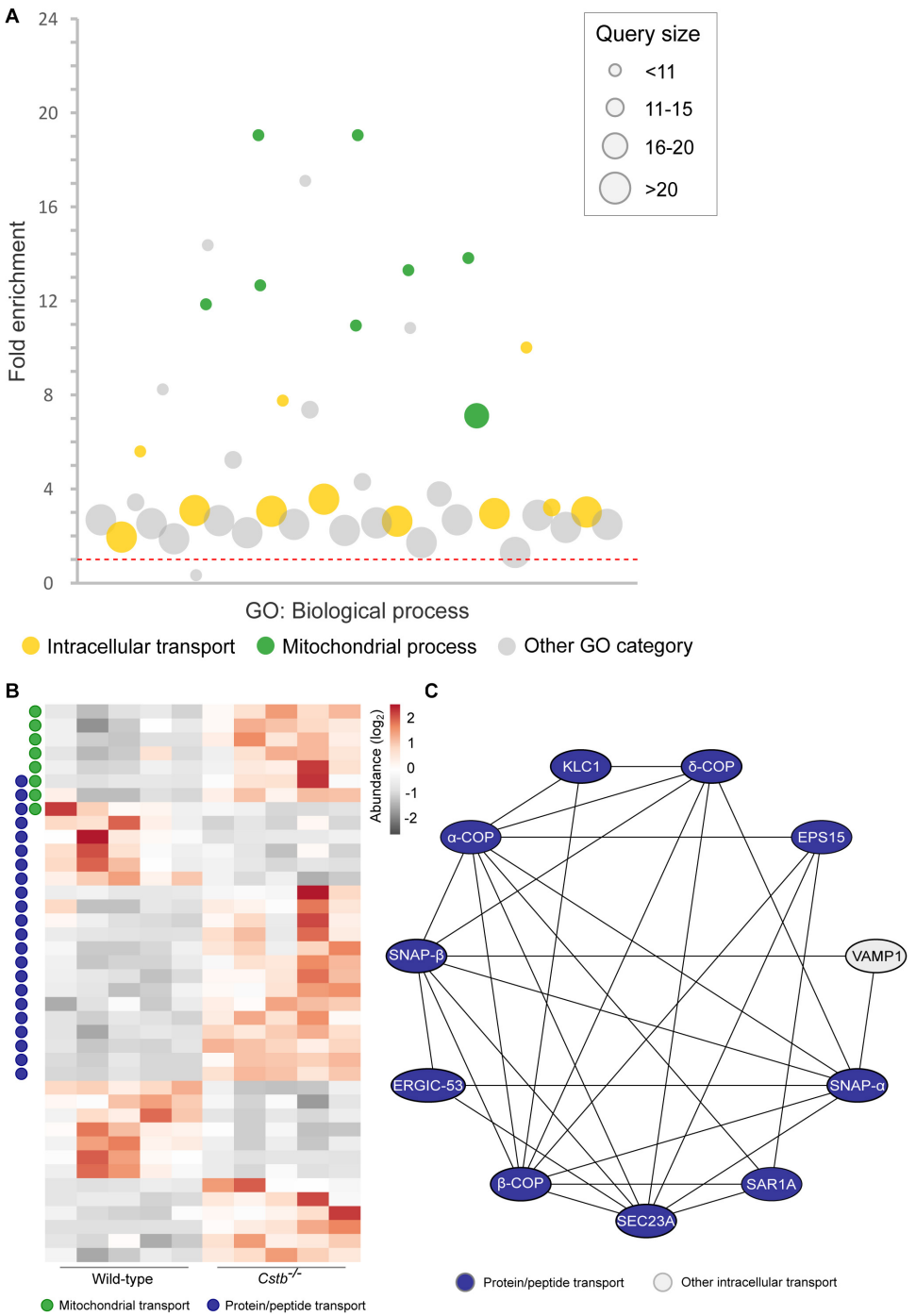

FIGURE 2 | Differentially abundant intracellular transport proteins in *Cstb*$^{-/-}$ synaptosomes. **(A)** Manhattan plot of enriched (FDR < 0.05) GO terms show a high number of intracellular transport (yellow circles; GO:0006810; GO:0071702; GO:0071705; GO:0046907; GO:0015031; GO:0015833; GO:0042886; GO:0006886; GO:0006839; GO:0048193; GO:0006888) and mitochondrial process (green circles; GO:0007005; GO:0007006; GO:0022904; GO:0022900; GO:0032981; GO:0010257; GO:0006119; GO:0033108) -related biological processes in the DAPs dataset. Each circle represents a GO term, circle size corresponding to the annotated number of proteins in the DAPs dataset (query size). GO term fold enrichment is plotted on the *y*-axis, and the threshold limit of 1 (no fold change) is plotted as a red dotted line. **(B)** Heatmap of 40 differentially abundant transport proteins in *Cstb*$^{-/-}$ synaptosomes, with 13 and 27 proteins having decreased and increased fold changes, respectively. Proteins involved in mitochondrial or protein/peptide transport are marked with green or blue circles, respectively. Each column represents an independent sample, and each row represents a protein. See **Supplementary Table S3** for complete list of proteins. **(C)** Predicted protein-protein interaction network, with a majority of interactors grouping to the GO term protein/peptide transport (blue). Networks with less than three members, or interactions below the combined interaction score threshold of 0.7, are not shown.

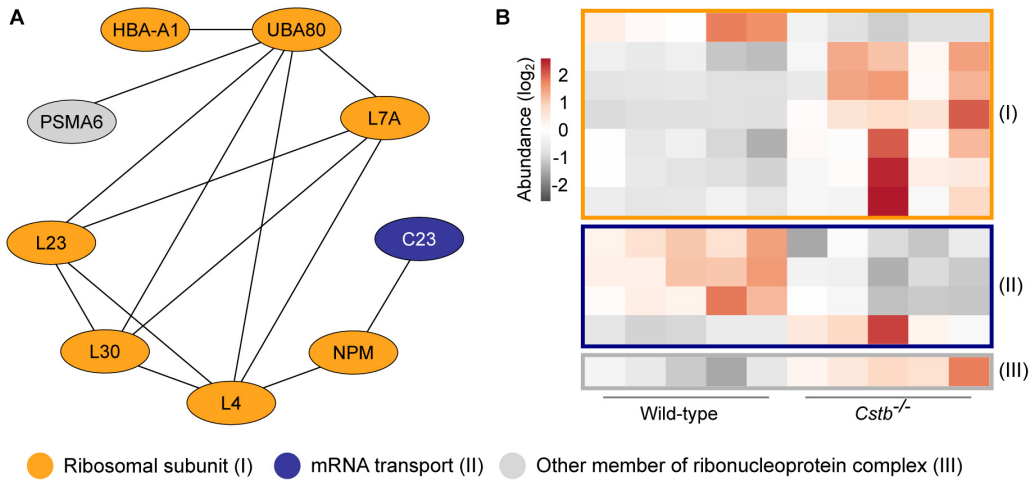

FIGURE 3 | Differentially abundant proteins of the ribonucleoprotein complex in *Cstb*$^{-/-}$ synaptosomes. **(A)** Protein-protein interaction network shows the predicted relation between ribosomal subunits (orange) and proteins involved in mRNA transport (blue). Other proteins of the ribonucleoprotein complex are plotted in gray. Protein classification was performed based on GO terms. **(B)** Heatmap of 12 differentially abundant ribonucleoprotein complex members in *Cstb*$^{-/-}$ synaptosomes, with 4 and 8 proteins having decreased and increased fold changes, respectively. Proteins are grouped by key function. Each column represents an independent sample, and each row represents a protein. See **Supplementary Table S3** for complete list of proteins.

of the ribosome and increased in abundance in *Cstb*$^{-/-}$ synaptosomes (**Figure 3B**).

Several Differentially Abundant Synaptic Proteins in *Cstb*$^{-/-}$ Synaptosomes

A synapse-specific location of the DAPs could provide an explanation for the previously reported alterations in GABAergic signaling. To investigate this hypothesis, we compared the DAPs dataset to the SynSysNet –online database for synaptic proteins (von Eichborn et al., 2013), and identified 31 of 128 proteins with reported synaptic location (**Supplementary Table S5**). Ten of these were associated with GABA- or glutamate-mediated neurotransmission (**Table 1**), and we studied these further by identifying their disease associations and mouse model phenotypes. GAT-1 was the only protein in the dataset exclusively associated with inhibitory GABAergic signaling, and its abundance was decreased by 0.9 fold ($\log_2$) in *Cstb*$^{-/-}$ synaptosomes. Defects in GAT-1 function have previously been associated with myoclonus, epilepsy (Johannesen et al., 2018) and altered GABAergic signaling (Jensen et al., 2003), unlike any of the other synaptic proteins we identified in our analyses.

Unaltered GAT-1 Activity in *Cstb*$^{-/-}$ Cerebellar Granule Neurons

To investigate GAT-1 activity in cerebellar granule neurons we turned to electrophysiology. *Cstb*$^{-/-}$ mice are born healthy but develop progressive clinical symptoms at one month of age. Thus, we decided to test GAT-1 activity at two time points in development: P14 (presymptomatic) and P30 (early symptomatic). Tonic $GABA_AR$ -mediated currents are known to increase in response to GAT-1 inhibition and with increased extracellular GABA (Wall and Usowicz, 1997; Rossi et al., 2003). We inhibited GAT-1 with the antagonist NNC-711 (Suzdak et al., 1992) in voltage-clamp experiments, using the drug-induced change in tonic $GABA_AR$ -mediated current as a read-out of GAT-1 function.

Whole-cell voltage clamp recordings were obtained from a total of 39 cerebellar granule neurons (n = 6 and 13, and 8 and 12 for P14 and P30 *Cstb*$^{-/-}$ and wt, respectively) exhibiting similar morphological and electrophysiological features. The median membrane capacitance (pF), reflecting cell size, was 3.75 and 3.70 at P14 and 3.65 and 3.90 at P30 for *Cstb*$^{-/-}$ and wt, respectively (**Supplementary Table S6**). This is consistent with previous reports from cerebellar granule neurons (Kaneda et al., 1995; Brickley et al., 1996; Carta et al., 2004).

GAT-1 inhibition caused an increase in tonic $GABA_AR$ -mediated currents in both genotypes (**Figure 4A**). However, the maximum effect of blocking GAT-1 with 10 μM NNC-711 showed large variability in both age groups (**Figure 4B**). A high cell-to-cell variation was also observed in the total amplitude of the tonic current as seen following its complete block by 100 μM picrotoxin (**Figure 4C**). The median effect of blocking GAT-1 was not different between *Cstb*$^{-/-}$ and wt mice at either age point (**Figure 4B** and **Supplementary Table S6**). To normalize the quantifications of the GAT-1 mediated currents for each individual neuron, the ratio between GAT-1 induced maximum current (**Figure 4B**) and total available tonic current given by the picrotoxin-induced shift (**Figure 4C**) was calculated. The median values for these ratios did not indicate for differences between the two genotypes at either age point (**Supplementary Table S6**).

DISCUSSION

We undertook a proteomics approach to gain insight into the molecular basis behind altered synaptic functions in the cerebella of presymptomatic *Cstb*$^{-/-}$ mice. Our analysis reveals that

TABLE 1 | Differentially abundant GABA and glutamate -associated proteins in *Cstb*$^{-/-}$ synaptosomes.

Gene	Protein	log_2 FC	Neurotransmitter	Disease association	Mouse model phenotype
Slc6a1	Sodium- and chloride-dependent GABA transporter 1 (GAT-1)	−0.87	GABA	MAE; ID (Johannesen et al., 2018)	Altered GABAergic signaling (Jensen et al., 2003)
Bcan	Brevican core protein	2.29	GABA, Glu	No reported disease association	Impaired LTP (Brakebusch et al., 2002)
Tnr	Tenascin-R	1.31	Glu	No reported disease association	Increased neuronal excitability (Brenneke et al., 2004)
Napa	Alpha-soluble NSF attachment protein	1.31	Glu	TLE (Xi et al., 2015); polymorphisms associated with PD severity (Agliardi et al., 2019)	
Napb	Beta-soluble NSF attachment protein	0.94	Glu	Possible contribution to EIEE1 (Conroy et al., 2016)	Epileptic seizures, ataxia (Burgalossi et al., 2010)
Dbn1	Drebrin	−0.68	Glu	Decreased spine plasticity in AD (Harigaya et al., 1996)	
Actn1	Alpha-actinin-1	−0.78	Glu	Trombocytopenia (Westbury et al., 2017)	
Vamp1	Vesicle-associated membrane protein 1	−1.13	Glu	SPAX1 (Bourassa et al., 2012); CMS25 (Shen et al., 2017)	Neurological defect, prewean death (Nystuen et al., 2007)
Pura	Transcriptional activator protein Pur-alpha	−1.35	Glu	5q31.3 microdeletion syndrome (Lalani et al., 2014)	Tremors, seizures, death at young age (Khalili et al., 2003)
Dynll2	Dynein light chain 2, cytoplasmic	−1.79	Glu	No reported disease association	

GABA, gamma-aminobutyric acid; Glu, glutamate; MAE, myoclonic atonic epilepsy; ID, intellectual disability; LTP, long-term potentiation; TLE, temporal lobe epilepsy; PD, Parkinson's disease; EIEE1, early infantile epileptic encephalopathy 1; AD, Alzheimer's disease; SPAX1, spastic ataxia 1; CMS25, congenital myasthenic syndrome-25.

mitochondrial dysfunction might be a critical factor in the early pathogenesis of CSTB deficiency, establishing for the first time an early role for mitochondria in the molecular pathogenesis of EPM1. However, in contrast to our initial hypothesis [see (Joensuu et al., 2014], we did not detect significant changes related to GABAergic signaling.

We found one third of the differentially abundant proteins identified in the cerebellar synaptosomes of presymptomatic *Cstb*$^{-/-}$ mice were part of the mitochondrial proteome. The fold changes of these proteins were among the highest in the dataset. Disruption of the mitochondrial proteome could affect ATP production and reactive oxygen species (ROS) scavenging, among other functions, shifting redox-balance to generate progressive mitochondrial dysfunction. In other neurological disorders, such as Alzheimer's and Parkinson's disease, early changes in synaptic mitochondrial density, energy metabolism, dynamics, and function have been reported to precede the onset of neurological symptoms and brain pathology (Arnold et al., 2011; Van Laar et al., 2018; Tang et al., 2019).

Considering the central role that mitochondria play in oxidative stress, it was perhaps not surprising to identify disruptions in the mitochondrial proteome because redox homeostasis was previously implicated in the disease mechanisms of CSTB deficiency (Lehtinen et al., 2009). Loss of CSTB function appears to sensitize cerebellar granule neurons to oxidative stress induced cell death with increased lipid peroxidation and depletion of antioxidants in the cerebellum of *Cstb*$^{-/-}$ mice. Further, loss of mitochondrial membrane integrity has been reported in lipopolysaccharide stimulated primary bone marrow -derived macrophages from *Cstb*$^{-/-}$ mice (Maher et al., 2014). A consequence of mitochondrial dysfunction is the production of ROS, which affects intracellular signal transduction pathways and generates oxidative damage (Fatokun et al., 2008). Indeed, our proteomic data show changes to the abundance of ROS-associated proteins. Notably, SOD1, an enzyme converting ROS to hydrogen peroxide limiting its potential toxicity (Wang et al., 2018) was reduced, in line with the decreased activity of SOD in cerebella of *Cstb*$^{-/-}$ mice (Lehtinen et al., 2009). We also observed alterations to the nuclear-encoded mitochondrial protein ROMO1, and the hemoglobin subunits HBA and HBB. The latter are linked to superoxide production, increased oxidative stress, and neural pathogenesis (Nishi et al., 2008; Biagioli et al., 2009; Norton et al., 2014; Lee et al., 2018). Mitochondrial ROS has been reported to modulate GABAergic signaling in cell-type-specific mechanisms (Beltrán González et al., 2019). In cerebellar granule cells, $GABA_AR$ subunit α6 -mediated inhibitory currents are strengthened in response to mitochondrial ROS, although the mechanism is currently unknown (Accardi et al., 2015). Previously, we reported increased expression of both *Gabra6* and *Gabrd*, encoding the α6 and δ subunits of the $GABA_AR$, in the cerebella of *Cstb*$^{-/-}$ mice (Joensuu et al., 2014).

Our proteomic data also revealed altered abundance of key transport proteins, suggesting the potential for altered transport from the soma to the synapse. These may reflect dysfunctions in global transport mechanisms or in targeted trafficking of a subset of cargo, collectively affecting synaptic plasticity. Such mechanisms have previously been described for several neurodegenerative disorders and mitochondrial dysfunction (Liu et al., 2012). Intracellular trafficking is tied

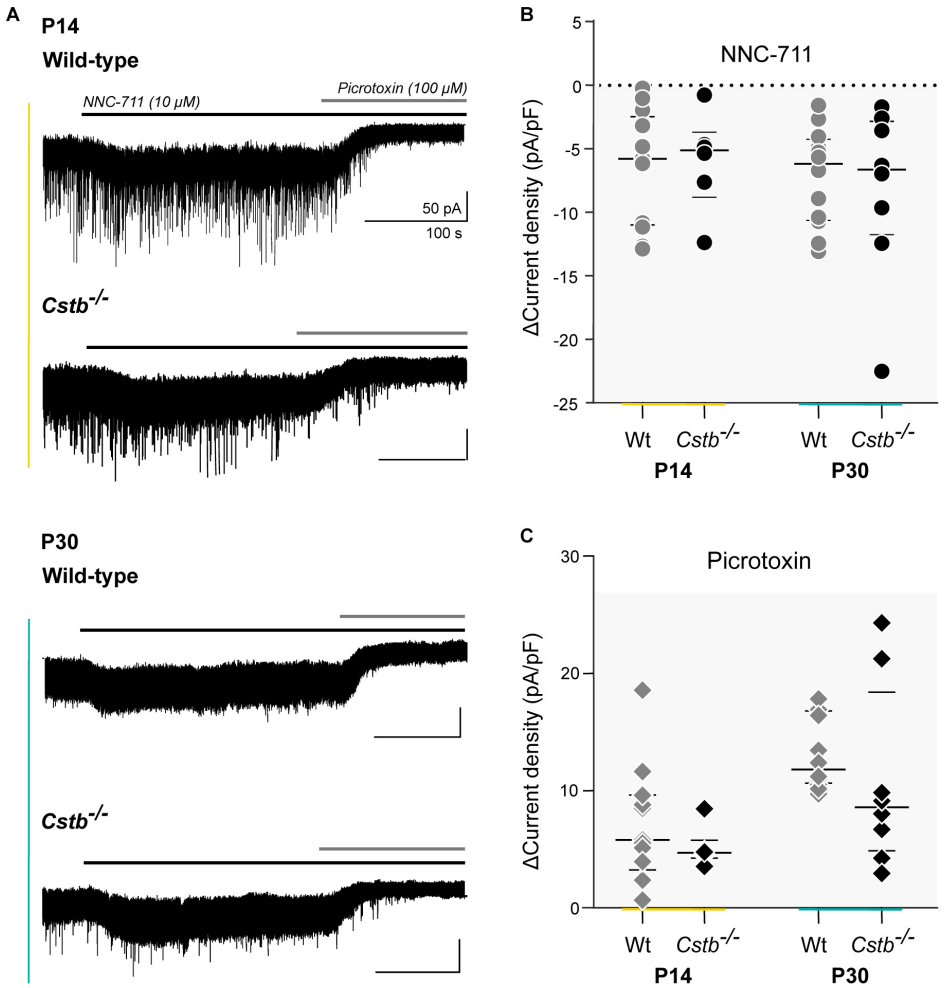

FIGURE 4 | GAT-1 activity and total tonic $GABA_AR$ –mediated currents in cerebellar granule cells of *Cstb*$^{-/-}$ and wild-type mice. **(A)** Experimental traces of whole-cell voltage clamped cerebellar granule neurons of P14 and P30 *Cstb*$^{-/-}$ and wt mice. NNC-711 (10 μM) blocks GAT-1 activity. Picrotoxin (100 μM) blocks $GABA_AR$ -mediated tonic conductance. Recordings were obtained in the presence of CNQX (10 μM) and D-AP5 (20 μM). **(B,C)** Summary of NNC-711 and picrotoxin application. Horizontal bars represent median and interquartile range values of the change (Δ) in current density (pA/pF), induced by NNC-711 and picrotoxin application. See **Supplementary Table S6** for more details.

to local protein synthesis and is critical for synaptic plasticity, enabling spatio-temporal regulation of translation (Steward and Schuman, 2001; Liu et al., 2012). Consistent with this interpretation, our data revealed differential abundance of several ribonucleoproteins and ribosomal subunits in the synaptosomes of *Cstb*$^{-/-}$ mice. Future studies will clarify the importance of these functions to the molecular pathogenesis of EPM1.

How does mitochondrial dysfunction and intracellular transport link to CSTB deficiency? Since 99% of the mitochondrial proteome is encoded in the nucleus, transport of the organelle back to the soma is required to maintain its function. This is paramount when the proteome has a differential turnover rate even among subunits of the same oxidative phosphorylation complex (Karunadharma et al., 2015). Thus, mitochondrial dysfunction could arise as a secondary effect of the cellular pathology at synapses.

The CSTB protein was robustly detected in our synaptosome preparations from wt mice, and has also been observed in synaptosomes from rat cortex and human cerebral organoids (Penna et al., 2019). The specific role of CSTB in synapses is not clear, but its function appears to be protective and crucial for synaptic physiology, as it is locally translated in synaptosomes of rat cerebral cortex (Penna et al., 2019). Furthermore, loss of CSTB function triggers a cascade of early pathological events, including mitochondrial dysfunction, compromised axonal transport, and altered local translation, leading to progressive neurodegeneration.

We did not identify factors in any major pathway that are known to specifically affect the GABAergic system. Our data, however, revealed a decreased abundance of GAT-1 in the synaptosomes of *Cstb*$^{-/-}$ mice. GAT-1 is a crucial member of the GABA recycling system, clearing GABA from the synaptic cleft of mature GABAergic neurons, and terminating its inhibitory

actions by preventing excessive activation of extrasynaptic $GABA_A$Rs that mediate tonic inhibition (Guastella et al., 1990). Moreover, mutations in *SLC6A1*, the gene encoding GAT-1, have previously been linked with neurological human phenotypes, including myoclonus and epilepsy (Johannesen et al., 2018). *Gat-1* deficiency in mice increased the tonic postsynaptic $GABA_A$R -mediated conductance in hippocampus (Jensen et al., 2003). No difference in GAT-1 activity in cerebellar granule cells was detected between *Cstb*$^{-/-}$ and wt mice, which may reflect heterogeneity in the cells at P14, as the cerebellum is still developing and maturing (Altman, 1972). Indeed, GAT-1 expression in the cerebellum is dependent on the maturation of neurons. Localization of GAT-1 to the GABAergic axons does not begin until the second and third postnatal weeks, paralleling synapse formation and following the expression of vesicular GABA transporter (VGAT) (Takayama and Inoue, 2005). However, our electrophysiological analysis of GAT-1 activity at P30, when the cerebellum is further matured and *Cstb*$^{-/-}$ mice enter the early symptomatic stage, also failed to detect any differences between the genotypes. These results are consistent with our previous studies, which showed less VGAT immunopositive puncta in the cerebellar molecular layer of P14 *Cstb*$^{-/-}$ mice, reaching control levels by P20 (Joensuu et al., 2014). This may indicate delayed maturation of GABAergic synapses in *Cstb*$^{-/-}$ mice. Our proteomics and electrophysiology data demonstrate that despite decreased abundance of total GAT-1 in the synaptosomes, its activity as GABA transporter in the synapse is sufficient to retain the electrophysiological properties of the cell. Its impact on other functions in the developing synapse, however, cannot be distinguished from these data, and is to be investigated in future studies.

In conclusion, our study confirms the role for CSTB in synaptic physiology and reveals a role for mitochondrial dysfunction in the early molecular pathogenesis of CSTB deficiency. The proposed hypothesis on early mitochondrial dysfunction could be the mechanism linking ROS signaling and GABAergic inhibition (Joensuu et al., 2014). Detailed understanding on how CSTB deficiency leads to mitochondrial dysfunction and the mechanisms underlying synaptic dysfunction need to be explored in future detailed studies.

DATA AVAILABILITY STATEMENT

All datasets presented in this study are included in the article/supplementary material. The mass spectrometry proteomics data have been deposited to the PRIDE database with the dataset identifier PXD019370.

ETHICS STATEMENT

The animal study was reviewed and approved by the Animal Ethics Committee of the State Provincial Office of Southern Finland.

AUTHOR CONTRIBUTIONS

KG, AS, KK, BB, and A-EL contributed the study design. KG and AS performed the experiments. KG, AS, TN, and BB analyzed the data. KG, BB, and A-EL wrote the manuscript. All authors discussed and commented on the manuscript.

FUNDING

We wish to acknowledge the following funding sources: Folkhälsan Research Foundation, the Sigrid Jusélius Foundation, the Finnish Epilepsy Association, Medicinska Understödsföreningen Liv och Hälsa r.f., Finnish Epilepsy Research Foundation (KG) and the Academy of Finland (KK; grant numbers 294375 and 319237). A-EL and KK are HiLIFE Fellows at the University of Helsinki.

ACKNOWLEDGMENTS

We acknowledge Paula Hakala and Veronika Rezov for their skilled technical assistance, animal caretakers at the Laboratory Animal Center (University of Helsinki) for flexible cooperation and professional care of animals, Anne Rokka and Saara Tegelberg for technical advice, Tarja Joensuu, Saara Tegelberg, and Christopher Jackson for scientific advice. Mass spectrometry analysis and mass spectrometry data analysis were performed at the Turku Proteomics Facility, and at the Bioinformatics Unit at the Turku Centre for Biotechnology, University of Turku and Åbo Akademi University. The facilities are supported by Biocenter Finland.

SUPPLEMENTARY MATERIAL

The Supplementary Material for this article can be found online at: https://www.frontiersin.org/articles/10.3389/fnmol.2020.570640/full#supplementary-material

REFERENCES

Accardi, M. V., Brown, Patricia, M. G. E., Miraucourt, L. S., Orser, B. A., and Bowie, D. (2015). α6-Containing GABA(A) receptors are the principal mediators of inhibitory synapse strengthening by insulin in cerebellar granule cells. *J. Neurosci.* 35, 9676–9688. doi: 10.1523/JNEUROSCI.0513-15.2015

Agliardi, C., Guerini, F. R., Zanzottera, M., Riboldazzi, G., Zangaglia, R., Sturchio, A., et al. (2019). SNAP25 gene polymorphisms protect against Parkinson's disease and modulate disease severity in patients. *Mol. Neurobiol.* 56, 4455–4463. doi: 10.1007/s12035-018-1386-0

Altman, J. (1972). Postnatal development of the cerebellar cortex in the rat. II. Phases in the maturation of Purkinje cells and of the

molecular layer. *J. Comp. Neurol.* 145, 399–463. doi: 10.1002/cne.901450402

Arnold, B., Cassady, S. J., Van Laar, V. S., and Berman, S. B. (2011). Integrating multiple aspects of mitochondrial dynamics in neurons: age-related differences and dynamic changes in a chronic rotenone model. *Neurobiol. Dis.* 41, 189–200. doi: 10.1016/j.nbd.2010.09.006

Beltrán González, A. N., López Pazos, M. I., and Calvo, D. J. (2019). Reactive oxygen species in the regulation of the GABA mediated inhibitory neurotransmission. *Neuroscience* 4522, 30395–30401. doi: 10.1016/j.neuroscience.2019.05.064

Biagioli, M., Pinto, M., Cesselli, D., Zaninello, M., Lazarevic, D., Roncaglia, P., et al. (2009). Unexpected expression of alpha- and beta-globin in mesencephalic dopaminergic neurons and glial cells. *Proc. Natl. Acad. Sci. U.S.A.* 106, 15454–15459. doi: 10.1073/pnas.0813216106

Bourassa, C. V., Meijer, I. A., Merner, N. D., Grewal, K. K., Stefanelli, M. G., Hodgkinson, K., et al. (2012). VAMP1 mutation causes dominant hereditary spastic ataxia in Newfoundland families. *Am. J. Hum. Genet.* 91, 548–552. doi: 10.1016/j.ajhg.2012.07.018

Brakebusch, C., Seidenbecher, C. I., Asztely, F., Rauch, U., Matthies, H., Meyer, H., et al. (2002). Brevican-deficient mice display impaired hippocampal CA1 long-term potentiation but show no obvious deficits in learning and memory. *Mol. Cell. Biol.* 22, 7417–7427. doi: 10.1128/mcb.22.21.7417-7427.2002

Brenneke, F., Bukalo, O., Dityatev, A., and Lie, A. A. (2004). Mice deficient for the extracellular matrix glycoprotein tenascin-r show physiological and structural hallmarks of increased hippocampal excitability, but no increased susceptibility to seizures in the pilocarpine model of epilepsy. *Neuroscience* 124, 841–855. doi: 10.1016/j.neuroscience.2003.11.037

Brickley, S. G., Cull-Candy, S. G., and Farrant, M. (1996). Development of a tonic form of synaptic inhibition in rat cerebellar granule cells resulting from persistent activation of GABAA receptors. *J. Physiol.* 497(Pt 3), 753–759. doi: 10.1113/jphysiol.1996.sp021806

Burgalossi, A., Jung, S., Meyer, G., Jockusch, W. J., Jahn, O., Taschenberger, H., et al. (2010). SNARE protein recycling by αSNAP and βSNAP supports synaptic vesicle priming. *Neuron* 68, 473–487. doi: 10.1016/j.neuron.2010.09.019

Buzzi, A., Chikhladze, M., Falcicchia, C., Paradiso, B., Lanza, G., Soukupova, M., et al. (2012). Loss of cortical GABA terminals in Unverricht-Lundborg disease. *Neurobiol. Dis.* 47, 216–224. doi: 10.1016/j.nbd.2012.04.005

Canafoglia, L., Gennaro, E., Capovilla, G., Gobbi, G., Boni, A., Beccaria, F., et al. (2012). Electroclinical presentation and genotype-phenotype relationships in patients with Unverricht-Lundborg disease carrying compound heterozygous CSTB point and indel mutations. *Epilepsia* 53, 2120–2127. doi: 10.1111/j.1528-1167.2012.03718.x

Carta, M., Mameli, M., and Valenzuela, C. F. (2004). Alcohol enhances GABAergic transmission to cerebellar granule cells via an increase in Golgi cell excitability. *J. Neurosci.* 24, 3746–3751. doi: 10.1523/JNEUROSCI.0067-04.2004

Ceru, S., Konjar, S., Maher, K., Repnik, U., Krizaj, I., Bencina, M., et al. (2010). Stefin B interacts with histones and cathepsin L in the nucleus. *J. Biol. Chem.* 285, 10078–10086. doi: 10.1074/jbc.M109.034793

Cohen, N. R., Hammans, S. R., Macpherson, J., and Nicoll, J. A. R. (2011). New neuropathological findings in Unverricht-Lundborg disease: neuronal intranuclear and cytoplasmic inclusions. *Acta Neuropathol.* 121, 421–427. doi: 10.1007/s00401-010-0738-2

Conroy, J., Allen, N. M., Gorman, K. M., Shahwan, A., Ennis, S., Lynch, S. A., et al. (2016). NAPB - a novel SNARE-associated protein for early-onset epileptic encephalopathy. *Clin. Genet.* 89, E1–E3. doi: 10.1111/cge.12648

Danner, N., Julkunen, P., Khyuppenen, J., Hukkanen, T., Könönen, M., Säisänen, L., et al. (2009). Altered cortical inhibition in Unverricht-Lundborg type progressive myoclonus epilepsy (EPM1). *Epilepsy Res.* 85, 81–88. doi: 10.1016/j.eplepsyres.2009.02.015

Eldridge, R., Iivanainen, M., Stern, R., Koerber, T., and Wilder, B. J. (1983). "Baltic" myoclonus epilepsy: hereditary disorder of childhood made worse by phenytoin. *Lancet* 2, 838–842. doi: 10.1016/s0140-6736(83)90749-3

Elo, L. L., Filén, S., Lahesmaa, R., and Aittokallio, T. (2008). Reproducibility-optimized test statistic for ranking genes in microarray studies. *IEEE/ACM Trans. Comput. Biol. Bioinform.* 5, 423–431. doi: 10.1109/tcbb.2007.1078

Fatokun, A. A., Stone, T. W., and Smith, R. A. (2008). Oxidative stress in neurodegeneration and available means of protection. *Front. Biosci.* 13:3288–3311. doi: 10.2741/2926

Franceschetti, S., Sancini, G., Buzzi, A., Zucchini, S., Paradiso, B., Magnaghi, G., et al. (2007). A pathogenetic hypothesis of Unverricht-Lundborg disease onset and progression. *Neurobiol. Dis.* 25, 675–685. doi: 10.1016/j.nbd.2006.11.006

Gentleman, R. C., Carey, V. J., Bates, D. M., Bolstad, B., Dettling, M., Dudoit, S., et al. (2004). Bioconductor: open software development for computational biology and bioinformatics. *Genome Biol.* 5:R80. doi: 10.1186/gb-2004-5-10-r80

Guastella, J., Nelson, N., Nelson, H., Czyzyk, L., Keynan, S., Miedel, M. C., et al. (1990). Cloning and expression of a rat brain GABA transporter. *Science* 249, 1303–1306. doi: 10.1126/science.1975955

Haltia, M., Kristensson, K., and Sourander, P. (1969). Neuropathological studies in three Scandinavian cases of progressive myoclonus epilepsy. *Acta Neurol. Scand.* 45, 63–77. doi: 10.1111/j.1600-0404.1969.tb01220.x

Harigaya, Y., Shoji, M., Shirao, T., and Hirai, S. (1996). Disappearance of actin-binding protein, drebrin, from hippocampal synapses in Alzheimer's disease. *J. Neurosci. Res.* 43, 87–92. doi: 10.1002/jnr.490430111

Jensen, K., Chiu, C., Sokolova, I., Lester, H. A., and Mody, I. (2003). GABA transporter-1 (GAT1)-deficient mice: differential tonic activation of GABAA versus GABAB receptors in the hippocampus. *J. Neurophysiol.* 90, 2690–2701. doi: 10.1152/jn.00240.2003

Joensuu, T., Kuronen, M., Alakurtti, K., Tegelberg, S., Hakala, P., Aalto, A., et al. (2007). Cystatin B: mutation detection, alternative splicing and expression in progressive myclonus epilepsy of Unverricht-Lundborg type (EPM1) patients. *Eur. J. Hum. Genet.* 15, 185–193. doi: 10.1038/sj.ejhg.5201723

Joensuu, T., Lehesjoki, A. E., and Kopra, O. (2008). Molecular background of EPM1-Unverricht-Lundborg disease. *Epilepsia* 49, 557–563. doi: 10.1111/j.1528-1167.2007.01422.x

Joensuu, T., Tegelberg, S., Reinmaa, E., Segerstrale, M., Hakala, P., Pehkonen, H., et al. (2014). Gene expression alterations in the cerebellum and granule neurons of Cstb(-/-) mouse are associated with early synaptic changes and inflammation. *PLoS One* 9:e89321. doi: 10.1371/journal.pone.0089321

Johannesen, K. M., Gardella, E., Linnankivi, T., Courage, C., de Saint Martin, A., Lehesjoki, A. E., et al. (2018). Defining the phenotypic spectrum of SLC6A1 mutations. *Epilepsia* 59, 389–402. doi: 10.1111/epi.13986

Julkunen, P., Säisänen, L., Könönen, M., Vanninen, R., Kälviäinen, R., and Mervaala, E. (2013). TMS-EEG reveals impaired intracortical interactions and coherence in Unverricht-Lundborg type progressive myoclonus epilepsy (EPM1). *Epilepsy Res.* 106, 103–112. doi: 10.1016/j.eplepsyres.2013.04.001

Kälviäinen, R., Khyuppenen, J., Koskenkorva, P., Eriksson, K., Vanninen, R., and Mervaala, E. (2008). Clinical picture of EPM1-Unverricht-Lundborg disease. *Epilepsia* 49, 549–556. doi: 10.1111/j.1528-1167.2008.01546.x

Kaneda, M., Farrant, M., and Cull-Candy, S. G. (1995). Whole-cell and single-channel currents activated by GABA and glycine in granule cells of the rat cerebellum. *J. Physiol.* 485(Pt 2), 419–435. doi: 10.1113/jphysiol.1995.sp020739

Karunadharma, P. P., Basisty, N., Chiao, Y. A., Dai, D., Drake, R., Levy, N., et al. (2015). Respiratory chain protein turnover rates in mice are highly heterogeneous but strikingly conserved across tissues, ages, and treatments. *FASEB J.* 29, 3582–3592. doi: 10.1096/fj.15-272666

Kennedy, M. J., and Ehlers, M. D. (2006). Organelles and trafficking machinery for postsynaptic plasticity. *Annu. Rev. Neurosci.* 29, 325–362. doi: 10.1146/annurev.neuro.29.051605.112808

Khalili, K., Del Valle, L., Muralidharan, V., Gault, W. J., Darbinian, N., Otte, J., et al. (2003). Puralpha is essential for postnatal brain development and developmentally coupled cellular proliferation as revealed by genetic inactivation in the mouse. *Mol. Cell. Biol.* 23, 6857–6875. doi: 10.1128/mcb.23.19.6857-6875.2003

Koskenkorva, P., Hyppönen, J., Aikiä, M., Mervaala, E., Kiviranta, T., Eriksson, K., et al. (2011). Severer phenotype in Unverricht-Lundborg disease (EPM1) patients compound heterozygous for the dodecamer repeat expansion and the c.*202C*>T mutation in the CSTB gene. *Neurodegener. Dis.* 8, 515–522. doi: 10.1159/000323470

Koskenkorva, P., Khyuppenen, J., Niskanen, E., Könönen, M., Bendel, P., Mervaala, E., et al. (2009). Motor cortex and thalamic atrophy in Unverricht-Lundborg disease: voxel-based morphometric study. *Neurology* 73, 606–611. doi: 10.1212/WNL.0b013e3181b3888b

Koskenkorva, P., Niskanen, E., Hyppönen, J., Könönen, M., Mervaala, E., Soininen, H., et al. (2012). Sensorimotor, visual, and auditory cortical atrophy in Unverricht-Lundborg disease mapped with cortical thickness analysis. *AJNR Am. J. Neuroradiol.* 33, 878–883. doi: 10.3174/ajnr.A2882

Koskiniemi, M., Donner, M., Majuri, H., Haltia, M., and Norio, R. (1974). Progressive myoclonus epilepsy. A clinical and histopathological study. *Acta Neurol. Scand.* 50, 307–332.

Lalani, S. R., Zhang, J., Schaaf, C. P., Brown, C. W., Magoulas, P., Tsai, A. C., et al. (2014). Mutations in PURA cause profound neonatal hypotonia, seizures, and encephalopathy in 5q31.3 microdeletion syndrome. *Am. J. Hum. Genet.* 95, 579–583. doi: 10.1016/j.ajhg.2014.09.014

Lee, G. Y., You, D., Lee, H., Hwang, S. W., Lee, C. J., and Yoo, Y. D. (2018). Romo1 is a mitochondrial nonselective cation channel with viroporin-like characteristics. *J. Cell Biol.* 217, 2059–2071. doi: 10.1083/jcb.201709001

Lehtinen, M. K., Tegelberg, S., Schipper, H., Su, H., Zukor, H., Manninen, O., et al. (2009). Cystatin B deficiency sensitizes neurons to oxidative stress in progressive myoclonus epilepsy, EPM1. *J. Neurosci.* 29, 5910–5915. doi: 10.1523/JNEUROSCI.0682-09.2009

Liu, X., Rizzo, V., and Puthanveettil, S. (2012). Pathologies of axonal transport in neurodegenerative diseases. *Translat. Neurosci.* 3, 355–372. doi: 10.2478/s13380-012-0044-7

Maher, K., Jerič Kokelj, B., Butinar, M., Mikhaylov, G., Manček-Keber, M., Stoka, V., et al. (2014). A role for stefin B (cystatin B) in inflammation and endotoxemia. *J. Biol. Chem.* 289, 31736–31750. doi: 10.1074/jbc.M114.609396

Mancini, G. M. S., Schot, R., de Wit, Marie Claire, Y., de Coo, R. F., Oostenbrink, R., et al. (2016). CSTB null mutation associated with microcephaly, early developmental delay, and severe dyskinesia. *Neurology* 86, 877–878. doi: 10.1212/WNL.0000000000002422

Manninen, O., Koskenkorva, P., Lehtimäki, K. K., Hyppönen, J., Könönen, M., Laitinen, T., et al. (2013). White matter degeneration with Unverricht-Lundborg progressive myoclonus epilepsy: a translational diffusion-tensor imaging study in patients and cystatin B-deficient mice. *Radiology* 269, 232–239. doi: 10.1148/radiol.13122458

Metsalu, T., and Vilo, J. (2015). ClustVis: a web tool for visualizing clustering of multivariate data using principal component analysis and heatmap. *Nucleic Acids Res.* 43, W566–W570. doi: 10.1093/nar/gkv468

Mi, H., Muruganujan, A., Casagrande, J. T., and Thomas, P. D. (2013). Large-scale gene function analysis with the PANTHER classification system. *Nat. Protoc.* 8, 1551–1566. doi: 10.1038/nprot.2013.092

Nishi, H., Inagi, R., Kato, H., Tanemoto, M., Kojima, I., Son, D., et al. (2008). Hemoglobin is expressed by mesangial cells and reduces oxidant stress. *J. Am. Soc. Nephrol.* 19, 1500–1508. doi: 10.1681/ASN.2007101085

Nolt, M. J., Lin, Y., Hruska, M., Murphy, J., Sheffler-Colins, S. I., Kayser, M. S., et al. (2011). EphB controls NMDA receptor function and synaptic targeting in a subunit-specific manner. *J. Neurosci.* 31, 5353–5364. doi: 10.1523/JNEUROSCI.0282-11.2011

Norton, M., Ng, A. C., Baird, S., Dumoulin, A., Shutt, T., Mah, N., et al. (2014). ROMO1 is an essential redox-dependent regulator of mitochondrial dynamics. *Sci. Signal.* 7:ra10. doi: 10.1126/scisignal.2004374

Nystuen, A. M., Schwendinger, J. K., Sachs, A. J., Yang, A. W., and Haider, N. B. (2007). A null mutation in VAMP1/synaptobrevin is associated with neurological defects and prewean mortality in the lethal-wasting mouse mutant. *Neurogenetics* 8, 1–10. doi: 10.1007/s10048-006-0068-7

O'Brien, A., Marshall, C. R., Blaser, S., Ray, P. N., and Yoon, G. (2017). Severe neurodegeneration, progressive cerebral volume loss and diffuse hypomyelination associated with a homozygous frameshift mutation in CSTB. *Eur. J. Hum. Genet.* 25, 775–778. doi: 10.1038/ejhg.2017.39

Okuneva, O., Korber, I., Li, Z., Tian, L., Joensuu, T., Kopra, O., et al. (2015). Abnormal microglial activation in the Cstb(-/-) mouse, a model for progressive myoclonus epilepsy, EPM1. *Glia* 63, 400–411. doi: 10.1002/glia.22760

Penna, E., Cerciello, A., Chambery, A., Russo, R., Cernilogar, F. M., Pedone, E. M., et al. (2019). Cystatin B involvement in synapse physiology of rodent brains and human cerebral organoids. *Front. Mol. Neurosci.* 12:195. doi: 10.3389/fnmol.2019.00195

Pennacchio, L. A., Bouley, D. M., Higgins, K. M., Scott, M. P., Noebels, J. L., and Myers, R. M. (1998). Progressive ataxia, myoclonic epilepsy and cerebellar apoptosis in cystatin B-deficient mice. *Nat. Genet.* 20, 251–258. doi: 10.1038/3059

Pennacchio, L. A., Lehesjoki, A. E., Stone, N. E., Willour, V. L., Virtaneva, K., Miao, J., et al. (1996). Mutations in the gene encoding cystatin B in progressive myoclonus epilepsy (EPM1). *Science* 271, 1731–1734. doi: 10.1126/science.271.5256.1731

R Core Team (2016). *R: A Language and Environment for Statistical Computing*. Vienna: R Foundation for Statistical Computing.

Rossi, D. J., Hamann, M., and Attwell, D. (2003). Multiple modes of GABAergic inhibition of rat cerebellar granule cells. *J. Physiol.* 548(Pt 1), 97–110. doi: 10.1113/jphysiol.2002.036459

Shannon, P., Markiel, A., Ozier, O., Baliga, N. S., Wang, J. T., Ramage, D., et al. (2003). Cytoscape: a software environment for integrated models of biomolecular interaction networks. *Genome Res.* 13, 2498–2504. doi: 10.1101/gr.1239303

Shen, X., Scola, R. H., Lorenzoni, P. J., Kay, C. S. K., Werneck, L. C., Brengman, J., et al. (2017). Novel synaptobrevin-1 mutation causes fatal congenital myasthenic syndrome. *Ann. Clin. Transl. Neurol.* 4, 130–138. doi: 10.1002/acn3.387

Silver, R. A., Traynelis, S. F., and Cull-Candy, S. G. (1992). Rapid-time-course miniature and evoked excitatory currents at cerebellar synapses in situ. *Nature* 355, 163–166. doi: 10.1038/355163a0

Sipilä, S. T., Huttu, K., Soltesz, I., Voipio, J., and Kaila, K. (2005). Depolarizing GABA Acts on intrinsically bursting pyramidal neurons to drive giant depolarizing potentials in the immature hippocampus. *J. Neurosci.* 25, 5280–5289. doi: 10.1523/JNEUROSCI.0378-05.2005

Steward, O., and Schuman, E. M. (2001). Protein synthesis at synaptic sites on dendrites. *Annu. Rev. Neurosci.* 24, 299–325. doi: 10.1146/annurev.neuro.24.1.299

Suzdak, P. D., Frederiksen, K., Andersen, K. E., Sørensen, P. O., Knutsen, L. J., and Nielsen, E. B. (1992). NNC-711, a novel potent and selective gamma-aminobutyric acid uptake inhibitor: pharmacological characterization. *Eur. J. Pharmacol.* 224, 189–198. doi: 10.1016/0014-2999(92)90804-d

Szklarczyk, D., Gable, A. L., Lyon, D., Junge, A., Wyder, S., Huerta-Cepas, J., et al. (2019). STRING v11: protein-protein association networks with increased coverage, supporting functional discovery in genome-wide experimental datasets. *Nucleic Acids Res.* 47, D607–D613. doi: 10.1093/nar/gky1131

Takayama, C., and Inoue, Y. (2005). Developmental expression of GABA transporter-1 and 3 during formation of the GABAergic synapses in the mouse cerebellar cortex. *Brain Res. Dev. Brain Res.* 158, 41–49. doi: 10.1016/j.devbrainres.2005.05.007

Tang, J., Oliveros, A., and Jang, M. (2019). Dysfunctional mitochondrial bioenergetics and synaptic degeneration in Alzheimer disease. *Int. Neurourol. J.* 23(Suppl. 1), S5–S10. doi: 10.5213/inj.1938036.018

Tegelberg, S., Kopra, O., Joensuu, T., Cooper, J. D., and Lehesjoki, A. E. (2012). Early microglial activation precedes neuronal loss in the brain of the Cstb-/- mouse model of progressive myoclonus epilepsy, EPM1. *J. Neuropathol. Exp. Neurol.* 71, 40–53. doi: 10.1097/NEN.0b013e31823e68e1

Turk, V., Stoka, V., and Turk, D. (2008). Cystatins: biochemical and structural properties, and medical relevance. *Front. Biosci.* 13:5406–5420. doi: 10.2741/3089

Van Laar, V. S., Arnold, B., Howlett, E. H., Calderon, M. J., St. Croix, C. M., Greenamyre, J. T., et al. (2018). Evidence for compartmentalized axonal mitochondrial biogenesis: mitochondrial DNA replication increases in distal axons as an early response to parkinson's disease-relevant stress. *J. Neurosci.* 38, 7505–7515. doi: 10.1523/JNEUROSCI.0541-18.2018

Vizcaíno, J. A., Côté, R. G., Csordas, A., Dianes, J. A., Fabregat, A., Foster, J. M., et al. (2013). The PRoteomics IDEntifications (PRIDE) database and associated tools: status in 2013. *Nucleic Acids Res.* 41, D1063–D1069. doi: 10.1093/nar/gks1262

von Eichborn, J., Dunkel, M., Gohlke, B. O., Preissner, S. C., Hoffmann, M. F., Bauer, J. M. J., et al. (2013). SynSysNet: integration of experimental data on synaptic protein-protein interactions with drug-target relations. *Nucleic Acids Res.* 41, D834–D840. doi: 10.1093/nar/gks1040

Wall, M. J., and Usowicz, M. M. (1997). Development of action potential-dependent and independent spontaneous GABAA receptor-mediated currents

in granule cells of postnatal rat cerebellum. *Eur. J. Neurosci.* 9, 533–548. doi: 10.1111/j.1460-9568.1997.tb01630.x

Wang, Y., Branicky, R., Noë, A., and Hekimi, S. (2018). Superoxide dismutases: dual roles in controlling ROS damage and regulating ROS signaling. *J. Cell Biol.* 21, 1915–1928. doi: 10.1083/jcb.201708007

Westbury, S. K., Shoemark, D. K., and Mumford, A. D. (2017). ACTN1 variants associated with thrombocytopenia. *Platelets* 28, 625–627. doi: 10.1080/09537104.2017.1356455

Xi, Z., Deng, W., Wang, L., Xiao, F., Li, J., Wang, Z., et al. (2015). Association of alpha-soluble NSF attachment protein with epileptic seizure. *J. Mol. Neurosci.* 57, 417–425. doi: 10.1007/s12031-015-0596-4

Conflict of Interest: The authors declare that the research was conducted in the absence of any commercial or financial relationships that could be construed as a potential conflict of interest.

frontiers in Molecular Neuroscience

MINI REVIEW
published: 23 December 2020
doi: 10.3389/fnmol.2020.564446

Recent Developments in Data Independent Acquisition (DIA) Mass Spectrometry: Application of Quantitative Analysis of the Brain Proteome

Ka Wan Li, Miguel A. Gonzalez-Lozano, Frank Koopmans and August B. Smit*

Department of Molecular and Cellular Neurobiology, Center for Neurogenomics and Cognitive Research, Amsterdam Neuroscience, Faculty of Science, Vrije Universiteit Amsterdam, Amsterdam, Netherlands

Mass spectrometry is the driving force behind current brain proteome analysis. In a typical proteomics approach, a protein isolate is digested into tryptic peptides and then analyzed by liquid chromatography–mass spectrometry. The recent advancements in data independent acquisition (DIA) mass spectrometry provide higher sensitivity and protein coverage than the classic data dependent acquisition. DIA cycles through a pre-defined set of peptide precursor isolation windows stepping through 400–1,200 m/z across the whole liquid chromatography gradient. All peptides within an isolation window are fragmented simultaneously and detected by tandem mass spectrometry. Peptides are identified by matching the ion peaks in a mass spectrum to a spectral library that contains information of the peptide fragment ions' pattern and its chromatography elution time. Currently, there are several reports on DIA in brain research, in particular the quantitative analysis of cellular and synaptic proteomes to reveal the spatial and/or temporal changes of proteins that underlie neuronal plasticity and disease mechanisms. Protocols in DIA are continuously improving in both acquisition and data analysis. The depth of analysis is currently approaching proteome-wide coverage, while maintaining high reproducibility in a stable and standardisable MS environment. DIA can be positioned as the method of choice for routine proteome analysis in basic brain research and clinical applications.

Keywords: proteomics, neuroscience, brain, synapse, LC-MS, quantitative analyses

OPEN ACCESS

Edited by:
Matthew L. MacDonald, University of Pittsburgh, United States

Reviewed by:
Maciej Maurycy Lalowski, University of Helsinki, Finland
Elena V. Romanova, University of Illinois at Urbana-Champaign, United States
Lindsay K. Pino, University of Pennsylvania, United States

****Correspondence:***
Ka Wan Li
k.w.li@vu.nl

Received: *21 May 2020*
Accepted: *02 December 2020*
Published: *23 December 2020*

Citation:
Li KW, Gonzalez-Lozano MA, Koopmans F and Smit AB (2020) Recent Developments in Data Independent Acquisition (DIA) Mass Spectrometry: Application of Quantitative Analysis of the Brain Proteome. Front. Mol. Neurosci. 13:564446. doi: 10.3389/fnmol.2020.564446

INTRODUCTION

The brain is the most complex organ in the human body. It consists of about 85 billion neurons of different types, and an equal number of non-neuronal cells (Herculano-Houzel, 2009). The neurons communicate within the central nervous system and with the body periphery through the use of hundreds of trillions of synapses for neurotransmission. In support of these, glia cells nourish the brain and in part regulate neurotransmission (Allen, 2014). The brain's computational capacity to act as signal receiver, integrator, and output device crucially depends on its neuronal network connectivity and synaptic features (Caroni et al., 2012). In particular, activity-dependent plasticity of synapses in specific brain regions is thought to underlie learning and memory

(von Engelhardt et al., 2010; Humeau and Choquet, 2019), whereas aberrant spatial-temporal changes of cells and synapses/organelles are underlying causes of psychiatric and neurodegenerative disorders (Counotte et al., 2011; Kanellopoulos et al., 2020).

Over the last decade, advances in mass spectrometry-based proteomics have contributed significantly to the understanding of the underlying molecular mechanisms at stake in health and disease. In particular, proteomics has been extensively used to catalog protein constituents, specifically the synapse. More recently, quantitative proteomics that interrogates thousands of proteins has been applied to examine specific regions of the brain (Sharma et al., 2015), synaptic proteomes (Biesemann et al., 2014; Loh et al., 2016; Pandya et al., 2017), neurodegenerative brain tissues (Hondius et al., 2016; Li et al., 2019; Bai et al., 2020; Johnson et al., 2020), and cell cultures (Frese et al., 2017). Although data dependent acquisition (DDA) has been the most commonly used comprehensive and quantitative proteomics methodology, more recently, data independent acquisition (DIA) has gained popularity due to its improved detection and quantitation. Multiplexed proteomics, based on isobaric mass tags such as the commercially available iTRAQ and TMT reagents, is another popular quantitative proteomics technology that allows the simultaneous identification and quantitation of up to 16 samples (using TMTpro 16-plex labeling reagents). This method is outside the scope of the present review; we refer the reader to another recent review (Pappireddi et al., 2019).

QUANTITATIVE PROTEOMICS BY DATA DEPENDENT ACQUISITION (DDA)

Proteomics critically depends on the use of a mass spectrometer (MS) with good mass accuracy and high sensitivity. In a typical proteomics approach, proteins biochemically extracted from the tissue or organelle of interest are enzymatically digested into tryptic peptides. Peptides are fractionated by liquid chromatography (LC), usually based on their hydrophobicity on a reversed phase column. The eluted peptides are electro-sprayed online into the MS for analysis.

DDA has been the predominant method for quantitative proteomics. The eluted peptides from LC are detected by first stage MS1 generally within a mass range 400–1,200 m/z. A fixed number of most abundant peptides are then selected sequentially for second stage tandem mass spectrometry (MS/MS). Depending on the scan speed and sensitivity of the MS, 3–20 MS/MS can be performed in each cycle. Once the high intensity peak has been sequenced it will be excluded for re-analysis so that less abundant peptides can be identified. MS/MS of each selected precursor generates a fragment ion spectrum, which can be compared to all predicted fragments for all hypothetical peptides of the appropriate molecular mass. The most common format for this protein sequence database is the FASTA format. Each peptide match can then be linked to its corresponding protein.

In case there are more co-eluted peptides than the maximum number of MS/MS performed, the less abundant ones would not be selected for MS/MS and escape identification (Michalski et al., 2011). Furthermore, due to the semi-stochastic nature of precursor selection for MS/MS, each peptide may not be consistently detected in all samples, resulting in many missing values.

A single cycle of MS1 and MS/MS analysis usually takes 2–3 s, but it can vary depending on the LC-MS configuration. The MS switches back to the MS1 to detect and quantify the peptides and repeat the sequential MS/MS analysis. For accurate quantitation, enough data points should be acquired to accurately observe each peptide's elution profile. The total peptide peak area under the MS1 elution profile represents the quantity of the peptide. An alternative method is spectral counting where quantification of a protein relies on the number of spectra identified. The run time per LC-MS/MS is often between 0.5 and 2 h, but longer run times have also been reported that could increase the number of identified proteins (Muntel et al., 2019).

DATA INDEPENDENT ACQUISITION (DIA) IS EMERGING AS METHOD OF CHOICE FOR QUANTITATIVE PROTEOMICS

DIA (Ludwig et al., 2018; Zhang et al., 2020), also known as SWATH (Liu et al., 2013), enables the quantitation of thousands of proteins with low variation and high reproducibility, as demonstrated in a multi-laboratory evaluation study (Collins et al., 2017). In principle, DIA interrogates all peptides within the selected m/z windows, typically between 400 and 1,200 m/z, that contain >90% of all tryptic peptides (Koopmans et al., 2018a; Pino et al., 2020). First, the MS1 scans the entire mass range in one go. In the MS/MS mode, the precursor isolation window of 25 m/z is initially set at, for example, 400–425 m/z. All the peptides within this mass range would be fragmented and detected simultaneously for 50–100 ms. Then, the isolation window steps up by another 25 m/z to 425–450 m/z for peptide fragmentation and detection. This process repeats 32 times, stepping through the whole mass range. A single cycle of MS1 and MS/MS usually takes 3 s, and cycles through the whole LC gradient. As MS/MS fragments, all the peptide precursors within a mass range of interest are used, and a highly complex fragment ion mass spectrum is generated. This is challenging for data analysis using a conventional genome-wide species-specific database. While proteins from DIA data can be identified by using a search engine, such as DIA-Umpire (Tsou et al., 2015), PECAN (Ting et al., 2017), or DirectDIA (Koopmans et al., 2018a; Muntel et al., 2019) in Spectronaut, a higher coverage of protein identities is achieved when the search is performed with a project-specific spectral library (Koopmans et al., 2018a). A project-specific spectral library is typically acquired from multiple fractionated DDA analysis of the same type of sample on the same instrument, and searched against a protein sequence database to identify peptides. The library is comprised of the elution time of each identified peptide and its fragment ions' pattern. Matching of the elution time and fragment ions' pattern from the DIA data to the spectral library aids with peptide

detection. DIA MS/MS quantification is reported as the sum of the integrated fragment ion peak areas.

For a complex sample, the 25 m/z window may contain too many peptides that could create an interference problem, i.e., some fragment ions from different co-eluted precursors may have very similar masses and be difficult to distinguish. Furthermore, the fragment ion intensities of the lower abundant peptides may be suppressed. For this reason, current DIA protocols often use isolation windows <10 m/z. However, this narrower isolation window requires more MS/MS steps per cycle to cover the same overall m/z range, which increases the cycle time and therefore reduces the number of measurement points per peptide. This could compromise quantitation. An alternative is to use variable isolation windows. For example, a narrower window is set for mass ranges within 400–800 m/z because the majority of peptides are contained in this mass range, and a wider window for >800 m/z that has a lower peptide complexity.

DIA is finding various applications in brain research (**Figure 1**). An early study examined the synaptic proteome in Alzheimer's disease patients (Chang et al., 2015), however, it still had to rely on the use of a sub-optimal data analysis tool. Easy to use and reliable DIA analysis platforms have since been launched, in particular the popular commercial software Spectronaut (Bruderer et al., 2015), the open-source OpenSWATH (Rost et al., 2014), EncyclopeDIA (Searle et al., 2018), Skyline (Egertson et al., 2015), the more recently developed DIA-NN (Demichev et al., 2020), DIA-Umpire that allows DirectDIA (Tsou et al., 2015), and more [see overview in Zhang et al. (2020)].

APPLICATION OF DIA FOR BRAIN RESEARCH

DIA has been applied successfully for the comparative analysis of hippocampal synaptosome preparations from two rodent and two primate species (Koopmans et al., 2018b). A time-of-flight mass spectrometer was used for the measurement. The spectral library contained about 3,600 proteins that were generated from the same samples and measured on the same mass spectrometer operated in DDA mode. Peptides that were unique to one species were excluded for data analysis, resulting in the full comparative quantification of about 2,000 proteins. When comparing mouse with human, there were 644 proteins with higher abundance in human and 663 proteins with higher abundance in mouse. Of particular note were the sodium channels, in which specific subunits had a strong differential expression profile between rodents and primates. As sodium channels are involved in the formation and propagation of action potentials, the differences in expression pattern may qualify them for the distinct physiology of human neurons (Testa-Silva et al., 2014). When considering the changes globally, the differentially expressed proteins were highly enriched for synaptic plasticity-related processes. A similar mouse synaptosome preparation has also been analyzed by another high-end mass spectrometer, the Orbitrap Fusion Lumos, using a similar LC gradient as the previous experiment. About 4,600 proteins were quantified by DIA from a spectral library of about 5,000 proteins (Koopmans et al., 2018a), demonstrating the increase in protein coverage from technological advancement.

DIA has also been used for the analysis of whole cell lysates that are more complex than isolated organelles. Two recent studies have reported protein changes in primary neuronal culture after knockdown of candidate genes of interest (Rosato et al., 2019) or overexpression of a microRNA (He et al., 2018) related to schizophrenia. Currently, there are >100 known independent genetic risk loci associated with schizophrenia (Schizophrenia Working Group of the Psychiatric Genomics, 2014), but their contribution to the disease is unclear. Rosato et al. (2019) examined the neuronal phenotypes by knocking down 41 risk genes each by shRNA, and showed that three of them, Tcf4, Tbr1, and Top3b, caused similar changes in synaptic development. DIA analysis of the neuronal cultures with the individual knockdown of these three genes revealed limited overlap in protein changes. Interestingly, when the effect of Tcf4, Tbr1, and Top3b knockdown of all 210 regulated proteins was taken together, protein-protein interaction enrichment analysis identified a set of proteins involved in neurotransmitter release, including the core proteins SNAP25, SNAP29, NAPB, STX7, and STXBP5. This strongly suggests that polygenic risk in schizophrenia may converge onto common cellular pathways. The mir-137 locus is another genetic risk factor for schizophrenia. He et al. (2018) overexpressed mir-137 in primary neuronal culture, and showed by DIA that the proteins that changed significantly were enriched for cell adhesion and cell development, including NFASC, NLGN, NRXN, and HAPLN. Together with the electrophysiological and morphological data, it was concluded that mir-137 regulates synaptic function by regulating synaptogenesis, synaptic ultrastructure, and synapse function.

A recent study has used DIA to quantify the dynamics of a thousand surface N-glycoproteins in primary cortical neurons at 4, 6, 8, 16, 18, and 20 days *in vitro* (van Oostrum et al., 2020). Most surface protein abundance changes occurred within the first week prior to the time window for synapse formation. Interestingly, many synaptic proteins were present on the surface at the time when synapse counts began to increase, and they reached peak abundance 2 days before the peak of synapse counts at 18 days *in vitro*. This suggests that many synaptic proteins are produced and trafficked to the membrane surface before synapses are formed and only later are these proteins organized into synaptic micro-domains by surface diffusion. In another experimental paradigm that induced synaptic scaling by activation or inhibition of neuronal activity, about 30% of the surface proteins showed significant changes whereas total proteome showed <10% significant changes. This also suggests an extensive dynamic reorganization of the neuronal membrane surface that is largely independent of global protein abundance change. Both these studies demonstrate the successful implementation of DIA in the neuroscience field.

DIA is capable of analyzing very complex samples, such as a brain tissue extract. Bruderer (Bruderer et al., 2017) optimized the DIA protocol with a Q-Exactive HF mass spectrometer to examine the developmental changes of about 6,000 proteins in mouse somatosensory cortex 1-barrel field at P9, P15, P30,

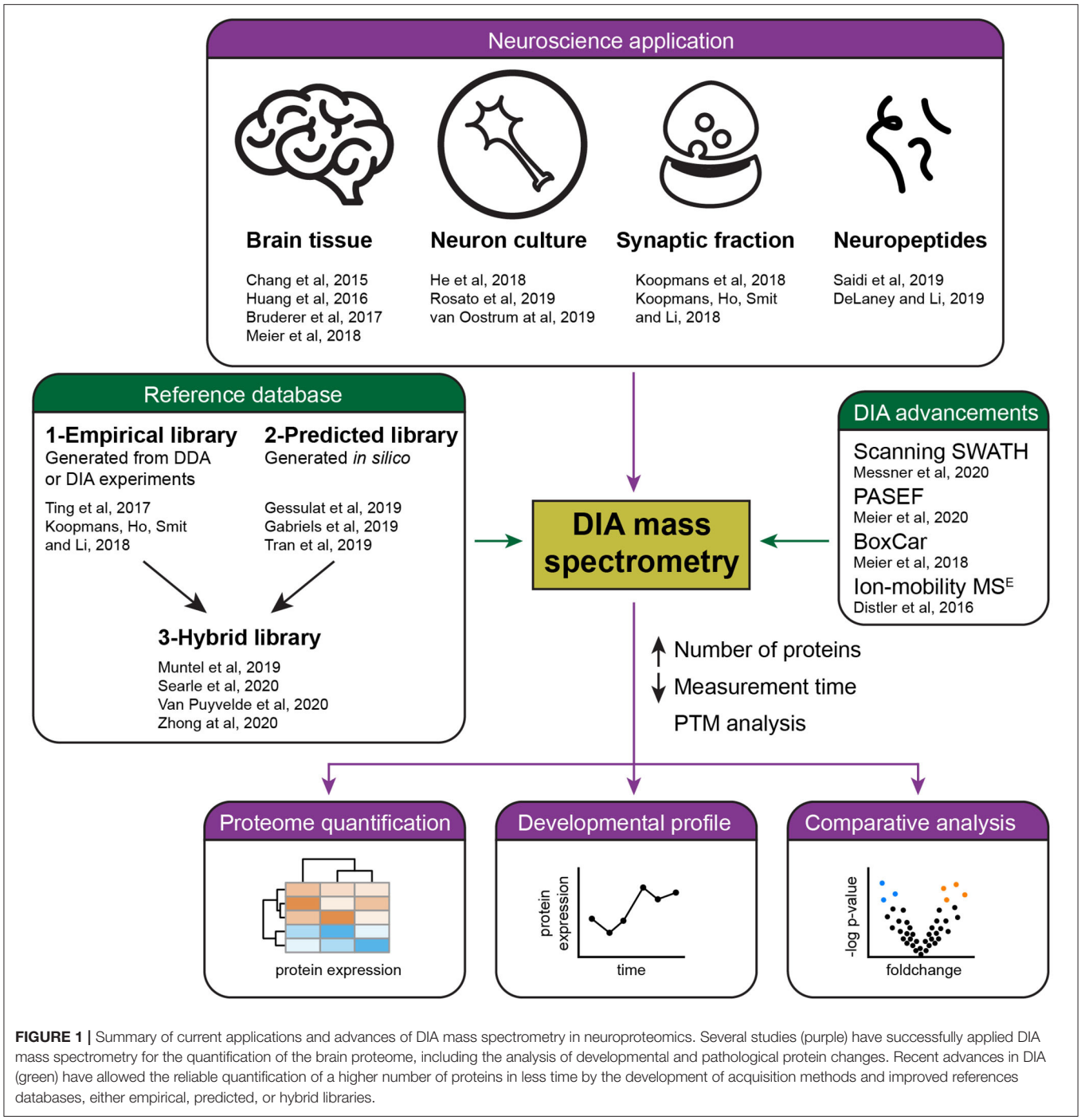

FIGURE 1 | Summary of current applications and advances of DIA mass spectrometry in neuroproteomics. Several studies (purple) have successfully applied DIA mass spectrometry for the quantification of the brain proteome, including the analysis of developmental and pathological protein changes. Recent advances in DIA (green) have allowed the reliable quantification of a higher number of proteins in less time by the development of acquisition methods and improved references databases, either empirical, predicted, or hybrid libraries.

and P54. During early development, synaptic transmission-related proteins displayed a strong increase in expression and leveled off thereafter. Proteins of the mitochondrial respiratory chain showed a smooth increase over the whole developmental period. The down regulated proteins belonged to functional groups involved in axonogenesis, RNA splicing, or UBL conjugation processes.

DIA has also found application in some specific research fields, including the analysis of neuropeptides in mammals (Saidi et al., 2019) and in invertebrate model systems (DeLaney and Li, 2019), and the reporting of increase in detection of G-protein coupled receptors when a targeted virtual library is applied on top of the original project-specific spectral library (Lou et al., 2020).

RECENT ADVANCEMENT OF DIA

DIA is rapidly improving and approaching proteome-wide levels of detection. Advancements are achieved through better

acquisition protocols and innovative computational data analysis (**Figure 1**), in conjunction with increased MS sensitivity and scan rate.

An early form of DIA, the MS^E, was first introduced in 2005 (Silva et al., 2005). It uses a wide band-pass filter for precursor selection, resulting in highly complex fragment ion spectra in MS^E workflows that is challenging for data analysis. More recently, the coupling of an ion-mobility device to the mass spectrometer offers the possibility to fragment precursor ions after ion-mobility separation, thereby reducing complexity. Furthermore, the ramping of collision energies according to ion mobility improved the fragmentation efficiency and hence peptide identification rates (Distler et al., 2016). MS^E has been applied to study the effect of hippocampal proteins with the goal of determining protein alteration associated with low-dose whole body ionizing radiation on the changes of the hippocampal proteome. Out of about 400 identified proteins, about 70 have shown significant alteration (Huang et al., 2016). Using a similar approach, more than 2,000 proteins have been identified from post-synaptic density (Distler et al., 2014).

Recent algorithmic developments led to predicted spectral libraries that can be used instead of empirical libraries, with a performance on par in some settings/situations. Furthermore, the combined use of the predicted and empirical spectral libraries seems to improve the search results. Deep-learning-based models (Zhou et al., 2017; Gabriels et al., 2019; Tran et al., 2019) with neural networks have been applied on large DDA datasets to learn features of peptide fragment ions and their chromatographic retention time. For example, Prosit (Gessulat et al., 2019) used the ProteomeTools resource that contains 21,764,501 high-quality spectra from 576,256 unique precursors belonging to the synthetic peptide library that together covers 19,749 of the 20,040 human protein coding genes. The training enables subsequent prediction of relative intensities of peptide fragments and retention time, from which an extensive and precise predicted spectral library can be generated. One caveat to use all possible tryptic peptides in a database is its huge number contributing to false discovery rate correction, while the majority of the peptides are not detected. To mitigate this problem a hybrid method has been developed. A subset of the biological samples is analyzed by DIA with a narrow precursor isolation window and searched with the predicted spectral library (Searle et al., 2020; Van Puyvelde et al., 2020). The resulting data forms an empirically corrected library for database search. As the DIA injections for the empirically corrected library uses the same acquisition parameters, chromatographic conditions, and sample matrix as quantitative single injection DIA experiments, it gives an improved peptide detection rate over searching a project-specific DDA library. Recently, the deep learning model for spectrum prediction has been extended to include the post-translation modifications of the peptides (Zeng et al., 2019). An alternative strategy is to construct a hybrid library from the combined project-specific library with the directDIA analysis (Muntel et al., 2019; Zhong et al., 2020). With a LC gradient of 4 h or longer in a single shot analysis, >10,000 proteins have been quantified with the hybrid library at 1% protein FDR (Muntel et al., 2019).

The dynamic post-translation modification is an important molecular event that may change the properties of the protein, such as its activity, stability, subcellular localization, and interactions with other proteins. DIA is applicable to quantify post-translational modifications at a high throughput manner, as exemplified by a recent study (Bekker-Jensen et al., 2020). The phosphoproteome of retinal pigment epithelium cells was analyzed from 200 μg of whole-cell tryptic digests and enriched by Ti-IMAC. A short run time with 15-min liquid chromatography gradients identified about 20,000 phosphopeptides by DDA. The number of phosphopeptides was substantially increased to about 30,000 using a project-specific spectral library.

In addition, there are other less explored but equally promising DIA methodologies. In Scanning SWATH, precursor ions are fragmented using a "scanning" isolation window of 5 m/z, which is continuously scanned with the first quadrupole rather than the conventional DIA that used the stepwise windowed acquisition. The workflow quantified 2000–3000 proteins in 5–10 min run-time and can measure around 180 samples/day (https://doi.org/10.1101/656793). In another study, DIA has been coupled to the "parallel accumulation followed by serial fragmentation" in a trapped ion mobility quadrupole-TOF mass spectrometer for diaPASEF analysis (https://doi.org/10.1101/656207). Using a 17-min gradient separation (50 samples per day), about 6,000 proteins were quantified per sample. Higher throughput is feasible with 5 min gradients (180 samples per day), but the protein identification is then decreased to about 2,800 proteins. When a high resolution-high mass accuracy MS is used, DIA can be measured at the MS1 level, for example using WiSIM (Koopmans et al., 2018a) and BoxCar (Meier et al., 2018). In particular, the BoxCar-library-based workflow was shown to identify 10,000 protein groups from the mouse cerebellum extract in a single shot 100 min MS run (Meier et al., 2018).

ALTERNATIVE METHODOLOGIES APPLICABLE TO QUANTITATIVE PROTEOMICS

It is reported that DIA is superior to DDA in reproducibility, specificity, and accuracy of relative protein quantification (Barkovits et al., 2020). Nevertheless, the apparent deficit of DDA can be offset with innovations in data analysis. The IonStar software demonstrated the quantification of 7,000 proteins in 100 brain samples with no missing data (Shen et al., 2018). A recent study demonstrated that using a spectral library search in DDA, in a manner similar to a DIA data analysis strategy, led to substantial improvement of reproducibility in protein identification and quantitation with lower coefficient of variation and reduced missing values (Fernandez-Costa et al., 2020).

In cases where a spectral library may not be readily obtainable, for instance when only limited input samples are available, DDA could be a better analysis choice. The use of a mass spectrometer gas phase cleavable chemical crosslinker to examine protein-protein interactions has recently been successfully applied to elucidate a global protein interactome in the synapse; around

12,000 unique lysine crosslinks from 2,362 proteins were identified (Gonzalez-Lozano et al., 2020). Given the stochastic nature of intra- and inter-protein crosslinking events at various lysine sites, a single spectral library for their identification is not favorable and therefore DDA was used. In experiments where the identification of peptides is the main goal, DDA is generally the method of choice.

Recently, proteomics analysis at the single cell level has been demonstrated, where isobaric labeling of samples with TMT measured by DDA improved sensitivity by the stacking effect of pooling TMT-labeled samples, in addition to the increase in through-put from the simultaneous analysis of multiple samples (Dou et al., 2019; Tsai et al., 2020).

For peptides specific to a low abundant protein-isoform or post-translational modifications present in a highly complex background, such as total tissue lysate, DIA may not have enough sensitivity and specificity for their detection and quantitation. In these cases, a targeted DIA strategy, the parallel reaction monitoring assay (Rauniyar, 2015), that focuses on tens to hundreds of pre-defined peptides and provides several fold higher sensitivity than DIA, could be a better choice, but only for the selected proteins of interest.

Therefore, for quantitative proteomics to be optimal the selection of a method, and specifically the advantages and limitations for the analysis of the samples, needs consideration. Isobaric multiplexing with isobaric labeling is advantageous for quantitation of a small sample size that matches the number of the available tags, for example a maximum of eight samples for iTRAQ and 16 for TMT. DDA is the method for label-free quantitation and is especially useful for experimental designs with only a few samples or specific applications, such as crosslink experiments. A parallel reaction monitoring assay has the highest sensitivity and specificity, and can be adopted for high throughput workflow on selected peptides/proteins. DIA is applicable to general quantitative proteomics. Due to its low missing value and good reproducibility, DIA has good potential for large-scale quantitative proteomics.

CONCLUSION AND FUTURE OUTLOOK

When is DIA the method of choice, and how could it advance our knowledge of brain function and disorders? Previous studies demonstrated the general applicability of DIA for neuroscience studies, including the analysis of the synapse, primary neuronal culture, brain tissues, human stem cells derived neurons and glial cells, and the dynamics of neuronal membrane proteins. These studies characterized the proteomes from mostly large populations of organelles or cells. For example, the synapse proteome characterized by proteomics is an average of all synapses isolated from a brain region (Pandya et al., 2017; Koopmans et al., 2018b). However, the size, shape, and functioning of synapses changes with neuronal activity, implicating compositional adaptation of their proteomes (Mansilla et al., 2018; Kulik et al., 2019). Important questions that have remained unanswered relate to the extent of the molecular diversity of synapses and how changes in synapse protein composition connect to neurological and psychiatric disorders. As DIA can be used for the analysis of multiple samples while maintaining good reproducibility and a low number of missing values, it would be used for systematic interrogation of these organelles under various conditions. Similar strategies will be applied to the studies of specific cell types and their proteome changes.

Considering that DIA has high-throughput capability with deep proteome analysis and good sensitivity, it is an advantageous method to be integrated in a platform for large-scale biomarker studies. For example, cerebrospinal fluid and blood proteome may be measured in a clinical environment as a routine diagnostical screen to reveal brain disorders and their disease stages. The feasibility to perform such large-scale analysis was recently demonstrated on the analysis of nearly 200 cerebrospinal fluid samples from Alzheimer's disease patients and healthy controls. Each DIA experiment quantified approximately a thousand proteins from a few microliters of sample (Bader et al., 2020). In the future, standardization of DIA protocols should be developed and adopted by large communities for meaningful comparison and interpretation of data, and to minimize batch effects across different laboratories.

Neurological and psychiatric disorders are frequently heterogeneous in nature. Each may further exhibit typical spatio-temporal malfunctions in the brain. Often, large sample sizes are necessary to reveal the global and subtype-specific analysis of the diseases. DIA, with its high reproducibility and low missing values, and good coverage of the proteome, is the preferred choice for such analysis. To accommodate comparative analysis of high numbers of samples, multi-laboratory projects would benefit from DIA. To be successful, standardization of protocols and hardware used for data acquisition, and the unified downstream data analysis, should be firmly established.

AUTHOR CONTRIBUTIONS

KL wrote the manuscript. MG-L drew the figure and critically reviewed the manuscript. FK provided input on all aspects of proteomics/DIA. AS assisted the writing of the manuscript. All authors contributed to the article and approved the submitted version.

REFERENCES

Allen, N. J. (2014). Synaptic plasticity: astrocytes wrap it up. *Curr. Biol.* 24, R697–699. doi: 10.1016/j.cub.2014.06.030

Bader, J. M., Geyer, P. E., Muller, J. B., Strauss, M. T., Koch, M., Leypoldt, F., et al. (2020). Proteome profiling in cerebrospinal fluid reveals novel biomarkers of Alzheimer's disease. *Mol. Syst. Biol.* 16:e9356. doi: 10.15252/msb.20199356

Bai, B., Wang, X., Li, Y., Chen, P. C., Yu, K., Dey, K. K., et al. (2020). Deep multilayer brain proteomics identifies molecular networks

in alzheimer's disease progression. *Neuron*. 105, 975–991.e977. doi: 10.1016/j.neuron.2019.12.015

Barkovits, K., Pacharra, S., Pfeiffer, K., Steinbach, S., Eisenacher, M., Marcus, K., et al. (2020). Reproducibility, specificity and accuracy of relative quantification using spectral library-based data-independent acquisition. *Mol. Cell. Proteomics* 19, 181–197. doi: 10.1074/mcp.RA119.001714

Bekker-Jensen, D. B., Bernhardt, O. M., Hogrebe, A., Martinez-Val, A., Verbeke, L., Gandhi, T., et al. (2020). Rapid and site-specific deep phosphoproteome profiling by data-independent acquisition without the need for spectral libraries. *Nat. Commun*. 11:787. doi: 10.1038/s41467-020-14609-1

Biesemann, C., Gronborg, M., Luquet, E., Wichert, S. P., Bernard, V., Bungers, S. R., et al. (2014). Proteomic screening of glutamatergic mouse brain synaptosomes isolated by fluorescence activated sorting. *EMBO J*. 33, 157–170. doi: 10.1002/embj.201386120

Bruderer, R., Bernhardt, O. M., Gandhi, T., Miladinovic, S. M., Cheng, L. Y., Messner, S., et al. (2015). Extending the limits of quantitative proteome profiling with data-independent acquisition and application to acetaminophen-treated three-dimensional liver microtissues. *Mol. Cell. Proteomics* 14, 1400–1410. doi: 10.1074/mcp.M114.044305

Bruderer, R., Bernhardt, O. M., Gandhi, T., Xuan, Y., Sondermann, J., Schmidt, M., et al. (2017). Optimization of experimental parameters in data-independent mass spectrometry significantly increases depth and reproducibility of results. *Mol. Cell. Proteomics* 16, 2296–2309. doi: 10.1074/mcp.RA117.000314

Caroni, P., Donato, F., and Muller, D. (2012). Structural plasticity upon learning: regulation and functions. *Nat. Rev. Neurosci*. 13, 478–490. doi: 10.1038/nrn3258

Chang, R. Y., Etheridge, N., Nouwens, A. S., and Dodd, P. R. (2015). SWATH analysis of the synaptic proteome in Alzheimer's disease. *Neurochem. Int*. 87, 1–12. doi: 10.1016/j.neuint.2015.04.004

Collins, B. C., Hunter, C. L., Liu, Y., Schilling, B., Rosenberger, G., Bader, S. L., et al. (2017). Multi-laboratory assessment of reproducibility, qualitative and quantitative performance of SWATH-mass spectrometry. *Nat. Commun*. 8:291. doi: 10.1038/s41467-017-00249-5

Counotte, D. S., Goriounova, N. A., Li, K. W., Loos, M., van der Schors, R. C., Schetters, D., et al. (2011). Lasting synaptic changes underlie attention deficits caused by nicotine exposure during adolescence. *Nat. Neurosci*. 14, 417–419. doi: 10.1038/nn.2770

DeLaney, K., and Li, L. (2019). Data independent acquisition mass spectrometry method for improved neuropeptidomic coverage in crustacean neural tissue extracts. *Anal. Chem*. 91, 5150–5158. doi: 10.1021/acs.analchem.8b05734

Demichev, V., Messner, C. B., Vernardis, S. I., Lilley, K. S., and Ralser, M. (2020). DIA-NN: neural networks and interference correction enable deep proteome coverage in high throughput. *Nat. Methods*. 17, 41–44. doi: 10.1038/s41592-019-0638-x

Distler, U., Kuharev, J., Navarro, P., and Tenzer, S. (2016). Label-free quantification in ion mobility-enhanced data-independent acquisition proteomics. *Nat. Protoc*. 11, 795–812. doi: 10.1038/nprot.2016.042

Distler, U., Schmeisser, M. J., Pelosi, A., Reim, D., Kuharev, J., Weiczner, R., et al. (2014). In-depth protein profiling of the postsynaptic density from mouse hippocampus using data-independent acquisition proteomics. *Proteomics* 14, 2607–2613. doi: 10.1002/pmic.201300520

Dou, M., Clair, G., Tsai, C. F., Xu, K., Chrisler, W. B., Sontag, R. L., et al. (2019). High-Throughput single cell proteomics enabled by multiplex isobaric labeling in a nanodroplet sample preparation platform. *Anal. Chem*. 91, 13119–13127. doi: 10.1021/acs.analchem.9b03349

Egertson, J. D., MacLean, B., Johnson, R., Xuan, Y., and MacCoss, M. J. (2015). Multiplexed peptide analysis using data-independent acquisition and skyline. *Nat. Protoc*. 10, 887–903. doi: 10.1038/nprot.2015.055

Fernandez-Costa, C., Martinez-Bartolome, S., McClatchy, D. B., Saviola, A. J., Yu, N. K., and Yates, J. R. 3rd. (2020). Impact of the identification strategy on the reproducibility of the DDA and DIA Results. *J. Proteome Res*. 19, 3153–3161. doi: 10.1021/acs.jproteome.0c00153

Frese, C. K., Mikhaylova, M., Stucchi, R., Gautier, V., Liu, Q., Mohammed, S., et al. (2017). Quantitative map of proteome dynamics during neuronal differentiation. *Cell Rep*. 18, 1527–1542. doi: 10.1016/j.celrep.2017.01.025

Gabriels, R., Martens, L., and Degroeve, S. (2019). Updated MS(2)PIP web server delivers fast and accurate MS(2) peak intensity prediction for multiple fragmentation methods, instruments and labeling techniques. *Nucleic Acids Res*. 47, W295–W299. doi: 10.1093/nar/gkz299

Gessulat, S., Schmidt, T., Zolg, D. P., Samaras, P., Schnatbaum, K., Zerweck, J., et al. (2019). Prosit: proteome-wide prediction of peptide tandem mass spectra by deep learning. *Nat. Methods*. 16, 509–518. doi: 10.1038/s41592-019-0426-7

Gonzalez-Lozano, M. A., Koopmans, F., Sullivan, P. F., Protze, J., Krause, G., Verhage, M., et al. (2020). Stitching the synapse: cross-linking mass spectrometry into resolving synaptic protein interactions. *Sci Adv*. 6:eaax5783. doi: 10.1126/sciadv.aax5783

He, E., Lozano, M. A. G., Stringer, S., Watanabe, K., Sakamoto, K., den Oudsten, F., et al. (2018). MIR137 schizophrenia-associated locus controls synaptic function by regulating synaptogenesis, synapse maturation and synaptic transmission. *Hum. Mol. Genet*. 27, 1879–1891. doi: 10.1093/hmg/ddy089

Herculano-Houzel, S. (2009). The human brain in numbers: a linearly scaled-up primate brain. *Front. Hum. Neurosci*. 3:31. doi: 10.3389/neuro.09.031.2009

Hondius, D. C., van Nierop, P., Li, K. W., Hoozemans, J. J., van der Schors, R. C., van Haastert, E. S., et al. (2016). Profiling the human hippocampal proteome at all pathologic stages of Alzheimer's disease. *Alzheimers. Dement*. 12, 654–668. doi: 10.1016/j.jalz.2015.11.002

Huang, L., Wickramasekara, S. I., Akinyeke, T., Stewart, B. S., Jiang, Y., Raber, J., et al. (2016). Ion mobility-enhanced MS(E)-based label-free analysis reveals effects of low-dose radiation post contextual fear conditioning training on the mouse hippocampal proteome. *J. Proteomics* 140, 24–36. doi: 10.1016/j.jprot.2016.03.032

Humeau, Y., and Choquet, D. (2019). The next generation of approaches to investigate the link between synaptic plasticity and learning. *Nat. Neurosci*. 22, 1536–1543. doi: 10.1038/s41593-019-0480-6

Johnson, E. C. B., Dammer, E. B., Duong, D. M., Ping, L., Zhou, M., Yin, L., et al. (2020). Large-scale proteomic analysis of Alzheimer's disease brain and cerebrospinal fluid reveals early changes in energy metabolism associated with microglia and astrocyte activation. *Nat. Med*. 26, 769–780. doi: 10.1038/s41591-020-0815-6

Kanellopoulos, A. K., Mariano, V., Spinazzi, M., Woo, Y. J., McLean, C., Pech, U., et al. (2020). Aralar sequesters GABA into hyperactive mitochondria, causing social behavior deficits. *Cell* 180, 1178–1197.e1120. doi: 10.1016/j.cell.2020.02.044

Koopmans, F., Ho, J. T. C., Smit, A. B., and Li, K. W. (2018a). Comparative analyses of data independent acquisition mass spectrometric approaches: DIA, WiSIM-DIA, and untargeted DIA. *Proteomics* 18:1700304. doi: 10.1002/pmic.201700304

Koopmans, F., Pandya, N. J., Franke, S. K., Phillippens, I., Paliukhovich, I., Li, K. W., et al. (2018b). comparative hippocampal synaptic proteomes of rodents and primates: differences in neuroplasticity-related proteins. *Front. Mol. Neurosci*. 11:364. doi: 10.3389/fnmol.2018.00364

Kulik, Y. D., Watson, D. J., Cao, G., Kuwajima, M., and Harris, K. M. (2019). Structural plasticity of dendritic secretory compartments during LTP-induced synaptogenesis. *eLife*. 8:e46356. doi: 10.7554/eLife.46356.030

Li, K. W., Ganz, A. B., and Smit, A. B. (2019). Proteomics of neurodegenerative diseases: analysis of human post-mortem brain. *J. Neurochem*. 151, 435–445. doi: 10.1111/jnc.14603

Liu, Y., Huttenhain, R., Surinova, S., Gillet, L. C., Mouritsen, J., Brunner, R., et al. (2013). Quantitative measurements of N-linked glycoproteins in human plasma by SWATH-MS. *Proteomics* 13, 1247–1256. doi: 10.1002/pmic.201200417

Loh, K. H., Stawski, P. S., Draycott, A. S., Udeshi, N. D., Lehrman, E. K., Wilton, D. K., et al. (2016). Proteomic analysis of unbounded cellular compartments: synaptic clefts. *Cell* 166, 1295–1307.e1221. doi: 10.1016/j.cell.2016.07.041

Lou, R., Tang, P., Ding, K., Li, S., Tian, C., Li, Y., et al. (2020). Hybrid spectral library combining DIA-MS data and a targeted virtual library substantially deepens the proteome coverage. *iScience* 23:100903. doi: 10.1016/j.isci.2020.100903

Ludwig, C., Gillet, L., Rosenberger, G., Amon, S., Collins, B. C., and Aebersold, R. (2018). Data-independent acquisition-based SWATH-MS for quantitative proteomics: a tutorial. *Mol. Syst. Biol*. 14:e8126. doi: 10.15252/msb.20178126

Mansilla, A., Jordan-Alvarez, S., Santana, E., Jarabo, P., Casas-Tinto, S., and Ferrus, A. (2018). Molecular mechanisms that change synapse number. *J. Neurogenet*. 32, 155–170. doi: 10.1080/01677063.2018.1506781

Meier, F., Geyer, P. E., Virreira Winter, S., Cox, J., and Mann, M. (2018). BoxCar acquisition method enables single-shot proteomics at a depth of 10,000 proteins in 100 minutes. *Nat. Methods*. 15, 440–448. doi: 10.1038/s41592-018-0003-5

Michalski, A., Cox, J., and Mann, M. (2011). More than 100,000 detectable peptide species elute in single shotgun proteomics runs but the majority is inaccessible to data-dependent LC-MS/MS. *J. Proteome Res.* 10, 1785–1793. doi: 10.1021/pr101060v

Muntel, J., Gandhi, T., Verbeke, L., Bernhardt, O. M., Treiber, T., Bruderer, R., et al. (2019). Surpassing 10 000 identified and quantified proteins in a single run by optimizing current LC-MS instrumentation and data analysis strategy. *Mol Omics*. 15, 348–360. doi: 10.1039/C9MO00082H

Pandya, N. J., Koopmans, F., Slotman, J. A., Paliukhovich, I., Houtsmuller, A. B., Smit, A. B., et al. (2017). Correlation profiling of brain sub-cellular proteomes reveals co-assembly of synaptic proteins and subcellular distribution. *Sci. Rep.* 7:12107. doi: 10.1038/s41598-017-11690-3

Pappireddi, N., Martin, L., and Wuhr, M. (2019). A review on quantitative multiplexed proteomics. *Chembiochem* 20, 1210–1224. doi: 10.1002/cbic.201800650

Pino, L. K., Just, S. C., MacCoss, M. J., and Searle, B. C. (2020). Acquiring and analyzing data independent acquisition proteomics experiments without spectrum libraries. *Mol. Cell Proteomics* 19, 1088–1103. doi: 10.1074/mcp.P119.001913

Rauniyar, N. (2015). Parallel reaction monitoring: a targeted experiment performed using high resolution and high mass accuracy mass spectrometry. *Int. J. Mol. Sci.* 16, 28566–28581. doi: 10.3390/ijms161226120

Rosato, M., Stringer, S., Gebuis, T., Paliukhovich, I., Li, K. W., Posthuma, D., et al. (2019). Combined cellomics and proteomics analysis reveals shared neuronal morphology and molecular pathway phenotypes for multiple schizophrenia risk genes. *Mol. Psychiatry.* doi: 10.1038/s41380-019-0436-y. [Epub ahead of print].

Rost, H. L., Rosenberger, G., Navarro, P., Gillet, L., Miladinovic, S. M., Schubert, O. T., et al. (2014). OpenSWATH enables automated, targeted analysis of data-independent acquisition MS data. *Nat. Biotechnol.* 32, 219–223. doi: 10.1038/nbt.2841

Saidi, M., Kamali, S., and Beaudry, F. (2019). Neuropeptidomics: comparison of parallel reaction monitoring and data-independent acquisition for the analysis of neuropeptides using high-resolution mass spectrometry. *Biomed. Chromatogr.* 33:e4523. doi: 10.1002/bmc.4523

Schizophrenia Working Group of the Psychiatric Genomics, C. (2014). Biological insights from 108 schizophrenia-associated genetic loci. *Nature* 511, 421–427. doi: 10.1038/nature13595

Searle, B. C., Pino, L. K., Egertson, J. D., Ting, Y. S., Lawrence, R. T., MacLean, B. X., et al. (2018). Chromatogram libraries improve peptide detection and quantification by data independent acquisition mass spectrometry. *Nat. Commun.* 9:5128. doi: 10.1038/s41467-018-07454-w

Searle, B. C., Swearingen, K. E., Barnes, C. A., Schmidt, T., Gessulat, S., Kuster, B., et al. (2020). Generating high quality libraries for DIA MS with empirically corrected peptide predictions. *Nat. Commun.* 11:1548. doi: 10.1038/s41467-020-15346-1

Sharma, K., Schmitt, S., Bergner, C. G., Tyanova, S., Kannaiyan, N., Manrique-Hoyos, N., et al. (2015). Cell type- and brain region-resolved mouse brain proteome. *Nat. Neurosci.* 18, 1819–1831. doi: 10.1038/nn.4160

Shen, X., Shen, S., Li, J., Hu, Q., Nie, L., Tu, C., et al. (2018). IonStar enables high-precision, low-missing-data proteomics quantification in large biological cohorts. *Proc. Natl. Acad. Sci. U.S.A.* 115, E4767–E4776. doi: 10.1073/pnas.1800541115

Silva, J. C., Denny, R., Dorschel, C. A., Gorenstein, M., Kass, I. J., Li, G. Z., et al. (2005). Quantitative proteomic analysis by accurate mass retention time pairs. *Anal. Chem.* 77, 2187–2200. doi: 10.1021/ac048455k

Testa-Silva, G., Verhoog, M. B., Linaro, D., de Kock, C. P., Baayen, J. C., Meredith, R. M., et al. (2014). High bandwidth synaptic communication and frequency tracking in human neocortex. *PLoS Biol.* 12:e1002007. doi: 10.1371/journal.pbio.1002007

Ting, Y. S., Egertson, J. D., Bollinger, J. G., Searle, B. C., Payne, S. H., Noble, W. S., et al. (2017). PECAN: library-free peptide detection for data-independent acquisition tandem mass spectrometry data. *Nat. Methods* 14, 903–908. doi: 10.1038/nmeth.4390

Tran, N. H., Qiao, R., Xin, L., Chen, X., Liu, C., Zhang, X., et al. (2019). Deep learning enables *de novo* peptide sequencing from data-independent-acquisition mass spectrometry. *Nat. Methods* 16, 63–66. doi: 10.1038/s41592-018-0260-3

Tsai, C. F., Zhao, R., Williams, S. M., Moore, R. J., Schultz, K., Chrisler, W. B., et al. (2020). An improved boosting to amplify signal with isobaric labeling (iBASIL) strategy for precise quantitative single-cell proteomics. *Mol. Cell. Proteomics* 19, 828–838. doi: 10.1074/mcp.RA119.001857

Tsou, C. C., Avtonomov, D., Larsen, B., Tucholska, M., Choi, H., Gingras, A. C., et al. (2015). DIA-umpire: comprehensive computational framework for data-independent acquisition proteomics. *Nat Methods*. 12, 258–264. doi: 10.1038/nmeth.3255

van Oostrum, M., Campbell, B., Seng, C., Muller, M., Tom Dieck, S., Hammer, J., et al. (2020). Surfaceome dynamics reveal proteostasis-independent reorganization of neuronal surface proteins during development and synaptic plasticity. *Nat. Commun.* 11:4990. doi: 10.1038/s41467-020-18494-6

Van Puyvelde, B., Willems, S., Gabriels, R., Daled, S., De Clerck, L., Vande Casteele, S., et al. (2020). Removing the hidden data dependency of DIA with predicted spectral libraries. *Proteomics* 20:e1900306. doi: 10.1002/pmic.201900306

von Engelhardt, J., Mack, V., Sprengel, R., Kavenstock, N., Li, K. W., Stern-Bach, Y., et al. (2010). CKAMP44: a brain-specific protein attenuating short-term synaptic plasticity in the dentate gyrus. *Science* 327, 1518–1522. doi: 10.1126/science.1184178

Zeng, W. F., Zhou, X. X., Zhou, W. J., Chi, H., Zhan, J., and He, S. M. (2019). MS/MS Spectrum prediction for modified peptides using pDeep2 trained by transfer learning. *Anal. Chem.* 91, 9724–9731. doi: 10.1021/acs.analchem.9b01262

Zhang, F., Ge, W., Ruan, G., Cai, X., and Guo, T. (2020). Data-independent acquisition mass spectrometry-based proteomics and software tools: a glimpse in 2020. *Proteomics* 10:e1900276. doi: 10.1002/pmic.201900276

Zhong, C. Q., Wu, R., Chen, X., Wu, S., Shuai, J., and Han, J. (2020). Systematic assessment of the effect of internal library in targeted analysis of SWATH-MS. *J. Proteome Res.* 19, 477–492. doi: 10.1021/acs.jproteome.9b00669

Zhou, X. X., Zeng, W. F., Chi, H., Luo, C., Liu, C., Zhan, J., et al. (2017). pDeep: predicting MS/MS spectra of peptides with deep learning. *Anal. Chem.* 89, 12690–12697. doi: 10.1021/acs.analchem.7b02566

Conflict of Interest: The authors declare that the research was conducted in the absence of any commercial or financial relationships that could be construed as a potential conflict of interest.

frontiers in Molecular Neuroscience

REVIEW
published: 07 January 2021
doi: 10.3389/fnmol.2020.604158

Neuroproteomics in Epilepsy: What Do We Know so Far?

Amanda M. do Canto[1,2], *Amanda Donatti*[1,2], *Jaqueline C. Geraldis*[1,2], *Alexandre B. Godoi*[1,2], *Douglas C. da Rosa*[1,2] *and Iscia Lopes-Cendes*[1,2]*

[1]*Department of Medical Genetics and Genomic Medicine, School of Medical Sciences, University of Campinas (UNICAMP), Campinas, Brazil,* [2]*Brazilian Institute of Neuroscience and Neurotechnology (BRAINN), Campinas, Brazil*

Epilepsies are chronic neurological diseases that affect approximately 2% of the world population. In addition to being one of the most frequent neurological disorders, treatment for patients with epilepsy remains a challenge, because a proportion of patients do not respond to the antiseizure medications that are currently available. This results in a severe economic and social burden for patients, families, and the healthcare system. A characteristic common to all forms of epilepsy is the occurrence of epileptic seizures that are caused by abnormal neuronal discharges, leading to a clinical manifestation that is dependent on the affected brain region. It is generally accepted that an imbalance between neuronal excitation and inhibition generates the synchronic electrical activity leading to seizures. However, it is still unclear how a normal neural circuit becomes susceptible to the generation of seizures or how epileptogenesis is induced. Herein, we review the results of recent proteomic studies applied to investigate the underlying mechanisms leading to epilepsies and how these findings may impact research and treatment for these disorders.

Keywords: mesial temporal lobe epilepsy, hippocampal sclerosis, malformations of cortical development, proteomics, epileptogenesis, seizures

OPEN ACCESS

Edited by:
Tija Carey Jacob, University of Pittsburgh, United States

Reviewed by:
Eva Maria Jimenez-Mateos, Trinity College Dublin, Ireland
Jeffrey Loeb, University of Illinois at Chicago, United States

***Correspondence:**
Iscia Lopes-Cendes
icendes@unicamp.br

Received: *08 September 2020*
Accepted: *09 December 2020*
Published: *07 January 2021*

Citation:
do Canto AM, Donatti A, Geraldis JC, Godoi AB, da Rosa DC and Lopes-Cendes I (2021) Neuroproteomics in Epilepsy: What Do We Know so Far? Front. Mol. Neurosci. 13:604158. doi: 10.3389/fnmol.2020.604158

INTRODUCTION

Epilepsies are a group of life-threatening chronic neurological diseases affecting over 50 million people worldwide (Hauser et al., 1996; Borges et al., 2004; World Federation of Neurology and World Health Organization, 2017). While heterogeneous, these disorders have in common the presence of spontaneous recurrent seizures (Laidlaw, 1988; England et al., 2012). Epileptic seizures are induced by abnormal neuronal discharges, which lead to variable clinical manifestations that depend on the affected brain regions (Fisher et al., 2014; Devinsky et al., 2018). Despite the high number of antiseizure drugs (ASDs) available, some patients do not respond to treatment and have so-called pharmacoresistant or refractory epilepsy (Kwan et al., 2010). Also, the current available ASDs target only the symptoms rather than the cause of epilepsy, thus requiring the continuous use of ASDs, which can affect overall brain functioning and lead to many side effects (Kwan et al., 2010; Löscher and Schmidt, 2011; Brodie et al., 2012; Crepeau and Sirven, 2017). Therefore, understanding the biological mechanisms underlying human epilepsy is critical to developing new and more effective medications to treat these patients.

Because of its complexity, different mechanisms can be involved in the various types of epilepsy, such as the imbalance between inhibitory and excitatory neurotransmission, high levels of inflammation, neuronal damage in specific brain regions, and abnormalities in neuronal and cortical development (Crespel et al., 2002; Blümcke et al., 2013; Devinsky et al., 2013, 2018;

Staley, 2015; Gales and Prayson, 2017; Ye and Kaszuba, 2017). All these mechanisms may be caused by environmental or genetic factors and, most likely, by interactions among them. Genetic and developmental abnormalities are more prevalent in children, whereas, in adults and elderly patients, acquired causes, such as brain tumors, trauma, and stroke, are more frequent (Allone et al., 2017; Magalhães et al., 2019; Thijs et al., 2019). However, it is still unclear how a normal neural circuit becomes more susceptible to the generation of seizures or how epileptogenesis is induced. Also, it is unlikely that a single factor or mechanism can lead to all the changes seen in the various types of epilepsy.

Even with all the significant developments achieved over the last few decades in biomedical sciences, there is still a substantial part of the cellular machinery that remains poorly understood. Therefore, by studying proteins and their dynamics, presence, and abundance, one can gain new insights into cellular functions in normal and pathological tissues. Hence, proteomic studies can help researchers understand the biological mechanisms leading to epilepsy, the development of new treatments, and the discovery of biomarkers of disease, which may assist in predicting the best responses to treatment. Proteomics is best performed in the target tissue where the molecular changes may take place; thus, in epilepsy, there are two main sources: human tissue, primarily resected brain samples obtained from epilepsy surgery, and tissue from animal models of epilepsy, which can be induced by different strategies or genetic models (**Figure 1**; Grone and Baraban, 2015; Becker, 2018; Devinsky et al., 2018).

Herein, we reviewed the recent findings of proteomic studies on epilepsy and discussed how these findings might impact research and the clinical management of epileptic patients. A summary of the main neuroproteomics findings in epilepsy is presented in **Table 1** and **Figure 2**. The studies are reviewed in chronological order because there has been a significant impact from technological developments in proteomics over the past few years. Please note that the proteins discussed in the text are presented in their abbreviated form. **Table 1** provides the full name of the discussed proteins.

PROTEOMIC STUDIES IN HUMAN EPILEPSY

In most proteomic studies, evaluating the affected tissue is an essential approach to measure molecular dynamics at a determined point in the time course of the disease (Al Diffalha et al., 2019). Thus, the availability of tissue to be studied by different proteomic techniques is a central issue in neuroproteomics. Human tissues are restricted in studies on epilepsy because brain tissue is only available *postmortem* or from surgery performed on patients with focal epilepsy who do not respond to treatment with ASDs. When using tissue from an autopsy, it is important to observe the *postmortem* interval (PMI), which is the time between death and the autopsy procedure. This time usually varies from 1 h to over 24 h. Given that autopsy material is widely used as control tissue in human neuroscience, tissue preservation must be considered and the PMI is a significant factor that can interfere with the tissue quality (Chandana et al., 2009; Blair et al., 2016). Some studies have investigated the impact of the PMI on biomolecule integrity and found that the *postmortem* protein changes are dependent on the evaluated protein. Even though studies suggest that proteins are stable in a short PMI (Nagy et al., 2015; Blair et al., 2016), comparison of *postmortem* and biopsy tissues requires caution because the identified molecular differences may be due to a confounding factor.

The two most important types of medically refractory focal epilepsy, which can benefit from surgical tissue resection, are temporal lobe epilepsy (TLE) and malformations of cortical development (Cendes, 2005; Kwan et al., 2010).

Temporal Lobe Epilepsy

TLE is a common form of focal epilepsy in humans, with seizures originating in the temporal lobe (Cendes, 2005). In addition to seizures being frequent, a significant proportion of patients with TLE do not respond to treatment with ASDs, leading to the diagnosis of pharmacoresistant epilepsy in about 30% of these patients (Kwan et al., 2010; Allone et al., 2017; Luan et al., 2018). TLE can be divided into two sub-types: mesial temporal lobe epilepsy (MTLE), the most common and a usually severe form of epilepsy, and neocortical temporal lobe epilepsy (NTLE; Cendes, 2005; Tassi et al., 2009; Allone et al., 2017). In most patients with MTLE, seizure onset occurs in the hippocampus, entorhinal cortex, or amygdala (Cendes, 2005; Lévesque et al., 2018). Mesial temporal sclerosis (MTS), including hippocampal sclerosis (HS), is the main histopathological finding in these patients, and it is present in 60–70% of patients with MTLE who undergo a surgical procedure to treat medically refractory seizures. MTS is the histopathological term for neuronal loss and gliosis involving the hippocampus, and frequently also the amygdala, uncus, and parahippocampal gyrus (Blümcke et al., 1999, 2013; Cendes, 2005).

As described above, most proteomic studies using human tissue are derived from surgical specimens obtained from patients with MTLE who underwent resection of the mesial temporal structures to treat medically refractory epilepsy. It is known that dysregulation of synaptic processes is the most common mechanism in epileptic seizures. However, due to the disease's complexity, several biological processes are probably interacting to determine the epileptogenic lesion seen in patients with MTLE, including energetic, signaling, and cytoskeleton pathways (Yang et al., 2004, 2006; Persike et al., 2012; Fukata and Fukata, 2017). The first studies to evaluate changes at the protein level related to epilepsy reported findings involved with abnormal neuronal excitability. In 2000, an enzymatic study analyzed, through spectrophotometry (SPCT), the levels of NADH:CoQ1 oxidoreductase and cytochrome *c* oxidase in hippocampal tissue of patients with MTLE (Kunz et al., 2000). There was a loss in complex I of the mitochondrial respiratory chain complex in the *Cornu Ammonis* CA(3) of the hippocampus and the dentate gyrus (DG). Alterations in complex I of this chain have been described as promoting changes in excitability and selective neuronal vulnerability in the hippocampal regions (Kunz et al., 2000; Yang et al., 2004). Kunz et al. (2000) analyzed 19 TLE samples and one control using histochemistry and electron microscopy. Despite having a good

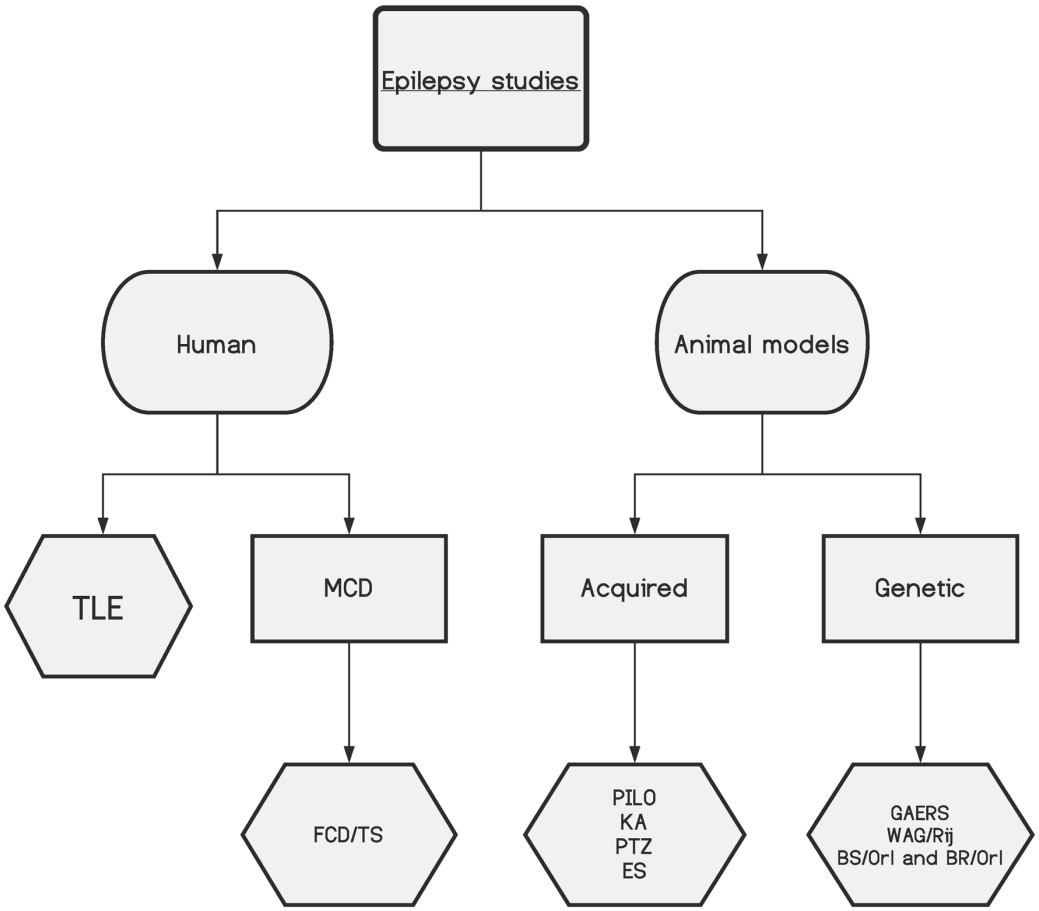

FIGURE 1 | A schematic of the main epilepsy studies and their divisions, highlighting the complexity of the disease. TLE, temporal lobe epilepsy; MCD, malformations of cortical development; FCD, focal cortical dysplasia; TS, tuberous sclerosis; PILO, pilocarpine model; KA, kainic acid model; PTZ, pentylenetetrazol model; ES, electrical stimulation models; GAERS, genetic absence epilepsy rats from Strasbourg; WAG/Rij, Wistar Albino Glaxo/Rijswijk rat; BS/Orl and BR/Orl, mouse strains.

number of patient samples ($n = 57$), there was high heterogeneity among them. Some patients presented severe segmental loss in the hippocampus, others presented moderate hippocampal neuronal loss, and some even showed no signs of pathological abnormalities. Also, the authors analyzed only two controls, normal tissue obtained from a patient with a non-epileptogenic tumor within the mesial temporal lobe. Furthermore, the main focus of that study was enzymatic activity and energy metabolism influences over neuronal excitability.

Leite et al. (2002) identified a reduced amount of neuronal nitric oxide synthase (nNOS) in hippocampal sections (CA1–CA4) of samples from patients with MTLE and HS by immunohistochemistry (IHC) and western blot (WB) experiments. Nitric oxide impacts the neuronal membrane potential by changing the dynamics of neurotransmitter release and ion channels, phenomena that alter cell excitability (Leite et al., 2002; Fukata and Fukata, 2017). The tissues were obtained from patients with pathological signs of HS evaluated with high-resolution magnetic resonance imaging (MRI), and the controls were obtained from the autopsies of patients with no neurological conditions (Leite et al., 2002). This study was hypothesis-driven; its main purpose was to describe nNOS expression in the hippocampus of patients with MTLE and how it could be related to disease mechanisms.

The first evidence of changes in neuronal plasticity and the axonal organization at the protein level was published by Czech et al. (2004). A study of the middle segment of the hippocampal body from patients with drug-resistant MTLE (rMTLE) associated with typical imaging and pathological features of HS, compared with autopsy material, was conducted by 2DE (two-dimension electrophoresis), and spots were then analyzed by a MALDI-TOF PMF (Matrix-Assisted Laser Desorption Ionization Time of Flight Mass Spectrometry Peptide Mass Fingerprint) and MALDI LIFT-TOF/TOF MS/MS (matrix-assisted laser desorption/ionization time-of-flight/time-of-flight mass spectrometer). The researchers identified 13 different spots, including CRMP-2 at 65 and 55 kDa. The authors suggested that the expression of the two isoforms represents alternative splicing forms of post-translational modifications (PTMs; Czech et al., 2004). CRMP-2 is related to axonal outgrowth and neuronal

polarity, which guides axonal pathfinding and is essential to brain plasticity (Babb et al., 1991; Isokawa et al., 1993; Blümcke et al., 1999; Furtinger et al., 2001; Gorter and Lopes da Silva, 2002). Therefore, reduced CRMP-2 could induce aberrant axonal reorganization and be related to HS. Recent studies have shown a relationship between elevated CRMP-2 and epilepsy, including the usage of lacosamide, a CRMP-2 antagonist, in the treatment of refractory partial epilepsy seizures (Wilson and Khanna, 2015; Keren-Aviram et al., 2018).

After the previous study (Czech et al., 2004), the same group analyzed hippocampal samples from patients with rMTLE and HS using 2DE followed by MS, comparing them with *postmortem* controls; they identified a reduction ACOT in patients (Yang et al., 2004). ACOT regulates intracellular levels of coenzyme A (CoASH), acyl-CoA, and free fatty acids (Yamada et al., 1999). These molecules are involved in fatty acid metabolism, influencing the electrochemical gradient by a cascade reaction (Yamada et al., 1999; Yang et al., 2004; Sousa et al., 2018). Another study from the same group revealed altered expression of ApoA-I in the hippocampus from patients with MTLE compared with autopsy controls. However, this change seems to be due to plasma extravasates and partly by gliosis, as shown by IHC analysis (Yang et al., 2005).

Subsequently, a pilot study using 2DE followed by MALDI-TOF/TOF MS compared the proteomic profile of a biopsy specimen of the human temporal lobe obtained from a patient with rMTLE to an autopsy specimen of the same brain region, from a patient with no prior history of neurodegenerative conditions (He et al., 2006). Enzymes and structural proteins represented the majority of the identified proteins, while channel and regulator proteins were rare. The neurotransmitter metabolic enzymes, such as DDAH1, are reduced in TLE patients; these changes could indirectly lead to alterations in the homeostasis and central functions of nitric oxide, like neuronal plasticity. Another enzyme that is decreased, glutamate-ammonia ligase (glutamine synthase), could be related to the extracellular accumulation of glutamate and excitotoxicity (Eid et al., 2004; He et al., 2006). Meanwhile, decreased aspartate aminotransferase and the GABA catabolic enzyme (4-aminobutyrate transaminase) would reduce the metabolism of glutamate and the catabolism of GABA, leading to the perturbation of a wide range of synaptic processes (He et al., 2006). Decreased UNG and SIR2 levels were also identified in the patient and could lead to neuronal death by impairing oxidative DNA damage repair (Rose et al., 2003; Kruman et al., 2004; He et al., 2006). Also, the cytoprotective protein CRYAB is associated with the tubulin cytoskeleton and could be related to some neurodegenerative conditions and TLE (He et al., 2006; Xi et al., 2006). Moreover, researchers have suggested that decreased levels of neurofilament three and septins are related to neuronal cytoskeleton damage: these changes impair cytoskeleton remodeling and tissue organization and function (Perez-Olle et al., 2004; Spiliotis, 2006; Xi et al., 2006). Besides, reduced DPYSL2 could also impair tissue organization due to abnormalities in axon guidance and neural growth cone collapse. A decrease in the level of enzymes related to glycolysis and tricarboxylic acids, such as ALDOA, PGK1, MDH1, IDH3A, LDH, and TPI1, could reduce the cellular energy supply (He et al., 2006). Despite the identified alterations, He et al. (2006) only analyzed one patient and one control, which makes it very difficult to relate these findings to the disease mechanism. The use of *postmortem* tissue as a control—with no description of the histological features—also makes it difficult to assess the validity of the results.

Another study has also described several proteins related to cytoskeleton function and tissue structure from patients with rMTLE compared with autopsy tissue from patients with no history of brain disease (Yang et al., 2006). In that work, 2DE and MALDI-TOF spectrometry identified reduced levels of α-1-tubulin and β-tubulin in two and three spots, respectively. Tubulin β-5 chain, ezrin, and the anchoring protein vinculin were increased in the patient samples. Profilin II and neuronal tropomodulin were decreased, while the presence of β-actin was not identified in the samples. The absence of tropomodulin can reduce neuronal death and affect the cytoskeleton integrity of those patients (Yang et al., 2006). The authors also described the alteration of oxidative stress proteins: they observed an increase in PRDX6 and a decrease in PRDX3, changes that were associated with reactive oxygen species (ROS) attacks and production, respectively, in MTLE patients. This protein responds to oxidative stress by modulating cytoskeletal dynamics (Wang et al., 2003; Yang et al., 2006). Reduced levels of chaperone 1 and T complex protein were observed in the same patient samples. T complex protein facilitates tubulin protein folding, while chaperone is proportionally involved in the cytoskeleton development level (Yang et al., 2006). Some reduced synaptic proteins were also associated with cytoskeletal mechanisms in MTLE patients. Low levels of MAPKK1 impairs the phosphorylation activity of cytoskeleton proteins, changing their functionality. SYTI and SCNA are substrates for the mitogen-activated protein kinase (MAPK) pathway. Their reduction in MTLE patients can regulate neurotransmitter release and transport and the formation of filamentous aggregates, causing synaptic deficits and cytoskeletal abnormalities (Yang et al., 2006). However, these alterations in cytoskeleton proteins could also be related to the gliosis and neuronal loss characteristic of HS; also, this study did not evaluate the histopathological features of the analyzed tissue.

The same MALDI-TOF technique was used to evaluate the untargeted proteomic profile of hippocampal samples from MTLE patients (Persike et al., 2012) compared with hippocampal tissue from autopsy controls. Overall, the authors identified nine altered proteins associated with metabolic disturbance and oxidative damage. There were increased levels of ALB, HSP70, DPYSL2, MBP, ATP6V1A, and the DLAT complex. There were decreased levels of SPTAN isoform 3, and two proteins were found only in samples from patients: GSTP1 and PARK7 (Persike et al., 2012).

In an elegant study performed in 2014, MALDI mass spectrometry imaging (MSI) was used to examine tissue protein from specific microdissected layers of the mesial temporal structures from patients with MTLE and autopsy controls (Mériaux et al., 2014). Histological observation of the hippocampus indicated HS with a localized loss of neurons in the

TABLE 1 | The main proteins associated with epilepsy and their contributions to the phenotype.

Tissue	Method	Protein	ID	Relation	Biological effect	Reference
Focal epilepsies						
Temporal lobe epilepsy						
Hipp	SPCT	Mitochondrial complex I (NADH dehydrogenase).	NADH	Decrease	Excitability and selective neuronal vulnerability. Increased calcium ions in the cytosolic environment.	Kunz et al. (2000)
Hipp	IHC + WB	Neuronal nitric oxide synthase.	nNOS	Decrease	Decreased neurotransmitter release and ion channel dynamics.	Leite et al. (2002)
Hipp	2DE + MALDI/TOF	Collapsin response mediator protein 2.	CRMP-2	Decrease	Aberrant axonal reorganization.	Czech et al. (2004)
Hipp	2DE + MS	Acyl-CoA thioester hydrolase.	ACOT	Decrease	Fatty acid metabolism.	Yang et al. (2004)
Hipp	2DE + MALDI-TOF	Apolipoprotein A-I	ApoAI	Increase	BBB integrity	Yang et al. (2005) and He et al. (2006)
Hipp	2DE + MALDI-TOF	Dimethylarginine dimethylaminohydrolase 1.	DDAH1	Decrease	Decrease of neurotransmitter release.	He et al. (2006)
Hipp	2DE + MALDI-TOF	Glutamine synthetase	GS	Decrease	Excitotoxicity	He et al. (2006)
Hipp	2DE + MALDI-TOF	4-aminobutyrate transaminase.	ABAT	Decrease	Glutamate metabolism	He et al. (2006)
Hipp	2DE + MALDI-TOF	Uracil DNA glycosylase	UNG	Decrease	Neuronal death	He et al. (2006)
Hipp	2DE + MALDI-TOF	Silent information regulator 2 protein.	SIR2	Decrease	DNA repair and cytoprotection.	He et al. (2006)
Hipp	2DE + MALDI-TOF	Alpha-crystallin B	CRYAB	Decrease	Inhibits the aggregation of unfolded proteins.	He et al. (2006) and Keren-Aviram et al. (2018)
Hipp	2DE + MALDI-TOF	Neurofilament 3/Septin-8/alpha tubulin, isoform 1/beta tubulin.	NEF3/Sept8/α-1-tubulin/β-tubulin.	Decrease	Cytoskeleton damage	He et al. (2006)
Hipp	2DE + MALDI-TOF	Dihydropyrimidinase-like 2	DPYSL2	Decrease	Cytoskeleton damage	He et al. (2006) and Persike et al. (2012)
Hipp	2DE + MALDI-TOF	Beta tubulin, isoform 5/Ezrin/Vinculin	β5-tubulin/EZR/VCL.	Increase	Cytoskeleton damage	Yang et al. (2006)
Hipp	2DE + MALDI-TOF	Profilin II	PFN2	Decrease	Cytoskeleton damage	Yang et al. (2006)
Hipp	2DE + MALDI-TOF	Neuronal tropomodulin	TMOD2	Decrease	Neuronal death and cytoskeleton integrity.	Yang et al. (2006)
Hipp	2DE + MALDI-TOF	Peroxiredoxin 3/ Peroxiredoxin 6	PRDX3/PRDX6	Decrease/ increase	Attack to reactive oxygen species.	Yang et al. (2006)
Hipp	2DE + MALDI-TOF	T complex protein I alpha	TCP1	Decrease	Cytoskeleton structure	Yang et al. (2006)
Hipp	2DE + MALDI-TOF	Mitogen-activated protein kinase kinase 1.	MPKK1	Decrease	Phosphorylation of cytoskeleton proteins.	Yang et al. (2006)
Hipp	2DE + MALDI-TOF	Synaptotagmin I	Syt I	Decrease	Regulation of neurotransmitter release and transport.	Yang et al. (2006)
Hipp	2DE + MALDI-TOF	Alpha-synuclein	SNCA	Decrease/ increase	Regulation of neurotransmitter release and transport.	Yang et al. (2006) and Keren-Aviram et al. (2018)
Hipp	2DE + MALDI-TOF	Spectrin alpha chain, isoform 3	SPTAN1	Decrease	Electrophysiological activity of the NMDA receptor.	Persike et al. (2012)
Hipp	2DE + MALDI-TOF	Dihydrolipoyllysine-residue acetyltransferase component of pyruvate dehydrogenase complex, mitochondrial.	DLAT	Increase	Metabolic disturbance and oxidative damage.	Persike et al. (2012)
Hipp	2DE + MALDI-TOF	Parkinson disease protein 7	PARK7	Presence	Protection against oxidative stress and cell death in this condition.	Persike et al. (2012)

(Continued)

TABLE 1 | Continued

Tissue	Method	Protein	ID	Relation	Biological effect	Reference
Hipp	2DE + MALDI-TOF	Glutathione S transferase P	GSTP1	Presence	Hydrophobic electrophiles maintenance.	Persike et al. (2012)
Hipp	2DE + MALDI-TOF	Heat shock-related 70 kDa protein 2	HSPA2	Increase	Cytoskeleton development.	Persike et al. (2012)
Hipp	MALDI MSI/MS	Neuropeptide Y	NPY	Increase	Seizure induces neurogenesis.	Mériaux et al. (2014)
Hipp	MALDI MSI/MS	Somatostatin 1	Somatostatin	Increase	Neuromodulator	Mériaux et al. (2014)
Hipp	LC-LTQ MS/MS	Leucine-rich glioma inactivated 1.	LIGI1	Presence	Male autosomal dominant partial epilepsy with auditory features (ADPEAF).	Mériaux et al. (2014)
Neocort	LC/MS	Collapsin response mediator protein 2.	CRMP-2	Increase	Synaptic plasticity related to the epileptic neocortex.	Keren-Aviram et al. (2018)
Neocort	LC/MS	Glial fibrillary acidic protein.	GFAP	Decrease	BBB function and cell communication.	Keren-Aviram et al. (2018)
Neocort	LC/MS	Guanine nucleotide-binding protein G(o) subunit α/LIM and SH3 protein 1.	GNAO1/LASP1	Decrease	Astrocyte origin	Keren-Aviram et al. (2018)
Neocort	LC/MS	Synapsin II/Stathmin 1	SYN2/STMN1	Increase	Neuritogenesis and synaptic transmission.	Keren-Aviram et al. (2018)
Hipp	LC/MS	O-GlcNAcase	GOA	Absence	Increase OGlcNacetylation in tissues.	Sánchez et al. (2019)
Hipp	IHC	Mitochondrial ATP synthase	ATP5B	Decrease	Neuronal cell maintenance	Mota et al. (2019)
Focal cortical dysplasia						
Neocort	LC-MS/MS + WB + IHC	Fascin/dihydropyrimidinase-related protein 1/microtubule-associated protein 4.	FSCN1/CRMP1/MAP4	Increase	Neuron migration, neurite outgrowth, and abnormal dendrite orientation.	Qin et al. (2017)
Neocort	LC-MS/MS + WB + IHC	Protein NDRG1	NDRG1	Increase	Reactive oligodendroglial hyperplasia.	Qin et al. (2017)
Neocort	LC-MS/MS + WB + IHC	Peroxiredoxin-6	PRDX6	Decrease	Oxidative stress	Qin et al. (2017)
Neocort	LC-MS/MS + WB + IHC	Prosaposin	PSAP	Decrease	Neuroprotection/ neurotoxicity.	Qin et al. (2017)
Tuberous sclerosis						
Tubers	LC-MS/MS	Hamartin	TSC1	Decrease	Synaptic signaling and inflammation.	Dombkowski et al. (2016)
Neocort	LC-MS/MS	Brefeldin A-inhibited guanine nucleotide-exchange protein 2/neuronal migration protein doublecortin.	ARFGEF2/DCX	Decrease/ increase	Intellectual disability and abnormal neuronal migration.	Liu et al. (2020)
Neocort	LC-MS/MS	Ubiquitin-like protein ATG12.	ATG12	Decrease	Autophagy	Liu et al. (2020)
Neocort	LC-MS/MS	Potassium voltage-gated channel subfamily A member 2.	KCNA2/KCNA2B	Decrease	Membrane excitability.	Liu et al. (2020)

2DE, two-dimensional electrophoresis; BBB, blood-brain barrier; Hipp, hippocampus; IHC, immunohistochemistry; LC, liquid chromatography; MALDI, matrix-assisted laser desorption ionization; MS, mass spectrometry; Neocort, neocortex; SPCT, spectrophotometry; TOF, time of flight; WB, Western Blot.

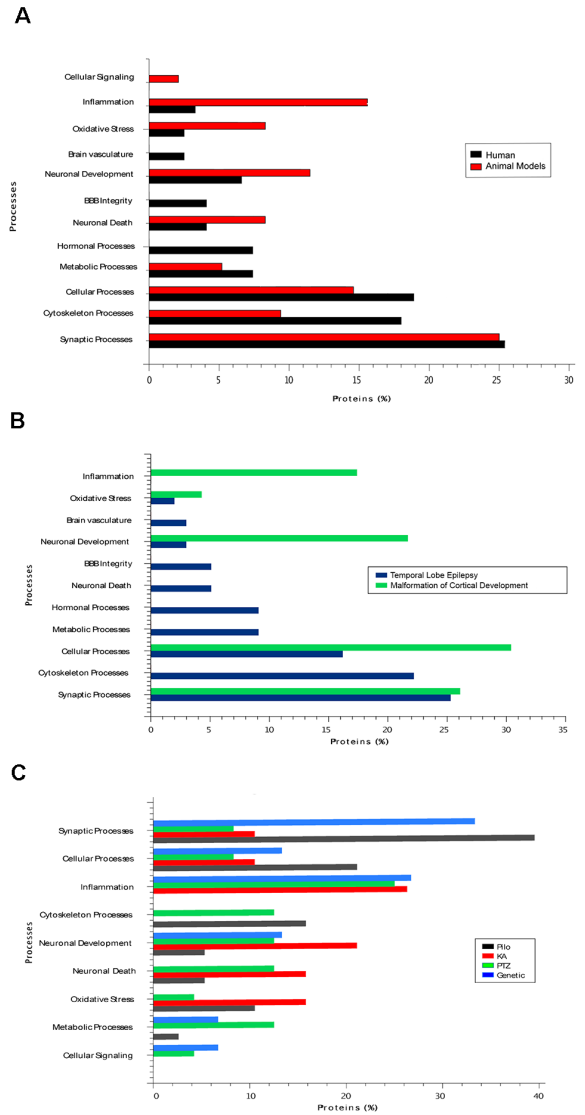

FIGURE 2 | (A) The main biological processes associated with epilepsy in human tissue and in tissues from rodent models of the disease. **(B)** The biological processes present in two types of human epilepsy, namely temporal lobe epilepsy (TLE) and malformations of cortical development. **(C)** The main biological processes present in studies with different animal models of epilepsy. Pilo, pilocarpine model; KA, kainic acid model; PTZ, pentylenetetrazol model.

CA1 and the granular layer of the DG. Due to the putative role of the DG in regulating the entrance of excitatory/inhibitory nerve signals in the hippocampus and its influences on the balance of the limbic system, the authors performed an MSI experiment using protein extracts from specific layers of the DG. They analyzed the data using hierarchical unsupervised clustering and reconstruction of the areas with different profiles (Hsu, 2007; Mériaux et al., 2014). These authors were the first to identify specific peptides in different layers of the DG. In the granular layer, there were galanin and neurokinin B; in the hilar layer, there was the C-terminally truncated fragment NPY(1–30); and in the molecular layer, they found somatostatin 1. Remarkably, these results are in accordance with previous findings, indicating that NYP and somatostatin are present in DG GABAergic interneurons, and the upregulation of NYP and its receptor in the DG is related to the seizure-induced neurogenesis (Furtinger et al., 2001; Kokaia, 2011; Gøtzsche et al., 2012; Mériaux et al., 2014). Somatostatin is a critical neuromodulator in the DG, and its levels are sensitive to excitotoxicity. Also, Mériaux et al. (2014) extracted proteins of 20 μm of microdissected hippocampal tissue sections and performed in-gel digestion and analysis by nanoLC-LTQ MS/MS (nano Liquid Chromatography Linear Trap Quadrupole in tandem Mass Spectrometry). Among the proteins with altered expression in the hippocampus of patients with MTLE, the authors found LIGI1, a protein involved with a hereditary form of NTLE, autosomal dominant partial epilepsy with auditory features (ADPEAF; Ottman et al., 2004).

Furthermore, researchers have found sex-specific proteins, such as tumor suppressor proteins, hormones (FSTL4 and BPIFB1), neurite outgrowth proteins (SRGP3, GPRIN3), and proteins implicated in Alzheimer's disease (APP) in male patients with MTLE, whereas female patients had a specific signature for proteins involved in brain synaptic plasticity (OPTN, OPALIN, and LIN7C), odorant receptors, growth factors (SESN1, IGF1R, BMPR1A, IRF-2, and ABI1), and actin-associated cytoskeleton proteins (cortactin, APS2; Mériaux et al., 2014). Label-free quantification confirmed the presence of sex-specific neuropeptide precursors and their receptors. In male patients with MTLE, there were secretogranin-1, secretogranin-2, galanin, and appetite-regulated hormone isoform 2, and angiotensinogen, neuroendocrine convertase 2, NPY type 2 receptor, vasopressin, and the mu-type opioid variant receptors. In female patients, they identified pro-enkephalin B and growth hormone 2, and VIP and leptin receptors. Furthermore, there were sex-specific patterns for endocrine hormones and their receptors: steroid hormone and FSH receptors (Follicle-stimulating hormone) in male patients, and growth hormone 2 (GH2) and LHRH receptors (Luteinizing hormone-releasing hormone) in females with MTLE (Mériaux et al., 2014).

Researchers recently used neocortex samples obtained from patients who underwent cortical resections to treat refractory seizures. These neocortical tissues displayed high spike frequency during electroencephalography (EEG) monitoring, and their proteomic findings were compared with nearby tissue with no or low spike frequency. This interesting approach made it possible to compare protein expression in tissue from the same patient, thus decreasing the impact of individual variability (Keren-Aviram et al., 2018). The authors used a 2D-DIGE (two-dimensional difference gel electrophoresis) approach followed by LC/MS and an in-line microfluidic Chip LC. Eight proteins were upregulated in the high-spiking regions (SNCA, STMN1, UGP2, DSP, CA1, PRDX2, SYN2, and DPYSL2), and 10 were downregulated in the same regions (GFAP, HNRNPK, CPNE6, CRYAB, GNAO1, PHYHIP, HNRPDL, ALDH2, GAPDH, and LASP1; Keren-Aviram et al., 2018). By using specific histological staining, the authors concluded that most of the upregulated proteins were found predominantly in the high spiking neocortex's blood vessels. Thus, they interpreted the

finding of a highly expressed erythrocyte protein cluster as a part of the increased vascularity in high-spiking samples. The process of angiogenesis has been associated with brain injury and increased blood-brain barrier (BBB) permeability in TLE, suggesting that this process may be related to metabolic changes and increased cortical activity (Greenberg and Jin, 2005; Papageorgiou et al., 2011; Visanji et al., 2012; Keren-Aviram et al., 2018). However, it was not possible to indicate whether the vascular changes cause epileptic activity or result from increased activity. Also, researchers have identified changes in adherens junction proteins, which can be involved in blood vessels or the BBB.

Several other abnormally regulated pathways have also been found in epilepsy, such as "acute phase response signaling," "Semaphorin signaling in neurons," and "axonal guidance signaling," indicating a high degree of changes in synaptic plasticity related to the epileptic neocortex. The identification of these pathways specifies the presence of CRMP isoforms, specially CRMP-2, which was upregulated in high-spike tissues. Moreover, GFAP, 50 kDa, total nuclear GFAP, and CRYAB were decreased in the neocortical tissues with high-spike frequencies. These results were unexpected because these proteins have been reported to be upregulated in neocortical epileptic tissue (Oberheim et al., 2008; Keren-Aviram et al., 2018). However, as previously discussed, He et al. (2006) also identified reduced CRYAB. CRYAB regulates GFAP assembly and it is strongly induced in reactive astrocytes. It plays a cytoprotective role with an anti-inflammatory and an anti-apoptotic function in those cells (Che et al., 2001; Ousman et al., 2007; Hagemann et al., 2009; Sarnat and Flores-Sarnat, 2009). Keren-Aviram et al. (2018) hypothesized that the co-reduction may be related to CRYAB–GFAP complex formation, reduced reactive astrocytes, or astrocyte apoptosis due to the lack of CRYAB. Furthermore, they showed that another candidate for the astrocyte marker, ALDH1L1, was also decreased. For all these results, they suggested that GFAP-positive astrocytes may be reduced and related to epilepsy, but the nature of the changes in these cells is unclear. Besides those patterns, they also identified significant individual proteins. In high-spiking neurons, they found downregulation of GNAO1, LIM, and LASP1, which may also be related to the astrocyte origin and plenty of other functions, and upregulation of SNCA, SYN2, and STMN1 which may be linked to neurite sprouting and synapse remodeling, because they interact with cytoskeletal proteins in the nerve growth cone and microtubule regulation (Keren-Aviram et al., 2018).

A recent study with histopathology and IHC showed reduced levels of mitochondrial ATP synthase (ATP5B) in all hippocampal regions of patients with MTLE and HS compared with *postmortem* control hippocampal tissue. The decreased level of ATP5B might be associated with neuronal cell maintenance (Mota et al., 2019). ATPases maintain an adequate neuronal transmembrane electrical potential, and, consequently, dissipate ionic transients and protect brain functions (Yang et al., 2004).

Furthermore, PTMs can lead to protein dysfunction and affect the phenotype. A recent study evaluated the cycling and disruptions of two PTM enzymes and their effect on hippocampal tissues from an animal model and patients with rMTLE compared with age-matched *postmortem* hippocampus as controls (Sánchez et al., 2019). Using HPLC and MS/MS analysis, electrophysiology, WB, pharmacological tests, immunofluorescence, and animal MRI, the authors found that the absence of OGA increases OGlcNacetylation modification of the tissue, reducing the duration of seizures and epileptic spike events. They concluded that OGA can be a potential therapeutic target for seizure control (Sánchez et al., 2019).

Also, the phosphorylation of amino acid residues in proteins with the potential to lead to changes in the functioning of neurons has been described in epilepsy. A work evaluating differences between patients with rMTLE associated with HS (MTLE-HS), who may or may not present a clinical sign called ictal fear (IF), showed a difference in the phosphorylation of a residue belonging to a subunit of the AMPA receptor, GluA1-Ser845. The authors used hippocampal and amygdalar homogenates from surgeries and determined the phosphorylation levels and the total amount of target proteins using WB, and, for the detection of proteins, selective antibodies. Thus, the authors demonstrated that patients with MTLE and IF had a significant decrease in p-GluA1-Ser845 in the anterior portion of the hippocampus and decreased GluA1 subunit levels in the amygdala ipsilateral to the HS compared with patients without IF (Leal et al., 2020). Of note, the authors did not use controls: they analyzed only the epileptic tissue.

Malformations of Cortical Development

Another important cause of refractory epilepsy is abnormal cortical development. These structural abnormalities are caused by disturbances during the development of the cortical layers, networks, and columns (Palmini et al., 1992). Many studies addressing the anatomical, molecular and electrophysiological characteristics of these malformations have been performed over the past two decades; however, it is still unclear how the size and location of the abnormalities are correlated with the severity of the seizure (Kilb et al., 2011; Schwartzkroin and Wenzel, 2012; Luhmann et al., 2014). Although abnormal cortical development is an important cause of focal epilepsy, proteomic studies exploring their mechanisms and biological responses are still scarce. Among the most common types of cortical malformations are focal cortical dysplasia (FCD), which is commonly found in children and is one of the main causes of medically refractory seizures in this group of patients with focal seizures (Blümcke et al., 2011).

A recent study evaluated brain tissue from patients with childhood cortical dysplasia (CCD) compared with surgical control tissue from patients with traumatic intracranial hypertension (TIH), by using iTRAQ (Isobaric tag for relative and absolute quantitation) labeling and MS/MS to perform a screening of the differentially expressed (DE) proteins (Qin et al., 2017). The authors identified 153 DE proteins in the CCD tissues and further validated their findings with WB and IHC. Through gene ontology, these were classified mainly into groups facilitating catalytic activity, binding, transporter activity, enzyme regulation, and molecule-structuring activity. Among the upregulated proteins, they identified FSCN1, CRMP1,

NDRG1, DPYSL5, MAP4, and FABP3, while PRDX6 and PSAP were downregulated. This was the first report of these proteins being associated with CCD. The increased levels of the proteins FSCN1, CRMP1, and MAP4 may be involved with abnormal neuron migration, neurite outgrowth, abnormal dendrite orientation, and the later involved with microtubules movement (Bast et al., 2006; Yamashita et al., 2006; Tokuraku et al., 2007; Higurashi et al., 2012; Wu et al., 2014; Qin et al., 2017). NDRG1 was also upregulated in CCD tissues and seemed to be part of a complex mechanism involved with reactive oligodendroglial hyperplasia (Shepherd et al., 2013; Qin et al., 2017). Meanwhile, decreased PRDX6 levels are associated with oxidative stress, a mechanism highly associated with brain damage and epilepsy, as discussed previously (Singh and Trevick, 2016; Qin et al., 2017). PSAP has been associated with animal models with neuroprotection, suggesting that its decrease could have an important role in neurotoxicity (Nabeka et al., 2014; Qin et al., 2017).

Tuberous sclerosis (TSC) is a multisystem autosomal dominant condition with a prevalence of 1 in 6,000 live births. TSC shares many histopathologic features with FCD, and most patients with the disease present mutations in *TSC1* or *TSC2*. The classical TSC lesions are hamartomas, but neurologic issues represent some of the most relevant clinical complications (Saxena and Sampson, 2015; Canevini et al., 2018). Genetic mutations in both genes result in the abnormal activation of the mammalian target of rapamycin (mTOR) pathway. This mTOR overactivity may lead to aberrant migration and orientation of neuronal cells that, consequently, drive atypical cortical lamination and dendritic arborization (Canevini et al., 2018). Epilepsy is the most prevalent clinical manifestation of TSC, affecting 85% of patients; infantile spasms are frequently accompanied by other seizure types, resulting in 75% of cases with pharmacoresistant epilepsy (Saxena and Sampson, 2015; Curatolo et al., 2018).

A study characterized overexpression of four microRNAs from cortical tubers resected from patients with a mutation in *TSC1* and *TSC2*. The authors compared epileptogenic tuberous tissue with adjacent non-tuberous tissue using quantitative LC-MS/MS proteomics to assess alterations in the abundance of the microRNA-targeted proteins; they identified significant repression in the expression of these proteins. The set of transcripts that were repressed has been associated with synaptic signaling and inflammation. Among these repressed proteins, they identified hamartin, which is a product of the *TSC1* gene. Based on the study results and data from the literature, the authors proposed a possible role for these aberrantly expressed microRNAs, especially miRs-23a and miRs-34a, in the tuber pathology. Furthermore, aberrantly expressed microRNAs are likely involved with alterations in synaptic density and loss of neuronal elements of TSC patients (Dombkowski et al., 2016).

A very recent study (Liu et al., 2020) reported mutation analyses, clinical features, and tissue proteomic profiles of three patients with epilepsy caused by truncating *TSC1* mutations. The authors used a DIA (Data-independent acquisition) workflow to explore the proteomic profile of these patients compared with control tissue from craniocerebral trauma surgery and found downregulation of ARFGEF2, which has been associated with intellectual disability and abnormal neuronal migration (Hong et al., 2018; Liu et al., 2020). DCX upregulation may also be involved with intellectual disability, abnormal neuronal localization, epilepsy (des Portes et al., 1998; Lee et al., 2003; Liu et al., 2020), and decreased levels of ATG12, a protein related to autophagy (Wang et al., 2019). Moreover, Liu et al. (2020) identified decreased levels of K^+ channel proteins (KCNA2 and KCNAB2) in the *TSC1* mutation group compared with the controls; these changes have been associated with epilepsy due to the proteins' role in membrane excitability (Jan and Jan, 1997; Liu et al., 2020). In summary, through the enrichment gene ontology analysis, the researchers found that DE proteins were mainly the components of synaptic membranes; the biological processes that were highly enriched were amino acid metabolism and the molecular functions related to antioxidant activity, ligase activity, and tetrapyrrole binding, which had an especially high number of DE proteins. Taken together, these data suggest that TSC mutations or alterations in patients' synaptic proteins may affect the information transmission in the cells, and changes in patients' amino acid metabolism can be a new mechanism to be explored in the TSC complex context (Liu et al., 2020).

Notably, despite the many efforts to explore and describe epilepsy-related changes at the protein level, most published neuroproteomics studies are limited by technical constraints and have mainly used low in-depth coverage techniques. The first published neuroproteomics study, from the early 2000s, used predominantly two-dimensional polyacrylamide gel electrophoresis (2D-PAGE). Unfortunately, besides being time-consuming, 2D-PAGE requires large amounts of input material, it is labor-intensive, and it is limited to detecting low-abundance and hydrophobic proteins (Zhang et al., 2014; Yokota, 2019). It was only around 2014 that studies using LC-MS started to appear in the epilepsy field; this technique has allowed for more extended coverage of the proteome and enhanced dynamic range and sensitivity. Another challenge, specific to studies with human specimens, is the limitations imposed by the use of *postmortem* tissue as controls, and the lack of age-matched subjects. As mentioned previously, this approach may introduce confounding factors in data interpretation due to the delay in tissue collection and processing, which directly affects the rate of protein degradation (ElHajj et al., 2016; Ferreira et al., 2018). Hence, studies in animal models may provide relevant information that can complement the results obtained with human samples by overcoming the lack of proper controls for human tissue (Becker, 2018).

PROTEOMIC STUDIES IN TISSUE FROM ANIMAL MODELS OF EPILEPSY

Animal models, mainly rodents, which present physiological characteristics that mimic human epilepsy, are often used to study the mechanisms and possible therapeutic strategies for epilepsy. They can be divided into two main categories: acquired models, usually induced through a stimulus like an injury trauma, the use of chemo convulsant, and electrical stimulation of brain regions; or genetic models caused by

genetic modifications that lead to spontaneous recurrent seizures (Löscher, 2017). Here, we will review the main findings of proteomic studies using tissue from animal models of epilepsy.

Acquired Models

Pilocarpine

The pilocarpine models of MTLE are based on the induction of a *status epilepticus* (SE, a seizure that lasts at least 5 min uninterrupted), and its physiological features reflect pathologic patterns of human MTLE, with the occurrence of spontaneously recurrent seizures and interictal activity patterns (Cavalheiro et al., 1991; Sharma et al., 2007; Curia et al., 2008). Pilocarpine is a drug that acts as a muscarinic acetylcholine receptor partial agonist, specifically the M1 receptor. It induces long-term epileptic activity and neuronal damage with structural alterations and neuronal death mainly in the limbic regions (Cavalheiro et al., 1991; Curia et al., 2008). Using 2DE-based proteomics to evaluate changes in the hippocampal tissue from pilocarpine-treated animals 2 days after SE (Greene et al., 2007), the most significant difference was the upregulation of HSP27, which is linked with responses to cellular stress and could also be performing a neuroprotective role in these cells (Kalwy et al., 2003; Arimura et al., 2004; Czech et al., 2004). DRP-2 was also changed: it was downregulated in the hippocampus of epileptic animals. This protein is related to the development of newborn neurons and axon growth, which are directly involved with neuronal development. Furthermore, there was elevated expression of α-tubulin, which is also related to axon outgrowth and microtubule functions, indicating that structural abnormalities are a significant contributing factor to epileptogenesis in this model. Moreover, an observed increase in DHPR in the hippocampus from pilocarpine-treated rats could result in elevated BH_4 levels (Cho et al., 1999), contributing to neuronal damage following SE. The authors suggested it as a possible therapeutic target (Greene et al., 2007).

Another study using hippocampal tissue from a pilocarpine-induced model evaluated two-time points, 12 h (acute) and 72 h (latent) after SE compared with controls; the authors identified 57 DE proteins using 2DE coupled with MALDI-MS and MS/MS (Liu et al., 2008). This study demonstrated that abnormal expression of structural (actins and tubulins) and mitochondrial (PKM2, ATP5A1, ATP5B, VDAC2, HSP60, and others) proteins and impairment in synaptic transmission and plasticity (HOMER2, SYN2, and SNAP25) could be involved with the pathological mechanisms underlying epilepsy. Among these mechanisms, the authors suggested that these alterations could lead to modifications in information storage, long-term plasticity, structural alterations of neural circuits, synaptic impairment, inadequate energy supply, changes in ion homeostasis, apoptosis, oxidative stress, and protein misfolding, which could be related to seizure-induced neuronal damage and neuroprotection (Liu et al., 2008).

Li et al. (2010) analyzed the DG from a pilocarpine model of epilepsy using 2DE combined with LC-MS/MS to identify the protein abundance and phosphorylation state of these neurons. The authors reported eight functional protein categories: metabolism, synaptic, energy, structural, stress response, apoptosis, transcription, and growth. Among the structural proteins, β-actin was downregulated and profilin-1 and vimentin were upregulated. From synaptic proteins, α-synuclein and UCH-L1 were upregulated. The researchers also identified several proteins involved with metabolism, such as carbonic anhydrase II, which was enhanced phosphorylated in the epileptic hippocampus. Another protein that was enhanced and phosphorylated by SE was NSE2, a marker of neuronal damage. There was also a 141% increase in the expression of the cathepsin D. The cell stress response was exacerbated through increased expression of PRDX6, a potent antioxidant, and increased expression of the HSP27 and CRYAB (Li et al., 2010).

A more recent study used the pilocarpine model to analyze the right and left hippocampus using 2DE and MALDI-TOF-MS (Sadeghi et al., 2017). Lateralization has been reported to be very relevant, especially with the predominance of the left hemisphere in human epilepsy (Gatzonis et al., 2002). When analyzing only the control hippocampus (healthy) to evaluate changes in both hemispheres, the researchers found a significant increase in the expression of the proteins DJ-1, SPR, BASP1, α-Inx, AADC, CLCA, and CLCB in the right hippocampus. These proteins are related to dopamine synthesis. Overall, the study revealed a decrease in the proteins involved in dopamine pathways (DJ-1, SPR, AADC, β-synuclein, BASP1, CLCA, CLCB, SNAP25, α-Inx, and STMN1) in the pilocarpine model. Also, there was an increase in polyamine regulatory enzymes (mitochondrial ornithine transporter and ODC), which were higher in the left epileptic hippocampal tissue. This lateralization could lead to a lower seizure threshold in the left hemisphere in the epilepsy context (Sadeghi et al., 2017).

In a very recent study performed by our group in 2020, we employed the pilocarpine model to broadly assess changes in the proteome and transcriptome of Wistar rats (Canto et al., 2020). We isolated different regions of the hippocampal formation, DG and CA3, as well as different areas (dorsal and ventral), using laser microdissection and determined their protein and transcriptional profiles—the transcriptomic study used next-generation sequencing, while the proteomic study used a label-free mass spectrometry approach. After integrating the data between the two molecular techniques, we found several pathways suggestive of enhanced epileptogenesis in the CA3 compared with the DG. Also, we described a complex network of cellular pathways that contribute to the generation of epileptogenesis in different regions and areas of the hippocampal formation, such as: (i) upregulation in pathways related to inflammation and immune response; (ii) downregulation in calcium/calmodulin-dependent protein kinases (CAMKs); and (iii) abnormal regulation of ion channels, such as some voltage-gated K^+ and voltage-gated Na^+ channels. We also found upregulation of genes from pathways associated with neurogenesis in the DG (*Notch1-201* and *Ephb6-201*) and the LRRK2 (Leucine-rich repeat kinase 2) pathway in the dorsal region of the DG. By contrast, there was a downregulation in the WNT signaling pathway in the CA3. These findings

also highlight the heterogeneity in the transcriptome and proteome of different hippocampal regions and areas (Canto et al., 2020).

Kainic Acid

The intra-hippocampal administration of kainic acid (KA) is another animal model for MTLE; it is widely used in the study of the histopathological changes occurring in MTS because many of the characteristic changes found in human MTS are seen in this model (Bouilleret et al., 1999; Heinrich et al., 2011). Thus, it is believed that characterizing the proteomes of these animals can provide information about the cellular mechanisms involved in the establishment of epileptogenesis and cellular events triggered by the establishment and progression of the disease (Kim et al., 2004). Many studies have used this approach to identify determining factors for the recurrent onset of seizures and the mesial lesions commonly found in patients with MTLE. With this focus, a study evaluated the hippocampal proteome of KA-induced mice using high-resolution Orbitrap LC-MS/MS combined with label-free quantification at three different times after the injection of the chemical (1, 3, and 30 days), with NaCl-injected mice as controls, to evaluate molecular patterns that may provide information about the evolution of the disease (Bitsika et al., 2016). The authors reported decreased expression of proteins related to axonal regeneration and neuroplasticity, mainly in the chronic phase of the disease (30 days after KA injection). Downregulated proteins such as neurochondrin, Homer1, Ataxin-10, and Neurabin-2 suggest dysfunctions in neuroplasticity. By contrast, changes in MAP2, tau (Mapt), and BRSK1 may characterize the neurodegeneration profile observed in this model. Therefore, these changes could trigger characteristic histopathological findings in MTLE, such as neuronal loss observed in hippocampal regions including the DG (Bitsika et al., 2016).

Bitsika et al. (2016) also reported increased expression of other proteins related to inflammatory processes, such as a link with the activation of microglia/astrocyte, which extends from the stage of development of the disease (3 days after KA injection) to the chronic phase. This process was characterized by elevated expression of proteins linked to neuroprotection resulting from inflammatory processes, such as clusterin and gelsolin, as well as pro-inflammatory cytokines such as C4B, α-2-macroglobulin, CD44, and some integrin receptors in T cells (Bitsika et al., 2016).

In addition to the quantitative analysis of protein expression, it is also possible to analyze PTMs, which may provide information regarding protein activity (Kumar and Prabhakar, 2008). In this context, a study published in 2014 showed downregulation in 12 phosphorylation sites of Nav1.2 channels in rats with acute seizures induced by systemic KA injection, using the immunopurification of Nav1.2 and subsequent gel-based proteomics by nano-LC tandem LTQ-FT MS (Baek et al., 2014). One of the target regions for the insertion of a phosphate group identified by this approach, the ID I-II linker, when downregulated, leads to an increase in ionic currents, a phenomenon possibly related to the onset of seizures and the subsequent epileptogenesis. Besides, increased methylation in some arginine residues (R472, R563, and R570) from these channels, which can contribute to the development of seizures, has also been described (Baek et al., 2014).

Mitochondrial protein PTMs also play an important role in overall cellular functioning: These modifications participate in the regulation of central metabolism pathways, such as those related to bioenergetics. It is well known that epileptogenesis and seizure development is closely associated with mitochondrial dysfunctions because this organelle plays a determining role in the production of ATP and the control of oxidative damage (Kovac et al., 2013; Rowley and Patel, 2013). Therefore, a study sought to demonstrate, through WB analysis of the mitochondrial isolate from hippocampal homogenates, which PTMs have great relevance to cellular processes that culminate in the establishment of recurrent epileptic seizures (Gano et al., 2018). The authors reported a decrease in SIRT3, a protein responsible for NAD^+-dependent deacetylation of mitochondrial proteins, bioenergetics, and antioxidant mechanisms, especially in the chronic phase of the model. This reduction was correlated with some of the main characteristic cellular changes of the disease, including alterations in bioenergetics, antioxidant pathways, and epileptogenesis. Thus, as a result of this finding, the acetylation levels of mitochondrial proteins would appear to be increased. Also, there were other alterations, such as a decrease in NAMPT, with an effect on NAD^+ levels. Also, increased acetylation of MnSOD and IDH2 may lead to impairment in the oxidative equilibrium of hippocampal cells with the potential to contribute to the commonly observed neurodegeneration pattern in MTLE (Gano et al., 2018).

Pentylenetetrazol

Another biologically active molecule that can generate acute or chronic seizures is pentylenetetrazol (PTZ; Takechi et al., 2012). The pro-convulsive action of PTZ is due to its antagonistic activity on $GABA_A$ receptors, thus generating a decrease in the inhibitory effect produced by GABA when it binds to its receptors (Ramanjaneyulu and Ticku, 1984). Although this model has been studied since the mid-1960s, the process of elucidating the proteins involved in the mechanism of PTZ-induced seizures is not yet complete (Löscher, 2011). However, it has already been shown that increased susceptibility to seizures through the administration of this molecule is linked to increased expression of tissue plasminogen activator (tPA) and some structural proteins, such as MAP1B and GAP43, in hippocampal tissue (Junker et al., 2005). Also, the authors demonstrated, through a gel-based proteomic analysis followed by a MALDI-TOF approach using hippocampal tissues from rats induced with PTZ that molecular modifications—possibly linked to PTM—of the Rieske iron-sulfur protein may be related to the seizure development process in this model. Given that the Rieske iron-sulfur protein participates in the protein structure of the mitochondrial cytochrome bc_1 complex, it was proposed that changes in its activity are characterized by the decrease in the energetic state of the cells—a development with the potential to facilitate the occurrence of seizures and leading to some histopathological findings, such as the

damage in the CA1 subfield of the hippocampal formation (Junker et al., 2005).

Electrical Stimulation

The electrical stimulation approach of specific neuronal pathways also has great importance in the induction of epilepsy in animal models, mainly rodents. This method retains considerable relevance in the scope of animal models due to the generation of cell lesions similar to those found in human MTLE, with less extra-hippocampal injury (Norwood et al., 2010). Despite being a well-characterized model, the molecular mechanisms that lead animals to recurrent seizures are still poorly understood (Norwood et al., 2010; Will et al., 2013). In this sense, to offer molecular bases for such pathophysiological changes, a study published in 2017 showed that the hippocampal tissue and the parahippocampal cortex of Sprague Dawley rats were induced by stimulation of the right anterior basolateral region of the amygdala for proteomic analysis by LC-MS/MS at different stages of the disease (Keck et al., 2018). In the hippocampus, the authors identified 121 DE proteins 2 days after SE, 276 DE proteins after 10 days, and 14 DE proteins after 8 weeks. In the parahippocampal cortex, there were 218, 419, and 223 DE proteins 2 days, 10 days, and 8 weeks, respectively, after SE. Therefore, it was possible to describe temporal changes in molecular profiles that were possibly linked to the histopathophysiological changes observed in the animals. These profiles displayed, in the hippocampus, enriched pathways commonly linked to the regulation of cell death (14-3-3 and HIPPO signaling), cellular plasticity (cytoskeletal dynamics and axonal guidance), and carbohydrate and amino acid metabolism (Keck et al., 2018). More recently, our group analyzed the proteome of the DG from perforant pathway–stimulated rats by LC-MS/MS; we identified different proteomic profiles for the DG layers (granular and molecular) and regions (ventral and dorsal; do Canto et al., 2020). In all layers and regions, there were two enriched pathways that are important for determining the molecular bases for epileptogenesis and the cellular changes observed: inflammation and energy metabolism. The enriched inflammation pathways (immune response-CRTH2 signaling in Th2 cells, IL-16 signaling pathway, and others) contained abnormally regulated proteins such as PKC and 14-3-3 proteins. Those related to bioenergetics (citric acid cycle, gluconeogenesis, and amino acid metabolism) exhibited several downregulated proteins, pointing to a dysfunction in the energy generation process of the cells. In addition to these pathways and proteins, others were linked to specific DG layers and regions. Proteins such as PARK7 and connexin 31/gap junction were differentially regulation in the ventral portion of the DG, and RACK1 expressed opposite differential regulation in the dorsal and ventral part of the DG (do Canto et al., 2020).

Due to the relevance of the inflammatory processes concerning human MTLE and animal models, some researchers have examined proteins closely linked to inflammatory pathways to determine their role in the main histopathological findings observed in the hippocampal tissue. In a study aiming to establish such a role, Walker et al. (2016) explored the proteome of the hippocampus and the parahippocampal cortex of rats induced with electrical stimulation of the right anterior basolateral nucleus of the amygdala was obtained by LC-MS/MS. The authors also evaluated the proteome in three stages of the disease—the early post-insult (2 days after SE), the latency phase (10 days after SE), and the chronic phase (8 weeks after SE)—to assess changes in the inflammatory profile as a function of disease progression. They showed an early induction for inflammatory pathways through the enrichment analyses of these two regions, with a sustained activity during the latency phase that preceded recurrent seizures. Moreover, in the phase where the disease is established (chronic phase), inflammatory pathways are predominant in the parahippocampal cortex compared with the hippocampus. Part of the inflammatory outcomes was related to the modulation of TLR (Toll-like receptors) signaling molecules, such as an increased expression of RPS27A, ITGB2, and ITGAM, mainly during the first two phases of the disease.

In addition to TLR signaling, some molecules related to purinergic receptors were found, such as P2RX7 upregulated in the hippocampus during epileptogenesis. These findings suggest that these receptors contribute to the maintenance of neuroinflammatory processes (Walker et al., 2016).

Genetic Models

Among the animal models of epilepsy, genetically predisposed species display a similar pattern of spontaneous seizures and clinical phenotypes that is seen in some human epilepsy. In these models, the seizures occur spontaneously or in response to a stimulus (Löscher, 1984). The genetic models of absence epilepsy have been frequently studied. The Genetic Absence Epilepsy from Strasbourg (GAERS) and Wistar Albino Glaxo/Rijswijk (WAG/Rij) rats are widely used as rat models; they present behavioral and EEG characteristics that mimic the generalized human absence epilepsy (Depaulis and van Luijtelaar, 2006). Meanwhile, the BS/Orl and BR/Orl are genetic "in-mirror" mouse models (Chapouthier et al., 1998).

Absence Seizures

Absence seizures (AS) are a generalized type of epileptic seizures that frequently occur in children. AS are characterized by an abrupt loss of consciousness, motionless stare, and suspension of ongoing actions. The common hallmark of AS is bilaterally generalized synchronous "spike and wave" discharges (SWDs). It is broadly accepted that the alternation from healthy states to SWDs occurs after changes in corticothalamic connectivity, such as increasing excitatory connections between the cortex and the thalamus. The thalamic contribution to SWD triggering has been observed in *in vivo* studies (Maksimenko et al., 2017; Deeba et al., 2018). Searching for altered intracellular proteins in AS, a study using 2DE coupled with Nano-LC-ESI-MS/MS analyzed three brain structures from the GAERS rat model compared with non-epilepsy animals: the parietal cortex, thalamus, and hippocampus (Danış et al., 2011). The delta subunit of ATP synthase and the 14-3-3 zeta isoform were upregulated in the parietal cortex. Myelin basic proteins and macrophage migration inhibitory factor was upregulated in the thalamus and, in the hippocampus, the migration

inhibitory factor was upregulated. At the same time, 0-β-2-globulin was downregulated. These findings indicate that, while intracellular proteins have not been seen as primarily responsible for neuronal excitability in seizures, they are relevant for maintaining neuronal functions and are linked to several mechanisms. Here are some examples: (i) the generation of energy through changes in ATP synthase; (ii) inflammatory responses represented by the macrophage inhibitory factor; (iii) ion channel and signal transduction with the alteration of 14-3-3 zeta and membrane potassium conductance; and (iv) abnormal expression of myelin basic protein and 0-β-2-globulin (Danış et al., 2011).

While Lagarrigue et al. (2012) aimed to develop a new proteomics workflow using MSI to detect possible disease markers, they used the BR/Orl and BS/Orl mouse models, compared them with the non-epileptic controls, and identified some interesting proteins. Among the findings, the SYN1 fragment was one of the most statistically significant fragments identified in the epileptic tissue. It was a potential marker of absence epilepsy because it is thought to control excitability (Garcia et al., 2004; Lagarrigue et al., 2012). The findings also identified DE of myelin basic protein, neurogranin, PCP4, ubiquitin, and thymosin β-4. These proteins have essential roles in the central nervous system and can contribute to the pathogenesis of the disease (Lagarrigue et al., 2012). Another study, using 2DE-MALDI-TOF MS, found two DE membrane proteins in the epileptic tissue compared with controls, namely 14-3-3 (upregulated) and the membrane-anchored protein GNBPs1 (downregulated). These data suggest that both of them can be important targets for the neuropharmacology studies of this disease (Yuce-Dursun et al., 2014).

Tuberous Sclerosis

There is interesting research that focuses on the role of abnormal proteins in animal models of TSC. A study published in 2016 aimed to explore the role of mTORC1 in regulating regional protein expression during disease and normal states used MS/MS combined with protein-protein interaction (PPI) analysis. The authors identified PARK7 protein as increased in dendrites and colocalized with post-synaptic density protein-95 (PSD95). To confirm these predicted results in the context of the disease state, they tested a *Tsc1* conditional knockout (cKO) mouse model and performed IHC. The *Tsc1*-cKO mouse model presents elevated mTORC1 activity due to TSC1 protein reduction, and it exhibits behavioral features of both epilepsy and autism. The mouse model results indicated that the expression of PARK7 increases in regions where the activity of mTORC1 is higher (Niere et al., 2016).

FUTURE DIRECTIONS

In recent years, proteomic studies have become more advanced, mostly due to the incorporation of new technology, such as MS. These advances have led to increased accuracy and sensitivity, fast acquisition rates, high resolution, and the use of small input samples (Hosp and Mann, 2017). The variations detected in the proteome may result from different physiological states, differential gene expression, and regulation, or translational modifications (Ramadan et al., 2017; Li et al., 2019). Although neuroproteomics can help disentangle some of the brain's biological complexity in normal and disease states, the results are limited by the disease complexity, variability in etiology, and brain areas analyzed.

These studies must account for the remarkable individual variation among human subjects and the intrinsic limitations in the characterization of physiological and, most importantly, disease-related phenotypes. Indeed, one of the most critical drawbacks identified in the neuroproteomics literature is the limited clinical characterization of the studied patients (Li et al., 2019). However, even with all the aforementioned constraints, systems biology combined with neuroproteomics analyses can lead to a new level of visualization and interpretation of the molecular information (Jaber et al., 2016a,b; Ramadan et al., 2017). Thus, generating new biological hypotheses about the molecular mechanisms of disease that can be further explored in depth in follow-up studies, especially in those with a multi-omics approach. In epilepsy, the most critical findings in proteomic studies have been the changes detected in structural proteins, especially those that comprise the cytoskeleton, oxidative stress, and energy metabolism—with an emphasis on the lipid metabolism identified especially in human studies; alterations of ion channels, inflammation, and synaptic proteins have been prevalent in most of the described studies (**Figure 2**). These changes could directly or indirectly affect the neurotransmission processes, which are mainly impaired in epilepsy. However, which mechanisms are more related to the cause or consequence of the disease remains unknown. Gliosis and extensive neuronal damage, as much as inflammatory responses, are frequently found in epilepsy patients and animal models. One of the greatest challenges when investigating the molecular mechanisms of epilepsy is to identify which abnormal biological pathways are the result of the histopathological changes that occur in the epileptic tissue and which ones are related to the mechanism leading to the lesions in the first place. Furthermore, it remains to be determined whether abnormally expressed proteins and enriched molecular pathways are indeed leading to seizures or maybe protecting against it.

The majority of the proteomic analyses of epilepsy are not hypothesis-driven (Ramadan et al., 2017); therefore, they have identified a broad set of biological mechanisms that can now guide future studies with defined, critical, and correct questions to be explored, such as a specific protein or PTM changes, or a dysregulated network involved with one particular pathological state. More important, future applications of more advanced technology in proteomic studies are essential to improve data quality and coverage and the acquisition of relevant biological information.

Furthermore, these protein identifications and quantifications can help researchers understand the disease progression and prognosis because some of the studies have analyzed the disease at various time points to better evaluate its biological effects. These findings can also, soon, contribute to the clinical diagnosis by being applied to the biomarker studies, helping predict and understand the drug-resistance mechanisms.

CONCLUSION

Epilepsies represent a large group of heterogeneous conditions with complex molecular mechanisms. Neuroproteomic studies exploring different epilepsy types have made significant contributions, pointing to an array of biological processes that are involved in these conditions, especially energy metabolism, oxidative stress, inflammation, and excitatory imbalance. Proteomic analyses in epilepsy are useful because the analyzed tissue sample closely represents the pathogenic process involved in human epilepsies. However, the lack of an ideal experimental model that can faithfully reproduce the condition seen in patients has created difficulties in interpreting proteomic findings in animal models. At the same time, the use of human tissue samples can also be problematic because they are usually not available at a critical point in time when epileptogenesis actually occurs.

Furthermore, one cannot rely on human tissue to understand how the disease progresses over time. Another limitation of using tissue samples from patients is the remarkable individual variability among patients, a factor that may create confounding factors when interpreting the proteomic findings. It is clear that there are no simple solutions for the aforementioned limitations; thus, the field will significantly benefit from additional studies performed with large samples of well-characterized tissue so that the full array of proteomic changes occurring in epileptogenic abnormalities can be well characterized. Also, studies comparing the findings using similar proteomic techniques in different models and human tissue will be of great value in future studies.

AUTHOR CONTRIBUTIONS

All the authors contributed equally to the development, elaboration, and writing of this work. All authors contributed to the article and approved the submitted version.

FUNDING

This work was supported by a grant from Fundação de Amparo à Pesquisa do Estado de São Paulo (FAPESP, grant number # 2013/07559-3), SP, Brazil. AC, AD, JG, AG, and DR are supported by fellowships from FAPESP (grants # 2015/12960-4, 2015/25607-0, 2017/23954-0, 2019/00213-0, and 2019/00048-0, respectively). IL-C is supported by grants from Conselho Nacional de Pesquisa (CNPq), Brazil (grants # 403299/2016-0 and 309494/2014-1) and Coordenação de Aperfeiçoamento de Pessoal de Nível Superior (CAPES), Brazil (grant # 001).

REFERENCES

Al Diffalha, S., Sexton, K. C., Watson, P. H., and Grizzle, W. E. (2019). The importance of human tissue bioresources in advancing biomedical research. *Biopreserv. Biobank.* 17, 209–212. doi: 10.1089/bio.2019.0039

Allone, C., Lo Buono, V., Corallo, F., Pisani, L. R., Pollicino, P., Bramanti, P., et al. (2017). Neuroimaging and cognitive functions in temporal lobe epilepsy: a review of the literature. *J. Neurol. Sci.* 381, 7–15. doi: 10.1016/j.jns.2017.08.007

Arimura, N., Menager, C., Fukata, Y., and Kaibuchi, K. (2004). Role of CRMP-2 in neuronal polarity. *J. Neurobiol.* 58, 34–47. doi: 10.1002/neu.10269

Babb, T. L., Kupfer, W. R., Pretorius, J. K., Crandall, P. H., and Levesque, M. F. (1991). Synaptic reorganization by mossy fibers in human epileptic fascia dentata. *Neuroscience* 42, 351–363. doi: 10.1016/0306-4522(91)90380-7

Baek, J.-H., Rubinstein, M., Scheuer, T., and Trimmer, J. S. (2014). Reciprocal changes in phosphorylation and methylation of mammalian brain sodium channels in response to seizures. *J. Biol. Chem.* 289, 15363–15373. doi: 10.1074/jbc.M114.562785

Bast, T., Ramantani, G., Seitz, A., and Rating, D. (2006). Focal cortical dysplasia: prevalence, clinical presentation and epilepsy in children and adults. *Acta Neurol. Scand.* 113, 72–81. doi: 10.1111/j.1600-0404.2005.00555.x

Becker, A. J. (2018). Review: animal models of acquired epilepsy: insights into mechanisms of human epileptogenesis. *Neuropathol. Appl. Neurobiol.* 44, 112–129. doi: 10.1111/nan.12451

Bitsika, V., Duveau, V., Simon-Areces, J., Mullen, W., Roucard, C., Makridakis, M., et al. (2016). High-throughput LC-MS/MS proteomic analysis of a mouse model of mesiotemporal lobe epilepsy predicts microglial activation underlying disease development. *J. Proteome Res.* 15, 1546–1562. doi: 10.1021/acs.jproteome.6b00003

Blair, J. A., Wang, C., Hernandez, D., Siedlak, S. L., Rodgers, M. S., Achar, R. K., et al. (2016). Individual case analysis of postmortem interval time on brain tissue preservation. *PLoS One* 11:e0151615. doi: 10.1371/journal.pone.0151615

Blümcke, I., Beck, H., Lie, A. A., and Wiestler, O. D. (1999). Molecular neuropathology of human mesial temporal lobe epilepsy. *Epilepsy Res.* 36, 205–223. doi: 10.1016/s0920-1211(99)00052-2

Blümcke, I., Thom, M., Aronica, E., Armstrong, D. D., Bartolomei, F., Bernasconi, A., et al. (2013). International consensus classification of hippocampal sclerosis in temporal lobe epilepsy: a task force report from the ILAE commission on diagnostic methods. *Epilepsia* 54, 1315–1329. doi: 10.1111/epi.12220

Blümcke, I., Thom, M., Aronica, E., Armstrong, D. D., Vinters, H. V., Palmini, A., et al. (2011). The clinicopathologic spectrum of focal cortical dysplasias: a consensus classification proposed by an *ad hoc* Task Force of the ILAE Diagnostic Methods Commission1: the ILAE classification system of FCD. *Epilepsia* 52, 158–174. doi: 10.1111/j.1528-1167.2010.02777.x

Borges, M. A., Min, L. L., Guerreiro, C. A. M., Yacubian, E. M. T., Cordeiro, J. A., Tognola, W. A., et al. (2004). Urban prevalence of epilepsy: populational study in São José do Rio Preto, a medium-sized city in Brazil. *Arq. Neuropsiquiatr.* 62, 199–204. doi: 10.1590/s0004-282x2004000200002

Bouilleret, V., Ridoux, V., Depaulis, A., Marescaux, C., Nehlig, A., and Le Gal La Salle, G. (1999). Recurrent seizures and hippocampal sclerosis following intrahippocampal kainate injection in adult mice: electroencephalography, histopathology and synaptic reorganization similar to mesial temporal lobe epilepsy. *Neuroscience* 89, 717–729. doi: 10.1016/s0306-4522(98)00401-1

Brodie, M. J., Barry, S. J. E., Bamagous, G. A., Norrie, J. D., and Kwan, P. (2012). Patterns of treatment response in newly diagnosed epilepsy. *Neurology* 78, 1548–1554. doi: 10.1212/WNL.0b013e3182563b19

Canevini, M. P., Kotulska-Jozwiak, K., Curatolo, P., La Briola, F., Peron, A., Sowińska, M., et al. (2018). Current concepts on epilepsy management in tuberous sclerosis complex. *Am. J. Med. Genet. C Semin. Med. Genet.* 178, 299–308. doi: 10.1002/ajmg.c.31652

Canto, A. M., Matos, A. H. B., Godoi, A. B., Vieira, A. S., Aoyama, B. B., Rocha, C. S., et al. (2020). Multi-omics analysis suggests enhanced epileptogenesis in the Cornu Ammonis 3 of the pilocarpine model of mesial temporal lobe epilepsy. *Hippocampus* doi: 10.1002/hipo.23268. [Epub ahead of print].

Cavalheiro, E. A., Leite, J. P., Bortolotto, Z. A., Turski, W. A., Ikonomidou, C., and Turski, L. (1991). Long-term effects of pilocarpine in rats: structural damage of the brain triggers kindling and spontaneous recurrent seizures. *Epilepsia* 32, 778–782. doi: 10.1111/j.1528-1157.1991.tb05533.x

Cendes, F. (2005). Mesial temporal lobe epilepsy syndrome: an updated overview. *J. Epilepsy Clin. Neurophysiol.* 11, 141–144. doi: 10.1586/ern.10.53

Chandana, R., Mythri, R. B., Mahadevan, A., Shankar, S. K., and Srinivas Bharath, M. M. (2009). Biochemical analysis of protein stability in human brain collected at different post-mortem intervals. *Indian J. Med. Res.* 129, 189–199.

Chapouthier, G., Launay, J.-M., Venault, P., Breton, C., Roubertoux, P. L., and Crusio, W. E. (1998). Genetic selection of mouse lines differing in sensitivity to a benzodiazepine receptor inverse agonist. *Brain Res.* 787, 85–90. doi: 10.1016/s0006-8993(97)01483-2

Che, Y., Piao, C. S., Han, P.-L., and Lee, J.-K. (2001). Delayed induction of α B-crystallin in activated glia cells of hippocampus in kainic acid-treated mouse brain. *J. Neurosci. Res.* 65, 425–431. doi: 10.1002/jnr.1170

Cho, S., Volpe, B. T., Bae, Y., Hwang, O., Choi, H. J., Gal, J., et al. (1999). Blockade of tetrahydrobiopterin synthesis protects neurons after transient forebrain ischemia in rat: a novel role for the cofactor. *J. Neurosci.* 19, 878–889. doi: 10.1523/JNEUROSCI.19-03-00878.1999

Crepeau, A. Z., and Sirven, J. I. (2017). Management of adult onset seizures. *Mayo Clin. Proc.* 92, 306–318. doi: 10.1016/j.mayocp.2016.11.013

Crespel, A., Coubes, P., Rousset, M.-C., Brana, C., Rougier, A., Rondouin, G., et al. (2002). Inflammatory reactions in human medial temporal lobe epilepsy with hippocampal sclerosis. *Brain Res.* 952, 159–169. doi: 10.1016/s0006-8993(02)03050-0

Curatolo, P., Nabbout, R., Lagae, L., Aronica, E., Ferreira, J. C., Feucht, M., et al. (2018). Management of epilepsy associated with tuberous sclerosis complex: updated clinical recommendations. *Eur. J. Paediatr. Neurol.* 22, 738–748. doi: 10.1016/j.ejpn.2018.05.006

Curia, G., Longo, D., Biagini, G., Jones, R. S. G., and Avoli, M. (2008). The pilocarpine model of temporal lobe epilepsy. *J. Neurosci. Methods* 172, 143–157. doi: 10.1016/j.jneumeth.2008.04.019

Czech, T., Yang, J.-W., Csaszar, E., Kappler, J., Baumgartner, C., and Lubec, G. (2004). Reduction of hippocampal collapsin response mediated protein-2 in patients with mesial temporal lobe epilepsy. *Neurochem. Res.* 29, 2189–2196. doi: 10.1007/s11064-004-7025-3

Danış, Ö., Demir, S., Günel, A., Aker, R. G., Gülçebi, M., Onat, F., et al. (2011). Changes in intracellular protein expression in cortex, thalamus and hippocampus in a genetic rat model of absence epilepsy. *Brain Res. Bull.* 84, 381–388. doi: 10.1016/j.brainresbull.2011.02.002

Deeba, F., Sanz-Leon, P., and Robinson, P. A. (2018). Dependence of absence seizure dynamics on physiological parameter evolution. *J. Theor. Biol.* 454, 11–21. doi: 10.1016/j.jtbi.2018.05.029

Depaulis, A., and van Luijtelaar, G. (2006). "Genetic models of absence epilepsy in the rat," in *Models of Seizures and Epilepsy*, eds A. Pitkänen, P. A. Schwartkroin, and S. L. Moshé (Amsterdam: Elsevier), 233–248.

des Portes, V., Francis, F., Pinard, J.-M., Desguerre, I., Moutard, M.-L., Snoeck, I., et al. (1998). Doublecortin is the major gene causing X-linked subcortical laminar heterotopia (SCLH). *Hum. Mol. Genet.* 7, 1063–1070. doi: 10.1093/hmg/7.7.1063

Devinsky, O., Vezzani, A., Najjar, S., De Lanerolle, N. C., and Rogawski, M. A. (2013). Glia and epilepsy: excitability and inflammation. *Trends Neurosci.* 36, 174–184. doi: 10.1016/j.tins.2012.11.008

Devinsky, O., Vezzani, A., O'Brien, T. J., Jette, N., Scheffer, I. E., de Curtis, M., et al. (2018). Epilepsy. *Nat. Rev. Dis. Primer* 4:18024. doi: 10.1038/nrdp.2018.24

do Canto, A. M., Vieira, A. S., Matos, A. H. B., Carvalho, B. S., Henning, B., Norwood, B. A., et al. (2020). Laser microdissection-based microproteomics of the hippocampus of a rat epilepsy model reveals regional differences in protein abundances. *Sci. Rep.* 10:4412. doi: 10.1038/s41598-020-61401-8

Dombkowski, A. A., Batista, C. E., Cukovic, D., Carruthers, N. J., Ranganathan, R., Shukla, U., et al. (2016). Cortical tubers: windows into dysregulation of epilepsy risk and synaptic signaling genes by MicroRNAs. *Cereb. Cortex* 26, 1059–1071. doi: 10.1093/cercor/bhu276

Eid, T., Thomas, M., Spencer, D., Rundén-Pran, E., Lai, J., Malthankar, G., et al. (2004). Loss of glutamine synthetase in the human epileptogenic hippocampus: possible mechanism for raised extracellular glutamate in mesial temporal lobe epilepsy. *Lancet* 363, 28–37. doi: 10.1016/s0140-6736(03)15166-5

ElHajj, Z., Cachot, A., Müller, T., Riederer, I. M., and Riederer, B. M. (2016). Effects of postmortem delays on protein composition and oxidation. *Brain Res. Bull.* 121, 98–104. doi: 10.1016/j.brainresbull.2016.01.005

England, M. J., Liverman, C. T., Schultz, A. M., and Strawbridge, L. M. (2012). Epilepsy across the spectrum: promoting health and understanding. *Epilepsy Behav.* 25, 266–276. doi: 10.1016/j.yebeh.2012.06.016

Ferreira, P. G., Muñoz-Aguirre, M., Reverter, F., Sá Godinho, C. P., Sousa, A., Amadoz, A., et al. (2018). The effects of death and post-mortem cold ischemia on human tissue transcriptomes. *Nat. Commun.* 9:490. doi: 10.1038/s41467-017-02772-x

Fisher, R. S., Acevedo, C., Arzimanoglou, A., Bogacz, A., Cross, J. H., Elger, C. E., et al. (2014). ILAE official report: a practical clinical definition of epilepsy. *Epilepsia* 55, 475–482. doi: 10.1111/epi.12550

Fukata, Y., and Fukata, M. (2017). Epilepsy and synaptic proteins. *Curr. Opin. Neurobiol.* 45, 1–8. doi: 10.1016/j.conb.2017.02.001

Furtinger, S., Pirker, S., Czech, T., Baumgartner, C., Ransmayr, G., and Sperk, G. (2001). Plasticity of Y1 and Y2 receptors and neuropeptide Y fibers in patients with temporal lobe epilepsy. *J. Neurosci.* 21, 5804–5812. doi: 10.1523/JNEUROSCI.21-15-05804.2001

Gales, J. M., and Prayson, R. A. (2017). Chronic inflammation in refractory hippocampal sclerosis-related temporal lobe epilepsy. *Ann. Diagn. Pathol.* 30, 12–16. doi: 10.1016/j.anndiagpath.2017.05.009

Gano, L. B., Liang, L.-P., Ryan, K., Michel, C. R., Gomez, J., Vassilopoulos, A., et al. (2018). Altered mitochondrial acetylation profiles in a kainic acid model of temporal lobe epilepsy. *Free Radic. Biol. Med.* 123, 116–124. doi: 10.1016/j.freeradbiomed.2018.05.063

Garcia, C. C., Blair, H. J., Seager, M., Coulthard, A., Tennant, S., Buddles, M., et al. (2004). Identification of a mutation in synapsin I, a synaptic vesicle protein, in a family with epilepsy. *J. Med. Genet.* 41, 183–186. doi: 10.1136/jmg.2003.013680

Gatzonis, S. D., Roupakiotis, S., Kambayianni, E., Politi, A., Triantafyllou, N., Mantouvalos, V., et al. (2002). Hemispheric predominance of abnormal findings in electroencephalogram (EEG). *Seizure* 11, 442–444. doi: 10.1053/seiz.2001.0642

Gorter, J. A., and Lopes da Silva, F. H. (2002). "Abnormal plastic changes in a rat model for mesial temporal lobe epilepsy: a short review," in *Progress in Brain Research*, eds M. A. Hofman, G. J. Boer, A. J. G. D. Holtmaat, E. J. W. Van Someren, J. Verhaagenand, and D. F. Swaab (Amsterdam, Netherlands: Elsevier), 61–72.

Gøtzsche, C. R., Nikitidou, L., Sørensen, A. T., Olesen, M. V., Sørensen, G., Christiansen, S. H. O., et al. (2012). Combined gene overexpression of neuropeptide Y and its receptor Y5 in the hippocampus suppresses seizures. *Neurobiol. Dis.* 45, 288–296. doi: 10.1016/j.nbd.2011.08.012

Greenberg, D. A., and Jin, K. (2005). From angiogenesis to neuropathology. *Nature* 438, 954–959. doi: 10.1038/nature04481

Greene, N. D. E., Bamidele, A., Choy, M., de Castro, S. C. P., Wait, R., Leung, K.-Y., et al. (2007). Proteome changes associated with hippocampal MRI abnormalities in the lithium pilocarpine-induced model of convulsive status epilepticus. *Proteomics* 7, 1336–1344. doi: 10.1002/pmic.200601027

Grone, B. P., and Baraban, S. C. (2015). Animal models in epilepsy research: legacies and new directions. *Nat. Neurosci.* 18, 339–343. doi: 10.1038/nn.3934

Hagemann, T. L., Boelens, W. C., Wawrousek, E. F., and Messing, A. (2009). Suppression of GFAP toxicity by αB-crystallin in mouse models of Alexander disease. *Hum. Mol. Genet.* 18, 1190–1199. doi: 10.1093/hmg/ddp013

Hauser, W. A., Annegers, J. F., and Rocca, W. A. (1996). Descriptive epidemiology of epilepsy: contributions of population-based studies from Rochester, Minnesota. *Mayo Clin. Proc.* 71, 576–586. doi: 10.4065/71.6.576

He, S., Wang, Q., He, J., Pu, H., Yang, W., and Ji, J. (2006). Proteomic analysis and comparison of the biopsy and autopsy specimen of human brain temporal lobe. *Proteomics* 6, 4987–4996. doi: 10.1002/pmic.200600078

Heinrich, C., Lähteinen, S., Suzuki, F., Anne-Marie, L., Huber, S., Häussler, U., et al. (2011). Increase in BDNF-mediated TrkB signaling promotes epileptogenesis in a mouse model of mesial temporal lobe epilepsy. *Neurobiol. Dis.* 42, 35–47. doi: 10.1016/j.nbd.2011.01.001

Higurashi, M., Iketani, M., Takei, K., Yamashita, N., Aoki, R., Kawahara, N., et al. (2012). Localized role of CRMP1 and CRMP2 in neurite outgrowth and growth cone steering. *Dev. Neurobiol.* 72, 1528–1540. doi: 10.1002/dneu.22017

Hong, E.-H., Kim, J.-Y., Kim, J.-H., Lim, D.-S., Kim, M., and Kim, J.-Y. (2018). BIG2-ARF1-RhoA-mDia1 signaling regulates dendritic golgi polarization in hippocampal neurons. *Mol. Neurobiol.* 55, 7701–7716. doi: 10.1007/s12035-018-0954-7

Hosp, F., and Mann, M. (2017). A primer on concepts and applications of proteomics in neuroscience. *Neuron* 96, 558–571. doi: 10.1016/j.neuron.2017.09.025

Hsu, D. (2007). "The dentate gyrus as a filter or gate: a look back and a look ahead," in *Progress in Brain Research*, ed H. E. Scharfman (Amsterdam, Netherlands: Elsevier), 601–613.

Isokawa, M., Levesque, M., Babb, T., and Engel, J. (1993). Single mossy fiber axonal systems of human dentate granule cells studied in hippocampal slices from patients with temporal lobe epilepsy. *J. Neurosci.* 13, 1511–1522. doi: 10.1523/JNEUROSCI.13-04-01511.1993

Jaber, Z., Aouad, P., Al Medawar, M., Bahmad, H., Abou-Abbass, H., Ghandour, H., et al. (2016a). "Role of systems biology in brain injury biomarker discovery: neuroproteomics application," in *Injury Models of the Central Nervous System Methods in Molecular Biology*, eds F. H. Kobeissy, C. E. Dixon, R. L. Hayes, and S. Mondello (New York, NY: Springer), 157–174.

Jaber, Z., Aouad, P., Al Medawar, M., Bahmad, H., Abou-Abbass, H., and Kobeissy, F. (2016b). "Application of systems biology to neuroproteomics: the path to enhanced theranostics in traumatic brain injury," in *Injury Models of the Central Nervous System Methods in Molecular Biology*, eds F. H. Kobeissy, C. E. Dixon, R. L. Hayes, and S. Mondello (New York, NY: Springer), 139–155.

Jan, L. Y., and Jan, Y. N. (1997). Cloned potassium channels from eukaryotes and prokaryotes. *Annu. Rev. Neurosci.* 20, 91–123. doi: 10.1146/annurev.neuro.20.1.91

Junker, H., Späte, K., Suofu, Y., Walther, R., Schwarz, G., Kammer, W., et al. (2005). Proteomic identification of the involvement of the mitochondrial rieske protein in epilepsy. *Epilepsia* 46, 339–343. doi: 10.1111/j.0013-9580.2005.46904.x

Kalwy, S. A., Akbar, M. T., Coffin, R. S., de Belleroche, J., and Latchman, D. S. (2003). Heat shock protein 27 delivered *via* a herpes simplex virus vector can protect neurons of the hippocampus against kainic-acid-induced cell loss. *Mol. Brain Res.* 111, 91–103. doi: 10.1016/s0169-328x(02)00692-7

Keck, M., van Dijk, R. M., Deeg, C. A., Kistler, K., Walker, A., von Rüden, E.-L., et al. (2018). Proteomic profiling of epileptogenesis in a rat model: focus on cell stress, extracellular matrix and angiogenesis. *Neurobiol. Dis.* 112, 119–135. doi: 10.1016/j.nbd.2018.01.013

Keren-Aviram, G., Dachet, F., Bagla, S., Balan, K., Loeb, J. A., and Dratz, E. A. (2018). Proteomic analysis of human epileptic neocortex predicts vascular and glial changes in epileptic regions. *PLoS One* 13:e0195639. doi: 10.1371/journal.pone.0195639

Kilb, W., Kirischuk, S., and Luhmann, H. J. (2011). Electrical activity patterns and the functional maturation of the neocortex: shaping of developing cortical circuits by electrical activity. *Eur. J. Neurosci.* 34, 1677–1686. doi: 10.1111/j.1460-9568.2011.07878.x

Kim, S. I., Voshol, H., van Oostrum, J., Hastings, T. G., Cascio, M., and Glucksman, M. J. (2004). Neuroproteomics: expression profiling of the brain's proteomes in health and disease. *Neurochem. Res.* 29, 1317–1331. doi: 10.1023/b:nere.0000023618.35579.7c

Kokaia, M. (2011). Seizure-induced neurogenesis in the adult brain: seizure-induced neurogenesis. *Eur. J. Neurosci.* 33, 1133–1138. doi: 10.1111/j.1460-9568.2011.07612.x

Kovac, S., Abramov, A. Y., and Walker, M. C. (2013). Energy depletion in seizures: anaplerosis as a strategy for future therapies. *Neuropharmacology* 69, 96–104. doi: 10.1016/j.neuropharm.2012.05.012

Kruman, I. I., Schwartz, E., Kruman, Y., Cutler, R. G., Zhu, X., Greig, N. H., et al. (2004). Suppression of uracil-DNA glycosylase induces neuronal apoptosis. *J. Biol. Chem.* 279, 43952–43960. doi: 10.1074/jbc.M408025200

Kumar, G. K., and Prabhakar, N. R. (2008). Post-translational modification of proteins during intermittent hypoxia. *Respir. Physiol. Neurobiol.* 164, 272–276. doi: 10.1016/j.resp.2008.05.017

Kunz, W. S., Kudin, A. P., Vielhaber, S., Blümcke, I., Zuschratter, W., Schramm, J., et al. (2000). Mitochondrial complex I deficiency in the epileptic focus of patients with temporal lobe epilepsy. *Ann. Neurol.* 48, 766–773. doi: 10.1002/1531-8249(200011)48:5<766::aid-ana10>3.0.co;2-m

Kwan, P., Arzimanoglou, A., Berg, A. T., Brodie, M. J., Allen Hauser, W., Mathern, G., et al. (2010). Definition of drug resistant epilepsy: consensus proposal by the *ad hoc* Task Force of the ILAE Commission on Therapeutic Strategies. *Epilepsia* 51, 1069–1077. doi: 10.1111/j.1528-1167.2009.02397.x

Lagarrigue, M., Alexandrov, T., Dieuset, G., Perrin, A., Lavigne, R., Baulac, S., et al. (2012). New analysis workflow for MALDI imaging mass spectrometry: application to the discovery and identification of potential markers of childhood absence epilepsy. *J. Proteome Res.* 11, 5453–5463. doi: 10.1021/pr3006974

Laidlaw, J. (ed.). (1988). *A Textbook of Epidemiology*. 3rd Edn. Edinburgh: Churchill Livingstone.

Leal, R. B., Lopes, M. W., Formolo, D. A., de Carvalho, C. R., Hoeller, A. A., Latini, A., et al. (2020). Amygdala levels of the GluA1 subunit of glutamate receptors and its phosphorylation state at serine 845 in the anterior hippocampus are biomarkers of ictal fear but not anxiety. *Mol. Psychiatry* 25, 655–665. doi: 10.1038/s41380-018-0084-7

Lee, A., Maldonado, M., Baybis, M., Walsh, C. A., Scheithauer, B., Yeung, R., et al. (2003). Markers of cellular proliferation are expressed in cortical tubers. *Ann. Neurol.* 53, 668–673. doi: 10.1002/ana.10579

Leite, J. P., Chimelli, L., Terra-Bustamante, V. C., Costa, E. T., Assirati, J. A., De Nucci, G., et al. (2002). Loss and sprouting of nitric oxide synthase neurons in the human epileptic hippocampus. *Epilepsia* 43, 235–242. doi: 10.1046/j.1528-1157.43.s.5.29.x

Lévesque, M., Shiri, Z., Chen, L.-Y., and Avoli, M. (2018). High-frequency oscillations and mesial temporal lobe epilepsy. *Neurosci. Lett.* 667, 66–74. doi: 10.1016/j.neulet.2017.01.047

Li, A., Choi, Y.-S., Dziema, H., Cao, R., Cho, H.-Y., Jung, Y. J., et al. (2010). Proteomic profiling of the epileptic dentate gyrus. *Brain Pathol. Zurich Switz.* 20, 1077–1089. doi: 10.1111/j.1750-3639.2010.00414.x

Li, K. W., Ganz, A. B., and Smit, A. B. (2019). Proteomics of neurodegenerative diseases: analysis of human post-mortem brain. *J. Neurochem.* 151, 435–445. doi: 10.1111/jnc.14603

Liu, Y.-D., Ma, M.-Y., Hu, X.-B., Yan, H., Zhang, Y.-K., Yang, H.-X., et al. (2020). Brain proteomic profiling in intractable epilepsy caused by TSC1 truncating mutations: a small sample study. *Front. Neurol.* 11:475. doi: 10.3389/fneur.2020.00475

Liu, X.-Y., Yang, J.-L., Chen, L.-J., Zhang, Y., Yang, M.-L., Wu, Y.-Y., et al. (2008). Comparative proteomics and correlated signaling network of rat hippocampus in the pilocarpine model of temporal lobe epilepsy. *Proteomics* 8, 582–603. doi: 10.1002/pmic.200700514

Löscher, W. (1984). Genetic animal models of epilepsy as a unique resource for the evaluation of anticonvulsant drugs. A review. *Methods Find. Exp. Clin. Pharmacol.* 6, 531–547. doi: 10.1016/j.chemosphere.2020.129167

Löscher, W. (2011). Critical review of current animal models of seizures and epilepsy used in the discovery and development of new antiepileptic drugs. *Seizure* 20, 359–368. doi: 10.1016/j.seizure.2011.01.003

Löscher, W. (2017). Animal models of seizures and epilepsy: past, present, and future role for the discovery of antiseizure drugs. *Neurochem. Res.* 42, 1873–1888. doi: 10.1007/s11064-017-2222-z

Löscher, W., and Schmidt, D. (2011). Modern antiepileptic drug development has failed to deliver: ways out of the current dilemma: ways out of the current dilemma with new AEDs. *Epilepsia* 52, 657–678. doi: 10.1111/j.1528-1167.2011.03024.x

Luan, L., Sun, Y., and Yang, K. (2018). Surgical strategy for temporal lobe epilepsy with dual pathology and incomplete evidence from EEG and neuroimaging. *Exp. Ther. Med.* 16, 4886–4892. doi: 10.3892/etm.2018.6774

Luhmann, H. J., Kilb, W., and Clusmann, H. (2014). "Malformations of cortical development and neocortical focus," in *International Review of Neurobiology*, eds Premysl Jiruska, Marco de Curtis, and John G. R. Jefferys (San Diego, CA: Elsevier), 35–61.

Magalhães, P. H. M., Moraes, H. T., Athie, M. C. P., Secolin, R., and Lopes-Cendes, I. (2019). New avenues in molecular genetics for the diagnosis and application of therapeutics to the epilepsies. *Epilepsy Behav.* doi: 10.1016/j.yebeh.2019.07.029. [Epub ahead of print].

Maksimenko, V. A., van Heukelum, S., Makarov, V. V., Kelderhuis, J., Lüttjohann, A., Koronovskii, A. A., et al. (2017). Absence seizure control by a brain computer interface. *Sci. Rep.* 7:2487. doi: 10.1038/s41598-017-02626-y

Mériaux, C., Franck, J., Park, D. B., Quanico, J., Kim, Y. H., Chung, C. K., et al. (2014). Human temporal lobe epilepsy analyses by tissue proteomics. *Hippocampus* 24, 628–642. doi: 10.1002/hipo.22246

Mota, M. V. B., Zaidan, B. C., do Canto, A. M., Ghizoni, E., Tedeschi, H., de Souza Queiroz, L., et al. (2019). ATP synthase subunit β immunostaining is

reduced in the sclerotic hippocampus of epilepsy patients. *Cell. Mol. Neurobiol.* 39, 149–160. doi: 10.1007/s10571-018-0641-2

Nabeka, H., Uematsu, K., Takechi, H., Shimokawa, T., Yamamiya, K., Li, C., et al. (2014). Prosaposin overexpression following kainic acid-induced neurotoxicity. *PLoS One* 9:e110534. doi: 10.1371/journal.pone.0110534

Nagy, C., Maheu, M., Lopez, J. P., Vaillancourt, K., Cruceanu, C., Gross, J. A., et al. (2015). Effects of postmortem interval on biomolecule integrity in the brain. *J. Neuropathol. Exp. Neurol.* 74, 459–469. doi: 10.1097/NEN.0000000000000190

Niere, F., Namjoshi, S., Song, E., Dilly, G. A., Schoenhard, G., Zemelman, B. V., et al. (2016). Analysis of proteins that rapidly change upon mechanistic/mammalian target of rapamycin complex 1 (mTORC1) repression identifies Parkinson protein 7 (PARK7) as a novel protein aberrantly expressed in tuberous sclerosis complex (TSC). *Mol. Cell. Proteomics* 15, 426–444. doi: 10.1074/mcp.M115.055079

Norwood, B. A., Bumanglag, A. V., Osculati, F., Sbarbati, A., Marzola, P., Nicolato, E., et al. (2010). Classic hippocampal sclerosis and hippocampal-onset epilepsy produced by a single "cryptic" episode of focal hippocampal excitation in awake rats. *J. Comp. Neurol.* 518, 3381–3407. doi: 10.1002/cne.22406

Oberheim, N. A., Tian, G.-F., Han, X., Peng, W., Takano, T., Ransom, B., et al. (2008). Loss of astrocytic domain organization in the epileptic brain. *J. Neurosci.* 28, 3264–3276. doi: 10.1523/JNEUROSCI.4980-07.2008

Ottman, R., Winawer, M. R., Kalachikov, S., Barker-Cummings, C., Gilliam, T. C., Pedley, T. A., et al. (2004). LGI1 mutations in autosomal dominant partial epilepsy with auditory features. *Neurology* 62, 1120–1126. doi: 10.1212/01.wnl.0000120098.39231.6e

Ousman, S. S., Tomooka, B. H., van Noort, J. M., Wawrousek, E. F., O'Conner, K., Hafler, D. A., et al. (2007). Protective and therapeutic role for αB-crystallin in autoimmune demyelination. *Nature* 448, 474–479. doi: 10.1038/nature05935

Palmini, A., Andermann, F., Tampieri, D., Andermann, E., Robitaille, Y., and Olivier, A. (1992). Epilepsy and cortical cytoarchitectonic abnormalities: an attempt at correlating basic mechanisms with anatomoclinical syndromes. *Epilepsy Res. Suppl.* 9, 19–29; discussion 29–30.

Papageorgiou, I. E., Gabriel, S., Fetani, A. F., Kann, O., and Heinemann, U. (2011). Redistribution of astrocytic glutamine synthetase in the hippocampus of chronic epileptic rats. *Glia* 59, 1706–1718. doi: 10.1002/glia.21217

Perez-Olle, R., Lopez-Toledano, M. A., and Liem, R. K. H. (2004). The G336S variant in the human neurofilament-M gene does not affect its assembly or distribution: importance of the functional analysis of neurofilament variants. *J. Neuropathol. Exp. Neurol.* 63, 759–774. doi: 10.1093/jnen/63.7.759

Persike, D., Lima, M., Amorim, R., Cavalheiro, E., Yacubian, E., Centeno, R., et al. (2012). Hippocampal proteomic profile in temporal lobe epilepsy. *J. Epilepsy Clin. Neurophysiol.* 18, 53–56. doi: 10.1590/s1676-26492012000200007

Qin, L., Liu, X., Liu, S., Liu, Y., Yang, Y., Yang, H., et al. (2017). Differentially expressed proteins underlying childhood cortical dysplasia with epilepsy identified by iTRAQ proteomic profiling. *PLoS One* 12:e0172214. doi: 10.1371/journal.pone.0172214

Ramadan, N., Ghazale, H., El-Sayyad, M., El-Haress, M., and Kobeissy, F. H. (2017). "Neuroproteomics studies: challenges and updates," in *Neuroproteomics Methods in Molecular Biology*, eds F. H. Kobeissy and S. M. Stevens (New York, NY: Springer), 3–19.

Ramanjaneyulu, R., and Ticku, M. K. (1984). Interactions of pentamethylenetetrazole and tetrazole analogues with the picrotoxinin site of the benzodiazepine-gaba receptor-ionophore complex. *Eur. J. Pharmacol.* 98, 337–345. doi: 10.1016/0014-2999(84)90282-6

Rose, G., Dato, S., Altomare, K., Bellizzi, D., Garasto, S., Greco, V., et al. (2003). Variability of the SIRT3 gene, human silent information regulator Sir2 homologue, and survivorship in the elderly. *Exp. Gerontol.* 38, 1065–1070. doi: 10.1016/s0531-5565(03)00209-2

Rowley, S., and Patel, M. (2013). Mitochondrial involvement and oxidative stress in temporal lobe epilepsy. *Free Radic. Biol. Med.* 62, 121–131. doi: 10.1016/j.freeradbiomed.2013.02.002

Sadeghi, L., Rizvanov, A. A., Salafutdinov, I. I., Dabirmanesh, B., Sayyah, M., Fathollahi, Y., et al. (2017). Hippocampal asymmetry: differences in the left and right hippocampus proteome in the rat model of temporal lobe epilepsy. *J. Proteomics* 154, 22–29. doi: 10.1016/j.jprot.2016.11.023

Sánchez, R. G., Parrish, R. R., Rich, M., Webb, W. M., Lockhart, R. M., Nakao, K., et al. (2019). Human and rodent temporal lobe epilepsy is characterized by changes in O-GLCNAC homeostasis that can be reversed to dampen epileptiform activity. *Neurosci. Dis.* 124, 531–543. doi: 10.1016/j.nbd.2019.01.001

Sarnat, H. B., and Flores-Sarnat, L. (2009). α-B-crystallin as a tissue marker of epileptic foci in paediatric resections. *Can. J. Neurol. Sci.* 36, 566–574. doi: 10.1017/s0317167100008052

Saxena, A., and Sampson, J. (2015). Epilepsy in tuberous sclerosis: phenotypes, mechanisms, and treatments. *Semin. Neurol.* 35, 269–276. doi: 10.1055/s-0035-1552616

Schwartzkroin, P. A., and Wenzel, H. J. (2012). Are developmental dysplastic lesions epileptogenic? Are dysplasias epileptogenic? *Epilepsia* 53, 35–44. doi: 10.1111/j.1528-1167.2012.03473.x

Sharma, A. K., Reams, R. Y., Jordan, W. H., Miller, M. A., Thacker, H. L., and Snyder, P. W. (2007). Mesial temporal lobe epilepsy: pathogenesis, induced rodent models and lesions. *Toxicol. Pathol.* 35, 984–999. doi: 10.1080/01926230701748305

Shepherd, C., Liu, J., Goc, J., Martinian, L., Jacques, T. S., Sisodiya, S. M., et al. (2013). A quantitative study of white matter hypomyelination and oligodendroglial maturation in focal cortical dysplasia type II. *Epilepsia* 54, 898–908. doi: 10.1111/epi.12143

Singh, A., and Trevick, S. (2016). The epidemiology of global epilepsy. *Neurol. Clin.* 34, 837–847. doi: 10.1016/j.ncl.2016.06.015

Sousa, J. S., D'Imprima, E., and Vonck, J. (2018). "Mitochondrial respiratory chain complexes," in *Membrane Protein Complexes: Structure and Function, Subcellular Biochemistry*, eds J. R. Harris and E. J. Boekema (Singapore: Springer Singapore), 167–227.

Spiliotis, E. T. (2006). Here come the septins: novel polymers that coordinate intracellular functions and organization. *J. Cell Sci.* 119, 4–10. doi: 10.1242/jcs.02746

Staley, K. (2015). Molecular mechanisms of epilepsy. *Nat. Neurosci.* 18, 367–372. doi: 10.1038/nn.3947

Takechi, K., Suemaru, K., Kawasaki, H., and Araki, H. (2012). Impaired memory following repeated pentylenetetrazol treatments in kindled mice. *Yakugaku Zasshi* 132, 179–182. doi: 10.1248/yakushi.132.179

Tassi, L., Meroni, A., Deleo, F., Villani, F., Mai, R., Lo Russo, G., et al. (2009). Temporal lobe epilepsy: neuropathological and clinical correlations in 243 surgically treated patients. *Epileptic. Disord.* 11, 281–292. doi: 10.1684/epd.2009.0279

Thijs, R. D., Surges, R., O'Brien, T. J., and Sander, J. W. (2019). Epilepsy in adults. *Lancet* 393, 689–701. doi: 10.1016/S0140-6736(18)32596-0

Tokuraku, K., Noguchi, T. Q. P., Nishie, M., Matsushima, K., and Kotani, S. (2007). An isoform of microtubule-associated protein 4 inhibits kinesin-driven microtubule gliding. *J. Biochem.* 141, 585–591. doi: 10.1093/jb/mvm063

Visanji, N. P., Wong, J. C., Wang, S. X., Cappel, B., Kleinschmidt-DeMasters, B. K., Handler, M. H., et al. (2012). A proteomic analysis of pediatric seizure cases associated with astrocytic inclusions: Proteomics Seizure Astrocytic Inclusions. *Epilepsia* 53, e50–e54. doi: 10.1111/j.1528-1167.2011.03369.x

Walker, A., Russmann, V., Deeg, C. A., von Toerne, C., Kleinwort, K. J. H., Szober, C., et al. (2016). Proteomic profiling of epileptogenesis in a rat model: focus on inflammation. *Brain. Behav. Immun.* 53, 138–158. doi: 10.1016/j.bbi.2015.12.007

Wang, X., Phelan, S. A., Forsman-Semb, K., Taylor, E. F., Petros, C., Brown, A., et al. (2003). Mice with targeted mutation of peroxiredoxin 6 develop normally but are susceptible to oxidative stress. *J. Biol. Chem.* 278, 25179–25190. doi: 10.1074/jbc.M302706200

Wang, L., Song, L.-F., Chen, X.-Y., Ma, Y.-L., Suo, J.-F., Shi, J.-H., et al. (2019). MiR-181b inhibits P38/JNK signaling pathway to attenuate autophagy and apoptosis in juvenile rats with kainic acid-induced epilepsy *via* targeting TLR4. *CNS Neurosci. Ther.* 25, 112–122. doi: 10.1111/cns.12991

Will, J. L., Eckart, M. T., Rosenow, F., Bauer, S., Oertel, W. H., Schwarting, R. K. W., et al. (2013). Enhanced sequential reaction time task performance in a rat model of mesial temporal lobe epilepsy with classic hippocampal sclerosis. *Behav. Brain Res.* 247, 65–72. doi: 10.1016/j.bbr.2013.03.019

Wilson, S. M., and Khanna, R. (2015). Specific binding of lacosamide to collapsin response mediator protein 2 (CRMP2) and direct impairment of its canonical function: implications for the therapeutic potential of lacosamide. *Mol. Neurobiol.* 51, 599–609. doi: 10.1007/s12035-014-8775-9

World Federation of Neurology and World Health Organization. (2017). *Atlas: Country Resources for Neurological Disorders.* 2nd Edn. Geneva: World Health Organization.

Wu, Q., Liu, J., Fang, A., Li, R., Bai, Y., Kriegstein, A. R., et al. (2014). The dynamics of neuronal migration. *Adv. Exp. Med. Biol.* 800, 25–36. doi: 10.1007/978-94-007-7687-6_2

Xi, J., Bai, F., McGaha, R., and Andley, U. P. (2006). α-crystallin expression affects microtubule assembly and prevents their aggregation. *FASEB J.* 20, 846–857. doi: 10.1096/fj.05-5532com

Yamada, J., Kurata, A., Hirata, M., Taniguchi, T., Takama, H., Furihata, T., et al. (1999). Purification, molecular cloning, and genomic organization of human brain long-chain Acyl-CoA hydrolase. *J. Biochem.* 126, 1013–1019. doi: 10.1093/oxfordjournals.jbchem.a022544

Yamashita, N., Uchida, Y., Ohshima, T., Hirai, S., Nakamura, F., Taniguchi, M., et al. (2006). Collapsin response mediator protein 1 mediates reelin signaling in cortical neuronal migration. *J. Neurosci.* 26, 13357–13362. doi: 10.1523/JNEUROSCI.4276-06.2006

Yang, J. W., Czech, T., Felizardo, M., Baumgartner, C., and Lubec, G. (2006). Aberrant expression of cytoskeleton proteins in hippocampus from patients with mesial temporal lobe epilepsy. *Amino Acids* 30, 477–493. doi: 10.1007/s00726-005-0281-y

Yang, J. W., Czech, T., Yamada, J., Csaszar, E., Baumgartner, C., Slavc, I., et al. (2004). Aberrant cytosolic acyl-CoA thioester hydrolase in hippocampus of patients with mesial temporal lobe epilepsy. *Amino Acids* 27, 269–275. doi: 10.1007/s00726-004-0138-9

Yang, J.-W., Czech, T., Gelpi, E., and Lubec, G. (2005). Extravasation of plasma proteins can confound interpretation of proteomic studies of brain: a lesson from apo A-I in mesial temporal lobe epilepsy. *Mol. Brain Res.* 139, 348–356. doi: 10.1016/j.molbrainres.2005.06.010

Ye, H., and Kaszuba, S. (2017). Inhibitory or excitatory? Optogenetic interrogation of the functional roles of GABAergic interneurons in epileptogenesis. *J. Biomed. Sci.* 24:93. doi: 10.1186/s12929-017-0399-8

Yokota, H. (2019). Applications of proteomics in pharmaceutical research and development. *Biochim. Biophys. Acta Proteins Proteom.* 1867, 17–21. doi: 10.1016/j.bbapap.2018.05.008

Yuce-Dursun, B., Danis, O., Demir, S., Ogan, A., and Onat, F. (2014). Proteomic changes in the cortex membrane fraction of genetic absence epilepsy rats from Strasbourg. *J. Integr. Neurosci.* 13, 633–644. doi: 10.1142/S021963521450023X

Zhang, Z., Wu, S., Stenoien, D. L., and Paša-Tolić, L. (2014). High-throughput proteomics. *Annu. Rev. Anal. Chem.* 7, 427–454. doi: 10.1146/annurev-anchem-071213-020216

Conflict of Interest: The authors declare that the research was conducted in the absence of any commercial or financial relationships that could be construed as a potential conflict of interest.

frontiers in Molecular Neuroscience

ORIGINAL RESEARCH
published: 02 March 2021
doi: 10.3389/fnmol.2021.633398

Analysis of Chronic Mild Stress-Induced Hypothalamic Proteome: Identification of Protein Dysregulations Associated With Vulnerability and Resiliency to Depression or Anxiety

Weibo Gong[1,2†], Wei Liao[1,2†], Chui Fang[3†], Yanchen Liu[1,2], Hong Xie[1,4], Faping Yi[1,2], Rongzhong Huang[5], Lixiang Wang[3] and Jian Zhou[1,2]**

[1] Institute of Neuroscience, Chongqing Medical University, Chongqing, China, [2] Basic Medical College, Chongqing Medical University, Chongqing, China, [3] Shenzhen Wininnovate Bio-Tech Co., Ltd., Shenzhen, China, [4] Department of Pharmacy, Chongqing Renji Hospital, University of Chinese Academy of Sciences, Chongqing, China, [5] ChuangXu Institute of Life Science, Chongqing, China

OPEN ACCESS

Edited by:
Mark Oliver Collins,
The University of Sheffield,
United Kingdom

Reviewed by:
Peter Hamilton,
Virginia Commonwealth University,
United States
Yoko Hirata,
Gifu University, Japan

***Correspondence:**
Lixiang Wang
leon.wang@hotmail.com
Jian Zhou
zhoujian@cqmu.edu.cn

† These authors have contributed equally to this work

Received: 25 November 2020
Accepted: 10 February 2021
Published: 02 March 2021

Citation:
Gong W, Liao W, Fang C, Liu Y, Xie H, Yi F, Huang R, Wang L and Zhou J (2021) Analysis of Chronic Mild Stress-Induced Hypothalamic Proteome: Identification of Protein Dysregulations Associated With Vulnerability and Resiliency to Depression or Anxiety. Front. Mol. Neurosci. 14:633398. doi: 10.3389/fnmol.2021.633398

Chronic stress as a known risk factor leads to hyperactivity of the hypothalamus-pituitary-adrenal (HPA) axis in both depression and anxiety. However, the stress-induced dysfunction of the HPA axis in these disorders especially the common and unique molecular dysregulations have not been well-explored. Previously, we utilized a chronic mild stress (CMS) paradigm to segregate and gain depression-susceptible, anxiety-susceptible, and insusceptible groups. In this study, we continue to examine the possible protein expression alterations of the hypothalamus as the center of the HPA axis in these three groups by using a proteomic approach. Though isobaric tags for relative and absolute quantitation (iTRAQ)-based quantitative analysis, a total of 593 dysregulated proteins were identified. These were potentially associated with vulnerability and adaptability of CMS-caused depression or anxiety and therefore might become novel investigative protein targets. Further independent analysis using parallel reaction monitoring (PRM) indicated that 5, 7, and 21 dysregulated proteins were specifically associated with depression-susceptible, anxiety-susceptible, and insusceptible groups, respectively, suggesting that the same CMS differently affected the regulation system of the rat hypothalamic proteome. In summary, the current proteomic research on the hypothalamus provided insights into the specific and common molecular basis for the HPA dysfunction mechanisms that underlie resiliency and vulnerability to stress-induced depression or anxiety.

Keywords: anxiety, chronic mild stress, depression, hypothalamus, quantitative proteomics

INTRODUCTION

Depression and anxiety are two common and chronic mental illnesses that negatively affect the social interactions, career, and well-being of patients, families, and society (Larson et al., 2007; Almeida et al., 2012; Hamilton et al., 2015). Clinically, depression and anxiety disorders show different core symptoms, but they usually coexist (Brodbeck et al., 2011; Melton et al., 2016;

Yun et al., 2016). Due to their considerable overlap in comorbidities and pathophysiology, most clinical and basic investigation data were frequently mixed, which may obscure the understanding of the factors that regulate these two disorders (Chiba et al., 2012; Yun et al., 2016). Consequently, some recent studies are beginning to separately investigate non-complicated individuals with the two diseases to unravel the common and distinct features of the central nervous systems (Lotan et al., 2014; Frick, 2017; Zhao et al., 2017; Chen et al., 2018).

Anxiety and depression are two complex and heterogeneous disorders. Numerous studies have shown that there are common risk factors between these two disorders, such as life event stress and chronic stress (Pittenger and Duman, 2008; Mathew et al., 2011; Leuner and Shors, 2013). Increasing evidence shows that chronic stressful life events such as deleterious environmental factors cause anxiety and depression (Chang and Grace, 2014; Yun et al., 2016). However, even when exposed to chronic stress, many individuals do not show symptoms of anxiety and depression (Krishnan et al., 2007; Uchida et al., 2011; Henningsen et al., 2012; Russo et al., 2012). To model some environmental factors that affect humans, researchers commonly subject rodents to chronic mild stress (CMS) in order to generate behaviors that are useful for the study of depression- and anxiety-like disorders (Henningsen et al., 2012; Chang and Grace, 2014). To illustrate the potential biological cause and pathophysiology of the two disorders, the focus on the neural and molecular substrates that are sensitive and adaptable to the stress-induced diseases will be very significant (Uchida et al., 2011; Henningsen et al., 2012; Russo et al., 2012; Chang and Grace, 2014).

Mounting studies have illustrated that depression and anxiety as stress-related disorders involve hyperactivity of the hypothalamic-pituitary-adrenal (HPA) axis (Lucassen et al., 2013; Renoir et al., 2013; Borrow et al., 2016). As the key brain region of the HPA axis, the hypothalamus plays an important role in the physiological stress response (Pittenger and Duman, 2008; Rao et al., 2016). Hypothalamic and limbic areas coordinate cognitive, emotional, neuroendocrine, and autonomic inputs in the classic neuroendocrine circuit, and jointly determine the specificity and magnitude of the behavioral, neural, and hormonal responses of an individual to stress (Lucassen et al., 2013). Brain imaging studies of depressive and anxious disorders have indicated that the volume of the hypothalamus as well as its interactions and coherence were altered by stress (Dedovic et al., 2009; Pruessner et al., 2010; Sousa and Almeida, 2012; Oliveira et al., 2013). This stress-induced hypothalamic morphological change inevitably causes cellular and molecular dysfunctions in depression and anxiety (Sousa and Almeida, 2012). Although the hypothalamic plasticity is potentially abnormal in the two disorders, the corresponding molecular basis may be intrinsically different and still obscure. Therefore, the identification of common and unique molecular characteristics of mal-adaptability and adaptability to depression or anxiety has become an urgent need.

In our previous study, we quantitatively profiled the hippocampal proteome to discover common and unique protein components correlated to anxiety-like and depression-like behavioral phenotypes induced by CMS (Tang et al., 2019). Through the behavioral tests, the depression-susceptible, anxiety-susceptible, and insusceptible groups were segregated as the three different responses to stress (Tang et al., 2019). To probe continuously into stress-related anxiety and depression, in the current study we utilized the hypothalamic tissues from the same batch of our previously-established CMS rat model. The proteomes of the hypothalamus from the three stressed groups and the control group were comparatively analyzed, offering the significant molecular basis associated with maladaptive and adaptive behavioral phenotypes to anxiety or depression. Our proteomic data could provide a window into the understanding of the common and distinct molecular mechanisms underlying stress resistance and stress-induced anxiety or depression.

MATERIALS AND METHODS

CMS Rat Model and Behavioral Testing

The animal experiments in our study were approved by the Ethics Committee of Chongqing Medical University. All procedures were performed in accordance with the National Institutes of Health protocols for the use and care of laboratory animals. We purchased male Sprague-Dawley albino rats with a bodyweight of approximately 250 g from the local animal center. We individually housed all rats and allowed them *ad libitum* access to food and water. The rats were maintained under the following conditions: the relative humidity was 55 ± 5%; the room temperature was 21–22°C with a 12 h light/dark cycle.

As described previously (Tang et al., 2019), we conducted the CMS procedure after the rats were habituated to sucrose consumption. Following a baseline sucrose preference test, the rats were randomly allocated to the control group and stressed group. Rats in the control group were provided with standard daily care. Those in the stressed group were exposed to the 8 week CMS procedure, which involved a variety of stressors; namely, strobe light, continuous lighting, white noise, paired housing, a 45° cage tilt, a soiled cage, water deprivation, and an empty water bottle.

During this CMS exposure, depression-like behavior (anhedonia) of the rats was assessed using the sucrose preference test (SPT) as previously described (Tang et al., 2019). We utilized the formula to calculate sucrose preference: sucrose preference = (sucrose intake/total fluid intake) × 100%. Then, we performed a forced swimming test (FST) to evaluate the despair-like behavior of the rats using a water-filled Plexiglas cylinder and a video monitoring system as described previously (Tang et al., 2019). At the same time, we employed an elevated plus maze test (EMT) to determine the rat anxiety-like behavior as illustrated previously (Tang et al., 2019). Also, we recorded the animal body weights every week during this process.

Extraction and Digestion of Hypothalamic Tissue Proteins

After the behavioral tests were completed, the rats were sacrificed and their whole brains were excised rapidly. The hypothalamus tissues were dissected from the brain, and quickly frozen in liquid nitrogen, and kept at −80°C. To extract hypothalamic proteins,

we homogenized the tissues with SDT lysis buffer (100 mM Tris–HCl, pH 8.0, 100 mM dithiothreitol, 4% SDS, and protease inhibitors). The resulting extracts were heated at 100°C for 5 min. After centrifugation, the protein contents in the supernatant were measured with the Pierce bicinchoninic acid assay method.

Afterward, we used filter-aided sample preparation (FASP)-based method to digest the proteins. As in our previously-described procedure (Qiao et al., 2017), the 10 kD ultrafiltration centrifuge tubes were utilized for effective protein digestion. In brief, the protein solutions were diluted by adding urea buffer containing 8 M urea, 150 mM Tris-HCl, pH 8.0, and subsequently alkylated in the dark using 50 mM iodoacetamide for half an hour. The protein solutions were centrifuged and washed twice by adding the urea buffer. Then the proteins were incubated overnight with trypsin at 37°C. After centrifugation, the tryptic peptides were obtained by repeatedly washing. The collected peptides were lyophilized in a Speed Vac.

Peptide iTRAQ Labeling and High-pH Reversed-Phase Liquid Chromatography (RPLC) Fractionation

We labeled the tryptic peptides using 8-plex iTRAQ reagents as described previously (Tang et al., 2019). Eight samples from the three stressed groups (depression-susceptible, anxiety-susceptible, and insusceptible) and the control group were labeled with the iTRAQ reagents 113–121. Each sample was from two or three rats in each group. After the peptides were labeled, the eight samples were pooled and then fractionated utilizing off-line high-pH RPLC. The peptide mixture was separated by 80 min gradient elution, in which the high-pH buffer (25% ACN, 10 mM ammonium formate, 90% acetonitrile, pH 10.0) was linearly increased from 5 to 38% at a flow rate of 0.3 ml/min. The collected sixteen fractions were desalted and dried for the following liquid chromatography-tandem mass spectrometry (LC-MS/MS) analysis.

Q-Exactive LC-MS/MS Analysis

The labeled peptides were re-dissolved with 0.1% formic acid and then loaded into a nanoViper trapping column (C18, 3 μm, 100 Å). A Thermo Scientific Easy-nLC 1200 system was employed for the online chromatographic separation of peptides. The peptides were effectively desalted by elution of 100% solution A (0.1% formic acid). Subsequently, we used an analytical column (50 μm × 150 mm, 3 μm C18 100 Å) to separate the peptides along with a 50 min elution gradient. In the gradient, solution B (0.1% formic acid/80% acetonitrile) was linearly increased from 8 to 38%. Afterward, the MS analysis was conducted on a Q-Exactive Orbitrap mass spectrometer (Thermo Fisher Scientific) equipped with a Nano Flex ion source. For the MS operation, a 275°C interface heater temperature and a 1.9 kV ion spray voltage were used. The tandem MS data were acquired by using a data-dependent acquisition mode with full MS scans, where MS1 spectra were collected in the m/z range from 350 to 1,200, and MS2 spectra were collected in the m/z range from 110 to 1,200. The 250 ms survey scans were acquired along with up to fourteen MS/MS product ion scans of 50 ms. MS spectra with two and above charge-state were selected and fragmented by using higher-energy collision dissociation. We set the dynamic exclusion time for 25 s.

Data Analysis

We employed the software Proteome Discoverer (version 2.1, ThermoFisher) with the Sequest HT search engine for identification and quantitation of peptides and proteins. The UniProt_Rat release 2017_12 database was introduced into the software. The search parameters were as follows: two trypsin missed cleavages, iTRAQ 8plex on N-term and Lys and Carbamidomethylation on Cys as fixed modifications, Oxidation on Met, acetylation on protein N-term, deamidation on Asn and Gln, and Pyro-Glu as variable modifications, precursor fragment mass tolerance of 10 ppm, and fragment mass tolerance of 0.05 Da. For peptide and protein identifications, we used the Percolator module to control the peptide-spectrum-match false discovery rate (FDR) below 1.0%, as described previously (Han et al., 2015). Further, we utilized Reporter Ions Quantifier and Peptide and Protein Quantifier nodes to calculate the relative ratios of peptides and proteins across samples. The quantified data were introduced to Microsoft Excel for manual processing. Then, the protein ratios were analyzed by a two-tailed Student's *t*-test. Those proteins with a 1.2-fold alteration and *p*-values less than 0.05 were deemed to be significant differences, as used in previous studies (Tian et al., 2018; Zhang et al., 2021). The raw data have been deposited to the ProteomeXchange Consortium[1] via the iProX partner repository (Ma et al., 2019) with the dataset identifier PXD022715.

Bioinformatics Analysis

The differential protein data were analyzed with the OmicsBean tool[2] to obtain the Gene Ontology (GO)[3] terms, as described previously (Xie et al., 2018; Tang et al., 2019). The GO terms in biological processes (GOBP), molecular functions (GOMF), and cellular components (GOCC) were enriched. A Kyoto Encyclopedia of Genes and Genomes (KEGG)[4] pathway analysis was performed using the same tool, in which a *p*-value of less than 0.05 was deemed significant. Furthermore, we evaluated protein-protein interaction (PPI) by use of the database of the Search Tool for the Retrieval of Interacting Genes/Proteins (STRING). The acquired network was further visualized using Cytoscape software, as described previously (Tang et al., 2019).

Parallel Reaction Monitoring (PRM) Analysis

Following the iTRAQ experiment, the sample preparation including protein extraction and digestion were carried out. The obtained peptides were injected into the Q-Exactive mass spectrometer and analyzed through LC-MS/MS. The 28 normalized collision energy was used for peptide fragmentation. The resulting fragments were examined in the Orbitrap

[1]http://proteomecentral.proteomexchange.org

[2]http://www.omicsbean.cn/

[3]http://www.geneontology.org/

[4]http://www.genome.jp/kegg/

at a resolution of 35,000. The raw data were acquired and subsequently analyzed by using the software Proteome Discoverer. Skyline software (version 19.1) was employed to process the MS data.

Statistical Analysis

SPSS software was used for the data statistical analysis. All data were subjected to Student's *t*-test and expressed as means ± standard error. The results with *p*-values less than 0.05 were deemed statistically significant.

RESULTS

Hypothalamic Proteomics Analysis of the CMS Model Rats

In the present study, SPT and FST were first used to evaluate the depression-like behavior (i.e., anhedonia and behavioral despair) induced by CMS. Then we conducted the EMT experiment to index the anxiety-like behavior. Taking into account the hypothalamic sample used from the same batch of CMS-induced rat model in our previous publication (Tang et al., 2019), thereby it was briefly mentioned that, compared with the other groups, the sucrose preference of the depression-susceptible group was reduced, while the immobility time was increased. As expected, some stressed rats did not exhibit depression-like behavior. Interestingly, we observed their anxiety-like behavior based on the EMT data and consequently defined them as an anxiety-susceptible group. Additionally, the SPT, FST, and EMT data of the insusceptible group were not significantly changed relative to the control group. This indicated that these insusceptible rats did not have any depressive and anxious behaviors. It should be mentioned that the body weight change of the insusceptible group was significantly different from that of the control group during 8 weeks, but similar to those of the other two stressed groups (Tang et al., 2019). Through these assessments, a subset of the control, depression-susceptible, anxiety-susceptible, and insusceptible groups were gained. These behavioral data indicated that the CMS procedure provided an effective preclinical model for exploring the molecular patterns associated with the vulnerability and adaptability of depression or anxiety induced by CMS. Next, we conducted the quantitative proteomics analysis on the hypothalamic tissues of the four groups. As illustrated in **Figure 1A**, the hypothalamic proteomes of the depression-susceptible, anxiety-susceptible, insusceptible, and the control groups were comparatively profiled by using iTRAQ-based quantitative strategy. The proteomics experiment was performed on five rats per group. As reported previously (Lenselink et al., 2015), we pooled with an equal amount of the hypothalamic proteins randomly taken from two or three individuals for each sample. As a result, a total of 4,181 non-redundant proteins were identified and quantified along with the FDR less than 1% (**Supplementary Table S1**). By comparing the hypothalamic proteomes of the four different groups, we identified a total of 593 CMS-responsive proteins using a cut-off of 1.2-fold change and a *p*-value of less than 0.05 (**Figure 1B**). As described in previous studies (Baughman et al., 2001; Andrews et al., 2004; Scagliotti et al., 2008; Bonati et al., 2015), we treated all proteomics data as independent hypotheses, and did not adjust for multiple comparisons. The results having *p*-values less than 0.05 can be taken to be suggestive of trends in hypothalamic protein expression changes (Zhang et al., 2021). A *p*-value smaller than this would correspond to a stronger suggestion. Herein, the proteomics profile of the hypothalamus was compared with that of the hippocampus from our previous study (Tang et al., 2019; **Supplementary Figure S1**). Although the overall proteins quantified in both the hippocampus and hypothalamus showed a similar profile with a 42–68% overlap, the sets of differentially regulated proteins of each region were considerably divergent, suggesting that the two regions had the different proteomic responses to the CMS.

Functional and Network Characterization of CMS-Affected Dysregulated Proteins

Through rat hypothalamic proteomics analysis, we determined that 593 proteins were differentially regulated under the CMS. Among these proteins, 89 proteins were down-regulated and 64 proteins were up-regulated in the depression-susceptible group, 154 down-regulated and 134 up-regulated in the anxiety-susceptible group, and 179 down-regulated and 181 up-regulated in the insusceptible group (**Figure 2A** and **Supplementary Table S2**). We observed 56 proteins with similar regulations in the two stress-susceptible groups, which may represent some common abnormal components between depression and anxiety. Furthermore, among the two susceptible and the insusceptible groups, 148 proteins were found to be similarly regulated as a result of CMS exposure. Interestingly, up to 72% of these dysregulated proteins were specifically related to these three behavioral phenotypes, suggesting that the three stress-related groups had different molecular features under the CMS. Notably, the differential proteins uniquely from the insusceptible group represented several potential molecular adaptations within the hypothalamus (Krishnan et al., 2007; Henningsen et al., 2012). Further unsupervised hierarchical cluster analysis of 593 dysregulated proteins divided them into three different groups, which also reflected the three different responses to CMS (**Figure 2B**).

To gain an in-depth understanding of significant biological functions and pathways related to behavioral phenotypes, we used the OmicsBean tool to investigate these dysregulated proteins in the three groups. Based on the GO and KEGG pathway databases, the 153 differentially regulated proteins in the depression-susceptible group were analyzed (**Supplementary Table S3**). As a result, a total of 447, 158, 137, and 20 terms in the GOBP, GOCC, GOMF, and KEGG pathway categories were identified to be significantly overrepresented, respectively. Herein we showed the top 10 enriched GO terms (**Figure 3A**). The GOBP analysis indicated that many proteins were involved in protein localization and targeting to the endoplasmic reticulum, localization, and transport. Most proteins in the GOCC category belonged to vesicle, cytoplasmic, intracellular, and organelle parts. GOMF category analysis showed that the majority of proteins were involved in transporter and enzyme

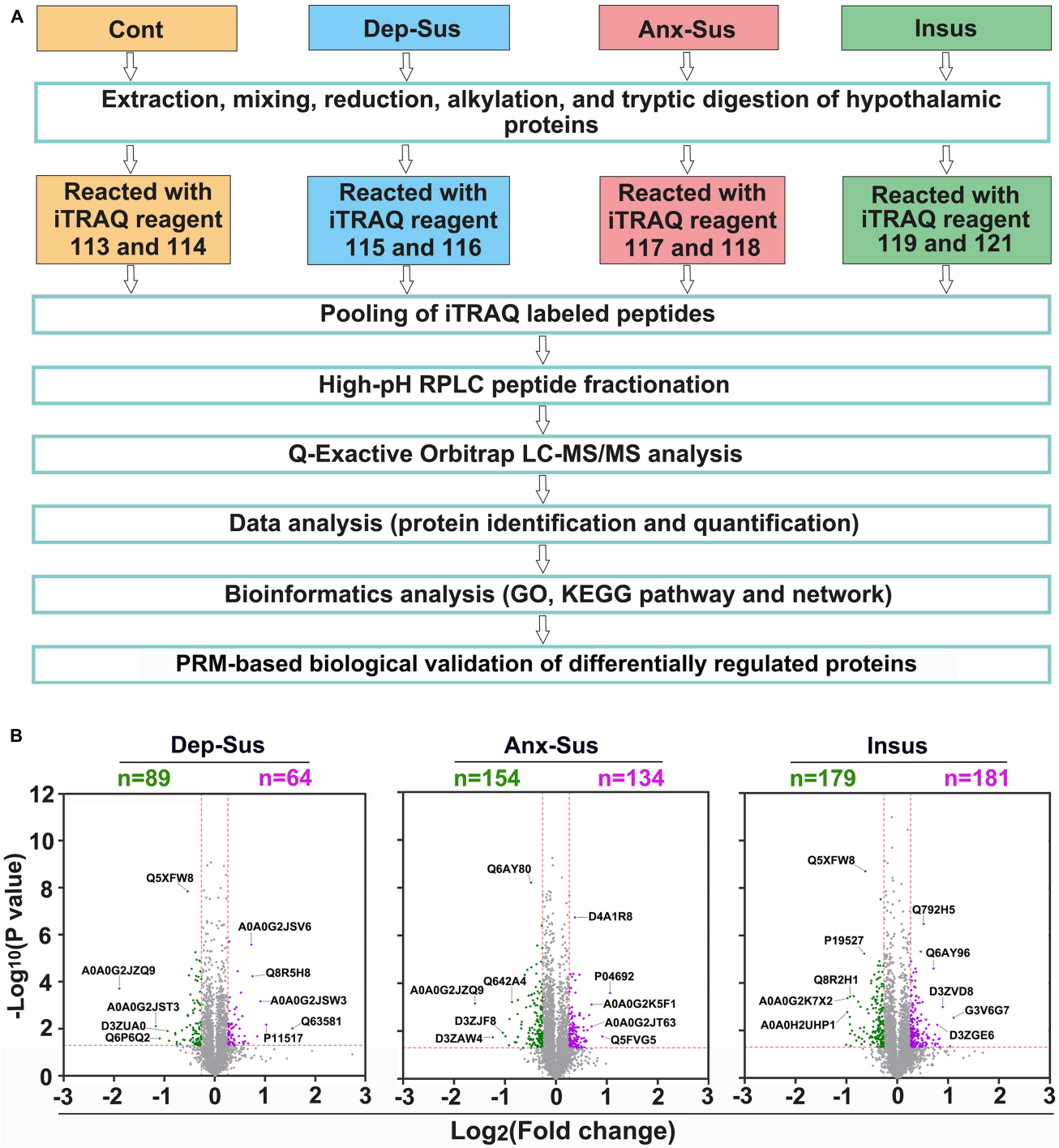

FIGURE 1 | Hypothalamic proteome profiling of the control (Cont), depression-susceptible (Dep-Sus), anxiety-susceptible (Anx-Sus), and insusceptible (Insus) groups. **(A)** Flow chart for the quantitative proteomic analysis. **(B)** Analysis of differentially regulated proteins in the hypothalamus. Volcano plot showing protein expression alternations in the Dep-Sus, Anx-Sus, and Insus groups. The X-axis represents the log2 fold-change, and the y-axis represents the log10 negative *p*-value. Green and purple, respectively, illustrate the low and high relative expressions. Examples of proteins that are differentially expressed with high significance are indicated with their Uniprot accessions.

activity, and protein and oxygen binding. The enrichment analysis of KEGG pathway showed that these dysregulated proteins were mainly involved in retrograde endocannabinoid, adrenergic, sphingolipid, and AMPK signaling, and GABAergic, cholinergic, glutamatergic, serotonergic, and dopaminergic synapse pathways (**Figure 3D**).

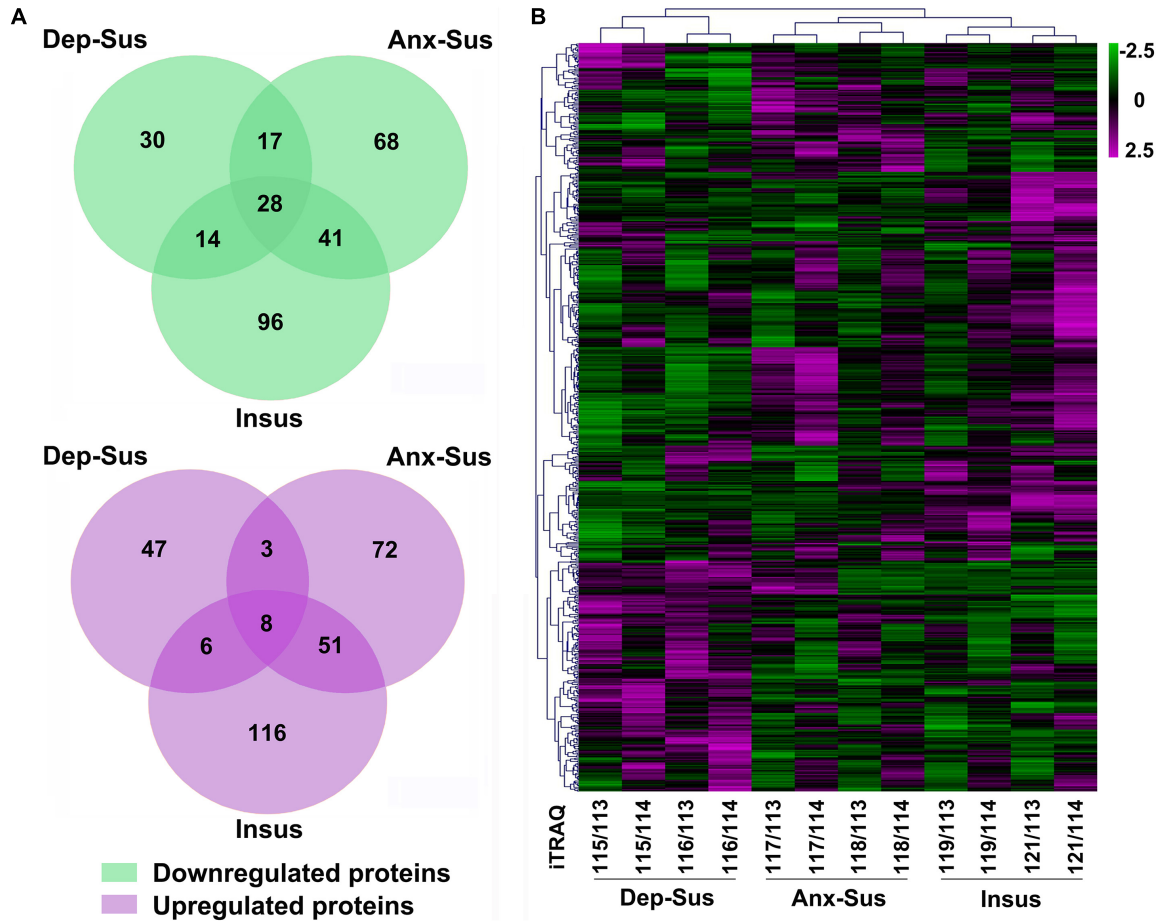

FIGURE 2 | Analysis of the differentially regulated proteins from the depression-susceptible (Dep-Sus), anxiety-susceptible (Anx-Sus), and insusceptible (Insus) groups. **(A)** Venn diagrams displaying the number of down-regulated and up-regulated proteins. Detailed information can be seen in **Supplementary Table S2**. **(B)** Heatmap-based clustering of differentially regulated proteins identified in the three groups. Lower expressions are indicated with green and higher expressions with purple. The intensities of various colors illustrate the expression levels. The color bar is log2 scaled.

At the same time, we conducted the GO and KEGG pathway enrichment of 288 proteins differentially regulated in the anxiety-susceptible group. A total of 829 GOBP, 223 GOCC, 194 GOMF, and 21 KEGG pathway terms were identified to be significantly enriched. The top 10 enriched GO terms were indicated (**Figure 3B**). The analysis of GOBP classification displayed that most proteins were related to cellular, macromolecule, and protein localization, and fibril, extracellular matrix, and structural organization. The analysis of GOCC category showed that most of the dysregulated proteins belonged to cytoplasmic, intracellular and organelle parts, extracellular exosome, organelle, and vesicle, while GOMF indicated most proteins were related to protein, RNA, anion, cell adhesion molecule, protein complex, carbohydrate derivative, purine ribonucleoside, and nucleoside binding. The analysis of KEGG pathways revealed these differential proteins were mainly associated with Huntington's, Alzheimer's, and Parkinson's diseases, metabolic, signaling, and synapse pathways (**Figure 3E**).

After that, we also enriched GO and KEGG pathway terms of 360 differentially regulated proteins from the insusceptible group. As a result, a total of 997 GOBP, 228 GOCC, 191 GOMF, and 20 KEGG pathway terms were identified to be significantly overrepresented. The top 10 overrepresented GO terms were shown in **Figure 3C**. GOBP category analysis showed that most proteins were involved in cellular component organization, biogenesis and assembly, protein complex biogenesis, assembly and subunit organization, and organelle organization. The GOCC classification analysis indicated that the majority of proteins were located in the extracellular exosome and organelle, vesicle, and cytoplasm. It was predicted that most proteins in the GOMF category were involved in protein, RNA, macromolecular and protein complex binding, and enzyme activity, and the enrichment of KEGG pathways demonstrated that these dysregulated proteins were mainly related to metabolic, signaling, Huntington's, Alzheimer's, and Parkinson's disease pathways (**Figure 3F**).

In addition, GO and KEGG pathway terms of 36 proteins that were commonly affected in all three groups were enriched. A total of 221 GOBP, 55 GOCC, 49 GOMF, and 9 KEGG pathway terms were identified to be significantly enriched

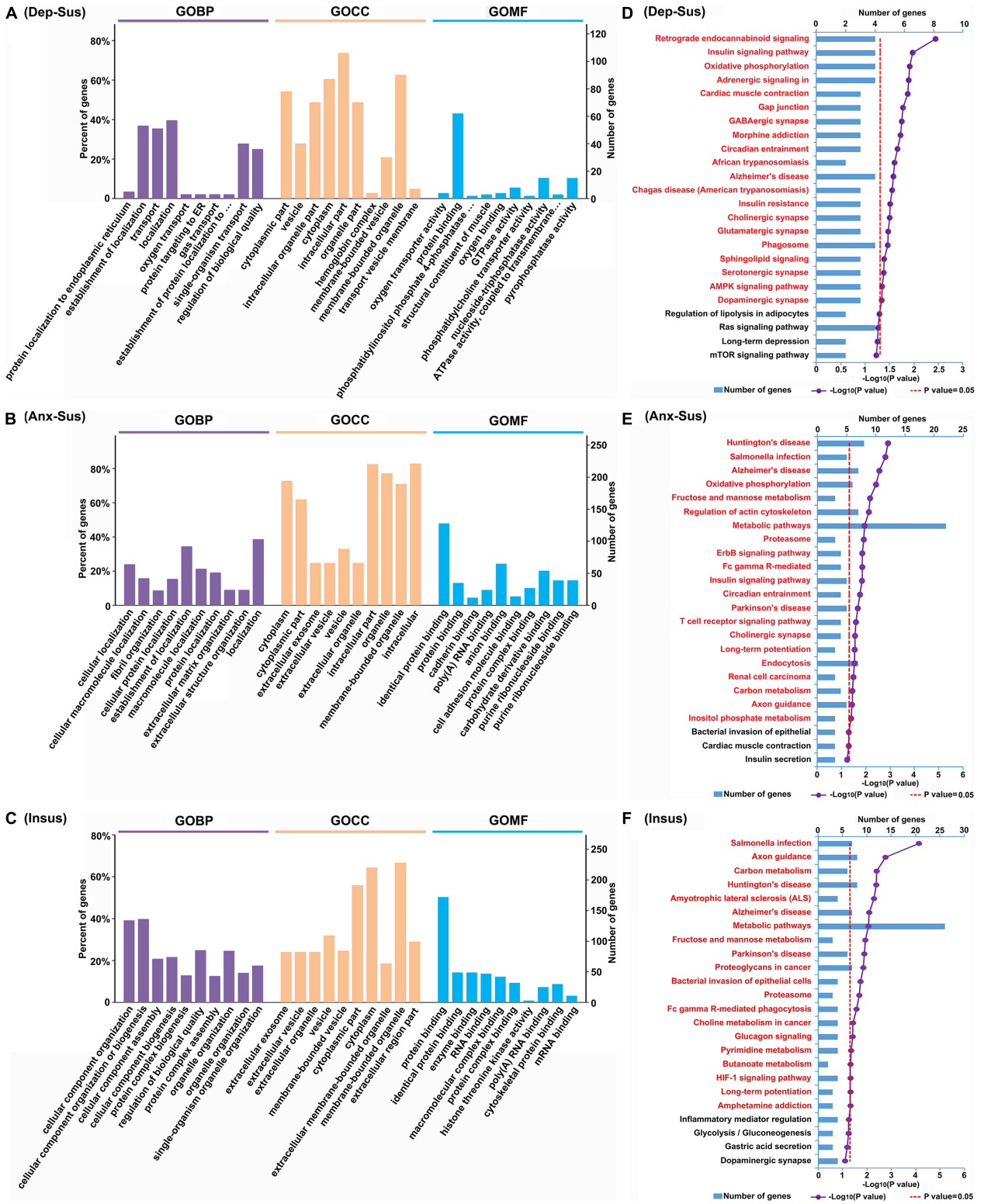

FIGURE 3 | Gene Ontology (GO) and Kyoto Encyclopedia of Genes and Genomes (KEGG) pathway enrichment analysis of the differentially regulated proteins from the depression-susceptible (Dep-Sus), anxiety-susceptible (Anx-Sus), and insusceptible (Insus) groups. **(A–C)** The top 10 enriched GO biological process (GOBP), cellular component (GOCC), and molecular function (GOMF) terms are indicated. **(D–F)** The significantly enriched KEGG pathway terms are showed by titles in red. The X-axis represents the log10 negative *p*-value.

(**Supplementary Table S4**). From the top 10 enriched GO terms, we observed that the majority of proteins in the GOBP category were classified into catabolic, biosynthetic and metabolic processes, and regulations of localization and transport; most of these proteins in the GOCC classification belonged to fiber, vesicle, and extracellular exosome and organelle; and most proteins in the GOMF analysis were involved in enzyme activity. KEGG analysis revealed that these proteins were mainly associated with metabolic and signaling pathways. Meanwhile, we also enriched GO and KEGG pathway terms of 56 proteins affected in both of the susceptible groups. A total of 290 GOBP, 103 GOCC, 64 GOMF, and 18 KEGG pathway terms were significantly enriched (**Supplementary Table S5**). From the top 10 enriched GO terms, it could be observed that most of these proteins in the GOBP analysis were involved in metabolic, catabolic, biosynthetic, and muscle system processes, and establishment of localization; the majority of proteins in the GOCC category were located in the fiber, vesicle, myosin, and actin filament and cytoskeleton; and most proteins in the GOMF classification were involved in catalytic and enzyme activities. The enrichment of KEGG pathways indicated that these proteins were mainly involved in oxidative phosphorylation, metabolic, signaling and synapse pathways.

Further, we focused on the protein-protein interaction (PPI) networks inferred by proteomics in the three groups (**Figures 4A–C**). The networks of the three stressed groups were built by using these dysregulated proteins along with the significantly-enriched KEGG pathways. It could be observed that the PPI network complexity of the anxiety-susceptible and insusceptible groups was higher than that of the depression-susceptible group, which suggested protein interactomes of the former two groups were more heavily affected by the CMS. This might represent differences in important protein dysregulation systems and active biological processes that occurred in these stressed groups. Based on a unified conceptual framework, we identified 16, 39, and 51 proteins as significant nodes in the networks from the depression-susceptible, anxiety-susceptible, and insusceptible groups, respectively. The PPI networks revealed the significant KEGG pathways and the corresponding dysregulated proteins and their close correlations, and thus provided a small pool of interactome that related to the three behavioral phenotypes.

PRM Analysis of CMS-Related Proteins

As an alternative method of targeted quantification, the PRM has been widely applied to validation of multiple proteins in complex sample (Yan et al., 2018; Wu et al., 2019; Zhang et al., 2021). In the current study, we further used the PRM-based approach to independently validate 54 dysregulated proteins of interest from the significantly enriched KEGG pathways and networks. On the whole, it can be observed that the results from the PRM mirrored the iTRAQ data (**Supplementary Figure S2**). As reported in other proteomics studies (Abdi et al., 2006; Cheng et al., 2011; Xu et al., 2012; Wu et al., 2019), some discrepancies objectively exist between the two iTRAQ- and PRM-based quantitative results. Besides the examination difference of these two approaches (Wu et al., 2019), another reason may be the additional pooling procedure in the iTRAQ proteomics experiment. As shown in **Figure 5**, the expressions of Atp6v1f, Arpc5, Ndufb6, and Psmc6 were significantly down-regulated while Adcyap1r1 was up-regulated in the depression-susceptible group compared with the control group. It was observed that the expressions of Gys1, Chka, Ncstn, and Ndufa6 were significantly down-regulated whereas Pgp, Klc1, and Kyat1 were up-regulated in the anxiety-susceptible group as compared to the control group. Moreover, we observed that the expressions of Arpc1b, Nefm, Pdpk1, Araf, Bace1, Arf5, Isyna1, Atp5l, Ctps1, Ppp1r12b, Psmd8, Nefh, Psd, and Plcb3 were significantly down-regulated while Aldoa, Psma1, Tpi1, Wasf1, Pak3, Cmpk2, and Ndufv3 were up-regulated in the insusceptible group when compared to the control group. In addition, a reduced level of Uqcrb in both the depression-susceptible and anxiety-susceptible groups, and elevated levels of Echs1 and Hspa8 in both the anxiety-susceptible and insusceptible groups were found as compared to the control group (**Supplementary Figure S3**). We also observed that the expression levels of Rab5a, Ephb1, Camk2a, Camk2d, Nefl, Tkfc, Fyn, Flot1, and Vdac1 were significantly down-regulated while Pak1, Cbr1, Dpysl2, Klc4, Klc2, Snx6, and Cttn were up-regulated in both the anxiety-susceptible and insusceptible groups compared with the control group.

DISCUSSION

As an unfavorable factor (Daviu et al., 2019), the CMS was usually employed to produce depressed and anxious behaviors in rodents (Henningsen et al., 2012; Chang and Grace, 2014). In our previous study (Tang et al., 2019), we used a well-established CMS rat model to identify the three different phenotypes (i.e., depression-susceptible, anxiety-susceptible, and insusceptible) based on the behavioral tests. The model supplied a valuable method for determining common and unique molecular characteristics of vulnerability and adaptability to depression or anxiety, which thus contributed to the biomedical translational research.

To unravel the possible protein dysregulations related to the three behavioral phenotypes, we carried out a comparative analysis of the hypothalamic proteomes of the stressed rats by the iTRAQ-based quantitative method. As a result, a total of 593 CMS-affected proteins were identified that were differentially regulated in the three stressed groups as compared to the control group. The overlapping proteome alterations between the two susceptible groups might represent a common molecular pattern of depression and anxiety.Intriguingly, the distinct protein dysfunctional profiles in the three stressed groups might represent differences of the three behavioral phenotypes. This proteome result will help researchers to discover protein systems and pathways related to vulnerability and adaptability to stress-induced anxiety or depression.

Our subsequent bioinformatics analysis suggested affected pathways in the hypothalamus particularly related to the three behavioral phenotypes. The pathway analysis indicated that the differentially regulated proteins were significantly overrepresented for signaling and synapse dysregulations

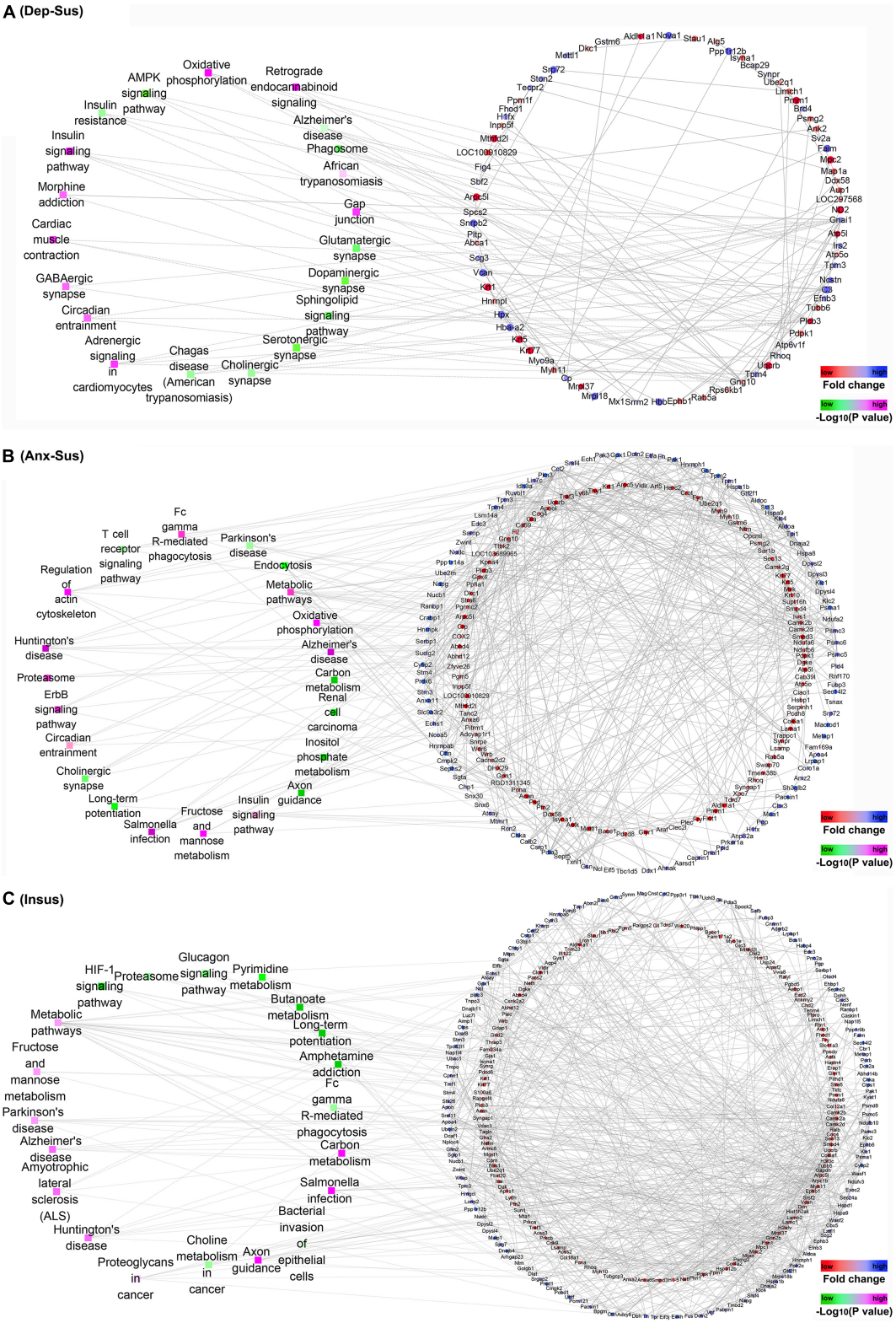

FIGURE 4 | Protein-protein interaction (PPI) analysis of the differentially regulated proteins in the depression-susceptible (Dep-Sus), anxiety-susceptible (Anx-Sus), and insusceptible (Insus) groups. **(A–C)** The PPI networks of the Dep-Sus **(A)**, Anx-Sus **(B)**, and Insus **(C)** groups are built on basis of altered protein expressions and overrepresented Kyoto Encyclopedia of Genes and Genomes (KEGG) pathways. Proteins/genes are indicated with circular nodes, and the KEGG pathways are indicated with the rectangle that is colored according to the *p*-values.

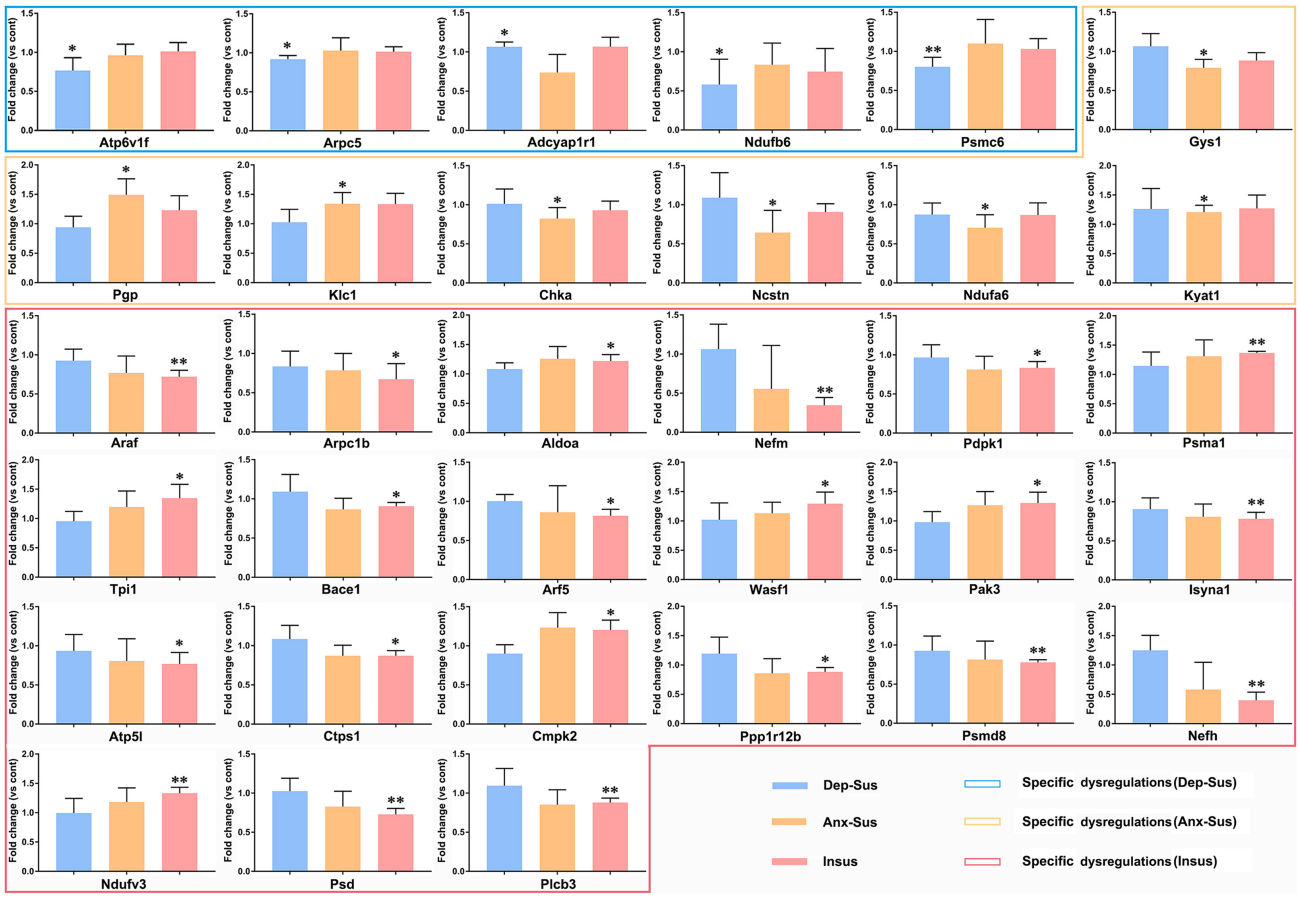

FIGURE 5 | Parallel reaction monitoring (PRM) analysis of the differentially regulated proteins in the depression-susceptible (Dep-Sus), anxiety-susceptible (Anx-Sus), and insusceptible (Insus) groups as compared to the control (Cont) group. The expression levels of Atp6v1f, Arpc5, Adcyap1r1, Ndufb6, Psmc6, Gys1, Pgp, Klc1, Chka, Ncstn, Ndufa6, Kyat1, Araf, Arpc1b, Aldoa, Nefm, Pdpk1, Psma1, Tpi1, Bace1, Arf5, Wasf1, Pak3, Isyna1, Atp5l, Ctps1, Cmpk2, Ppp1r12b, Psmd8, Nefh, Ndufv3, Psd, and Plcb3 were examined on the rat hypothalamic protein extracts and found to be specific dysregulations in the Dep-Sus, Anx-Sus and Insus groups. $n = 5$, $^{*}p < 0.05$, $^{**}p < 0.01$.

in the depression-susceptible group, metabolism, signaling, synapse, and neuropsychiatric disease-related dysfunctions in the anxiety-susceptible group, and metabolism, signaling, and neuropsychiatric disease-related repercussions in the insusceptible group. Meanwhile, the network analysis revealed the protein dysregulation systems along with these significant pathways, potentially providing some useful clues for the pathophysiological molecular basis of the three phenotypes.

Further, we independently analyzed the 54 differentially regulated proteins involved in the significant KEGG pathways by using the PRM method. The results indicated that Atp6v1f, Arpc5, Adcyap1r1, Ndufb6, and Psmc6 were distinctly dysregulated in the hypothalamus of the depression-susceptible group, while Gys1, Pgp, Klc1, Chka, Ncstn, Ndufa6, and Kyat1 were distinctly dysregulated in the anxiety-susceptible group. The specificity of molecular responses indicated that the same CMS differently affected the molecular functions, correspondingly providing an impetus to diverse biological processes and rat behavioral phenotypes. Intriguingly, the expressions of Arpc1b, Aldoa, Nefm, Pdpk1, Araf, Psma1, Tpi1, Bace1, Arf5, Wasf1, Pak3, Isyna1, Atp5l, Ctps1, Cmpk2, Ppp1r12b, Psmd8, Nefh, Ndufv3, Psd, and Plcb3 were found to be uniquely dysregulated in the insusceptible group, which suggested a potentially positive way to deal with the CMS-affected hypothalamic protein dysfunctions in the rats for stress protection (Krishnan et al., 2007; Uchida et al., 2011; Henningsen et al., 2012; Russo et al., 2012).

These phenotype-specific dysregulated proteins independently analyzed by PRM were mainly involved in signaling, metabolic, oxidative phosphorylation, endocytosis, and proteasome pathways. Gys1 and Plcb3 were involved in the glucagon signaling pathway, Pdpk1 and Araf involved in the insulin signaling pathway, and Pak3 involved in the ErbB signaling pathway. Of note, perturbations of the glucagon and insulin signaling pathways could significantly influence the corticotropin-releasing hormone promoter gene activity in the hypothalamus, thereby adjusting the CMS-activated HPA axis (Detka et al., 2019). Atp6v1f, Atp5l, Ndufa6, Ndufb6, and Ndufv3 were involved in oxidative phosphorylation, and Pgp, Chka, Kyat1, Aldoa, Tpi1, Wasf1, Isyna1, Ctps1, and Cmpk2

were involved in several metabolic pathways. The abnormal activity of the oxidative phosphorylation system along with the diverse metabolic processes in the hypothalamus would result in an energy imbalance of the HPA axis (Nieuwenhuizen and Rutters, 2008; Harris, 2015). Furthermore, Arpc5, Arf5, and Psd were involved in endocytosis, and Psmc6, Psma1, and Psmd8 were involved in the proteasome pathway, potentially leading to aberrant hypothalamic protein trafficking and degradation. Collectively, these significant pathways have been previously implicated in the HPA axis dysfunction of stress-related mood disorders (Pittenger and Duman, 2008; Leuner and Shors, 2013; Harris, 2015). In the current research, the protein expression disturbances distinctly related to the three different behavioral phenotypes could provide a more nuanced basis for future study. Despite the determination of an imbalance of protein expressions in the hypothalamus of the stressed rats, the detailed mechanisms behind these aberrations need further investigation.

CONCLUSION

In summary, we used iTRAQ- and PRM-based quantitative proteomics to analyze the CMS effect on the rat hypothalamic proteome. Our unbiased profile identified several hypothalamic protein candidates, which might be related to resiliency and vulnerability of stress-induced depression or anxiety, thus providing insights into the protein dysregulation mechanism behind CMS. The current results can serve as a significant molecular basis and deepen our understanding of the differences and similarities of stress resilience and stress-induced depression/anxiety concerning HPA axis dysfunction.

DATA AVAILABILITY STATEMENT

The proteomics raw data can be found in the ProteomeXchange Consortium with the identifier PXD022715.

ETHICS STATEMENT

The animal study was reviewed and approved by the Ethics Committee of Chongqing Medical University.

AUTHOR CONTRIBUTIONS

LW and JZ designed the project and prepared the manuscript. WG, WL, CF, and YL performed the experiments. WG, CF, HX, FY, and RH analyzed the data. All authors read and approved the final manuscript.

FUNDING

This work was supported by grants from the National Natural Science Foundation of China (Nos. 31770890 and 31570826) and the Health and Family Planning Commission of Chongqing Nanan District (No. 2018-03).

SUPPLEMENTARY MATERIAL

The Supplementary Material for this article can be found online at: https://www.frontiersin.org/articles/10.3389/fnmol.2021.633398/full#supplementary-material

Supplementary Figure 1 | Comparisons of the proteomic profiles of the hippocampus and hypothalamus. **(A)** Venn diagram showing the number of the total proteins quantified in each brain region. **(B–D)** The diagrams displaying the number of differential proteins in the depression-susceptible (Dep-Sus, **B**), anxiety-susceptible (Anx-Sus, **C**) and insusceptible (Insus, **D**). Hip, hippocampus; Hyp, hypothalamus.

Supplementary Figure 2 | Comparison of the data from the depression-susceptible (Dep-Sus), anxiety-susceptible (Anx-Sus), and insusceptible (Insus) groups relative to the control (Cont) group between isobaric tags for relative and absolute quantitation (iTRAQ)-based and parallel reaction monitoring (PRM)-based methods.

Supplementary Figure 3 | PRM analysis of the differentially regulated proteins in the depression-susceptible (Dep-Sus), anxiety-susceptible (Anx-Sus), and insusceptible (Insus) groups when compared to the control (Cont) group. The expression levels of Uqcrb, Echs1, Hspa8, Rab5a, Ephb1, Camk2a, Camk2d, Nefl, Pak1, Cbr1, Dpysl2, Tkfc, Klc4, Fyn, Flot1, Vdac1, Klc2, Snx6, and Cttn were examined on the rat hypothalamic protein extracts and shown to be altered in two or three stressed groups. $n = 5$, $^{*}p < 0.05$, $^{**}p < 0.01$.

Supplementary Table 1 | Identification of the hypothalamic proteins of the depression-susceptible (Dep-Sus), anxiety-susceptible (Anx-Sus), and insusceptible (Insus) groups through the isobaric tag for relative and absolute quantitation (iTRAQ)-based proteomics analysis. The differentially regulated proteins were indicated in blue.

Supplementary Table 2 | The Uniprot accessions of the proteins that comprise each region of the venn diagram in **Figure 2A**.

Supplementary Table 3 | Enrichment results of gene ontology (GO) biological process (GOBP), cellular component (GOCC), molecular function (GOMF), and Kyoto Encyclopedia of Genes and Genomes (KEGG) pathway terms of the differentially regulated proteins from the depression-susceptible (Dep-Sus), anxiety-susceptible (Anx-Sus), and insusceptible (Insus) groups. The significantly enriched terms were highlighted in blue.

Supplementary Table 4 | Enrichment results of gene ontology (GO) biological process (GOBP), cellular component (GOCC), molecular function (GOMF), and Kyoto Encyclopedia of Genes and Genomes (KEGG) pathway terms of 36 proteins that were commonly affected in all three groups. The significantly enriched terms were highlighted in blue.

Supplementary Table 5 | Enrichment results of gene ontology (GO) biological process (GOBP), cellular component (GOCC), molecular function (GOMF), and Kyoto Encyclopedia of Genes and Genomes (KEGG) pathway terms of 56 proteins affected in both of the susceptible groups. The significantly enriched terms were highlighted in blue.

REFERENCES

Abdi, F., Quinn, J. F., Jankovic, J., McIntosh, M., Leverenz, J. B., Peskind, E., et al. (2006). Detection of biomarkers with a multiplex quantitative proteomic platform in cerebrospinal fluid of patients with neurodegenerative disorders. *J. Alzheimer's Dis.* 9, 293–348. doi: 10.3233/jad-2006-9309

Almeida, O. P., Draper, B., Pirkis, J., Snowdon, J., Lautenschlager, N. T., Byrne, G., et al. (2012). Anxiety, depression, and comorbid anxiety and depression:

risk factors and outcome over two years. *Int. Psychogeriatr.* 24, 1622–1632. doi: 10.1017/S104161021200107X

Andrews, D. W., Scott, C. B., Sperduto, P. W., Flanders, A. E., Gaspar, L. E., Schell, M. C., et al. (2004). Whole brain radiation therapy with or without stereotactic radiosurgery boost for patients with one to three brain metastases: phase III results of the RTOG 9508 randomised trial. *Lancet* 363, 1665–1672. doi: 10.1016/s0140-6736(04)16250-16258

Baughman, R. P., Teirstein, A. S., Judson, M. A., Rossman, M. D., Yeager, H., Bresnitz, E. A., et al. (2001). Clinical characteristics of patients in a case control study of sarcoidosis. *Am. J. Respir. Crit. Care Med.* 164, 1885–1889. doi: 10.1164/ajrccm.164.10.2104046

Bonati, L. H., Dobson, J., Featherstone, R. L., Ederle, J., van der Worp, H. B., de Borst, G. J., et al. (2015). Long-term outcomes after stenting versus endarterectomy for treatment of symptomatic carotid stenosis: the International Carotid Stenting Study (ICSS) randomised trial. *Lancet* 385, 529–538. doi: 10.1016/s0140-6736(14)61184-61183

Borrow, A. P., Stranahan, A. M., Suchecki, D., and Yunes, R. (2016). Neuroendocrine regulation of anxiety: beyond the hypothalamic-pituitary-adrenal axis. *J. Neuroendocrinol.* 28, doi: 10.1111/jne.12403

Brodbeck, J., Abbott, R. A., Goodyer, I. M., and Croudace, T. J. (2011). General and specific components of depression and anxiety in an adolescent population. *BMC. Psychiatry* 11:191. doi: 10.1186/1471-244X-11-191

Chang, C. H., and Grace, A. A. (2014). Amygdala-ventral pallidum pathway decreases dopamine activity after chronic mild stress in rats. *Biol. Psychiatry* 76, 223–230. doi: 10.1016/j.biopsych.2013.09.020

Chen, J. J., Bai, S. J., Li, W. W., Zhou, C. J., Zheng, P., Fang, L., et al. (2018). Urinary biomarker panel for diagnosing patients with depression and anxiety disorders. *Transl. Psychiatry* 8:192. doi: 10.1038/s41398-018-0245-240

Cheng, P. J., Wang, T. H., Huang, S. Y., Kao, C. C., Lu, J. H., Hsiao, C. H., et al. (2011). Differential proteomics analysis of amniotic fluid in pregnancies of increased nuchal translucency with normal karyotype. *Prenat. Diagn.* 31, 274–281. doi: 10.1002/pd.2719

Chiba, S., Numakawa, T., Ninomiya, M., Richards, M. C., Wakabayashi, C., and Kunugi, H. (2012). Chronic restraint stress causes anxiety- and depression-like behaviors, downregulates glucocorticoid receptor expression, and attenuates glutamate release induced by brain-derived neurotrophic factor in the prefrontal cortex. *Prog. Neuropsychopharmacol. Biol. Psychiatry* 39, 112–119. doi: 10.1016/j.pnpbp.2012.05.018

Daviu, N., Bruchas, M. R., Moghaddam, B., Sandi, C., and Beyeler, A. (2019). Neurobiological links between stress and anxiety. *Neurobiol. Stress* 11:100191. doi: 10.1016/j.ynstr.2019.100191

Dedovic, K., Rexroth, M., Wolff, E., Duchesne, A., Scherling, C., Beaudry, T., et al. (2009). Neural correlates of processing stressful information: an event-related fMRI study. *Brain. Res.* 1293, 49–60. doi: 10.1016/j.brainres.2009.06.044

Detka, J., Ślusarczyk, J., Kurek, A., Kucharczyk, M., Adamus, T., Konieczny, P., et al. (2019). Hypothalamic insulin and glucagon-like peptide-1 levels in an animal model of depression and their effect on corticotropin-releasing hormone promoter gene activity in a hypothalamic cell line. *Pharmacol. Rep.* 71, 338–346. doi: 10.1016/j.pharep.2018.11.001

Frick, A. (2017). Common and distinct gray matter alterations in social anxiety disorder and major depressive disorder. *EBioMedicine* 21, 53–54. doi: 10.1016/j.ebiom.2017.06.021

Hamilton, J. P., Chen, M. C., Waugh, C. E., Joormann, J., and Gotlib, I. H. (2015). Distinctive and common neural underpinnings of major depression, social anxiety, and their comorbidity. *Soc. Cogn. Affect. Neurosci.* 10, 552–560. doi: 10.1093/scan/nsu084

Han, X., Shao, W., Liu, Z., Fan, S., Yu, J., Chen, J., et al. (2015). iTRAQ-based quantitative analysis of hippocampal postsynaptic density-associated proteins in a rat chronic mild stress model of depression. *Neuroscience* 298, 220–292. doi: 10.1016/j.neuroscience.2015.04.006

Harris, R. B. S. (2015). Chronic and acute effects of stress on energy balance: are there appropriate animal models? *Am. J. Physiol. Regul. Integr. Comp. Physiol.* 308, R250–R265. doi: 10.1152/ajpregu.00361.2014

Henningsen, K., Palmfeldt, J., Christiansen, S., Baiges, I., Bak, S., Jensen, O. N., et al. (2012). Candidate hippocampal biomarkers of susceptibility and resilience to stress in a rat model of depression. *Mol. Cell. Proteom.* 11:M111016428. doi: 10.1074/mcp.M111.016428

Krishnan, V., Han, M. H., Graham, D. L., Berton, O., Renthal, W., Russo, S. J., et al. (2007). Molecular adaptations underlying susceptibility and resistance to social defeat in brain reward regions. *Cell* 131, 391–404. doi: 10.1016/j.cell.2007.09.018

Larson, C. L., Nitschke, J. B., and Davidson, R. J. (2007). Common and distinct patterns of affective response in dimensions of anxiety and depression. *Emotion* 7, 182–191. doi: 10.1037/1528-3542.7.1.182

Lenselink, A. M., Rotaru, D. C., Li, K. W., van Nierop, P., Rao-Ruiz, P., Loos, M., et al. (2015). Strain differences in presynaptic function: proteomics, ultrastructure, and physiology of hippocampal synapses in DBA/2J and C57Bl/6J mice. *J. Biol. Chem.* 290, 15635–15645. doi: 10.1074/jbc.M114.628776

Leuner, B., and Shors, T. J. (2013). Stress, anxiety, and dendritic spines: what are the connections? *Neuroscience* 251, 108–119. doi: 10.1016/j.neuroscience.2012.04.021

Lotan, A., Fenckova, M., Bralten, J., Alttoa, A., Dixson, L., Williams, R. W., et al. (2014). Neuroinformatic analyses of common and distinct genetic components associated with major neuropsychiatric disorders. *Front. Neurosci.* 8:331. doi: 10.3389/fnins.2014.00331

Lucassen, P. J., Pruessner, J., Sousa, N., Almeida, O. F. X., Van Dam, A. M., Rajkowska, G., et al. (2013). Neuropathology of stress. *Acta Neuropathol.* 127, 109–135. doi: 10.1007/s00401-013-1223-1225

Ma, J., Chen, T., Wu, S., Yang, C., Bai, M., Shu, K., et al. (2019). iProX: an integrated proteome resource. *Nucleic Acids Res.* 47, D1211–D1217. doi: 10.1093/nar/gky869

Mathew, A. R., Pettit, J. W., Lewinsohn, P. M., Seeley, J. R., and Roberts, R. E. (2011). Co-morbidity between major depressive disorder and anxiety disorders: shared etiology or direct causation? *Psychol. Med.* 41, 2023–2034. doi: 10.1017/S0033291711000407

Melton, T. H., Croarkin, P. E., Strawn, J. R., and McClintock, S. M. (2016). Comorbid anxiety and depressive symptoms in children and adolescents: a systematic review and analysis. *J. Psychiatr. Pract.* 22, 84–98. doi: 10.1097/PRA.0000000000000132

Nieuwenhuizen, A. G., and Rutters, F. (2008). The hypothalamic-pituitary-adrenal-axis in the regulation of energy balance. *Physiol. Behav.* 94, 169–177. doi: 10.1016/j.physbeh.2007.12.011

Oliveira, J. F., Dias, N. S., Correia, M., Gama-Pereira, F., Sardinha, V. M., Lima, A., et al. (2013). Chronic stress disrupts neural coherence between cortico-limbic structures. *Front. Neural. Circuits.* 7:10. doi: 10.3389/fncir.2013.00010

Pittenger, C., and Duman, R. S. (2008). Stress, depression, and neuroplasticity: a convergence of mechanisms. *Neuropsychopharmacology* 33, 88–109. doi: 10.1038/sj.npp.1301574

Pruessner, J. C., Dedovic, K., Pruessner, M., Lord, C., Buss, C., Collins, L., et al. (2010). Stress regulation in the central nervous system: evidence from structural and functional neuroimaging studies in human populations - 2008 Curt Richter Award Winner. *Psychoneuroendocrinology* 35, 179–191. doi: 10.1016/j.psyneuen.2009.02.016

Qiao, R., Li, S., Zhou, M., Chen, P., Liu, Z., Tang, M., et al. (2017). In-depth analysis of the synaptic plasma membrane proteome of small hippocampal slices using an integrated approach. *Neuroscience* 353, 119–132. doi: 10.1016/j.neuroscience.2017.04.015

Rao, C., Shi, H., Zhou, C., Zhu, D., Zhao, M., Wang, Z., et al. (2016). Hypothalamic proteomic analysis reveals dysregulation of glutamate balance and energy metabolism in a mouse model of chronic mild stress-induced depression. *Neurochem. Res.* 41, 2443–2456. doi: 10.1007/s11064-016-1957-1952

Renoir, T., Hasebe, K., and Gray, L. (2013). Mind and body: how the health of the body impacts on neuropsychiatry. *Front. Pharmacol.* 4:158. doi: 10.3389/fphar.2013.00158

Russo, S. J., Murrough, J. W., Han, M.-H., Charney, D. S., and Nestler, E. J. (2012). Neurobiology of resilience. *Nat. Neurosci.* 15, 1475–1484. doi: 10.1038/nn.3234

Scagliotti, G. V., Parikh, P., von Pawel, J., Biesma, B., Vansteenkiste, J., Manegold, C., et al. (2008). Phase III study comparing cisplatin plus gemcitabine with cisplatin plus pemetrexed in chemotherapy-naive patients with advanced-stage non–small-cell lung cancer. *J. Clin. Oncol.* 26, 3543–3551. doi: 10.1200/jco.2007.15.0375

Sousa, N., and Almeida, O. F. X. (2012). Disconnection and reconnection: the morphological basis of (mal)adaptation to stress. *Trends. Neurosci.* 35, 742–751. doi: 10.1016/j.tins.2012.08.006

Tang, M., Huang, H., Li, S., Zhou, M., Liu, Z., Huang, R., et al. (2019). Hippocampal proteomic changes of susceptibility and resilience to depression or anxiety in a rat model of chronic mild stress. *Transl. Psychiatry* 9:260. doi: 10.1038/s41398-019-0605-604

Tian, Y., Jiang, F., Li, Y., Jiang, H., Chu, Y., Zhu, L., et al. (2018). Evaluation of the anti-hypertensive effect of Tengfu Jiangya tablet by combination of UPLC-Q-exactive-MS-based metabolomics and iTRAQ-based proteomics technology. *Biomed. Pharmacother* 100, 324–334. doi: 10.1016/j.biopha.2018.02.025

Uchida, S., Hara, K., Kobayashi, A., Otsuki, K., Yamagata, H., Hobara, T., et al. (2011). Epigenetic status of Gdnf in the ventral striatum determines susceptibility and adaptation to daily stressful events. *Neuron* 69, 359–372. doi: 10.1016/j.neuron.2010.12.023

Wu, X., Yan, J., Wu, Y., Zhang, H., Mo, S., Xu, X., et al. (2019). Proteomic analysis by iTRAQ-PRM provides integrated insight into mechanisms of resistance in pepper to *Bemisia tabaci* (Gennadius). *BMC Plant. Biol.* 19:270. doi: 10.1186/s12870-019-1849-1840

Xie, H., Huang, H., Tang, M., Wu, Y., Huang, R., Liu, Z., et al. (2018). iTRAQ-based quantitative proteomics suggests synaptic mitochondrial dysfunction in the hippocampus of rats susceptible to chronic mild stress. *Neurochem. Res.* 43, 2372–2383. doi: 10.1007/s11064-018-2664-y

Xu, H.-B., Zhang, R.-F., Luo, D., Zhou, Y., Wang, Y., Fang, L., et al. (2012). Comparative proteomic analysis of plasma from major depressive patients: identification of proteins associated with lipid metabolism and immunoregulation. *Int. J. Neuropsychopharmacol.* 15, 1413–1425. doi: 10.1017/s1461145712000302

Yan, X., Wu, Y., Zhong, F., Jiang, Q., Zhou, T., Guo, Y., et al. (2018). iTRAQ and PRM-based quantitative proteomics in T2DM-susceptible and -tolerant models of Bama mini-pig. *Gene* 675, 119–127. doi: 10.1016/j.gene.2018.06.103

Yun, S., Donovan, M. H., Ross, M. N., Richardson, D. R., Reister, R., Farnbauch, L. A., et al. (2016). Stress-Induced anxiety- and depressive-like phenotype associated with transient reduction in neurogenesis in adult Nestin-CreERT2/Diphtheria toxin fragment a transgenic mice. *PLoS One* 11:e0147256. doi: 10.1371/journal.pone.0147256

Zhang, Q., Wu, L., Bai, B., Li, D., Xiao, P., Li, Q., et al. (2021). Quantitative proteomics reveal neuron projection development genes ARF4, KIF5B and RAB8A associated with Hirschsprung disease. *Mol. Cell Proteom.* 20:100007. doi: 10.1074/mcp.RA120.002325

Zhao, Y., Chen, L., Zhang, W., Xiao, Y., Shah, C., Zhu, H., et al. (2017). Gray matter abnormalities in non-comorbid medication-naive patients with major depressive disorder or social anxiety disorder. *EBioMedicine* 21, 228–235. doi: 10.1016/j.ebiom.2017.06.013

Conflict of Interest: CF and LW were employed by the Shenzhen Wininnovate Bio-Tech Co., Ltd.

The remaining authors declare that the research was conducted in the absence of any commercial or financial relationships that could be construed as a potential conflict of interest.

frontiers in Molecular Neuroscience

ORIGINAL RESEARCH
published: 18 March 2021
doi: 10.3389/fnmol.2021.623659

Targeted Quantification of Detergent-Insoluble RNA-Binding Proteins in Human Brain Reveals Stage and Disease Specific Co-aggregation in Alzheimer's Disease

*Qi Guo[1], Eric B. Dammer[1,2], Maotian Zhou[1], Sean R. Kundinger[1], Marla Gearing[2,3], James J. Lah[2,4], Allan I. Levey[2,4], Joshua M. Shulman[5,6] and Nicholas T. Seyfried[1,2,4]**

[1] Department of Biochemistry, School of Medicine, Emory University, Atlanta, GA, United States, [2] Goizueta Alzheimer's Disease Research Center, School of Medicine, Emory University, Atlanta, GA, United States, [3] Department of Pathology and Laboratory Medicine, School of Medicine, Emory University, Atlanta, GA, United States, [4] Department of Neurology, School of Medicine, Emory University, Atlanta, GA, United States, [5] Departments of Neurology, Neuroscience and Molecular & Human Genetics, Baylor College of Medicine, Houston, TX, United States, [6] Jan and Dan Duncan Neurological Research Institute, Texas Children's Hospital, Houston, TX, United States

Core spliceosome and related RNA-binding proteins aggregate in Alzheimer's disease (AD) brain even in early asymptomatic stages (AsymAD) of disease. To assess the specificity of RNA-binding protein aggregation in AD, we developed a targeted mass spectrometry approach to quantify broad classes of RNA-binding proteins with other pathological proteins including tau and amyloid beta (Aβ) in detergent insoluble fractions from control, AsymAD, AD and Parkinson's disease (PD) brain. Relative levels of specific insoluble RNA-binding proteins across different disease groups correlated with accumulation of Aβ and tau aggregates. RNA-binding proteins, including splicing factors with homology to the basic-acidic dipeptide repeats of U1-70K, preferentially aggregated in AsymAD and AD. In contrast, PD brain aggregates were relatively depleted of many RNA-binding proteins compared to AsymAD and AD groups. Correlation network analyses resolved 29 distinct modules of co-aggregating proteins including modules linked to spliceosome assembly, nuclear speckles and RNA splicing. Modules related to spliceosome assembly and nuclear speckles showed stage-specific enrichment of insoluble RBPs from AsymAD and AD brains, whereas the RNA splicing module was reduced specifically in PD. Collectively, this work identifies classes of RNA-binding proteins that distinctly co-aggregate in detergent-insoluble fractions across the specific neurodegenerative diseases we examined.

Keywords: amyloid beta-protein, tau, RNA-binding proteins, Parkinson's disease, Alzheimer's disease, parallel reaction monitoring, mass spectrometry, human brains

OPEN ACCESS

Edited by:
Matthew L. MacDonald, University of Pittsburgh, United States

Reviewed by:
Nicolas Sergeant, Institut National de la Santé et de la Recherche Médicale, France
Robert Sweet, University of Pittsburgh Medical Center, United States
Becky Catherine Carlyle, Massachusetts General Hospital, Harvard Medical School, United States

***Correspondence:**
Nicholas T. Seyfried
nseyfri@emory.edu

Received: *30 October 2020*
Accepted: *12 February 2021*
Published: *18 March 2021*

Citation:
Guo Q, Dammer EB, Zhou M, Kundinger SR, Gearing M, Lah JJ, Levey AI, Shulman JM and Seyfried NT (2021) Targeted Quantification of Detergent-Insoluble RNA-Binding Proteins in Human Brain Reveals Stage and Disease Specific Co-aggregation in Alzheimer's Disease. Front. Mol. Neurosci. 14:623659. doi: 10.3389/fnmol.2021.623659

INTRODUCTION

Protein aggregation in the brain is one of the major pathologic hallmarks of neurodegenerative diseases (Taylor et al., 2002; Ross and Poirier, 2004). These aggregates cause both functional deficits and toxicity that is thought to lead to neurodegeneration. Detergent-insoluble β-amyloid (Aβ) in senile plaques and intracellular accumulation of neurofibrillary tangles (NFTs) composed of tau are the core pathologies of Alzheimer's disease (AD) (Masters et al., 1985; Grundke-Iqbal et al., 1986). Recent evidence indicates that detergent-insoluble RNA-binding proteins (RBPs) also accumulate and aggregate in AD (Bai et al., 2013; Diner et al., 2014; Hales et al., 2014, 2016; Bishof et al., 2018). For example, we previously discovered that a core component of the spliceosome complex, U1 small ribonucleoprotein 70 kDa (U1-70K), becomes insoluble in both symptomatic and early pre-symptomatic stages of AD where individuals had high brain amyloid pathology, yet were cognitively normal at death (Bai et al., 2013; Hales et al., 2016). The insolubility of additional U1 small nuclear ribonucleoprotein (snRNP) proteins, including U1-70K, was also observed in individuals with early-onset familial forms of AD caused by mutations in amyloid precursor protein (APP). Collectively this suggests that U1 snRNP aggregation in both familial and late-onset sporadic AD follows the loss of APP homeostasis and Aβ deposition (Hales et al., 2014). However, U1-70K does not co-aggregate with extracellular Aβ plaques in AD brains, yet in neurons mis-localizes from the nucleus to the cytoplasm were it co-aggregates with NFTs (Diner et al., 2014; Hales et al., 2016; Bishof et al., 2018; Hsieh et al., 2019). These co-aggregates between related U1 snRNP proteins and tau appear to be specific to AD as they are not observed in other tauopathies (Bai et al., 2013; Diner et al., 2014; Hales et al., 2016; Bishof et al., 2018). This supports a hypothesis that the cytoplasmic aggregation of U1-70K and functionally related RBPs provide a biological link between Aβ deposition and tau aggregation in AD.

Emerging evidence indicates that a diverse number of RBPs in addition to U1 snRNP proteins may also play an important role in mediating pathways of tau aggregation and subsequent neurodegeneration (Diner et al., 2014; Wolozin and Apicco, 2015; Bishof et al., 2018; Johnson et al., 2018; Maziuk et al., 2018; Raj et al., 2018; Hsieh et al., 2019). Notably, heterogeneous RBPs are found to mislocalize to the cytoplasm and co-aggregate with tau, which include the stress induced RBPs TIA1 (Vanderweyde et al., 2012; Vanderweyde et al., 2016) and G3BP that are reported to increasingly aggregate as disease severity progresses even in the absence of classic markers of tau pathology. Several of these RBPs that aggregate in neurodegenerative disease contain low complexity (LC) domains, including U1-70K, TDP-43, and FUS (Kwong et al., 2007; Neumann et al., 2009; Cohen et al., 2012). Our group and others have shown that U1-70K can aggregate independent from tau through self-assembly driven by multivalent interactions between structurally disordered basic-acidic dipeptide (BAD) LC domains (Diner et al., 2014; Bishof et al., 2018; Xue et al., 2019). However, whether other aggregation events occur systematically across an entire RBP class, or among specific RBPs expressed in human brain, is not clear.

Amyloidogenic and fibril-like aggregates, like Aβ and tau in AD, respectively, are highly resistant to biochemical or thermal denaturation and solubilization (Ramirez-Alvarado et al., 2000). It is therefore a challenge to purify and analyze aggregates through conventional biochemical methods (Ross and Poirier, 2004; Woltjer et al., 2005; Gozal et al., 2009; Seyfried et al., 2012; Diner et al., 2014; Nizhnikov et al., 2014; Hales et al., 2016). Ionic detergents such as N-lauryl-sarcosine (sarkosyl) can be used to enrich misfolded protein aggregates (Woltjer et al., 2005; Gozal et al., 2009; Diner et al., 2014, 2017; Hales et al., 2016). Despite solubilizing the majority of natively folded proteins in brain, sarkosyl is unable to solubilize aggregated proteins, which are pelleted out of solution following ultracentrifugation. The sarkosyl-insoluble pellet can be solubilized by a strong chaotropic agent like urea for subsequent proteomic analysis, revealing significant enrichment of β-amyloid or tau as well as RBPs such as U1-70K in AD brain (Seyfried et al., 2012; Bai et al., 2013; Diner et al., 2017). Emerging evidence demonstrates that specific subclasses of RBPs are insoluble in different neurodegenerative disease homogenates (Hasegawa et al., 2002; Miake et al., 2002; Neumann et al., 2006; Hales et al., 2016; Bishof et al., 2018; Cherry et al., 2018). As previous studies link RBP aggregation to AD and other neurodegenerative diseases, we sought to perform a comprehensive quantification of relative RBP abundance in sarkosyl-insoluble protein fractions across brains with a varying degree of AD pathology and Parkinson's disease (PD) as a disease control.

Mass spectrometry (MS) has emerged as an analytical tool to measure protein abundance in complex biological samples, providing excellent sensitivity, reproducibility and accuracy (Zhang et al., 2010; Gillette and Carr, 2013). In conventional discovery, or data-dependent acquisition (DDA) proteomic methods, the most abundant precursor peptide ions are selected for tandem MS analysis (MS/MS), which often biases measurement to the most abundant proteins in the sample. Thus, with highly complex proteomes, such as sarkosyl-insoluble brain extract, DDA approaches may result in some missing values across samples if the target of interest is not highly abundant. To circumvent these limitations, targeted data-independent acquisition (DIA) proteomic approaches such as parallel reaction monitoring (PRM) can be employed for sensitive and accurate quantification of peptides/proteins in brain tissue lysate (Peterson et al., 2012; Ronsein et al., 2015; Johnson et al., 2020). The PRM method can isolate and detect a select list of precursor ions simultaneously, mitigating abundance bias and minimizing missing peptide quantitation values.

Herein we describe a PRM method to monitor 870 peptides from 385 RBPs, plus microtubule-associated protein tau (MAPT), amyloid precursor protein (APP), Aβ, and internal standard peptides. We examined relative levels of these proteins in sarkosyl-insoluble fractions of 44 dorsolateral prefrontal cortex (DLPFC) tissues from control (CTL), AsymAD, AD, and PD cases. We confirmed the enrichment of Aβ, tau and U1-70K in the insoluble fractions of AsymAD and AD homogenates. In addition, several BAD RBPs showed enhanced insolubility in AD cases. We also discovered a variety of RBPs that were

differentially reduced in the sarkosyl-insoluble fractions of AD or PD cases. A systems-level weighted protein correlation network analysis displayed biological coherence for enrichment of RBP complexes and module-wise differences across disease groups. Modules of spliceosomal snRNP and nuclear speckle proteins showed a stage-specific enrichment in the insoluble fraction of AsymAD and AD, whereas modules related to transcription and translation were depleted from the insoluble fraction of AD or PD brain extracts, suggesting failure of normal RBP complex formation or less aggregation of these RBP complexes specific to these diseases. Collectively, this work identifies numerous novel signatures of co-aggregating RBPs in neurodegenerative disease, particularly during discrete stages of AD, holding promise to define mechanistic events during neurodegeneration.

MATERIALS AND METHODS

Materials

Primary antibodies used in this study include an in-house rabbit polyclonal antibody raised against a synthetic KLH-conjugated peptide corresponding to a C-terminal epitope of U1-70K (EM439) (Diner et al., 2014), a mouse monoclonal anti-tau phospho-threonine 231 antibody (clone MAB5450, EMD Millipore) and a rabbit polyclonal anti-TDP-43 antibody (10782-2-AP, ProteinTech Group). Secondary antibodies were conjugated to either Alexa Fluor 680 (Invitrogen) or IRDye800 (Rockland) fluorophores. Postmortem brain tissue from healthy control cases, pathologically confirmed AsymAD, AD, and PD cases were selected for comparison from the Emory Alzheimer's Disease Research Center (ADRC) brain bank (n = 44). Tissue from Brodmann Area 9 of the dorsolateral prefrontal cortex (DLPFC) was isolated. Human postmortem tissue was acquired in accordance with Institutional Review Board (IRB) protocols at Emory University. The AsymAD and AD cases were defined as described before (Boros et al., 2017) with the neuropathological examination of plaque distribution performed according to CERAD (Mirra et al., 1991) and neurofibrillary tau tangle pathology staging conducted according to the Braak system (Braak and Braak, 1991). All AD cases met the NIA-Reagan criteria for the diagnosis of Alzheimer disease (high likelihood) (Hyman and Trojanowski, 1997). The PD post-mortem diagnoses were also made in accordance with established criteria and guidelines (McKeith et al., 1996, 2005; Brown et al., 1998; Braak et al., 2003). The DLB Neocortex score included is a qualitative binary measure based on whether neocortical Lewy body pathology was observed (1) or whether the Lewy body pathology did not meet the consensus criteria (0) previously described (Brown et al., 1998; McKeith et al., 2005). All of the PD cases indeed presented synuclein pathology at autopsy, and all individuals were clinically diagnosed with PD. Cases were matched as closely as possible for age at death, gender, and post-mortem interval. A summary of case characteristics is provided in **Table 1**. All case metadata is provided in Supporting Information (**Supplementary Table 1**).

TABLE 1 | Characteristics of human subjects used in this study.

	Control	AsymAD	AD	PD
	(n = 12)	(n = 8)	(n = 12)	(n = 12)
Age at Death, mean years (SD)	76.0 (10.5)	82.5 (9.7)	76.4 (7.4)	75.1 (6.0)
Disease Duration, mean years (SD)			11.1 (4.0)	17.5 (9.6)
Sex, *n* (%)				
Male	6 (50.0)	5 (62.5)	8 (66.7)	9 (75.0)
Female	6 (50.0)	3 (37.5)	4 (33.3)	3 (25.0)
Race, *n* (%)				
White	9 (75.0)	8 (100.0)	12 (100.0)	12 (100.0)
Black	2 (16.7)	0 (0.0)	0 (0.0)	0 (0.0)
Hispanic	1 (8.3)	0 (0.0)	0 (0.0)	0 (0.0)
PMI, mean hrs (SD)	7.3 (3.9)	17.5 (9.6)	9.5 (8.2)	12.9 (7.6)
Amyloid & Tau Burden				
CERAD Score	0.2 (0.4)	2.8 (0.5)	3.0 (0.0)	0.2 (0.4)
Braak Score	1.6 (0.9)	3.0 (1.2)	5.9 (0.3)	2.2 (1.3)
ABC Score	0.5 (0.5)	1.8 (0.5)	3.0 (0.0)	0.4 (0.5)
DLB Neocortex Score, (SD)				0.5 (0.5)
ApoE Status, *n* (%)				
APOE2/2	0 (0.0)	0 (0.0)	0 (0.0)	0 (0.0)
APOE2/3	0 (0.0)	1 (12.5)	1 (8.3)	6 (50.0)
APOE2/4	0 (0.0)	1 (12.5)	0 (0.0)	0 (0.0)
APOE3/3	12 (100.0)	3 (37.5)	2 (16.7)	4 (33.3)
APOE3/4	0 (0.0)	2 (25.0)	6 (50.0)	2 (16.7)
APOE4/4	0 (0.0)	1 (12.5)	3 (25.0)	0 (0.0)

AsymAD, Asymptomatic Alzheimer's disease; AD, Alzheimer's disease; PD, Parkinson's disease; PMI. Post-Mortem Interval; CERAD, Consortium to Establish a Registry for Alzheimer's disease; ABC: Amyloid/Braak/CERAD aggregate score (none = 0, low = 1, intermediate = 2, high = 3); SD, Standard Deviation.

Extraction of Detergent-Insoluble Fraction From Human Brain

Extraction was performed with a fractionation protocol using the ionic detergent N-lauryl-sarcosine (sarkosyl) essentially as described (Diner et al., 2017). Approximately 200 mg of brain tissue was used for each case and the whole extraction process was performed on ice (**Supplementary Table 2**). Brain tissues were homogenized with 0.9-2.0 mm stainless steel homogenization beads (Next Advance, SSB14B) in 1 ml of low salt buffer (50 mM HEPES pH 7.0, 250 mM Sucrose and 1mM EDTA pH7.4 in H_2O) and 1× HALT protease/phosphatase inhibitor cocktail (Thermo Fisher Scientific) with a Bullet Blender® (Next Advance) for 2 × 5 min, generating a total homogenate (TH) lysate. A total of 800 µl of TH was aliquoted to a separate tube and mixed with 100 µl of 5M NaCl and 100 µl of 10% Sarkosyl (N-lauroylsarcosine), giving final concentrations of 0.5M NaCl and 1.0% Sarkosyl. The total homogenate-sarkosyl mix (TH-S) was then sonicated with a microtip probe (Sonic Dismembrator, Thermo Fisher Scientific) at 30% amplitude 3 × 5 s to shear nucleic acids. Protein concentrations were determined using the bicinchoninic acid (BCA) method (Pierce). Five milligrams of TH-S was diluted with Sark Buffer (1% Sarkosyl and 0.5M NaCl in low salt buffer) to a total volume of 500 µl in 700 µl ultracentrifuge tubes. Tubes were balanced and centrifuged at 64,000 rpm for 30 min at 4°C to obtain an insoluble pellet. The

supernatant was removed and saved, and the pellet was washed with 200 μl of Sark Buffer+1X HALT and centrifuged again. The resulting supernatant was discarded, and the pellet was washed with 500 μl PBS+1X HALT and centrifuged again. The final supernatant was discarded and 75 μl of 8M urea+1X HALT was added to solubilize the pellet, which was transferred into 1.5 ml Eppendorf tubes. Samples were then sonicated for 3 × 10 s on/off cycles at 20% amplitude to dissolve the pellet. The sonication was repeated every 30 min until the pellet was fully dissolved. The bicinchoninic acid assay (BCA) was performed to obtain protein concentration of the insoluble fraction. Insoluble fraction purity was then validated by western blot.

Western Blotting

Western blotting was performed according to standard procedures as reported previously (Dammer et al., 2012; Seyfried et al., 2012; Diner et al., 2014). Samples were loaded at 25 μg per lane. Samples denatured in Laemmli sample buffer were resolved by SDS-PAGE before being semi-dry transferred to nitrocellulose membranes (Invitrogen) using the iBlot2 system (Life Technologies). Membranes were blocked with casein blocking buffer (Sigma B6429) for 30 min at room temperature and then probed with primary antibodies (see "Materials") at a 1:1000 dilution overnight at 4°C. The next day, membranes were rinsed and incubated with secondary antibodies conjugated to Alexa Fluor 680 (Invitrogen) fluorophore at a 1:10000 dilution for 1 h at room temperature. Membranes were then rinsed and again incubated with secondary antibodies conjugated to a second 800 nm-emitting fluorophore at a 1:10000 dilution for 1 h at room temperature. Images were captured using an Odyssey Infrared Imaging System (Li-Cor Biosciences).

Protein Digestion and Sample Preparation

A total of 30 μg of each sample was prepared in 100 μl of 8M urea buffer (10 mM-Tris, 100 mM NaH_2PO_4, pH 8.5 with 1X HALT) for proteolytic digestion. Proteins were first reduced by DTT (final concentration of 1 mM) at room temperature for 30 min followed by alkylation with IAA (final concentration of 5 mM) in the dark at room temperature for 30 min. Proteins were then digested with Lys-C (enzyme ratio, 1:100) overnight at room temperature. The next day, samples were diluted 5 times to a final concentration < 2 M urea with 50 mM NH_4HCO_3 and digested with trypsin (enzyme ratio, 1:50) overnight at room temperature. Resulting peptides were desalted using an HLB column (10 mg, OASIS®) prior to liquid chromatography with tandem mass spectrometry (LC-MS/MS). A global pooled standard (GPS) sample was prepared for mass spectrometry analysis by pooling 10% of tryptic peptides from each case into a single tube. Then, 0.75 pmol/μl of 6 × 5 LC-MS/MS Peptide Reference Mix from Promega (6 peptides × 5 concentrations) was added into each of the 50 samples (44 case samples and 6 GPS technical replicates injected at different points throughout the sequence of 50 runs) before LC-MS/MS. The reference mix serves as an internal control to enable removal of any systematic variance. It is a mixture of 30 peptides: 6 sets of 5 isotopologues of the same peptide sequence, where the isotopologues of each peptide are present in a series of tenfold differences in molar abundance ranging from 0.0001X (lightest peptide) to 1X (heaviest peptide) (Promega, 2017).

Parallel Reaction Monitoring (PRM)

To create the RBP inclusion list for PRM quantification, the global pooled standard (GPS) sample was first deeply profiled on an Orbitrap Fusion using the DDA method (Dai et al., 2018). Raw files were processed by Maxquant (Version 1.5.7.4), using a human whole proteome sequence FASTA file downloaded from UniProt (UP000005640, date: 02-16-2016) (UniProt Consortium, 2019). The search engine Andromeda was used. Protein methionine oxidation (+15.9949 Da), protein N-terminal acetylation (+42.0106 Da), phosphorylation (S/T/Y, +79.9663 Da) and lysine ubiquitination (K, +114.0429 Da) were searched for as variable modifications (up to five allowed per peptide); cysteine was assigned a fixed carbamidomethyl modification (+57.0215 Da). Only fully tryptic peptides were considered with up to two missed cleavages in the database search. A precursor mass tolerance of ±20 ppm was applied prior to mass accuracy calibration, and a ± 4.5 ppm tolerance was applied after internal MaxQuant calibration. Other search settings included a maximum peptide mass of 6,000 Da, a minimum peptide length of six residues, and 0.6 Da tolerance for ion trap HCD MS/MS scans. The false discovery rate (FDR) for peptide spectral matches, proteins, and site decoy fraction were all set to 1%. Following database searches, the identified peptides were used to build a PRM list of proteins that have gene ontologies related to RNA binding by filtering for gene symbols present in gene ontologies of " spliceosome," "ribonucleoprotein," "mRNA processing," "RNA binding," "small nuclear ribonucleoprotein and Sm protein," in addition to the U1-70K interactome list generated by our group (Bishof et al., 2018). Peptides (and proteins) that were not suitable for protein quantification by unique peptide were removed. PRM analysis of peptides from the custom RBP list was then performed using a Q-Exactive Plus hybrid quadrupole-orbitrap mass spectrometer (Thermo Fisher Scientific), operated under Xcalibur software 3.0.63, equipped with a nano-electrospray ion source and coupled to a nano-Acquity system (Waters). Digested peptides were loaded and separated on a self-packed 1.9 μm C18 analytical column (New Objective, 70 cm × 75 μm inner diameter; 360 μm outer diameter). Elution was performed over a 160 min gradient at a rate of 240 nL/min with buffer B ranging from 1 to 99% (buffer A: 0.1% formic acid in water, buffer B: 0.1 % formic acid in acetonitrile). The Q-Exactive Plus MS was operated in PRM mode using an inclusion list, consisting of m/z values of targeted peptides (**Supplementary Table 6**). A normalized collision energy of 30% was employed for fragmentation. The following MS conditions were used: spray voltage, 2.0 kV; heated capillary temperature, 300°C; isolation windows, 1.6 m/z; resolution set to 17,500 at m/z 200; and an automatic gain control (AGC) target of 1×10^5. The mass spectrometry proteomics data have been deposited to the ProteomeXchange Consortium via the PRIDE repository with the dataset identifier PXD022144 (Perez-Riverol et al., 2019).

PRM Data Analysis

Before importing Thermo raw files into Skyline software (version 3.6), a spectral library was built. The library relied on global pooled standard (GPS) sample analyzed by an Orbitrap Fusion mass spectrometer described above with the same normalized collision energy as used for PRM analysis. For each peptide, three to six of the strongest product ions were selected in Skyline (MacLean et al., 2010). The Skyline software settings included: Precursor mass analyzer, centroided; MS1 mass accuracy of 20 ppm; Product mass analyzer, centroided; MS/MS mass accuracy of 20 ppm; Retention time filtering, including all matching scans. All product ion peak areas were calculated by Skyline, and endogenous peptide quantification was based on the normalized peak areas of at least 3 product ions. An example MS/MS spectrum of a tau peptide is included in **Supplementary Figure 3**.

Data Normalization

Quantitative proteomic data including PRM can be affected by a variety of systematic biases, defined as non-biological signal, e.g., artifacts generated by the MS instrument from tuning parameters or chromatographic drift. Normalization of measured peptide or protein abundances must be robust to contend with this technical bias in LC-MS/MS data, including ionization efficiency drift, LC column and signal drift, and the interplay of these with static data acquisition timing (Karpievitch et al., 2012). Thus, to correct for technical bias in comparisons between samples, it is necessary to normalize abundance data. Systematic technical variance occurring across MS runs was removed by data normalization of the linear drift of heavy labeled internal standard peptide signals as described (Zhou et al., 2020). Originally, there was signal depreciation of standard peptides in the dataset across the series of 50 injections with a coefficient of variance (CV) of 27.08% (**Supplementary Figure 4A**). To control for signal attenuation, we applied a correction factor to each peptide peak area, thereby calculating normalized peptide peak areas (**Supplementary Table 7**). Normalized protein abundances were then calculated by summing corrected intensity peptide values (**Supplementary Table 10**). In the final normalized quantitative matrices of PRM abundances used for statistics, rare missing (zero) values (0.73% of all 17,160 protein abundance values) were imputed as noise at one half of the minimum non-zero abundance measured for the peptide or protein. Finally, these normalized protein abundances were $\log_2$-transformed and regressed for age, sex and PMI and used to compare protein insolubility across disease groups (**Supplementary Table 11**). As described above, an isotopically labeled heavy peptide reference mix from Promega was added as internal control for normalization. Since the amount of standard peptides in each sample were fixed at known quantities, the variation in signal intensity for these peptide standard curves generated across all samples was due to unwanted technical drift. We chose the reference peptide (with peptide molar abundance of 0.01x) to calibrate normalization of drift slope to 0 using four reference peptides (#2-5), which had linear signal changes across the sequence of MS runs and had the highest coefficient of determination values (R^2) across all 50 samples. Correction factors for normalizing peptide/protein intensities were calculated using peak area. First, we averaged each of the four-reference peptide peak areas (intensities) $\bar{I}_{P2}$, $\bar{I}_{P3}$, $\bar{I}_{P4}$, and $\bar{I}_{P5}$ across all 50 injections, and then normalized each of the sample-reference-peptide peak areas $\bar{A}_{ij}$ (i = 2–5, j = 1–50) to an average of 1 by dividing $\bar{A}_{ij}$ by each corresponding peptide's average intensity:

$$Intensity\ Ratio(\mathrm{IRij}) == \bar{A}\mathrm{ij}/\bar{I}\mathrm{Pi}$$

A scatter plot including normalized intensity ratio of peptides 2–5 across 50 runs, where the *x*-axis represented MS injections 1 to 50 and the *y*-axis represented the intensity ratios as calculated above, showed a linear relationship between injection number and intensity ratio with the following best-fit regression line (**Supplementary Figure 4A**):

$$y\ -0.0167x1.417, \mathrm{R2}\ =\ 0.769$$

This confirmed that peptide intensity across MS injections decreased due to signal depreciation. The average intensity ratio ($\bar{I}_{Rj}$) of each injection (x = 1 to 50) was calculated using the equation above. Then, intensity ratios of all run positions were adjusted so that a fit line would have a slope of zero (**Supplementary Figure 4B**), and we divided 1 by each $\bar{I}_{Rj}$ to obtain a multiplier correction factor, in turn applied to all original peptide intensities for each injection position j:

$$Correction\ Factor = 1/\bar{I}\mathrm{Rj}$$

After normalization, the CVs of four-reference peptides across 50 runs became 14.69% as compared to pre-normalization values (CVs = 27.08%, **Supplementary Figure 4B**).

Protein Differential Abundance Analysis

Volcano plots were generated to visualize differential expression of RBPs in different case groups versus control. The *x*-axis, represented as $\log_2$ fold change, is the $\log_2$ ratio of average groupwise protein abundances in a pairwise comparison (e.g., AD/Control). Student *t*-test -$\log_{10}$(p) values represent statistical significance on the y-axes of volcano plots. Significantly altered proteins (p-Value < 0.05) are presented with p-Values and fold changes in **Supplementary Table 12**. For stacked bar plots, the fraction of co-expressed module members achieving differential abundance significance of $p < 0.05$ were counted (*y*-axis) for each of the indicated pairwise comparisons and coloring of the heat map scale was based on the range of minimum to maximum average $\log_2$ fold change of the significantly changed module member proteins. The limited sample size of our study limits power even without adjusting for multiple testing, so FDR adjustment of p-Values was not considered here.

Correlation Network and Pathology Correlation Analysis

The R package Weighted Gene Correlation Network Analysis (WGCNA) v1.68 was used to cluster proteins by abundance into groups of co-expressed proteins using a dissimilarity metric for clustering distance based on 1 minus the topology overlap matrix

(1-TOM), which is a calculation based on an adjacency matrix of correlations of all pairs of proteins in the abundance matrix supplied to WGCNA (Langfelder and Horvath, 2008). The power selected was the lowest power at which scale free topology R^2 was approximately 0.80, or in the case of not reaching 0.80, the power at which a horizontal asymptote (plateau) was nearly approached before further increasing the power had no more or a negative effect on scale free topology R^2. Other parameters were selected as previously optimized for protein abundance networks (Seyfried et al., 2017). Thus, for the signed network built on protein abundances obtained from PRM, parameters were input into the WGCNA::blockwiseModules() function as follows: Beta (power) 23, signed network type, biweight midcorrelation (bicor), mergeCutHeight = 0.07, pamStage TRUE, pamRespectsDendro TRUE, reassignThreshold $p < 0.05$, minKMEtoStay = 0.30, deepSplit = 4, minModuleSize = 5, TOMdenom = "mean," and maxBlockSize greater than the total number of proteins. To correlate RBP abundances to pathological aggregated insoluble Aβ and tau abundances, bicor rho values were calculated and reported.

Gene Ontology Enrichment and Co-clustering Analysis

GO-Elite v1.2.5 used a Fisher exact test $p < 0.05$ for determining significance of hypergeometric overlap and a minimum of 3 gene symbols per GO Term. The background insoluble proteome consisted of all 4313 gene symbols represented in a MaxQuant (Andromeda) search performed as described above on data-dependent acquisition data for the insoluble global pooled standard protein sample obtained on both Orbitrap Fusion and Q-Exactive mass spectrometers. Z-score equivalent of significant two-tailed Fisher exact test p-Values, i.e., $Z > 1.96$, was the threshold for over-representation of ontologies. Z-score bar graphs were plotted in R. The full table of Fisher exact test significance values and transformed as Z scores for cellular component ontologies enriched in any of the 29 WGCNA modules was also calculated by GO-Elite v1.2.5 using the same total insoluble proteome background. This Z-score table was co-clustered using the R NMF package a heatmap function, implementing Manhattan distance function, with a Ward metric.

RESULTS AND DISCUSSION

Enrichment and Targeted Mass Spectrometry Quantification of Detergent-Insoluble RNA-Binding Proteins Across Neurodegenerative Diseases

We enriched protein aggregates by sarkosyl detergent fractionation of dorsolateral prefrontal cortex (DLPFC) tissue in 44 cases of control, AsymAD, AD and PD cases (**Figure 1A**). Cases were matched as closely as possible for age at death, gender, and post-mortem interval (PMI)

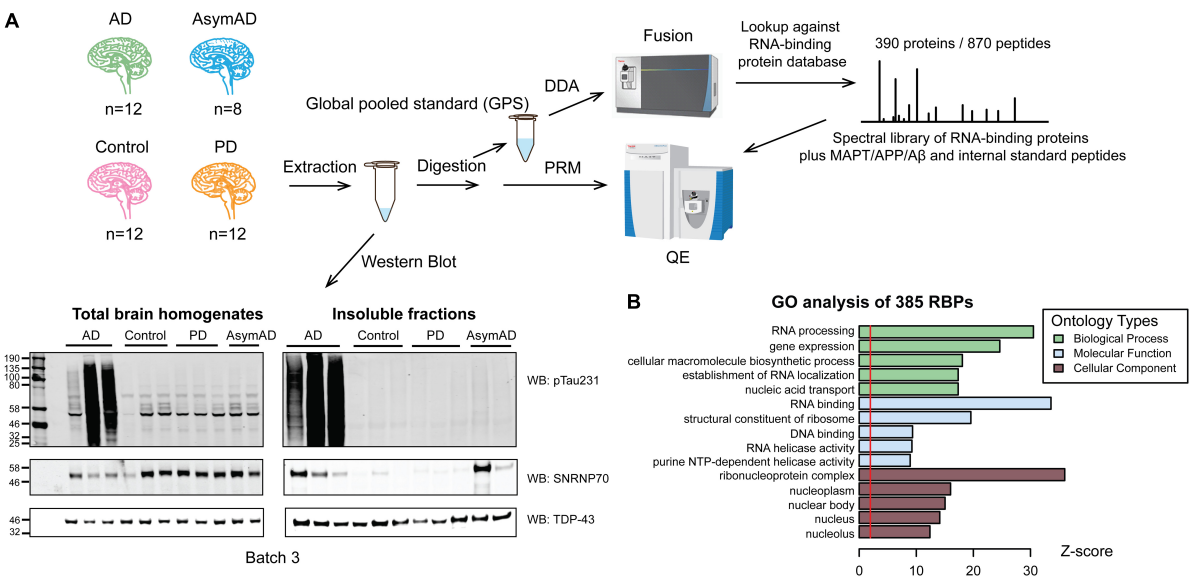

FIGURE 1 | Workflow of the targeted PRM method for quantification of RNA-binding proteins in detergent-insoluble fractions of human brains. **(A)** Workflow beginning with dorsolateral prefrontal cortex brain samples from control group (n = 12), Alzheimer's disease (AD, n = 12), Asymptomatic AD (AsymAD, n = 8), and Parkinson's disease (PD, n = 12) from which insoluble fractions were extracted and digested for subsequent quantification. Western blotting total homogenates and insoluble fractions of each group (n = 3, each) for TPD-43 (loading control), phosphorylated tau (pThr231-tau) and U1-70K indicates successful insoluble fraction extraction. A global pooled standard (GPS) was deeply profiled to identify the total insoluble proteome using an Orbitrap Fusion mass spectrometer. A custom targeted RNA-binding protein (RBP) peptide list and corresponding spectra library was designed for PRM, including 870 peptides from 385 RBPs plus tau, Aβ, APP and internal standard peptides. Finally, PRM was run on Q-Exactive mass spectrometer for all 44 samples using 6 GPS samples to normalize between batches. **(B)** GO analysis of detected 385 RBPs linked proteins to "RNA processing" and "RNA binding" biological processes and molecular functions, respectively.

(**Table 1** and **Supplementary Table 1**). PD cases served as a disease control, which do not show consistent evidence of U1 snRNP aggregation (Bai et al., 2013). Wet tissue amounts and insoluble protein yields were summarized to show no significant difference in the relative protein amounts of insoluble fractions between case groups (**Supplementary Table 2**). The aggregate enrichment was validated by western blot of pT231-tau, a marker of neurofibrillary tangles, and U1-70K (**Figure 1A** and **Supplementary Figure 1A**), counterposed with TDP-43 labeling as a loading control. Insolubility of tau and U1-70K are hallmarks of AD post-mortem brain (Bai et al., 2013; Hales et al., 2014, 2016). A large signal increase of insoluble pT231-tau was observed only in AD cases (**Supplementary Figure 1B**), while U1-70K was enriched in the insoluble fraction of both AsymAD and AD (**Supplementary Figure 1C**), with little to no enrichment of either hallmark observed in PD. These data are consistent with previous findings that showed insolubility of U1 snRNP components including U1-70K in early stages of preclinical AD, preceding that of tau (Hales et al., 2016).

After successfully enriching for insoluble proteins across different neurodegenerative disease cases, we comprehensively characterized the total insoluble proteome to build a target list of observable aggregating RNA-binding proteins (RBPs) across all disease groups. To generate the target list, a global pooled standard (GPS) consisting of an equivalent amount of tryptic peptides from all samples was analyzed by LC-MS/MS in data-dependent acquisition (DDA) mode. Of all the identified insoluble proteins, we prioritized 385 proteins involved in RNA biology and RNA binding (RBPs, see definition in "Methods" Section "Parallel Reaction Monitoring (PRM)"). As expected, gene ontology (GO) analysis of the custom 385 RBP list compared against the insoluble proteome used as background (**Figure 1B**) revealed predominant GO terms associated with the "RNA processing" biological process and the "RNA binding" molecular function. Furthermore, we observed an enrichment of "ribonucleoprotein complex," and "nucleus"-related cellular component GO terms, indicating that we captured a broad range of RBPs across divergent compartments of the cell. Using Skyline software (MacLean et al., 2010), we developed a targeted mass spectrometry-based PRM method to analyze 870 peptides from 385 RBPs, plus tau, APP and Aβ, and internal control spike-in peptides essentially as described (Zhou et al., 2019, 2020). Three hundred twenty four out of 390 proteins were common to previously published stochastic data dependent acquisition (untargeted) single-shot LC-MS/MS data (**Supplementary Figure 2A**; Johnson et al., 2020). About 97% of these 324 proteins have 0-5% missing PRM values, compared to 54% of proteins in the untargeted data (**Supplementary Figure 2B**). These analyses highlight the value of the targeted PRM method for quantifying RBPs with significantly less missingness than in an untargeted approach.

The PRM method achieved relative quantification of each target RBP peptide across all 44 case-samples, by which we could calculate abundance changes of each target RBP across different disease groups. A representative spectrum of a peptide from tau (IGSTENLK, residues 260-267) was selected to show how peptides were quantified by PRM (**Supplementary Figure 3**). Several fragment ions were detected from each peptide in the MS/MS spectra. The top five y-ions of the peptide were selected for PRM analysis (**Supplementary Figure 3A**). Peptides were quantified by integrating chromatographic areas of multiple fragment ions at the MS/MS level to determine relative abundance across the case-samples (**Supplementary Figure 3B**). At least three fragment ions were used to quantify each peptide using Skyline. The IGSTENLK tau peptide, mapping to the first repeat (R1) of the microtubule binding region (MTBR), was enriched specifically in AD group samples. This peptide is within the pronase-resistant region of tau and is a likely constituent of the protofilament core of AD tau (Fitzpatrick et al., 2017). Also, the IGSTENLK tau peptide harbors one of the KXGS motifs that regulate tau aggregation in a post-translational modification-dependent manner (Cook et al., 2014). Therefore, insoluble fraction abundance changes measured by PRM at the peptide level reflect insolubility or aggregation changes unique to heterogeneous diseases. We have also compared the signal intensities of western blot densitometry measurements to PRM quantification of pT231-tau (cor = 0.92, p = 1.1e–18, Student's p for Pearson rho; **Supplementary Figure 3C**) and U1-70K protein (cor = 0.81, p = 2.7e–11; Student's p for Pearson rho, **Supplementary Figure 3D**), observing a significant degree of correlation between the independent measurement procedures. This highlights the utility of PRM analysis for the interrogation of disease-specific attributes of the insoluble RBP proteome.

Region and Modification-Specific Peptides From APP and Tau Exhibit Increased Insolubility in AD

Amyloid beta plaques and tau neurofibrillary tangles are core pathological hallmarks of the AD brain (Glenner and Wong, 1984; Iqbal et al., 1984). To further confirm enrichment of insoluble protein species in our sarkosyl-insoluble, aggregate-enrichment method, we asked whether we could measure changes in this aggregate-enriched fraction at the peptide level. We created a schematic of the neuronal APP_{695} isoform, where all targeted peptides by PRM were aligned to their corresponding region in the protein. Mapped peptides were colored according to $-\log_{10}$ t-test p-Values of insoluble fraction abundance differences between the AD group and controls (**Figure 2A** and **Supplementary Table 7**). Individual boxplots of examined peptides across the entire APP_{695} sequence were generated to directly show differences in peptide abundance from the same protein across all disease groups. Notably, y-Values used in the boxplots were $\log_2$ transformed peptide area and those peptide areas with a zero value were imputed in order to perform statistical analysis (**Supplementary Table 7**). The imputation and $\log_2$ transformation compressed differences between groups contributing to more conservative p-Values (**Supplementary Tables 7, 8**). Still, peptides of Aβ and tau protein showed significant enrichment in AD cases. We observed that among the nine peptides mapping to APP, only those

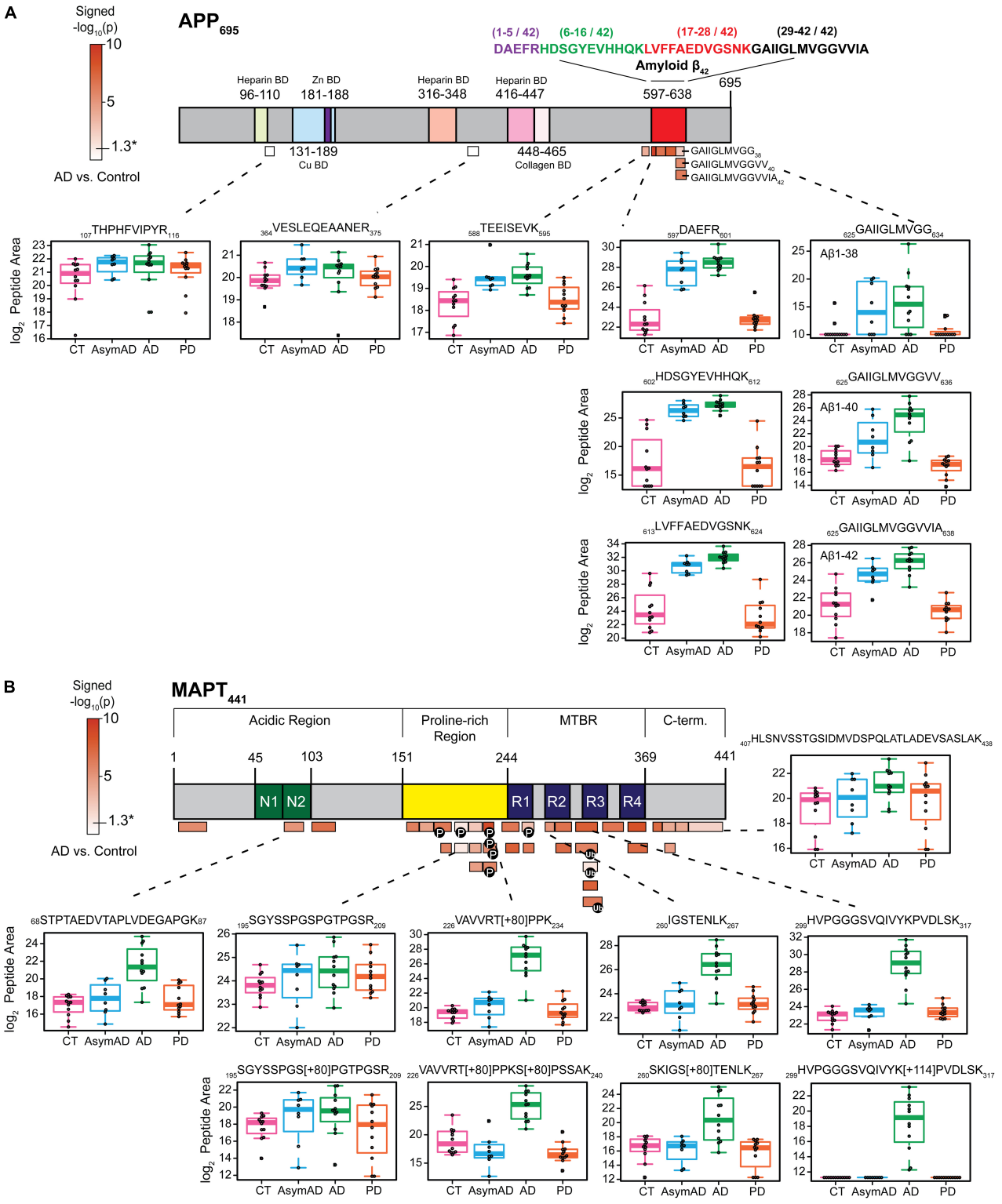

FIGURE 2 | Specific peptides from Aβ and tau exhibit disease-associated abundance changes in the detergent-insoluble fractions. **(A)** The schematic of APP_{695} where 9 peptides were identified and quantified across all 44 samples. The color scale represented -log10(*t*-test *p*) signed values, calculated on log_2-transformed data for AD vs. control case group comparison only. Subdomains identified from the UniProt database were marked with different colors. Peptides with significantly altered insoluble fraction abundances (*p*-Value < 0.05) are all mapped to the Aβ region. Box plots show the significant enrichment of Aβ peptides in AsymAD and AD while peptides mapping elsewhere in APP are unaltered across disease groups. **(B)** Peptides (n = 35) were mapped to the $MAPT_{441}$ (2N4R) and colored according to their corresponding *p*-Value as described above. Most identified peptides showed significant differences between AD and control group (*p*-Value < 0.05).

mapping to the Aβ region (residues 597-638) were highly enriched in AD (**Figure 2A**), consistent with previous findings (Seyfried et al., 2017), whereas peptides from the N-terminus of APP were unchanged in AD versus control cases. Enrichment of the Aβ-derived peptides in the insoluble fraction of AD brain is due to the AD-specific appearance of amyloid plaque aggregates (Seyfried et al., 2017) as a consequence of proteolytic cleavage by β- and γ-secretases, respectively (Vassar et al., 2009; Chen et al., 2017). Boxplots of all peptides mapping to APP further illustrate the differential regulation of peptide-level insolubility across different case groups. Whereas Aβ-derived insoluble peptides exhibited strong, stage-specific increased enrichment in AsymAD and AD, they were unchanged in PD, demonstrating the ability of our method to distinguish AD-specific amyloid aggregation.

Similarly, the 35 peptides mapping to tau (MAPT) (**Figure 2B**) show varying degrees of increased abundance in AD insoluble fractions compared to control. Peptides from the MTBR region were highly enriched in AD versus control cases. The MTBR region forms the highly insoluble and stable core of neurofibrillary tangles (Fitzpatrick et al., 2017), which are required for seeding tau aggregation. Phosphorylation and ubiquitination are PTMs that modulate signaling pathways and pathophysiological mechanisms in AD. Unsurprisingly, these classes of PTMs decorate the MTBR region of tau and are enriched in AD (Abreha et al., 2018; Ping et al., 2018, 2020; Arakhamia et al., 2020). Although highly enriched in AD, tau peptides were largely unchanged in AsymAD, demonstrating the late aggregation of tau protein during progression of AD pathology. This is in agreement with Braak staging and extensive molecular imaging and proteomic protein quantification studies in AD brain (Braak and Braak, 1991; Gozal et al., 2009; Bateman et al., 2012; Villemagne et al., 2013; Hales et al., 2016), and further highlights the reliability of our PRM method to detect and quantify changes in the insoluble proteome specific to AD.

Differential Aggregation of RNA-Binding Proteins Across Neurodegenerative Diseases

Although several neurodegenerative diseases are distinguished by RBP aggregation (Bai et al., 2013; Ramaswami et al., 2013; Diner et al., 2014; Hales et al., 2014; Wolozin and Apicco, 2015; Maziuk et al., 2017), different diseases contain aggregates of distinct classes or families of RBPs. To examine whether there were disease-specific RBP aggregation events in the brain proteomes of our cohort, we generated volcano plots of three pairwise comparisons of neurodegenerative disease groups versus controls (**Figure 3A**). Insoluble RBPs with a significant alteration in abundance within a disease group were considered as those beyond a 50 percent fold change (±1.5) with a p-Value < 0.05. A complete list of differentially insoluble RBPs is listed in **Supplementary Table 11** (t-test for control vs. disease) and **Supplementary Table 12** (ANOVA for all pairwise comparison). A few representative RBPs with significant changes in **Figure 3A** were shown in **Figure 3B**. Notably, U1 snRNP proteins SNRPA and U1-70K (SNRNP70) exhibited significant enrichment within the insoluble fraction of AsymAD brain, along with Aβ. This finding confirms our previous work that links U1 snRNP pathology to AD (Bai et al., 2013; Diner et al., 2014; Hales et al., 2014; Bishof et al., 2018), which coincides with Aβ plaque deposition. These events are likely to occur earlier than insoluble tau accumulation, which is primarily enriched in the insoluble fraction of symptomatic AD samples. Interestingly, tau is elevated in PD group as well. Other snRNP component RBPs belonging to the Sm ring of the spliceosome, including SNRPN, SNRPD1, SNRPD2, SNRPD3, SNRPE and SNRPG exhibit significant and robust insolubility increase in AD brain. In addition to core snRNP component RBPs, the splicing-associated RBPs LUC7L and LUC7L3, as well as U2AF2, DDX23 and PRPF4B, each with BAD repeats homologous to those of U1-70K, are enriched among insoluble proteins of AD-confirmed cases (Bishof et al., 2018; Kundinger et al., 2020). This suggests that proteins with BAD domains shift towards insolubility by way of some unknown mechanism in AD. In contrast, a noteworthy group of heterogeneous nuclear ribonucleoproteins (hnRNPs) called the FET (FUS/EWSR1/TAF15) family is more soluble in AD brain. In addition, a variety of RNA-binding proteins involved in protein translation or transcription were observed to be depleted preferentially from the insoluble fraction of PD cases, including pentatricopeptide repeat domain-containing protein 3 (PTCD3), 60S ribosomal protein L9 (RPL9), mitochondrial ribosomal protein L46 (MRPL46), cold-inducible mRNA binding protein (CIRBP) and DNA-directed RNA polymerase (POLRMT). This suggests a shift of RBPs involved in translation and transcription away from the insoluble fraction, specific to PD—though it is also commensurate with a possible decrease of these proteins in PD regardless of insoluble fraction enrichment. As we only measured the insoluble fraction, we were limited in the power to interpret an enrichment or depletion in the insoluble fraction of RBPs in the disease groups. Possible reasons for the significant depletion of an RBP from the insoluble fraction include increased degradation, preferential chaperone-mediated folding mechanisms or reduced expression of that protein (Bukau et al., 2006; Cohen et al., 2006; Balch et al., 2008). Significant enrichment of specific RBPs may also be dependent on the magnitude of their abundance in the total proteome. However, as we previously showed there were no obvious spliceosome changes via core snRNPs like U1-70K or U1A observed in the total proteome, and rather, bulk changes are driven by cell types instead of individual proteins (Higginbotham et al., 2020). We hypothesize the enrichment of core snRNP components in insoluble fractions is not driven by their abundance in the total proteome and may be considered as reflective of the insolubility shift of these proteins in specific disease groups. Nonetheless, the disease-specific increases and decreases in insoluble fraction enrichment of different groups of RBPs suggests that different protein-mediated RNA metabolism events are dysregulated in different neurodegenerative diseases (Liu et al., 2017). Our findings reveal several novel signatures of co-aggregating RBPs suggesting that RBPs are differentially dysregulated across different

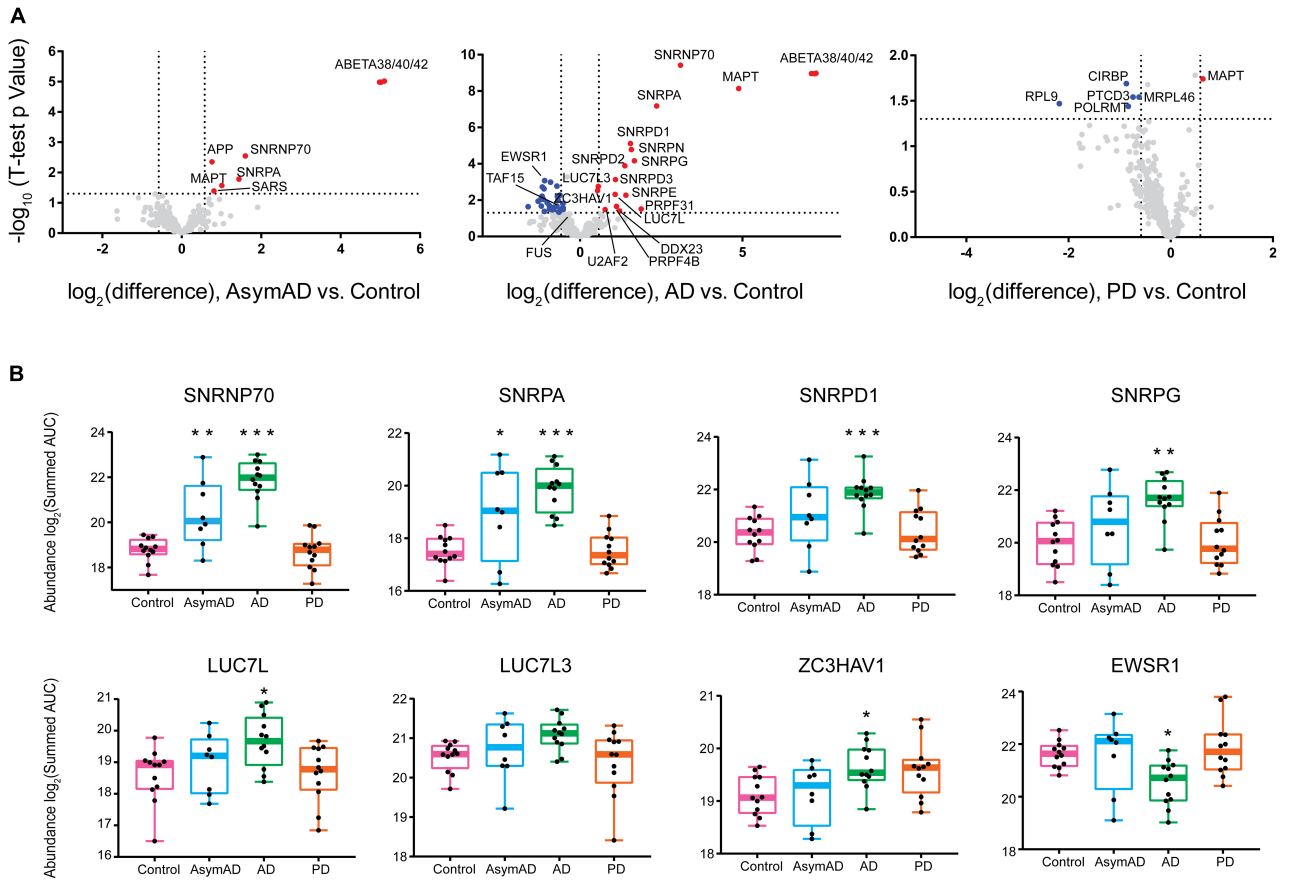

FIGURE 3 | RNA-binding proteins have different abundance patterns in the detergent-insoluble fractions across neurodegenerative diseases. **(A)** Differential abundance of RBPs across different groups was shown by volcano plot containing 385 RBPs, plus tau, APP and total β-amyloid. Fold-change, displayed on the *x*-axis, was the $\log_2$ protein abundance ratios for pairwise comparisons (AsymAD/Control, AD/Control, PD/Control). The t-statistic (−log10(*p*-Value)) was calculated for all proteins in each pairwise group and displayed on the *y*-axis. Insoluble fraction enriched proteins were highlighted in red (| Fold Change| $>$ 1.5, *p*-Value $<$ 0.05) while proteins with decreased insolubility were highlighted in blue, and gray dots represented proteins that remained unchanged. Several RBPs, including splicing factors, showed increased insolubility in AsymAD and AD while RBPs in PD were largely decreased in the insoluble fraction. **(B)** ANOVA boxplots of disease-signature RBPs (*$p < 0.05$, **$p < 0.01$, ***$p < 0.001$). SNRNP70 and SNRPA showed stage-specific increase in detergent-insoluble fraction of AsymAD and AD; SNRPD1, SNRPG, LUC7L, and ZC3HAV1 only showed significant increase in AD insoluble fractions; FET family member EWSR1 exhibited a decreased abundance in AD insoluble fractions.

neurodegenerative diseases, leading to diverse subsequent pathology, molecular pathophysiology, and symptoms.

Correlation Network Analysis Groups Detergent-Insoluble RNA-Binding Proteins Into Modules With Shared Biological Function

To further study the biology underlying co-aggregation between different RBPs, we performed a systems biology analysis using WeiGhted Co-expression Network Analysis (WGCNA) to cluster RBP abundances within sarkosyl-insoluble fractions across our multiple neurodegenerative disease brain cohort. The network reduced the data into 29 modules based on correlation (rank-ordered by size, M1-M29) that were each assigned a different color (**Figure 4A**). These modules are made up of proteins that highly correlated to each other which typically reflects their similarity in the biology or structure. An eigenprotein network was generated to show correlations between modules. An eigenprotein is defined as the first principal component of a given module and serves as a representative, weighted expression profile for the module (Seyfried et al., 2017). Individual RBP module membership is listed in **Supplementary Table 14**. Correlation of each module to post-mortem CERAD/Braak scores or disease states were illustrated as a heatmap, with significance visualized by a color scale and asterisks (*$p < 0.05$, **$p < 0.01$, ***$p < 0.001$). The M12 module, which contains tau and Aβ as well as all snRNP components measured, was the most highly correlated with CERAD scores (standard assessment of AD plaque pathology) and Braak staging (of tangle pathology extent). The M12 module insolubility profile across the cohort was also positively correlated with AD diagnosis ($p < 0.001$). The eigenproteins that drive the insolubility co-abundance of M12 are all snRNP components (SNRPN, U1-70K, U1A, SRNPD1/3,

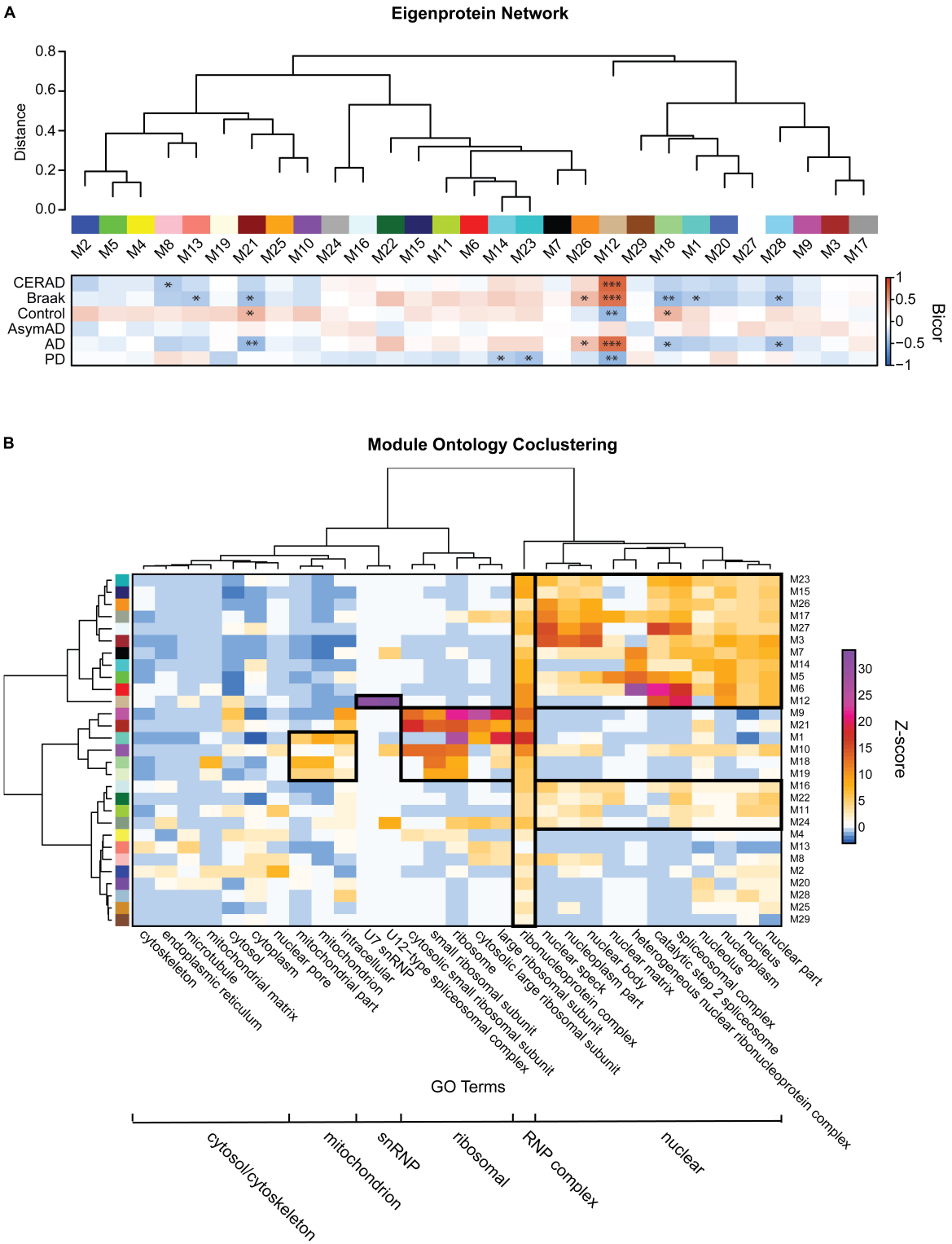

FIGURE 4 | Detergent-insoluble protein co-abundance network and ontology clusters. **(A)** 29 RBP modules were obtained by WGCNA network analysis. Modules were visualized in relatedness order, with the heatmap shown representing robust bicor correlation of each module to CERAD/Braak scores or each disease diagnoses. Bicor correlations are illustrated as a directional heatmap with a color scale and asterisks to display significance (*$p < 0.05$, **$p < 0.01$, and ***$p < 0.001$). Correlations between each module was shown by eigenprotein network indicated on the top. **(B)** For each module, a Z-score for Gene Ontology (GO) terms was calculated which reflects the over-representation of the components of that module to each GO term. Six "clusters" of RBP modules were grouped according to their over-representation of GO-terms involved in mitochondrion, snRNP, ribosomal, RNP, nuclear and cytoplasmic complexes.

SNRPG). These proteins are highly correlated with each other and with amyloid deposition even in early, preclinical stages of AD, consistent with previous observations (Hales et al., 2016). Another module, M26, containing the BAD proteins LUC7L, LUC7L3, DDX23 and RBM39, was also positively correlated with AD diagnosis and increased Braak staging. In agreement with the depletion of insoluble RBPs observed in PD (**Figure 3A**), there were several modules (M12, M14 and M23) with insolubility profiles that were anti-correlated to PD status. Therefore, we were able to observe biologically coherent groups of RBPs that correlated with disease status and relevant traits.

To reveal functionally distinct groups of modules, and thereby simplify the granularity of our network, we grouped RBP modules by their strength of association to different GO terms, using co-clustering analysis (**Figure 4B**). This illustrated the discrete enrichment of RBP modules to six different "macro" clusters. These included nuclear complexes, ribosomal units, RNP complexes, snRNPs, mitochondrion and cytoplasmic complexes. Because our hypothesis-driven MS approach targeted RBPs, every module grouped into the RNP complex cluster. A separate nuclear cluster consisted of a large group of RBP modules, as the nucleus is a hub for many membrane-less RBP organelles (Boeynaems et al., 2018). The M12 module, consisting almost entirely of snRNP component RBPs plus Aβ and tau, grouped into a separate snRNP cluster. Interestingly, the M12 module grouped with the nuclear cluster but adjacent to the mitochondrial and ribosomal clusters. This may recapitulate known subcellular localization and varied protein-protein interaction behaviors of snRNP proteins (Fischer et al., 1993, 1997; Romac et al., 1994; Liu et al., 1997; Bishof et al., 2018). The ribosome and mitochondrial clusters consisted of some of the same modules (M1, M10, M18, and M19), consistent with mitochondria utilizing independent translation machinery. Interestingly, one of these modules (M18) is significantly depleted from the insoluble fraction of AD brain, compared to control brain. In addition, the ribosome- and mitochondria-associated M19 module was depleted from the insoluble fraction in PD samples compared to control. These changes of translation machinery in the disease groups may indicate dysfunction of translation and links a recent finding of crosstalk between translation inhibition and aggresomal formation, involving nuclear capped-RNA-binding proteins like NCBP1 (Park et al., 2018). Notably, NCBP1, RAE1, XPOT, and EIF5A are involved in the passage of mature mRNAs from the nucleus to cytoplasm through nuclear pores, and all four of these proteins are members within M2, a module uniquely enriched for the gene ontology "nuclear pore." Trait correlations for M2 (**Figure 4A**) trend such that only control cases in the cohort have enhanced levels of insoluble M2 proteins, suggesting that the nuclear pore basket may be compromised in AD and PD. Taken together, these findings suggest that ribosome complexes and translation machinery may be less stable as large insoluble complexes in neurodegenerative diseases, perhaps downstream of defective mature mRNA export. Overall, by using bioinformatic and systems biology approaches, we were able to group RBPs and modules together to infer shifts in biological function specific to the different neurodegenerative diseases represented in our cohort.

Distinct Classes of Aggregated RNA-Binding Proteins Show Disease Specificity

To illustrate module-specific insolubility changes across disease groups, we generated box plots of insoluble proteome eigenproteins (**Figure 5A**). M12, with hubs involved in spliceosomal snRNP assembly, including U1-70K, SNRPA and other snRNPs-as well as Aβ and tau-was increasingly insoluble-enriched in control, AsymAD, and AD cases. M26, another key module the insolubility of which correlates with AD diagnosis, is enriched with GO term "nuclear speckle" proteins. Importantly, M26 includes the BAD proteins LUC7L, LUC7L3, DDX23 and RBM39 (Bishof et al., 2018; Kundinger et al., 2020). Given the positive correlation with AD diagnosis and CERAD and Braak scores of these RBP modules, we sought to rank RBPs by their correlation to the Aβ and tau insoluble protein profiles we measured across the 44 case samples of our cohort. To assess this, we calculated biweight midcorrelation (bicor) coefficients for all 385 RBPs as pairwise protein comparisons to $A\beta_{(1-42)}$ and tau insoluble fraction abundances across all 44 individual cases (**Supplementary Figures 5A,B** and **Supplementary Table 15**). Strikingly, the entire M12 module consisted of the highest correlated RBPs to both Aβ and tau insolubility. In addition, the next best ranking members included BAD proteins LUC7L, LUC7L3, and DDX23 of M26. This suggests that spliceosome associate RBPs may be a bridge between Aβ and tau aggregation pathologies in AD.

Among the RBPs most anti-correlated to insoluble tau abundance include the mitochondrial proteins MRPL46 and PTCD3, which are significantly depleted from the insoluble fractions of PD. Notably, tau protein facilitates an interaction between MRPL46 and stress-related RBP TIA1, and this interaction is eliminated when tau expression is lost (Vanderweyde et al., 2016). TIA1 and other stress granule RBPs including G3BP were not enriched in the sarkosyl-insoluble fractions in this work, consistent with previous studies (Vanderweyde et al., 2012; Wolozin, 2012; Hales et al., 2016). Instead, TIA1 preferentially stabilizes soluble oligomeric tau in stress granules, whereas TIA1 reduction promotes accumulation of fibrillar tau (Vanderweyde et al., 2016; Apicco et al., 2018). This highlights the potential of sarkosyl-soluble RBPs to regulate the aggregation of tau in addition to other RBPs. Some modules comprised of proteins that are anti-correlated to Aβ and tau show decreased insolubility in both AD and PD, such as M18, M21 and M28. The M28 module contains FET family members FUS/EWSR1/TAF15, and the other two are comprised of ribosomal subunit proteins. Over 50% of the members of M18, M21 and M28 are differentially soluble in AD (**Figure 5B**). As memory formation requires constant and activity-dependent adaptive protein biosynthesis, ribosomal protein solubility changes may indicate neuronal dysfunction and cognitive decline, consistent with a decrease in overall translation within neuronal cells (Meier et al., 2016; Koren et al., 2019). Two

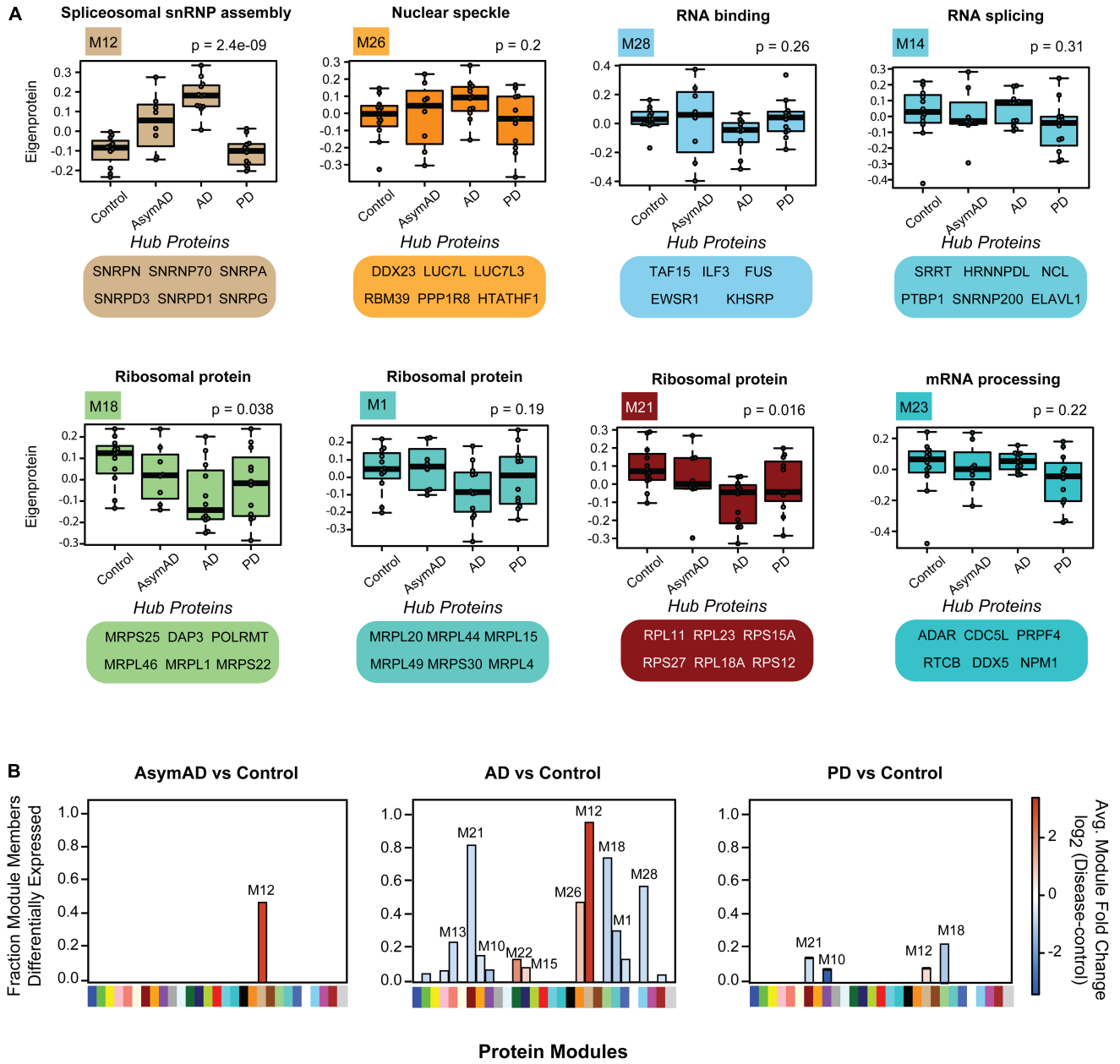

FIGURE 5 | Module-wise insolubility changes according to disease status. **(A)** A highlight of modules that were significantly correlated with disease groups. Top GO terms were highlighted for each module. All of 29 individual modules overrepresent gene ontologies. For example, M12 shows a group of proteins that belong to "spliceosome snRNP assembly;" M26 includes "nuclear speckle" proteins. The top six proteins which drive the module insolubility, called eigenproteins, are listed below each box plot. M12 and M26 showed stage-specific enrichment in detergent-insoluble fraction of AsymAD and AD. Modules M18, M21 and M28 exhibited decreased insolubility in AD. Modules M14 and M23 experience decreased insolubility in PD only. The central horizontal bar in each box is the 50th percentile (median), and hinges of the box extents represent the interquartile range of the two middle quartiles of data within a group. The farthest data points, up to 1.5 times the interquartile range away from box hinges, define the extent of whiskers (error bars). Significance was measured using one-way non-parametric ANOVA, Kruskal-Wallis *p*-Values. **(B)** Module eigenprotein levels for each pairwise comparison between disease groups and controls are shown. Direction of solubility change is colored according to $\log_2$ fold change colored scale. The percentage of module members that were differentially abundant in the insoluble fraction in disease compared with control is plotted on the *y*-axis.

modules (M14 and M23) related to mRNA processing and RNA splicing, respectively, are specifically depleted from the insoluble fractions of PD brain, which is consistent with a shift in solubility dynamics specific to PD. Overall, we have identified modules representing solubility changes specific to neurodegenerative diseases that can be leveraged to focus future investigations and hypotheses regarding of RBP-associated pathogenic and mechanisms tied to aggregation propensity of these proteins.

CONCLUSION

In this work, we developed a targeted MS method to quantify aggregated RBPs in neurodegenerative disease brain tissue. In total we analyzed ∼900 peptides mapping to 385 RBPs in addition to tau, Aβ, APP and internal standard peptides, and examined their relative abundance across detergent-insoluble fractions of 44 individual dorsolateral prefrontal cortex tissue samples of patients with pathologically confirmed diagnoses of control, AsymAD, AD or PD. Our findings recapitulate the known disease specific aggregation of tau and β-amyloid in AD progression. Additionally, we have found numerous novel co-aggregating RBPs across these disease groups and have discussed their potential pathological mechanisms involved in either initiation or progression of pathophysiology within these diseases. The insoluble RBPs with differential abundance across different groups might represent potential novel protein-RNA complexes that are targets for therapeutic development. Moreover, further studies targeting this panel of insoluble RBPs across other neurodegenerative disease, including tauopathies, may reveal additional links between tau pathology and co-aggregation RBPs. Finally, we reported a strong correlation between U1 snRNP proteins and AD pathology which supports a hypothesis that U1 snRNP aggregation provides a bridge between amyloid deposition with tau aggregation. The targeted approaches described in this study collectively hold promise in defining mechanistic events during distinct neurodegenerative states perturbing RBP homeostasis in the human brain, to be deciphered in future studies.

DATA AVAILABILITY STATEMENT

The datasets presented in this study can be found in online repositories. The names of the repository/repositories and accession number(s) can be found below: http://www.proteomexchange.org/, PXD022144.

AUTHOR CONTRIBUTIONS

QG and MZ carried out the experiments. QG, MZ, SK, and ED performed the data analyses. ED did the computational analyses. QG drafted the original manuscript and figures. QG, SK, ED, and NS wrote and edited the manuscript. NS supervised the project. QG, ED, MZ, SK, MG, JL, AL, JS, and NS reviewed and edited the manuscript. AL, JS, and NS carried out the funding acquisition. MG collected the resources. All authors contributed to the article and approved the submitted version.

FUNDING

Support for this research was provided by funding from the National Institute on Aging (R01AG053960, R01AG061800, RF1AG057471, RF1AG057470, R01AG057339, and RF1AG062181), the Accelerating Medicine Partnership for AD (U01AG046161 and U01AG061357), and the Emory Alzheimer's Disease Research Center (P30AG066511).

ACKNOWLEDGMENTS

We are grateful to the patients and families that donate tissue samples to the Emory University brain bank and for their contributions to this study.

SUPPLEMENTARY MATERIAL

The Supplementary Material for this article can be found online at: https://www.frontiersin.org/articles/10.3389/fnmol.2021.623659/full#supplementary-material

Supplementary Figure 1 | Western blot and PRM measurements for pT231-tau and U1-70K are highly correlated. **(A)** Western blot was performed on total brain homogenates before extraction and insoluble fractions after extraction for the remaining three batches which include 9 control, 9 AD, 5 AsymAD, and 9 PD cases. TDP-43 was blotted as loading control. **(B)** Scatter plot of insoluble pT231-tau western blot band intensities across all four groups. The AD group is the only group significantly changed from control (p-Value $\leq$ 0.0001, Dunnet's multiple comparisons test). **(C)** Group-wise scatter plot of insoluble U1-70K western blot. Both AsymAD (p-Value = 0.0427) and AD (p-Value = 0.0010) are significantly changed from control (Dunnet's multiple comparisons test).

Supplementary Figure 2 | Comparison of missing values in PRM targeted method and label free quantitation (discovery mode) untargeted method data. **(A)** A Venn diagram shows 324 common proteins in both PRM and data dependent acquisition (label free quantitation) method data. **(B)** Histogram of the percent of proteins with different levels of percent missing measurements for the 324 common proteins in PRM (*blue bars*) and untargeted Consensus LFQ (*yellow bars*) modes of analysis. Approximately 23% of the shared 324 proteins were removed in the untargeted LFQ analysis, while zero were removed in this current PRM analysis.

Supplementary Figure 3 | Parallel reaction monitoring analysis and peptide peak quantification confirms known changes of insoluble tau in AD at the peptide level. **(A)** MS/MS spectra of representative IGSTENLK peptide of tau. The *x*-axis is the m/z of each fragment ion and the *y*-axis displays the relative abundance of each fragment ion. The top-5 product ions were labeled and highlighted in different colors. The spectra was obtained from AD sample E06-155. **(B)** Corresponding chromatography of top-5 product ions of IGSTENLK peptide across GPS, control, AsymAD, AD and PD cases where *x*-axis is retention time and *y*-axis is intensity. Each ion was represented by a different color. **(C)** Scatter plot of western blot band intensities and PRM quantification of VAVVRT[+80]PPK (AA226-234) pT231-tau peptide in CTL (*magenta*), AsymAD (*turquoise*), AD (*green*), and PD (*orange*) samples. Significance of correlation is calculated between the two independent measurements of pT231-tau (Student's p for Pearson rho). **(D)** Scatter plot of western blot band intensities and PRM quantification of U1-70K protein. Significance of correlation is calculated between the two independent measurements of U1-70K (Student's p for Pearson rho).

Supplementary Figure 4 | The distribution of standard peptide response (standard peptide 2-5, isotope 3) across 50 runs before and after normalization. **(A)** The standard peptide intensity from each sample was averaged to 1 and plotted across all 50 runs. The *x*-axis indicates run number and *y*-axis displays the response. Theoretically, each of all 50 runs should exhibit the same response since an identical amount of standard peptides was added to each sample. However, due to systematic signal depreciation, the response gradually decreased before normalization. **(B)** After normalization, influence of technical variation was statistically eliminated with a final coefficient of variance (CV) of 14.69% by applying a correcting factor to each datapoint.

Supplementary Figure 5 | Bicor coefficients rank RBPs according to correlation with Aβ and tau. **(A)** The 385 RBPs were ranked by their correlation to $A\beta_{(1-42)}$

insolubility across all 44 cases examined. Each point is colored according to module membership of that RBP. The top 10 positively- and anti-correlated proteins are listed with their bicor coefficient value. **(B)** 385 RBPs were ranked by their correlation to tau insolubility across all 44 cases examined. Each point represents an individual RBP colored according to module memberships. The top 10 positively- and anti-correlated proteins are listed with their bicor coefficient value.

Supplementary Table 1 | Summary of case information.

Supplementary Table 2 | Sarkosyl-soluble and -insoluble protein yields.

Supplementary Table 3 | Protein bands quantification of insoluble tau and U1-70K.

Supplementary Table 4 | Correlation of pT231-tau /U1-70K quantification between western blot and PRM.

Supplementary Table 5 | Raw PRM quantified peptide peak area before normalization.

Supplementary Table 6 | Normalized peptide peak areas.

Supplementary Table 7 | Peptide differential abundance analysis (imputed missing values marked in blue, log_2-transformed, *t*-test).

Supplementary Table 8 | Peptide differential abundance analysis (ANOVA).

Supplementary Table 9 | Normalized protein quantification.

Supplementary Table 10 | Normalized protein quantification (log_2-transformed and regressed for age, sex, and PMI).

Supplementary Table 11 | Protein differential abundance analysis (*t*-test).

Supplementary Table 12 | Protein differential abundance analysis (ANOVA).

Supplementary Table 13 | Z-score table for module clustering by GO terms.

Supplementary Table 14 | Module assignment information.

Supplementary Table 15 | Correlation of all insoluble RNA-binding proteins quantified to $A\beta_{(1-42)}$ and tau.

REFERENCES

Abreha, M. H., Dammer, E. B., Ping, L., Zhang, T., Duong, D. M., Gearing, M., et al. (2018). Quantitative analysis of the brain ubiquitylome in Alzheimer's disease. *Proteomics* 18:e1800108. doi: 10.1002/pmic.201800108

Apicco, D. J., Ash, P. E. A., Maziuk, B., LeBlang, C., Medalla, M., Al Abdullatif, A., et al. (2018). Reducing the RNA binding protein TIA1 protects against tau-mediated neurodegeneration in vivo. *Nat. Neurosci.* 21, 72–80. doi: 10.1038/s41593-017-0022-z

Arakhamia, T., Lee, C. E., Carlomagno, Y., Duong, D. M., Kundinger, S. R., Wang, K., et al. (2020). Posttranslational modifications mediate the structural diversity of tauopathy strains. *Cell* 180, 633–644 e612. doi: 10.1016/j.cell.2020.01.027

Bai, B., Hales, C. M., Chen, P. C., Gozal, Y., Dammer, E. B., Fritz, J. J., et al. (2013). U1 small nuclear ribonucleoprotein complex and RNA splicing alterations in Alzheimer's disease. *Proc. Natl. Acad. Sci. U.S.A.* 110, 16562–16567. doi: 10.1073/pnas.1310249110

Balch, W. E., Morimoto, R. I., Dillin, A., and Kelly, J. W. (2008). Adapting proteostasis for disease intervention. *Science* 319, 916–919. doi: 10.1126/science.1141448

Bateman, R. J., Xiong, C., Benzinger, T. L., Fagan, A. M., Goate, A., Fox, N. C., et al. (2012). Clinical and biomarker changes in dominantly inherited Alzheimer's disease. *N. Engl. J. Med.* 367, 795–804. doi: 10.1056/NEJMoa1202753

Bishof, I., Dammer, E. B., Duong, D. M., Kundinger, S. R., Gearing, M., Lah, J. J., et al. (2018). RNA-binding proteins with basic-acidic dipeptide (BAD) domains self-assemble and aggregate in Alzheimer's disease. *J. Biol. Chem.* 293, 11047–11066. doi: 10.1074/jbc.RA118.001747

Boeynaems, S., Alberti, S., Fawzi, N. L., Mittag, T., Polymenidou, M., Rousseau, F., et al. (2018). Protein phase separation: a new phase in cell biology. *Trends Cell Biol.* 28, 420–435. doi: 10.1016/j.tcb.2018.02.004

Boros, B. D., Greathouse, K. M., Gentry, E. G., Curtis, K. A., Birchall, E. L., Gearing, M., et al. (2017). Dendritic spines provide cognitive resilience against Alzheimer's disease. *Ann.Neurol.* 82, 602–614. doi: 10.1002/ana.25049

Braak, H., and Braak, E. (1991). Neuropathological stageing of Alzheimer-related changes. *Acta Neuropathol.* 82, 239–259. doi: 10.1007/bf00308809

Braak, H., Del Tredici, K., Rüb, U., de Vos, R. A., Jansen Steur, E. N., and Braak, E. (2003). Staging of brain pathology related to sporadic Parkinson's disease. *Neurobiol. Aging* 24, 197–211. doi: 10.1016/s0197-4580(02)00065-9

Brown, D. F., Dababo, M. A., Bigio, E. H., Risser, R. C., Eagan, K. P., Hladik, C. L., et al. (1998). Neuropathologic evidence that the Lewy body variant of Alzheimer disease represents coexistence of Alzheimer disease and idiopathic Parkinson disease. *J. Neuropathol. Exp. Neurol.* 57, 39–46. doi: 10.1097/00005072-199801000-00006

Bukau, B., Weissman, J., and Horwich, A. (2006). Molecular chaperones and protein quality control. *Cell* 125, 443–451. doi: 10.1016/j.cell.2006.04.014

Chen, G. F., Xu, T. H., Yan, Y., Zhou, Y. R., Jiang, Y., Melcher, K., et al. (2017). Amyloid beta: structure, biology and structure-based therapeutic development. *Acta Pharmacol. Sin.* 38, 1205–1235. doi: 10.1038/aps.2017.28

Cherry, J. D., Zeineddin, A., Dammer, E. B., Webster, J. A., Duong, D., Seyfried, N. T., et al. (2018). Characterization of detergent insoluble proteome in chronic traumatic encephalopathy. *J. Neuropathol. Exp. Neurol.* 77, 40–49. doi: 10.1093/jnen/nlx100

Cohen, E., Bieschke, J., Perciavalle, R. M., Kelly, J. W., and Dillin, A. (2006). Opposing activities protect against age-onset proteotoxicity. *Science* 313, 1604–1610. doi: 10.1126/science.1124646

Cohen, T. J., Hwang, A. W., Unger, T., Trojanowski, J. Q., and Lee, V. M. (2012). Redox signalling directly regulates TDP-43 via cysteine oxidation and disulphide cross-linking. *EMBO J.* 31, 1241–1252. doi: 10.1038/emboj.2011.471

Cook, C., Carlomagno, Y., Gendron, T. F., Dunmore, J., Scheffel, K., Stetler, C., et al. (2014). Acetylation of the KXGS motifs in tau is a critical determinant in modulation of tau aggregation and clearance. *Hum. Mol. Genet.* 23, 104–116. doi: 10.1093/hmg/ddt402

Dai, J., Johnson, E. C. B., Dammer, E. B., Duong, D. M., Gearing, M., Lah, J. J., et al. (2018). Effects of APOE genotype on brain proteomic network and cell type changes in Alzheimer's disease. *Front. Mol. Neurosci.* 11:454. doi: 10.3389/fnmol.2018.00454

Dammer, E. B., Fallini, C., Gozal, Y. M., Duong, D. M., Rossoll, W., Xu, P., et al. (2012). Coaggregation of RNA-binding proteins in a model of TDP-43 proteinopathy with selective RGG motif methylation and a role for RRM1 ubiquitination. *PLoS One* 7:e38658. doi: 10.1371/journal.pone.0038658

Diner, I., Hales, C. M., Bishof, I., Rabenold, L., Duong, D. M., Yi, H., et al. (2014). Aggregation properties of the small nuclear ribonucleoprotein U1-70K in Alzheimer disease. *J. Biol. Chem.* 289, 35296–35313. doi: 10.1074/jbc.M114.562959

Diner, I., Nguyen, T., and Seyfried, N. T. (2017). Enrichment of detergent-insoluble protein aggregates from human postmortem brain. *J. Vis. Exp.* 128, 55835. doi: 10.3791/55835

Fischer, U., Liu, Q., and Dreyfuss, G. (1997). The SMN-SIP1 complex has an essential role in spliceosomal snRNP biogenesis. *Cell* 90, 1023–1029. doi: 10.1016/s0092-8674(00)80368-2

Fischer, U., Sumpter, V., Sekine, M., Satoh, T., and Lührmann, R. (1993). Nucleo-cytoplasmic transport of U snRNPs: definition of a nuclear location signal in the Sm core domain that binds a transport receptor independently of the m3G cap. *EMBO J.* 12, 573–583.

Fitzpatrick, A. W. P., Falcon, B., He, S., Murzin, A. G., Murshudov, G., Garringer, H. J., et al. (2017). Cryo-EM structures of tau filaments from Alzheimer's disease. *Nature* 547, 185–190. doi: 10.1038/nature23002

Gillette, M. A., and Carr, S. A. (2013). Quantitative analysis of peptides and proteins in biomedicine by targeted mass spectrometry. *Nat. Methods* 10, 28–34. doi: 10.1038/nmeth.2309

Glenner, G. G., and Wong, C. W. (1984). Alzheimer's disease: initial report of the purification and characterization of a novel cerebrovascular amyloid protein. *Biochem. Biophys. Res. Commun.* 120, 885–890. doi: 10.1016/s0006-291x(84)80190-4

Gozal, Y. M., Duong, D. M., Gearing, M., Cheng, D., Hanfelt, J. J., Funderburk, C., et al. (2009). Proteomics analysis reveals novel components in the detergent-insoluble subproteome in Alzheimer's disease. *J. Proteome Res.* 8, 5069–5079. doi: 10.1021/pr900474t

Grundke-Iqbal, I., Iqbal, K., Tung, Y. C., Quinlan, M., Wisniewski, H. M., and Binder, L. I. (1986). Abnormal phosphorylation of the microtubule-associated protein tau (tau) in Alzheimer cytoskeletal pathology. *Proc. Natl. Acad. Sci. U.S.A.* 83, 4913–4917. doi: 10.1073/pnas.83.13.4913

Hales, C. M., Dammer, E. B., Deng, Q., Duong, D. M., Gearing, M., Troncoso, J. C., et al. (2016). Changes in the detergent-insoluble brain proteome linked to amyloid and tau in Alzheimer's disease progression. *Proteomics* 16, 3042–3053. doi: 10.1002/pmic.201600057

Hales, C. M., Seyfried, N. T., Dammer, E. B., Duong, D., Yi, H., Gearing, M., et al. (2014). U1 small nuclear ribonucleoproteins (snRNPs) aggregate in Alzheimer's disease due to autosomal dominant genetic mutations and trisomy 21. *Mol. Neurodegener.* 9:15. doi: 10.1186/1750-1326-9-15

Hasegawa, M., Fujiwara, H., Nonaka, T., Wakabayashi, K., Takahashi, H., Lee, V. M., et al. (2002). Phosphorylated alpha-synuclein is ubiquitinated in alpha-synucleinopathy lesions. *J. Biol. Chem.* 277, 49071–49076. doi: 10.1074/jbc.M208046200

Higginbotham, L., Ping, L., Dammer, E. B., Duong, D. M., Zhou, M., Gearing, M., et al. (2020). Integrated proteomics reveals brain-based cerebrospinal fluid biomarkers in asymptomatic and symptomatic Alzheimer's disease. *Sci. Adv.* 6:eaaz9360. doi: 10.1126/sciadv.aaz9360

Hsieh, Y. C., Guo, C., Yalamanchili, H. K., Abreha, M., Al-Ouran, R., Li, Y., et al. (2019). Tau-mediated disruption of the spliceosome triggers cryptic RNA splicing and neurodegeneration in Alzheimer's disease. *Cell Rep.* 29, 301–316 e310. doi: 10.1016/j.celrep.2019.08.104

Hyman, B. T., and Trojanowski, J. Q. (1997). Consensus recommendations for the postmortem diagnosis of Alzheimer disease from the National Institute on Aging and the Reagan Institute Working Group on diagnostic criteria for the neuropathological assessment of Alzheimer disease. *J. Neuropathol. Exp. Neurol.* 56, 1095–1097. doi: 10.1097/00005072-199710000-00002

Iqbal, K., Zaidi, T., Thompson, C. H., Merz, P. A., and Wisniewski, H. M. (1984). Alzheimer paired helical filaments: bulk isolation, solubility, and protein composition. *Acta Neuropathol.* 62, 167–177. doi: 10.1007/BF00691849

Johnson, E. C. B., Dammer, E. B., Duong, D. M., Ping, L. Y., Zhou, M. T., Yin, L. M., et al. (2020). Large-scale proteomic analysis of Alzheimer's disease brain and cerebrospinal fluid reveals early changes in energy metabolism associated with microglia and astrocyte activation. *Nat. Med.* 26, 769–780. doi: 10.1038/s41591-020-0815-6

Johnson, E. C. B., Dammer, E. B., Duong, D. M., Yin, L., Thambisetty, M., Troncoso, J. C., et al. (2018). Deep proteomic network analysis of Alzheimer's disease brain reveals alterations in RNA binding proteins and RNA splicing associated with disease. *Mol. Neurodegener.* 13:52. doi: 10.1186/s13024-018-0282-4

Karpievitch, Y. V., Dabney, A. R., and Smith, R. D. (2012). Normalization and missing value imputation for label-free LC-MS analysis. *BMC Bioinformatics* 13(Suppl. 16):S5. doi: 10.1186/1471-2105-13-S16-S5

Koren, S. A., Hamm, M. J., Meier, S. E., Weiss, B. E., Nation, G. K., Chishti, E. A., et al. (2019). Tau drives translational selectivity by interacting with ribosomal proteins. *Acta Neuropathol.* 137, 571–583. doi: 10.1007/s00401-019-01970-9

Kundinger, S. R., Bishof, I., Dammer, E. B., Duong, D. M., and Seyfried, N. T. (2020). Middle-down proteomics reveals dense sites of methylation and phosphorylation in arginine-rich RNA-binding proteins. *J. Proteome Res.* 19, 1574–1591. doi: 10.1021/acs.jproteome.9b00633

Kwong, L. K., Neumann, M., Sampathu, D. M., Lee, V. M., and Trojanowski, J. Q. (2007). TDP-43 proteinopathy: the neuropathology underlying major forms of sporadic and familial frontotemporal lobar degeneration and motor neuron disease. *Acta Neuropathol.* 114, 63–70. doi: 10.1007/s00401-007-0226-5

Langfelder, P., and Horvath, S. (2008). WGCNA: an R package for weighted correlation network analysis. *BMC Bioinformatics* 9:559. doi: 10.1186/1471-2105-9-559

Liu, E. Y., Cali, C. P., and Lee, E. B. (2017). RNA metabolism in neurodegenerative disease. *Dis. Model. Mech.* 10, 509–518. doi: 10.1242/dmm.028613

Liu, Q., Fischer, U., Wang, F., and Dreyfuss, G. (1997). The spinal muscular atrophy disease gene product, SMN, and its associated protein SIP1 are in a complex with spliceosomal snRNP proteins. *Cell* 90, 1013–1021. doi: 10.1016/s0092-8674(00)80367-0

MacLean, B., Tomazela, D. M., Shulman, N., Chambers, M., Finney, G. L., Frewen, B., et al. (2010). Skyline: an open source document editor for creating and analyzing targeted proteomics experiments. *Bioinformatics* 26, 966–968. doi: 10.1093/bioinformatics/btq054

Masters, C. L., Simms, G., Weinman, N. A., Multhaup, G., McDonald, B. L., and Beyreuther, K. (1985). Amyloid plaque core protein in Alzheimer disease and down syndrome. *Proc. Natl. Acad. Sci. U.S.A.* 82, 4245–4249. doi: 10.1073/pnas.82.12.4245

Maziuk, B., Ballance, H. I., and Wolozin, B. (2017). Dysregulation of RNA binding protein aggregation in neurodegenerative disorders. *Front. Mol. Neurosci.* 10:89. doi: 10.3389/fnmol.2017.00089

Maziuk, B. F., Apicco, D. J., Cruz, A. L., Jiang, L., Ash, P. E. A., da Rocha, E. L., et al. (2018). RNA binding proteins co-localize with small tau inclusions in tauopathy. *Acta Neuropathol. Commun.* 6:71. doi: 10.1186/s40478-018-0574-5

McKeith, I. G., Dickson, D. W., Lowe, J., Emre, M., O'Brien, J. T., Feldman, H., et al. (2005). Diagnosis and management of dementia with Lewy bodies: third report of the DLB consortium. *Neurology* 65, 1863–1872. doi: 10.1212/01.wnl.0000187889.17253.b1

McKeith, I. G., Galasko, D., Kosaka, K., Perry, E. K., Dickson, D. W., Hansen, L. A., et al. (1996). Consensus guidelines for the clinical and pathologic diagnosis of dementia with Lewy bodies (DLB): report of the consortium on DLB international workshop. *Neurology* 47, 1113–1124. doi: 10.1212/wnl.47.5.1113

Meier, S., Bell, M., Lyons, D. N., Rodriguez-Rivera, J., Ingram, A., Fontaine, S. N., et al. (2016). Pathological Tau promotes neuronal damage by impairing ribosomal function and decreasing protein synthesis. *J. Neurosci.* 36, 1001–1007. doi: 10.1523/Jneurosci.3029-15.2016

Miake, H., Mizusawa, H., Iwatsubo, T., and Hasegawa, M. (2002). Biochemical characterization of the core structure of alpha-synuclein filaments. *J. Biol. Chem.* 277, 19213–19219. doi: 10.1074/jbc.M110551200

Mirra, S. S., Heyman, A., McKeel, D., Sumi, S. M., Crain, B. J., Brownlee, L. M., et al. (1991). The consortium to establish a registry for Alzheimer's disease (CERAD). Part II. Standardization of the neuropathologic assessment of Alzheimer's disease. *Neurology* 41, 479–486. doi: 10.1212/wnl.41.4.479

Neumann, M., Rademakers, R., Roeber, S., Baker, M., Kretzschmar, H. A., and Mackenzie, I. R. (2009). A new subtype of frontotemporal lobar degeneration with FUS pathology. *Brain* 132(Pt 11), 2922–2931. doi: 10.1093/brain/awp214

Neumann, M., Sampathu, D. M., Kwong, L. K., Truax, A. C., Micsenyi, M. C., Chou, T. T., et al. (2006). Ubiquitinated TDP-43 in frontotemporal lobar degeneration and amyotrophic lateral sclerosis. *Science* 314, 130–133. doi: 10.1126/science.1134108

Nizhnikov, A. A., Alexandrov, A. I., Ryzhova, T. A., Mitkevich, O. V., Dergalev, A. A., Ter-Avanesyan, M. D., et al. (2014). Proteomic screening for amyloid proteins. *PLoS One* 9:e116003. doi: 10.1371/journal.pone.0116003

Park, Y., Park, J., and Kim, Y. K. (2018). Crosstalk between translation and the aggresome–autophagy pathway. *Autophagy* 14, 1079–1081. doi: 10.1080/15548627.2017.1358849

Perez-Riverol, Y., Csordas, A., Bai, J., Bernal-Llinares, M., Hewapathirana, S., Kundu, D. J., et al. (2019). The PRIDE database and related tools and resources in 2019: improving support for quantification data. *Nucleic Acids Res.* 47, D442–D450. doi: 10.1093/nar/gky1106

Peterson, A. C., Russell, J. D., Bailey, D. J., Westphall, M. S., and Coon, J. J. (2012). Parallel reaction monitoring for high resolution and high mass accuracy quantitative, targeted proteomics. *Mol. Cell. Proteomics* 11, 1475–1488. doi: 10.1074/mcp.O112.020131

Ping, L., Duong, D. M., Yin, L., Gearing, M., Lah, J. J., Levey, A. I., et al. (2018). Global quantitative analysis of the human brain proteome in Alzheimer's and Parkinson's Disease. *Sci. Data* 5:180036. doi: 10.1038/sdata.2018.36

Ping, L., Kundinger, S. R., Duong, D. M., Yin, L., Gearing, M., Lah, J. J., et al. (2020). Global quantitative analysis of the human brain proteome and phosphoproteome in Alzheimer's disease. *Sci. Data* 7:315. doi: 10.1038/s41597-020-00650-8

Promega (2017). *6 × 5 LC-MS/MS Peptide Reference Mix [Online]*. Available online at: https://www.promega.com/products/mass-spectrometry/mass-spec-reference-reagents/6-x-5-lc_ms_ms-peptide-reference-mix/?catNum=V7491 (accessed December, 2017).

Raj, T., Li, Y. I., Wong, G., Humphrey, J., Wang, M., Ramdhani, S., et al. (2018). Integrative transcriptome analyses of the aging brain implicate altered splicing in Alzheimer's disease susceptibility. *Nat. Genet.* 50, 1584–1592. doi: 10.1038/s41588-018-0238-1

Ramaswami, M., Taylor, J. P., and Parker, R. (2013). Altered ribostasis: RNA-protein granules in degenerative disorders. *Cell* 154, 727–736. doi: 10.1016/j.cell.2013.07.038

Ramirez-Alvarado, M., Merkel, J. S., and Regan, L. (2000). A systematic exploration of the influence of the protein stability on amyloid fibril formation in vitro. *Proc. Natl. Acad. Sci. U.S.A.* 97, 8979–8984. doi: 10.1073/pnas.150091797

Romac, J. M., Graff, D. H., and Keene, J. D. (1994). The U1 small nuclear ribonucleoprotein (snRNP) 70K protein is transported independently of U1 snRNP particles via a nuclear localization signal in the RNA-binding domain. *Mol. Cell Biol.* 14, 4662–4670. doi: 10.1128/mcb.14.7.4662

Ronsein, G. E., Pamir, N., von Haller, P. D., Kim, D. S., Oda, M. N., Jarvik, G. P., et al. (2015). Parallel reaction monitoring (PRM) and selected reaction monitoring (SRM) exhibit comparable linearity, dynamic range and precision for targeted quantitative HDL proteomics. *J. Proteomics* 113, 388–399. doi: 10.1016/j.jprot.2014.10.017

Ross, C. A., and Poirier, M. A. (2004). Protein aggregation and neurodegenerative disease. *Nat. Med.* 10(Suppl.), S10–S17. doi: 10.1038/nm1066

Seyfried, N. T., Dammer, E. B., Swarup, V., Nandakumar, D., Duong, D. M., Yin, L., et al. (2017). A multi-network approach identifies protein-specific co-expression in asymptomatic and symptomatic Alzheimer's disease. *Cell Syst.* 4, 60–72 e64. doi: 10.1016/j.cels.2016.11.006

Seyfried, N. T., Gozal, Y. M., Donovan, L. E., Herskowitz, J. H., Dammer, E. B., Xia, Q., et al. (2012). Quantitative analysis of the detergent-insoluble brain proteome in frontotemporal lobar degeneration using SILAC internal standards. *J. Proteome Res.* 11, 2721–2738. doi: 10.1021/pr2010814

Taylor, J. P., Hardy, J., and Fischbeck, K. H. (2002). Toxic proteins in neurodegenerative disease. *Science* 296, 1991–1995. doi: 10.1126/science.1067122

UniProt Consortium (2019). UniProt: a worldwide hub of protein knowledge. *Nucleic Acids Res.* 47, D506–D515. doi: 10.1093/nar/gky1049

Vanderweyde, T., Apicco, D. J., Youmans-Kidder, K., Ash, P. E. A., Cook, C., Lummertz da Rocha, E., et al. (2016). Interaction of tau with the RNA-Binding Protein TIA1 Regulates tau pathophysiology and toxicity. *Cell Rep.* 15, 1455–1466. doi: 10.1016/j.celrep.2016.04.045

Vanderweyde, T., Yu, H., Varnum, M., Liu-Yesucevitz, L., Citro, A., Ikezu, T., et al. (2012). Contrasting pathology of the stress granule proteins TIA-1 and G3BP in tauopathies. *J. Neurosci.* 32, 8270–8283. doi: 10.1523/JNEUROSCI.1592-12.2012

Vassar, R., Kovacs, D. M., Yan, R., and Wong, P. C. (2009). The beta-secretase enzyme BACE in health and Alzheimer's disease: regulation, cell biology, function, and therapeutic potential. *J. Neurosci.* 29, 12787–12794. doi: 10.1523/JNEUROSCI.3657-09.2009

Villemagne, V. L., Burnham, S., Bourgeat, P., Brown, B., Ellis, K. A., Salvado, O., et al. (2013). Amyloid β deposition, neurodegeneration, and cognitive decline in sporadic Alzheimer's disease: a prospective cohort study. *Lancet Neurol.* 12, 357–367. doi: 10.1016/s1474-4422(13)70044-9

Wolozin, B. (2012). Regulated protein aggregation: stress granules and neurodegeneration. *Mol. Neurodegener.* 7:56. doi: 10.1186/1750-1326-7-56

Wolozin, B., and Apicco, D. (2015). RNA binding proteins and the genesis of neurodegenerative diseases. *Adv. Exp. Med. Biol.* 822, 11–15. doi: 10.1007/978-3-319-08927-0_3

Woltjer, R. L., Cimino, P. J., Boutté, A. M., Schantz, A. M., Montine, K. S., Larson, E. B., et al. (2005). Proteomic determination of widespread detergent-insolubility including Abeta but not tau early in the pathogenesis of Alzheimer's disease. *FASEB J.* 19, 1923–1925. doi: 10.1096/fj.05-4263fje

Xue, S., Gong, R., He, F., Li, Y., Wang, Y., Tan, T., et al. (2019). Low-complexity domain of U1-70K modulates phase separation and aggregation through distinctive basic-acidic motifs. *Sci. Adv.* 5:eaax5349. doi: 10.1126/sciadv.aax5349

Zhang, G., Ueberheide, B. M., Waldemarson, S., Myung, S., Molloy, K., Eriksson, J., et al. (2010). Protein quantitation using mass spectrometry. *Methods Mol. Biol.* 673, 211–222. doi: 10.1007/978-1-60761-842-3_13

Zhou, M., Duong, D. M., Johnson, E. C. B., Dai, J., Lah, J. J., Levey, A. I., et al. (2019). Mass spectrometry-based quantification of tau in human cerebrospinal fluid using a complementary tryptic peptide standard. *J. Proteome Res.* 18, 2422–2432. doi: 10.1021/acs.jproteome.8b00920

Zhou, M., Haque, R. U., Dammer, E. B., Duong, D. M., Ping, L., Johnson, E. C. B., et al. (2020). Targeted mass spectrometry to quantify brain-derived cerebrospinal fluid biomarkers in Alzheimer's disease. *Clin. Proteomics* 17:19. doi: 10.1186/s12014-020-09285-8

Conflict of Interest: The authors declare that the research was conducted in the absence of any commercial or financial relationships that could be construed as a potential conflict of interest.

frontiers in Molecular Neuroscience

REVIEW
published: 15 April 2021
doi: 10.3389/fnmol.2021.647451

Advances in Proteomics Allow Insights Into Neuronal Proteomes

*Erin Fingleton, Yan Li and Katherine W. Roche**

National Institute of Neurological Disorders and Stroke (NINDS), Bethesda, MD, United States

Protein–protein interaction networks and signaling complexes are essential for normal brain function and are often dysregulated in neurological disorders. Nevertheless, unraveling neuron- and synapse-specific proteins interaction networks has remained a technical challenge. New techniques, however, have allowed for high-resolution and high-throughput analyses, enabling quantification and characterization of various neuronal protein populations. Over the last decade, mass spectrometry (MS) has surfaced as the primary method for analyzing multiple protein samples in tandem, allowing for the precise quantification of proteomic data. Moreover, the development of sophisticated protein-labeling techniques has given MS a high temporal and spatial resolution, facilitating the analysis of various neuronal substructures, cell types, and subcellular compartments. Recent studies have leveraged these novel techniques to reveal the proteomic underpinnings of well-characterized neuronal processes, such as axon guidance, long-term potentiation, and homeostatic plasticity. Translational MS studies have facilitated a better understanding of complex neurological disorders, such as Alzheimer's disease (AD), Schizophrenia (SCZ), and Autism Spectrum Disorder (ASD). Proteomic investigation of these diseases has not only given researchers new insight into disease mechanisms but has also been used to validate disease models and identify new targets for research.

Keywords: neuroproteomics, schizophrenia, autism spectrum disorder, BONCAT, SILAC, mass spectrometry, proximity ligation assay, Alzheimer's disease

OPEN ACCESS

Edited by:
Matthew L. MacDonald,
University of Pittsburgh, United States

Reviewed by:
Yevgenia Kozorovitskiy,
Northwestern University,
United States
Maciej Maurycy Lalowski,
University of Helsinki, Finland
Jonathan Trinidad,
Indiana University, United States

***Correspondence:**
Katherine W. Roche
rochek@ninds.nih.gov

Received: *29 December 2020*
Accepted: *25 March 2021*
Published: *15 April 2021*

Citation:
Fingleton E, Li Y and Roche KW (2021) Advances in Proteomics Allow Insights Into Neuronal Proteomes. Front. Mol. Neurosci. 14:647451. doi: 10.3389/fnmol.2021.647451

INTRODUCTION

Elaborate and tightly regulated protein–protein interaction (PPI) networks underlie key neuronal processes like axon guidance and synaptic plasticity, which are essential for the initial wiring and ongoing plasticity of the brain. Every neuron contains a multitude of distinct PPI networks, which must be highly compartmentalized to permit efficient transmission and encoding of information. This proteomic intricacy is compounded by the various cell-types and substructures that make up the brain. Additionally, these networks must be dynamic and flexible to allow the neuron to respond to new patterns of information and changing extracellular environments. This level of complexity presents a major stumbling block for scientists trying to understand the brain through traditional biochemical techniques, which are limited in efficiency of throughput and level of resolution. Over the last few decades, mass spectrometry (MS) has gained popularity as a powerful tool for quantifying and identifying the constituent peptides of any proteome. Traditionally, weeks of MS analysis were required to fully catalog and identify even simple proteomes, such as baker's yeast (Bekker-Jensen et al., 2017). Modern techniques are not only faster but can

achieve a proteome coverage comparable to that of RNA-seq, while additionally granting insight to post-translational modifications (PTMs) (Bekker-Jensen et al., 2017). Combined with modern protein-labeling techniques, MS can also be used to identify and quantify cell-specific, subcellular, and temporally dynamic proteomes, filling important gaps that are not addressable using genomic and transcriptomic techniques. The details of MS are well-reviewed elsewhere, but generally most MS experiments can be viewed as comprising three steps: (1) sample preparation, (2) MS data acquisition, and (3) data analysis and interpretation (Liao et al., 2009; Aebersold and Mann, 2016; Hosp and Mann, 2017; **Figure 1**).

Sample preparation has become more sophisticated over the last decade and varies depending on the specific goals of the research. Given the large dynamic range of protein concentration and the low abundance of certain subcellular proteomes, thorough proteome screening and PTM profiling often require techniques to enrich specific protein populations. Besides increasing the sensitivity of the MS analysis, enrichment coupled with highly sensitive and accurate MS instruments also allows for more targeted datasets (Kitchen et al., 2014). To characterize interactomes, researchers can affinity purify a protein of interest prior to MS. Researchers interested in understanding PPI networks more broadly can use crosslinking MS to gain insight into how proteins interact within a proteome without restricting analysis to a specific protein's interactome (Gonzalez-Lozano et al., 2020). Other approaches do not offer insight into PPIs but allow purification of spatially and temporally restricted proteomes. Spatial resolution can be introduced at the brain region level though dissection and, more recently microdissection (MacDonald et al., 2019; **Figure 2A**). To achieve subcellular spatial resolution, researchers have traditionally relied on fractionation, which is a powerful technique for enriching organellar and synaptosomal proteomes (Biesemann et al., 2014; Itzhak et al., 2016, 2017). However, these techniques cannot specifically enrich neuronal proteomes over glial proteomes or excitatory synaptic proteomes over inhibitory synaptic proteomes, and is incapable of enriching some proteomes at all, at times rendering MS a blunt tool (Loh et al., 2016; Hosp and Mann, 2017; **Figure 2**). This shortcoming can be partially addressed through the use of cell sorting techniques, such as fluorescence activated cell sorting (FACS) and magnetic activated cell sorting (MACS), which can separate cellular material based on cell-type specific expression of a fluorophore or cell-type specific labeling with magnetic beads prior to analysis with MS. These techniques have been used to successfully purify nuclei, cell bodies, and synaptosomes from neurons (Biesemann et al., 2014; Poulopoulos et al., 2019). However, cell sorting approaches involve the dissociation and resuspension of tissues, which may shear the long processes characteristic of neurons, astrocytes, and other glial cell types, preventing these proteomes from being captured by cell sorting. Cell-type specificity can also be introduced, to some extent, *in vitro* through the use of cell culture protocols that enrich specific cell-types. Researchers looking for *in vivo* solutions capable of resolving the entire proteome of specific cell-types or otherwise unreachable subcellular proteomes, can turn to protein labeling techniques such as Bio-orthogonal non-canonical amino acid tagging (BONCAT), stochastic orthogonal recoding of translation (SORT), and Ascorbate Peroxidase (APEX) Labeling, which involve genetic expression of an enzyme or tRNA that facilitate the tagging of proteins (Dieterich et al., 2006; Roux et al., 2013; Elliott et al., 2014, 2016; Lobingier et al., 2017; Branon et al., 2018; Krogager et al., 2018; **Figures 2B**, **3B,C**). Due to the genetic nature of these approaches, they can be combined with conditional expression systems, such as Cre-loxP, to grant cell specificity (**Figure 2B**). Similarly, approaches involving tagging an organelle of interest can be combined with

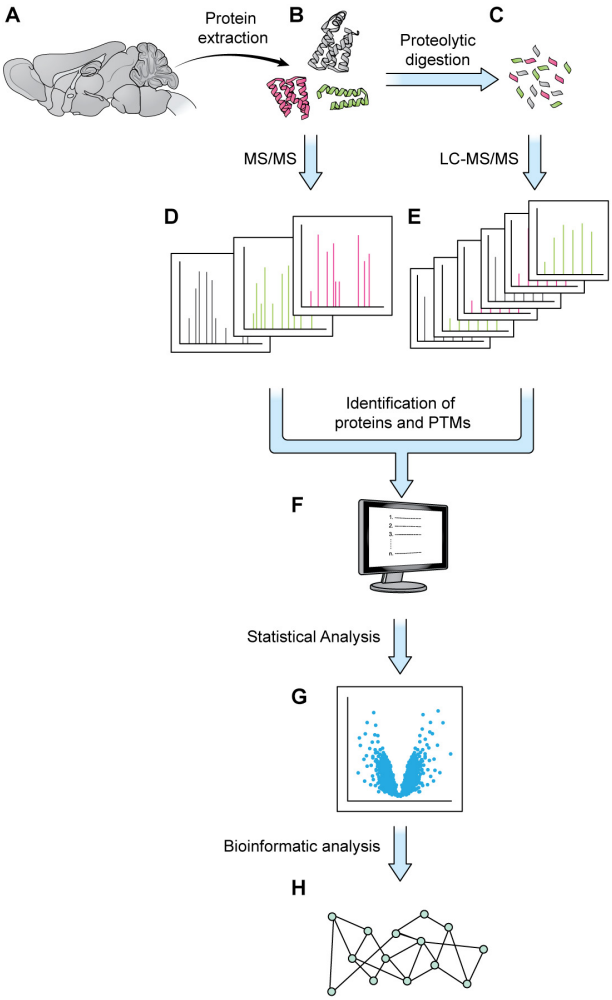

FIGURE 1 | Generic mass spectrometry-based proteomics workflow. Proteins are extracted from a biological sample. With the bottom-up approach, proteins are digested into shorter peptides, then used for LC-MS/MS data acquisition (steps **A–C**,**E**, without step **D**). With the top-down approach, the intact protein is subjected to MS/MS analysis without digestion (steps **A**,**B**,**D**, no steps **C,E**). MS1 and MS2 data are processed by a database search or a *de novo* sequencing algorithm to obtain protein sequence and PTM status **(F)**. The abundance of MS1 and/or MSn signal can be employed for protein quantitation and statistical analysis **(G)**. Various bioinformatics tools such as GO analysis or pathway analysis can be used to extract biologically relevant information from proteins of interest discovered in proteomics analysis **(H)**.

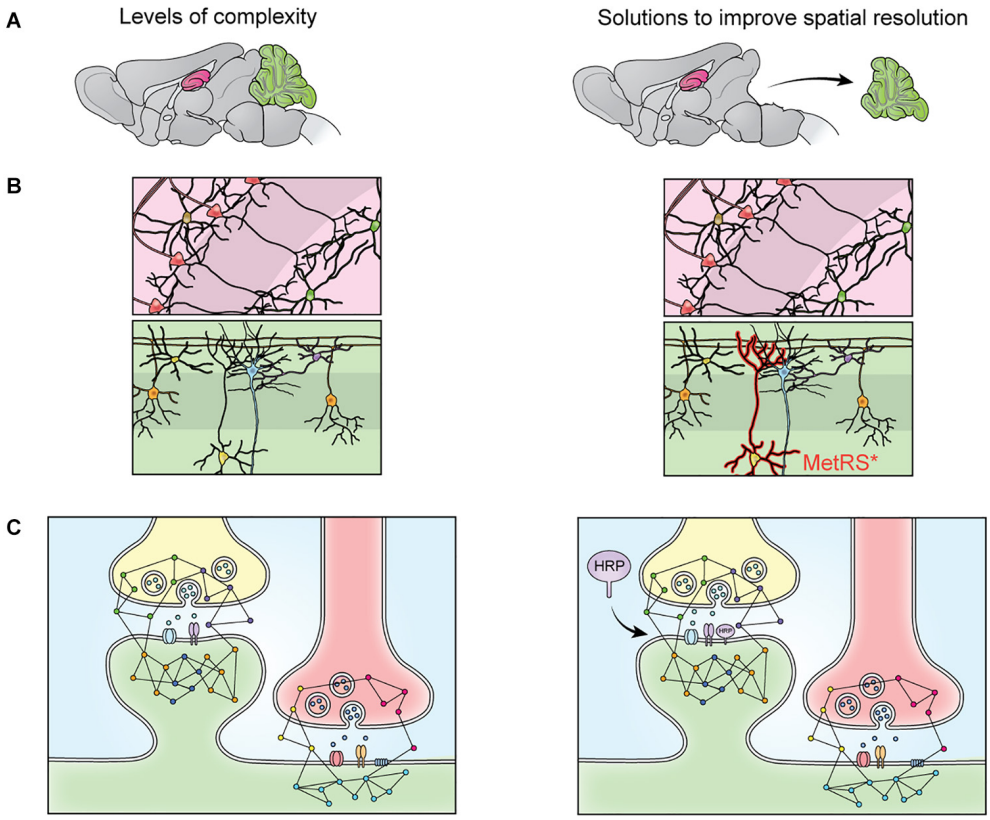

FIGURE 2 | The heterogeneity of the nervous system prevents isolation of specific proteomes though fractionation. The brain contains many substructures, such as the hippocampus (pink) and cerebellum (green) **(A)**. When the brain is homogenized, the proteomes of these structures are mixed and no longer distinguishable by MS. This limitation can be overcome via dissection **(A)**, but cellular heterogeneity remains **(B)**. When dissected brain areas are homogenized, the proteomes of specific cell types become indistinguishable via MS, this can be overcome by cell-specific tagging of proteins. For example, mutant methionine transferase (MetRS*) can be expressed in a cell specific manner to permit tagging and purification of proteins with a bio-orthogonal amino acid **(B)**. Cells of the nervous system are also highly compartmentalized. Specific cellular compartments, such as the synaptosome, can be isolated via fractionation, but isolation of specific synapse types is not possible with fractionation **(C)**. This can be addressed by targeting a protein labeling enzyme (here, HRP) to a specific subcellular locale, where it will label only nearby proteins **(C)**.

Cre-loxP to permit purification of specific organelles prior to MS (Fecher et al., 2019). Additionally, approaches that involve enzymatic modification of a protein, like APEX, can be used to grant further spatial resolution by targeting the modifying enzyme to a specific cellular locale, and thus only labeling proteins in that vicinity (**Figures 2C**, **3B**). These techniques, along with stable-isotope labeling with amino acids in cell culture (SILAC), involve introduction of an exogenous factor–either a modified amino acid or ligand–that labels the protein (Ong et al., 2002). By using pulse-chase approaches to the application of these exogenous factors, researchers can introduce temporal resolution to their studies. SILAC in particular has been used to great effect to study the role of protein turnover in neurons (Savas et al., 2012; Dörrbaum et al., 2018; Fornasiero et al., 2018; Heo et al., 2018). Coupled with sophisticated protein tagging techniques, MS can be used to study specific subsets of the proteome with considerable spatial and temporal resolution (Liao et al., 2009; Yuet and Tirrell, 2014; Hosp and Mann, 2017; **Figure 3**). Additionally, the development of techniques to enrich peptides with PTMs and sufficiently sensitive and accurate MS instruments affords researchers an exquisite level of insight into PTM-mediated signaling pathways.

Once proteins are extracted from a biological sample, often one of two principal approaches are employed during MS analysis: the conventional bottom-up or the less commonly used top-down method (Mann and Wilm, 1994; Yates et al., 1995; Kelleher et al., 1999). When the bottom-up method is used, proteins are digested into shorter peptides, then analyzed by liquid chromatography tandem mass spectrometry (LC-MS/MS). Whereas during a top-down analysis, the intact protein is isolated and subjected to MS/MS fragmentation without digestion. For both approaches, the survey scan (MS1) measures the molecular weight of peptides/proteins; during the product ion scan (MS2), peptides/proteins are dissociated with various fragmentation methods, and peptide/protein fragments are acquired. The pattern of the product ions is determined by the amino acid sequence of the specific peptide/protein. MS1 and MS2 data are processed through a database search or a *de novo* sequencing algorithm (Eng et al., 1994; Devabhaktuni and Elias, 2016). Protein sequence can thus be inferred directly (in top-down

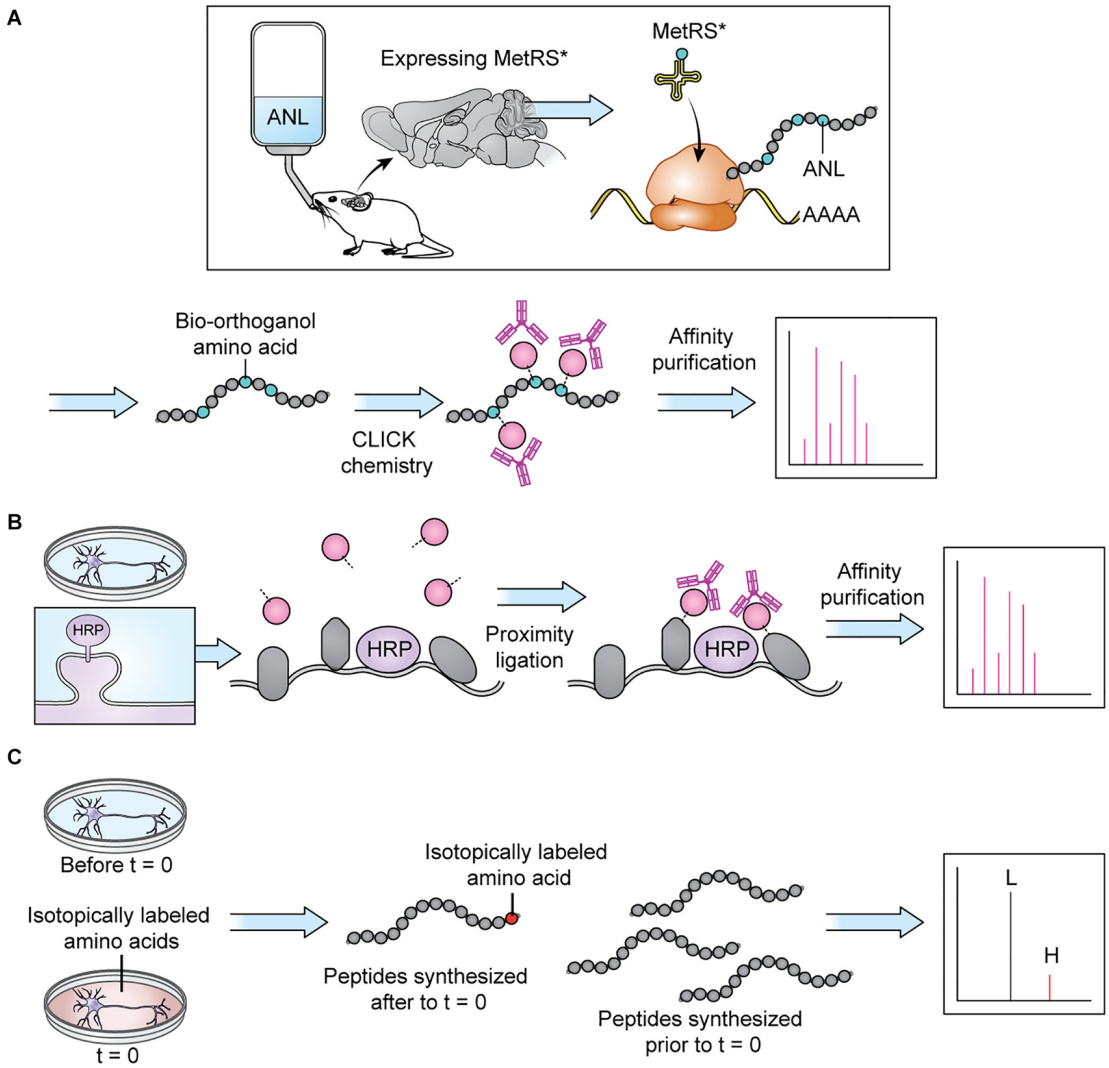

FIGURE 3 | Protein tagging techniques allow MS analysis of specific proteomes. **(A)** BONCAT: a modifiable bio-orthogonal amino acid (here: ANL) is incorporated into a newly synthesized protein via a mutant methionine transferase. During sample preparation, the bio-orthogonal amino acid is modified via CLICK chemistry to permit addition of a small molecule permitting affinity purification prior to MS. Stochastic orthogonal recoding of translation (SORT) operates by similar principles. For *in vivo* applications, the bio-orthogonal amino acid can be introduced in the animal's diet. Panel adapted from Alvarez-Castelao et al. (2017). **(B)** Proximity ligation: An enzyme (here: HRP) is targeted to a specific cellular locale where it catalyzes reactions allowing small molecule tagging of nearby proteins. Tagged proteins are then affinity purified before MS. In cell culture applications, the small molecule can be introduced in the cell culture media. Panel adapted from Loh et al. (2016). **(C)** SILAC: an isotopically labeled amino acid is incorporated into a newly synthesized protein, causing a shift in mass visible on m/z spectra, allowing spectra of newly synthesized peptides (H) to be distinguished from spectra of peptides synthesized prior to delivery of the isotopically labeled amino acids (L). In cell culture applications, the isotopically labeled amino acids can be introduced in the cell culture media.

workflow) or via peptides matched to the protein (in bottom-up workflow). PTMs can be identified as well, combining the information in MS1 and MS2 data. Product ions can be further fragmented (MSn) to more specifically determine protein sequence, detect specific modifications occurred, and obtain more accurate quantification (Schey et al., 1989). For quantitative analysis, label-free quantitation (LFQ) method directly compares precursor ion abundances of peptides among different LC-MS/MS runs. For label-based approaches, such as Isobaric Tags for Relative and Absolute Quantification (iTRAQ) and tandem mass tags (TMT), the N-terminus and the lysine side chain of peptides are isotopically labeled. After labeling, different samples are mixed and subjected to LC-MS/MS experiment. The abundance of MS2 or MSn reporter ions is used to quantify different samples. Another commonly used labeling methods is SILAC, in which a combination of 13C and 15N labeled Lysine and Arginine is incorporated into proteins by growing cells in "heavy" medium, resulting in a mass shift of peptides at MS1 level once the protein is digested with trypsin, allowing differentiation of peptides containing heavy isotopes from peptides with medium isotopes or without labeling (Ong et al., 2002; Schwanhäusser et al., 2009; Cagnetta et al., 2018).

In the past decade, advances in mass spectrometers include not only the improvement in mass accuracy and resolution, sensitivity, and scan speed, but also the development of robust fragmentation methods (Yates, 2019). With the increase in the power of MS, the list of protein hits returned from any experiment is much longer than those of early MS experiments, and demands a modern approach to analysis and interpretation. To address this need, researchers have developed bioinformatic approaches capable of grappling with the complexity and richness of MS-generated proteomic datasets, producing easily interpretable birds-eye views of proteomic data (Liao et al., 2009; Ghiassian et al., 2015). There is a variety of proprietary and open-access data analysis tools available to the modern researcher and covering all of them is beyond the scope of this review. They are well reviewed elsewhere (Wu et al., 2014; Chen et al., 2020). Here we will briefly describe the concepts underlying popular MS analysis approaches. Much of bioinformatic analysis relies on making inferences about a MS dataset based on what is already known about protein function. As such, bioinformatic analyses typically involve labeling each identified protein with its associated gene ontology (GO) term. GO terms can reflect the protein's biological function, cellular localization, biological pathway, or disease association, and can be sourced from several databases, such as GoMiner, KEGG, or the more recent SynGO. Based on GO term assignation, researchers can statistically identify GO terms that are enriched in their dataset–or appear more frequently than expected by chance–to gain insight into which biological processes, pathways, and locales might be reflected in their proteomic dataset. Additionally, software packages like Qiagen's Ingenuity Pathway Analysis tool, Thermo fisher's ProteinCenter, or the open-access Pathway Commons can be used to visualize the PPI networks and pathways represented in the MS dataset. Continuing advances made in areas from cell-specific purification, protein labeling, enrichment of peptides with PTM, MS instrumentation, data interpretation and bioinformatic analysis have elevated MS-based proteomics analysis from a general tool to a precision instrument with new relevance to research in both basic neuroscience and neurological disease.

MS IN BASIC BIOLOGY

To complete the computational work of the brain, neurons rely on very fast and highly compartmentalized signaling processes, and are supported by an array of glial cells, each with their own subcellular compartments and signaling pathways. Detailed proteomic snapshots of these cells are central to understanding the contours of how these signaling events unfold and the cellular processes they underlie. The power of MS in approaching questions in basic biology is demonstrated by research on the synaptic vesicle (SV) proteome. Using fractionation to purify SVs prior to MS, Takamori et al. (2006) were able to identify and quantify the proteomic content of the average SV, revealing important insights into how SVs are likely to function. Since then, significant advances in MS and protein enrichment techniques have opened access to previously unreachable proteomes, which will be the focus of this section. We will begin with efforts to target the proteomes of specific neuronal cell-types and subcellular domains. We will then review the use of stable isotope labeling in studies on newly synthesized peptides during axon guidance. Finally, we will discuss the use of phosphoproteomics in understanding signaling events in long-term potentiation (LTP). Interestingly, each of these subjects are well-studied, yet MS studies are still capable of unveiling new molecular players and pathways, providing researchers with new avenues for investigation.

Subcellular and Cell-Type Specific Mapping Efforts

As a cell-specific enrichment approach, BONCAT relies on the integration of a modifiable non-canonical amino acid into newly translated proteins (Dieterich et al., 2006; **Figure 3A**). Integration of the non-canonical amino acid is only possible with expression of a mutant methionine transferase (MetRS*). When MetRS* expression is coupled with a cell-specific Cre-loxP system, proteins are tagged with the non-canonical amino acid in a cell-specific manner. Subsequent CLICK chemistry modification of the non-canonical amino acid allows purification of proteins prior to MS (Dieterich et al., 2006; Alvarez-Castelao et al., 2017). Alvarez-Castelao et al. (2017) implemented BONCAT in a comparison of hippocampal excitatory and cerebellar inhibitory neurons. Interestingly, they found the MS profiles of dissected hippocampus and cerebellum to be more similar to glial MS profiles than the MS profiles of each brain area's major constituent neuronal cell type (CaMKII+ and GAD2+, respectively), suggesting that the glial proteome contributes significantly to MS datasets derived from dissected tissues. They also identified a number of significantly differentially expressed proteins in CaMKII+ and GAD2+ neurons. While some of their findings are unsurprising–PSD-95 is enriched in CaMKII+ neurons, and calbindin is enriched in GAD2+ neurons–their results also identify some unexpected proteins and lend insight into which cellular pathways are important for these two highly studied cell types. Although this study focused on adult tissue, application of cell type-specific BONCAT in younger animals may shed a light on how different cells in the nervous system initially develop and wire up with their neighbors.

Researchers can see beyond cellular proteomes and zero-in on specific subcellular locales using proximity labeling assays, like APEX, BioID, and TurboID (Roux et al., 2013; Lobingier et al., 2017; Branon et al., 2018; **Figure 3B**). These approaches involve targeting an enzyme to an area of interest where it can modify a freely diffusing molecule–usually biotin–which, once modified, can attach itself to nearby proteins, allowing their later purification. It is important to note that, much like BONCAT, this approach requires expression of an exogenous enzyme and as such requires use of a transfection method or development of a knock-in mouse line. Loh et al. (2016) targeted horseradish peroxidase (HRP) to inhibitory and excitatory synapses, allowing purification of excitatory

and inhibitory synaptic proteins with high specificity. Despite the relatively high focus these subcellular areas have received, Loh et al. (2016) were able to identify several synapse and synapse-type orphans: proteins that were not previously known to be synaptic or specific to a type of synapse, respectively. Intriguingly, they identify MDGA1 as an excitatory synaptic protein, which was unexpected due to its high sequence homology to MDGA2, which is inhibitory, and the fact that both have been shown to bind to neuroligin-2, an inhibitory synaptic adhesion molecule. As a group, neuroligins are synaptogenic. In overexpression paradigms, neuroligin-2 can stimulate excitatory synaptogenesis, despite its identity as an inhibitory neuroligin. Loh et al. (2016) go on to demonstrate that MDGA1 may be responsible for dampening neuroligin-2 mediated excitatory synaptogenesis, suggesting that in overexpression paradigms neuroligin-2 can overwhelm endogenous MDGA1, thus permitting excitatory synaptogenesis. Further study of MDGA1 and MDGA2 will likely lead to a new understanding of how synapse specificity arises and is maintained.

Axon Guidance

Axon guidance, the molecular signaling mechanism that allows axons to find their appropriate post-synaptic partners, is crucial for brain patterning and the development of neural circuits. As the axon extends, receptors on the growth cone, a fan shaped protrusion at the end of the axon, respond to attractive or repulsive guidance cues and initiate signaling cascades that remodel the cytoskeleton of the growth cone accordingly (Chilton, 2006; Bellon and Mann, 2018). A multitude of axon guidance receptors and cues exist, but all are generally thought to converge on the same cytoskeleton remodeling pathways, allowing integration of multiple signals which ultimately guide the axon toward attractive cues and away from repulsive cues (Chilton, 2006; Bellon and Mann, 2018). Local translation is key to this effort, necessitated by the fact that the axon guidance occurs at great distances from the soma, where most protein synthesis occurs (Spaulding and Burgess, 2017). Although axonal transcription is known to be crucial to axon guidance, how different guidance cues sculpt the transcriptional landscape is not well defined.

In their 2018 Neuron paper, Cagnetta et al. (2018) set out to answer this question using pulsed SILAC (pSILAC), an approach in which labeled lysine and arginine are incorporated into newly synthesized proteins of different cell states (Ong et al., 2002; Schwanhäusser et al., 2009; **Figure 3C**). The authors exposed isolated *Xenopus laevis* retinal ganglion cell (RGC) axons to three attractive guidance cues–netrin-1, Sema3a, and BDNF–paired with isotopically labeled amino acids and analyzed the resulting proteome via MS, thereby identifying the translational changes induced by each guidance cue. Their results indicate that while all three guidance cues cause the same translational changes in a subset of proteins–supporting the idea that guidance cues generally converge on the same pathways–each guidance cue also initiates a unique program of translational changes, which might grant insight into why several guidance cues are needed to signal what essentially boils down to "come here" vs. "go away."

Some guidance cues are attractive in one context, but repulsive in another (Chilton, 2006). Cagnetta et al. (2018) identified the translational changes induced by the same guidance cues in repulsive circumstances. Nearly 75% of newly synthesized proteins underwent the opposite translational change (i.e., if translation was down-regulated during the attractive cue, it was up-regulated during the repulsive cue and vice versa), supporting the idea that repulsive and attractive cues converge on the same pathways in opposite manners. The remaining ∼25% that undergo the same translational change regardless of the valence of the cue point to conserved aspects of attractive and repulsive axon guidance. In a later study, proteomic analysis of the guidance cue receptor interactomes revealed that different receptors interact with specific ribosomes, mRNAs, and mRNA binding proteins, which may explain the unique translational signature of each guidance cue (Koppers et al., 2019). These studies add to a rich and growing body of literature tackling the role of *de novo* peptide synthesis and axonal protein transport in axon guidance across model organisms (Poulopoulos et al., 2019; Schiapparelli et al., 2019).

Synaptic Plasticity

The incredible plasticity of the brain allows us to learn and consolidate knowledge in an ever-changing environment. There are many forms of synaptic plasticity, including LTP, long-term depression (LTD), and homeostatic plasticity, such as synaptic scaling (SS). LTP is the process by which synapses undergo an increase in synaptic efficacy after a period of high-frequency activity, whereas LTD is the loss of synaptic efficacy after a period of low-frequency activity. SS keeps LTP and LTD in check by dampening or strengthening synapses after long periods of high activity or low activity, respectively, which prevents synapses from undergoing LTP or LTD ad infinitum and maintains the dynamic range of synapses. These forms of plasticity are widely thought to be the molecular correlates of learning and memory, and appear key to the maintenance and tuning of neural networks.

NMDA receptors (NMDAR) play a central role in many forms of synaptic plasticity. They are a distinct class of Glutamate receptors that act as coincidence detectors by being activated upon depolarization and ligand binding. NMDARs allow calcium ion influx, which acts as a second messenger and promotes synaptic strengthening or weakening by regulating the synaptic protein content and density. The initial characterization of the NMDAR interactome via MS identified a 2–3 MDa multiprotein complex demonstrating the large and complicated nature of post-synaptic protein networks. This NMDAR multi-protein complex, referred to as the hebbosome by the authors of the initial study, comprises receptors, scaffolding proteins, and secondary messenger pathway effectors thought to be key to LTP/LTD induction (Husi et al., 2000; Grant and O'Dell, 2003).

Post-synaptic kinases and phosphatases have been the focus of intense investigation for their roles in coordinating the changes in synaptic protein composition, cytoskeletal architecture, and

gene expression that underlie synaptic plasticity (Thomas and Huganir, 2004; Lee, 2006; Coba, 2019). Li et al. (2016) turned the power of MS to cataloging phosphoproteomic changes after LTP, an undertaking made possible not only by the increased sensitivity and resolution of modern MS equipment, but also the wealth of bioinformatic information available to researchers (Bai et al., 2017). The authors began by identifying the kinases present at the synapse via MS analysis of the synaptic proteome and TiO2 enrichment of phosphopeptides, which identified 79 kinases representing all branches of the phylogenetic kinase tree, prompting the question: are these kinases active during LTP and what are they doing? Since kinases add phosphate groups to other proteins and are themselves often regulated by phosphorylation, a detailed inventory of changes in phosphorylation state during LTP could unearth insights into how different aspects of LTP are coordinated through cellular signaling events. Li and colleagues identified phosphorylation sites and quantified phosphopeptides by LC-MS/MS in synaptic proteins from hippocampal neurons with and without high frequency stimulation (i.e., with and without LTP). Interestingly a majority of the identified synaptic kinases were not differentially phosphorylated after LTP. This could be interpreted to mean less synaptic kinase activation during LTP than previously thought. However, the failure to detect changes in phosphorylation state in more synaptic kinases may also reflect certain technical limitations of the study. By inducing LTP via tetanic stimulation of Schaffer collateral fibers and analyzing the CA1 region of the hippocampal slice via MS, the authors introduce noise from non-neuronal cell-types and synapses in which LTP may not have been induced. However, it is notable that some of the changes in phosphorylation state of some substrates were profound enough to be detectable via western blot, suggesting activation strong enough to induce phosphorylation changes of some targets.

The authors identified proteins whose phosphorylation status was changed after LTP induction, and these represented many classes of proteins, including glutamate receptors, scaffolding proteins, and RasGAPs. Additionally, the authors predicted which class of kinase phosphorylated each phosphosite, by comparing the amino acid sequence of each phosphosite to known targets of different kinases. Their data suggest that CMCG and CAMK family kinases phosphorylate cell adhesion molecules, cytoskeletal molecules, and scaffolding molecules, whereas CAMK and AGC family molecules phosphorylate glutamate receptors, gap junction proteins, and RasGAPs. Thus, distinct signaling pathways may modulate different aspects of LTP. These findings will need to be validated with focused studies on particular kinases and their specific substrates. However, this is a good example of using phosphoproteomic screening approaches to open new avenues of investigation.

MS IN NEUROLOGICAL DISORDER

Because complex protein interaction networks underlie important neuronal structure and function, it follows that perturbations of these networks cause neurological disorders. Many studies on neurological disorders have leveraged high throughput sequencing techniques to either look for mutations in patients' genomes or changes in their transcriptomes. Although these techniques have yielded several key footholds, a full view of most neurological disorders remains elusive. This is, in part, because genomics and transcriptomics do not offer a full picture of disease states and can only serve as proxies when studying protein networks. Neither technique can accurately predict protein abundance or offer fine-grain information about protein localization, PTMs, or details about PPI. MS-based proteomics is capable of filling in some of these gaps. New proteomic studies on neurological disease are abundant. Here we do not offer an exhaustive review, but instead highlight studies in autism spectrum disorder (ASD), schizophrenia (SCZ), and Alzheimer's disease (AD) that illustrate the ways in which proteomic analysis can build on genomic and transcriptomic findings, refine popular hypotheses about disease etiology, and identify new targets for treatment.

Autism Spectrum Disorder

Autism spectrum disorder is a highly heritable, heterogeneous disorder, characterized by impairments in social communication and sensory perception, often accompanied by repetitive behaviors (Lord et al., 2018). Changes in brain connectivity have been observed in brain imaging studies with autistic participants, but ASD animal models point to a variety of possible causes, including altered excitatory to inhibitory ratio, dysregulated synaptic homeostasis, and irregular nervous system development (Mullins et al., 2016; Lord et al., 2018). As the name suggests, ASD encompasses a number of phenotypic subtypes (Lord et al., 2018). This variability is due in part to the varied genetic underpinnings of the disorder, which are thought to arise from complex inheritance involving large effect *de novo* mutations and small effect rare or common variants (Masi et al., 2017; Lord et al., 2018; Iakoucheva et al., 2019). Studies of high penetrance *de novo* gene mutations have been particularly fruitful in identifying ASD-related genes and the proteins they encode. However, the contribution of these genes to ASD is not always clear, despite their high penetrance, and often require further study to understand their role in ASD etiology. Proteomics is an ideal tool to better understand these proteins and their signaling pathways.

One such protein is Trio, a RhoGEF, in which mutations have been identified in ASD patients (Paskus et al., 2020). Interestingly, its highly homologous paralog, Kalirin, is not highly associated with ASD. In a recent study, Paskus et al. (2019, 2020) used a label-free IP-MS approach to quantify the Trio interactome alongside the interactome of its paralog protein, Kalirin, revealing differences in their interactomes that might explain why Trio, but not Kalirin, is implicated in ASD. Among the many proteins that differentially interact with Trio, Paskus and colleagues identified CRMP family proteins CRMP1-4 (also known as DPYSLs). These proteins regulate the collapse of the growth cone in response to repulsive guidance cues, play roles in modulating synaptic plasticity, and are implicated in a variety of diseases, including ASD (Wang and Strittmatter, 1996;

Stroedicke et al., 2015; Moutal et al., 2019; Li et al., 2020). The Trio-CRMP interactions may indicate a role for Trio in ASD through either regulation of network connectivity via axon guidance and dendritic patterning, or modulation of synaptic strength via LTP. Both cellular processes have been implicated in ASD, demonstrating that Trio likely impacts pathways common to different ASD genetic etiologies (Broek et al., 2014; Iakoucheva et al., 2019; Ruzzo et al., 2019).

Schizophrenia

Schizophrenia is a heterogeneous disorder characterized by a combination of positive, negative, and cognitive symptoms, which can include delusions and hallucinations (positive), social withdrawal and anhedonia (negative), and various cognitive dysfunctions (Kahn et al., 2015). Heritability accounts for 80% of SCZ risk, which is thought to be predominantly conferred by many low-penetrance common variants, with high penetrance rare variants and copy number variants also playing a role (Sullivan et al., 2003; Purcell et al., 2014; Kahn et al., 2015). Genetic studies have successfully identified many disease-associated loci, which have led to important revelations about SCZ, including the role of synaptic protein dysregulation and the immune system (Kenny et al., 2014; Ripke et al., 2014). However, a full understanding of SCZ remains elusive, despite the abundance of genetic leads available to researchers. This is, in part, because many of the identified disease-associated genetic loci confer marginal increases in risk, and so their effects may only become apparent when studied in combination with other disease-associated loci (Ripke et al., 2014; Kahn et al., 2015).

Proteomic studies based on the findings of genetic studies have been able to fill in some of the gaps. In a study by Rosato et al. (2019) cellomic screening of 41 SCZ risk genes identified in a genome wide association study via siRNA-mediated knock-down revealed three genes–Tcf4, Tbr1, Top3b–resulting in changes in synaptic morphology related to SCZ. MS-based analysis with data independent acquisition identified distinct proteomes regulated by each gene and PPI enrichment analysis indicated that the Tcf4 and Top3b knockdown proteomes were not significantly enriched for PPI, leaving it unclear which molecular pathway Tcf4 and Top3b act on. Although PPI analysis of Tbr1 identified a statistically significant PPI network, the network was small and contained only two proteins known to be dysregulated by Tbr1 knock-down. However, when the dysregulated proteins of all three knockdown conditions were analyzed in combination, PPI analysis identified a highly significant and large network containing molecules important for SNARE binding, demonstrating the importance of analyzing SCZ risk genes in concert rather than isolation. Alterations in neurotransmitter release, for which SNAREs are essential, are central to many theories of the mechanisms underlying SCZ, most notably hypotheses about the roles of glutamate, dopamine, and GABA, and thus the central finding of Rosato et al. (2019) is consistent with some current theories about SCZ (Kahn et al., 2015).

Identification of common pathways in SCZ can also be accomplished without screening candidate genes in advance. By using human inducible pluripotent stem cells (hiPSCs) from SCZ patients, researchers forgo the need to simultaneously knockdown several genes and search for the appropriate combination of risk factors to yield a disease phenotype. Use of hiPSCs also permits the study of the human PPIs, in contrast to animal models. This technology also circumvents issues in variability common to studies using post-mortem human tissue and shortcomings in verisimilitude common to animal disease models. Taking this approach, Tiihonen et al. (2019) used both transcriptomic and proteomic profiling to search for differential expression of genes in hiPSCs derived from monozygotic twins with one affected and one unaffected sibling. Proteomic analysis not only revealed commonly up- and down-regulated proteins in affected vs. unaffected individuals, but also identified a distinct dysregulated proteome in affected females compared to their unaffected counterparts. Thus, while there may be some molecular commonalities in SCZ across sex, there is a significant contribution of sex-specific molecular changes. Given the differences in SCZ presentation across patients of different sex, these results are unsurprising and warrant further investigation (Castle et al., 1998; Tandon et al., 2008; Kahn et al., 2015).

Alzheimer's Disease

Alzheimer's disease is a well-studied neurological disease involving the gradual loss of synapses in older adults and is characterized by the presence of amyloid plaques and tau tangles, which are thought to play converging roles in the pathogenesis of AD. Much of the research to date has focused on genomic and transcriptomic data, which successfully identified causative genes and risk genes for AD and broadened the scope of AD research to include interactions with the immune system (Masters et al., 2015). Despite the well-known genetic underpinnings and molecular hallmarks of AD, treatment options remain limited, demonstrating that our understanding of AD is incomplete. Proteomic analyses may offer a way to fill in the details missing from popular AD models.

In a recent paper, Dejanovic et al. (2018) studied proteomic changes in a mouse model for tauopathies, which may be relevant to our understanding of AD. Dejanovic et al. (2018) identified differentially expressed synaptic proteins in Tau P301S mice (Tg) vs. wild type mice using label-free quantitative MS. GO term analysis discovered enrichment of receptors, synaptic plasticity related proteins, and synaptic transmission related proteins in the dataset of proteins downregulated in Tg mice, consistent with synaptic loss, which is a hallmark of tauopathies. Although GO term analysis indicated enrichment of metabolism-related proteins in the dataset of proteins up-regulated in Tg mice, Dejanovic et al. (2018) focused on C1q, which is upregulated at the synapse in Tg mice. C1q is a component of the complement pathway, which helps target microglia to debris for engulfment. Microglia are hypothesized to erroneously engulf and sculpt away healthy synapses in AD brains, and so the upregulation of C1q at Tg synapses suggests a mechanism by which healthy synapses are marked for destruction by microglia (Hong et al., 2016; Salter and Stevens, 2017; Hansen et al., 2018; Shi and Holtzman, 2018; Ibrahim et al., 2020). Indeed, neutralization

of C1q via antibody prevents microglia engulfment of C1q and rescues synapse density in Tg mice.

It is important to note that studies in disease models come with advantages, but also important caveats. Disease models are rarely accurate representations of the disease, but rather useful tools to understand specific mechanisms of a disease. Mouse models of AD are no exception; several popular mouse models for AD exist, such as the APP/PS1 and 5 × FAD mice, and each capture different mechanistic details of the disease. Indeed, when mapped to the differentially regulated proteins identified in Dejanovic et al. (2018) several AD-related proteins are not significantly differentially expressed, indicating that the TauP301S mouse model does not fully recapitulate AD. Working with disease models in proteomic research also has important benefits, namely that sophisticated protein tagging techniques can be utilized. For example, mice expressing the mutant methionine transferase used in BONCAT under a microglia-specific promoter could be bred with Tau P301S mice to permit microglia-specific proteomic analysis, which may be instructive to our understanding of how microglia identify and attack neurons in AD. Expansion of proteomic techniques in disease research will be important to furthering our understanding of AD and other diseases.

LIMITATIONS AND FUTURE DIRECTIONS

Evidently, MS-based proteomics is a powerful tool that can be used to gain a more complete view of cellular processes, disease states, and specific sub-proteomes, and build on the knowledge gained through decades of genomic and transcriptomic research. In this review, we have curated a set of papers meant to illustrate the power of MS in neuroproteomics; however, it is important to note that this review is not exhaustive and leaves some issues unaddressed. The papers we have reviewed use bottom-up proteomics, in which proteins are digested into smaller peptides before being subjected to MS analysis. The MS and MS/MS data of these peptides are often searched against a protein database to identify sequences that best match the *in silico*-generated pattern. This approach permits identification of thousands of proteins per sample, and so has been widely adopted because peptides are easier to separate via liquid chromatography and have higher ionization efficiency compared to intact proteins. However, in bottom-up proteomics, only a portion of all peptides generated are recovered. An estimated 95% of human pre-mRNA is thought to undergo alternative splicing, and the diversity of protein isoforms is thought to play a major role in supporting the complexity of the nervous system (Pan et al., 2008; Wang et al., 2008). To recognize specific isoforms, a peptide sequence unique to the isoform must be detected; however, many isoforms are not identifiable from a unique peptide and can only be identified in their intact form (Brosch et al., 2011; Tran et al., 2011; Ezkurdia et al., 2012). Additionally, any protein isoform is necessarily lower abundance than the protein in general, which further complicates the issue of faithfully detecting protein isoforms (Heller et al., 2012). The incomplete sequence coverage in bottom-up proteomics also makes it very difficult to do in-depth PTM screening. Information about how PTMs interact with each other on an intact protein is lost. PTMs on the same protein are commonly expressed in patterns that bear biological significance. The ability to analyze these patterns is diminished when the protein is digested into smaller peptides (Duncan et al., 2010). Top-down MS, in which intact proteins are analyzed, can overcome these limitations, but come with significant technical challenges (Duncan et al., 2010). Off-line fractionation is often needed prior to on-line separation for top-down analysis, which affects the throughput of the analysis. Furthermore, detection and fragmentation of intact proteins demand high-performance mass spectrometers. The fast development in activation methods including electron transfer dissociation (ETD) and ultraviolet photodissociation (UVPD) have increased the chance of getting good sequence coverage; however, it is still difficult to accurately determine the monoisotopic mass, and therefore identify, proteins with mass larger than 50 kDa. In addition, top-down data processing and interpretation are very complicated (Catherman et al., 2014). Despite these challenges, top-down proteomics has been used to characterize full-length proteins, although typically with low-throughput (Boyne et al., 2006; Ge et al., 2009). Advances in protein fractionation techniques and ion analysis procedures have improved the throughput of top-down proteomics, making it a more viable alternative to bottom up proteomics than it has been in the past (Tran et al., 2011; Kafader et al., 2020). Until top-down techniques are widely adopted, these limitations must be acknowledged in data interpretation and resolved through alternative experimental approaches.

The field of proteomics is also inherently limited by the inability to amplify proteins. Genomic and transcriptomic analysis can derive increased sensitivity from DNA and RNA amplification techniques–namely PCR–which permits detection and sequencing of virtually all molecules. No such technique exists for proteins, and such increases in sensitivity are gained through advances in MS technology and protein enrichment schemes. Nevertheless, some protein species, though present, will remain undetectable. Even high sensitivity MS may not accurately identify some proteins. Bottom-up MS relies on peptide to protein matching, which relies on complete, well-annotated protein databases. Peptides representing proteins that are not in the database may be erroneously matched, or not matched at all (Duncan et al., 2010). Advances in technology and MS workflows may close the sensitivity gap between proteomics and nucleic acid-omics, and high-throughput approaches to *de novo* protein sequencing may eventually render database matching obsolete (Bekker-Jensen et al., 2017; Muth et al., 2018). In the meantime, researchers must be careful when interpreting their data and validate their results with orthogonal techniques.

CONCLUSION

To summarize, improvements in MS experiments over the last decade have reinvigorated our efforts to understand the brain's proteome and how it is dynamically regulated. Advances

in technology have allowed researchers access to specific protein networks, insight into PTMs, and proteomic snapshots of temporally dynamic neuronal processes. The application of MS in translational research has enhanced our understanding of neurological disorders and pointed to new molecular clues in our ongoing search for therapies. Although there are still roadblocks to studying certain populations of proteins (i.e., protein isoforms) via MS, the continuing development of new techniques and improvement of existing technology promises to expand the researcher's toolkit and eventually render the entire proteome accessible.

AUTHOR CONTRIBUTIONS

EF and YL wrote the manuscript. KWR and YL provided editorial guidance and supervision. All authors contributed to the article and approved the submitted version.

FUNDING

The authors were supported by the Intramural Research Program of the NINDS/NIH.

REFERENCES

Aebersold, R., and Mann, M. (2016). Mass-spectrometric exploration of proteome structure and function. *Nature* 537, 347–355. doi: 10.1038/nature19949

Alvarez-Castelao, B., Schanzenbächer, C. T., Hanus, C., Glock, C., tom Dieck, S., Dörrbaum, A. R., et al. (2017). Cell-type-specific metabolic labeling of nascent proteomes in vivo. *Nat. Biotechnol.* 35, 1196–1201. doi: 10.1038/nbt.4016

Bai, B., Tan, H., Pagala, V. R., High, A. A., Ichhaporia, V. P., Hendershot, L., et al. (2017). Deep profiling of proteome and phosphoproteome by isobaric labeling, extensive liquid chromatography, and mass spectrometry. *Methods Enzymol.* 585, 377–395. doi: 10.1016/bs.mie.2016.10.007

Bekker-Jensen, D. B., Kelstrup, C. D., Batth, T. S., Larsen, S. C., Haldrup, C., Bramsen, J. B., et al. (2017). An optimized shotgun strategy for the rapid generation of comprehensive human proteomes. *Cell Syst.* 4, 587.e4–599.e4. doi: 10.1016/j.cels.2017.05.009

Bellon, A., and Mann, F. (2018). Keeping up with advances in axon guidance. *Curr. Opin. Neurobiol.* 53, 183–191. doi: 10.1016/j.conb.2018.09.004

Biesemann, C., Grønborg, M., Luquet, E., Wichert, S. P., Bernard, V., Bungers, S. R., et al. (2014). Proteomic screening of glutamatergic mouse brain synaptosomes isolated by fluorescence activated sorting. *EMBO J.* 33, 157–170. doi: 10.1002/embj.201386120

Boyne, M. T., Pesavento, J. J., Mizzen, C. A., and Kelleher, N. L. (2006). Precise characterization of human histones in the H2A gene family by top down mass spectrometry. *J. Proteome Res.* 5, 248–253. doi: 10.1021/pr050269n

Branon, T. C., Bosch, J. A., Sanchez, A. D., Udeshi, N. D., Svinkina, T., Carr, S. A., et al. (2018). Efficient proximity labeling in living cells and organisms with TurboID. *Nat. Biotechnol.* 36, 880–887. doi: 10.1038/nbt.4201

Broek, J. A. C., Guest, P. C., Rahmoune, H., and Bahn, S. (2014). Proteomic analysis of post mortem brain tissue from autism patients: evidence for opposite changes in prefrontal cortex and cerebellum in synaptic connectivity-related proteins. *Mol. Autism* 5:41. doi: 10.1186/2040-2392-5-41

Brosch, M., Saunders, G. I., Frankish, A., Collins, M. O., Yu, L., Wright, J., et al. (2011). Shotgun proteomics aids discovery of novel protein-coding genes, alternative splicing, and "resurrected" pseudogenes in the mouse genome. *Genome Res.* 21, 756–767. doi: 10.1101/gr.114272.110

Cagnetta, R., Frese, C. K., Shigeoka, T., Krijgsveld, J., and Holt, C. E. (2018). Rapid cue-specific remodeling of the nascent axonal proteome. *Neuron* 99, 29.e4–46.e4. doi: 10.1016/j.neuron.2018.06.004

Castle, D., Sham, P., and Murray, R. (1998). Differences in distribution of ages of onset in males and females with schizophrenia. *Schizophr. Res.* 33, 179–183. doi: 10.1016/S0920-9964(98)00070-X

Catherman, A. D., Skinner, O. S., and Kelleher, N. L. (2014). Top down proteomics: facts and perspectives. *Biochem. Biophys. Res. Commun.* 445, 683–693. doi: 10.1016/j.bbrc.2014.02.041

Chen, C., Hou, J., Tanner, J. J., and Cheng, J. (2020). Bioinformatics methods for mass spectrometry-based proteomics data analysis. *Int. J. Mol. Sci.* 21:2873. doi: 10.3390/ijms21082873

Chilton, J. K. (2006). Molecular mechanisms of axon guidance. *Dev. Biol.* 292, 13–24. doi: 10.1016/j.ydbio.2005.12.048

Coba, M. P. (2019). Regulatory mechanisms in postsynaptic phosphorylation networks. *Curr. Opin. Struct. Biol.* 54, 86–94. doi: 10.1016/j.sbi.2019.01.003

Dejanovic, B., Huntley, M. A., De Mazière, A., Meilandt, W. J., Wu, T., Srinivasan, K., et al. (2018). Changes in the synaptic proteome in tauopathy and rescue of tau-induced synapse loss by C1q antibodies. *Neuron* 100, 1322.e7–1336.e7. doi: 10.1016/j.neuron.2018.10.014

Devabhaktuni, A., and Elias, J. E. (2016). Application of de novo sequencing to large-scale complex proteomics data sets. *J. Proteome Res.* 15, 732–742. doi: 10.1021/acs.jproteome.5b00861

Dieterich, D. C., Link, A. J., Graumann, J., Tirrell, D. A., and Schuman, E. M. (2006). Selective identification of newly synthesized proteins in mammalian cells using bioorthogonal noncanonical amino acid tagging (BONCAT). *Proc. Natl. Acad. Sci. U.S.A.* 103, 9482–9487. doi: 10.1073/pnas.0601637103

Dörrbaum, A. R., Kochen, L., Langer, J. D., and Schuman, E. M. (2018). Local and global influences on protein turnover in neurons and glia. *eLife* 7: e34202. doi: 10.7554/eLife.34202

Duncan, M. W., Aebersold, R., and Caprioli, R. M. (2010). The pros and cons of peptide-centric proteomics. *Nat. Biotechnol.* 28, 659–664. doi: 10.1038/nbt0710-659

Elliott, T. S., Bianco, A., Townsley, F. M., Fried, S. D., and Chin, J. W. (2016). Tagging and enriching proteins enables cell-specific proteomics. *Cell Chem. Biol.* 23, 805–815. doi: 10.1016/j.chembiol.2016.05.018

Elliott, T. S., Townsley, F. M., Bianco, A., Ernst, R. J., Sachdeva, A., Elsässer, S. J., et al. (2014). Proteome labeling and protein identification in specific tissues and at specific developmental stages in an animal. *Nat. Biotechnol.* 32, 465–472. doi: 10.1038/nbt.2860

Eng, J. K., McCormack, A. L., and Yates, J. R. (1994). An approach to correlate tandem mass spectral data of peptides with amino acid sequences in a protein database. *J. Am. Soc. Mass Spectrom.* 5, 976–989. doi: 10.1016/1044-0305(94)80016-2

Ezkurdia, I., Del Pozo, A., Frankish, A., Rodriguez, J. M., Harrow, J., Ashman, K., et al. (2012). Comparative proteomics reveals a significant bias toward alternative protein isoforms with conserved structure and function. *Mol. Biol. Evol.* 29, 2265–2283. doi: 10.1093/molbev/mss100

Fecher, C., Trovò, L., Müller, S. A., Snaidero, N., Wettmarshausen, J., Heink, S., et al. (2019). Cell-type-specific profiling of brain mitochondria reveals functional and molecular diversity. *Nat. Neurosci.* 22, 1731–1742. doi: 10.1038/s41593-019-0479-z

Fornasiero, E. F., Mandad, S., Wildhagen, H., Alevra, M., Rammner, B., Keihani, S., et al. (2018). Precisely measured protein lifetimes in the mouse brain reveal differences across tissues and subcellular fractions. *Nat. Commun.* 9:e12913. doi: 10.1038/s41467-018-06519-0

Ge, Y., Rybakova, I. N., Xu, Q., and Moss, R. L. (2009). Top-down high-resolution mass spectrometry of cardiac myosin binding protein C revealed that truncation alters protein phosphorylation state. *Proc. Natl. Acad. Sci. U.S.A.* 106, 12658–12663. doi: 10.1073/pnas.0813369106

Ghiassian, S. D., Menche, J., and Barabási, A.-L. (2015). A DIseAse MOdule detection (DIAMOnD) algorithm derived from a systematic analysis of connectivity patterns of disease proteins in the human interactome. *PLoS Comput. Biol.* 11:e1004120. doi: 10.1371/journal.pcbi.1004120

Gonzalez-Lozano, M. A., Koopmans, F., Sullivan, P. F., Protze, J., Krause, G., Verhage, M., et al. (2020). Stitching the synapse: cross-linking mass spectrometry into resolving synaptic protein interactions. *Sci. Adv.* 6:eaax5783. doi: 10.1126/sciadv.aax5783

Grant, S. G. N., and O'Dell, T. J. (2003). *The Hebbosome Hypothesis of Learning: Signaling Complexes Decode Synaptic Patterns of Activity and Distribute Plasticity*. Berlin: Springer, 23–43. doi: 10.1007/978-3-642-55543-5_3

Hansen, D. V., Hanson, J. E., and Sheng, M. (2018). Microglia in Alzheimer's disease. *J. Cell Biol.* 217, 459–472. doi: 10.1083/jcb.201709069

Heller, E. A., Zhang, W., Selimi, F., Earnheart, J. C., Ślimak, M. A., Santos-Torres, J., et al. (2012). The biochemical anatomy of cortical inhibitory synapses. *PLoS One* 7:e39572. doi: 10.1371/journal.pone.0039572

Heo, S., Diering, G. H., Na, C. H., Nirujogi, R. S., Bachman, J. L., Pandey, A., et al. (2018). Identification of long-lived synaptic proteins by proteomic analysis of synaptosome protein turnover. *Proc. Natl. Acad. Sci. U.S.A.* 115, E3827–E3836. doi: 10.1073/pnas.1720956115

Hong, S., Beja-Glasser, V. F., Nfonoyim, B. M., Frouin, A., Li, S., Ramakrishnan, S., et al. (2016). Complement and microglia mediate early synapse loss in Alzheimer mouse models. *Science* 352, 712–716. doi: 10.1126/science.aad8373

Hosp, F., and Mann, M. (2017). A primer on concepts and applications of proteomics in neuroscience. *Neuron* 96, 558–571. doi: 10.1016/j.neuron.2017.09.025

Husi, H., Ward, M. A., Choudhary, J. S., Blackstock, W. P., and Grant, S. G. N. (2000). Proteomic analysis of NMDA receptor-adhesion protein signaling complexes. *Nat. Neurosci.* 3, 661–669. doi: 10.1038/76615

Iakoucheva, L. M., Muotri, A. R., and Sebat, J. (2019). Getting to the Cores of Autism. *Cell* 178, 1287–1298. doi: 10.1016/j.cell.2019.07.037

Ibrahim, A. M., Pottoo, F. H., Dahiya, E. S., Khan, F. A., and Kumar, J. B. S. (2020). Neuron-glia interactions: molecular basis of alzheimer's disease and applications of neuroproteomics. *Eur. J. Neurosci.* 52, 2931–2943. doi: 10.1111/ejn.14838

Itzhak, D. N., Davies, C., Tyanova, S., Mishra, A., Williamson, J., Antrobus, R., et al. (2017). A mass spectrometry-based approach for mapping protein subcellular localization reveals the spatial proteome of mouse primary neurons. *Cell Rep.* 20, 2706–2718. doi: 10.1016/j.celrep.2017.08.063

Itzhak, D. N., Tyanova, S., Cox, J., and Borner, G. H. H. (2016). Global, quantitative and dynamic mapping of protein subcellular localization. *eLife* 5:e16950. doi: 10.7554/eLife.16950

Kafader, J. O., Melani, R. D., Durbin, K. R., Ikwuagwu, B., Early, B. P., Fellers, R. T., et al. (2020). Multiplexed mass spectrometry of individual ions improves measurement of proteoforms and their complexes. *Nat. Methods* 17, 391–394. doi: 10.1038/s41592-020-0764-5

Kahn, R. S., Sommer, I. E., Murray, R. M., Meyer-Lindenberg, A., Weinberger, D. R., Cannon, T. D., et al. (2015). Schizophrenia. *Nat. Rev. Dis. Primers* 1:15067. doi: 10.1038/nrdp.2015.67

Kelleher, N. L., Lin, H. Y., Valaskovic, G. A., Aaserud, D. J., Fridriksson, E. K., and McLafferty, F. W. (1999). Top down versus bottom up protein characterization by tandem high- resolution mass spectrometry. *J. Am. Chem. Soc.* 121, 806–812. doi: 10.1021/ja973655h

Kenny, E. M., Cormican, P., Furlong, S., Heron, E., Kenny, G., Fahey, C., et al. (2014). Excess of rare novel loss-of-function variants in synaptic genes in schizophrenia and autism spectrum disorders. *Mol. Psychiatry* 19, 872–879. doi: 10.1038/mp.2013.127

Kitchen, R. R., Rozowsky, J. S., Gerstein, M. B., and Nairn, A. C. (2014). Decoding neuroproteomics: integrating the genome, translatome and functional anatomy. *Nat. Neurosci.* 17, 1491–1499. doi: 10.1038/nn.3829

Koppers, M., Cagnetta, R., Shigeoka, T., Wunderlich, L. C. S., Vallejo-Ramirez, P., Qiaojin Lin, J., et al. (2019). Receptor-specific interactome as a hub for rapid cue-induced selective translation in axons. *eLife* 8:e48718. doi: 10.7554/eLife.48718

Krogager, T. P., Ernst, R. J., Elliott, T. S., Calo, L., Beránek, V., Ciabatti, E., et al. (2018). Labeling and identifying cell-specific proteomes in the mouse brain. *Nat. Biotechnol.* 36, 156–159. doi: 10.1038/nbt.4056

Lee, H. K. (2006). Synaptic plasticity and phosphorylation. *Pharmacol. Ther.* 112, 810–832. doi: 10.1016/j.pharmthera.2006.06.003

Li, J., Han, S., Li, H., Udeshi, N. D., Svinkina, T., Mani, D. R., et al. (2020). Cell-surface proteomic profiling in the fly brain uncovers wiring regulators. *Cell* 180, 373.e15–386.e15. doi: 10.1016/j.cell.2019.12.029

Li, J., Wilkinson, B., Clementel, V. A., Hou, J., O'Dell, T. J., and Coba, M. P. (2016). Long-term potentiation modulates synaptic phosphorylation networks and reshapes the structure of the postsynaptic interactome. *Sci. Signal.* 9:rs8. doi: 10.1126/scisignal.aaf6716

Liao, L., McClatchy, D. B., and Yates, J. R. (2009). Shotgun proteomics in neuroscience. *Neuron* 63, 12–26. doi: 10.1016/j.neuron.2009.06.011

Lobingier, B. T., Hüttenhain, R., Eichel, K., Miller, K. B., Ting, A. Y., von Zastrow, M., et al. (2017). An approach to spatiotemporally resolve protein interaction networks in living cells. *Cell* 169, 350.e12–360.e12. doi: 10.1016/j.cell.2017.03.022

Loh, K. H., Stawski, P. S., Draycott, A. S., Udeshi, N. D., Lehrman, E. K., Wilton, D. K., et al. (2016). Proteomic analysis of unbounded cellular compartments: synaptic clefts. *Cell* 166, 1295.e21–1307.e21. doi: 10.1016/j.cell.2016.07.041

Lord, C., Elsabbagh, M., Baird, G., and Veenstra-Vanderweele, J. (2018). Autism spectrum disorder. *Lancet* 392, 508–520. doi: 10.1016/S0140-6736(18)31129-2

MacDonald, M. L., Favo, D., Garver, M., Sun, Z., Arion, D., Ding, Y., et al. (2019). Laser capture microdissection–targeted mass spectrometry: a method for multiplexed protein quantification within individual layers of the cerebral cortex. *Neuropsychopharmacology* 44, 743–748. doi: 10.1038/s41386-018-0260-0

Mann, M., and Wilm, M. (1994). Error-tolerant identification of peptides in sequence databases by peptide sequence tags. *Anal. Chem.* 66, 4390–4399. doi: 10.1021/ac00096a002

Masi, A., DeMayo, M. M., Glozier, N., and Guastella, A. J. (2017). An overview of autism spectrum disorder, heterogeneity and treatment options. *Neurosci. Bull.* 33, 183–193. doi: 10.1007/s12264-017-0100-y

Masters, C. L., Bateman, R., Blennow, K., Rowe, C. C., Sperling, R. A., and Cummings, J. L. (2015). Alzheimer's disease. *Nat. Rev. Dis. Primers* 1:15056. doi: 10.1038/nrdp.2015.56

Moutal, A., White, K. A., Chefdeville, A., Laufmann, R. N., Vitiello, P. F., Feinstein, D., et al. (2019). Dysregulation of CRMP2 post-translational modifications drive its pathological functions. *Mol. Neurobiol.* 56, 6736–6755. doi: 10.1007/s12035-019-1568-4

Mullins, C., Fishell, G., and Tsien, R. W. (2016). Unifying views of autism spectrum disorders: a consideration of autoregulatory feedback loops. *Neuron* 89, 1131–1156. doi: 10.1016/j.neuron.2016.02.017

Muth, T., Hartkopf, F., Vaudel, M., and Renard, B. Y. (2018). A potential golden age to come-current tools, recent use cases, and future avenues for de novo sequencing in proteomics. *PROTEOMICS* 18:1700150. doi: 10.1002/pmic.201700150

Ong, S.-E., Blagoev, B., Kratchmarova, I., Kristensen, D. B., Steen, H., Pandey, A., et al. (2002). Stable Isotope labeling by amino acids in cell culture, silac, as a simple and accurate approach to expression proteomics. *Mol. Cell. Proteomics* 1, 376–386. doi: 10.1074/mcp.M200025-MCP200

Pan, Q., Shai, O., Lee, L. J., Frey, B. J., and Blencowe, B. J. (2008). Deep surveying of alternative splicing complexity in the human transcriptome by high-throughput sequencing. *Nat. Genet.* 40, 1413–1415. doi: 10.1038/ng.259

Paskus, J. D., Herring, B. E., and Roche, K. W. (2020). Kalirin and Trio: RhoGEFs in synaptic transmission, plasticity, and complex brain disorders. *Trends Neurosci.* 43, 505–518. doi: 10.1016/j.tins.2020.05.002

Paskus, J. D., Tian, C., Fingleton, E., Shen, C., Chen, X., Li, Y., et al. (2019). Synaptic Kalirin-7 and trio interactomes reveal a GEF protein-dependent Neuroligin-1 mechanism of action. *Cell Rep.* 29, 2944.e5–2952.e5. doi: 10.1016/j.celrep.2019.10.115

Poulopoulos, A., Murphy, A. J., Ozkan, A., Davis, P., Hatch, J., Kirchner, R., et al. (2019). Subcellular transcriptomes and proteomes of developing axon projections in the cerebral cortex. *Nature* 565, 356–360. doi: 10.1038/s41586-018-0847-y

Purcell, S. M., Moran, J. L., Fromer, M., Ruderfer, D., Solovieff, N., Roussos, P., et al. (2014). A polygenic burden of rare disruptive mutations in schizophrenia. *Nature* 506, 185–190. doi: 10.1038/nature12975

Ripke, S., Neale, B. M., Corvin, A., Walters, J. T. R., Farh, K. H., Holmans, P. A., et al. (2014). Biological insights from 108 schizophrenia-associated genetic loci. *Nature* 511, 421–427. doi: 10.1038/nature13595

Rosato, M., Stringer, S., Gebuis, T., Paliukhovich, I., Li, K. W., Posthuma, D., et al. (2019). Combined cellomics and proteomics analysis reveals shared neuronal morphology and molecular pathway phenotypes for multiple schizophrenia risk genes. *Mol. Psychiatry* 26, 784–799. doi: 10.1038/s41380-019-0436-y

Roux, K. J., Kim, D. I., and Burke, B. (2013). BioID: a screen for protein-protein interactions. *Curr. Protocols Protein Sci.* 74, 19.23.1–19.23.14. doi: 10.1002/0471140864.ps1923s74

Ruzzo, E. K., Pérez-Cano, L., Jung, J. Y., Wang, L. K., Kashef-Haghighi, D., Hartl, C., et al. (2019). Inherited and de novo genetic risk for autism impacts shared networks. *Cell* 178, 850.e26–866.e26. doi: 10.1016/j.cell.2019.07.015

Salter, M. W., and Stevens, B. (2017). Microglia emerge as central players in brain disease. *Nat. Med.* 23, 1018–1027. doi: 10.1038/nm.4397

Savas, J. N., Toyama, B. H., Xu, T., Yates, J. R., and Hetzer, M. W. (2012). Extremely long-lived nuclear pore proteins in the rat brain. *Science* 335:942. doi: 10.1126/science.1217421

Schey, K. L., Schwartz, J. C., Cooks, R. G., and Caprioli, R. M. (1989). Observation of sequence-specific peptide fragmentation using extended tandem mass spectrometry experiments. *Rapid Commun. Mass Spectrom.* 3, 305–309. doi: 10.1002/rcm.1290030910

Schiapparelli, L. M., Shah, S. H., Ma, Y., McClatchy, D. B., Sharma, P., Li, J., et al. (2019). The retinal ganglion cell transportome identifies proteins transported to axons and presynaptic compartments in the visual system in vivo. *Cell Rep.* 28, 1935.e5–1947.e5. doi: 10.1016/j.celrep.2019.07.037

Schwanhäusser, B., Gossen, M., Dittmar, G., and Selbach, M. (2009). Global analysis of cellular protein translation by pulsed SILAC. *Proteomics* 9, 205–209. doi: 10.1002/pmic.200800275

Shi, Y., and Holtzman, D. M. (2018). Interplay between innate immunity and Alzheimer disease: APOE and TREM2 in the spotlight. *Nat. Rev. Immunol.* 18, 759–772. doi: 10.1038/s41577-018-0051-1

Spaulding, E. L., and Burgess, R. W. (2017). Accumulating evidence for axonal translation in neuronal homeostasis. *Front. Neurosci.* 11:312. doi: 10.3389/fnins.2017.00312

Stroedicke, M., Bounab, Y., Strempel, N., Klockmeier, K., Yigit, S., Friedrich, R. P., et al. (2015). Systematic interaction network filtering identifies CRMP1 as a novel suppressor of huntingtin misfolding and neurotoxicity. *Genome Res.* 125, 701–713. doi: 10.1101/gr.182444.114

Sullivan, P. F., Kendler, K. S., and Neale, M. C. (2003). Schizophrenia as a complex trait. *Arch. Gen. Psychiatry* 60:1187. doi: 10.1001/archpsyc.60.12.1187

Takamori, S., Holt, M., Stenius, K., Lemke, E. A., Grønborg, M., Riedel, D., et al. (2006). Molecular anatomy of a trafficking organelle. *Cell* 127, 831–846. doi: 10.1016/j.cell.2006.10.030

Tandon, R., Keshavan, M. S., and Nasrallah, H. A. (2008). Schizophrenia, "Just the Facts" What we know in 2008. 2. Epidemiology and etiology. *Schizophr. Res.* 102, 1–18. doi: 10.1016/j.schres.2008.04.011

Thomas, G. M., and Huganir, R. L. (2004). MAPK cascade signalling and synaptic plasticity. *Nat. Rev. Neurosci.* 5, 173–183. doi: 10.1038/nrn1346

Tiihonen, J., Koskuvi, M., Storvik, M., Hyötyläinen, I., Gao, Y., Puttonen, K. A., et al. (2019). Sex-specific transcriptional and proteomic signatures in schizophrenia. *Nat. Commun.* 10:3933. doi: 10.1038/s41467-019-11797-3

Tran, J. C., Zamdborg, L., Ahlf, D. R., Lee, J. E., Catherman, A. D., Durbin, K. R., et al. (2011). Mapping intact protein isoforms in discovery mode using top-down proteomics. *Nature* 480, 254–258. doi: 10.1038/nature10575

Wang, E. T., Sandberg, R., Luo, S., Khrebtukova, I., Zhang, L., Mayr, C., et al. (2008). Alternative isoform regulation in human tissue transcriptomes. *Nature* 456, 470–476. doi: 10.1038/nature07509

Wang, L. H., and Strittmatter, S. M. (1996). A family of rat CRMP genes is differentially expressed in the nervous system. *J. Neurosci.* 16, 6197–6207. doi: 10.1523/jneurosci.16-19-06197.1996

Wu, X., Al Hasan, M., and Chen, J. Y. (2014). Pathway and network analysis in proteomics. *J. Theor. Biol.* 362, 44–52. doi: 10.1016/j.jtbi.2014.05.031

Yates, J. R. (2019). Recent technical advances in proteomics. *F1000Res.* 8:F1000FacultyRev-351. doi: 10.12688/f1000research.16987.1

Yates, J. R., Eng, J. K., McCormack, A. L., and Schieltz, D. (1995). Method to correlate tandem mass spectra of modified peptides to amino acid sequences in the protein database. *Anal. Chem.* 67, 1426–1436. doi: 10.1021/ac00104a020

Yuet, K. P., and Tirrell, D. A. (2014). Chemical tools for temporally and spatially resolved mass spectrometry-based proteomics. *Ann. Biomed. Eng.* 42, 299–311. doi: 10.1007/s10439-013-0878-3

Conflict of Interest: The authors declare that the research was conducted in the absence of any commercial or financial relationships that could be construed as a potential conflict of interest.

frontiers in Molecular Neuroscience

ORIGINAL RESEARCH
published: 27 April 2021
doi: 10.3389/fnmol.2021.627740

Unbiased Label-Free Quantitative Proteomics of Cells Expressing Amyotrophic Lateral Sclerosis (ALS) Mutations in *CCNF* Reveals Activation of the Apoptosis Pathway: A Workflow to Screen Pathogenic Gene Mutations

*Flora Cheng[1†], Alana De Luca[1†], Alison L. Hogan[1], Stephanie L. Rayner[1], Jennilee M. Davidson[1], Maxinne Watchon[1], Claire H. Stevens[2,3], Sonia Sanz Muñoz[2,3], Lezanne Ooi[2,3], Justin J. Yerbury[2,3], Emily K. Don[1], Jennifer A. Fifita[1], Maria D. Villalva[1], Hannah Suddull[1], Tyler R. Chapman[1], Thomas J. Hedl[4], Adam K. Walker[1,4], Shu Yang[1], Marco Morsch[1], Bingyang Shi[1], Ian P. Blair[1], Angela S. Laird[1], Roger S. Chung[1] and Albert Lee[1]**

[1] Centre for Motor Neuron Disease Research, Department of Biomedical Sciences, Faculty of Medicine, Health, and Human Sciences, Macquarie University, North Ryde, NSW, Australia, [2] Illawarra Health and Medical Research Institute (IHMRI), University of Wollongong, Wollongong, NSW, Australia, [3] School of Chemistry and Molecular Bioscience and Molecular Horizons, University of Wollongong, Wollongong, NSW, Australia, [4] Neurodegeneration Pathobiology Laboratory, Queensland Brain Institute, The University of Queensland, St Lucia, QLD, Australia

The past decade has seen a rapid acceleration in the discovery of new genetic causes of ALS, with more than 20 putative ALS-causing genes now cited. These genes encode proteins that cover a diverse range of molecular functions, including free radical scavenging (e.g., SOD1), regulation of RNA homeostasis (e.g., TDP-43 and FUS), and protein degradation through the ubiquitin-proteasome system (e.g., ubiquilin-2 and cyclin F) and autophagy (TBK1 and sequestosome-1/p62). It is likely that the various initial triggers of disease (either genetic, environmental and/or gene-environment interaction) must converge upon a common set of molecular pathways that underlie ALS pathogenesis. Given the complexity, it is not surprising that a catalog of molecular pathways and proteostasis dysfunctions have been linked to ALS. One of the challenges in ALS research is determining, at the early stage of discovery, whether a new gene mutation is indeed disease-specific, and if it is linked to signaling pathways that trigger neuronal cell death. We have established a proof-of-concept proteogenomic workflow to assess new gene mutations, using CCNF (cyclin F) as an example, in cell culture models to screen whether potential gene candidates fit the criteria of activating apoptosis. This can provide an informative and time-efficient output that can be extended further for

OPEN ACCESS

Edited by:
Mark Oliver Collins,
The University of Sheffield,
United Kingdom

Reviewed by:
Agnes Lumi Nishimura,
King's College London,
United Kingdom
Susan T. Weintraub,
The University of Texas Health Science Center at San Antonio,
United States

***Correspondence:**
Albert Lee
albert.lee@mq.edu.au

[†] These authors have contributed equally to this work

Received: 10 November 2020
Accepted: 19 March 2021
Published: 27 April 2021

Citation:
Cheng F, De Luca A, Hogan AL, Rayner SL, Davidson JM, Watchon M, Stevens CH, Muñoz SS, Ooi L, Yerbury JJ, Don EK, Fifita JA, Villalva MD, Suddull H, Chapman TR, Hedl TJ, Walker AK, Yang S, Morsch M, Shi B, Blair IP, Laird AS, Chung RS and Lee A (2021) Unbiased Label-Free Quantitative Proteomics of Cells Expressing Amyotrophic Lateral Sclerosis (ALS) Mutations in CCNF Reveals Activation of the Apoptosis Pathway: A Workflow to Screen Pathogenic Gene Mutations. Front. Mol. Neurosci. 14:627740. doi: 10.3389/fnmol.2021.627740

validation in a variety of *in vitro* and *in vivo* models and/or for mechanistic studies. As a proof-of-concept, we expressed cyclin F mutations (K97R, S195R, S509P, R574Q, S621G) in HEK293 cells for label-free quantitative proteomics that bioinformatically predicted activation of the neuronal cell death pathways, which was validated by immunoblot analysis. Proteomic analysis of induced pluripotent stem cells (iPSCs) derived from patient fibroblasts bearing the S621G mutation showed the same activation of these pathways providing compelling evidence for these candidate gene mutations to be strong candidates for further validation and mechanistic studies (such as E3 enzymatic activity assays, protein–protein and protein–substrate studies, and neuronal apoptosis and aberrant branching measurements in zebrafish). Our proteogenomics approach has great utility and provides a relatively high-throughput screening platform to explore candidate gene mutations for their propensity to cause neuronal cell death, which will guide a researcher for further experimental studies.

Keywords: proteomics, amyotrophic lateral sclerosis, induced pluripotent stem cell, proteogenomics, cell death, neurodegeneration, proteostasis cell stress and aging, zebrafish

INTRODUCTION

Proteogenomics is an integrated area of research that blends genomics and proteomics, which was originally described to use proteomics data to improve genome annotations and subsequent protein characterization (Jaffe et al., 2004; Nesvizhskii, 2014). In a typical proteogenomic experiment, high-resolution mass spectrometry is used to identify novel peptides in which the tandem mass spectra are searched against customized databases with predicted protein sequences to provide high-level validation and refinement of gene expression (Nesvizhskii, 2014). Moreover, integrated proteogenomic approaches can be employed to provide increased depth-in-biology to understand better disease mechanisms, perturbations to cellular pathways and dysfunctions in proteostasis arising from genetic variations that are implicated in the pathogenesis of a particular disease (Hedl et al., 2019). While genome-wide association studies (GWAS) have dramatically improved and sped-up the discovery of gene mutations for diseases such as neurodegenerative diseases, various unique challenges arise when trying to determine the downstream biological effects of newly discovered gene variants (Visscher et al., 2017). For example, unlike cancer research where the biology involves uncontrolled proliferation [and therefore cells can be easily immortalized and grown in culture (Mitra et al., 2013) or xenografts (Yada et al., 2018)]; neurodegenerative research is underpinned by finding the causative mechanisms that lead to cell death in specific cell types (e.g., neurons), by which a large population of cells have already perished before a patient even presents with symptoms (Sabatelli et al., 2011; Branch et al., 2016; Woollacott and Rohrer, 2016). This makes sourcing disease-affected neuronal cells from patients extremely challenging, and generating *in vitro* and *in vivo* models to recapitulate the multistep processes for the purposes of biomedical and therapeutic research even more difficult (Al-Chalabi et al., 2014; Morrice et al., 2018; Vucic et al., 2020). Because of the heterogeneity of onset and progression of many neurodegenerative diseases, there have been a number of models published to date reviewed in Van Damme et al. (2017); Morrice et al. (2018) that recapitulate various phenotypic aspects of disease (e.g., memory deficits). However, none are considered the 'classic' or 'benchmark' models given the numerous and converging signaling pathways that all affect the biology differently.

Amyotrophic lateral sclerosis (ALS) is typically a late-onset neurodegenerative disease characterized by the selective degeneration of upper and lower motor neurons of the cerebral cortex, brainstem, and spinal cord. It is the most common form of adult motor neuron disease (MND) with poor prognosis and limited treatment options. Given the complexity in molecular origins of ALS, it is not surprising that a catalog of molecular pathways has been implicated in the disease. These include disruption in DNA/RNA processing (Vance et al., 2009; Mitchell et al., 2013), oxidative stress (Duan et al., 2010), excitotoxicity (King et al., 2016), protein misfolding and aggregation (Ciryam et al., 2017; Yerbury et al., 2020), protein degradation (ubiquitin-proteasome and autophagy) (Shahheydari et al., 2017), proteostasis dysfunction (McAlary et al., 2019), ER stress (Jaronen et al., 2014; Prell et al., 2019), and neuroinflammation (Olesen et al., 2020). While environmental factors may play a role in the pathogenesis of the disease, the only established cause of ALS is genetic mutations. More than 20 putative ALS-causing genes are now cited and the pace of discovery is continually accelerating (Nguyen et al., 2018). However, one challenge that arises during genetic mutation discovery is determining whether newly discovered genetic variants are indeed causative of disease or are neutral mutations (i.e., mutations that do not cause a biological effect) (Lattante et al., 2020). Current methods use a range of bioinformatic prediction tools to classify whether gene variants are possibly pathogenic (Lattante et al., 2020), but few have used an experimental workflow to screen the activation of molecular pathways that cause apoptosis (Hogan et al., 2017). High-throughput technologies

such as proteogenomics can advance our understanding of both primary pathological proteins and associated proteins to gain insights into the biological effects of potential gene mutations (Hedl et al., 2019).

We have previously identified novel missense mutations in *CCNF* in patients with ALS and FTD (Williams et al., 2016). *CCNF* encodes for cyclin F, a 786 amino acid protein that forms part of the multi-protein Skp1-Cul1-F-Box ($SCF^{CyclinF}$) E3 ligase that is responsible for tagging substrates with ubiquitin for degradation by the proteasome. Protein degradation via the ubiquitin-proteasome system (UPS) involves three key steps, activation of ubiquitin by E1s, ubiquitin conjugation by E2s and ligation of protein substrates by E3s. Activation of this sequential process by ATP results in the covalent attachment of ubiquitin to specific lysine residues on target proteins, with specific polyubiquitin linkages generally marking them for degradation by the UPS (Lys48) or autophagy (Lys63) pathways. There are over 500 E3 ligases in the human proteome with each E3 being capable of binding their own specific set of substrates (Nakayama and Nakayama, 2006; Rayner et al., 2019). To date, the known substrates of cyclin F include RRM2 (D'Angiolella et al., 2012), CDC6 (Walter et al., 2016), CP110 (D'Angiolella et al., 2010), NuSAP (Emanuele et al., 2011), E2F (Clijsters et al., 2019), Exo1 (Elia et al., 2015), and SLBP (Dankert et al., 2016), all of which play a role in cell cycle progression and in DNA synthesis and maintaining genome stability (Galper et al., 2017). The cellular role of cyclin F in non-dividing cells such as neurons is presently not known; however, recent studies have revealed protein-protein interactions between cyclin F and ALS-associated proteins TDP-43, VCP and p62 (Yu et al., 2019).

We recently characterized the Ser621Gly (S621G) mutation in cyclin F, which induced apoptosis pathways and caused motor neuron axonopathies and reduced motor response in zebrafish (Hogan et al., 2017). Mechanistically, we also found that the enzymatic activity was aberrantly elevated in the mutant protein which results in the increased Lys-48 ubiquitylation of the proteome (Lee et al., 2017a,b). This suggests that hyperubiquitylation of protein substrates would also concomitantly increase protein trafficking and potentially impair proteasome activity as the cells' maximal degradation capacity is reached, leading to accumulation of ubiquitylated proteins and apoptosis. However, our studies have indicated that proteasome function remains unchanged and intact in neuronal cells expressing *CCNF* mutations (Williams et al., 2016) which suggests that cyclin F mutations triggers apoptosis through other mechanisms. While numerous other possible cellular mechanisms may link the S621G mutation to neurodegeneration, validating each hypothesis requires hundreds of biochemical assays to be tested. Given that other cyclin F mutations were also discovered and potentially linked to both sporadic and familial ALS and FTD in our previous GWAS study (Williams et al., 2016), we wanted to develop a relatively high-throughput, quick and informative strategy that could screen additional *CCNF* mutations (K97R, S195R, S509P and R574Q) to determine whether i) they were disease-causing and therefore used as model systems, and ii) verified by other biochemical and *in vivo* studies.

A direct method and output for determining whether a genetic mutation is disease-causing could be the determination of whether the apoptosis pathways have been activated in a model system expressing the chosen gene variant. Apoptosis can be activated by a range of exogenous and endogenous stimuli, such as DNA damage, ischemia, and oxidative stress (Payne et al., 1995). It plays an important function in development and in the elimination of damaged cells, which is facilitated by the release of cytochrome c from the mitochondria through the Bcl-2 family of regulatory proteins. Members of the Bcl-2 family of apoptotic molecules are substrates of the Lys-48 ubiquitin degradation process, and the regular turnover of these molecules by the UPS is an important factor in maintaining the balance between pro- and anti-apoptotic members of this family (Chen and Qiu, 2013). These proteins are classified into subfamilies according to their functionalities and their number of Bcl-2 homology (BH) domains. There are three subfamilies: the anti-apoptotic, which includes Bcl-2, Bcl-XL, Bcl-W, and MCL-1, the multi-BH protein effectors such as Bax and Bak and the BH_3-only proteins, Bad, Bim, Puma, and Bid. These proteins regulate the permeabilization of the mitochondrial outer membrane (MOMP) and therefore apoptosis via a complex network of heterodimeric interactions (Kale et al., 2018).

The direct activation model suggests that the anti-apoptotic members of the Bcl-2 family suppress apoptosis by sequestering the BH_3-only proteins, while other BH_3-only pro-apoptotic members compete to release activating pro-apoptotic proteins (Shamas-Din et al., 2013). Another model, the neutralization model (Chen et al., 2005) suggests that the pro-apoptotic activity of Bax and Bak is regulated by the anti-apoptotic proteins and upon activation, the BH_3-only proteins bind with and neutralize the anti-apoptotic proteins, allowing Bax and Bak to initiate apoptosis setting off a cascade of proteolytic events to activate caspase-3 and caspase-7 (Kalkavan and Green, 2018). Regardless of the exact mechanism, the delicate balance of pro- and anti-apoptotic molecules is essential for maintaining cellular homeostasis, which can be used to verify whether a newly discovered gene variant that can be expressed in a cell model is disease- and mechanistically-specific for further ALS research.

In this proteogenomic workflow, we have designed an unbiased proteomics workflow to determine whether familial and sporadic mutations in *CCNF* implicated in ALS were found to activate pathways that were susceptible to neuronal cell death and cause aberrant E3 ligase activity of the $SCF^{(cyclinF)}$ complex. Expression of selected ALS-linked *CCNF* mutations identified differences in the global proteome with many upregulated proteins found to cluster towards the Bad-Bax apoptosis pathway in transfected cells, while these same pathways were not activated in cells expressing the non-MND cyclin F mutation (R574Q) and *CCNF* wild-type control. Proteomics and biochemical analysis of induced pluripotent stem cells (IPSC) derived from patient fibroblasts bearing the ALS $CCNF^{S621G}$ mutation showed similar activation profiles of the Bad-Bax apoptosis pathway. This was confirmed *in vivo* using zebrafish injected with ALS mutant *CCNF* mRNA, which

increased activation of caspase-3 and caused aberrant branching of neurons in only disease-specific mutations, suggesting that ALS mutations in *CCNF* are highly specific in triggering neuronal cell death. Here, we thereby demonstrate a proof-of-concept proteogenomic workflow to screen new gene mutations (using *CCNF* as an example) to determine their potential to cause apoptosis and ALS pathogenesis using a combination of *in vitro* and *in vivo* models, proteomics, and biochemical assays. Our workflow aims to provide an efficient and timely means to prioritize gene candidates for further mechanistic studies, with potential application for the study of numerous disease-associated gene variants.

MATERIALS AND METHODS

Cell Culture and Transfection

HEK293 cells were plated at 1 x 10^6 cells in 100 mm plates and grown in high glucose DMEM supplemented with 10% heat inactivated FBS (F8192, Sigma Aldrich, MO, United States) in a 37°C heat-jacket humidified incubator with 5% CO_2. After 48 hours of growth the cells were transfected with FLAG-tagged or mCherry-tagged *CCNF* cDNA constructs using Lipofectamine 2000 as previously described (Lee et al., 2017a,b).

Fibroblasts were obtained by skin biopsy from a 59-year-old symptomatic familial ALS patient ($CCNF^{S621G}$) (Bax et al., 2019a), a 62-year-old pre-symptomatic familial ALS patient ($CCNF^{S621G}$) and two healthy controls aged 57 (Balez et al., 2016) and 59 years old. All experimental protocols were approved by the University of Wollongong and Macquarie University Human Research Ethics Committees. The methods were carried out in accordance with the guidelines as set out in the National Statement on Ethical Conduct in Research Involving Humans, and informed consent was obtained from all donors. Fibroblasts were reprogrammed into induced pluripotent stem cells (iPSCs) and confirmed as pluripotent as we previously described (Bax et al., 2019a,b). The iPSCs were cultured on Matrigel (Corning) coated 6 cm tissue culture plates in TeSR-E8 (Stem Cell Technologies) at 37°C, 5% CO_2 in a humidified incubator.

Cell Lysis and Immunoprecipitation

HEK293 cells were harvested in ice-cold PBS and lysed using probe-sonication (10 s, setting 3, Branson Sonifier 450) in lysis buffer [50 mM Tris-HCl, 150 mM NaCl, pH 7.4, 1% (v/v) NP-40 (I8896, Sigma Aldrich)], containing 2 mM EDTA, 10 mM N-ethylmaleimide, complete protease inhibitor cocktail (4693159001), and phosSTOP (4906837001, Sigma Aldrich). iPSCs were harvested by gently rinsing in 1x PBS followed by manual scraping in RIPA buffer (50 mM Tris-HCl pH 7.4, 1% NP-40, 0.25% Na-deoxycholate, 150 mM NaCl, 1 mM EDTA, phosphate (PhosSTOP, Roche) and protease (cOmplete Protease Inhibitor Cocktail, Roche) inhibitors. Cellular debris was pelleted by centrifugation at 10,000 g for 10 minutes at 4°C. The cleared protein lysate was quantified by BCA (PIE23225, Life Technologies, CA, United States). Typically, 10 μg protein was used for immunoblotting and MS analysis. Proteins were denatured by boiling at 95°C for 5 minutes in 1x LDS buffer (NP0008) with 1x NuPAGE Reducing Agent (NP0009, Life Technologies).

For the E3 Ligase activity assay, Flag-M2 antibody (F1804, Sigma Aldrich) was used to immunoprecipitate cyclin F and associated proteins. 2 μg antibody was used per 500 μg cellular protein. A pre-immune control IgG (5415, Genesearch, QLD, Australia) immunoprecipitation was carried out in triplicate and used as a negative control. Protein A/G beads (88803, Life Technologies) were used to capture the antibody: protein complex. The beads were washed in lysis buffer and resuspended in E3LITE Assay buffer (100 mM Tris-HCl, pH 8, 10 mM $MgCl_2$, 0.2 mM DTT).

Immunoblot Analysis

Denatured proteins were separated by gel electrophoresis using 4–15% Tris-glycine gels (4565083, BioRad, CA, United States) according to manufacturer instructions. Separated proteins were transferred to nitrocellulose membrane using the Bio-Rad Turbo Transfer System using the "Mixed molecular weight" protocol (7 mins, 13 V, 1.3 A). Membranes were rinsed with deionized water and blocked in Odyssey Blocking buffer (92740003, LI-COR, NE, United States) diluted 1:1 in TBS for 1 hour at room temperature with shaking. Membranes were then incubated in either antibodies (against actin (A1978, Sigma Aldrich), total Bad (9239), phospho-Bad ser136 (4366) Caspase-3 (96625), Bcl-2 (sc1382), Bik (sc365625), Bax (sc7480), Bid (sc373939), diluted 1:1000 in 3% (w/v) BSA in TBS-T [50 mM Tris-HCl pH 7.4, 150 mM NaCl, 0.1% (v/v) Tween-20] overnight at 4°C with rocking. Membranes were then incubated in fluorescently labeled IRDye 800CW Goat Anti-Rabbit IgG or IRDye 700CW Goat Anti-mouse IgG secondary antibodies (LI-COR). Proteins were imaged using a LI-COR CL-X, and densitometry analysis was conducted using Image Studio Lite ver 5.2.

E3 Ligase Activity Assay

The E3 ligase activity of the different cyclin F variants was assessed using E3LITE Customizable Ubiquitin Ligase Kit (E2 UBE2D3, Ubiquitin-Lys48 ubiquitin) (UC101, Life Sensors) and was carried out according to manufacturer's instructions (96-well plate format) with slight modifications to the incubation time which was increased from 30 to 90 minutes. Luminescence was measured using ECL on a Pherastar plate reader. Immunoprecipitation (IP) efficiency was confirmed by immunoblot to confirm E3 ligase measurements were carried out on equal immunoprecipitated cyclin F amounts.

Trypsin Digestion

Proteins were reduced and alkylated with 10 mM DTT and 55 mM iodoacetamide (IAA), respectively, and digested with trypsin (1:50 enzyme: protein) (V5111, Promega, WI, United States) overnight at 37°C. The digestion was inactivated by the addition of 2 μL of formic acid. Tryptic peptides were desalted on a pre-equilibrated C_{18} Sep-Pak cartridge

(A57003100K, Agilent, CA, United States) and eluted in 50 % (v/v) ACN, 0.1% (v/v) formic acid, and dried under vacuum centrifugation.

Reverse Phase C_{18} Liquid Chromatography-Mass Spectrometry (RP-LC-MS/MS)

Lyophilized peptides were resuspended in 0.1% FA and bath sonicated for 20 minutes. The resuspended peptides are then centrifuged at 14,000 g for 15 minutes to remove any insoluble debris, and the clarified peptides were analyzed by LC-MS/MS. The peptides were separated on an Ultimate 3000 nanoLC (Thermo Fisher Scientific) fitted with the Acclaim PepMap RSLC column particle size of 2 μm, diameter of 0.075 mm and length of 150 mm (Thermo Fisher Scientific), making use of a 60 min gradient (2–80% v/v acetonitrile, 0.1% v/v formic acid) running at a flow rate of 300 nl/min. Peptides eluted from the nano LC column were subsequently ionized into the Q Exactive Plus mass spectrometer (Thermo Fisher Scientific). The electrospray source was fitted with an emitter tip 10 μm (New Objective, Woburn, MA) and maintained at 1.6 kV electrospray voltage. The temperature of the capillary was set to 250°C. Precursor ions were selected for MS/MS fragmentation using a data-dependent "Top 10" method operating in FT acquisition mode with HCD fragmentation. FT-MS analysis on the Q Exactive Plus was carried out at 70,000 resolution and an AGC target of 1×10^6 ions in full MS. MS/MS scans were carried out at 17,500 resolution with an AGC target of 2×10^4 ions. Maximum injection times are set to 30 and 50 milliseconds, respectively. The charge exclusion was set to unassigned and 1+ with a dynamic exclusion of 20 seconds. The ion selection threshold for triggering MS/MS fragmentation was set to 25,000 counts, and an isolation width of 2.0 Da was used to perform HCD fragmentation with a normalized collision energy of 27.

Raw spectra files were processed using the Proteome Discoverer software 2.3 (Thermo) incorporating the Sequest search algorithm. Peptide identifications were determined using a 20-ppm precursor ion tolerance and a 0.1-Da MS/MS fragment ion tolerance for FT-MS and HCD fragmentation. Carbamidomethylation modification of cysteines was considered a static modification while oxidation of methionine, deamidation of asparagine and glutamine, GlyGly residues on lysine, and acetyl modification on N-terminal residues were set as variable modifications allowing for maximum two missed cleavages. The data was processed through Percolator for estimation of false discovery rates. Protein identifications were validated employing a q-value of 0.01. Label-free quantitation (LFQ) using intensity-based quantification was carried out. LFQ was carried out according to default parameter settings in the Proteome Discoverer 2.3 Software (Thermo). Briefly, peptide spectral matches (PSM) were filtered using a maximum delta Cn of 0.05, rank of 0, and delta mass of 0 ppm. PSMs and peptides were, respectively, validated using a strict FDR for PSMs of 0.01 and 0.05 for a relaxed FDR. Peptides shorter than 6 amino acids were filtered out. PSMs were chromatographically aligned for each input file in a sample set with a mass tolerance of 10 ppm and a maximum retention time (RT) shift of 10 minutes. Peptide groups used for protein quantification were analyzed using the default parameters which set a peptide as unique if it is included in only one protein group. The quantification was processed using unique and razor peptides (peptides shared among multiple proteins group or proteins) with the precursor abundance based on the intensity. Protein abundance was calculated as a sum of the individual peptide group abundances and the ratio was based on pairwise ratio using a geometric median of the peptide group ratios. An ANOVA test was used for the hypothesis test and uses the background population of ratios for all peptides and proteins to determine whether any given single peptide or protein is significantly changing relative to that background (Proteome Discoverer User Guide Software Version 2.3, Thermo).

Biological pathway analysis was carried out using PANTHER GO[1] (Mi et al., 2019) and predicted pathway and biological process activation was carried out using Ingenuity Pathway Analysis (QIAGEN, Version June 2018).

Generation of Zebrafish Overexpressing Cyclin F

Zebrafish were bred and maintained under established conditions (Westerfield, 2007) and all husbandry and experimental procedures were performed in compliance with the Animal Ethics Committee and Biosafety Committee, Macquarie University (AEC Reference No. 2015/034; 2017/019; NLRD 5201401007). Transgenic zebrafish that express blue fluorescent protein selectively in motor neurons on a TAB_WT background were used for this study [*Tg(-3mnx1:mTagBFP)*]^{mq10} (Don et al., 2017; Formella et al., 2018; Svahn et al., 2018). Only morphologically normal embryos were used for analysis, and all embryos were stage-matched through somite counts at 24 hpf.

The mCherry-*CCNF* plasmid (a gift from Michele Pagano, Addgene plasmid # 32975) (D'Angiolella et al., 2010) was used to generate constructs for this study. S621G, S195R and R574Q point mutations were introduced into *CCNF* within this plasmid using the Q5 Site-Directed Mutagenesis kit (NEB). Wild-type or mutant mCherry-tagged *CCNF* was then subcloned into the pCS2+ vector, and *CCNF* mRNA was generated from this vector using the mMESSAGE mMACHINE SP6 transcription kit (Thermo Fisher Scientific) as previously described (Hogan et al., 2017); 177 pg *CCNF* mRNA was injected into zebrafish embryos at the single-cell stage of development using a Picospritzer II (Parker Instrumentation) under a Nikon SMZ 745 stereomicroscope (Morsch et al., 2017). Embryos were screened for mCherry expression at approximately 6 hpf under a M165FC fluorescent stereomicroscope (Leica).

[1]www.pantherdb.org

Analysis of Axonal Branching in Zebrafish Embryos

Zebrafish embryos were manually dechorionated at 30 hours post-fertilization (hpf) and fixed in 4% PFA for one hour at room temperature. Fixed embryos were mounted in 3% methylcellulose and motor neurons expressing blue fluorescent protein imaged on a M165FC fluorescent stereomicroscope (Leica). The morphology of the ventral axonal projections of the first eight primary motor neurons immediately caudal to the yolk ball/tube boundary was assessed. Branching of the axon at or above the ventral edge of the notochord was considered aberrant (Lemmens et al., 2007). 41-46 embryos were assessed in each group across three experimental replicates.

Caspase-3 Staining of Zebrafish Embryos

Embryos were manually dechorionated and euthanized at 24 hpf, then fixed in 4% PFA for 1 hour at room temperature. Immunostaining was performed using rabbit polyclonal cleaved caspase-3 antibody at 1:500 dilution (Cell Signaling Technology) and donkey anti-rabbit Alexa Fluor® 488 secondary antibody at 1:500 dilution (Invitrogen) as previously described (Hogan et al., 2017). Embryos were mounted in 3% methylcellulose and imaged on a M165FC fluorescent stereomicroscope (Leica). Cleaved caspase-3 positive cells in the first five upper somites immediately caudal to the yolk ball/tube boundary were manually quantified. 30—40 embryos were assessed in each group across three experimental replicates.

Acridine Orange (AO) Staining

Zebrafish embryos were manually dechorinated at 24 hpf, then placed in 5 μg/ml acridine orange solution (Sigma Aldrich) for 10 minutes. Embryos were rinsed, then mounted in 3% methylcellulose and imaged on a M165FC fluorescent stereomicroscope (Leica) scope. The number of acridine orange positive cells in the first 5 upper somites immediately caudal to the yolk ball/tube boundary manually quantified; 38–61 embryos were assessed in each group across three experimental replicates.

RESULTS AND DISCUSSION

With the emergence of whole genome sequencing that have facilitated the rapid discovery of new genes for basic scientific research and in medicine, more than 20 putative genes are now cited as causing ALS (Mejzini et al., 2019). These genes encode proteins that cover a diverse range of molecular functions, including free radical scavenging (superoxide dismutase SOD1), regulation of RNA homeostasis [TAR DNA-binding protein 43 (TDP-43) and fused in sarcoma (FUS)], and protein degradation through the ubiquitin-proteasome system (ubiquilin-2, cyclin F) and autophagy (sequestosome-1/p62, dynactin). It is well established that familial origins represent about 10% of all ALS cases, and while more than 20 genes are now identified as causing ALS, only few have been fully validated to determine the full extent of the perturbed molecular mechanisms and pathways. While sporadic ALS makes up ∼90% of patients, the origins remain unresolved but environmental factors and gene-environment interactions are thought to be intimately involved. A clear example of this can be seen in discordant identical twin (n = 3 pairs) and triplets (n = 1 set), where one twin has died of ALS, but the other remains healthy (Tarr et al., 2019). Combined differences were observed in longitudinal methylation (epigenetic), and transcriptomes implicated the genes *CCNF, DPP6, RAMP3,* and *CCS* in one set of twins, while longitudinal transcriptomics showed an enrichment of immune function genes and under-representation of transcription and protein modification genes in ALS. A possible explanation for disease discordance is that there is a complex interaction between genetic susceptibility and environmental factors (that may influence gene expression or protein modification and function) that ultimately drives disease pathogenesis.

Given the complexity in molecular origins of ALS, various molecular pathways have been implicated in ALS including disruption in DNA/RNA processing (Zhang et al., 2015, 2018), oxidative stress (Pollari et al., 2014), excitotoxicity (Foran and Trotti, 2009), protein misfolding and aggregation (McAlary et al., 2019), protein degradation (ubiquitin-proteasome and autophagy) (Shahheydari et al., 2017), ER stress (Walker and Atkin, 2011), and neuroinflammation (Liu and Wang, 2017). It is likely that many of these cellular processes are implicated at some point during disease, but what is less clear is how these (and other) molecular pathways interact with each other and converge together to cause ALS. It seems likely that the various initial triggers of disease (either genetic, environmental, or gene–environment interactions) must converge upon a common set of molecular pathways that underlie the pathogenesis of ALS. The ultimate identification of such convergent molecular mechanisms will be a key discovery towards understanding disease etiology and ultimately developing therapeutic targets for intervention. In this regard, it would be highly informative to use an unbiased screening approach to assess the activity of multiple pathways at the same time and investigate how these change over the course of disease and the interactions between pathways.

We have developed a proof-of-concept integrated proteogenomics workflow (**Figure 1**) to provide broad insight into disease mechanisms through the identification of *CCNF* as a new ALS gene, and identification of disruption in multiple molecular pathways that converge to cause neuronal cell death (neurodegeneration). Pathways involved with activating apoptosis in cells expressing *CCNF* mutations were validated using various models, including cell lines, patient-derived iPSCs, and transgenic zebrafish. This integrated study demonstrates the utility and workflow for applying unbiased proteomics to ALS gene discoveries to determine whether new genetic variants are indeed potentially disease-causing mutations.

Unbiased Proteomics to Identify Perturbed Pathways From Disease-Specific Mutations

Mutations in the *CCNF* gene have been established as a cause of ALS and FTD in a large Australian family, and expression

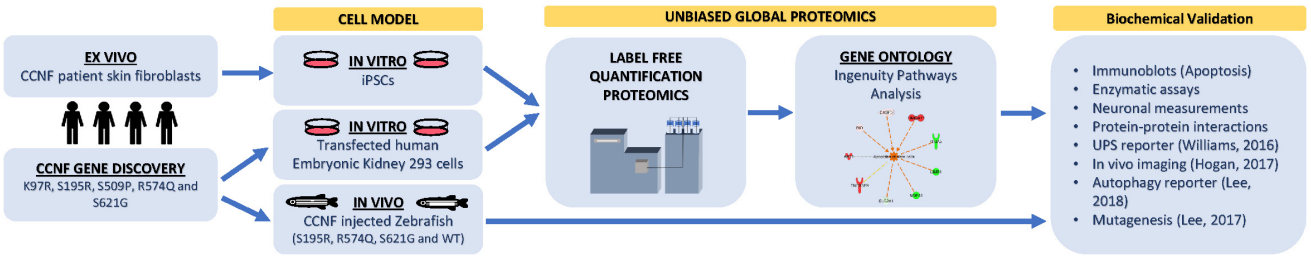

FIGURE 1 | Proteogenomic workflow to determine whether potential ALS gene candidates cause disease. Discovery of gene mutations by whole-genome, whole-exome, or targeted sequencing. cDNA gene constructs candidate mutations are inserted into cell models (e.g., HEK293 or Neuro2A cells). Ex vivo models such as patient fibroblasts (if available) that contain the gene mutation can also be used or converted into iPSCs for further differentiation. Label-free quantitative proteomics is used to analyze and provide a profile of protein expression changes that cluster to biological processes and signalling pathways. These biological pathways can then be validated using standard biochemical methods and/or in animal models. Animal models, such as zebrafish, have the advantage of generating progeny relatively quickly and can be extended to study motor phenotypes.

of mutant cyclin F proteins in both cell line and zebrafish models have been shown to cause dysregulation of the UPS system (Williams et al., 2016; Hogan et al., 2017; Lee et al., 2017a,b). In previous studies, we have shown that expression of mutant cyclin F^{S621G} causes elevated Lys48 ubiquitylation of proteins and increased autophagy in human cell lines (Lee et al., 2017a,b). Additionally, injection of $CCNF^{S621G}$ mRNA into zebrafish caused motor neuron axonopathies (Hogan et al., 2017). We aimed to explore whether this proteogenomics workflow would be useful for establishing whether a gene mutation(s) was indeed disease-causing, by using *CCNF* mutations previously reported by Williams et al. (2016) as a test case.

In this study, we selected familial ALS mutations in cyclin F (K97R, S195R, S509P, S621G) and one non-ALS public database SNP (R574Q) for analysis in our unbiased proteogenomic workflow. Expression of familial and ALS-specific (K97R, S195R, S509P, S621G) and non-ALS *CCNF* mutations (wild type and R574Q) were carried out in HEK293 cells, lysed and tryptically digested, and analyzed by LC-MS/MS. In total, we identified 5231 proteins with approximately 91% found in common between all samples indicating a high level of consistency from each proteome dataset. Using label-free quantitative proteomics to measure the relative abundance of each protein, we observed differential hierarchical clustering of the proteome datasets where both cyclin F wild type and R574Q displayed similar proteomic profiles across all identified and differentially expressed proteins, while the proteomic profiles of cells expressing cyclin F S621G, K97R and S509P appeared to cluster together (**Figure 2A**). This was intriguing as the proteome profile of cells expressing only the ALS-specific mutations clustered together. To ensure that these observations were not due technical variations, we examined the expression levels of cyclin F by immunoblot analysis (**Figure 2B**) and as measured by mass spectrometry (**Figure 2C**) and confirmed that the proteome similarities between ALS and non-ALS mutations were not due to the effects of transient transfections and differences in cyclin F protein expression. We next carried out an additional data quality control by principal component analysis (PCA) to examine whether there were variations between the individual biological replicates analyzed that may explain how the proteomes of ALS-specific mutations in cyclin F clustered together. Two-dimensional PCA analysis showed a high level of consistency amongst the samples analyzed, with biological replicates grouped together by cyclin F mutation (**Figure 2D**). Therefore, the data quality provided us with confidence that the proteomic profiles (and the lists of differentially expressed proteins) were due specifically to the expression of cyclin F mutations, which enabled us to extend the analysis to focus on perturbed cellular pathways.

Proteome profiles for HEK293 cells expressing cyclin F gene variants were analyzed by Gene Ontology using PANTHER GO[2] and observed the distribution of proteins within "Protein Class" categories with nucleic acid binding (21%), hydrolase (13%), and transferase (10%) making up the top three functional categories for proteins identified (**Figure 3A**). The distribution of the different protein classes was similar and consistent across all proteomic profiles, and no differences were distinguished between proteins from each *CCNF* variant. Therefore, we carried out an analysis of protein identifications found uniquely in each of the *CCNF* variants (compared to the WT) (**Figure 3B**) and filtered the signaling pathways to those relevant to ALS pathogenesis and neuroinflammation. Interestingly, we observed unique proteins in cells expressing the *CCNF* ALS gene mutations but not in the wild type that are classified in the GO categories: ubiquitin-proteasome (such as UBE2E2 and WWP2), inflammation (such as STAT6 and CAMK2B), Huntington's (such as TNFAIP8 and OPTN), Parkinson's (such as MAPK7 and NDUFV2) and apoptosis signaling (such as JUN and MAP4K5). While these unique proteins identified in cyclin F variants gave us some clues to the pathways affected, we analyzed the proteomics data with their expressional changes using ingenuity pathway analysis[3] (IPA) to calculate activation Z-scores using individual protein expression values and grouped according to their canonical cellular pathways. The predicted activation or inhibition scores enabled us to interrogate our dataset further and to provide confidence to direct our validation studies.

We analyzed the proteomic profiles of the different cyclin F variants using each protein's abundance ratio (relative to the wild

[2]http://pantherdb.org

[3]https://www.qiagenbioinformatics.com/products/ingenuity-pathway-analysis

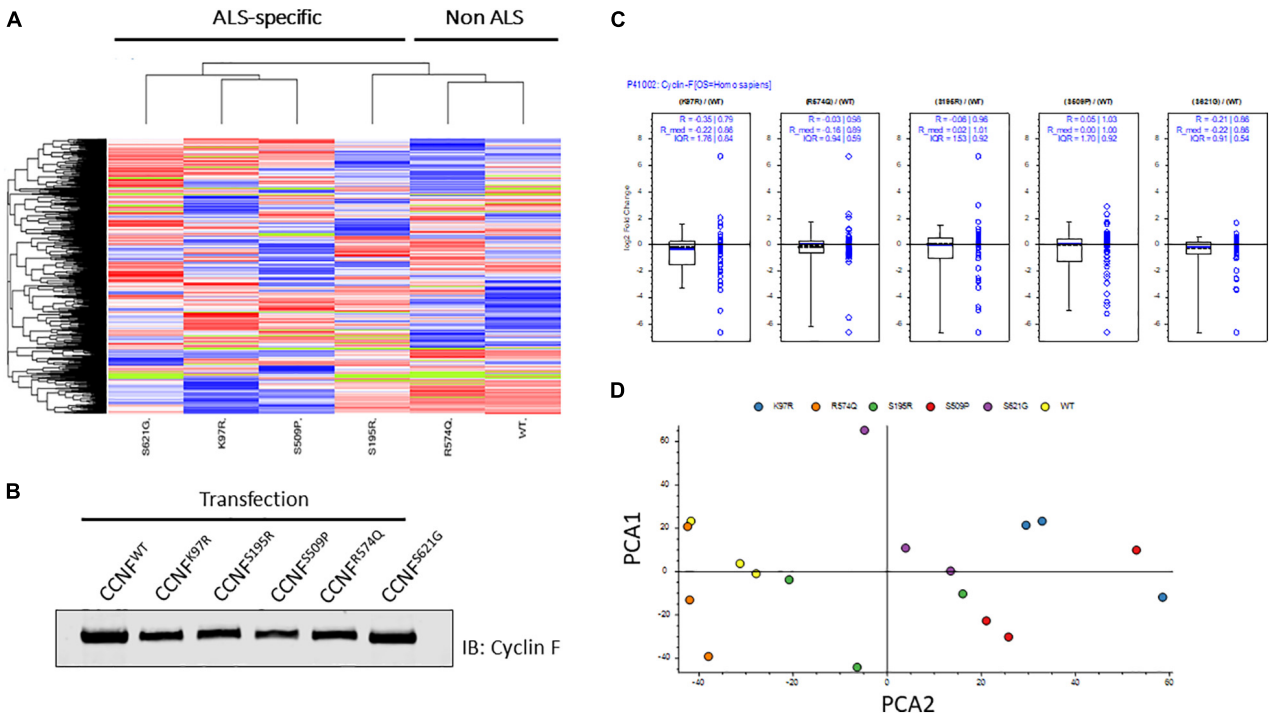

FIGURE 2 | Label-free quantitative proteomics of HEK293 cells transfected with different cyclin F mutations (wild type, K97R, S195R, S509P, R574Q, S621G). **(A)** Hierarchical group clustering of proteome profiles from transfected cells showed ALS-specific and non-ALS mutations grouped together. Immunoblot analysis **(B)** and LFQ proteomics **(C)** of relatively equal cyclin F expression levels in transiently transfected HEK293 cells. **(D)** Two-dimensional principle component analysis (PCA) reflects the data quality and similarities of the proteome profiles between each biological replicate that are grouped by cyclin F mutations. Figures **(A,C,D)** were generated using Proteome Discoverer 2.3 (Thermo).

type control) as calculated by label-free proteomics. Interestingly, IPA determined that various canonical pathways were similarly predicted to be activated (such as actin cytoskeleton signaling) or inhibited (such as sirtuin signaling) in cells expressing the cyclin F variants with K97R, S195R, S509P and S621G mutations (**Figure 3C**). These four mutations were identified in various patients with ALS and FTD (Williams et al., 2016). In contrast, the cyclin F variant R574Q had a similar pathway profile to the wild type control and was characterized to be a database SNP and not found in ALS and FTD patient cohorts. This database SNP also ensured that an appropriate negative control was included in this proteomic study that is not known to cause ALS and/or FTD. Given the various reported cellular pathways that are perturbed at the onset and during ALS and FTD pathogenesis, our goal was to determine (i) whether mutations identified by GWAS studies were disease-causing and (ii) to focus on the end-point of disease which is fundamentally characterized by neuronal cell death (apoptosis).

Ingenuity pathway analysis predicted activation of the apoptosis signaling pathway in cells expressing cyclin F K97R, S195R, and S621G and therefore we focused on the identified proteins within the apoptosis pathway that were differentially expressed or perturbed (**Figure 3D**). Using the label-free proteomics data and IPA, we observed that the intrinsic pathway of apoptosis was predicted to be activated with various key pro-apoptosis players such as the Bcl-2 family including the pro-apoptotic proteins Bcl-2 associated agonist of cell death (Bad), Bcl-2 homologous antagonist killer (Bax), and BH3-interacting domain death agonist (Bid), which were all differentially upregulated in disease-causing cyclin F variants. The activation of the apoptosis pathway in K97R, S195R and S621G was not due to the transient transfection procedure since both cyclin F wild-type and the R574Q variants were also transfected using the same procedure without activating the apoptosis pathway. Since these pathways are based on IPA predictions using experimentally obtained label-free proteomics data, we validated various components of the apoptosis pathway by immunoblot analysis.

Biochemical Validation of the Bad-Bax Apoptosis Pathway in Cells Expressing Cyclin F Variants

The Bcl-2 family consists of approximately 25 proteins that are involved with promoting or inhibiting apoptosis by controlling mitochondrial outer membrane permeabilization and release of cytochrome c (Kale et al., 2018). Bad/Bax/Bak are believed to initiate apoptosis by forming a pore in the mitochondrial outer membrane that allows cytochrome c to escape into the cytoplasm and activate the pro-apoptotic caspase cascade (Kalkavan and Green, 2018). While the anti-apoptotic Bcl-2 and Bcl-xL proteins promote cell survival by binding to Bad and Bak

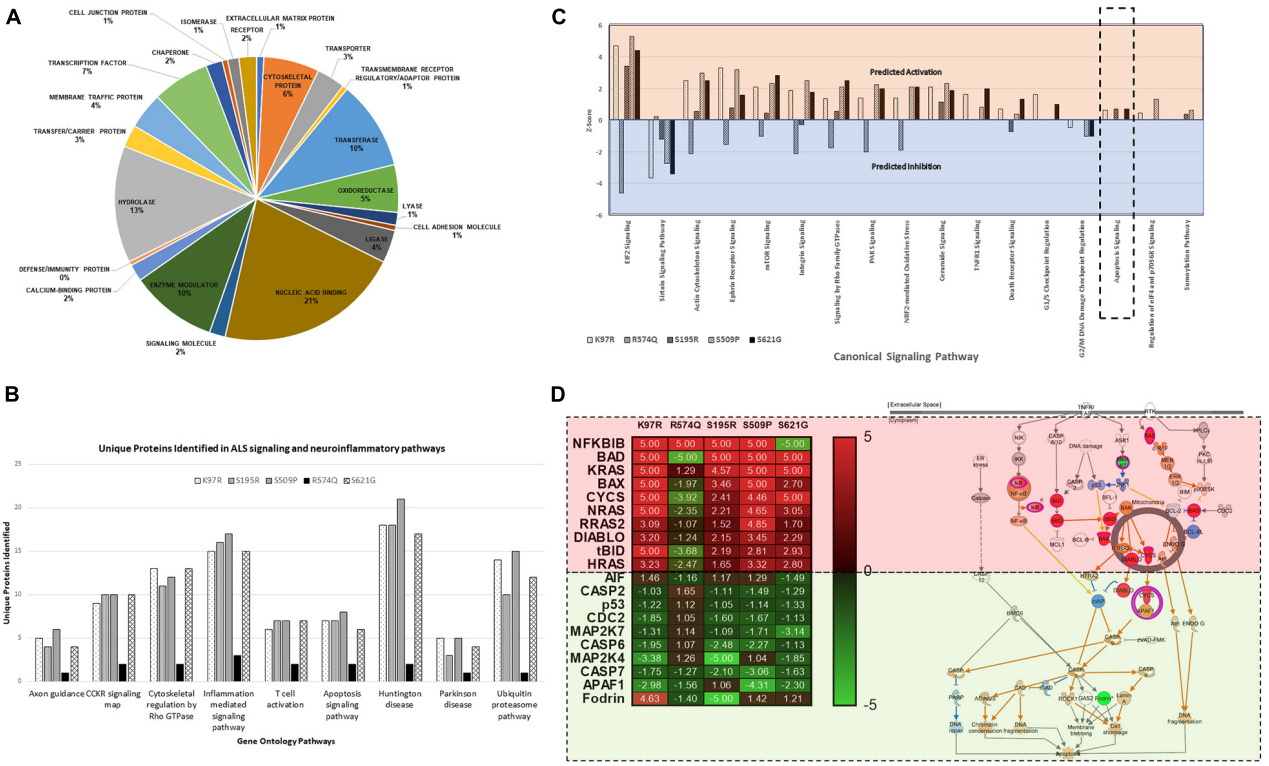

FIGURE 3 | (A) Gene ontology (GO) distribution of the global proteome of HEK293 cells expressing cyclin F variants under the "Protein Class" category demonstrating proteins are classified as having molecular functions: nucleic acid binding, hydrolase, and transferase activity. **(B)** Selected gene ontology (GO) annotations of unique proteins clustered to selected pathways in neuroinflammation and ALS signalling. **(C)** Ingenuity pathway analysis (IPA) of the proteomic profile of cyclin F variants predicts activation and inhibition of various canonical cellular pathways. Apoptosis signaling was predicted to be activated in cells expressing cyclin F K97R, S195R, and S621G. Orange and blue annotation refer, respectively, to predicted activation and inhibition as determined by IPA. **(D)** Heatmap of label-free proteomics of differentially expressed proteins in the apoptosis signaling pathway and IPA prediction of downstream effects (log2 values shown; values shown as 5 and −5, respectively, indicate detection of the presence and absence of a protein and are not measured values). Red and green annotations refer, respectively, to experimentally measured values. Orange and blue annotations and lines refer, respectively, to predicted activation and inhibition as determined by IPA. Filled and dashed lines, respectively, refer to direct and indirect causal relationships.

and inhibiting cytochrome c release through the mitochondrial pore and preventing the activation of the cytoplasmic caspase cascade (Shamas-Din et al., 2013). Bad mediates cell survival by heterodimerizing two anti-apoptotic proteins: Bcl-xL and Bcl-2. Following the activation of the Bad's targeted proteins is the oligomerization of Bax and Bak monomers by Bim and truncated tBid to mediate the mitochondrial outer membrane permeability. Cytochrome c is released from the mitochondria to promote caspase-9 activation, which leads to the cleavage of caspase-3, caspase-7 and poly(ADP-ribose) polymerase (PARP), activating cellular apoptosis.

Moreover, the pro-apoptotic activity of Bad is regulated through its phosphorylation and sequestration to the cytosol by 14-3-3. Thus, one of the main markers to determine the level of apoptosis activation through this pathway is to measure the phosphorylation status of Bad. Seven phosphorylation sites have been identified on Bad: Ser112, Ser128, Ser136, Ser155, Ser170, Thr117 and Thr201. These sites are phosphorylated and regulated by a variety of kinases (Klumpp and Krieglstein, 2002; Burlacu, 2003). For example, dephosphorylated or reduced phosphorylation levels of Bad at Ser112, Ser136, and/or Ser155 (which are regulated by Akt, p70S6 kinase, and PKA) allows Bad to form a heterodimer with Bcl-2 and Bcl-xL blocking the Bcl-2 pro-survival activity and thus allowing Bax/Bak-triggered apoptosis to occur. Immunoblot analysis of phospho-Bad at Ser112, 136 and Ser155 from cells expressing the cyclin F wild type and variants K97R, S195R, S509P, R574Q, and S621G revealed no statistically significant phosphorylation differences at Ser136. However, there were observable decreases in phosphorylation at Bad, pBad (Ser112) and pBad (Ser155) (**Figure 4A**).

Notably, pBad (Ser112) was decreased in the cyclin F variants K97R (0.385-fold, $p = 0.0001$, $n = 4$), S195R (0.529-fold, $p = 0.0025$, $n = 4$), S509P (0.413-fold, $p = 0.0002$, $n = 4$), and S621G (0.508-fold, $p = 0.0015$, $n = 4$) when compared to the cyclin F wild-type control (**Figure 4A**). In addition, pBad (Ser155) was decreased in only S195R (0.616-fold, $p = 0.0274$, $n = 4$), S509 (0.578-fold, $p = 0.0141$, $n = 4$) and surprisingly R574Q (0.37-fold, $p = 0.0003$, $n = 4$) when compared to the cyclin F wild-type control (**Figure 4A**). The levels of pBad at the different sites can be regulated at various stoichiometries as they are influenced by i) specific environmental cues and ii) various upstream

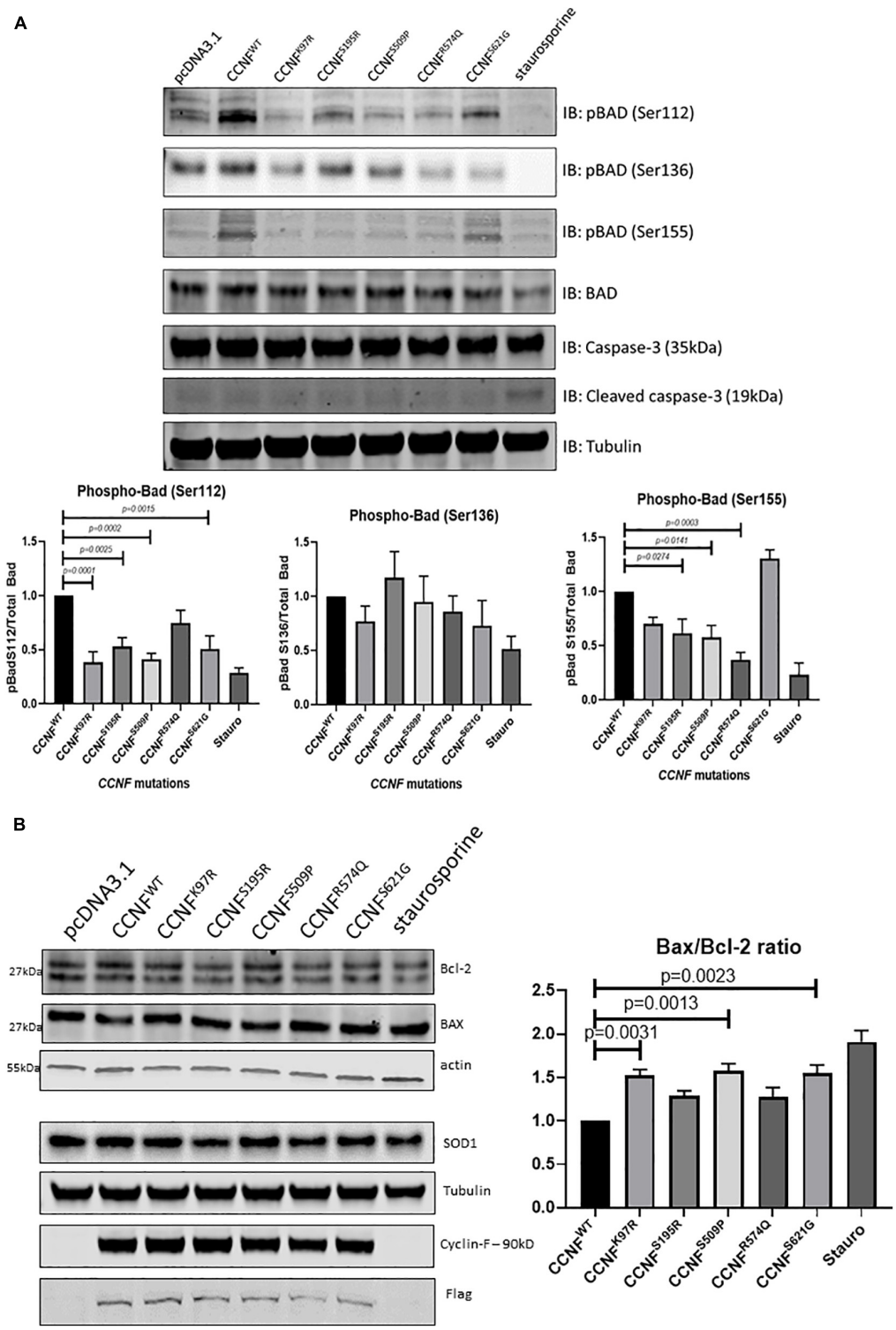

FIGURE 4 | (A) Phosphorylation of Bcl-2 associated agonist of cell death (Bad) at Ser112, Ser136, and Ser155 reveals activation of the intrinsic apoptosis pathway. pBad (Ser112) was decreased in the cyclin F variants K97R (0.385-fold, $p = 0.0001$, $n = 4$), S195R (0.529-fold), S509P (0.413-fold), and S621G (0.508-fold) when compared to the cyclin F wild-type control (one-way ANOVA with Dunnett's multiple comparison test, $n = 4$). pBad (Ser155) was decreased in only S195R (0.616-fold), S509 (0.578-fold), and R574Q (0.37-fold) when compared to the cyclin F wild-type control (one-way ANOVA with Dunnett's multiple comparison test, $n = 4$). **(B)** Immunoblot analysis of Bcl-2, Bax, and SOD1 from cells expressing cyclin F wild-type and variants (K97R, S195R, S509P, R574Q, S621G) reveals increased Bax/Bcl-2 ratios in K97R (1.53-fold), S509P (1.58-fold), and S621G (1.55-fold) (one-way ANOVA with Dunnet's multiple comparison test, $n = 3$) suggesting increased stimulation of apoptosis.

kinase(s) since multiple kinases can converge to phosphorylate the same site. This makes it difficult to determine the upstream changes that have led to the activation of Bad and the apoptosis pathway. What is apparent in this study, however, is that the decreased pBad levels at Ser112 and Ser155 would suggest that cells expressing cyclin F disease variants have increased apoptosis activity which supports the IPA predictions of the global proteomics analysis (**Figure 3D**).

To determine whether other components of the Bad-Bax apoptosis pathway were also activated in cells expressing cyclin F variants, we immunoblotted the pro-apoptotic protein Bax and compared the ratio to the anti-apoptotic Bcl-2 (Bax/Bcl-2) (**Figure 4B**). We observed increased ratio of Bax/Bcl-2 (pro-apoptosis/anti-apoptosis) in cyclin F variants K97R (1.53-fold, $p = 0.0031$, $n = 3$), S509P (1.58-fold, $p = 0.0013$, $n = 3$) and S621G (1.55-fold, $p = 0.0023$, $n = 3$) compared to the wild-type control. Superoxide dismutase is an enzyme responsible for reducing free superoxide radicals and is implicated in apoptosis and familial ALS. In this study, SOD1 and SOD2 were upregulated in only cyclin F disease-causing variants; however, immunoblot validations did not detect any observable differences in SOD1 abundance between the cyclin F variants. Importantly, we did not observe any differences in apoptosis in cells expressing the non-MND cyclin F mutation (R574Q). Taken together, immunoblot validation of the Bad-Bax apoptosis pathway (i.e., phosphorylation of Bad and Bax/Bcl-2 ratios) confirmed that cells expressing the cyclin F ALS variants activated apoptosis, giving us confidence that our proteogenomic workflow was capable of determining whether potential gene mutations are indeed disease-causing.

Induced Pluripotent Stem Cells From ALS Patients Harboring the Cyclin F S621G Mutation Activate the Apoptosis Pathway

Given the limitations of overexpressing a transgene in a non-neuronal cell line (HEK293) for ALS research, we next tested iPSCs from a symptomatic ALS patient with the cyclin F S621G mutation, an asymptomatic or pre-symptomatic family member with the same mutation, and two healthy controls. The advantage of using iPSCs for this proteogenomic study is i) the uniform expression of the cyclin F S621G at endogenous levels and ii) the increased amount of material that can be obtained from these cultures that are sufficient for biochemical and proteomic analysis. We carried out proteomics analysis of the iPSCs from both the pre-symptomatic and symptomatic individuals. We detected differentially expressed proteins (such as Bid, caspase-3, and calpain) that are responsible for various stages of apoptosis signaling (**Figure 5A**) – the same pathway that was activated in the HEK293 cell lines expressing cyclin F variants. While the activation of apoptosis was anticipated in iPSCs (Activation Z-score = 1.67, p-value = 0.000396) derived from the symptomatic patient, it was also similarly predicted from iPSCs derived from the pre-symptomatic patient.

We carried out immunoblot analysis of calpain-1, calpain-2, Bid, Bax and caspase-3 to validate the proteomics results (**Figure 5B**). Calpain-1, calpain-2, and caspase-3 were detected, and their expression was determined to be similar (i.e., no statistical difference) between iPSCs derived from asymptomatic and symptomatic cyclin F S621G patients and healthy controls. Interestingly, we observed increased expression of the pro-apoptotic protein Bid and increased ratio of Bid/Bcl-2 in iPSCs derived from the symptomatic (Bid/Bcl-2 ratio 1.9-fold, $p = 0.0255$, $n = 3$) cyclin F S621G patient when compared to the healthy controls. There were no apparent differences in the Bid/Bcl-2 ratio between the pre-symptomatic patient and healthy controls. Additionally, increased expression of the pro-apoptotic protein Bax and increased ratio of Bax/Bcl-2 was also observed in iPSCs derived from pre-symptomatic (Bax/Bcl-2 ratio 1.7-fold, $p = 0.0237$, $n = 3$) and symptomatic (Bax/Bcl-2 ratio 1.87-fold, $p = 0.0091$, $n = 3$) cyclin F S621G patients when compared to the healthy controls (**Figure 5B**). The immunoblot analyses validate much of the proteomics data and the bioinformatics analyses with respect to predicting the activation of apoptosis from iPSCs from ALS patients expressing the cyclin F S621G mutation. This validation step also demonstrates a high level of confidence that the screening of HEK293 cell lines expressing cyclin F variants was indeed highly accurate in proteomic profiling to determine the activation status of apoptosis signaling and potentially other affected cellular pathways. The expression of transgenes in a cell- and/or species-specific model can be highly effective for determining how 'pathogenic' a gene is as well as identifying the cellular pathways that may be perturbed and driving the biological processes towards cellular death.

Cyclin F Mutations Cause Aberrant Lys48-Ubiquitin E3 Ligase Ubiquitylation Activity

To gain insights into the mechanistic changes of these mutations to cyclin F activity, *in vitro* E3 ligase activity assays were carried out. Cyclin F is an F-box protein that is a component of the $SCF^{(cyclinF)}$ complex, which is an E3 ligase responsible for ubiquitylating substrates for proteasomal degradation. To measure the enzymatic activity of cyclin F, we employed the E3LITE *in vitro* ubiquitylation assay with Lys48-ubiquitin using immunoprecipitated FLAG-cyclin F from biological replicates ($n = 3$) as previously described (Lee et al., 2017a,b) (**Figure 6A**). We observed increased E3 ligase activity from cyclin F variants K97R (1.324-fold, $p = 0.0153$, $n = 3$), S195R (1.73-fold, $p \leq 0.0001$, $n = 3$) and S621G (2.83-fold, $p \leq 0.0001$, $n = 3$) compared to the wild-type control. We have previously reported that the S621G mutation in cyclin F increases its E3 ligase activity by approximately 30–40% (measured for 30 minutes) compared to the wild type. We detected similar increases in ubiquitylation activity with the K97R and S195R mutations suggesting a gain-of-function in these cyclin F variants. Interestingly, the cyclin F variant S509P had dramatically reduced E3 ligase activity by 0.42-fold ($p = 0.0002$, $n = 3$) and suggests a loss-of-function to cyclin F. While the cyclin F variants examined in this study (except R574Q) activated apoptotic pathways that lead to neuronal loss [as determined by proteomics, immunoblot validations and patient information (Williams et al., 2016)], it suggests that both

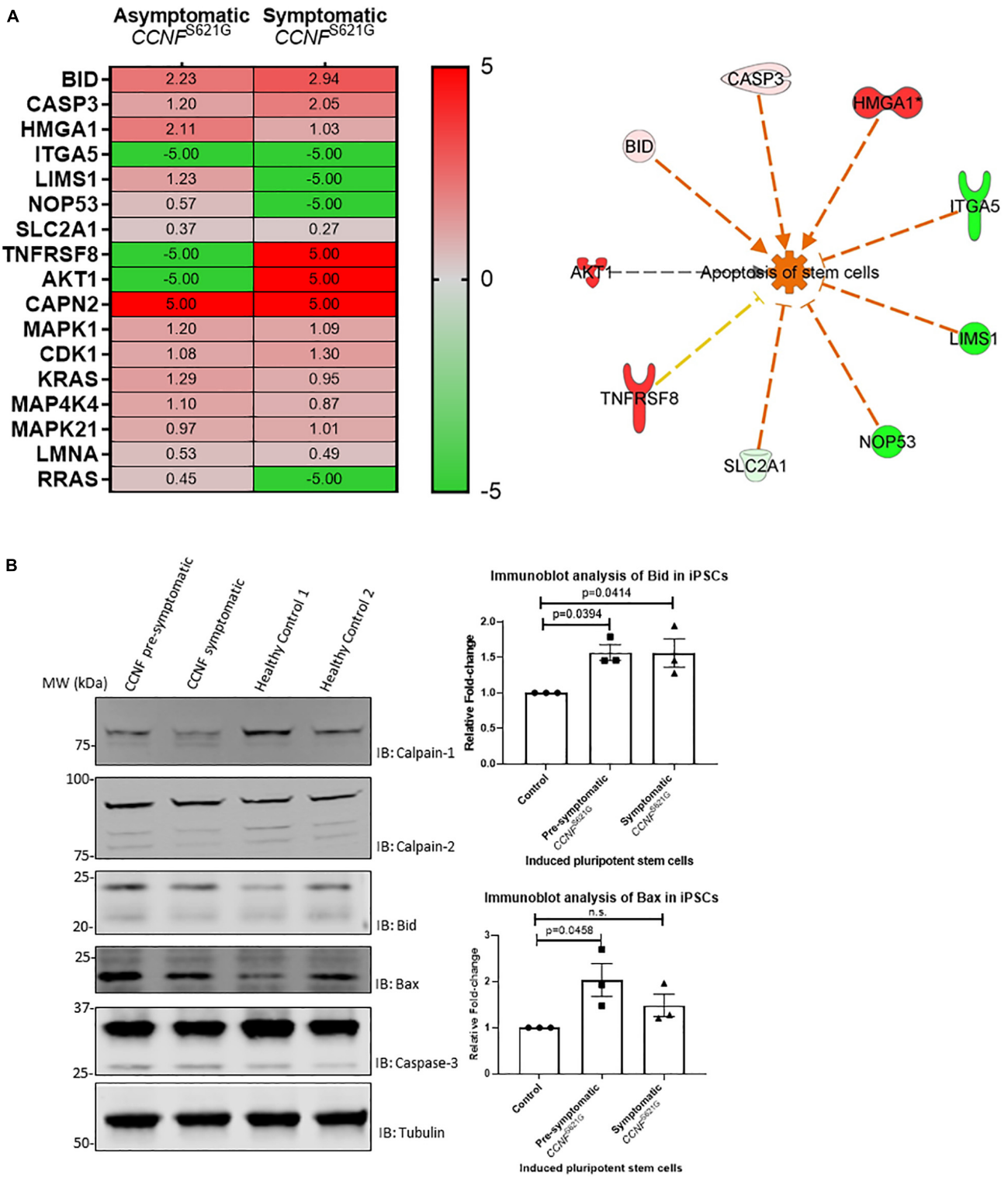

FIGURE 5 | (A) iPSCs from asymptomatic and symptomatic ALS patients harboring the *CCNF* S621G mutation were subjected to global proteomics analysis. IPA of the quantitative proteomics data predicted activation of the apoptosis pathway. Red and green annotations refer, respectively, to experimentally measured values. Orange and blue annotations and lines refer, respectively, to predicted activation and inhibition as determined by IPA. Dashed lines indicate an indirect causal relationship (log2 values shown; values shown as 5 and −5, respectively, indicate detection of the presence and absence of a protein and are not measured values). **(B)** Immunoblot analysis of iPSCs from asymptomatic and symptomatic ALS patients harboring the *CCNF* S621G mutation compared to healthy controls reveals increased expression of pro-apoptotic proteins Bid and Bax. One-way ANOVA with Dunnett's multiple comparison test ($n = 3$).

gain- and loss-of-function mutations in cyclin F are associated with the perturbation of downstream cellular pathways and cause proteostasis dysfunction. Therefore, the fine-tuning and regulation of cyclin F's E3 ligase activity is highly important in maintaining cellular homeostasis.

Cyclin F Interacts With Caspase-3

Given that caspase-3 can be regulated by ubiquitylation (Arama et al., 2007; Parrish et al., 2013) and is typically ubiquitylated for degradation by the proteasome (Choi et al., 2009), we hypothesized that cyclin F could potentially interact and/or ubiquitylate caspase-3. Caspase-3 contains two R-X-L motifs (residue 79–81 and 149–151) in its sequence, and cyclin F typically interacts with its substrates via this region (D'Angiolella et al., 2010). HEK293 cells expressing mCherry only, mCherry-cyclin F^{WT} and mCherry-cyclin F^{S621G} were immunoprecipitated using an RFP-Trap and immunoblotted for caspase 3 (**Figure 6B**). Immunoblot analysis revealed that caspase-3 co-immunoprecipitated with cyclin F. We performed the reverse immunoprecipitations of endogenous caspase 3 and immunoblotted for cyclin F, which revealed a direct interaction between caspase 3 and cyclin F.

Cyclin F S195R and S621G Cause Increased Caspase-3 Activity and Aberrant Neuron Branching in Zebrafish

To determine whether apoptosis pathway activation could be recapitulated *in vivo*, we injected zebrafish with *CCNF* mRNA as previously described (Hogan et al., 2017). The mRNA of *CCNF* variants S621G, S195R, and R574Q and wild-type *CCNF* were injected into zebrafish embryos at the single-cell stage of development, and various blinded measurements were made that included (i) the aberrant number branches per fish, (ii) the number of cells positively stained for cleaved caspase-3, and (iii) the number of cells stained with acridine orange as a measure of apoptotic cells (**Figure 7**). A blinded-analysis was carried out and determined that zebrafish expressing cyclin F S621G and S195R, respectively, had 2.01-fold (p-value = 0.006, n = 42) and 2.4-fold (p-value = 0.0011, n = 46) more aberrantly branched motor neurons compared to the wild-type and uninjected controls. The incidence of aberrant axonal branching in zebrafish expressing the non-ALS cyclin F variant R574Q did not change significantly (1.27-fold) compared to fish expressing wild-type cyclin F (**Figure 7A**). We then carried out immunohistochemistry analysis of cleaved caspase-3 by counting the number of positive cells in injected zebrafish, as a crude measure of the level of enzymatic activity of caspase-3. Similarly, both cyclin F S621G and S195R injected zebrafish had increased cleaved caspase-3 activity by 2.08-fold (p-value = 0.0029, n = 39) and 2.79-fold (p-value = 0.0004, n = 28), respectively, when compared to the cyclin F wild-type (**Figure 7B**). The cyclin F R574Q (1.03-fold) did not show any significant differences compared to the wild type. Lastly, we carried out acridine orange (AO) staining to determine the number of apoptotic cells in zebrafish injected with *CCNF* variants. Consistent with the previous results, the number of AO positive cells in S621G and S195R were 1.4-fold (p-value = 0.0496, n = 37) and 1.45-fold (p-value = 0.0115, n = 57) higher, respectively, compared to the wild type. The number of AO stained cells in zebrafish injected with R574Q (1.07-fold) and the wild type was not significantly different (**Figure 7C**). Collectively, these three *in vivo* experiments to measure (i) aberrant neuron branching, (ii) level of cleaved caspase-3, and (iii) the amount of apoptotic cells provide further validation that increased activation of apoptosis occurs in zebrafish injected with ALS-specific *CCNF* gene variants.

Proteogenomics Workflow Reveals Potential Disease-Causing Mutations

The pathological hallmark in almost all cases of ALS is the presence of aggregated, acetylated (Cohen et al., 2015), ubiquitylated (Neumann et al., 2006), and phosphorylated (Hasegawa et al., 2008) TDP-43 in post-mortem patient brain tissue (Neumann et al., 2007). Numerous mechanisms have been implicated in the pathogenesis of ALS which are related to mutations and/or proteostasis dysfunction that impact on various cellular pathways including intracellular transport (Walker and Atkin, 2011), protein folding and degradation (Shahheydari et al., 2017), cellular stress (Ling et al., 2013), and RNA metabolism (Zhang et al., 2015, 2018). However, the initial trigger(s) that sets off a chain of biological events that lead to motor neuron loss (and eventually ALS) is still not known.

Genome-wide association studies has rapidly accelerated the identification of new genetic causes of ALS with more than 20 putative ALS-causing genes now cited. This series of discoveries have led to a better understanding of disease mechanisms that have helped draw connections between these gene discoveries (and their reported canonical functions) to the pathological features observed in ALS patients. Moreover, identification of gene variants has also enabled the generation of *in vitro* and *in vivo* models that recapitulate various features of the disease despite most models artificially over-expressing a disease-linked protein. While there are bioinformatic tools available to predict if a gene variant may be pathogenic, one major challenge is actually verifying these in a model system with a method to confirm that changes to pathways related to neuronal damage and/or loss have occurred or are predicted to occur.

Using our proteogenomics workflow with *CCNF* gene variants, as a proof-of-concept, we expressed cyclin F into a HEK293 cell line given its utility to be grown easily in culture, withstand the transient transfection procedure, and express the transgene-of-interest with consistent high copy numbers without compromising cell viability. Label-free quantitative proteomics was used to identify and quantitate the proteome which has various advantages mostly because it is a cheaper and more suitable approach for the main purpose of identifying the effect of transgene expression on perturbed cellular pathways. Other quantitative proteomics techniques such as SILAC and TMT (Hedl et al., 2019) are much more accurate in their measurements of protein expression; however, they can often be costly and have limited benefit when determining bioinformatic predictions on perturbed cell pathways compared to LFQ proteomics. Given that the underlying biology for ALS, much

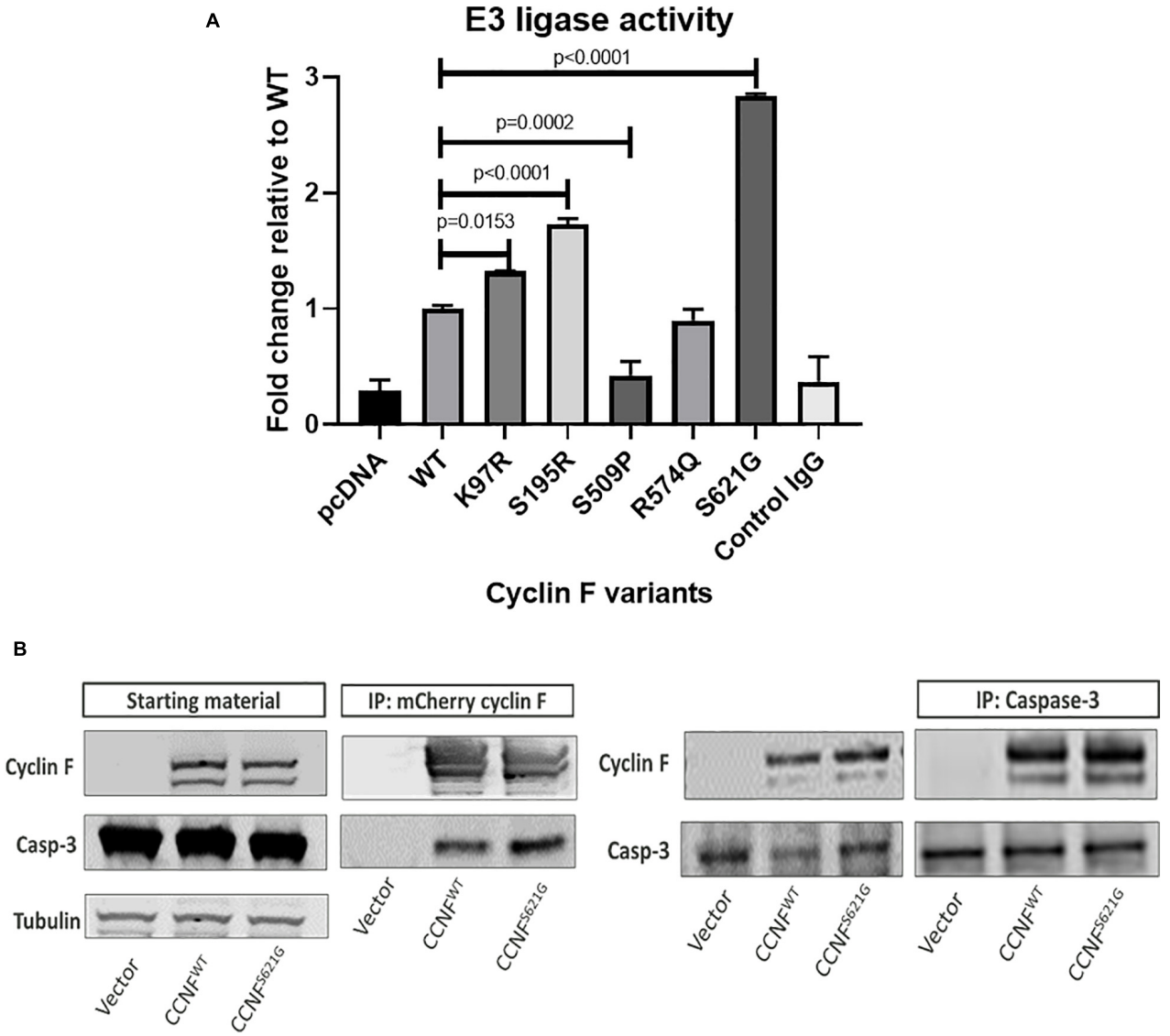

FIGURE 6 | (A) Lys48-ubiquitylation E3 ligase activity assay of immunoprecipitated cyclin F from cells expressing cyclin F wild-type, K97R, S195R, S509P, R574Q, and S621G. **(B)** Cyclin F interacts with caspase 3. HEK293 cells transfected with mCherry-cyclin F and immunoprecipitated (left blot) shows interaction with endogenous caspase-3. The reverse immunoprecipitation to enrich caspase-3 showed the same interaction with cyclin F (right blot).

like other neurodegenerative diseases, involves neuronal cell death, our criteria for determining whether a gene variant was pathogenic was to make predictions using our experimental proteomics data and bioinformatic tools (IPA) to establish if apoptosis pathways were activated or predicted to be activated. Other bioinformatic tools such as Reactome, MetaCore, and PathVisio can also be used to visualize -omics data matched to pathways (Cirillo et al., 2017). It should be noted that in our study, other molecular pathways were also predicted to be affected; however, our emphasis was to screen for gene variants and evaluate their effects on apoptotic pathways as a key feature of ALS.

Our proteomic findings provide us with confidence and experimental options with which to validate our *CCNF* gene variants (i) in various models (iPSCs and zebrafish) and (ii) for mechanistic studies (immunoblot analysis, enzymatic activity assays, and protein–protein interaction). Other validation experiments, such as GFPu reporter (Yang et al., 2015), FloIT (Whiten et al., 2016), live-cell imaging (Farrawell et al., 2018), and toxicity assays (McAlary et al., 2016), may also be considered to support predictions made from the proteomics experiments. Here, we demonstrated by proteomics analysis of iPSCs derived from fibroblasts of $CCNF^{S621G}$ patients that transfection of HEK293 cells was an appropriate model of apoptosis pathway activation as verified by immunoblot analysis of the Bad-Bax pathway. Measurements of aberrant neuron branching, cleaved caspase-3, and acridine orange staining for apoptotic cells in zebrafish reaffirmed the predicted activation

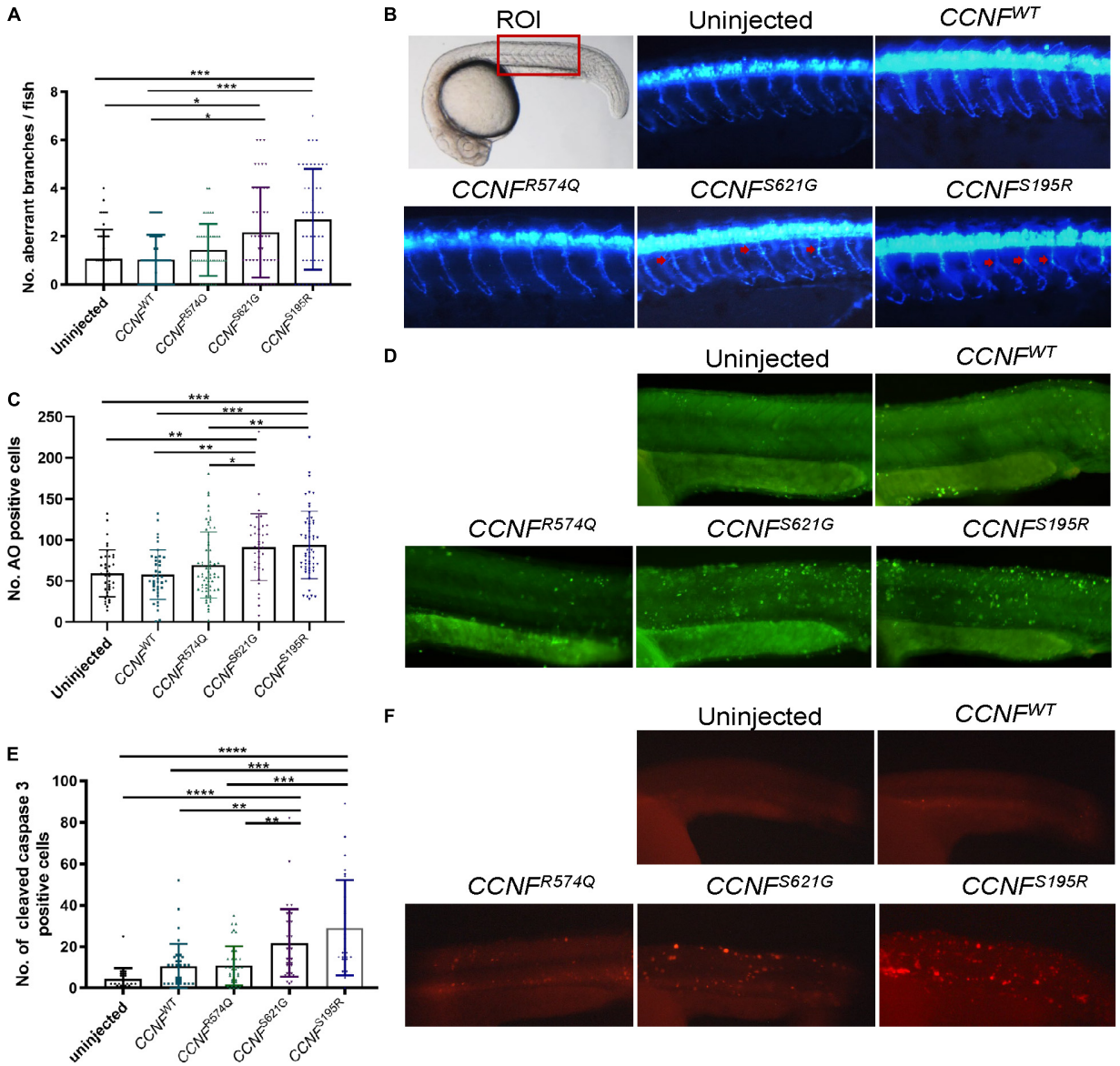

FIGURE 7 | Measurements of aberrant neuron branching and apoptosis activation in zebrafish injected with *CCNF* gene variants S621G, S195R, R574Q, and wild type. **(A)** Blinded analysis of the number of aberrant branches in zebrafish expressing cyclin F S621G and S195R, respectively, had 2.01-fold (p-value = 0.006, n = 42) and 2.4-fold (p-value = 0.0011, n = 46) more aberrantly branched motor neurons compared to the wild type (one-way ANOVA). Region of interest (ROI) in zebrafish used for imaging. **(B)** Representative images of zebrafish expressing blue fluorescent protein in motor neurons used to analyse primary motor axon branching. Examples of aberrant branching indicated by red arrows. **(C)** Cyclin F S621G and S195R had displayed increased cleaved caspase-3 activity by 2.08-fold (n = 39, p-value = 0.0029 and 2.79-fold (n = 28, p-value = 0.0004) (one-way ANOVA adjusted with Kruskal–Wallis test). (**D**) Representative images of live zebrafish staining with AO. **(E)** AO positive cells in S621G and S195R were 1.4-fold (p-value = 0.0496, n = 37) and 1.45-fold (p-value = 0.0115, n = 57) higher, respectively, compared to the wild type (one-way ANOVA). (**F**) Representative images of zebrafish immunostained with cleaved caspase-3 primary antibody. $^*p \leq 0.05$, $^{**}p \leq 0.01$, $^{***}p \leq 0.001$, $^{****}p \leq 0.0001$.

status of apoptosis from the initial proteomics screening of transfected HEK293 cells.

To provide some mechanistic insights, we demonstrate that *CCNF* gene variants found in patients with ALS had impaired cyclin F activity with increased E3 ligase activity in mutations K97R, S195R and S621G (gain-of-function), while the S509P mutation showed reduced/loss of E3 ligase activity (loss-of-function). Our non-ALS SNP mutation R574Q did not display any aberrant activity when compared to the wild-type control. This suggests that mutations in *CCNF* dysregulate the E3 ligase activity of the cyclin F protein. To correlate the proteomics screening which predicted apoptosis activation together with impairments to cyclin F E3 ligase activity, we hypothesized that cyclin F may be involved in the ubiquitylation of a key component in the apoptosis pathway. We performed immunoprecipitations of cyclin F and caspase-3, given that

it contained two R-X-L binding motifs and as one of the main players of apoptosis, and confirmed that these proteins interact endogenously. The interaction between these proteins may provide important insight into the pathogenesis of ALS and warrant further investigation.

Taken together, we have demonstrated the advantage of employing a proteogenomics workflow to screen new ALS gene mutations and determine their pathogenic potential. Our approach allows for rapid unbiased analysis which generates a wealth of biological information to enable new hypotheses and new disease models to be developed.

DATA AVAILABILITY STATEMENT

The mass spectrometry proteomics data and additional tables are available on the ProteomeXchange Consortium via the PRIDE (Perez-Riverol et al., 2019) partner repository with the dataset identifier PXD021793 and doi: 10.6019/PXD021793.

ETHICS STATEMENT

The studies involving human participants were reviewed and approved by the University of Wollongong Human Ethics Committee (HE 13/272). The patients/participants provided their written informed consent to participate in this study. The animal study was reviewed and approved by the Animal Ethics Committee and Biosafety Committee, Macquarie University (AEC Reference Nos. 2015/034 and 2017/019; NLRD 5201401007).

AUTHOR CONTRIBUTIONS

All authors were responsible for drafting, writing, and editing the manuscript, and all authors read and approved the final manuscript. FC, AD, AH, SR, JD, MV, and AL were responsible for carrying out the cell line and proteomics experiments, and bioinformatics analyses. CS, SM, and LO were responsible for generating the IPSC cells. AH, MW, ED, and ASL were responsible for all zebrafish work. JY, TC, TH, AW, SY, MM, BS, IB, and RC provided intellectual input and design of some of the experiments.

FUNDING

This work and related studies were supported by funding from Motor Neuron Disease Research Association (MNDRA) (Innovator grants IG1910, IG2029, and IG2036 and a Betty and John Laidlaw grant BLP1901), the Australian National Health and Medical Research Council (NHMRC) (Project grants GNT1124005, 1095215, 1107644, and 1146750 and RD Wright Career Development Fellowship GNT1140386), the Australian Rotary Health, the Canadian Natural Science and Engineering Research Council Doctoral Scholarship, the Australian Government Department of Education and Training RTP, QBI Research Higher Degree Top Up Scholarship, the Ross Maclean Fellowship, and the Brazil Family Program for Neurology. LO is supported by an NHMRC Boosting Dementia Research Leadership Fellowship (APP1135720). We wish to thank the Snow Foundation for their generous support towards establishing the Transgenic Zebrafish Facility at Macquarie University and continued support of the researchers.

ACKNOWLEDGMENTS

We would like to thank the patients, families, and donors for their support of the Macquarie University Centre for MND Research. We also wish to thank the Zebrafish Facility staff (past and present) for assistance in zebrafish care.

REFERENCES

Al-Chalabi, A., Calvo, A., Chio, A., Colville, S., Ellis, C. M., Hardiman, O., et al. (2014). Analysis of amyotrophic lateral sclerosis as a multistep process: a population-based modelling study. *Lancet Neurol.* 13, 1108–1113. doi: 10.1016/S1474-4422(14)70219-4

Arama, E., Bader, M., Rieckhof, G. E., and Steller, H. (2007). A ubiquitin ligase complex regulates caspase activation during sperm differentiation in Drosophila. *PLoS Biol.* 5:e251. doi: 10.1371/journal.pbio.0050251

Balez, R., Steiner, N., Engel, M., Munoz, S. S., Lum, J. S., Wu, Y., et al. (2016). Neuroprotective effects of apigenin against inflammation, neuronal excitability and apoptosis in an induced pluripotent stem cell model of Alzheimer's disease. *Sci. Rep.* 6:31450. doi: 10.1038/srep31450

Bax, M., Balez, R., Munoz, S. S., Do-Ha, D., Stevens, C. H., Berg, T., et al. (2019a). Generation and characterization of a human induced pluripotent stem cell line UOWi005-A from dermal fibroblasts derived from a CCNF(S621G) familial amyotrophic lateral sclerosis patient using mRNA reprogramming. *Stem Cell Res.* 40:101530. doi: 10.1016/j.scr.2019.101530

Bax, M., McKenna, J., Do-Ha, D., Stevens, C. H., Higginbottom, S., Balez, R., et al. (2019b). The ubiquitin proteasome system is a key regulator of pluripotent stem cell survival and motor neuron differentiation. *Cells* 8:581. doi: 10.3390/cells8060581

Branch, S. Y., Chen, C., Sharma, R., Lechleiter, J. D., Li, S., and Beckstead, M. J. (2016). Dopaminergic neurons exhibit an age-dependent decline in electrophysiological parameters in the mitopark mouse model of Parkinson's disease. *J. Neurosci.* 36, 4026–4037. doi: 10.1523/JNEUROSCI.1395-15.2016

Burlacu, A. (2003). Regulation of apoptosis by Bcl-2 family proteins. *J. Cell Mol. Med.* 7, 249–257. doi: 10.1111/j.1582-4934.2003.tb00225.x

Chen, L., Willis, S. N., Wei, A., Smith, B. J., Fletcher, J. I., Hinds, M. G., et al. (2005). Differential targeting of prosurvival Bcl-2 proteins by their BH3-only ligands allows complementary apoptotic function. *Mol. Cell* 17, 393–403. doi: 10.1016/j.molcel.2004.12.030

Chen, Y. S., and Qiu, X. B. (2013). Ubiquitin at the crossroad of cell death and survival. *Chin. J. Cancer* 32, 640–647. doi: 10.5732/cjc.012.10283

Choi, Y. E., Butterworth, M., Malladi, S., Duckett, C. S., Cohen, G. M., and Bratton, S. B. (2009). The E3 ubiquitin ligase cIAP1 binds and ubiquitinates caspase-3 and -7 via unique mechanisms at distinct steps in their processing. *J. Biol. Chem.* 284, 12772–12782. doi: 10.1074/jbc.M807550200

Cirillo, E., Parnell, L. D., and Evelo, C. T. (2017). A review of pathway-based analysis tools that visualize genetic variants. *Front. Genet.* 8:174. doi: 10.3389/fgene.2017.00174

Ciryam, P., Lambert-Smith, I. A., Bean, D. M., Freer, R., Cid, F., Tartaglia, G. G., et al. (2017). Spinal motor neuron protein supersaturation patterns are

associated with inclusion body formation in ALS. *Proc. Natl. Acad. Sci. U.S.A.* 114, E3935–E3943. doi: 10.1073/pnas.1613854114

Clijsters, L., Hoencamp, C., Calis, J. J. A., Marzio, A., Handgraaf, S. M., Cuitino, M. C., et al. (2019). Cyclin F controls cell-cycle transcriptional outputs by directing the degradation of the three activator E2Fs. *Mol. Cell* 74, 1264–1277.e7. doi: 10.1016/j.molcel.2019.04.010

Cohen, T. J., Hwang, A. W., Restrepo, C. R., Yuan, C. X., Trojanowski, J. Q., and Lee, V. M. (2015). An acetylation switch controls TDP-43 function and aggregation propensity. *Nat. Commun.* 6:5845. doi: 10.1038/ncomms6845

D'Angiolella, V., Donato, V., Forrester, F. M., Jeong, Y. T., Pellacani, C., Kudo, Y., et al. (2012). Cyclin F-mediated degradation of ribonucleotide reductase M2 controls genome integrity and DNA repair. *Cell* 149, 1023–1034. doi: 10.1016/j.cell.2012.03.043

D'Angiolella, V., Donato, V., Vijayakumar, S., Saraf, A., Florens, L., Washburn, M. P., et al. (2010). SCF(Cyclin F) controls centrosome homeostasis and mitotic fidelity through CP110 degradation. *Nature* 466, 138–142. doi: 10.1038/nature09140

Dankert, J. F., Rona, G., Clijsters, L., Geter, P., Skaar, J. R., Bermudez-Hernandez, K., et al. (2016). Cyclin F-mediated degradation of SLBP limits H2A.X accumulation and apoptosis upon genotoxic stress in G2. *Mol. Cell* 64, 507–519. doi: 10.1016/j.molcel.2016.09.010

Don, E. K., Formella, I., Badrock, A. P., Hall, T. E., Morsch, M., Hortle, E., et al. (2017). A Tol2 gateway-compatible toolbox for the study of the nervous system and neurodegenerative disease. *Zebrafish* 14, 69–72. doi: 10.1089/zeb.2016.1321

Duan, W., Li, X., Shi, J., Guo, Y., Li, Z., and Li, C. (2010). Mutant TAR DNA-binding protein-43 induces oxidative injury in motor neuron-like cell. *Neuroscience* 169, 1621–1629. doi: 10.1016/j.neuroscience.2010.06.018

Elia, A. E., Boardman, A. P., Wang, D. C., Huttlin, E. L., Everley, R. A., Dephoure, N., et al. (2015). Quantitative proteomic atlas of ubiquitination and acetylation in the DNA damage response. *Mol. Cell* 59, 867–881. doi: 10.1016/j.molcel.2015.05.006

Emanuele, M. J., Elia, A. E., Xu, Q., Thoma, C. R., Izhar, L., Leng, Y., et al. (2011). Global identification of modular cullin-RING ligase substrates. *Cell* 147, 459–474. doi: 10.1016/j.cell.2011.09.019

Farrawell, N. E., Lambert-Smith, I., Mitchell, K., McKenna, J., McAlary, L., Ciryam, P., et al. (2018). SOD1(A4V) aggregation alters ubiquitin homeostasis in a cell model of ALS. *J. Cell Sci.* 131:jcs209122. doi: 10.1242/jcs.209122

Foran, E., and Trotti, D. (2009). Glutamate transporters and the excitotoxic path to motor neuron degeneration in amyotrophic lateral sclerosis. *Antioxid. Redox Signal.* 11, 1587–1602. doi: 10.1089/ars.2009.2444

Formella, I., Svahn, A. J., Radford, R. A. W., Don, E. K., Cole, N. J., Hogan, A., et al. (2018). Real-time visualization of oxidative stress-mediated neurodegeneration of individual spinal motor neurons *in vivo*. *Redox Biol.* 19, 226–234. doi: 10.1016/j.redox.2018.08.011

Galper, J., Rayner, S. L., Hogan, A. L., Fifita, J. A., Lee, A., Chung, R. S., et al. (2017). Cyclin F: a component of an E3 ubiquitin ligase complex with roles in neurodegeneration and cancer. *Int. J. Biochem. Cell Biol.* 89, 216–220. doi: 10.1016/j.biocel.2017.06.011

Hasegawa, M., Arai, T., Nonaka, T., Kametani, F., Yoshida, M., Hashizume, Y., et al. (2008). Phosphorylated TDP-43 in frontotemporal lobar degeneration and amyotrophic lateral sclerosis. *Ann. Neurol.* 64, 60–70. doi: 10.1002/ana.21425

Hedl, T. J., San Gil, R., Cheng, F., Rayner, S. L., Davidson, J. M., De Luca, A., et al. (2019). Proteomics approaches for biomarker and drug target discovery in ALS and FTD. *Front. Neurosci.* 13:548. doi: 10.3389/fnins.2019.00548

Hogan, A. L., Don, E. K., Rayner, S. L., Lee, A., Laird, A. S., Watchon, M., et al. (2017). Expression of ALS/FTD-linked mutant CCNF in zebrafish leads to increased cell death in the spinal cord and an aberrant motor phenotype. *Hum. Mol. Genet.* 26, 2616–2626. doi: 10.1093/hmg/ddx136

Jaffe, J. D., Berg, H. C., and Church, G. M. (2004). Proteogenomic mapping as a complementary method to perform genome annotation. *Proteomics* 4, 59–77. doi: 10.1002/pmic.200300511

Jaronen, M., Goldsteins, G., and Koistinaho, J. (2014). ER stress and unfolded protein response in amyotrophic lateral sclerosis-a controversial role of protein disulphide isomerase. *Front. Cell Neurosci.* 8:402. doi: 10.3389/fncel.2014.00402

Kale, J., Osterlund, E. J., and Andrews, D. W. (2018). BCL-2 family proteins: changing partners in the dance towards death. *Cell Death Differ.* 25, 65–80. doi: 10.1038/cdd.2017.186

Kalkavan, H., and Green, D. R. (2018). MOMP, cell suicide as a BCL-2 family business. *Cell Death Differ.* 25, 46–55. doi: 10.1038/cdd.2017.179

King, A. E., Woodhouse, A., Kirkcaldie, M. T., and Vickers, J. C. (2016). Excitotoxicity in ALS: overstimulation, or overreaction? *Exp. Neurol.* 275(Pt 1), 162–171. doi: 10.1016/j.expneurol.2015.09.019

Klumpp, S., and Krieglstein, J. (2002). Serine/threonine protein phosphatases in apoptosis. *Curr. Opin. Pharmacol.* 2, 458–462. doi: 10.1016/s1471-4892(02)00176-5

Lattante, S., Marangi, G., Doronzio, P. N., Conte, A., Bisogni, G., Zollino, M., et al. (2020). High-throughput genetic testing in ALS: the challenging path of variant classification considering the ACMG guidelines. *Genes (Basel)* 11:1123. doi: 10.3390/genes11101123

Lee, A., Rayner, S. L., De Luca, A., Gwee, S., Morsch, M., Sundaramoorthy, V., et al. (2017a). Casein Kinase II phosphorylation of cyclin F at Serine 621 regulates the Lys48-ubiquitylation E3 ligase activity of the SCF(cyclin F) complex. *Open Biol.* 7:170058.

Lee, A., Rayner, S. L., Gwee, S., De Luca, A., Shahherydari, H., Sundaramoorthy, V., et al. (2017b). Pathogenic mutation in the ALS/FTD gene, CCNF, causes elevated Lys48-linked ubiquitylation and defective autophagy. *Cell. Mol. Life Sci.* 75, 335–354.

Lemmens, R., Van Hoecke, A., Hersmus, N., Geelen, V., D'Hollander, I., Thijs, V., et al. (2007). Overexpression of mutant superoxide dismutase 1 causes a motor axonopathy in the zebrafish. *Hum. Mol. Genet.* 16, 2359–2365. doi: 10.1093/hmg/ddm193

Ling, S. C., Polymenidou, M., and Cleveland, D. W. (2013). Converging mechanisms in ALS and FTD: disrupted RNA and protein homeostasis. *Neuron* 79, 416–438. doi: 10.1016/j.neuron.2013.07.033

Liu, J., and Wang, F. (2017). Role of neuroinflammation in amyotrophic lateral sclerosis: cellular mechanisms and therapeutic implications. *Front. Immunol.* 8:1005. doi: 10.3389/fimmu.2017.01005

McAlary, L., Aquilina, J. A., and Yerbury, J. J. (2016). Susceptibility of mutant SOD1 to form a destabilized monomer predicts cellular aggregation and toxicity but not *In vitro* aggregation propensity. *Front. Neurosci.* 10:499. doi: 10.3389/fnins.2016.00499

McAlary, L., Plotkin, S. S., Yerbury, J. J., and Cashman, N. R. (2019). Prion-like propagation of protein misfolding and aggregation in amyotrophic lateral sclerosis. *Front. Mol. Neurosci.* 12:262. doi:10.3389/fnmol.2019.00262

Mejzini, R., Flynn, L. L., Pitout, I. L., Fletcher, S., Wilton, S. D., and Akkari, P. A. (2019). ALS genetics, mechanisms, and therapeutics: where are we now? *Front. Neurosci.* 13:1310. doi: 10.3389/fnins.2019.01310

Mi, H., Muruganujan, A., Ebert, D., Huang, X., and Thomas, P. D. (2019). PANTHER version 14: more genomes, a new PANTHER GO-slim and improvements in enrichment analysis tools. *Nucleic Acids Res.* 47(D1), D419–D426. doi: 10.1093/nar/gky1038

Mitchell, J. C., McGoldrick, P., Vance, C., Hortobagyi, T., Sreedharan, J., Rogelj, B., et al. (2013). Overexpression of human wild-type FUS causes progressive motor neuron degeneration in an age- and dose-dependent fashion. *Acta Neuropathol.* 125, 273–288. doi: 10.1007/s00401-012-1043-z

Mitra, A., Mishra, L., and Li, S. (2013). Technologies for deriving primary tumor cells for use in personalized cancer therapy. *Trends Biotechnol.* 31, 347–354. doi: 10.1016/j.tibtech.2013.03.006

Morrice, J. R., Gregory-Evans, C. Y., and Shaw, C. A. (2018). Animal models of amyotrophic lateral sclerosis: a comparison of model validity. *Neural. Regen. Res.* 13, 2050–2054. doi: 10.4103/1673-5374.241445

Morsch, M., Radford, R. A., Don, E. K., Lee, A., Hortle, E., Cole, N. J., et al. (2017). Triggering cell stress and death using conventional UV laser confocal microscopy. *J. Vis. Exp.* 120:54983. doi: 10.3791/54983

Nakayama, K. I., and Nakayama, K. (2006). Ubiquitin ligases: cell-cycle control and cancer. *Nat. Rev. Cancer* 6, 369–381. doi: 10.1038/nrc1881

Nesvizhskii, A. I. (2014). Proteogenomics: concepts, applications and computational strategies. *Nat. Methods* 11, 1114–1125. doi: 10.1038/nmeth.3144

Neumann, M., Kwong, L. K., Sampathu, D. M., Trojanowski, J. Q., and Lee, V. M. (2007). TDP-43 proteinopathy in frontotemporal lobar degeneration and amyotrophic lateral sclerosis: protein misfolding diseases without amyloidosis. *Arch. Neurol.* 64, 1388–1394. doi: 10.1001/archneur.64.10.1388

Neumann, M., Sampathu, D. M., Kwong, L. K., Truax, A. C., Micsenyi, M. C., Chou, T. T., et al. (2006). Ubiquitinated TDP-43 in frontotemporal lobar degeneration and amyotrophic lateral sclerosis. *Science* 314, 130–133. doi: 10.1126/science.1134108

Nguyen, H. P., Van Broeckhoven, C., and van der Zee, J. (2018). ALS genes in the genomic era and their implications for FTD. *Trends Genet.* 34, 404–423. doi: 10.1016/j.tig.2018.03.001

Olesen, M. N., Wuolikainen, A., Nilsson, A. C., Wirenfeldt, M., Forsberg, K., Madsen, J. S., et al. (2020). Inflammatory profiles relate to survival in subtypes of amyotrophic lateral sclerosis. *Neurol. Neuroimmunol. Neuroinflamm.* 7:e697. doi: 10.1212/NXI.0000000000000697

Parrish, A. B., Freel, C. D., and Kornbluth, S. (2013). Cellular mechanisms controlling caspase activation and function. *Cold Spring Harb. Perspect. Biol.* 5:a008672. doi: 10.1101/cshperspect.a008672

Payne, C. M., Bernstein, C., and Bernstein, H. (1995). Apoptosis overview emphasizing the role of oxidative stress, DNA damage and signal-transduction pathways. *Leuk Lymphoma* 19, 43–93. doi: 10.3109/10428199509059662

Perez-Riverol, Y., Csordas, A., Bai, J., Bernal-Llinares, M., Hewapathirana, S., Kundu, D. J., et al. (2019). The PRIDE database and related tools and resources in 2019: improving support for quantification data. *Nucleic Acids Res.* 47(D1), D442–D450. doi: 10.1093/nar/gky1106

Pollari, E., Goldsteins, G., Bart, G., Koistinaho, J., and Giniatullin, R. (2014). The role of oxidative stress in degeneration of the neuromuscular junction in amyotrophic lateral sclerosis. *Front. Cell Neurosci.* 8:131. doi: 10.3389/fncel.2014.00131

Prell, T., Stubendorff, B., Le, T. T., Gaur, N., Tadic, V., Rodiger, A., et al. (2019). Reaction to endoplasmic reticulum stress via ATF6 in amyotrophic lateral sclerosis deteriorates with aging. *Front. Aging Neurosci.* 11:5. doi: 10.3389/fnagi.2019.00005

Rayner, S. L., Morsch, M., Molloy, M. P., Shi, B., Chung, R., and Lee, A. (2019). Using proteomics to identify ubiquitin ligase-substrate pairs: how novel methods may unveil therapeutic targets for neurodegenerative diseases. *Cell. Mol. Life Sci.* 76, 2499–2510. doi: 10.1007/s00018-019-03082-9

Sabatelli, M., Zollino, M., Luigetti, M., Grande, A. D., Lattante, S., Marangi, G., et al. (2011). Uncovering amyotrophic lateral sclerosis phenotypes: clinical features and long-term follow-up of upper motor neuron-dominant ALS. *Amyotroph. Lateral. Scler.* 12, 278–282. doi: 10.3109/17482968.2011.580849

Shahheydari, H., Ragagnin, A., Walker, A. K., Toth, R. P., Vidal, M., Jagaraj, C. J., et al. (2017). Protein quality control and the amyotrophic lateral sclerosis/frontotemporal dementia continuum. *Front. Mol. Neurosci.* 10:119. doi: 10.3389/fnmol.2017.00119

Shamas-Din, A., Kale, J., Leber, B., and Andrews, D. W. (2013). Mechanisms of action of Bcl-2 family proteins. *Cold Spring Harb. Perspect. Biol.* 5:a008714. doi: 10.1101/cshperspect.a008714

Svahn, A. J., Don, E. K., Badrock, A. P., Cole, N. J., Graeber, M. B., Yerbury, J. J., et al. (2018). Nucleo-cytoplasmic transport of TDP-43 studied in real time: impaired microglia function leads to axonal spreading of TDP-43 in degenerating motor neurons. *Acta Neuropathol.* 136, 445–459. doi: 10.1007/s00401-018-1875-2

Tarr, I. S., McCann, E. P., Benyamin, B., Peters, T. J., Twine, N. A., Zhang, K. Y., et al. (2019). Monozygotic twins and triplets discordant for amyotrophic lateral sclerosis display differential methylation and gene expression. *Sci. Rep.* 9:8254. doi: 10.1038/s41598-019-44765-4

Van Damme, P., Robberecht, W., and Van Den Bosch, L. (2017). Modelling amyotrophic lateral sclerosis: progress and possibilities. *Dis. Model Mech.* 10, 537–549. doi: 10.1242/dmm.029058

Vance, C., Rogelj, B., Hortobagyi, T., De Vos, K. J., Nishimura, A. L., Sreedharan, J., et al. (2009). Mutations in FUS, an RNA processing protein, cause familial amyotrophic lateral sclerosis type 6. *Science* 323, 1208–1211. doi: 10.1126/science.1165942

Visscher, P. M., Wray, N. R., Zhang, Q., Sklar, P., McCarthy, M. I., Brown, M. A., et al. (2017). 10 years of GWAS discovery: biology, function, and translation. *Am. J. Hum. Genet.* 101, 5–22. doi: 10.1016/j.ajhg.2017.06.005

Vucic, S., Higashihara, M., Sobue, G., Atsuta, N., Doi, Y., Kuwabara, S., et al. (2020). ALS is a multistep process in South Korean, Japanese, and Australian patients. *Neurology* 94, e1657–e1663. doi: 10.1212/WNL.0000000000009015

Walker, A. K., and Atkin, J. D. (2011). Stress signaling from the endoplasmic reticulum: a central player in the pathogenesis of amyotrophic lateral sclerosis. *IUBMB Life* 63, 754–763. doi: 10.1002/iub.520

Walter, D., Hoffmann, S., Komseli, E. S., Rappsilber, J., Gorgoulis, V., and Sorensen, C. S. (2016). SCF(Cyclin F)-dependent degradation of CDC6 suppresses DNA re-replication. *Nat. Commun.* 7:10530. doi: 10.1038/ncomms10530

Westerfield, M. (2007). *The Zebrafish Book : a Guide for the Laboratory use of Zebrafish (Danio Rerio)*. Eugene, OR: University. of Oregon Press.

Whiten, D. R., San Gil, R., McAlary, L., Yerbury, J. J., Ecroyd, H., and Wilson, M. R. (2016). Rapid flow cytometric measurement of protein inclusions and nuclear trafficking. *Sci. Rep.* 6:31138. doi: 10.1038/srep31138

Williams, K. L., Topp, S., Yang, S., Smith, B., Fifita, J. A., Warraich, S. T., et al. (2016). CCNF mutations in amyotrophic lateral sclerosis and frontotemporal dementia. *Nat. Commun.* 7:11253. doi: 10.1038/ncomms11253

Woollacott, I. O., and Rohrer, J. D. (2016). The clinical spectrum of sporadic and familial forms of frontotemporal dementia. *J. Neurochem.* 138 Suppl 1, 6–31. doi: 10.1111/jnc.13654

Yada, E., Wada, S., Yoshida, S., and Sasada, T. (2018). Use of patient-derived xenograft mouse models in cancer research and treatment. *Future Sci. OA* 4:FSO271. doi: 10.4155/fsoa-2017-0136

Yang, S., Zhang, K. Y., Kariawasam, R., Bax, M., Fifita, J. A., Ooi, L., et al. (2015). Evaluation of skin fibroblasts from amyotrophic lateral sclerosis patients for the rapid study of pathological features. *Neurotox Res.* 28, 138–146. doi: 10.1007/s12640-015-9532-1

Yerbury, J. J., Farrawell, N. E., and McAlary, L. (2020). Proteome homeostasis dysfunction: a unifying principle in ALS pathogenesis. *Trends Neurosci.* 43, 274–284. doi: 10.1016/j.tins.2020.03.002

Yu, Y., Nakagawa, T., Morohoshi, A., Nakagawa, M., Ishida, N., Suzuki, N., et al. (2019). Pathogenic mutations in the ALS gene CCNF cause cytoplasmic mislocalization of Cyclin F and elevated VCP ATPase activity. *Hum. Mol. Genet.* 28, 3486–3497. doi: 10.1093/hmg/ddz119

Zhang, K., Daigle, J. G., Cunningham, K. M., Coyne, A. N., Ruan, K., Grima, J. C., et al. (2018). Stress granule assembly disrupts nucleocytoplasmic transport. *Cell* 173, 958–971.e17. doi: 10.1016/j.cell.2018.03.025

Zhang, K., Donnelly, C. J., Haeusler, A. R., Grima, J. C., Machamer, J. B., Steinwald, P., et al. (2015). The C9orf72 repeat expansion disrupts nucleocytoplasmic transport. *Nature* 525, 56–61. doi: 10.1038/nature14973

Conflict of Interest: The authors declare that the research was conducted in the absence of any commercial or financial relationships that could be construed as a potential conflict of interest.

frontiers in Molecular Neuroscience

REVIEW
published: 09 June 2021
doi: 10.3389/fnmol.2021.678837

Proteomic Approaches to Study Cysteine Oxidation: Applications in Neurodegenerative Diseases

Trong Khoa Pham[1,2], Weronika A. Buczek[2], Richard J. Mead[1†], Pamela J. Shaw[1†] and Mark O. Collins[2†]*

[1] Sheffield Institute for Translational Neuroscience (SITraN), University of Sheffield, Sheffield, United Kingdom, [2] Department of Biomedical Science, University of Sheffield, Sheffield, United Kingdom

OPEN ACCESS

Edited by:
Andrei Surguchov, University of Kansas Medical Center, United States

Reviewed by:
Irina G. Sourgoutcheva, University of Kansas Medical Center, United States
Jennifer Geddes-McAlister, University of Guelph, Canada

***Correspondence:**
Mark O. Collins
mark.collins@sheffield.ac.uk

† These authors have contributed equally to this work and share last authorship

Specialty section:
This article was submitted to Molecular Signalling and Pathways, a section of the journal Frontiers in Molecular Neuroscience

Received: *10 March 2021*
Accepted: *03 May 2021*
Published: *09 June 2021*

Citation:
Pham TK, Buczek WA, Mead RJ, Shaw PJ and Collins MO (2021) Proteomic Approaches to Study Cysteine Oxidation: Applications in Neurodegenerative Diseases. Front. Mol. Neurosci. 14:678837. doi: 10.3389/fnmol.2021.678837

Oxidative stress appears to be a key feature of many neurodegenerative diseases either as a cause or consequence of disease. A range of molecules are subject to oxidation, but in particular, proteins are an important target and measure of oxidative stress. Proteins are subject to a range of oxidative modifications at reactive cysteine residues, and depending on the level of oxidative stress, these modifications may be reversible or irreversible. A range of experimental approaches has been developed to characterize cysteine oxidation of proteins. In particular, mass spectrometry-based proteomic methods have emerged as a powerful means to identify and quantify cysteine oxidation sites on a proteome scale; however, their application to study neurodegenerative diseases is limited to date. Here we provide a guide to these approaches and highlight the under-exploited utility of these methods to measure oxidative stress in neurodegenerative diseases for biomarker discovery, target engagement and to understand disease mechanisms.

Keywords: oxidation, oxidative stress, proteomics, neurodegenerative disease, amyotrophic lateral sclerosis (ALS), Alzheimer's disease

INTRODUCTION

Post-translational modifications (PTMs) of cysteine (Cys) residues play a crucial role in protein function and cellular homeostasis. In particular, cysteine residues are sensitive to oxidative stress and are subject to a range of reversible and irreversible oxidations. Many mass spectrometry (MS)-based proteomics approaches have been developed to identify and measure levels of oxidized cysteine residues (Oxi-Cys) in a range of biological systems. These quantitative proteomics approaches include the analysis of reversible, irreversible and specific sub-types of Oxi-Cys PTMs. Oxidative stress is a pathological feature of a range of neurodegenerative diseases, but proteomics methods to study Oxi-Cys PTMs in this context are underexploited. In this review, we survey state-of-the-art approaches for Oxi-Cys PTMs analysis to guide researchers who wish to exploit proteomics to probe cysteine oxidation in neurodegenerative disease.

Cysteine Oxidation

Among four common sulfur-containing amino acids, homocysteine, taurine, methionine and cysteine, only the latter two are incorporated into proteins. Although both of these two play essential roles in cell metabolism, cysteine plays a crucial role in the structure of proteins and protein-folding pathways because of its ability to form intra- (inside a protein) and inter-chain (different proteins) linkages with other cysteine residues (Brosnan and Brosnan, 2006). Only 2.3% of the human proteome encodes Cys residues, but their activities vary depending on their states, mainly reduced or oxidized forms, within proteins. Many attempts have been performed to characterize oxidation states of specific Cys residues, but success has been limited because of the low abundance of oxidatively modified Cys in biological systems and the diversity of its oxidative products. The oxidation of other amino acids also plays an important role in neurodegenerative diseases (such as methionine and tyrosine oxidation) (Shi and Carroll, 2020), but they are not the focus of this review.

There are two primary levels of Oxi-Cys residues in proteins depending on the level of cellular oxidative stress, reversible and irreversible Cys oxidations. The reversible oxidation of Cys, such as *S*-nitrosylation (*S*-NO), *S*-sulfenylation (*S*-OH), *S*-glutathionylation (*S*-SG), and disulphide formation (*S*–*S*) (**Figure 1**), is found under low oxidative conditions and acts to modulate protein function (Dalle-Donne et al., 2005). However, at higher levels of oxidative stress, the oxidative state of Cys is elevated and harder to reverse (*S*-sulfinylation, *S*-O_2H) or becomes irreversible (*S*-sulfonylation, *S*-O_3H, or *S*-sulfinylation) (**Figure 1**), causing the loss of protein function (Murray and Eyk, 2012). The determination of dynamic changes in site-specific Cys oxidation will provide vital information to understand the distribution of redox balance states in neurodegenerative diseases and to characterize dysregulated oxidation in patients compared to healthy control (HC) groups. The reversible oxidation states of Cys may also reflect the fluctuations of cellular oxidation status, and both reversible and irreversible oxidation status of Cys may serve as biomarkers of neurodegenerative diseases associated with oxidative stress.

Oxidative Stress in Neurodegeneration

Multiple lines of evidence point to a role for elevated oxidative stress in driving neuronal degeneration in neurodegenerative diseases such as Alzheimer's disease (AD) (Markesbery and Carney, 1999), Parkinson's disease (PD) (Puspita et al., 2017) and amyotrophic lateral sclerosis (ALS) (Barber and Shaw, 2010). We are still unsure whether oxidative stress is a cause or consequence of neuronal degeneration. In addition, many therapeutic approaches have been tested in clinical studies in an attempt to limit pro-oxidative mediated neuronal injury. However, few of these approaches, except Edaravone for ALS (Group, 2017), have been successful.

Oxidative stress has broadly been considered an imbalance in pro and anti-oxidant processes, leading to elevated pro-oxidant activity in cells, leading to cellular injury and death (Guo et al., 2013; Song et al., 2021). For example, a common denominator in neurodegenerative diseases is the presence of oxidatively damaged macromolecules in neurons and glia and other biosamples. However, oxidative stress is probably better understood as a disruption of the interplay between different inter-related cellular redox systems and their control (Jones, 2006). Therefore, to understand and therapeutically modulate redox control and signaling in neurodegeneration, it is critical to measure the status of these different redox systems. Cysteine redox cycling is a key component of these systems, and the study of this pathway has been relatively neglected to date. However, it is eminently accessible *via* proteomic approaches, enabling a global view of cysteine redox regulation.

The refinement of measures of complex redox biology in the central nervous system (CNS) directly in patients, as disease progresses, would greatly facilitate both the understanding of the role that redox regulation plays in neurodegeneration, but importantly would also enable identification of novel biomarkers for evaluating therapeutic interventions targeted at oxidative stress. So-called target engagement biomarkers are considered critical in the development of novel therapeutics (Durham and Blanco, 2015).

The misfolding and aggregation of amyloid-beta (Aβ) and tau in AD and superoxide dismutase type-1 (SOD1) in ALS results in a progressive loss of specific populations of neurons that is strongly associated with mitochondrial dysfunction,

Abbreviations: 2-D gel, two-dimensional gel; 2-ME, 2-mercaptoethanol; AD, Alzheimer's disease; ALS, amyotrophic lateral sclerosis; Aβ, amyloid-beta; Biotin–HPDP, *N*-[6-(biotinamido) hexyl]-3′-(2′-pyridyldithio) propionamide; BME, β-mercaptoethanol; BST, biotin switch technique; CAM, carbamidomethyl group; CBK, photocaged bromomethyl ketone; CIK4, iodomethyl; CNS, central nervous system; CSF, cerebrospinal fluid; Ctrl, control; CuAAC, copper(I)-catalyzed azide–alkyne cycloaddition; Cys, cysteine; CysTMT, cysteine-reactive tandem mass tag; CysTMTRAQ, cysteine-reactive tandem mass tag and isobaric tags for relative and absolute quantitation; DDA, data-dependent acquisition; DIA, data-independent acquisition; DTBA, dithiobutylamine; DTT, dithiothreitol; EBX, ethynyl benziodoxolone; ELISA, enzyme-linked immunosorbent assay; ERW3, fluoronitrobenzene; ESI, electrospray ionization; FFI, fatal familial insomnia; FTD, frontotemporal dementia; HC, healthy control; HPDP, *N*-[6-(biotinamido) hexyl]-3′-(2′-pyridyldithio) propionamide (biotin–HPDP); HRMS1, high resolution MS1; IA, immunoaffinity; IAA, iodoacetic acid; IAM, iodoacetamide; iCAT, isotope-coded affinity tag; iodoTMT, iodoacetyl isobaric tandem mass tags; IPL, inferior parietal lobule; isoTOP-ABPP, isotopic tandem orthogonal proteolysis-activity-based protein profiling; iTRAQ, isobaric tags for relative and absolute quantitation; LFQ, label free quantification; MCI, mild cognitive impairment; MMTS, methanethiosulfonate; MND, motor neuron disease; MnSOD, manganese superoxide dismutase; MRM, multiple reaction monitoring; MS, mass spectrometry; MS, multiple sclerosis; MTRP, multiplexed thiol reactivity profiling; NaAsc, sodium ascorbate; ND, neurodegenerative diseases; NEM, *N*-ethylmaleimide; NLRP3, NOD-like receptor family, pyrin domain containing 3; NMDA, *N*-methyl-D-aspartate; NOD, nucleotide-binding and oligomerization domain; NPH, normal pressure hydrocephalus; NPM, *N*-propargylmaleimide; OxcyscPILOT, oxidized cysteine-selective combined precursor isotopic labeling and isobaric tagging; Oxi-Cys, oxidative cysteine; PD, Parkinson's disease; PRM, parallel reaction monitoring; p-SRM, pseudo-selected reaction monitoring; PTM, post-translational modification; RAC, resin-assisted capture; RB2, chloropyridine; ROS, reactive oxygen species; sCJD, Creutzfeldt–Jakob disease; SDS–PAGE, sodium dodecyl sulfate –polyacrylamide-gel electrophoresis; SH, sulfhydryl; SILAC, stable isotope labeling by amino acids in cell culture; *S*-NO, *S*-nitrosylation; *SNO*TRAP, *S*-NO trapping by triaryl phosphine; *S*-O_2H, *S*-sulfinylation; *S*-O_3H, *S*-sulfonylation; SOD1, superoxide dismutase type-1; *S*-OH, *S*-sulfenylation; SPS, synchronous precursor selection; SRM, selected reaction monitoring; *S*-SG, *S*-glutathionylation; SWATH-MS, sequential window acquisition of all theoretical mass spectra; TCA, trichloroacetic acid; TCEP, Tris(2-carboxyethyl)phosphine; TEV, tobacco etch virus; TMT, isobaric tandem mass tags; TOF, time-of-flight; TOP, tandem orthogonal proteolysis; TTP, transthyretin; UPLC, ultra performance liquid chromatography; XIC, extracted ion chromatogram.

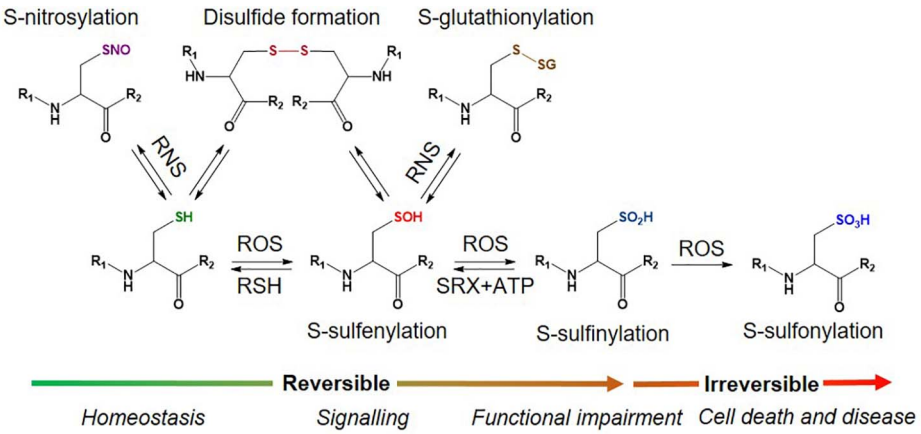

FIGURE 1 | Different types of Oxy-Cys PTMs occurring in proteins.

neuroinflammation and excitotoxicity (Andersen, 2004; Guo et al., 2013; Song et al., 2021). These pathological processes lead to increased generation of free radicals, redox imbalance which further impairs cellular function, leading to neuronal cell death.

Protein aggregates are formed by oxidatively altered proteins that misfold and accumulate. Multiple PTMs may contribute to protein misfolding; one of these is Cys oxidation (Olzscha, 2019). Several mutations in the Cu/Zn superoxide dismutase gene (SOD1) cause familial amyotrophic lateral sclerosis (FALS). There is also evidence to suggest that oxidized wild-type SOD1 adopts a conformation similar to mutant SOD1, which could be pathogenic in sporadic ALS (Bosco et al., 2010). In another study, the oxidation of C_{111} on SOD1 *via* glutathionylation (*S*-SG) was found to decrease the stabilization of SOD1 dimer, increasing the potential for the unfolding of the monomer and subsequent aggregation and, as a result, leads to loss of SOD1 activity and promotion of cell death (Redler et al., 2011). Peroxiredoxins (Prxs), enzymes that neutralize reactive oxygen/nitrogen species, have been implicated in several neurodegenerative diseases, including AD and PD. They act to reduce peroxynitrite and other hydroperoxides through a redox-sensitive Cys within their active sites; they reduce peroxide substrates *via* the formation of intramolecular disulphide bonds or oxidation to sulfinic acid or sulfonic acid (Hall et al., 2009). The protective function of PRDX2, the most abundant peroxiredoxin in neurons, against oxidative stress is inhibited by oxidation of the enzyme itself. *S*-NO of PRDX2 at the active-site residues Cys 51 and 172 inhibits the enzyme activity, the level of which is increased in human PD brains (Fang et al., 2007).

In AD, *S*-NO can have both neuroprotective and neurotoxic functions (Zhao et al., 2015). For example, *S*-NO of the *N*-methyl-D-aspartate (NMDA) receptor inhibits its overactivation and promotes neuronal survival (Nakamura and Lipton, 2007). In contrast, many proteins that are key to normal synaptic function are aberrantly *S*-nitrosylated in AD, which results in synaptic damage and neurodegeneration (Nakamura et al., 2013). Therefore, targeting protein *S*-NO can prove useful as a new therapeutic intervention for AD neurodegeneration.

Neurons are particularly susceptible to oxidative stress because of the high energy demand, which depends heavily on robust mitochondrial function. Under physiological conditions, mitochondria serve as a primary source of reactive oxygen species (ROS) in the cell and in normal conditions, the physiological antioxidant defense systems can neutralize these. However, mitochondrial dysfunction leads to increased ROS levels and has been implicated in AD pathology (Lin and Beal, 2006). Swerdlow and Khan (2004) and Swerdlow et al. (2014) proposed a 'mitochondrial cascade hypothesis,' which suggests that oxidative stress and amplified generation of ROS trigger Aβ aggregation and neurodegeneration. *In vitro* models of both AD and ALS provided evidence that mitochondrial fragmentation and dysfunction trigger ROS production by microglia, resulting in neuronal damage (Joshi et al., 2019). In a mouse model of AD, partial deficiency of manganese superoxide dismutase (MnSOD) is known to induce oxidative stress, elevated Aβ levels and plaque deposition (Li et al., 2004). In another AD mouse model, pharmacological inhibition of energy production was also amyloidogenic, and metabolic dysregulation has been suggested to be an early pathological event in AD (Velliquette et al., 2005). These results support the hypothesis that altered energy metabolism is a key mechanism in AD.

Studies on neuroinflammation have generated more evidence showing the role of ROS in AD. For example, activation of the NOD-like receptor family, pyrin domain containing 3 (NLRP3) inflammasome, has been widely implicated in various neurological disorders (Shao et al., 2018). One of the main features of AD is microglial activation, which enhances the release of pro-inflammatory molecules, including ROS, and contributes to the propagation of the disease. Aβ promotes the accumulation of mitochondrial ROS, which causes NLRP3 inflammasome activation (Wang et al., 2017). The activation of the NLRP3 inflammasome is thought to seed and spread the Aβ pathology within and between brain structures (Venegas et al., 2017). Moreover, there is strong evidence suggesting that NLRP3 inflammasome activation by ROS also drives tau pathology (Ising et al., 2019). Therefore, this example shows a clear

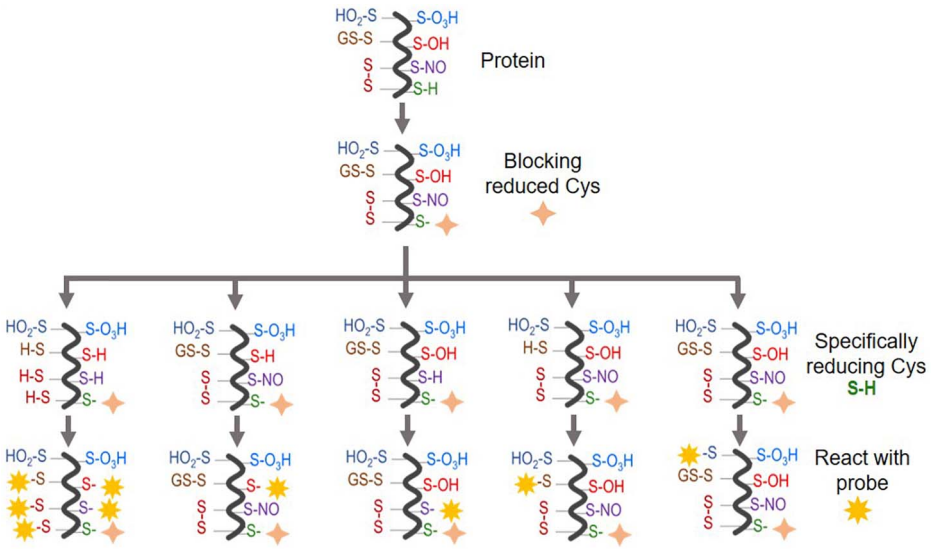

FIGURE 2 | An overview of Oxi-Cys quantitative proteomics approaches for different types of Cys oxidations. Chemicals used for selective Oxi-Cys proteomics analysis. Free reduced Cys residues are firstly labeled with alkylating reagents (IAM, NEM, MMTS, *etc.*) while different PTMs of reversible Oxi-Cys residues are selectively alkylated by specific reducing regents; for example, DTT/TCEP for reducing all reversible Cys, arsenite for *S*-sulfenylation (*S*-OH), ascorbate for *S*-nitrosylation (*S*-NO), glutaredoxin for *S*-glutathionylation (*S*-SG). These newly formed reduced Cys residues then, theoretically, can be labeled by different alkylating reagents or specific probes coupled with tags for purification/enrichment. The quantitation is performed based on comparing intensities of tags from diseased compared to control groups. *S*-OH probes include: dimedone and bicyclononyne BCN; *S*-O_2H probes include: *C*-nitroso esters, diazenes and *S*-nitrosothiols as detailed in **Figures 5A,B**.

connection between neuroinflammation and ROS production occurring in Aβ- and tau-related neurodegeneration. Since oxidative damage is associated with both healthy aging and disease, understanding the mechanisms of cellular oxidation status in aging and neurodegeneration may lead to new strategies for their prevention.

Overview of Oxi-Cys Proteomics

In the field of Oxi-Cys proteomics, one of the main challenges lies in the sample preparation methods used to access (and preserve) the initial oxidation state of proteins within oxidative environments. A general protocol for MS-based Oxi-Cys proteomics includes two main steps: chemical labeling reduced and oxidized cysteine residues and MS-based analysis to identify and quantify peptides (bottom-up) or intact proteins (top-down) containing labeled cysteine residues. The key steps for sample preparation and labeling of cysteine-containing proteins consist of extracting proteins using appropriate buffers, blocking free reduced cysteine residues, reducing reversibly oxidized cysteines using either reducing reagents or targeting the type of oxidation of interest using suitable probes. Subsequently, labeled and/or purified proteins/peptides are analyzed by MS. For the bottom-up proteomics approach, labeled proteins are enzymatically digested into peptides (typically using trypsin) to generate a complex mixture of peptides, which is then analyzed directly by MS analysis or fractionated using HPLC to reduce the complexity of peptide mixture before MS analysis of each fraction. For top-down analysis, an intact protein is enriched/purified using suitable techniques before being directly analyzed and fragmented in a tandem mass spectrometer (Virág et al., 2020). As the intact protein is analyzed, the context of multiple PTMs and protein isoforms is retained (Tran et al., 2011), unlike bottom-up proteomics, where the connection between PTMs on different peptides is lost. However, sequence coverage is generally much lower in top-down versus bottom-up proteomics. Top-down proteomics is not currently well suited for the analysis of complex mixtures of proteins (Lorenzatto et al., 2015), and data analysis can be complex and time-consuming. As a result, this approach is not currently routinely used for high-throughput proteomic analysis, and only a few studies have used this approach to study protein oxidation (Tran et al., 2011; Ansong et al., 2013; Auclair et al., 2014; Reinwarth et al., 2014). Therefore, in this review, we will highlight the most currently used bottom-up proteomics approaches for the studies of Oxi-Cys proteomes.

CHEMICAL-LABELING APPROACHES FOR OXI-CYS PTMs

There are many considerations for the experimental design for proteomic analysis of Oxi-Cys PTMs. These include the types of Cys-oxidations of interest, number of biological samples, selection of approaches (reactive thiols or oxidized Cys), incorporation of chemical tags, enrichment method, availability of antibodies, and type of quantitation (Gu and Robinson, 2016b). In Oxi-Cys based analysis, abundance changes

TABLE 1 | Advantages and disadvantages of current Oxi-Cys proteomic approaches.

Approach	Advantages	Disadvantages	References
SICyLIA	Simple protocol. Saves time and cost. Increased detection of low abundance oxidized Cys. High oxi-proteome coverage. Accurate quantitation.	Cannot distinguish different forms of reversible oxidized Cys. Need to control IAM reaction carefully to reduce the loss of deuterium in heavy IAM. Only two samples can be compared in a single experiment.	van der Reest et al., 2018
IodoTMT	Multiple samples (up to 6 samples per experiment).	Low selectivity. Antibody based purification.	Qu et al., 2014
cysTMTRAQ	Multiplexing analysis. Analyze both Oxi-Cys dynamics and protein-level changes in a single experiment. Can perform either Cys enrichment or not. Determine stoichiometry of redox modifications. High confidence and accuracy for oxi-Cys proteome analysis.	Costly and complicated protocol. Interference of both TMT and iTRAQ ion reporters cause ratio compression.	Parker et al., 2015
isoTOP-ABPP	Measure/monitor directly functions of enzymes in native biological systems. Exact sites of Cys reactivity. Low (μM) of IA used to allow differentiate the extent of alkylation. The isoTOP-ABPP ratio is independent with both peptide and protein abundances. Proteome-wide profiles of Cys reactivity in complex biological systems.	Incomplete precipitation of proteins after click chemistry (∼50% of total proteins). Low accurate characterization of too large or too short peptides. Combination of digested enzymes need to be used to increase proteome coverage. Limit in software that can be used for data analysis. Long protocol.	Weerapana et al., 2007; van der Reest et al., 2018
QTRP	High yield of biotinylated as click chemistry reaction performed on a peptide level.	Control concentration of IPM for alkylation.	van der Reest et al., 2018
DiaAlk	Measure directly *S*-sulfinylation and *S*-sulfenylation. High selectivity of *S*-sulfinated peptides/proteins.	Applicable for 2 biological samples only. Complicated sample preparation. Prolonged and costly protocol. Availability of chemicals. Many chemical reactions Not optimized to measure global level of *S*-sulinylated Cys directly in cells. Requires biotin based purification and photo-cleavage to release tags.	Akter et al., 2018
OxiMRM	Benefit for low abundance oxidized proteins. Detect/measure both reversibly and irreversibly oxidized Cys.	Two different alkylating steps. Many precipitation steps. Need specific antibodies. Low number of peptides detected.	Held et al., 2010
UPLC-pSRM	Label free approach. No affinity purification required. Detect/measure irreversibly oxidized Cys.	Underestimation of low abundance oxidized protein detection. Requires specific antibody for immunoaffinity purification. Prior knowledge of targets required.	Sherrod et al., 2012
Cys-DIA	High coverage of Cys proteome.	Only used with certain MS instruments. Need to run DDA to create customized database. Samples run individually does not support multiplexing. Need to purify Cys.	Tahir et al., 2020

in peptides containing oxidized Cys will directly reflect the oxidation level in a given sample/experiment. In thiol reactivity profiling experiments, abundance changes in reduced Cys will reflect the oxidative level of Cys inversely. Generally, a typical

workflow for Oxi-Cys proteomics analysis in neurodegenerative diseases should cover:

- Types of Oxi-Cys PTMs of interest (global or selected PTMs as seen in **Figure 1**) to ensure that, in the case of selected Oxi-Cys, the (affinity) purification method is available and suitable.
- Quantitative approaches to be used, as this will determine the types of thiol alkylations, appropriate reagents, protein/peptide enrichment and labeling, MS [$MS/MS^{(n)}$] operation, and cost-effectiveness.
- Type of MS instrument available for sample analysis.

These key factors will affect the selection of appropriate approaches, MS (MS/MS) mode operation, and downstream data processing. We have summarized the main proteomic approaches for different types of Oxi-Cys PTM analyses in **Figure 2**, and their applications, advantages and disadvantages are shown in **Table 1** and **Supplementary Table 1**, respectively. The details of these approaches are discussed in the following sections.

There are two main types of Oxi-Cys analysis: global Oxi-Cys and selective Oxi-Cys measurement (**Figure 2**). Traditionally, for any relative quantitative analysis of Oxi-Cys, at least two different biological groups are required. The global quantitative Oxi-Cys analysis can be performed based on the ratio of Cys-containing peptide XIC (extracted ion chromatogram) intensities detected by MS (either reduced or oxidized Cys intensities) between samples. This type of analysis includes two different alkylating steps (e.g., IAM and NEM), stable isotopic labeling (SICyLIA), resin-assisted capture (RAC) combined with isobaric labeling reagents (TMT, iTRAQ, and iCAT). Irreversible cysteine oxidations are typically stable during sample processing and LC-MS conditions; thus, direct analysis of these modifications in a complex sample is feasible.

Differential Alkylation

Chemically Distinct Alkylation Reagents

One of the biggest challenges of reversible Oxi-Cys analysis is to preserve the endogenous redox state. This can be affected by either oxidation or reduction of Cys during sample preparation leading to inaccurate cellular redox balance measurement. To minimize the artefactual oxidation, alkylating reagents such as Iodoacetamide (IAM) or *N*-ethylmaleimide (NEM) are added at the first step during protein denaturation to alkylate reduced Cys residues (McDonagh et al., 2014). This is a crucial step for relative quantification, and it is required that the alkylating reagent should completely block all reduced Cys. Subsequently, all reversible Oxi-Cys residues are reduced by reducing agents, such as dithiothreitol (DTT), dithiobutylamine (DTBA), β-mercaptoethanol (BME), or tris(2-carboxyethyl)phosphine (TCEP) to generate free sulfhydryl groups. This is followed by the second alkylation step, where newly formed sulfhydryl groups are chemically blocked with an alkylating reagent distinct from that used in the first step [e.g., NEM, IAM, 2-chloroacetamide, iodoacetic acid (IAA), 4-vinylpyridine, methanethiosulfonate (MMTS)] (McDonagh et al., 2014). Proteins are then enzymatically digested, and the generated peptides can then be fractionated, if necessary, *via* an off-line HPLC and fractions analyzed by LC-MS/MS (**Figure 3A**). Intensities of reduced Cys and Oxi-Cys-containing peptides from samples are compared to estimate the ratio of Oxi-Cys. This approach is relatively straightforward, and from the same analysis, protein expression measurement can be performed using label-free quantification of non-cysteine containing peptides. However, given that this approach does not include a cysteine enrichment step, the coverage of Cys-containing peptides for complex samples may be lower than that achievable using other methods that do incorporate an enrichment step.

Stable Isotopic Labeling With Iodoacetamide (SICyLIA)

An approach using stable isotope cysteine labeling with IAM, termed SICyLIA, has been recently developed to investigate global Oxi-Cys proteomes (van der Reest et al., 2018). This approach utilizes light or heavy isotope-labeled IAM to differently label reduced Cys thiols between two groups (e.g., control and experimental). A detailed workflow of this approach is shown in **Figure 3B**. During denaturing, free reduced Cys residues in control and experimental samples are alkylated using either light ($^{12}C_2H_4INO$) or heavy ($^{13}C_2D_2H_2INO$) IAM, respectively which results in the addition of a carbamidomethyl group (CAM), adding an extra of 57 or 61 Da to cysteine residues (**Figure 4A**); or free reduced Cys can be also alkylated with either light or heavy NEM (**Figure 4B**). These two samples are then combined and reduced using DTT; newly reduced Cys generated from reversible Oxi-Cys are alkylated with NEM and subjected to tryptic digestion to generate labeled peptides. The mixture of these peptides is then fractionated off-line by a high pH reversed-phase chromatography to reduce the complexity of the peptide mixture to increase proteome coverage. Peptide fractions of labeled peptides are then analyzed by LC-MS/MS. The ratio (of signal intensity) between heavy and light IAM-labeled Cys-containing peptides will estimate reduced cysteine levels between two samples with an assumption that any decrease in CAM-modified peptides will reflect an increase in the level of oxidation (van der Reest et al., 2018). Given that the reduced Cys portion of proteins is more abundant in cells, this approach does not require an enrichment step and allows enhanced detection of oxidation changes in cells (van der Reest et al., 2018). However, this approach cannot distinguish specific forms of reversible Oxi-Cys, as all reversible Oxi-Cys residues are labeled and analyzed.

Isobaric Tags

Iodoacetyl Isobaric Tandem Mass Tags – IodoTMT

Iodoacetyl isobaric tandem mass tags (iodoTMT) allows the pooling and analysis of up to six samples in a single Oxi-proteomics experiment. The iodoTMTsixplex reagents consist of six different isobaric isomers that can react with the sulfhydryl (-SH) group of protein *via* irreversible labeling step by forming an iodoacetyl-activated covalent bond (Bomgarden et al., 2012). The workflow of this approach is presented in **Figure 3C**, and the chemical structures of iodoTMTsixplex reagents with

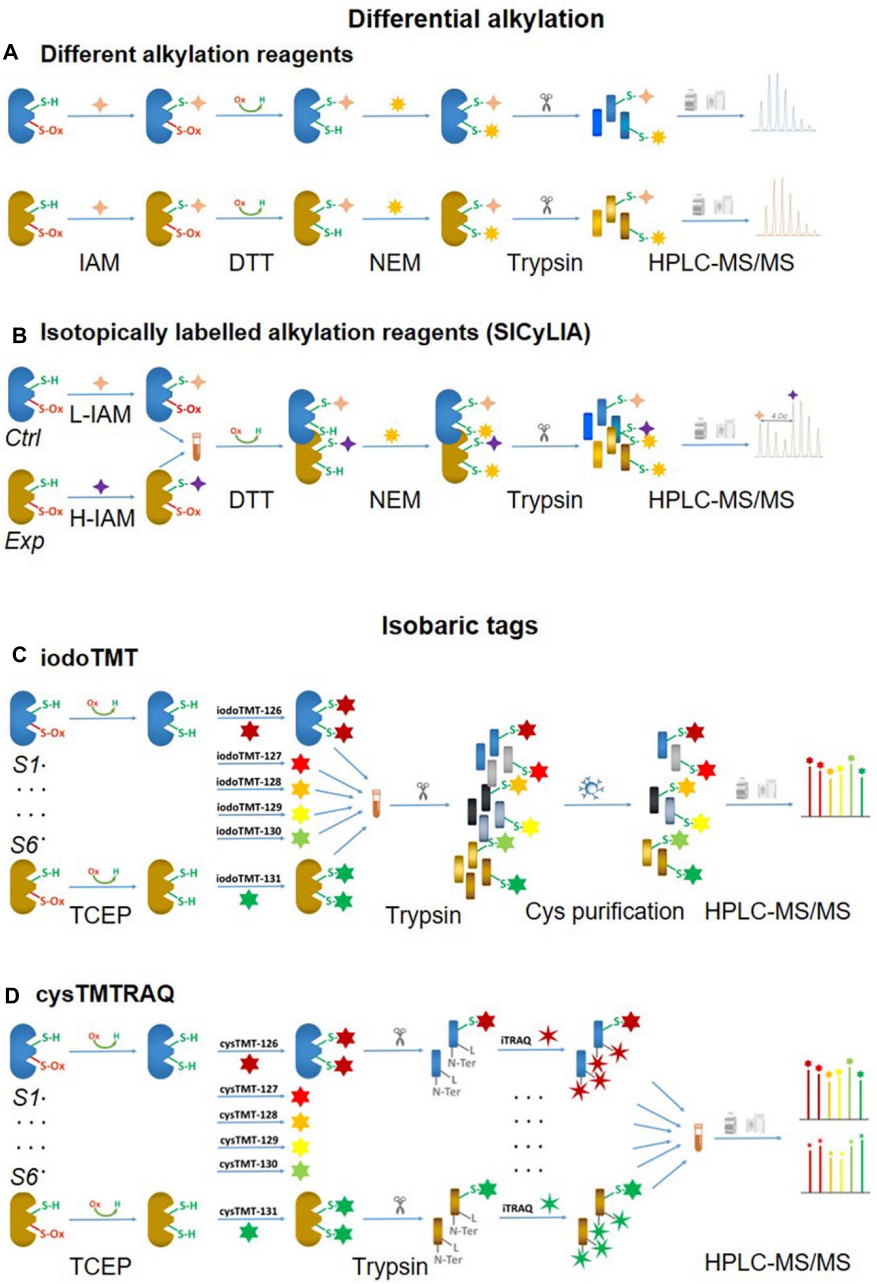

FIGURE 3 | Non-click chemistry-based thiol-reactive workflows. Different alkylation methods: **(A)** two chemically distinct alkylation reagents and **(B)** SICyLIA; isobariac tags: **(C)** iodoTMT and **(D)** cysTMTTRAQ.

the distribution of isotopes and their reaction with reduced Cys are shown in **Figure 4C**. Each iodoTMT reagent contains three distinctive groups (**Figure 4C**), including a reporter (used for quantitation), mass normaliser (balance group) and a Cys reactive group (to react with a sulfhydryl group) (Bomgarden et al., 2012). Different iodoTMT reagents can be used to label either reduced or oxidized Cys residues (reduced before labeling) depending on the design of the experiment. The ion reporters (isobaric mass tags) are cleaved during MS2 (fragmentation) analysis generating unique reporter ions ranging from 126 – 131 *m/z* (**Figure 4C**). Their intensities in fragmentation spectra are then used to calculate the level of Cys oxidation from the samples (Bomgarden et al., 2012).

This approach can be used for either global Cys (reduced and reversible oxidized forms) or Oxi-Cys analyses. If it is used for global Cys analysis, all proteins are denatured and

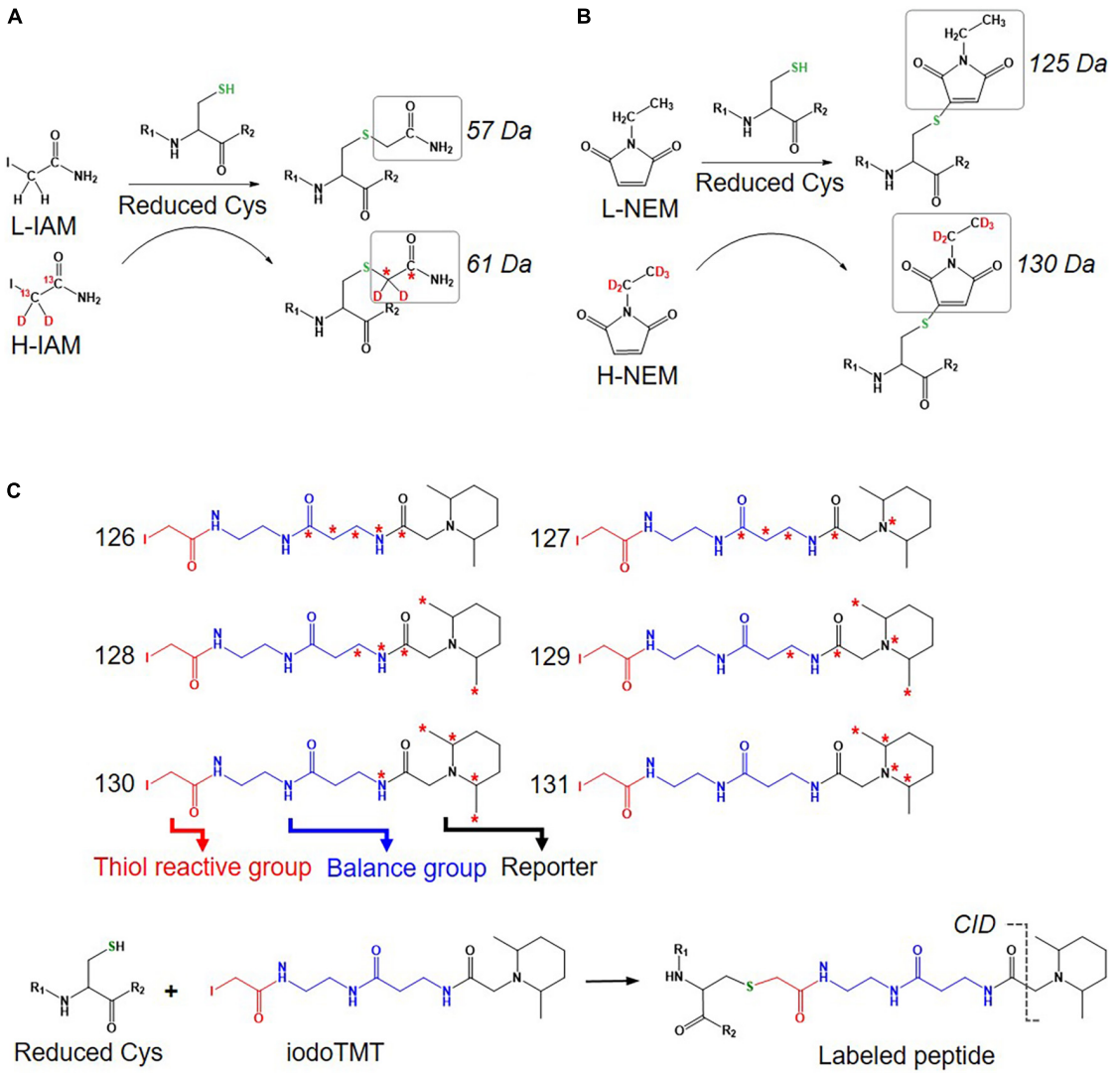

FIGURE 4 | Isotope labeled reagents and probes used for Oxi-Cys proteomics. Isotopic chemicals and their adding extra mass for PTM search: **(A)** L-IAM and H-IAM, **(B)** L-NEM, and H-NEM, **(C)** iodoTMT reagents and the cleavage site to release ion reporters by CID during MS/MS analysis.

reduced with TCEP to ensure that all reversible Oxi-Cys are reduced. All initially and newly reduced Cys-containing proteins in each sample are then labeled with appropriate iodoTMT reagent; up to six samples can be labeled with six specific iodoTMT reagents (**Figure 3C**). If an iodoTMT approach is used for analyzing reversible Oxi-Cys, proteins are firstly denatured in the presence of IAM to block reduced Cys; the excess IAM is removed via trichloroacetic acid (TCA) precipitation of proteins. Subsequently, proteins are reduced with DTT to covert reversible Oxi-Cys to free thiols that are then labeled with iodoTMT reagents. All labeled proteins are pooled and precipitated by TCA to remove the excess iodoTMT reagents, followed by tryptic digestion (Bomgarden et al., 2012). Labeled iodoTMT peptides are enriched using immobilized anti-TMT antibody resin and eluates analyzed by LC-MS/MS. The intensity of ion reporters generated during MS2 analysis will be used for relative quantitation of Oxi-Cys while other MS2 information is used for peptide/protein sequencing.

This iodoTMT approach can also be used for selective Oxi-Cys analysis. Qu et al. (2014) combined biotin switch technique (BST) [adopted from (Jaffrey et al., 2001), see section Biotin Switch Technique (BST) for details] with iodoTMT labeling to improve the iodoTMT approach, such as robust workflow for *S*-NO PTM analysis, effective peptide digestion, unambiguous *S*-NO-Cys mapping, and enhanced high throughput (Qu et al., 2014). In brief, Cys residues containing free thiols are alkylated with MMTS, while nitrosylated Cys residues are selectively reduced with ascorbate and labeled with iodoTMT reagents. Six different iodoTMT labeled samples are then combined, reduced (by DTT) and alkylated (by IAM), digested by trypsin. Labeled peptides are enriched by anti-TMT antibody resin before being

analyzed by LC-MS/MS. The enrichment efficiency of iodoTMT labeled peptides is low but optimization of elution conditions has increased the efficiency from 6% using standard conditions to 21% (Qu et al., 2014). In theory, iodoTMT can be used for the investigation of most common reversible Oxi-Cys by a combination of selected methods for enrichment of different kinds of Oxi-Cys (as shown in **Figure 2**) and iodoTMT for labeling of interested Oxi-Cys PTM.

Cysteine-Reactive Tandem Mass Tag (cysTMT) and Isobaric Tags for Relative and Absolute Quantitation (iTRAQ) – cysTMTRAQ

Conventional multiplexing approaches such as iodoTMT, which provide a readout of the changes in thiol redox state, do not allow measurement of global changes in protein expression. To overcome this, the double-labeling approach termed cysTMTRAQ combining two different isobaric tag approaches, the cysTMT and iTRAQ, was developed (Parker et al., 2015). The cysTMT approach utilizes two different isobaric tag groups with two different purposes: the cysTMT tags are used to label thiol groups on Cys in up to six samples (126, 127, 128, 129, 130, and 131 *m/z*), while the iTRAQ tags are used to label N-terminal and lysine residues of peptides in up to six various samples (114, 115, 116, 117, 119, and 121 *m/z*). This approach, therefore, allows the simultaneous measurement of the changes in Cys oxidation (from cysTMT) and changes in global protein expression (from iTRAQ). This allows cysteine oxidation data to be normalized to protein expression data to correct for changes in protein turnover (Parker et al., 2015). To enhance the coverage of Oxy-Cys proteomes, the enrichment of labeled proteins can be performed using a specific anti-TMT antibody after two labeling steps, coupled with HPLC based fractionation before MS analysis. The workflow of this approach is shown in **Figure 3D**, and its benefits are shown in **Table 2**. Although this approach offers many advantages, one of the main problems is the ratio compression in quantitation caused by the interference of both TMT and iTRAQ ion reporters; however, the use of advanced modes of data acquisition such as synchronous precursor selection (SPS) implemented in the current generation of Orbitrap analyzers can solve this issue (Erickson et al., 2015).

Click Chemistry Approaches

Unlike SiCyLIA or iodoTMT, in which different isotopic labeling reagents directly react with Cys residues in proteins without any other further reactions, click chemistry-based approaches (DiaAlk, TOP-ABPP) employ two reactions. Firstly, a probe (containing specified alkyne and an IAM group) will react with the thiol group in a protein (*via* IAM group) to form the probe-protein intermediate. This is then biotinylated with isotope labeled–biotin tags using a click chemistry reaction (*via* alkyne group) to allow subsequent purification of tagged proteins using avidin/streptavidin resins. Common probes used for selective Oxy-Cys proteomics analysis and click chemistry approaches are shown in **Figure 5**. Proteins labeled with either light or heavy isotope tags are usually tryptically digested to generate labeled peptides. Subsequently, the biotin group in these labeled peptides will be cleaved off by either enzymes (isoTOP-BPP approach) or UV (QTRP and DiaAlk approaches) at a specific wavelength, allowing labeled peptides to be readily analyzed by LC-MS/MS (see **Figure 6**). Based on signals of the (light and heavy) tag-labeled peptides obtained at MS1 level, a ratio of light/heavy (or versa) can be calculated to estimate the oxidation level of Cys in different samples/conditions.

Isotopic Tandem Orthogonal Proteolysis-Activity-Based Protein Profiling (isoTOP-ABPP)

IsoTOP-ABPP was developed as an advanced approach to quantify/measure the reactivity of Cys residues directly in native biological samples. It combines two different strategies; tandem orthogonal proteolysis (TOP) and activity-based protein profiling and has been used to predict functions of cysteine residues in proteomes (Weerapana et al., 2007). This approach consists of three main steps, alkylating reduced Cys in proteins with a probe, click chemistry-based incorporation of isotopically-labeled cleavable tags, protein purification and on-bead digestion (Weerapana et al., 2007). A probe consists of two main components: a reactive group to label reduced Cys residues in proteins coupled with an alkyne group for tagging click chemistry (**Figure 4C**). The TEV-biotin tag contains three different components: a biotin group for streptavidin affinity purification, a TEV (Tobacco etch virus) protease recognition domain (ENLYFQG) conjugated to an isotopically labeled Valine (heavy or light), and an azide handle for click chemistry, and a linker between a reporter and the reactive group (Weerapana et al., 2007; Chen et al., 2017) (**Figure 7**). The mass shift between light and heavy version tags is 6.014 Da (Weerapana et al., 2010).

A typical workflow of the isoTOP-ABPP approach employs two different (light and heavy) isotopically labeled cleavable biotin-azide tags that are reacted with IA-alkyne probes. Copper(I)-catalyzed azide-alkyne cycloaddition (CuAAC) is used to label two different experimental Cys-proteomes (**Figure 6A**). Reactive cysteines in proteins from two distinct proteomes are firstly alkylated with IA-alkyne probe, subsequently conjugated with isotopically differentiated cleavable biotin-azide tag using CuAAC (Kolb et al., 2001). IA-labeled proteins from two different proteomes are combined and subjected to affinity purification on streptavidin beads, followed by on-bead tryptic digestion. All labeled cysteine-containing peptides are then released by sodium dithionite before analysis by LC-MS/MS (**Figure 6A**). The calculated heavy/light ratio of each labeled Cys peptide, obtained from MS1 level analysis, will reflect Cys reactivity changes between two proteomes.

Many attempts have been performed to improve the performance of isoTOP-ABPP, mainly focused on cysteine reactive electrophile probes, cleavable biotin-azide tags, and heavy isotope incorporations (Maurais and Weerapana, 2019).

- Various probes recently introduced (summarized in **Figure 5C**) include (i) IA-alkyne based probes such as chloropyridine (RB2) and fluoronitrobenzene (ERW3) (Shannon et al., 2014), a photocaged bromomethyl ketone (CBK) (Abo and Weerapana, 2015), iodomethyl ketone

TABLE 2 | List of (potential and confirmed) biomarkers in neurodegenerative diseases from Oxy-Cys proteomics studies.

Neurodegenerative diseases	Human specimens. Sample sizes	Method used	PTMs	Biomarkers	Cys sites	References
Multiple sclerosis	CSF	Modified proteomics approach (No reduction and alkylation applied) and a targeted database search		Extracellular Superoxide dismutase (ECSOD) α1-antitrypsin (A1AT) Phospholipid transfer protein (PLTP) Alpha-2-HS-glycoprotein Ectonucleotide pyrophosphate (ENPP-2) Gelsolin Interleukin-18 (IL-18) Ig heavy chain V III region POM	195 232 318 340 773 304 38 22	Srivastava et al., 2019
	7 MS patients (2 males + 5 females), ages 35.6 ± 10.5 5 idiopathic intracranial hypertension (IIH) patients used as control group (1 male + 4 females), age 26.2 ± 7.6					
AD	CSF	Online immunoaffinity chromatography -mass spectrometry of intact protein		Transthyretin (TTR) isoforms (TTR-Cys10-Cys (cysteinylated), TTR-Cys10-CysGly (cysteine-glycinylated), and TTR-Cys10-SG (glutathionylated)/)	10	Poulsen et al., 2014
	AD 37 patients Mild cognitive impairment (MCI) 17 Normal pressure hydrocephalus (NPH) Healthy control (HC) 7					
AD and PD	Human brain tissues	2D gel, immunostaining and MS	*S*-sulfonylation	Targets: sulfonic acid UCH-L1	220	Choi et al., 2004
AD	Inferior parietal lobule from patients	2D-Oxyblots and MS	*S*-glutathionylation	Deoxyhemoglobin, α-crystallin B, α-enolase Glyceraldehyde phosphate dehydrogenase (GAPDH)		Newman et al., 2007
AD	Hippocampus, substantia nigra and cortex, AD patients (n = 9) control (n = 5)	2D-Oxyblot and MS	*S*-NO	Voltage-dependent anion-selective channel protein 2 (VDAC2). Superoxide dismutase [Mn] (SOD2). Fructose-bisphosphate aldolase C (ALDOC).		Zahid et al., 2014
AD	Human Hippocampus	2D-Oxyblots and MS	*S*-OH, *S*-O2H, *S*-O3H Sulfenic acid, sulfinic acid, and sulfonic acid	Pin1	113	Chen et al., 2015
Human Prion Diseases	Human cortex and cerebellum	BST, avidin enrichment, iTRAQ, gel-free	*S*-NO	1509 *S*-nitrosylated proteins (*SNO*-proteins) were identified		Chen et al., 2016

(Continued)

TABLE 2 | Continued

Neurodegenerative diseases	Human specimens. Sample sizes	Method used	PTMs	Biomarkers	Cys sites	Reference
AD	Human cortical brain Tissues *n* = 30 healthy control, *n* = 30 MCI and *n* = 30 AD	Immunoblots, IodoTMT	*S*-NO	Myelin-oligodendrocyte glycoprotein (MOG) Glutathione *s*-transferase Mu 3 (GSTM3) Four and a half LIM domains protein 1 (FHL1)	53, 127 3 65	Wijasa et al., 2020

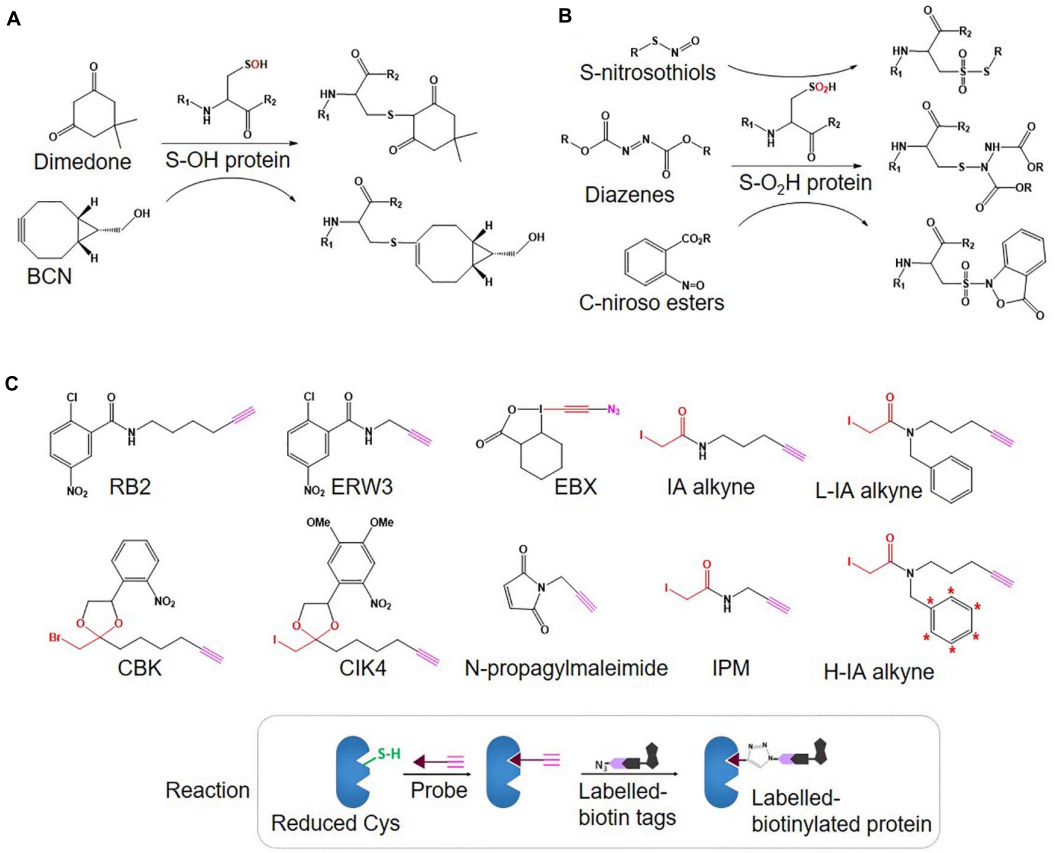

FIGURE 5 | Structure of probes used for selective Oxi-Cys (**A:** *S*-OH and **B:** *S*-O_2H) and click chemistry-based **(C)** approaches.

(CIK4), ethynyl benziodoxolone (EBX) (Abo et al., 2017), and (ii) light and heavy isotopic IA-alkyne tags (Abo et al., 2018), (iii) thiol-reactive probe (*N*-propargylmaleimide, NPM) (McConnell et al., 2020).

- Different cleavable biotin-azide tags: protease-cleavable biotin-azide tags for CuAAC-mediated conjugation (TEV protease), chemically cleavable azobenzene (Azo) linkers (Qian and Weerapana, 2017) (**Figure 7**), and photocleavable biotin-azide tags such as reductive dimethyl labeling (termed rdTOP-ABPP for triplex quantification) (Yang et al., 2018) and multiplexed thiol reactivity profiling (MTRP) (Tian et al., 2017), maleimide-activated (**Figure 8**).
- Heavy isotope incorporation: for duplex analysis including stable isotope labeling by amino acids in cell culture (SILAC), isotopes of IA-alkyne tags (Abo et al., 2018) (**Figure 5C**), light and heavy isotopic biotin-azide linkers (**Figure 7**); for triplex analysis including reductive dimethylation rdTOP-ABPP (Yang et al., 2018); and multiplex including isobaric tags (iTRAQ, TMT).

The synthesis of isotope containing cleavable biotin tags [L-Valine-N-Fmoc ($^{13}C_5$, $^{15}N_1$)] is usually expensive and low yield, but recently, a more cost-effective version of light and heavy isotopes of IA-alkyne tags (**Figure 5C**) has been developed (Abo et al., 2018). The availability of these three crucial developments

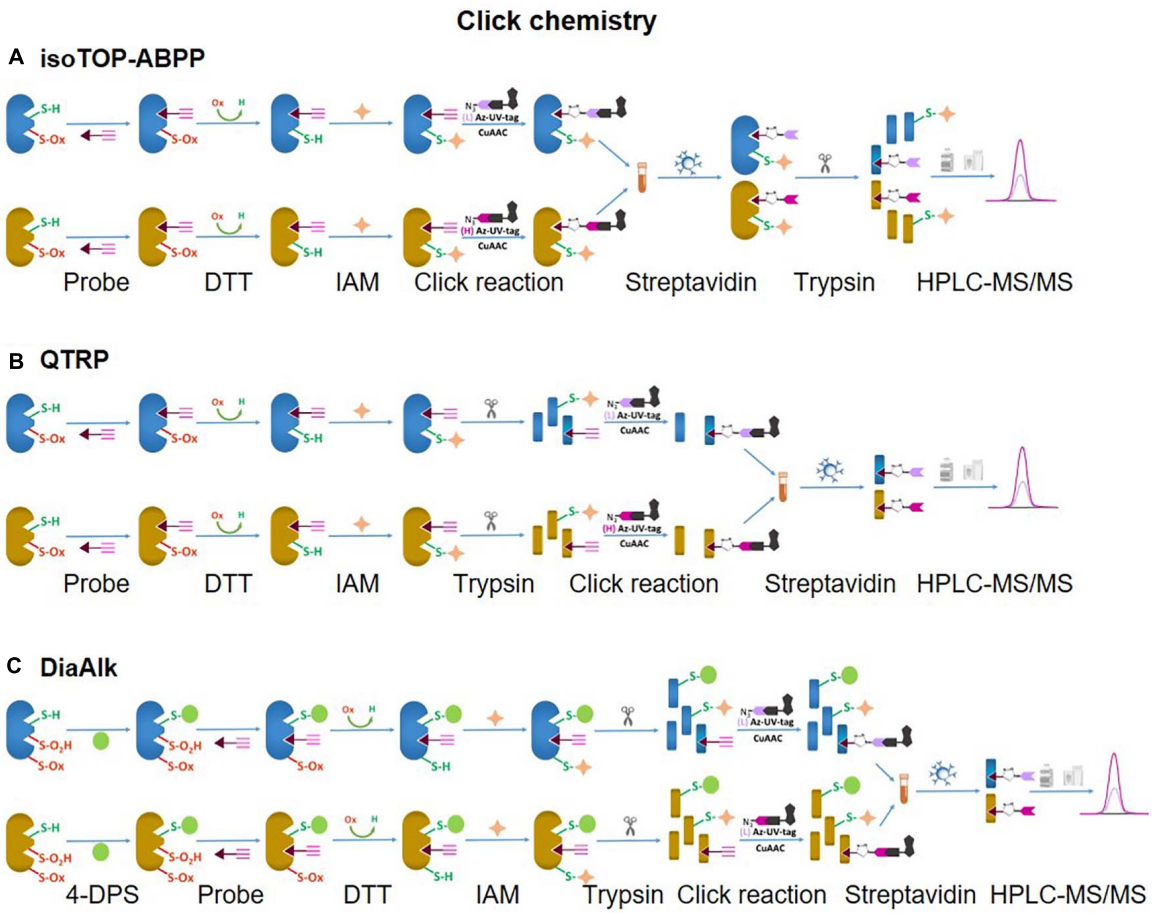

FIGURE 6 | Click chemistry thiol-reactive workflows. **(A)** isoTOP-ABPP; **(B)** QTRP; **(C)** DiAlk. The Oxy-Cys quantitation of these approaches is based on MS1 level.

offers many combinations to tailor isoTOP-ABPP workflow to suit specific experimental designs. Furthermore, when combined with other MS-based approaches (next Section), different variants of isoTOP-ABPP can be customized to maximize Oxi-Cys detection and quantitation.

Quantitative Thiol Reactivity Profiling (QTRP)

In a strategy similar to isoTOP-ABPP, a quantitative thiol reactivity profiling (QTRP) approach was introduced for Oxi-proteomics analysis in which IAM-alkyne probes are used together with click chemistry for light and heavy isotope labeling (Fu et al., 2017). This approach also uses an electrophilic IAM-alkyne probe (2-iodo-*N*-(prop-2-yn-1-yl)acetamide, IPM, **Figure 5C**) coupled with isotopically light (^{12}C) and heavy (^{13}C) UV-cleavable azido-biotin tags via a click chemistry reaction (CuAAC) (**Figure 8**). All free reduced Cys thiol groups are firstly alkylated with IPM while reversible Cys are reduced by DTT, alkylated with IAM and then digested into peptides (**Figure 6B**). The peptides containing the IPM probe, from each sample, are then conjugated with light or heavy UV-cleavable azido-biotin tags (for control and compared samples) *via* copper catalyzed alkyne azide cycloaddition reaction (CuAAC, click chemistry) (Fu et al., 2017). Equal amounts of each sample (light or heavy labeled peptides) are combined and purified by streptavidin. Isotopically labeled peptides are then released *via* a photorelease step (irradiated with 365 nm UV light) (Fu et al., 2017). Mixed labeled peptides are then analyzed by MS, and the light/heavy ratio of a given precursor peptide derived from all isotopically labeled Cys peptides will indicate the oxidation level of control against experimental samples. The key difference between isoTOP-ABPP and QTRP is the order of the labeling steps; while a chemistry click reaction is performed at the protein level in isoTOP-ABPP approach, its reaction is carried out at the peptide level in the QTRP approach, offering a higher yield of biotinylated peptides (Fu et al., 2017), and high selectivity. Recently an updated QTRP approach has been introduced and enabled to detect 5,000 unique Cys-containing peptides (Fu et al., 2020).

Electrophilic Diazene Probe (DiaAlk)

There is controversy regarding the biological functions of *S*-sulfinylation and the extent of its reversibility. Furthermore, the analysis of *S*-sulfinylation is challenged by other canonical forms of Oxi-Cys, such as *S*-sulfhydration (-SSH). Indeed, a

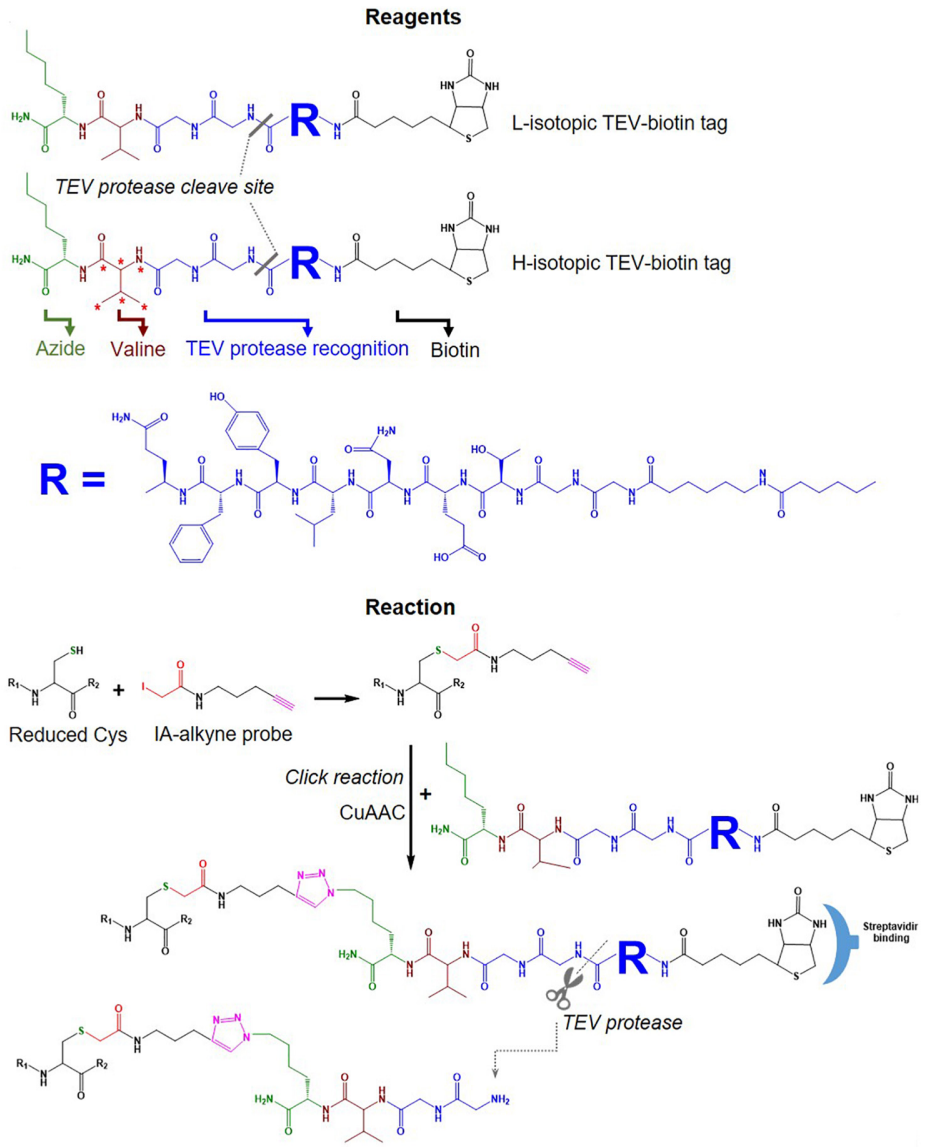

FIGURE 7 | Tags used in the isoTOP-ABPP workflow. Structure of light and heavy isotopic TEV-biotin tags used in isoTOP-ABP, their reaction with reduced Cys, purification using streptavidin and release of labeled proteins using TEV protease.

mass difference of 32 Da between unmodified and *S*-sulfinylated proteins in a standard proteomics workflow has been used to detect *S*-sulfinic acid by MS (*S*-O_2H). However, this type of analysis has faced challenges, for example, the problem of oxidation during sample preparation, the interference of other PTMs with the same nominal mass shift [*S*-sulfhydration (-SSH), for example] (Lee et al., 2013). To overcome these problems, an alkyne derivative of di-t-butyl azodicarboxylate (DBAD) (termed DiaAlk), coupled with isotopic tags, has been used (Akter et al., 2018). The addition of the single alkyne tag to convert DBAD into an asymmetrical molecule enables sulfinic acid to be tagged at both positions of the N = N link in DiaAlk (Akter et al., 2018) (**Figure 8**). Reduced Cys residues in proteins (in both control and experimental samples) are blocked with 4,4′-dipyridyldisulfide (4-DPS) to prevent thiol-mediated probe consumption whilst sulfinylated Cys residues are reacted with DiaAlk probe (**Figure 6C**). Subsequently, other remaining types of Oxi-Cys residues are reduced (by DTT) and alkylated (by IAM) to prevent the re-oxidation of newly formed reduced Cys. Proteins are enzymatically digested (with trypsin), and *S*-sulfinylated peptides are then conjugated to light and heavy azide-biotin to form a photocleavable linker (Az-UV-biotin) *via* Cu(I)-catalyzed azide-alkyne cycloaddition (**Figure 8**) (for two distinct proteomes). Peptides from control and experimental samples are combined before being purified using streptavidin resin. Labeled-biotinylated peptides are released by photocleavage of the biotin linker by irradiation under UV light at 395 nm (Akter et al., 2018) and analyzed by LC-MS/MS.

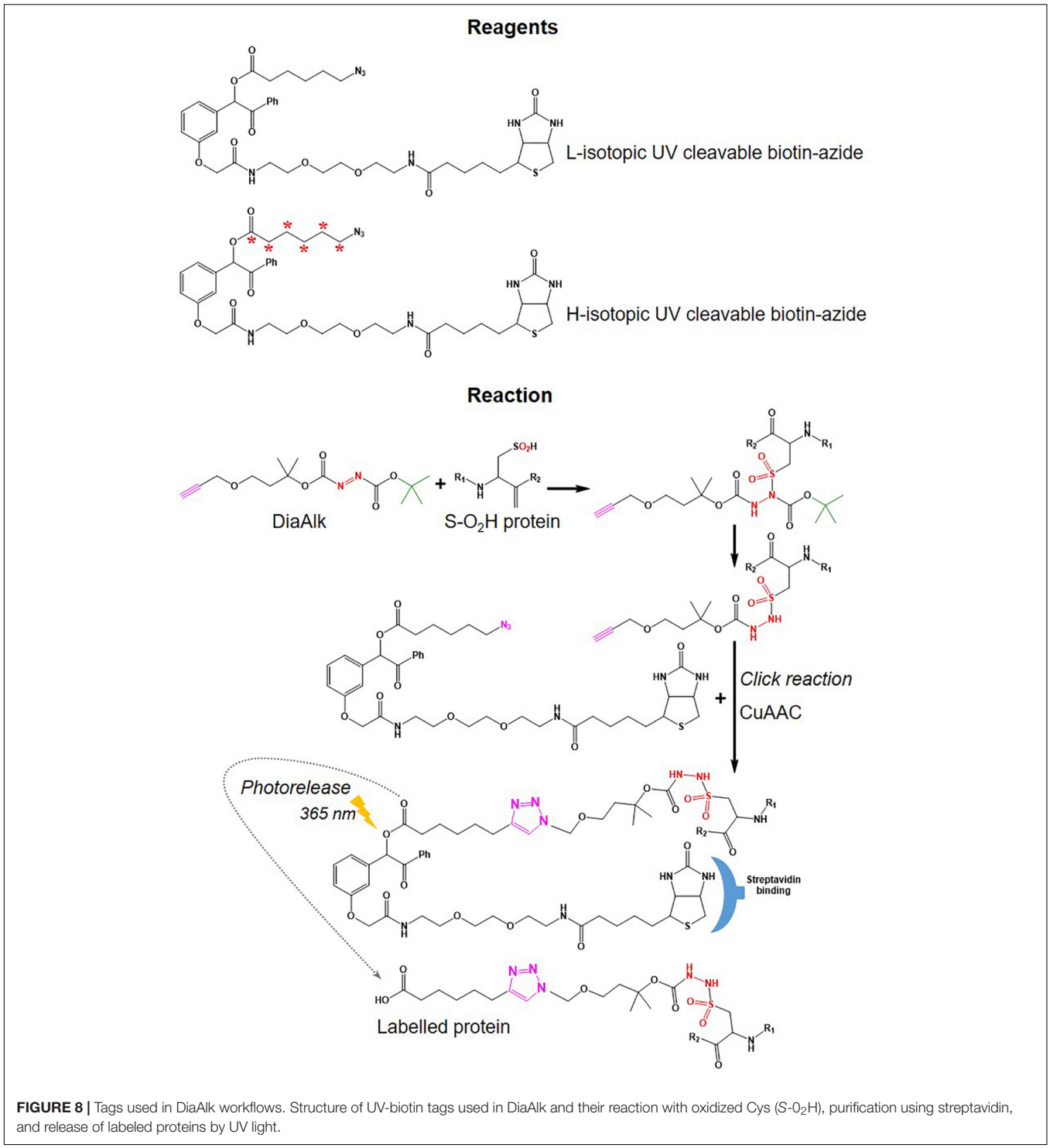

FIGURE 8 | Tags used in DiaAlk workflows. Structure of UV-biotin tags used in DiaAlk and their reaction with oxidized Cys (*S*-0_2H), purification using streptavidin, and release of labeled proteins by UV light.

ENRICHMENT OF OXI-CYS PTMs

Given the content of Cys in proteins is low and oxidized Cys is present at even lower levels, Cys enrichment is an important step to increase the coverage of Oxi-Cys by MS. There are three main methods to enrich Cys [details see Gu and Robinson (2016b)] as listed below:

- Biotin switch technique (BST): ICAT, iTRAQ, SILAC.
- Thiol-affinity RAC: OxcysDML, OxcyscPILOT.
- Immunoaffinity purification: iodoTMT, light and heavy isotopes NEM.

When Oxi-Cys quantitative analysis is performed across multiple samples, it is required that the level of Cys oxidation

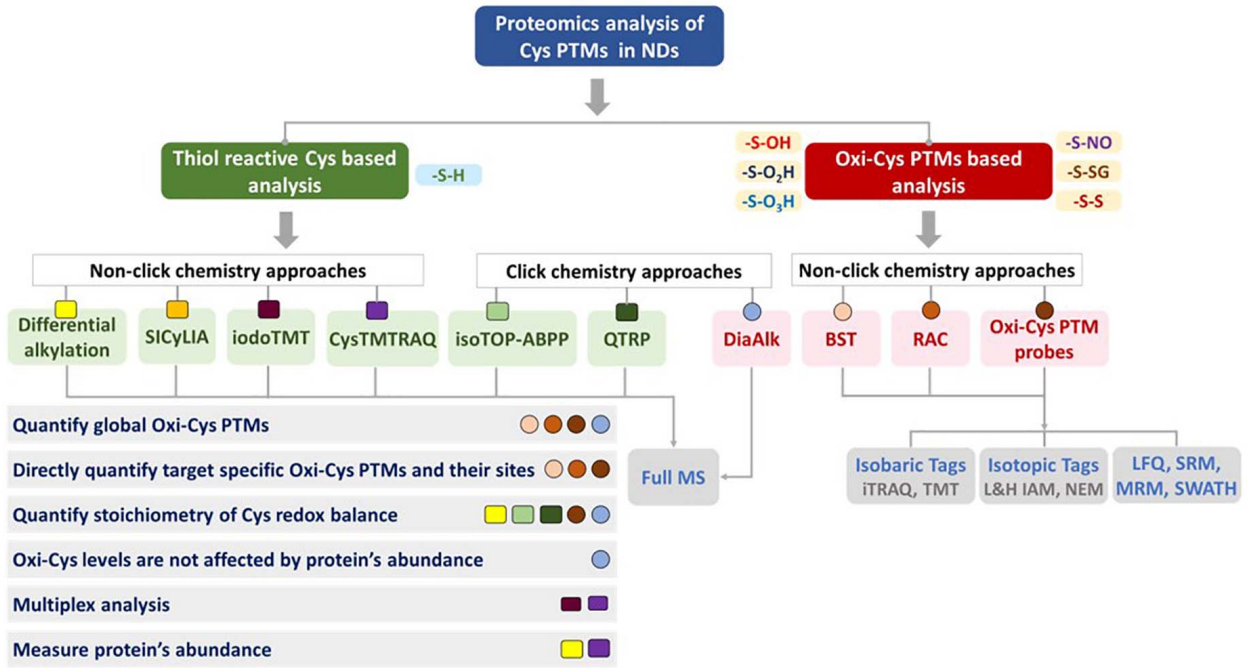

FIGURE 9 | Considerations for choosing strategies for proteomic analysis of cysteine oxidation. Various features of each approach are included to help guide the choice of methods. The shape (□,○) and color code each represent a distinct method but are grouped according to the different overall approaches.

needs to be normalized to the level of protein expression, usually requiring a separate experiment for global proteome quantitation. However, approaches have been developed to generate Cys oxidation ratios and measure protein expression in the same experiment. In a differential alkylation approach, peptides containing Cys (either chemically alkylated or initially oxidized) are used to estimate Cys oxidation levels, while peptides not containing Cys are used for measurement of protein expression. Likewise, in cysTMTRAQ, differential isotope tagging of Cys-containing and peptides that do not contain Cys allow for measurement of both Cys oxidation and protein expression. Therefore, if access to MS instrument time is limited, choosing an approach that generates oxidation and protein expression data is worth considering (**Figure 9**).

Biotin Switch Technique (BST)

The BST technique exploits the specificity and strong binding affinity of biotin with avidin resin to enrich biotinylated Cys-containing peptides from complex samples. Many approaches such as iodoTMT, CysTMTRAQ, QTRP, TOP-ABPP use BST to enrich Cys-containing peptides/proteins. This is an important step in these approaches to enhance the abundance and coverage of Oxi-Cys in biological samples. BST is widely used as a robust technique to enrich Cys; however, non-specific interactions might also occur if wash steps are not sufficiently stringent and bound peptides/proteins are challenging to elute if cleavable biotin is not used. In addition, the size of the biotin tags could also prevent appropriate interactions with the Cys residue (Gu and Robinson, 2016b).

Jaffrey et al. (2001) used BST to investigate *S*-nitrosylated proteins. All Cys-containing free thiols are alkylated with MMTS, while nitrosothiols are selectively reduced with ascorbate to form free thiols, which are then blocked with thiol-modifying reagent biotin–HPDP (*N*-[6-(biotinamido) hexyl]-3′-(2′-pyridyldithio) propionamide). The biotinylated proteins are then purified using streptavidin-agarose resin and selectively eluted with 2-mercaptoethanol (2-ME) to break the disulphide linkage in biotin-HPDP. However, cysteine residues modified by MMTS and endogenous disulphides are also reduced to form free thiol during this elution step (Jaffrey et al., 2001). Therefore, other alkylating reagents such as IAM or NEM should be used to alkylate Cys irreversibly to avoid this problem. Proteins are separated on a Sodium dodecyl sulfate –polyacrylamide-gel electrophoresis (SDS–PAGE), selected bands are then subjected to tryptic digestion and MS analysis for identification of *S*-NO PTMs (Jaffrey et al., 2001).

Another BST-based approach, *SNO*TRAP (*S*-NO trapping by triaryl phosphine) was developed to selectively target *S*-nitrosylated proteins to reveal those involved in the early stages of neurodegeneration in a mouse model of Alzheimer's disease (Seneviratne et al., 2016). All initially reduced Cys are blocked with IAM while *S*-nitrosylated proteins are directly reacted with a biotin-*SNO*TRAP (*b*-SNOTRAP) probe to yield an azaylide intermediate to form the disulfide–iminophosphorane compound, which then is subject to reduction by TCEP before blocking with NEM (Seneviratne et al., 2016). The biotin-based enrichment of *S*-NO is performed at either protein or peptide levels.

Thiol-Affinity Resin-Assisted Capture (RAC)

The enrichment of Cys-containing peptides/proteins based on thiol-affinity RAC has been widely used in quantitative proteomics analysis of reversible Oxi-Cys. Coupled with different quantitative proteomics approaches (e.g., isotopic labeling, isobaric tags, and LFQ), thiol-affinity resin has been used for the purification of various kinds of selected Oxi-Cys PTMs, including *S*-NO [SNO-RAC coupled with iTRAQ (Forrester et al., 2009), OxcyscPILOT/SNO-RAC coupled with TMT (Gu and Robinson, 2016a), *S*-SG (Guo et al., 2014), and global Oxi-Cys PTMs RAC coupled with LFQ (Paulech et al., 2013)]. The most popular RAC is Thiopropyl sepharose® 6B resin that consists of a chemically stable ether linkage formed by an interaction between a reactive 2-thiopyridyl disulfide group with sepharose (**Supplementary Figure 2**). RAC is used for the enrichment of Cys-containing peptides through the formation of a covalent disulfide bond between the Cys and the thiopropyl group of the resin. Non-Cys-containing peptides are washed away by washing buffer (see Guo et al., 2014 for details), and Cys-containing peptides are eluted using a reducing reagent (DTT). Eluted peptides can be directly analyzed by LC-MS/MS with label-free quantification or can be labeled with either stable isotopic labeling or isobaric tags if higher quantitative accuracy is required.

QUANTITATIVE MS-BASED APPROACHES FOR ANALYSIS OF OXI-CYS PTMs

There are two main types of data acquisition strategies, data-dependent acquisition (DDA) and data-independent acquisition (DIA). In DDA mode, a fixed number (Top N approach) of peptides are selected based on their intensity in MS1 scans, for fragmentation in MS2 scans. MS1 (intact peptide mass) and MS2 (fragment ion masses) data are analyzed using database-searching algorithms to score peptide-spectral matches (PSMs) for peptide/protein identification. Peptides are usually quantified using either MS1 or MS2 data, and well-established statistical and bioinformatics strategies are used to identify significantly different levels of peptides/proteins between conditions.

Many approaches use DDA for Oxi-Cys analysis, such as differential alkylation, iodoTMT, SICyCLIA *etc.*, but missing values across multiplex/multiple samples is an issue that can affect the statistical analysis of quantitative data. To overcome this, an unbiased technology in quantitative proteomics – DIA, such as sequential window acquisition of all theoretical mass spectra (SWATH-MS) and targeted DIA (SRM/MRM), can be used (Gillet et al., 2012). In a typical DIA analysis, a relatively wide mass/charge window is used for the isolation of peptides for fragmentation. In doing so, all detectible peptides are fragmented and quantified, which results in improved accuracy and precision of quantitation at the protein level with fewer missing values. The complexity of MS2 data in DIA, however, results in a challenge for data analysis, as it requires more sophisticated computation compared to DDA to identify peptides from spectra generated by the fragmentation of several peptides in a single MS2 scan. Approaches, where specific proteins/peptide are targeted for analysis (SRM/MRM and PRM) are also widely used for a robust quantitation of selected peptides/proteins and their PTMs.

Label-Free Quantification (LFQ)

The development of advanced MS instrumentation (with high mass accuracy, resolution and sensitivity), together with highly reproducible nanoflow chromatography, has allowed the widespread use of LFQ-based quantification in bottom-up proteomics. LFQ can be used instead of labeling approaches (stable isotopic labeling or isobaric tags) to quantify proteins/peptides using sequential LC-MS/MS analysis of samples. Compared to labeling approaches, LFQ offers a higher dynamic range than isotope labeling methods, but the quantitative accuracy is lower, and typically, more replicates are required for robust quantitation. In this approach, each digested proteome is run separately on an LC-MS/MS platform, and the quantitation is carried out based on XIC (extracted ion chromatogram) intensities (Wang et al., 2008). In XIC, the ion current signal (in MS1) associated with each individual peptide is used to reconstruct the area under the curve during chromatography which is proportional to the amount of peptide present. The performance of LFQ-based quantification can be improved by the incorporation of more advanced data processing. For example, retention time alignment across samples and "matching between runs" in which missing values are reduced by transferring peptide identifications based on narrow mass and retention time windows. This minimizes missing values due to poor fragmentation data or cases where a peptide is not selected for fragmentation because it was present at a lower amount in one sample compared to others in an experiment.

Stable-Isotope Dimethyl Labeling

Stable-isotope dimethyl labeling employs different isotopomers of formaldehyde and cyanoborohydride to introduce dimethyl groups to the N-termini and side chains of lysine residues which differ by at least 4 Da. This is used to label usually 2–3 samples, but up to 5 samples (5-plex) can be labeled and pooled in a single experiment if other formaldehyde/cyanoborohydride isotopomers are used (Wu et al., 2014). The application of multiplexing for labeling multiple samples in a single experiment offers many benefits as analysis of multiple samples can be performed in the same experiment and thereby reduced the amount of instrument time required. On the one hand, given that samples are pooled and analyzed within an LC-MS/MS acquisition, this type of quantification is more accurate than sequential label-free quantification approaches. However, because the samples are pooled, the peptide complexity is increased, and up-front peptide fractionation may be required depending on the initial sample complexity and acquisition speed of the MS instrument.

Multiplex Isobaric Tagging

Multiplex approaches (iodoTMT and cysTMTRAQ) allow the analysis of up to six different samples in a single experiment.

This is achieved by labeling samples with chemical tags which add the same overall mass to each peptide (same mass addition in MS1), but when labeled peptides are fragmented in MS2 scans, they generate signature (barcoded) ions used for quantitation of each individual sample. The key difference between isobaric tags and isotopic labeling approaches is that all isobaric tags are identical in total mass (see **Figure 4C**). In contrast, isotopic labeling masses are different when labeling peptides and peptides are distinguished by a mass difference in MS1 scans. The quantitation of peptides using isotopic labeling is performed based on the intensity of peptides measured in MS1 spectra, while that of the isobaric tagging approach is carried out based on the intensity of tags cleaved from labeled peptides in MS2 spectra with signature masses (e.g., 126, 127, 128, 129, 130, and 131 m/z). In a complex digested sample, co-elution (from online-HPLC) and co-isolation (at MS1) of peptides with others with a similar m/z result can result in a combination of the reporter ion intensity from different peptides, resulting in a bias in the relative ratio of a peptide from different proteomes. This is a particular challenge for quantifying low abundance peptides/proteins as the interference is much higher. Specific data acquisition strategies and statistical analysis packages have been developed to address this issue of ratio compression (Pappireddi et al., 2019).

Multiple Reaction Monitoring (MRM)

MRM (also known as SRM, Selected Reaction Monitoring) is used to analyze specific proteins/peptides of interest in a complex sample by selectively targeting peptides to enhance the reproducibility and accuracy of quantitation, especially for low abundance proteins/peptides. This approach involves the isolation of targeted peptides (enzymatically digested from proteins of interest) and specific fragment ions from the targeted peptides. This is typically performed in a triple quadrupole mass spectrometer. The first and third quadrupoles are used as filters to specifically select the targeted ions (m/z) corresponding to peptides of interest and specific fragment ions fragmented from the targeted peptides. The second quadrupole acts as a collision cell for fragmentation of the targeted ions. The transition of ion pairs (precursors/fragment ions) are monitored continuously during the MS run to generate a spectrum that contains signal intensities of specific transitions as a function of time (Lange et al., 2008). Given that this approach uses a selective ion pair technique, not a "full scan" technique like others, it can improve sensitivity by up to two orders of magnitude and the linear response over a wide dynamic range up to five orders of magnitude compared to "full scan" technique (Lange et al., 2008). MRM can measure peptides from more than 100 proteins per acquisition using high-speed triple quadrupole MS in line with accurate retention time scheduling (Percy et al., 2014). A variant of this approach, Parallel-reaction monitoring (PRM), can be performed using a high-resolution instrument such as the Orbitrap instrument. Unlike MRM in which typically three fragment ions are monitored in transitions, in PRM all fragment ions are measured for the set of targeted peptides (Meyer and Schilling, 2017).

An approach named OxiMRM has been developed for targeted Oxi-Cys proteomics analysis. It utilizes a stable isotopic approach to label Cys residues *via* two different alkylating steps, light (d_0) and heavy (d_5) stable isotope labeled NEM to label reduced and Oxi-Cys, respectively (**Figure 4B**). These labeled proteins are then subjected to immunoaffinity purification to enrich a specific protein of interest before being digested with trypsin and quantified using a multiple reaction monitoring (MRM) method (Held et al., 2010). This technique offers a highly sensitive and reproducible approach to target specific Cys residues in proteins of interest that can be used to quantify both sulfinic and sulfonic acid oxidation levels (Held et al., 2010). Another method in this category, UPLC-pSRM (combination of nano-UPLC and pseudo-SRM performed on a LTQ-Orbitrap), has been introduced to detect and quantify irreversible Cys oxidation (Lee et al., 2013) without any enrichment step. The approach employs a high chromatographic resolution (using a long reverse-phase nano-UPLC column) to separate different forms of Oxi-Cys and a high mass accuracy, resolution and sensitivity of an Orbitrap instrument for identification and quantitation of modified Cys sites (Lee et al., 2013). The benefit of this technique is that it allows direct detection of irreversibly linked Oxi-Cys residues in peptides/proteins.

Cysteine-Specific Data Independent Analysis (Cys-DIA)

The ultimate benefit of DIA is that it can measure most detectible peptides falling in a selected *m/z* window to improve the accuracy and precision of peptide quantitation with minimal missing values. In that context, Cys-DIA was used to analyze Cys-containing peptides purified with Thiopropyl Sepharose^{TM} 6B beads (as discussed in section "Thiol-affinity resin-assisted capture") to increase Cys-proteome coverage up to 35% compared to conventional DIA/SWATH approach. In brief, all reversible Oxi-Cys residues are reduced by (DTT or TECP), and all free reduced Cys residues (newly formed and native reduced Cys) are subjected to Cys purification. These purified Cys-peptides are then analyzed on an Orbitrap instrument (Q-Exactive HF-X) operated in high-resolution MS1 DIA mode (HRMS1-DIA) to quantify Cys-containing peptides (Tahir et al., 2020). A typical selection of 25–50 *m/z* windows covering from 400 to 1500 *m/z* is used, and all ionized peptides within that range are fragmented, generating complex spectra of fragmented ions. Unlike DDA data, DIA data can be searched against a peptide spectral reference library generated from separate DDA experiments to identify and quantitate peptides (Tahir et al., 2020).

CYSTEINE OXIDATION IN NEURODEGENERATIVE DISEASES

We have surveyed published articles using PubMed[1], from the last 20 years, for studies that include proteomic analysis of Cys oxidation in neurodegenerative diseases with different keywords, as shown in Figure S1. Keywords for searching included: proteo* and oxida* and cysteine (used as fixed keywords), and then other

[1]https://pubmed.ncbi.nlm.nih.gov/

variables such as neuro*, human, AD, Parkinson disease (PD), multiple sclerosis (MS), and motor neuron disease (MND)/ALS. Generally, Oxy-Cys studies have steadily increased over the last two decades. However, when specific neurodegenerative disease keywords (AD, PD, MS, MND, and ALS) were included, the number of proteomics studies of Cys oxidation in the context of neurodegenerative disease is strikingly low. Many hits were found for PD and AD, but when these hits were manually inspected, the total number of studies for Oxi-Cys proteomics was less than ten; especially a combination of fixed keywords with human and MND (or ALS) resulted in no hits.

Moreover, we have also examined data from the CSF (cerebrospinal fluid) Proteome Resource[2] containing 128 human CSF proteomics datasets (4,192 proteins) available from 31 research articles for neurodegenerative disease studies (AD, MS, PD, and ALS) from 2010 to 2019 (Guldbrandsen et al., 2017), there were no Oxy-Cys proteomic studies. This indicates that despite the oxidative state of Cys playing important roles in neurodegenerative diseases, very little (or no) studies have been performed to investigate how global changes in Cys oxidation are altered in neurodegenerative diseases or how it changes in response to disease progression and treatment. Here, we review recent Oxi-Cys PTMs studies to characterize oxidation changes in neurodegenerative diseases.

Alzheimer's Disease

S-NO is implicated in AD through its association with impaired metabolism, mitochondrial dysfunction, neuronal loss, and protein misfolding and aggregation (Dyer et al., 2017). Various methods have been used to measure changes in *S*-NO in mouse models of AD and clinical samples. Using the OxcyscPILOT approach, Dyer et al. (2017) identified 135 *S*-NO modified proteins, of which 11 proteins were differentially regulated in an AD (APP/PS1) mouse model. This approach allows comparison of *S*-NO levels across different samples (up to 6 samples) as well as measuring total (reduced and reversibly oxidized) cysteine-containing peptides so that the levels of *S*-NO can be easily normalized in a single experiment (Dyer et al., 2017). However, this technique has not yet been applied to the analysis of clinical samples.

Synaptic loss and neuroinflammation contribute to early pathophysiological changes in AD. The induction of nitric oxide synthase type 2 leads to increased nitric oxide levels and *S*-NO of cysteine residues (Paula et al., 2010). An isobaric tag approach, iodoTMT, was used to reveal the *S*-NO sites on Cys residues of NOS2-dependent *S*-NO of synaptic proteins in mild cognitive impairment (MCI) and AD and human control brain tissues (Wijasa et al., 2020). Of 291 and 295 *S*-NO proteins identified in synaptosome fractions, 16 and 9 *S*-NO proteins were significantly increased in AD vs. MCI brains and AD vs. Ctrl, respectively (Wijasa et al., 2020). Of these up-regulated *S*-NO proteins, three proteins, myelin-oligodendrocyte glycoprotein (MOG), glutathione *s*-transferase Mu 3 (GSTM3), and four and a half LIM domains protein 1 (FHL1), were found at a higher level in AD compared to either MCI or Ctrl cases (Wijasa et al., 2020). Furthermore, this study identified 23 potential *S*-NO biomarkers (see Wijasa et al., 2020 for details). The up-regulation of MOG was associated with an increased production of autoantibodies against MOG protein in AD, indicating early demyelination of the hippocampal region (Papuć et al., 2015). The exact functions of FHL1 or GSTM3 in synapses are still unclear (Wijasa et al., 2020). Other *S*-NO modified proteins such as neurocan core protein (NCAN), calmodulin-dependent protein kinase type II subunit gamma (CAMK2G), CD44 and aspartate aminotransferase (GOT1) were also reported to be increased in abundance in AD brains as well as in human CSF (Wijasa et al., 2020), representing potential AD biomarkers for future study.

Antibodies to measure specific Cys oxidation types have been used for the detection and measurement of protein oxidation in neurodegenerative diseases, e.g., *S*-nitrosocysteine antibody for *S*-NO. In an early Oxi-Cys proteomics study, Choi et al. (2004) applied a 2-D protein gel-based approach coupled with immunostaining and MS analysis to discover three human brain UCH-L1 isoforms that contain Oxi-Cys, suggesting the oxidation might damage the ubiquitination/de-ubiquitination machinery involved in the etiology of AD and PD. Newman et al. (2007) utilized 2-D-Oxyblots and MS analysis to identify specific targets of *S*-glutathionylated Cys in AD inferior parietal lobule (IPL) compared to control IPL, in which three proteins, deoxyhemoglobin, α-crystallin B, glyceraldehyde phosphate dehydrogenase (GAPDH), and α-enolase, were significantly *S*-glutathionylated in AD IPL (Newman et al., 2007). The exact functions of these *S*-glutathionylated proteins were not elucidated, but the study identified several proteins sensitive to oxidative stress in the AD brain (Newman et al., 2007). Using a similar approach, Zahid et al. (2014) reported three proteins [voltage-dependent anion-selective channel protein 2 (VDAC2), superoxide dismutase [Mn] (SOD2), and fructose-bisphosphate aldolase C (ALDOC)] that were *S*-glutathionylated in autopsied brain specimens (hippocampus, substantia nigra and cortex) (Zahid et al., 2014). Although MS was used to identify *S*-glutathionylated proteins, the exact location of Oxi-Cys sites within these proteins was only predicted by *in silico* analysis. The altered levels of *S*-NO in AD might contribute to disease-related consequences (Zahid et al., 2014).

Transthyretin (TTR), an abundant CSF protein, contains both free and oxidized Cys residues. The relative changes between these two states generate different TTR isoforms under oxidative stress conditions (Poulsen et al., 2014). This protein can bind to beta-amyloid peptide, and familial amyloidosis diseases (e.g., familial amyloid polyneuropathy) have been associated with its variants (Biroccio et al., 2006). In a later study, Poulsen et al. (2014) adopted this approach to characterize the oxidation isoforms of TTR in CSF from AD, MCI, and normal pressure hydrocephalus (NPH) patients and HCs, and an increased oxidation level of Cys_{10} in TTR isoforms was observed in AD and MCI compared to other groups. This offers a potential novel biomarker for the diagnosis of AD in patients but would need to be investigated in larger cohorts of patients for validation.

[2]https://proteomics.uib.no/csf-pr/

Multiple Sclerosis

Multiple sclerosis is a neuroinflammatory disease associated with demyelination and axonal damage (Compston and Coles, 2002). Oxidative stress is a crucial factor contributing to the disease pathology *via* demyelination and oligodendroglia degeneration (Konat and Wiggins, 1985). Using a modified proteomics approach, which excluding reduction and alkylation steps to retain glutathione attached to cysteine through disulfide linkage, coupled with a targeted database search, Srivastava et al. (2019) characterized *S*-glutathionylation of CSF proteins in MS. In particular, they identified several proteins that were glutathionylated in patients with MS during a relapse, including three proteins (ECSOD, A1AT, and PLTP) which were oxidized at functionally important positions in their structure (Srivastava et al., 2019). This indicates that *S*-glutathionylation may negatively regulate the function of these proteins in MS (Liedhegner et al., 2012). However, given that this study has a limited sample size, validation of these oxidation changes needs to be performed in larger patient cohorts to confirm a link between *S*-glutathionylation and MS (Srivastava et al., 2019).

DISCUSSION AND FUTURE DIRECTIONS

Over the last 20 years, proteomic analysis of Cys oxidation has revealed global profiles of the redox network in many biological systems. Two main types of analyses have been performed, oxidation site mapping and quantitation and thiol reactivity profiling (Fu et al., 2020). The site mapping Oxi-Cys strategy has many approaches (BST, RAC, iodoTMT, *etc.*) to identify redox-sensitive cysteines in proteins and quantitation of dynamic changes in cysteine oxidation in response to a variety of perturbations (Jaffrey et al., 2001; Forrester et al., 2009; Guo et al., 2014; Gu and Robinson, 2016a). A summary of approaches used for the analysis of Cys PTMs and their applications is shown in **Figure 9**, and further details of the advantages and disadvantages of each method are listed in **Supplementary Table 1**.

Advantages and Disadvantages

The identification and quantitation of various forms of cysteine oxidation remain challenging because of the low abundance of cysteine in the proteome and the sub-stoichiometric nature of oxidation. It requires robust tools to characterize the Oxi-Cys proteome. As discussed above, many approaches, mostly attempting to enrich Oxi-Cys residues or Cys-containing peptides, have been established, such as iodoTMT, isoTOP-ABPP, QTRP, and DiaAlk. Selective Oxi-Cys proteomics approaches, mainly based on BST or probes, offer higher sensitivity, specificity and precision (Mnatsakanyan et al., 2019) than methods that don't incorporate an enrichment step (differential alkylation, SICyLIA, or CysTMTRAQ). However, Oxi-Cys approaches, which rely on an enrichment step, might not directly capture the native oxidized state of proteins under physiological conditions. An alternative to this is the SICyLIA approach, a simple, unbiased and robust method to sensitively detect and accurately quantify global oxidized Cys-proteomes since it does not require Cys enrichment (van der Reest et al., 2018). However, given the lack of an enrichment step in the SICyLIA approach, it may be less suitable for the analysis of low abundance proteins and cases where the stoichiometry of oxidation is low.

Most of the approaches listed in **Figure 9** (apart from Differential alkylation and DiaAlk) require an extra experiment/additional MS time to measure protein expression levels which is necessary for the normalization of Cys oxidation levels. This is an important consideration if protein expression differences are likely to occur between experimental and control conditions.

Most of the methods shown in **Figure 9** are not directly compatible with the analysis of irreversible cysteine oxidation. However, in some cases, data from some approaches such as differential alkylation or SICyLIA can allow the identification of irreversible Cys oxidation (*S*-O_3H or *S*-O_2H) if these modifications are selected in database searching algorithms. Click chemistry-based approaches offer many benefits for the study of reversible Oxi-Cys residues, such as high selectivity and direct measurement and determination of exact sites of Cys containing PTMs. However, there are no available probes designed for targeting and purifying peptides/proteins containing irreversible Oxi-Cys (*S*-O_3H), but a few for *S*-O_2H, such as the DiaAlk probe have been developed (**Figure 5B**).

Isobaric tag-based approaches (iodoTMT and CysTMTRAQ) have been used in several Oxy-Cys PTM studies, redox and electrophile reactive Cys proteome applications (Gygi et al., 1999; Jaffrey et al., 2001; Chouchani et al., 2017) because of the commercial availability of reagents as well as their multiplexing capability. However, the high cost of reagents and high-end MS instrumentation required to avoid ratio compression due to co-isolated peptides is potentially a barrier to the wide adoption of these approaches. Furthermore, the large structure of isobaric tag labeling reagents may have reduced accessibility to react with sterically buried Cys in native conditions (Fu et al., 2020).

Perspectives

Recent advances in MS-based proteomics, biomarker discovery in the context of neurodegenerative disease has significant potential. Applications include the identification of biomarkers for earlier diagnosis of disease and biomarkers of drug-target engagement that can be used for the development and testing of new therapies.

Recent studies using protein biomarkers for AD diagnosis highlight the advances in biomarker discovery for neurodegenerative diseases. The diagnosis of AD relies on a combination of clinical criteria, brain scans and a neurological exam. Disease pathology is reflected in biomarkers, including amyloid-beta 1–42 peptide ($A\beta_{1-42}$), tau protein (t-tau), and tau phosphorylated at Thr-181 (p-tau181) in CSF (Begcevic et al., 2018). However, only two validated methods have been used to identify amyloid-beta in the brain; measurement of levels in CSF or positron-emission tomography (PET) brain imaging (Nakamura et al., 2018). Nakamura et al. (2018) recently developed an immunoprecipitation-MS (IP-MS) based assay to measure amyloid-beta precursor protein $(APP)_{669-711}$/amyloid-β $(A\beta)_{1-42}$ and $A\beta_{1-40}/A\beta_{1-42}$ ratios in plasma to predict

brain amyloid-β burden. The performance of this composite biomarker was high [areas under the receiver operating characteristic curves (AUCs) in both data sets (discovery, 96.7%, n = 121 and validation, 94.1%, n = 111)]. It had an accuracy of 90% compared to diagnosis with PET imaging, demonstrating the potential clinical utility of this MS-based biomarker assay (Nakamura et al., 2018).

Going beyond protein expression level biomarkers to protein modification markers in neurodegenerative disease is the next step toward accessing, for example, earlier markers of disease progression and a means to evaluate therapeutic efficacy. For example, the application of Oxi-Cys proteomics approaches to study changes in oxidation in CSF from patients in longitudinal studies may reveal proteins with an oxidation status that correlates to disease progression. The efficacy of therapeutics designed to reduce oxidative stress in patients could be tested for their ability to reduce the level of these oxidation biomarkers and would therefore allow measurement of target engagement in clinical studies. There is also a variety of preclinical applications of Oxi-Cys proteomics in which the impact of specific human disease mutations on oxidation profiles can be assessed in animal models.

It is necessary to develop reliable proteomics approaches to build a global resource of (reversibly and irreversibly) Oxi-Cys proteomes in different clinical samples and types of neurodegenerative diseases (brain tissues, CSF, blood serum, *etc.*) that can be used to identify biomarkers in diagnosis and drug development studies. This resource could focus on: specific cell types of global Oxi-Cys proteomes to understand the disease mechanism of neurodegenerative diseases; integration of Oxi-Cys proteomics networks in brain tissue, CSF or plasma. Furthermore, these will also contribute to the understanding of neurodegenerative disease pathogenesis, progression, monitoring and treatment. Indeed, the integration of Oxi-proteomics data and data from the metabolomics of oxidative stress combined with *in silico* computational models, will provide a clearer picture of oxidative stress processes in neurodegenerative diseases.

AUTHOR CONTRIBUTIONS

TP, WB, and RM wrote the first draft of the manuscript. PS and MC edited the manuscript. All authors contributed to the article and approved the submitted version.

FUNDING

The authors acknowledge funding support from the UK Medical Research Council (MR/S004920/1) and the Sheffield NIHR Biomedical Research Centre (IS-BRC-1215-20017). PS was supported as an NIHR Senior Investigator (NF-SI-0617–10077).

SUPPLEMENTARY MATERIAL

The Supplementary Material for this article can be found online at: https://www.frontiersin.org/articles/10.3389/fnmol.2021.678837/full#supplementary-material

REFERENCES

Abo, M., Bak, D. W., and Weerapana, E. (2017). Optimization of caged electrophiles for improved monitoring of cysteine reactivity in living cells. *Chembiochem* 18, 81–84. doi: 10.1002/cbic.201600524

Abo, M., Li, C., and Weerapana, E. (2018). Isotopically-labeled iodoacetamide-alkyne probes for quantitative cysteine-reactivity profiling. *Mol. Pharm.* 15, 743–749. doi: 10.1021/acs.molpharmaceut.7b00832

Abo, M., and Weerapana, E. (2015). A caged electrophilic probe for global analysis of cysteine reactivity in living cells. *J. Am. Chem. Soc.* 137, 7087–7090. doi: 10.1021/jacs.5b04350

Akter, S., Fu, L., Jung, Y., Conte, M. L., Lawson, J. R., Lowther, W. T., et al. (2018). Chemical proteomics reveals new targets of cysteine sulfinic acid reductase. *Nat. Chem. Biol.* 14, 995–1004. doi: 10.1038/s41589-018-0116-2

Andersen, J. K. (2004). Oxidative stress in neurodegeneration: cause or consequence? *Nat. Med.* 10, 18–25.

Ansong, C., Wu, S., Meng, D., Liu, X., Brewer, H. M., Deatherage Kaiser, B. L., et al. (2013). Top-down proteomics reveals a unique protein S-thiolation switch in *Salmonella* Typhimurium in response to infection-like conditions. *Proc. Natl. Acad. Sci. U S A* 110, 10153–10158. doi: 10.1073/pnas.1221210110

Auclair, J. R., Salisbury, J. P., Johnson, J. L., Petsko, G. A., Ringe, D., Bosco, D. A., et al. (2014). Artifacts to avoid while taking advantage of top-down mass spectrometry based detection of protein S-thiolation. *Proteomics* 14, 1152–1157. doi: 10.1002/pmic.201300450

Barber, S. C., and Shaw, P. J. (2010). Oxidative stress in ALS: key role in motor neuron injury and therapeutic target. *Free Radic. Biol. Med.* 48, 629–641. doi: 10.1016/j.freeradbiomed.2009.11.018

Begcevic, I., Brinc, D., Brown, M., Martinez-Morillo, E., Goldhardt, O., Grimmer, T., et al. (2018). Brain-related proteins as potential CSF biomarkers of Alzheimer's disease: a targeted mass spectrometry approach. *J. Proteomics* 182, 12–20. doi: 10.1016/j.jprot.2018.04.027

Biroccio, A., Del Boccio, P., Panella, M., Bernardini, S., Di Ilio, C., Gambi, D., et al. (2006). Differential post-translational modifications of transthyretin in Alzheimer's disease: a study of the cerebral spinal fluid. *Proteomics* 6, 2305–2313. doi: 10.1002/pmic.200500285

Bomgarden, R. D., Viner, R. I, Kuhn, K., Pike, I., and Rogers, J. C. (2012). Iodoacetyl tandem mass tags for cysteine peptide modification, enrichment and quantitation. *iHUPO*

Bosco, D. A., Morfini, G., Karabacak, N. M., Song, Y., Gros-Louis, F., Pasinelli, P., et al. (2010). Wild-type and mutant SOD1 share an aberrant conformation and a common pathogenic pathway in ALS. *Nat. Neurosci.* 13, 1396–1403. doi: 10.1038/nn.2660

Brosnan, J. T., and Brosnan, M. E. (2006). The sulfur-containing amino acids: an overview. *J. Nutr.* 136, 1636s–1640s.

Chen, C.-H., Li, W., Sultana, R., You, M.-H., Kondo, A., Shahpasand, K., et al. (2015). Pin1 cysteine-113 oxidation inhibits its catalytic activity and cellular function in Alzheimer's disease. *Neurobiol. Dis.* 76, 13–23. doi: 10.1016/j.nbd.2014.12.027

Chen, L.-N., Shi, Q., Zhang, B.-Y., Zhang, X.-M., Wang, J., Xiao, K., et al. (2016). Proteomic analyses for the global S-Nitrosylated proteins in the brain tissues of different human prion diseases. *Mol. Neurobiol.* 53, 5079–5096. doi: 10.1007/s12035-015-9440-7

Chen, X., Wong, Y. K., Wang, J., Zhang, J., Lee, Y.-M., Shen, H.-M., et al. (2017). Target identification with quantitative activity based protein profiling (ABPP). *Proteomics* 17:1600212. doi: 10.1002/pmic.201600212

Choi, J., Levey, A. I., Weintraub, S. T., Rees, H. D., Gearing, M., Chin, L. S., et al. (2004). Oxidative modifications and down-regulation of ubiquitin carboxyl-terminal hydrolase L1 associated with idiopathic Parkinson's and Alzheimer's diseases. *J. Biol. Chem.* 279, 13256–13264. doi: 10.1074/jbc.m314124200

Chouchani, E. T., James, A. M., Methner, C., Pell, V. R., Prime, T. A., Erickson, B. K., et al. (2017). Identification and quantification of protein S-nitrosation by nitrite in the mouse heart during ischemia. *J. Biol. Chem.* 292, 14486–14495. doi: 10.1074/jbc.m117.798744

Compston, A., and Coles, A. (2002). Multiple sclerosis. *Lancet* 359, 1221–1231.

Dalle-Donne, I., Scaloni, A., Giustarini, D., Cavarra, E., Tell, G., Lungarella, G., et al. (2005). Proteins as biomarkers of oxidative/nitrosative stress in diseases: the contribution of redox proteomics. *Mass Spectrom Rev.* 24, 55–99. doi: 10.1002/mas.20006

Durham, T. B., and Blanco, M. J. (2015). Target engagement in lead generation. *Bioorg. Med. Chem. Lett.* 25, 998–1008. doi: 10.1016/j.bmcl.2014.12.076

Dyer, R. R., Gu, L., and Robinson, R. A. S. (2017). "S-nitrosylation in Alzheimer's disease using oxidized cysteine-selective cPILOT," in *Current proteomic approaches applied to brain function*, eds E. Santamana and J. Fernández-Irigoyen (New York: Springer), 225–241. doi: 10.1007/978-1-4939-7119-0_14

Erickson, B. K., Jedrychowski, M. P., Mcalister, G. C., Everley, R. A., Kunz, R., and Gygi, S. P. (2015). Evaluating multiplexed quantitative phosphopeptide analysis on a hybrid quadrupole mass filter/linear ion trap/orbitrap mass spectrometer. *Anal. Chem.* 87, 1241–1249. doi: 10.1021/ac503934f

Fang, J., Nakamura, T., Cho, D.-H., Gu, Z., and Lipton, S. A. (2007). S-nitrosylation of peroxiredoxin 2 promotes oxidative stress-induced neuronal cell death in Parkinson's disease. *Proc. Natl. Acad. Sci.* 104, 18742–18747. doi: 10.1073/pnas.0705904104

Forrester, M. T., Thompson, J. W., Foster, M. W., Nogueira, L., Moseley, M. A., and Stamler, J. S. (2009). Proteomic analysis of S-nitrosylation and denitrosylation by resin-assisted capture. *Nat. Biotechnol.* 27, 557–559. doi: 10.1038/nbt.1545

Fu, L., Li, Z., Liu, K., Tian, C., He, J., He, J., et al. (2020). A quantitative thiol reactivity profiling platform to analyze redox and electrophile reactive cysteine proteomes. *Nat. Protoc.* 15, 2891–2919. doi: 10.1038/s41596-020-0352-2

Fu, L., Liu, K., Sun, M., Tian, C., Sun, R., Morales Betanzos, C., et al. (2017). Systematic and quantitative assessment of hydrogen peroxide reactivity with cysteines across human proteomes. *Mol. Cell. Proteomics* 16, 1815–1828. doi: 10.1074/mcp.ra117.000108

Gillet, L. C., Navarro, P., Tate, S., Röst, H., Selevsek, N., Reiter, L., et al. (2012). Targeted data extraction of the MS/MS spectra generated by data-independent acquisition: a new concept for consistent and accurate proteome analysis. *Mol. Cell. Proteomics* 11:16717.

Group, W. G. E. M.-A. S. (2017). Safety and efficacy of edaravone in well defined patients with amyotrophic lateral sclerosis: a randomised, double-blind, placebo-controlled trial. *Lancet Neurol.* 16, 505–512.

Gu, L., and Robinson, R. A. (2016a). High-throughput endogenous measurement of S-nitrosylation in Alzheimer's disease using oxidized cysteine-selective cPILOT. *Analyst* 141, 3904–3915. doi: 10.1039/c6an00417b

Gu, L., and Robinson, R. A. (2016b). Proteomic approaches to quantify cysteine reversible modifications in aging and neurodegenerative diseases. *Proteomics Clin. Appl.* 10, 1159–1177. doi: 10.1002/prca.201600015

Guldbrandsen, A., Farag, Y., Kroksveen, A. C., Oveland, E., Lereim, R. R., Opsahl, J. A., et al. (2017). CSF-PR 2.0: an interactive literature guide to quantitative cerebrospinal fluid mass spectrometry data from neurodegenerative disorders. *Mol. Cell. Proteomics* 16, 300–309. doi: 10.1074/mcp.o116.064477

Guo, C., Sun, L., Chen, X., and Zhang, D. (2013). Oxidative stress, mitochondrial damage and neurodegenerative diseases. *Neural. Regen. Res.* 8, 2003–2014.

Guo, J., Gaffrey, M. J., Su, D., Liu, T., Camp, D. G. II, Smith, R. D., et al. (2014). Resin-assisted enrichment of thiols as a general strategy for proteomic profiling of cysteine-based reversible modifications. *Nat. Protoc.* 9, 64–75. doi: 10.1038/nprot.2013.161

Gygi, S. P., Rist, B., Gerber, S. A., Turecek, F., Gelb, M. H., and Aebersold, R. (1999). Quantitative analysis of complex protein mixtures using isotope-coded affinity tags. *Nat. Biotechnol.* 17, 994–999. doi: 10.1038/13690

Hall, A., Karplus, P. A., and Poole, L. B. (2009). Typical 2-Cys peroxiredoxins – structures, mechanisms and functions. *FEBS J.* 276, 2469–2477. doi: 10.1111/j.1742-4658.2009.06985.x

Held, J. M., Danielson, S. R., Behring, J. B., Atsriku, C., Britton, D. J., Puckett, R. L., et al. (2010). Targeted quantitation of site-specific cysteine oxidation in endogenous proteins using a differential alkylation and multiple reaction monitoring mass spectrometry approach. *Mol. Cell. Proteomics* 9, 1400–1410. doi: 10.1074/mcp.m900643-mcp200

Ising, C., Venegas, C., Zhang, S., Scheiblich, H., Schmidt, S. V., Vieira-Saecker, A., et al. (2019). NLRP3 inflammasome activation drives tau pathology. *Nature* 575, 669–673.

Jaffrey, S. R., Erdjument-Bromage, H., Ferris, C. D., Tempst, P., and Snyder, S. H. (2001). Protein S-nitrosylation: a physiological signal for neuronal nitric oxide. *Nat. Cell. Biol.* 3, 193–197. doi: 10.1038/35055104

Jones, D. P. (2006). Redefining oxidative stress. *Antioxid. Redox. Signal.* 8, 1865–1879. doi: 10.1089/ars.2006.8.1865

Joshi, A. U., Minhas, P. S., Liddelow, S. A., Haileselassie, B., Andreasson, K. I., Dorn, G. W., et al. (2019). Fragmented mitochondria released from microglia trigger A1 astrocytic response and propagate inflammatory neurodegeneration. *Nat. Neurosci.* 22, 1635–1648. doi: 10.1038/s41593-019-0486-0

Kolb, H. C., Finn, M. G., and Sharpless, K. B. (2001). Click chemistry: diverse chemical function from a few good reactions. *Angew. Chem. Int. Ed. Engl.* 40, 2004–2021. doi: 10.1002/1521-3773(20010601)40:11<2004::aid-anie2004>3.0.co;2-5

Konat, G. W., and Wiggins, R. C. (1985). Effect of reactive oxygen species on myelin membrane proteins. *J. Neurochem.* 45, 1113–1118. doi: 10.1111/j.1471-4159.1985.tb05530.x

Lange, V., Picotti, P., Domon, B., and Aebersold, R. (2008). Selected reaction monitoring for quantitative proteomics: a tutorial. *Mol. Syst. Biol.* 4:222. doi: 10.1038/msb.2008.61

Lee, C.-F., Paull, T. T., and Person, M. D. (2013). Proteome-wide detection and quantitative analysis of irreversible cysteine oxidation using long column UPLC-pSRM. *J. Proteome Res.* 12, 4302–4315. doi: 10.1021/pr400201d

Li, F., Calingasan, N. Y., Yu, F., Mauck, W. M., Toidze, M., Almeida, C. G., et al. (2004). Increased plaque burden in brains of APP mutant MnSOD heterozygous knockout mice. *J. Neurochem.* 89, 1308–1312. doi: 10.1111/j.1471-4159.2004.02455.x

Liedhegner, E. A. S., Gao, X.-H., and Mieyal, J. J. (2012). Mechanisms of altered redox regulation in neurodegenerative diseases—Focus on S-glutathionylation. *Antioxidants Redox Signal.* 16, 543–566. doi: 10.1089/ars.2011.4119

Lin, M. T., and Beal, M. F. (2006). Mitochondrial dysfunction and oxidative stress in neurodegenerative diseases. *Nature* 443, 787–795. doi: 10.1038/nature05292

Lorenzatto, K. R., Kim, K., Ntai, I., Paludo, G. P., Camargo De Lima, J., Thomas, P. M., et al. (2015). Top down proteomics reveals mature proteoforms expressed in subcellular fractions of the *Echinococcus granulosus* preadult stage. *J. Proteome Res.* 14, 4805–4814. doi: 10.1021/acs.jproteome.5b00642

Markesbery, W. R., and Carney, J. M. (1999). Oxidative alterations in Alzheimer's disease. *Brain Pathol.* 9, 133–146.

Maurais, A. J., and Weerapana, E. (2019). Reactive-cysteine profiling for drug discovery. *Curr. Opin. Chem. Biol.* 50, 29–36. doi: 10.1016/j.cbpa.2019.02.010

McConnell, E. W., Smythers, A. L., and Hicks, L. M. (2020). Maleimide-based chemical proteomics for quantitative analysis of cysteine reactivity. *J. Am. Soc. Mass Spectrometry* 31, 1697–1705. doi: 10.1021/jasms.0c00116

McDonagh, B., Sakellariou, G. K., Smith, N. T., Brownridge, P., and Jackson, M. J. (2014). Differential cysteine labeling and global label-free proteomics reveals an altered metabolic state in skeletal muscle aging. *J. Proteome Res.* 13, 5008–5021. doi: 10.1021/pr5006394

Meyer, J. G., and Schilling, B. (2017). Clinical applications of quantitative proteomics using targeted and untargeted data-independent acquisition techniques. *Expert Rev. Proteomics* 14, 419–429. doi: 10.1080/14789450.2017.1322904

Mnatsakanyan, R., Markoutsa, S., Walbrunn, K., Roos, A., Verhelst, S. H. L., and Zahedi, R. P. (2019). Proteome-wide detection of S-nitrosylation targets and motifs using bioorthogonal cleavable-linker-based enrichment and switch technique. *Nat. Commun.* 10:2195.

Murray, C. I., and Eyk, J. E. V. (2012). Chasing cysteine oxidative modifications: proteomic tools for characterizing cysteine redox status. *Circ. Cardiovasc. Genet.* 5:591. doi: 10.1161/circgenetics.111.961425

Nakamura, A., Kaneko, N., Villemagne, V. L., Kato, T., Doecke, J., Doré, V., et al. (2018). High performance plasma amyloid-β biomarkers for Alzheimer's disease. *Nature* 554, 249–254.

Nakamura, T., and Lipton, S. A. (2007). S-Nitrosylation and uncompetitive/fast off-rate (UFO) drug therapy in neurodegenerative disorders of protein misfolding. *Cell. Death Differ.* 14, 1305–1314. doi: 10.1038/sj.cdd.4402138

Nakamura, T., Tu, S., Akhtar, M. W., Sunico, C. R., Okamoto, S., and Lipton, S. A. (2013). Aberrant protein s-nitrosylation in neurodegenerative diseases. *Neuron* 78, 596–614. doi: 10.1016/j.neuron.2013.05.005

Newman, S. F., Sultana, R., Perluigi, M., Coccia, R., Cai, J., Pierce, W. M., et al. (2007). An increase in S-glutathionylated proteins in the Alzheimer's disease inferior parietal lobule, a proteomics approach. *J. Neurosci. Res.* 85, 1506–1514. doi: 10.1002/jnr.21275

Olzscha, H. (2019). Posttranslational modifications and proteinopathies: how guardians of the proteome are defeated. *Biol. Chem.* 400, 895–915. doi: 10.1515/hsz-2018-0458

Pappireddi, N., Martin, L., and Wühr, M. (2019). A review on quantitative multiplexed proteomics. *Chembiochem* 20, 1210–1224. doi: 10.1002/cbic.201800650

Papuć, E., Kurys-Denis, E., Krupski, W., Tatara, M., and Rejdak, K. (2015). Can antibodies against glial derived antigens be early biomarkers of hippocampal demyelination and memory loss in Alzheimer's disease? *J. Alzheimer's Dis.* 48, 115–121. doi: 10.3233/jad-150309

Parker, J., Balmant, K., Zhu, F., Zhu, N., and Chen, S. (2015). cysTMTRAQ-An integrative method for unbiased thiol-based redox proteomics. *Mol. Cell. Proteomics* 14, 237–242. doi: 10.1074/mcp.o114.041772

Paula, A., Rodrigo, A. C., and Catarina, O. (2010). Neuroinflammation, oxidative stress and the pathogenesis of Alzheimers disease. *Curr. Pharm. Design* 16, 2766–2778. doi: 10.2174/138161210793176572

Paulech, J., Solis, N., Edwards, A. V., Puckeridge, M., White, M. Y., and Cordwell, S. J. (2013). Large-scale capture of peptides containing reversibly oxidized cysteines by thiol-disulfide exchange applied to the myocardial redox proteome. *Anal. Chem.* 85, 3774–3780. doi: 10.1021/ac400166e

Percy, A. J., Chambers, A. G., Yang, J., Hardie, D. B., and Borchers, C. H. (2014). Advances in multiplexed MRM-based protein biomarker quantitation toward clinical utility. *Biochim. Biophys. Acta* 1844, 917–926. doi: 10.1016/j.bbapap.2013.06.008

Poulsen, K., Bahl, J. M., Simonsen, A. H., Hasselbalch, S. G., and Heegaard, N. H. (2014). Distinct transthyretin oxidation isoform profile in spinal fluid from patients with Alzheimer's disease and mild cognitive impairment. *Clin. Proteomics* 11:12. doi: 10.1186/1559-0275-11-12

Puspita, L., Chung, S. Y., and Shim, J. W. (2017). Oxidative stress and cellular pathologies in Parkinson's disease. *Mol. Brain* 10:53.

Qian, Y., and Weerapana, E. (2017). "A quantitative mass-spectrometry platform to monitor changes in cysteine reactivity," in *Activity-based proteomics: methods and protocols*, eds H. S. Overkleeft and B. I. Florea (New York City, NY: Springer), 11–22. doi: 10.1007/978-1-4939-6439-0_2

Qu, Z., Meng, F., Bomgarden, R. D., Viner, R. I., Li, J., Rogers, J. C., et al. (2014). Proteomic quantification and site-mapping of S-nitrosylated proteins using isobaric iodoTMT reagents. *J. Proteome Res.* 13, 3200–3211. doi: 10.1021/pr401179v

Redler, R. L., Wilcox, K. C., Proctor, E. A., Fee, L., Caplow, M., and Dokholyan, N. V. (2011). Glutathionylation at Cys-111 induces dissociation of wild type and FALS mutant SOD1 dimers. *Biochemistry* 50, 7057–7066. doi: 10.1021/bi200614y

Reinwarth, M., Avrutina, O., Fabritz, S., and Kolmar, H. (2014). Fragmentation follows structure: top-down mass spectrometry elucidates the topology of engineered cystine-knot miniproteins. *PLoS One* 9:e108626. doi: 10.1371/journal.pone.0108626

Seneviratne, U., Nott, A., Bhat, V. B., Ravindra, K. C., Wishnok, J. S., Tsai, L.-H., et al. (2016). S-nitrosation of proteins relevant to Alzheimer's disease during early stages of neurodegeneration. *Proc. Natl. Acad. Sci.* 113:4152. doi: 10.1073/pnas.1521318113

Shannon, D. A., Banerjee, R., Webster, E. R., Bak, D. W., Wang, C., and Weerapana, E. (2014). Investigating the proteome reactivity and selectivity of aryl halides. *J. Am. Chem. Soc.* 136, 3330–3333. doi: 10.1021/ja4116204

Shao, B.-Z., Cao, Q., and Liu, C. (2018). Targeting NLRP3 inflammasome in the treatment of CNS Diseases. *Front. Mol. Neurosci.* 11:320. doi: 10.3389/fnmol.2018.00320

Sherrod, S. D., Myers, M. V., Li, M., Myers, J. S., Carpenter, K. L., Maclean, B., et al. (2012). Label-free quantitation of protein modifications by pseudo selected reaction monitoring with internal reference peptides. *J. Proteome Res.* 11, 3467–3479. doi: 10.1021/pr201240a

Shi, Y., and Carroll, K. S. (2020). Activity-based sensing for site-specific proteomic analysis of cysteine oxidation. *Acc. Chem. Res.* 53, 20–31. doi: 10.1021/acs.accounts.9b00562

Song, M., Zhao, X., and Song, F. (2021). Aging-dependent mitophagy dysfunction in Alzheimer's disease. *Mol. Neurobiol.* 58, 2362–2378. doi: 10.1007/s12035-020-02248-y

Srivastava, D., Kukkuta Sarma, G. R., Dsouza, D. S., Muralidharan, M., Srinivasan, K., and Mandal, A. K. (2019). Characterization of residue-specific glutathionylation of CSF proteins in multiple sclerosis – A MS-based approach. *Anal. Biochem.* 564-565, 108–115. doi: 10.1016/j.ab.2018.10.015

Swerdlow, R. H., Burns, J. M., and Khan, S. M. (2014). The Alzheimer's disease mitochondrial cascade hypothesis: progress and perspectives. *Biochim. Biophys. Acta* 1842, 1219–1231. doi: 10.1016/j.bbadis.2013.09.010

Swerdlow, R. H., and Khan, S. M. (2004). A "mitochondrial cascade hypothesis" for sporadic Alzheimer's disease. *Medical Hypotheses* 63, 8–20. doi: 10.1016/j.mehy.2003.12.045

Tahir, M., Nawrocki, A., Ditzel, H. J., and Larsen, M. R. (2020). Increasing proteome coverage using cysteine-specific DIA mass spectrometry – Cys-DIA. *bioRxiv* 2020:966861.

Tian, C., Sun, R., Liu, K., Fu, L., Liu, X., Zhou, W., et al. (2017). Multiplexed thiol reactivity profiling for target discovery of electrophilic natural products. *Cell. Chem. Biol.* 24, 1416–1427. doi: 10.1016/j.chembiol.2017.08.022

Tran, J. C., Zamdborg, L., Ahlf, D. R., Lee, J. E., Catherman, A. D., Durbin, K. R., et al. (2011). Mapping intact protein isoforms in discovery mode using top-down proteomics. *Nature* 480, 254–258. doi: 10.1038/nature10575

van der Reest, J., Lilla, S., Zheng, L., Zanivan, S., and Gottlieb, E. (2018). Proteome-wide analysis of cysteine oxidation reveals metabolic sensitivity to redox stress. *Nat. Commun.* 9:1581.

Velliquette, R. A., O'connor, T., and Vassar, R. (2005). Energy inhibition elevates beta-secretase levels and activity and is potentially amyloidogenic in APP transgenic mice: possible early events in Alzheimer's disease pathogenesis. *J. Neurosci.* 25, 10874–10883. doi: 10.1523/jneurosci.2350-05.2005

Venegas, C., Kumar, S., Franklin, B. S., Dierkes, T., Brinkschulte, R., Tejera, D., et al. (2017). Microglia-derived ASC specks cross-seed amyloid-β in Alzheimer's disease. *Nature* 552, 355–361. doi: 10.1038/nature25158

Virág, D., Dalmadi-Kiss, B., Vékey, K., Drahos, L., Klebovich, I., Antal, I., et al. (2020). Current trends in the analysis of post-translational modifications. *Chromatographia* 83, 1–10. doi: 10.1007/s10337-019-03796-9

Wang, H. M., Zhang, T., Huang, J. K., Xiang, J. Y., Chen, J., Fu, J. L., et al. (2017). Edaravone attenuates the proinflammatory response in Amyloid-β-Treated Microglia by inhibiting NLRP3 inflammasome-mediated IL-1β Secretion. *Cell. Physiol. Biochem.* 43, 1113–1125. doi: 10.1159/000481753

Wang, M., You, J., Bemis, K. G., Tegeler, T. J., and Brown, D. P. (2008). Label-free mass spectrometry-based protein quantification technologies in proteomic analysis. *Brief Funct. Genomic. Proteomic.* 7, 329–339.

Weerapana, E., Speers, A. E., and Cravatt, B. F. (2007). Tandem orthogonal proteolysis-activity-based protein profiling (TOP-ABPP)—a general method for mapping sites of probe modification in proteomes. *Nat. Protoc.* 2, 1414–1425. doi: 10.1038/nprot.2007.194

Weerapana, E., Wang, C., Simon, G. M., Richter, F., Khare, S., Dillon, M. B. D., et al. (2010). Quantitative reactivity profiling predicts functional cysteines in proteomes. *Nature* 468, 790–795. doi: 10.1038/nature09472

Wijasa, T. S., Sylvester, M., Brocke-Ahmadinejad, N., Schwartz, S., Santarelli, F., Gieselmann, V., et al. (2020). Quantitative proteomics of synaptosome S-nitrosylation in Alzheimer's disease. *J. Neurochem.* 152, 710–726. doi: 10.1111/jnc.14870

Wu, Y., Wang, F., Liu, Z., Qin, H., Song, C., Huang, J., et al. (2014). Five-plex isotope dimethyl labeling for quantitative proteomics. *Chem. Commun.* 50, 1708–1710. doi: 10.1039/c3cc47998f

Yang, F., Gao, J., Che, J., Jia, G., and Wang, C. (2018). A dimethyl-labeling-lased strategy for site-specifically quantitative chemical proteomics. *Anal. Chem.* 90, 9576–9582. doi: 10.1021/acs.analchem.8b02426

Zahid, S., Khan, R., Oellerich, M., Ahmed, N., and Asif, A. R. (2014). Differential S-Nitrosylation of proteins in Alzheimer's disease. *Neuroscience* 256, 126–136. doi: 10.1016/j.neuroscience.2013.10.026

Zhao, Q.-F., Yu, J.-T., and Tan, L. (2015). S-Nitrosylation in Alzheimer's disease. *Mol. Neurobiol.* 51, 268–280.

Conflict of Interest: The authors declare that the research was conducted in the absence of any commercial or financial relationships that could be construed as a potential conflict of interest.

frontiers in Molecular Neuroscience

ORIGINAL RESEARCH
published: 17 June 2021
doi: 10.3389/fnmol.2021.658339

Broad Influence of Mutant Ataxin-3 on the Proteome of the Adult Brain, Young Neurons, and Axons Reveals Central Molecular Processes and Biomarkers in SCA3/MJD Using Knock-In Mouse Model

*Kalina Wiatr[1], Łukasz Marczak[1], Jean-Baptiste Pérot[2], Emmanuel Brouillet[2], Julien Flament[2] and Maciej Figiel[1]**

[1] Institute of Bioorganic Chemistry, Polish Academy of Sciences, Poznań, Poland, [2] Université Paris-Saclay, Centre National de la Recherche Scientifique, Commissariat à l'Energie Atomique, Direction de la Recherche Fondamentale, Institut de Biologie François Jacob, Molecular Imaging Research Center, Neurodegenerative Diseases Laboratory, Fontenay-aux-Roses, France

Spinocerebellar ataxia type 3 (SCA3/MJD) is caused by CAG expansion mutation resulting in a long polyQ domain in mutant ataxin-3. The mutant protein is a special type of protease, deubiquitinase, which may indicate its prominent impact on the regulation of cellular proteins levels and activity. Yet, the global model picture of SCA3 disease progression on the protein level, molecular pathways in the brain, and neurons, is largely unknown. Here, we investigated the molecular SCA3 mechanism using an interdisciplinary research paradigm combining behavioral and molecular aspects of SCA3 in the knock-in ki91 model. We used the behavior, brain magnetic resonance imaging (MRI) and brain tissue examination to correlate the disease stages with brain proteomics, precise axonal proteomics, neuronal energy recordings, and labeling of vesicles. We have demonstrated that altered metabolic and mitochondrial proteins in the brain and the lack of weight gain in Ki91 SCA3/MJD mice is reflected by the failure of energy metabolism recorded in neonatal SCA3 cerebellar neurons. We have determined that further, during disease progression, proteins responsible for metabolism, cytoskeletal architecture, vesicular, and axonal transport are disturbed, revealing axons as one of the essential cell compartments in SCA3 pathogenesis. Therefore we focus on SCA3 pathogenesis in axonal and somatodendritic compartments revealing highly increased axonal localization of protein synthesis machinery, including ribosomes, translation factors, and RNA binding proteins, while the level of proteins responsible for cellular transport and mitochondria was decreased. We demonstrate the accumulation of axonal vesicles in neonatal SCA3 cerebellar neurons and increased phosphorylation of SMI-312 positive adult cerebellar axons, which indicate axonal dysfunction in SCA3. In summary, the SCA3 disease mechanism is based on the broad influence of mutant ataxin-3 on the neuronal proteome. Processes

OPEN ACCESS

Edited by:
Matthew L. MacDonald, University of Pittsburgh, United States

Reviewed by:
Clevio Nobrega, University of Algarve, Portugal
Utpal Das, University of California, San Diego, United States

***Correspondence:**
Maciej Figiel
mfigiel@ibch.pozan.pl

Received: *25 January 2021*
Accepted: *01 April 2021*
Published: *17 June 2021*

Citation:
Wiatr K, Marczak Ł, Pérot J-B, Brouillet E, Flament J and Figiel M (2021) Broad Influence of Mutant Ataxin-3 on the Proteome of the Adult Brain, Young Neurons, and Axons Reveals Central Molecular Processes and Biomarkers in SCA3/MJD Using Knock-In Mouse Model. Front. Mol. Neurosci. 14:658339. doi: 10.3389/fnmol.2021.658339

central in our SCA3 model include disturbed localization of proteins between axonal and somatodendritic compartment, early neuronal energy deficit, altered neuronal cytoskeletal structure, an overabundance of various components of protein synthesis machinery in axons.

Keywords: spinocerebellar ataxia type 3 (SCA3), Machado-Joseph disease (MJD), ataxin-3, neurodegenerative, proteome, axon, vesicular transport, energy metabolism

INTRODUCTION

Spinocerebellar ataxia type 3 (SCA3), also known as Machado–Joseph disease (MJD), is a neurodegenerative, late-onset, genetic disorder caused by the expansion of CAG repeats in the coding region of the ATXN3 gene (>50 in patients) (McLoughlin et al., 2020). This mutation leads to an expanded polyglutamine (polyQ) tract in the ataxin-3 protein, causing a toxic gain of function (Orr and Zoghbi, 2007). SCA3 patients most typically display imbalance, motor incoordination, and neurodegeneration in the cerebellum, brainstem, spinal cord, and cerebral cortex (Bettencourt and Lima, 2011). Although the disease-causative mutation is known, the exact molecular and cellular mechanisms of SCA3 remain unclear. Several lines of evidence point to the disruption of axon organization and, therefore, connections between brain structures as one of the main traits in SCA3 pathogenesis (de Rezende et al., 2015; Farrar et al., 2016; Lu et al., 2017). Moreover, axonal impairment was observed in central nervous system (CNS) and peripheries in the form of white mater defects on magnetic resonance imaging (MRI) and peripheral axonal neuropathy in SCA3 patients (D'Abreu et al., 2009; Graves and Guiloff, 2011; Rezende et al., 2018). Axonal impairment may be related to the fact that mutant ataxin-3 aberrantly interacts with microtubules affecting cytoskeleton dynamics in neurons and forms inclusions in axons (Mazzucchelli et al., 2009; Seidel et al., 2010; Chen et al., 2012). Also, mitochondrial impairment is a component of axonal damage in neurodegeneration, and likely plays a role in SCA3 pathogenesis (Da Silva et al., 2019). We recently demonstrated that gross transcriptional changes are absent in the pre-symptomatic SCA3 brain of the Ki91 mouse model; however, dysregulations of proteins and phosphoproteins occurred in these animals, pointing at protein homeostasis as a more general and early trait in disease pathogenesis (Switonski et al., 2015; Wiatr et al., 2019).

The ataxin-3 protein is a particular type of protease, a deubiquitinase, and it has been previously demonstrated that the function in the mutant version of the protein is compromised (Neves-Carvalho et al., 2015), which should have a significant influence on the brain proteome. Therefore, the investigation of proteins seems to be the strongest candidate to discover pathogenic mechanisms or identify the cluster of disease mechanisms. The number of known biomarkers and proteins reliably linked to SCA3 pathogenic processes is still relatively low. Surprisingly, the global model picture of SCA3 disease progression on the protein level, showing the most crucial proteins and pathways in the brain, and neurons, has not been generated and published previously. Therefore in the present work, we aimed to identify protein dysregulations and pathogenic processes in SCA3 on various levels, *in vitro*, and *in vivo*. We designed a research pipeline consisting of three complementary proteomic approaches, mouse behavior, and necessary functional validation assays to unveil with increased resolution the most critical processes influencing the SCA3 pathogenesis. The pipeline combines proteomics paralleled to behavioral milestones of SCA3 Ki91 and correlative proteomics for displaying the proteome linked to disease severity. In the third and the most focused approach, we used targeted proteomics of somatodendritic and axonal compartments from young SCA3 neurons. Our results indicate that the SCA3 disease mechanism is based on the broad influence of mutant ataxin-3 on the neuronal proteome affecting classes of proteins responsible for several central molecular processes. These include disturbed localization of proteins between axonal and somatodendritic compartment, early neuronal energy deficit, altered neuronal cytoskeletal structure, an overabundance of protein synthetic machinery in axons, and altered vesicular trafficking pointing at affected axonal maintenance.

Abbreviations: ANOVA, analysis of variance; BP, biological process;CPDB, ConsensusPath Database; CC, cellular compartment; CNS, central nervous system; DIV, days in vitro; ECAR, extracellular acidification rate; FC, fold change; MJD, Machado-Joseph disease; MS, mass spectrometry; mo, month-old, MF, molecular function; mRFP, monomeric red fluorescent protein; MRI, magnetic resonance imaging; mRNP, messenger ribonucleoprotein; NF, neurofilament; OCR, oxygen consumption rate; OXPHOS, oxidative phosphorylation; polyQ, polyglutamine; PCA, principal component analysis; SCA3, Spinocerebellar ataxia type 3; TCA, tricarboxylic acid cycle; WT, wildtype.

RESULTS

The SCA3 in Ki91 Mice Gradually Progresses and Demonstrates Discrete Early and Late Phenotypes

We have previously demonstrated that by 2 months of age, Ki91 mice show no motor symptoms or other behavioral abnormalities, and we additionally defined the spectrum of Ki91 motor deficits using 14-month-old animals (Wiatr et al., 2019). Upon completing our longitudinal behavioral tests (4–18 months), we now demonstrate that the homozygous Ki91 model gradually develops disease symptoms resembling disease progression in SCA3 patients. Based on the large volume of longitudinal behavioral data (**Figure 1**), we have distinguished three stages of behavioral symptom development in Ki91 animals (n = 36). The first stage consists of progressive failure to gain body weight (4-month-old) followed by the early symptomatic stage (12-month-old), characterized by gait

A

Age	Weight	Time to traverse	Scoring	Time to turn	Rotarod	Muscle strength	Footprint	Open field
4	*							N/A
6	**							N/A
8	***							N/A
10	***							N/A
12	***	*						N/A
14	***	**	***					N/A
16	***	**	***	**				N/A
18	***	***	***	**	*	***	**	***

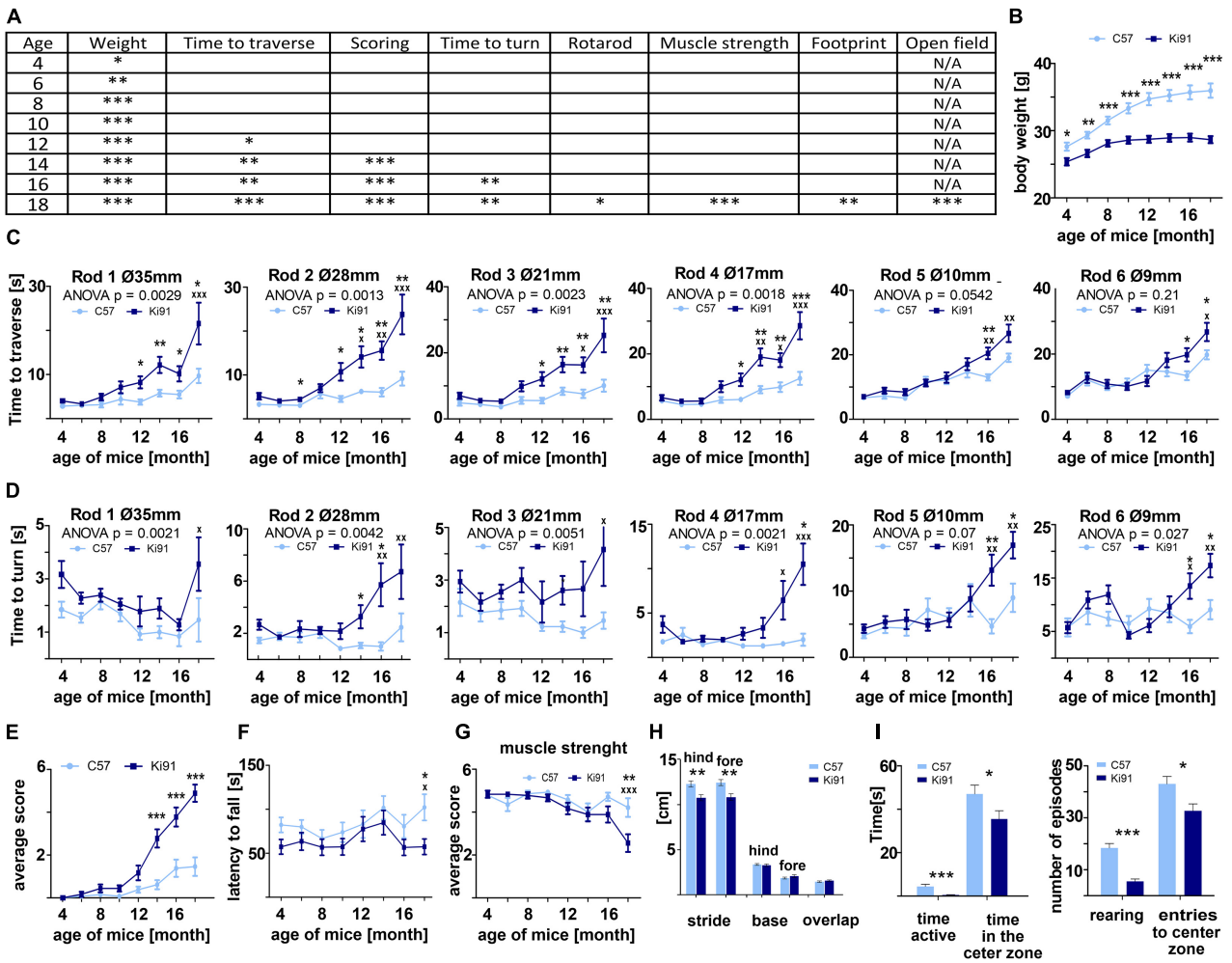

FIGURE 1 | Progressive motor deficits and other disease symptoms in Ki91 SCA3/MJD mice. Ki91 mice presented a gradual decline in several motor and non-motor functions measured by elevated beam walk, rotarod, monitoring of body weight, muscle weakness, and other tests. **(A)** Progressive reduction of body weight gain was observed starting from 4-month-old mice; on average, mut/mut animals at 12 months of age displayed 16.4% less body weight compared to WT animals ($p < 0.001$; two-sample *t*-test) **(B)**. In the elevated beam walk test **(C,D)** "time to turn" and "traverse time" parameters were measured on six rods with decreasing diameter (diameter of rods are indicated by Ø in mm). A total of 12-month-old Ki91 mice needed significantly more time to traverse on rods 1–4, whereas older 16-month-old mice also needed more time on rods 5–6. **(C)** A total of 16-month-old animals needed more time to turn on all rods **(D)**. In the scoring test, 14-month-old Ki91 mice presented symptoms characteristic for SCA3: incoordination, gait disturbances, kyphosis, and hind limb clasping **(E)**. A total of 18-month-old mice showed motor incoordination in accelerated rotarod (4–40 rpm in 9.5 min) **(F)**, muscle weakness **(G)**, and differences in stride length in footprint test **(H)**. A total of 18-month-old mice also presented a cognitive deterioration marked by a decreased amount of time spent in the center zone in the Open field test and a decreased number of rearing **(I)**. Two-way ANOVA with Bonferroni *post hoc* test ($p \leq 0.05$; total number of biological replicates: $n = 36$, $n = 18$ per genotype), error bars: SEM. Asterisks denotes a two-way ANOVA calculated separately for each test consisted of 4 days at each age ($^{*}p < 0.05$, $^{**}p < 0.01$, $^{***}p < 0.001$); x-symbol represent two-way ANOVA calculated after completion of testing all ages ($^{x}p < 0.05$, $^{xx}p < 0.01$, $^{xxx}p < 0.001$).

ataxia and motor incoordination. The final, symptomatic phase (18-month-old animals) is characterized by severe loss of balance and coordination, gait ataxia, dystonia, and muscle weakness (**Figure 1A**). Reduced rate of body weight gain was observed as the first symptom in 4-month-old Ki91 mice ($p < 0.05$; two-sample *t*-test), and the difference between Ki91 and wild-type (WT) littermates increased with age [$p < 0.001$; two-sample *t*-test, two-way analysis of variance (ANOVA), Bonferroni; **Figure 1B**]. At the age of 8 months, Ki91 mice stopped gaining weight, and their weight was stable across further ages (**Figure 1B**) while the WT animals still regularly gained weight. First motor symptoms occurred in 12-month-old animals, which performed worse in the elevated beam walk (**Figure 1C**). Ki91 took more time to traverse rods (diameter: 35, 28, 21, and 17 mm) and committed more foot slips while performing the task ($p < 0.05$; two-way ANOVA, Bonferroni). As the disease progressed, 14-month-old Ki91 demonstrated overall deterioration of phenotype, including gait disturbances, loss of coordination, and balance, and several Ki91 animals demonstrated hindlimb clasping and kyphosis in the scoring test ($p < 0.0001$; one- and two-way ANOVA, Bonferroni) (**Figure 1E**). Next, 16-month-old Ki91 mice needed more time

to turn on a rod (diameter: 28, 17, 10, and 9 mm) in the elevated beam walk test ($p < 0.05$; two-way ANOVA, Bonferroni), showing loss of balance (**Figure 1D**). Besides, 18-month-old Ki91 mice demonstrated incoordination in the Rotarod ($p < 0.05$; two-way ANOVA, Bonferroni; **Figure 1F**), reduced muscle strength ($p < 0.001$; one- and two-way ANOVA, Bonferroni; **Figure 1G**), shorter stride, which indicated further gait disturbances in the footprint test ($p < 0.001$; two-sample *t*-test, ANOVA, Bonferroni; **Figure 1H**), and decreased activity and anxiety in the open field test ($p < 0.05$; two-sample *t*-test; **Figure 1I**). In this last test, Ki91 mice showed significantly less time spent moving ($p < 0.0001$; two-sample *t*-test), as well as decreased vertical activity (rearing) ($p < 0.0001$; two-two-sample *t*-test), a smaller number of the entries, and less time spent in the center zone ($p < 0.05$; two-sample *t*-test). Since mice showed differences in body weight, we ensured that no correlation existed between body weight and behavioral tests in each age to exclude the effect of the animals' weight on the results ($p < 0.05$, correlation test).

Ki91 SCA3/MJD Mice Demonstrate Multiple Brain Region Atrophy and the Presence of Atxn3 Inclusions Throughout the Brain

Magnetic resonance imaging was used on *ex vivo* brains of 18 months old animals ($n = 6$ per genotype) to measure brain volumes in Ki91 and WT mice (**Figures 2A,B**). As measured by MRI image segmentation, whole-brain volume showed significant global atrophy of the brain in Ki91 mice (−7%, $p < 0.001$; **Figure 2A**). When looking at regions volume, several structures seem particularly atrophied as parietal-temporal cortex (−11%, $p < 0.01$), entorhinal, piriform and motor cortexes (−11% each, $p < 0.05$), corpus callosum (−7.5%, $p < 0.05$), striatum (−11%, $p < 0.05$), septum (−11%, $p < 0.01$), pons (−12%, $p < 0.01$), and hypothalamus (−8%, $p < 0.05$) (**Figure 2B**). There was no significant atrophy in the hippocampus, and cerebellar atrophy was not determined due to MRI coil performance at the end of the brain. Fractional Anisotropy (FA) was also investigated as a biomarker of the integrity of tissue organization. FA was significantly decreased in dentate gyrus (−17%, $p < 0.01$), and stratum granulosum (−19%, $p < 0.05$) (**Figure 2C**).

Next, we have performed brain sections from 18-month-old Ki91 and staining using the anti-ataxin-3 antibody (**Figure 3**). We found that all brain areas, including the cerebral cortex, striatum, midbrain, hippocampus, cerebellum, DCN, and pons, demonstrated intensive positive signals in the form of both inclusions and diffuse staining of cellular structures ($n = 4$; **Figures 3A–E**). In particular, intense anti-ataxin-3 staining was present in cell nuclei, and many cells demonstrated large inclusions (**Figure 3A**). Interestingly, a significant number of smaller and larger ataxin-3-positive inclusions were scattered along the neurites (particularly axons labeled by SMI-312 axonal marker) in the cerebellum (**Figures 3C,E**). Although we could not measure cerebellum atrophy by MRI, we determined that the inclusions are rich in the cerebellum, indicating an intense pathogenic process. In the cerebellum, the large inclusions were predominantly present in the DCN area, white matter, and in some cells located in the granular layer (**Figures 3B,D**). Many of the atxn3 inclusions were ubiquitinated (**Supplementary Figures 1A,B, 2**). Considering widespread brain atrophy and the inclusions in all regions, we reasoned that the brain pathogenic SCA3 processes are multi-region and multi-thread. Therefore we selected the cerebellum and cerebral cortex to represent both classically reported SCA3 pathogenesis in the hindbrain and postulated SCA3 pathogenesis in more frontal parts of the brain.

Proteomics Parallel to Behavioral Milestones Implicates Disturbed Metabolism, Cytoskeleton, and Vesicular Trafficking in Ki91 SCA3/MJD Mice

Parallel to behavioral experiments and based on the occurrence of symptoms in behavioral tests, we have selected four mouse ages (4, 10, 12, and 14-month-old, $n = 4$ per genotype) to analyze proteomic changes in the cerebral cortex (entire region collected for analysis) and cerebellum. In detail, 4-month-old Ki91 animals displayed reduced body weight gain; a 10-months stage was just before the onset of motor symptoms, while 12 and 14-month-old mice showed a decline in motor functions (**Figure 1**); therefore, the protein dysregulation in those ages would be most relevant. The principal component analysis (PCA) mostly demonstrated distinct clustering of the Ki91 and WT datasets (**Supplementary Figures 3A,B**). Altogether, we identified 115, 126, 212, and 75 proteins that were significantly dysregulated ($p < 0.05$; two-sample *t*-test) in the cerebellum of 4-, 10-, 12-, and 14-month-old Ki91 mice, respectively (**Supplementary Table 1** and **Supplementary Figure 3C**). In comparison, 178, 89, 170, and 279 proteins were significantly dysregulated ($p < 0.05$; two-sample *t*-test) in the cerebral cortex of 4-, 10-, 12-, and 14-month-old Ki91 animals, respectively (**Supplementary Table 2** and **Supplementary Figure 3C**).

In order to reveal molecular pathways and cellular compartments (CCs), which might contribute to the SCA3 pathogenesis, we performed an analysis of dysregulated proteins using the ConsensusPath database (CPDB; pathways and GO CC for each age; level 4 and 5; $q < 0.01$). For simplicity, we have arbitrarily grouped pathways and CCs identified in CPDB into five categories for the cerebral cortex (**Figure 4A**) and cerebellum (**Figure 4B**) based on their biological relations and similarity. Lists of proteins with the highest log2-fold changes (log2-FC) belonging to five categories are presented for the cerebral cortex (**Figure 4C**) and cerebellum (**Figure 4D**).

The first category was related to vesicular transport and endocytosis. Cytoplasmic vesicles and extracellular exosomes were the localization for 24–32 and 33–51% of dysregulated proteins in every dataset from the cortex (**Figure 4A**) and similarly 21–24 and 45–51% in the cerebellum (**Figure 4B**). Moreover, vesicle-mediated transport and clathrin-mediated endocytosis are predicted to be disturbed in both the cerebral cortex (Vamp2, Cltb, and Rab10; **Figure 4C**) and cerebellum (Rab11b, Napa, Nsf, and Rab3d; **Figure 4D**).

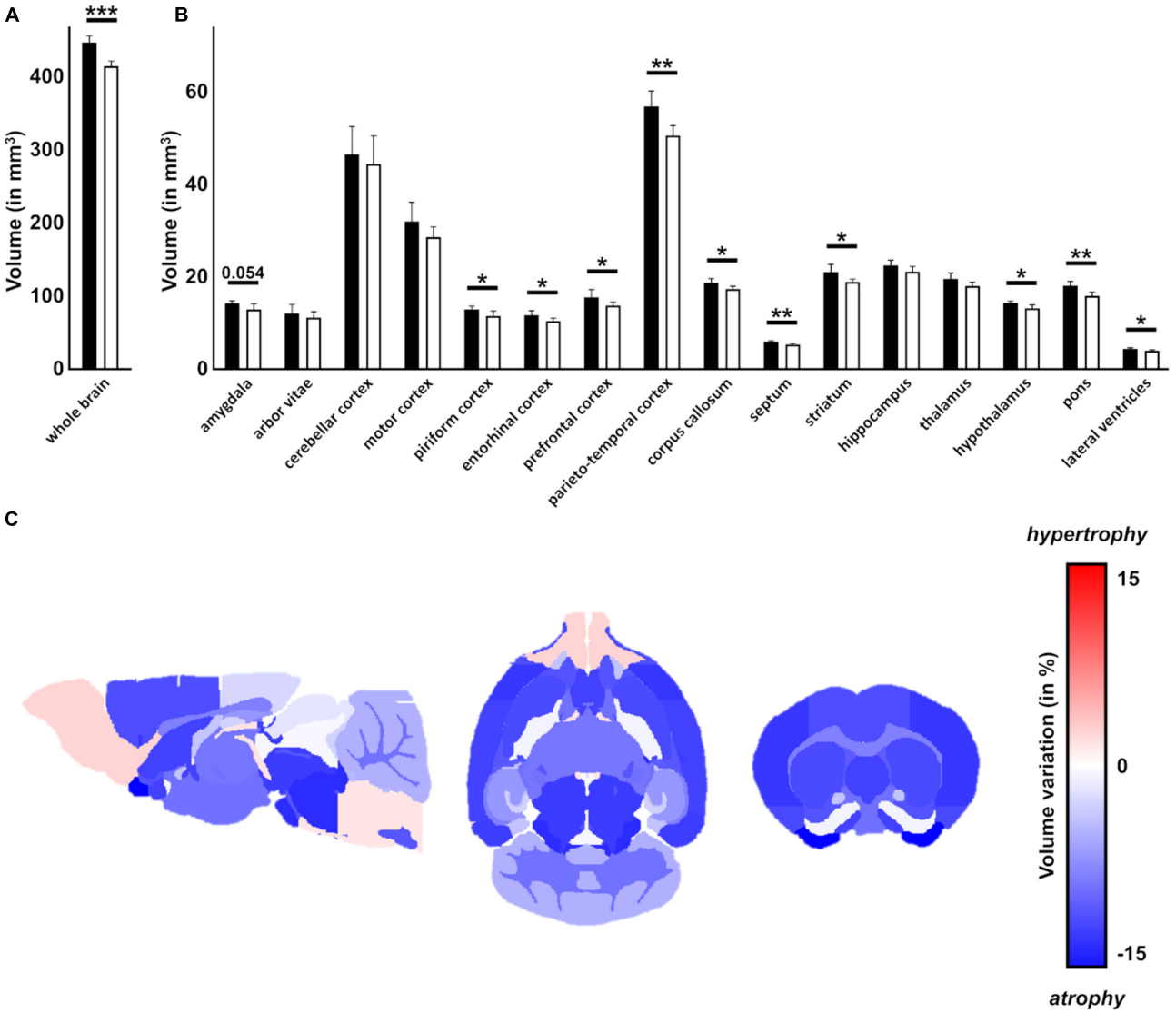

FIGURE 2 | Atrophy of multiple regions including white matter in the Ki91 SCA3/MJD brain. MRI image segmentation was used to measure whole brain volume *ex vivo* of 18-month-old Ki91 and WT mice ($n = 6$ per genotype) and revealed significant global atrophy (–7%, $p < 0.001$) **(A)** and reduction of volume of many regions, such as parieto-temporal cortex (–11%, $p < 0.01$), entorhinal, piriform and motor cortexes (–11% each, $p < 0.05$), corpus callosum (–7,5%, $p < 0.05$), striatum (–11%, $p < 0.05$), septum (–11%, $p < 0.01$), pons (–12%, $p < 0.01$) and hypothalamus (–8%, $p < 0.05$) **(B)**. Schematic representation of brain regions atrophy in Ki91 mice **(C)**. Atrophy of many brain regions might suggest impaired connections between those structures. The gradient of red color is for hypertrophy, the gradient of blue color for the atrophy. Two-sample *t*-test (*$p < 0.05$, **$p < 0.01$, ***$p < 0.001$), error bars: SEM.

The second category included dysregulated proteins involved in synaptic transmission. There was a relative increase in the number of altered proteins in older 12–14 month-old Ki91 mice in the cerebral cortex compared to younger ages (4–10-month-old). For instance, pathways such as "transmission across chemical synapses" contained ∼ 6% of dysregulated proteins in 4–10-month-old vs. ∼ 10% in 12–14% and "synaptic vesicle cycle" ∼ 3% vs. 7%, respectively (**Figure 4A**). Proteins related to SNARE complex and synaptic vesicles such as Syn3, Syp, Sv2a, and Syt7 were dysregulated (**Figure 4C**). Interestingly, most of the proteins with a function in the synapse showed decreased levels in the cerebral cortex of older 12–14-month-old Ki91 mice (**Figure 4C**). In the cerebellum, dysregulated proteins of synaptic vesicles or synapses were less frequent compared to the cortex (**Figure 4B**) and included Sv2a, Syt2, and Kcnab2 (**Figure 4D**). In both tested tissues, downregulation of Car2, Qdpr, and Glul, were detected in most of the tested ages (**Figures 4C,D**), which we also validated using vacuum dot-blot assay ($p < 0.05$; two-sample *t*-test; **Supplementary Figure 4**). Glul, Car2, and Qdpr play a role in the metabolism of amino acids and neurotransmitters, and Qdpr level is slightly and gradually dropping down across ages (**Supplementary Tables 1**, **2**).

The third category was referring to altered proteins playing a role in regulating cytoskeletal structure and function.

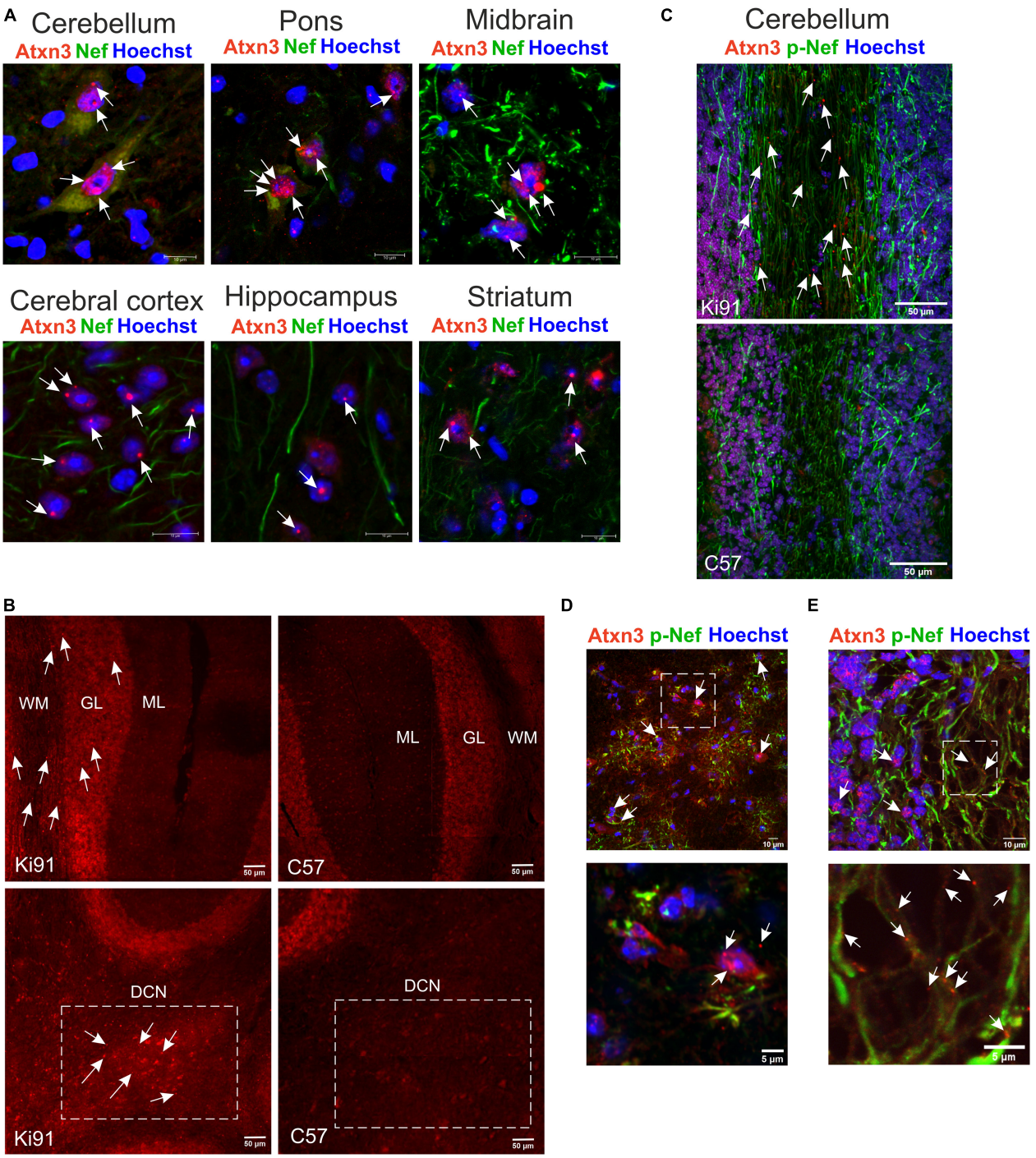

FIGURE 3 | The presence of multi-region intra-nuclear and intra-axonal inclusions in Ki91 SCA3/MJD brain. The ataxin-3 immunostaining of the 18-month-old Ki91 brain sections revealed a large number of cells within the cerebellum, midbrain, pons, cerebral cortex, hippocampus, and striatum with ataxin-3 (red; rabbit anti-ataxin-3 antibody) localizing mainly in the cell nucleus (blue; Hoechst 33342) **(A)**. White arrows indicate large intra-nuclear inclusions; however, many smaller inclusions throughout the brain were present. A rich representation of Atxn3 aggregates (red; rabbit anti-ataxin-3 antibody) was present in DCN, granular layer (gl), and white matter (wm) of the Ki91 cerebellum **(B–D)**. A significant number of small and large ataxin-3 inclusions were detected in the neurites (green; Smi-32, pan-neuronal or Smi-312, axon-specific antibody) of the Ki91 cerebellum **(C,E)**. White box and arrows in **(D)** mark prominent Atxn3 aggregates in the DCN area (lower panel represents the magnification of selected region in the upper panel). White box and arrows in **(E)** mark the magnified area containing multiple intra-axonal inclusions of Atxn3 (lower panel). Scale bars: 50 µm **(B,C)**; 10 µm **(A)**; 5 µm on inserts **(D,E)**. *N* = 4 biological replicates; at least 4 pictures per brain region of each kind were collected.

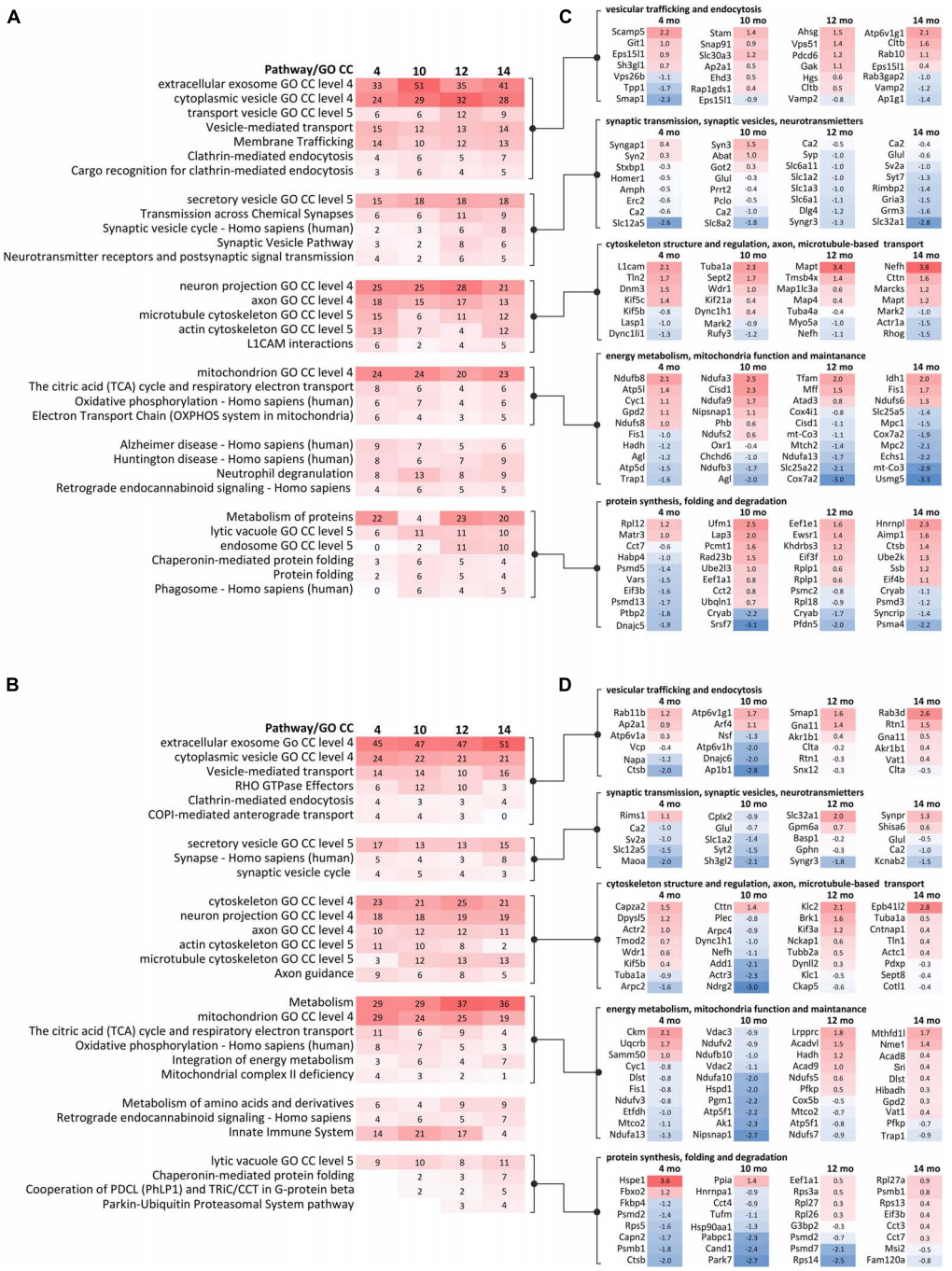

FIGURE 4 | GO term and pathway analysis of dysregulated proteins identified in proteomics at behavioral milestones in the Ki91 SCA3/MJD mouse brain implicate vesicular transport, cytoskeleton, protein metabolism, and mitochondrial function. Bioinformatic analysis of biological pathways and subcellular localization of dysregulated proteins ($p < 0.05$; two-sample *t*-test, $n = 4$ per genotype) during disease progression in the cerebral cortex **(A)** and cerebellum **(B)** was assessed using ConsensusPath database (CPDB; pathways *p*-value cut-off < 0.01; GO terms cellular component, *p*-value cut-off < 0.01, level 3, 4). The heatmaps present changes of pathways and subcellular localization involving dysregulated proteins ($p < 0.05$; two-sample *t*-test) over the course of the disease in four tested ages (4, 10, 12, and 14-month-old) by showing what percentage of dysregulated proteins in each set is assigned to the particular pathway or subcellular region (numbers). The gradient of red color denotes a higher percentage of dysregulated proteins (more intense color) to a lower percentage of dysregulated proteins (less intense color). The five groups of pathways and GO terms arranged in blocks in **(A,B)** are linked to the corresponding lists of dysregulated proteins ($p < 0.05$; two-sample *t*-test) with the highest log2-FC in each tested age, assigned to five arbitrary categories in the cerebral cortex **(C)** and cerebellum **(D)**. The categories were formed based on the analysis of pathways and GO terms and are as follows: (1) vesicular trafficking and endocytosis; (2) synaptic transmission, synaptic vesicles, and neurotransmitters; (3) cytoskeleton structure and regulation, axon, and microtubule-based transport; (4) energy metabolism, mitochondria function, and maintenance; and (5) protein synthesis, folding, and degradation. The lists of dysregulated proteins are also presented as heatmaps with numbers representing log2-FC **(C,D)**. The gradient of red color is for upregulated proteins, blue color for downregulated proteins.

Dysregulated proteins localized to neuronal projections (axons and dendrites) constituted between 21 and 28% in the cortex and ∼ 18% in the cerebellum (**Figures 4A,B**). Proteins assigned to cytoskeletal localization included actin (cortex: Actr1a; cerebellum: Arpc2 and Actr3), microtubules (cortex: Tuba1a and Mapt) and neurofilaments (cortex and cerebellum: Nefh) (**Figures 4C,D**). Disturbances of the cytoskeleton structure may lead to cellular transport defects, and there were many proteins directly regulating anterograde and retrograde axonal transport. For instance, in the cerebral cortex, dysregulated proteins involved in anterograde microtubule-based transport were Kif5c, Kif5b, and Kif21a and retrograde transport: Dnm3, Dync1li1, Dync1h1, and microtubule-associated proteins: Map1lc3a and Mark2 (**Figure 4C**). In the cerebellum, proteins involved in the anterograde microtubule-based transport included Kif5b, Klc1, Klc2, and Kif3a, and in retrograde transport Dync1h1 and Dynll2 (**Figure 4D**).

The fourth category involved many dysregulated proteins related to energy metabolism and mitochondria maintenance (**Figures 4A–D**). Proteins predicted to localize in mitochondrion were between 20–24 and 19–29% in the cortex and cerebellum, respectively (**Figures 4A,B**). The top pathway involving dysregulated proteins in the Ki91 cerebellum was metabolism (**Figure 4B**). Moreover, the number of proteins dysregulated in the cerebellum and associated with metabolism increases with age (4–10-month-old: ∼ 29%; 12–14-month-old: ∼ 36%; **Figure 4B**). Proteins related to tricarboxylic acid cycle (TCA) and oxidative phosphorylation (OXPHOS) are dysregulated in the cerebral cortex (mitochondrial proteins Ndufb8 with; Ndufa3, Ndufs6, and mt-Co3; **Figure 4C**) and cerebellum (Ndufa13, Ndufa10, and Ndufs7; **Figure 4D**). There were also dysregulated proteins responsible for mitochondria fission (Fis1 and Mff) and mitochondrial chaperons (Hspd1 and Trap1) (**Figures 4C,D**). Also, several proteins with altered levels mostly related to metabolism were linked to Alzheimer's and Huntington disease in both the cerebellum and cerebral cortex (**Figures 4A,B**).

The fifth category included dysregulated proteins involved in protein metabolism. In the case of the cerebral cortex, there are 4–23% dysregulated proteins involved in the metabolism of proteins (**Figure 4A**). Noteworthy, the number of dysregulated proteins predicted to localize in lysosomes, endosomes, and phagosomes is higher in the cortex of older mouse (**Figures 4A,B**). Similarly, the number of altered proteins involved in protein folding and "Parkin-Ubiquitin Proteasomal System pathway" is increasing with age in the Ki91 cerebellum (**Figure 4B**). Dysregulated proteins in this category involve also various ribosomal subunits and translation factors (cortex: Rpl12 and Eif3b; cerebellum: Rpl27a), proteasome subunits (cortex: Psmd13 and Psma4; cerebellum: Psmb1 and Psmd7), and chaperons (cortex: Dnajc5 and Cryab; cerebellum: Hspe1 and Park7) (**Figures 4C,D**). Downregulation of Cryab, which was one of the most frequently identified proteins implicated in the pathology of neurodegenerative disease (Zhu and Reiser, 2018), was confirmed with vacuum dot blot assay ($p < 0.05$; two-sample t-test) in the cerebral cortex (10, 14, and 18-month-old; **Supplementary Figure 4A**) and cerebellum (18-month-old; **Supplementary Figure 4B**). Of note, most of the proteasome subunits and chaperons demonstrated decreased levels in both tested tissues (**Figures 4C,D**).

Proteomics Correlative With SCA3 Behavioral Phenotype in 18-Month-Old Ki91 Mice Reveals Dysregulated Proteins Involved in Transport, Cytoskeleton, Synapse, and Mitochondria

Our correlative proteomic approach aimed to discover dysregulated proteins in the brain of animals that demonstrated consistent behavioral phenotype to establish a more exact relationship between the protein biomarkers and the degree of SCA3 disease severity (**Supplementary Figure 5**). Therefore, after the endpoint of behavioral studies (18 months), the animals were grouped by the intensity of phenotype, and three phenotype subgroups were established in the Ki91 cohort: severe, moderate, and mild ($n = 4$). The selection was based on score assessment on the 0–5 scale (Kruskal–Wallis test, $p < 0.05$) (**Supplementary Figure 6A**). The scores 0 or 1 represented the "mild phenotype" group, score 2 or 3 was the "moderate phenotype" group, and 4 or 5 was the "severe phenotype" group. The cerebellum and cerebral cortex were collected from each group, and the tissues were subjected to proteomics (**Supplementary Table 3** and **Supplementary Figures 5A,B**). The analysis of dysregulated proteins revealed that protein levels in the moderate group were mostly in between the level of the severe and mild group, demonstrating a gradual pattern of protein dysregulation in Ki91 mice (**Supplementary Figures 6B,C**). Therefore in further data processing, we focused on the protein levels in severe and mild phenotype.

We found that in the cerebellum of the Ki91 animals with the severe phenotype ($n = 4$), there were heat shock protein Dnaja1 and a nuclear importin Kpna4 upregulated compared to WT animals (WT; $n = 10$) (**Supplementary Figure 6B**). Another member of the importin family, Kpna3, was previously shown to control the nuclear localization of ataxin-3 (Sowa et al., 2018). There were also five upregulated proteins in the mild phenotype ($n = 4$) – Pvalb, Pak1, Kif5c, and neurofilaments (Nefl and Nefm). Pak1, a kinase implicated in vesicle-mediated transport and regulation of cytoskeleton dynamics, and Kif5c involved in microtubule-based transport, were also downregulated in severe phenotype (**Supplementary Figure 6B**). Moreover, in the severe group, there were also other downregulated proteins playing a pivotal role in transport along the microtubule (Klc1, Kif5c, Vatl1, and Map4) and notably Purkinje cell protein 4 (Pcp4), which was not dysregulated in mild phenotype (**Supplementary Figure 6B**). Noteworthy, mitochondrial proteins were downregulated in both severe and mild phenotypes. Mitochondrial chaperone Timm9 showed lower levels in the "severe" group, while Ndufb5 and Fasn were downregulated in the "mild" group (**Supplementary Figure 6B**).

In the cerebellar cortex, the only upregulated protein was a subunit of mitochondrial ATP synthase, Atp5a1 (**Supplementary Figure 6C**). Proteins commonly downregulated in both severe and mild phenotype (**Supplementary Figure 6C**) included Glul, already identified in the proteomics performed

parallel to behavioral milestones and myelin protein Cnp, ubiquitinating enzyme Ube2n, transcription factor Tceb1, and Snx12 involved in intracellular trafficking. In the mild group only, there were downregulated proteins associated with synaptic vesicles and post-synaptic density (Akap5, Bsn, Pclo, and Gprin1; **Supplementary Figure 6C**). Whereas in a "severe" group, there were downregulated proteins related to intracellular transport and cytoskeleton (Snx12, Dlg3, Dnm2, Cap2, and Atcay), and mitochondrial protein Cox7a2 (**Supplementary Figure 6C**).

Altogether, we identified a set of proteins involved in intracellular and microtubule-based transport downregulated in the cerebellum and cerebral cortex of Ki91 mice displaying severe phenotype. Downregulated proteins in the "mild" phenotype were related to mitochondria in the cerebellum and synapse in the cerebral cortex. Proteins upregulated in the cerebellum were associated with cytoskeleton and neurofilaments in the "mild" group. Cellular processes and compartments associated with dysregulated proteins in "severe" phenotype were related to mitochondria, intracellular and microtubule-based transport, synaptic vesicles, and the cytoskeleton. Most of these processes and compartments were also identified in our approach parallel to behavioral milestones. An essential neuronal structure, which connected those terms, is the axon, which requires high energy production, highly efficient trafficking of cargoes toward its end, and is a location of synaptic vesicle release. Therefore, we further decided to go to the next level of neuronal complexity in our proteomic investigation and selectively explore proteins dysregulated in the SCA3 axons.

Targeted Axonal Proteomics Indicates the Abnormal Localization of Proteins Between Axons and Soma Such as Cytoskeletal, Vesicular Proteins, and Highly Increased Translation Machinery in Ki91 SCA3 Neurons

Our next aim was to define with high precision the specific processes which highly contribute to axonal dysfunction in SCA3 already at a very early level of neuronal maturation stage, where no neuronal damage takes place, and therefore no secondary post-symptomatic events occur. Therefore, we performed the analysis of enriched or decreased proteins in axons of the cerebellar (young postnatal; P5) and cortical neurons (embryonal; E18) growing in Boyden chambers (n = 4 per genotype; **Figure 5A**).

Both somatodendritic and axonal protein extracts were subjected to MS/MS proteomics, and the "raw levels" for each protein for both compartments were determined (**Supplementary Table 4**). To normalize the protein levels within fractions originating from neurons on the same filter, we calculated the protein level ratio between the axonal and somatodendritic compartments for each WT and Ki91 sample/filter (**Supplementary Table 4**). Such normalization has proved very solid since the comparison of soma/axon ratios within the single genotype (WT or Ki91) demonstrated that the most significant difference was the abundance of nuclear proteins, such as histones, and nuclear enzymes characteristic for the somatodendritic compartment (ratio axon to soma < -3; **Supplementary Table 4**). Coherently, the PCA graph demonstrates a clear separation between axonal and somatodendritic samples (**Supplementary Figures 7C,D**).

Subsequently, we compared protein level ratios between WT and Ki91 SCA3/MJD neurons to calculate the fold change and estimate if the protein was enriched or depleted in axons ($p < 0.05$; two-sample t-test; **Supplementary Table 4**). In the cerebellar neurons, there were 34 proteins enriched (ratio axon/soma > 1, $p < 0.05$; two-sample t-test; $n = 4$) and 41 proteins depleted (ratio axon/soma < 1, $p < 0.05$; two-sample t-test; $n = 4$) in Ki91 vs. WT axons (**Figures 5B,C** and **Supplementary Tables 5**, **6**). There were 27 and 20 such proteins in cortical neurons, respectively (**Figures 5D,E** and **Supplementary Tables 7**, **8**). The analysis of proteins in both cerebellar and cortical Ki91 axons revealed a common functional characteristic. The majority of the axon-enriched proteins in SCA3 samples were related to the upregulation of protein production and degradation (**Figures 5B,D, 6A,B** and **Supplementary Tables 6, 8**). Strongly upregulated was the translation machinery, in particular the initiation step and nonsense-mediated decay together with the RNA binding proteins, including Cirbp (FC = 4.92; **Figure 5B**), which stabilizes mRNAs involved in cell survival during stress (Liao et al., 2017). Highly upregulated were the proteasome subunits and chaperones enriched in cerebellar Ki91 axons (Psmd14, Psma5, and Hspa8; **Supplementary Table 6**) and cortical Ki91 axons (Sel1l and Cct2; **Supplementary Table 8**), which altogether might be related to the neuronal response to cellular stress and misfolded proteins in SCA.

In contrast, proteins that were reduced in Ki91 axons comparing to WT were in the majority related to the actin cytoskeleton and vesicle-mediated transport, which may indicate the axonal structural dysfunction (**Figures 5C,E**, **6A,B** and **Supplementary Tables 5, 7**). In Ki91 cerebellar axons, there were reduced levels of 13 proteins related to cytoskeleton, including 8 proteins regulating actin function (**Figures 5C**, **6A** and **Supplementary Table 5**). The actin cytoskeleton is involved not only in maintaining the proper structure of the axon but also plays a pivotal role in the short-range transport, selection of cargoes targeted to the axon tip, formation of synapses, and scaffold for the mitochondria in the growth cone (Kevenaar and Hoogenraad, 2015). Along this line, we identified eight mitochondrial proteins with a lower ratio axon vs. soma in cerebellar SCA3 samples as compared to WT (**Figures 5C, 6A** and **Supplementary Table 5**). Altogether, this may indicate the disrupted delivery of mitochondria to the proper axon area due to the deregulated function of the actin cytoskeleton. Moreover, there are also proteins with a reduced level in cerebellar Ki91 axons directly related to intracellular trafficking (Actr1a, Ank2, Arf6, Nsf, and Rhob), synaptic/SNARE vesicles (Sv2b, Napa, and Vti1b), and COPI-mediated transport from ER to Golgi (Napa, Actr1a, Nsf,

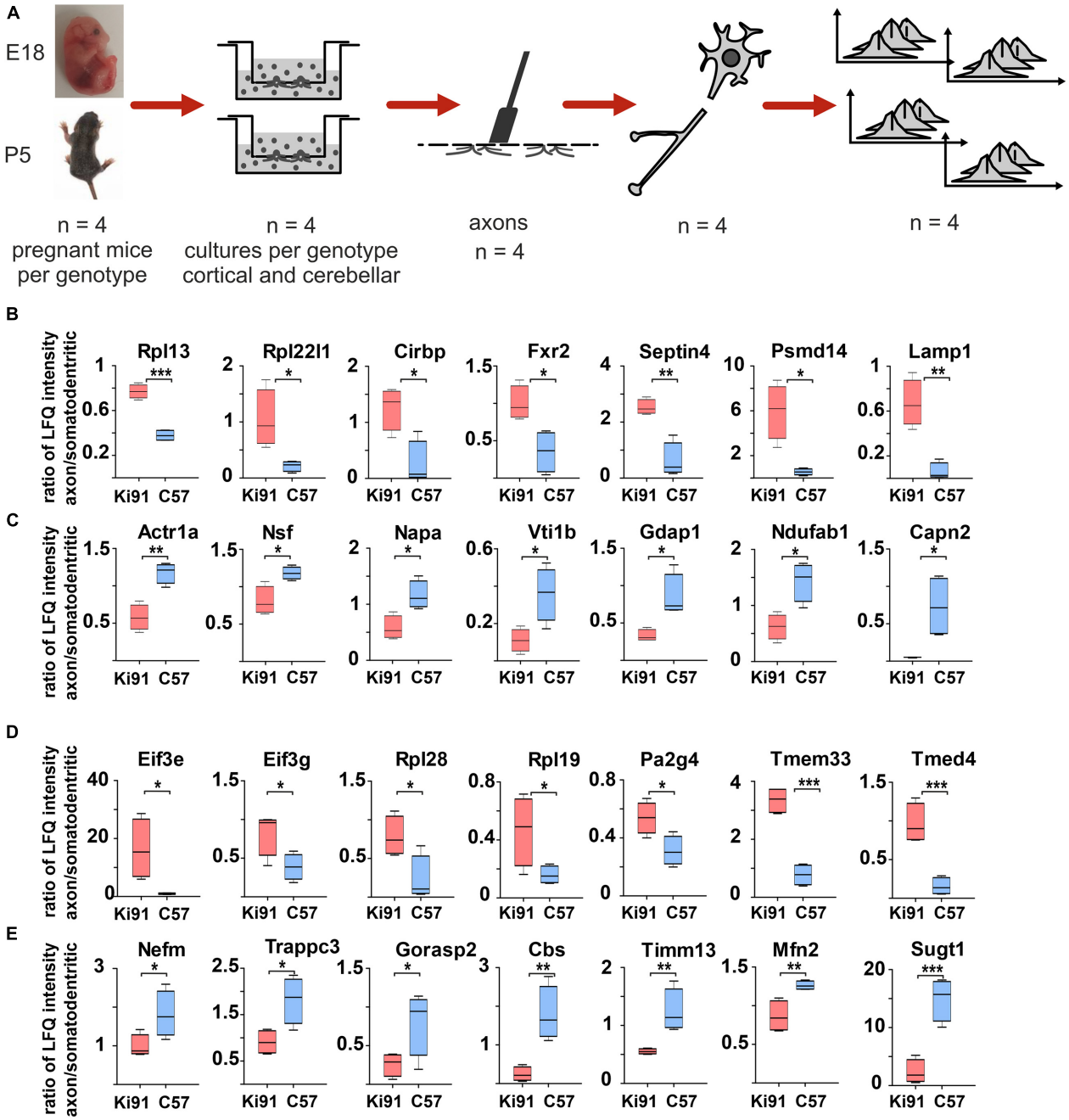

FIGURE 5 | Targeted axonal proteomics reveals sets of proteins enriched or depleted in the Ki91 SCA3/MJD cerebellar and cortical axons. Identification of proteins differentially localized in SCA3 neuronal compartments was performed by isolating two neuronal fractions (axonal and somatodendritic) from the same culture (Boyden chambers) obtained from E18 embryo (cortical) or P5 pups (cerebellar) – derived neurons. In brief, neurons were seeded on the inner side of the Boyden chamber inserts with a 1-μm porous filter. After the period of neuronal differentiation and axonal growth through and toward the outer side of the insert membrane, both the inner side of the insert (somatodendritic) and the outer side (axonal) were scraped, and the fractions were collected for MS/MS analysis **(A)**. Graphs present proteins with abnormal localization between axon and soma with the highest ratio between those compartments ($p < 0.05$; two-sample *t*-test) in the primary cerebellar **(B,C)** and cortical Ki91 neurons **(D,E)**. In the P5-derived Ki91 cerebellar axons, there were enriched proteins related to ribosomes (Rpl13 and Rpl22l1), RNA-binding (Cirbp and Fxr2), and proteasome or lysosome (Psmd14 and Lamp1) **(B)**. Proteins depleted in the Ki91 cerebellar axons involved important modulators of vesicular transport (Actr1a, Nsf, Napa, and Vti1b) **(C)**. In the E18-derived Ki91 cortical axons, there were enriched translation factors (Eif3e and Eif3g), ribosome subunits (Rpl28 and Rpl19), RNA-binding (Pa2g4), and ER and Golgi (Tmed4 and Tmem33) **(D)**. Proteins that were depleted in the Ki91 cortical axons included neurofilament (Nefm), related to intracellular trafficking (Trappc3 and Gorasp2), and mitochondria (Timm13 and Mfn2) **(E)**. two-sample *t*-test (*$p < 0.05$, **$p < 0.01$, ***$p < 0.001$), $n = 36$, $n = 4$ per phenotype, error bars: SEM.

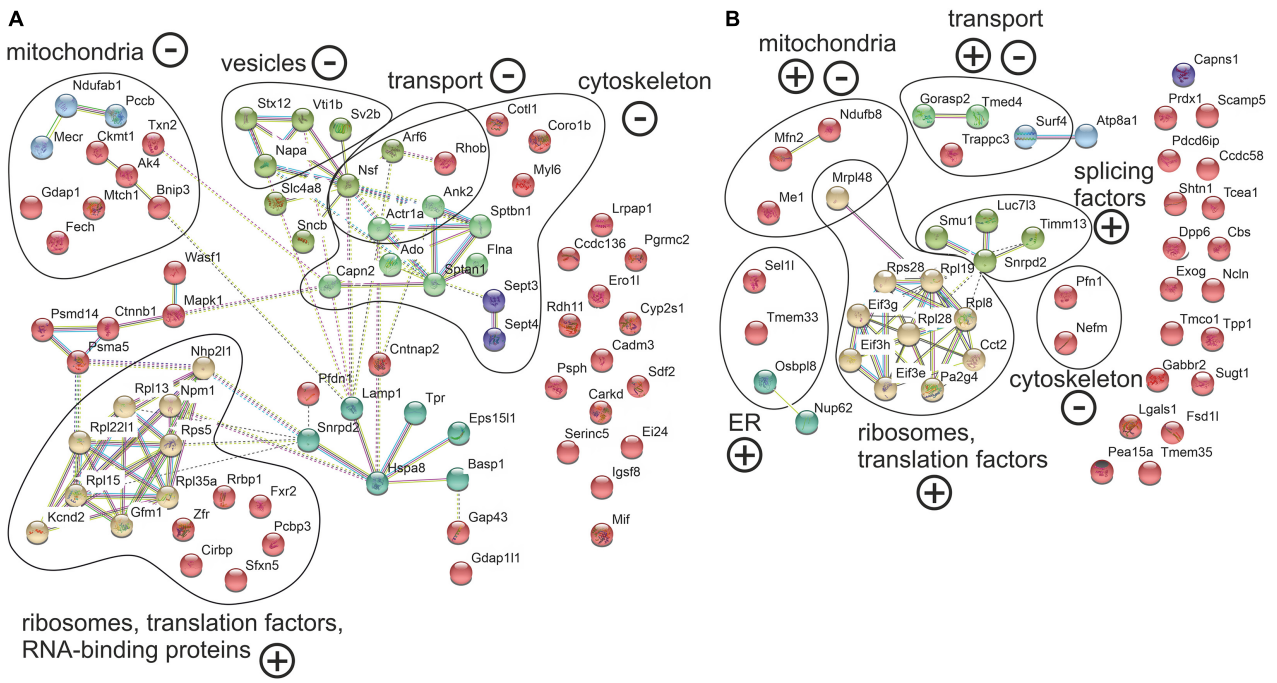

FIGURE 6 | Abnormal localization between axon and soma in the cerebellar and cortical neurons of Ki91 SCA3/MJD build an intensely interconnected network of proteins of translation machinery, vesicles, and transport machinery, cytoskeletal and mitochondrial proteins. The network of proteins displaying altered ratio between axon and soma in cerebellar **(A)** and cortical neurons **(B)** of Ki91 mice were generated using String database and clustering (https://string-db.org/). Number of proteins enriched in cerebellar axons $n = 34$ (ratio axon/soma > 1, $p < 0.05$; two-sample t-test); reduced in cerebellar axons $n = 41$ (ratio axon/soma < 1, $p < 0.05$; two-sample t-test); enriched in cortical axons $n = 27$ (ratio axon/soma > 1, $p < 0.05$; two-sample t-test); reduced in cortical axons $n = 20$ (ratio axon/soma < 1, $p < 0.05$; two-sample t-test), four biological replicates per genotype. Distinct colors denote clusters of proteins generated by the String algorithm, which grouped functionally associated proteins into specific sets, such as translational machinery (ribosomes and translation factors), cytoskeletal-modulators, and vesicular proteins. Functional groups are marked and named based on GO annotations (BP, M Level 3, 4, and 5; $q < 0.01$) using CPDB or GO term search if not available in CPDB. "+" and "–" denote for enrichment or depletion of protein groups in axons based on F.C. of the majority of proteins in the group. Blue and pink edges represent known interactions, green, red, and dark blue represent predicted interactions, while black and purple are other interactions.

Sptan1, Sptbn, and Ank2) (**Figures 5C**, **6A** and **Supplementary Table 5**).

In cortical Ki91 axons, there were generally fewer proteins identified with lower ratio axons to the soma (**Figure 5E** and **Supplementary Table 7**). However, there were also proteins related to mitochondria, transport, and cytoskeleton, including neurofilament medium-chain (Nefm), playing an essential role in axonal function (**Figures 5E, 6B** and **Supplementary Table 7**).

Impairment of Mitochondrial Metabolic Potential in Ki91 SCA3/MJD Primary Cerebellar Neurons

Spinocerebellar ataxia type 3 patients show decreased BMI, and similarly, SCA3 Ki91 mice fail to gain weight. Moreover, our proteomic approaches identified mitochondria and energy metabolism failure in Ki91. The direct investigation of energy metabolism in presymptomatic young SCA3 neurons was not performed previously; therefore, it is unknown if the mitochondrial phenotype occurs early in SCA3 and if mitochondrial dysfunction is a primary contributor to the SCA3 pathology or only the secondary result of putative mice and patient dysphagia. To address whether energy metabolism is disturbed in Ki91 neurons, we performed Cell Energy Phenotype Test with Seahorse XFp analyzer. The assay was performed on primary cerebellar neurons in days *in vitro* 3 (DIV3), 11, 18, and 21 ($n = 6$ per genotype and stage; **Figures 7A–C**). The oxygen consumption rate (OCR) and extracellular acidification rate (ECAR) were measured over time at baseline and stressed conditions (injection of oligomycin and FCCP mixture) (**Supplementary Figure 8**). Then, the metabolic potential of neurons was evaluated by calculating changes after stress conditions relative to baseline. The test demonstrated a significant increase in the ECAR metabolic potential in both Ki91 and WT neurons in every tested stage ($p < 0.0001$; two-sample t-test; **Figures 7A,B**). Likewise, an increase of the OCR metabolic potential was observed in WT neurons and Ki91 neurons, but only in DIV11 and 21 ($p < 0.05$; two-sample t-test; **Figures 7A,B**). Furthermore, under stressed conditions, the levels of ECAR were diminished in Ki91 neurons compared to WT in DIV3, 18, and 21 ($p < 0.001$; two-sample t-test; **Figures 7A,C**). Interestingly, both baseline and stressed OCR was increased in Ki91 neurons compared to WT in DIV 3 and 11 ($p < 0.0001$; two-sample t-test; DIV11 baseline $p = 0.13$; **Figures 7A,C**),

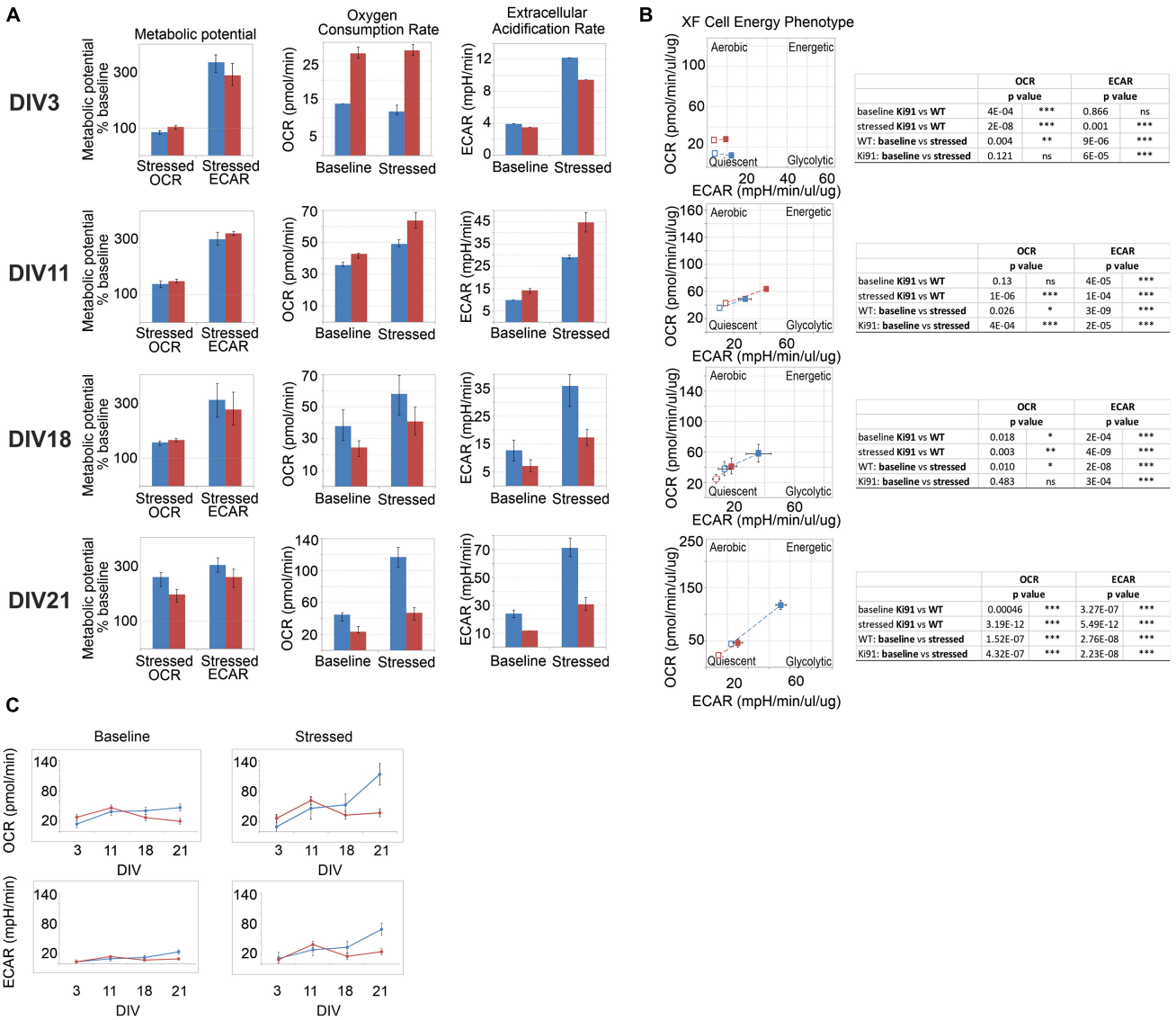

FIGURE 7 | The energy metabolism measured by Seahorse XFp Cell Energy Phenotype Test is impaired in the P5 cerebellar neurons of Ki91 SCA3/MJD. The assays were performed with cerebellar neurons at DIV3, 11, 18, and 21. The rate of mitochondrial respiration (OCR, oxygen consumption rate) and glycolysis (ECAR, extracellular acidification rate) were measured under baseline and stressed conditions, which were evoked by specific stressors: 1 μM of oligomycin and 1 μM of FCCP. The bioenergetic parameters are shown for OCR (pmol/min), ECAR (mpH/min), and metabolic potential [(stressed OCR or ECAR/baseline OCR or ECAR) × 100%)] in **(A)**. In DIV3 and DIV11, OCR in neurons is elevated in Ki91 compared to WT ($p < 0.001$; two-sample *t*-test), but in later stages (DIV21), both OCR and ECAR are severely decreased in Ki91 neurons ($p < 0.001$; two-sample *t*-test) under both baseline and stressed conditions **(A)**. WT cerebellar neurons transform from the quiescent phenotype in DIV3 toward energetic in DIV21, but Ki91 does not undergo such transformation **(B)**. The profiles of OCR and ECAR during tested developmental stages *in vitro* are presented in **(C)**. The blue color is for WT neurons; red is for Ki91 neurons. Experiments were performed in $n = 6$ per genotype and stage. Two-sample *t*-test (*$p < 0.05$, **$p < 0.01$, ***$p < 0.001$), error bars: SEM.

while in later stages, the trend was reversed and in DIV18 and 21 it was significantly decreased ($p < 0.01$; two-sample *t*-test; **Figures 7A,C**).

Overall, these data demonstrate that the potential for energy production is impaired in cerebellar Ki91 neurons. The glycolysis rate shows fluctuations in both baseline and stressed conditions. On the other hand, mitochondrial respiration shows a coherent pattern, which starts with an increase under both tested conditions, following by a decrease. The study demonstrates that energy deficit occurs early in SCA3 neurons, and therefore it is not a secondary event resulting from previous neuronal damage.

Assessment of Vesicle State in Neurites of Ki91 SCA3/MJD Cerebellar Neurons

All proteomic approaches collectively demonstrated altered levels of proteins building cellular vesicles or regulating intracellular

vesicular trafficking. Therefore, our next goal was to assess a state of vesicles using the functional assay based on the labeling of neuronal vesicles using Rab7, a vesicular protein commonly occurring in late endosomes, lysosomes, and other types of vesicles that are undergoing active transport in axons and dendrites. Therefore we transfected monomeric red fluorescent protein (mRFP)-tagged Rab7 to SCA3 primary cerebellar neurons (neuron cultures isolated from three different sets of P5 pups, five independent transfections, with 5–10 neurons analyzed each time; **Figure 8A**).

We found that the average area of vesicles labeled with fluorescently tagged Rab7 was significantly (*t*-test, $p < 0.01$) increased by 40% in Ki91 as compared to WT neurons (**Figure 8B**). Distribution of vesicle size showed that Ki91 neurons had a lower number of small vesicles ($<0.25\ \mu m^2$) and a higher number of large vesicles ($>0.5\ \mu m^2$) (*t*-test, $p < 0.01$; **Figure 8C**). We did not detect any differences in the shape of vesicles. However, there was a significant increase in the number of vesicles normalized to the length of the measured axon (*t*-test, $p < 0.05$; **Figure 8D**). To assess whether Rab7-loaded vesicles accumulate in either the axon's proximal or distal region, we also calculated the number of vesicles in those regions, arbitrarily defined as 1/8 of the axon length starting either from the axon hillock or axon tip. There was a significant increase in the number of vesicles in the proximal region (*t*-test, $p < 0.01$) by 58% in Ki91 as compared to WT neurons and in the distal part (*t*-test, $p < 0.001$) by 110% (**Figure 8D**).

Ki91 SCA3/MJD Neurons Show Increased Phosphorylation of Axon-Specific Neurofilaments, Indicating the Stress of the Axonal Cytoskeleton

The proteomic approaches and, in particular, the axonal proteomics demonstrated that several classes of dysregulated proteins in SCA3 are located in the axonal compartment. We also found the ataxin-3-positive inclusions along axons in the cerebellum by co-staining with axon-specific marker smi-312 antibody (axon-specific p-Nef). The phosphorylation state of axonal neurofilaments reflects the health of the neuronal cytoskeleton. Therefore we further explored whether the structure and phosphorylation status of neurofilaments are disturbed in the SCA3 model. We assessed the phosphorylated and non-phosphorylated neurofilaments (axon-specific p-Nef and neuronal Nef; **Figure 9**) on immunostained sagittal brain slices from 12-month-old Ki91 and WT mice using. Increased phosphorylation of neurofilaments is often a sign of defective transport and maintenance also related to mitochondria. We found that both p-Nef levels (SMI-312 antibody) and non-phosphorylated Nef levels (SMI-32 antibody) were significantly increased in the cerebellum of SCA3 mice compared to WT animals (*t*-test, $p < 0.001$; $n = 3$ and five pictures per genotype; **Figures 9A–D**). In detail, we found increased levels of Nef in soma, dendrites, and axons of Purkinje cells (*t*-test, $p < 0.01$; **Figures 9A,C**). The increased level of axon-specific p-Nef was detected in axons of the molecular layer and axons of the granular

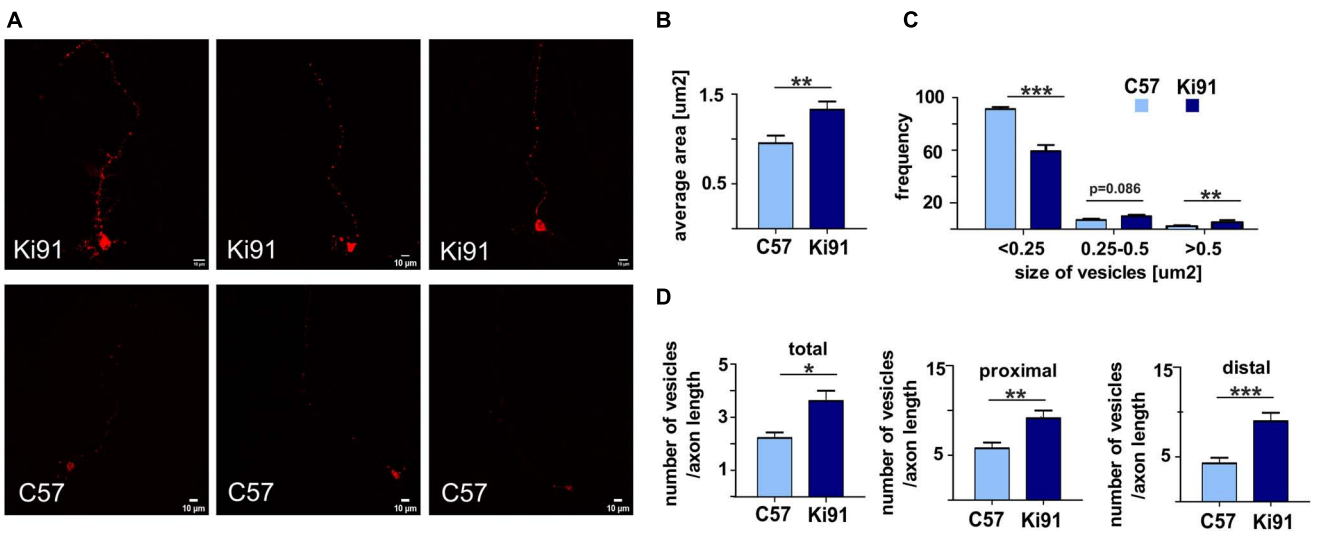

FIGURE 8 | Accumulation and enlargement of vesicles in Ki91 SCA3/MJD P5 cerebellar neurons. To investigate if the consensus vesicular and transport process identified by various types of proteomics in Ki91 impacts vesicle appearance and number, we transfected the primary cerebellar neurons (DIV8-9) with RFP-labeled Rab7. The Rab7 was selected as a useful vesicle tag since it is often recruited to several types of vesicles, including late endosomes and lysosomes (red). Representative images show fluorescently tagged vesicles in cerebellar neurons from Ki91 mice (upper panel) and WT neurons (lower panel) **(A)**. The sizes and the number of tagged vesicles were quantified using ImageJ. The average area of fluorescently tagged vesicles was 1.33 μm^2 ($n = 45$) for Ki91, 0.95 μm^2 ($n = 34$) for WT ($p < 0.01$; two-sample *t*-test) **(B)**. The size distribution of tagged vesicles in Ki91 cerebellar neurons showed a shift from smaller to larger sizes in comparison to WT ($p < 0.001$; two-sample *t*-test) **(C)**. The number of vesicles per axon length was higher in Ki91 neurons, also measured separately for both proximal and distal parts (defined as 1/8 of the axon length starting either from the axon hillock or axon tip) **(D)**. The measurements were from five independent experiments, with 5–10 cells analyzed each time. Scale bars: 10 μm. Two-sample *t*-test (*$p < 0.05$, **$p < 0.01$, ***$p < 0.001$), error bars: SEM.

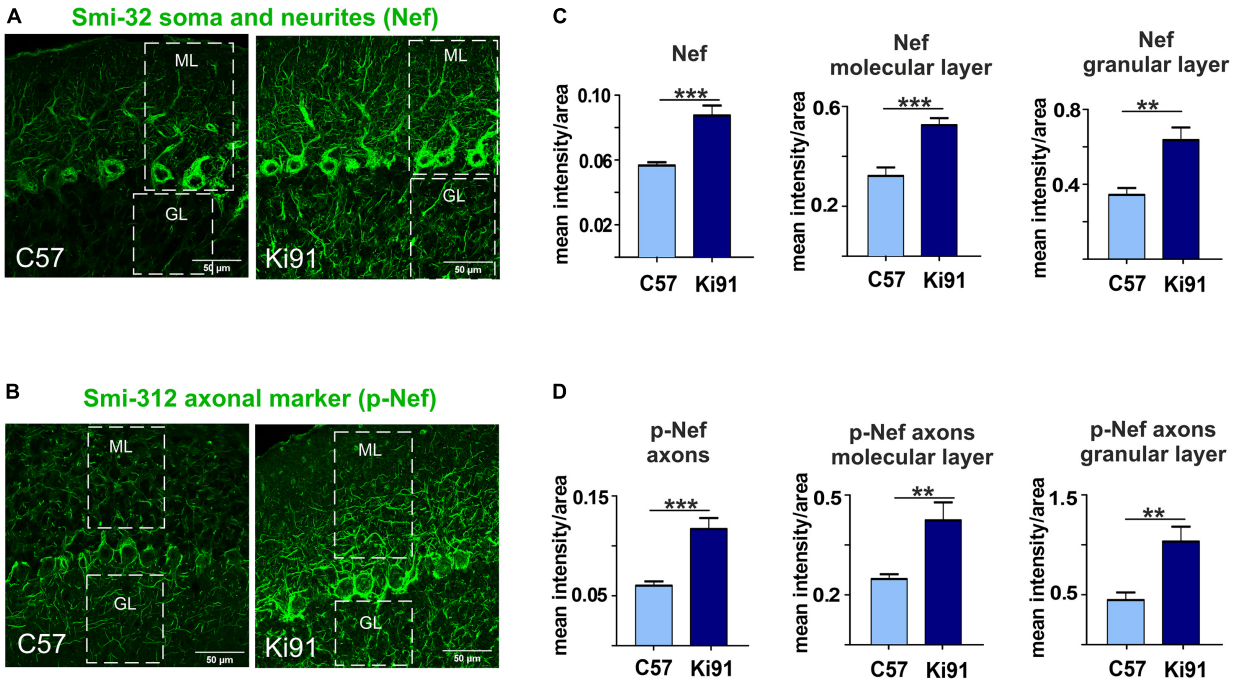

FIGURE 9 | Accumulation of neurofilaments in the cerebellar neurons of Ki91 SCA3/MJD brain. Immunofluorescent staining of the cerebellar sections from 12-month-old mice evaluates the condition of neuronal cytoskeleton and phosphorylation state of neurofilaments in axons. The staining shows the accumulation of phosphorylated neurofilaments in SCA3 cerebellar axons, which is often a sign of axonal stress. Also, the non-phosphorylated pan-neuronal neurofilaments also show increased staining intensity indicating altered cytoskeleton in SCA3 neurons. Scale bars: 50 µm **(A,B)**. Non-phosphorylated heavy neurofilaments (Nef) detected with SMI-32 antibody (pan-neuronal) are presented in panel **(A)**. Phosphorylated neurofilaments H and M detected with SMI-312 (p-Nef; axon-specific) are shown in **(B)**. White boxes inside pictures **(A,B)** mark the area, which was used for measuring the mean intensity of the fluorescence comprising the molecular and granular layer of the cerebellum. Measurement of mean intensity of fluorescence using ImageJ and statistics ($p < 0.05$; two-sample *t*-test) performed for sections as a whole and for both layers separately is presented on the graphs **(C,D)**. Axon-specific SMI-312-positive neurofilaments were highly phosphorylated in both layers in the cerebellum of the Ki91 animals (molecular layer, $p < 0.001$; granular layer, $p < 0.01$; two-sample *t*-test) **(B,D)**. Moreover, the level of dephosphorylated neurofilaments was also elevated in both cerebellar layers of the Ki91 ($p < 0.01$; two-sample *t*-test) **(A,C)**. *N* = 3 biological replicates and 10 confocal images per genotype were collected. Two-sample t-test (*$p < 0.05$, **$p < 0.01$, ***$p < 0.001$), error bars: SEM.

layer and white matter (*t*-test, $p < 0.001$; **Figures 9B,D**). The altered phosphorylation of axons in the SCA3 Ki91 model may be related to disturbed protein and mitochondria localization and their transport in axons.

DISCUSSION

Very little is known about the proteome in the SCA3 brain, and it may be one of the reasons for the incomplete understanding of the disease mechanism and delay in finding a cure. Although there are transcriptomic alterations in symptomatic SCA3 animal models, knowledge about changes in levels of the proteins is still missing (Toonen et al., 2018; Zeng et al., 2018). Moreover, we previously demonstrated the lack of transcriptomic changes in the pre-symptomatic SCA3 mice (Wiatr et al., 2019). Here, we aimed to investigate the brain profile of altered proteins in the SCA3 knock-in model to unveil a consensus set of most critical molecular programs governing the disease and identify protein biomarkers. In detail, we aimed to investigate the proteome using three different approaches: at the *in vivo* level, at the CC level, and in relation to disease progression and severity. Once the consensus set of altered candidate processes was established, we aimed to test if we can identify their physiological fingerprints by simple, functional assays, preferably using primary presymptomatic neurons.

We first performed a longitudinal behavioral study between 4 and 18 months of age of Ki91 (Switonski et al., 2015) to establish SCA3 behavioral and phenotypic milestones suitable for the investigation of brain proteome. The first milestone in symptomatic Ki91 mice was the reduced body weight gain identified in 4-month-old animals. Statistically significant gait ataxia at 12-month-old Ki91 was the second milestone, and the last milestone was the severe motor disturbances and progression of other symptoms in 18-month-old animals. Altogether, homozygous Ki91 represents a model of SCA3 progression and gradation of symptoms observed in SCA3 patients (Coutinho and Andrade, 1978; Jacobi et al., 2015; Pulido-Valdeolivas et al., 2016; Coarelli et al., 2018).

In the next step, we determined a range of affected brain areas by the MRI and detection of ataxin-3-positive inclusions using advanced, symptomatic Ki91 animals. The inclusions were present in almost all brain areas of both the posterior and frontal brain parts. The intra-nuclear inclusions dominated

in the cerebellum, mainly in the white matter, DCN, and in pons and midbrain; however, they were also present in the cerebral cortex, hippocampus, and striatum. Importantly, we have seen highly abundant ataxin-3-positive inclusions in SMI-312-positive cerebellar axons in white matter. The intra-axonal inclusions were also previously detected in nerves and various tracts in SCA3/MJD patients (Seidel et al., 2010). Also, the changes observed by brain MRI in Ki91 were not localized to one structure, but the atrophy was spreading on several brain regions, including frontal parts, cerebellum, and brainstem. Moreover, brain areas rich in axons such as the corpus callosum are atrophied in Ki91. Therefore, exploring our behavioral, neuropathologic, and MRI results led to selecting the consensus set of brain regions for further experiments. To identify molecular SCA3 pathogenesis by our three-way proteomic approach, we selected two representative brain regions: the cerebellum and cerebellar cortex. Both regions demonstrated a high number of inclusions; particularly, the cerebellum was affected more than other brain regions. Besides, the cerebral cortex demonstrated very pronounced atrophy on MRI. Even if it was not possible to determine cerebellar volume change on MRI (technical limitation of MRI setup), our previous works detected atrophy of Purkinje cells and occurrence of reactive gliosis by immunohistochemistry (Switonski et al., 2015). Also, the behavioral motor signs indicated the involvement of cerebellum atrophy. Such a selection of brain regions for further experiments involves both classically reported SCA3 pathogenesis in the hindbrain and postulated SCA3 pathogenesis in more frontal parts of the brain (Schmidt et al., 2019; Guo J. et al., 2020).

Our first proteomic approach corresponded to Ki91 behavioral milestones where we selected tissue from animals at the age of 4 months (lack of weight gain), 10 months (mice on the verge of behavioral phenotype), 12 months (motor decline statistically significant), and 14 months (an additional symptomatic age). The second proteomic approach, called "correlative," was aimed to identify dysregulated proteins and processes in mouse subjects with carefully characterized and matching phenotype severity. The first two proteomic approaches offered insights into the disease pathogenesis at the level of tissue and disease stage; however, the perspective of cellular level and CCs were still missing in both approaches. Therefore we employed a third, targeted proteomics approach where we separately assessed proteins in somatodendritic and axonal compartments of primary neurons isolated from embryos or pups. An additional advantage of such primary neuronal SCA3 culture is the possibility of validation if processes discovered in two other approaches may occur early in the disease development.

The first pathogenic process, which was consensus among the proteomic approaches in our work, is the disturbed energy metabolism. We demonstrated many dysregulated proteins related to the mitochondrial compartment, which corresponds with the reduced body weight gain in Ki91. Notably, the BMI of SCA3 patients is significantly lower, and BMI decrease correlated with faster disease progression (Diallo et al., 2017; Yang et al., 2018). The energy metabolism was the most common pathway, and the proteins related to metabolism were dysregulated already in 4-month-old presymptomatic Ki91 mice. For instance, many OXPHOS-related proteins, such as Nduf subunits, Aco2, and mt-Co proteins and several metabolic proteins such as Gpd2, Cs, Gpi, Pkm, Wdr1, Sdha, Ddx1, and Aldh1l1 demonstrated altered levels and were previously identified in AD, HD, and SCA1 (Sorolla et al., 2008; Sánchez et al., 2016; Lunnon et al., 2017). Similarly, the correlative approach also revealed downregulated mitochondrial proteins such as mitochondrial chaperone Timm9, Ndufb5, and Fasn in both "mild" and 'severe" phenotype, which suggest that disturbances of energy production is the primary pathology of SCA3. Several mitochondrial proteins were also depleted in axons compared to the somatodendritic compartment in SCA3 neurons, which may indicate the disrupted delivery of mitochondria to nerve terminals. The most frequently dysregulated protein, which we propose as one of a SCA3 biomarker candidate in both tested brain regions, is carbonic anhydrase 2 (Ca2). Ca2 is linked to a mechanism controlling an increased transport of lactate, which is an important energy source for neurons (Stridh et al., 2012; Karus et al., 2015).

Since many proteomic changes pointed out pathways related to energy metabolism, our first functional assay measured mitochondrial respiration and glycolysis rate in cultured cerebellar Ki91 neurons kept for DIV 3, 11, 18, and 21, which reflected the culture differentiating from young to more mature neurons. Commonly, the typical culture of such neurons and also our WT neurons represented a developing dependency on OXPHOS since mature neurons rely on OXPHOS to meet energy demands. In turn, SCA3 neurons demonstrated a lack of increase in OXPHOS dependency and even a slight drop in oxygen consumption during neuronal maturation. SCA3 neurons under stress reached their maximal OCR already as young as DIV 11 as compared to WT neurons, which reached the maximum at DIV 21. At DIV 3 and 11, SCA3 neuronal progenitors show higher overall oxygen consumption; therefore, at this early stage, the neurons may already be in deficiency of energy, or its production is aberrant. In the case of older SCA3 neurons with highly developed processes, a dramatic difference in energy metabolism compared to WT neurons can also be related to the failure of energy production in axons.

Overall, we demonstrated that the number of dysregulated proteins related to metabolism, lysosomes, endosomes, and protein folding increases with Ki91 age and is noticeably higher in older 10–14-month-old Ki91 mice, which represent the phase of the motor symptoms development. Moreover, the most advanced disease stage marked by highly reduced body weight, anxiety, and severe motor symptoms in 18-month-old animals is also characterized by the excessive size of Atxn3 inclusions and were observed both in the nuclei and axons, whereas in pre-symptomatic 2-month old SCA3 mice ataxin-3-positive aggregates were relatively smaller and detected only in cell nuclei (Wiatr et al., 2019).

Recent discoveries emphasize the role of degeneration of "wiring" between brain structures and axonal deficits as one of the main pathogenic events in neurodegenerative disorders (Sánchez-Valle et al., 2016; Ferrari Bardile et al., 2019; Casella et al., 2020). Also, in SCA3, the axonal defects and white matter

abnormalities are prominent disease symptoms (de Rezende et al., 2015; Farrar et al., 2016; Lu et al., 2017). Our proteomic approaches jointly demonstrated that the largest population of proteins with altered levels was involved in vesicular transport and endocytosis as a second consensus molecular process candidate in SCA3. Vesicular trafficking is crucial for axon maintenance, synaptic signaling, releasing, and recycling of neurotransmitters. Our proteomic data demonstrate highly downregulated levels of proteins related to vesicle transport or trans-synaptic signaling (Nrgn, Sh3gl1, Vamp2, Syngap1, Bsn, Syt7, Homer1, Rims1, Pclo, and Erc2; SNARE complex). Several vesicular Rab proteins were also dysregulated, such as Rab11b, Rab3d, and Rab10. Other Rab proteins were also dysregulated in SCA3/MJD patients (Sittler et al., 2018). Besides, there were dysregulated proteins related to protein metabolism localized to endosomes, exosomes, and lysosomes. Many of these proteins are involved in neurodegenerative diseases such as AD and HD (Skotte et al., 2018; Mendonça et al., 2019), and their loss brings significant neurological consequences (Yoo et al., 2001; Santos et al., 2017; Salpietro et al., 2019; Falck et al., 2020). Moreover, Qdpr (human homolog: DHPR) and Glul proteins responsible for neurotransmitters' metabolism are progressively downregulated throughout the SCA3 course in the Ki91 cerebellum and cortex. Both proteins are essential for proper CNS function (Breuer et al., 2019; Kurosaki et al., 2019; Zhou et al., 2019).

The 3rd consensus SCA3 candidate process was termed by us "the regulation of cytoskeletal structure and function" with dysregulated proteins localizing to neuronal processes. Coherently with vesicle trafficking, our proteomic results also revealed dysregulation of neurofilament proteins (NFs), such as heavy chain NF-H in both the cerebral cortex and cerebellum. Disturbed energy metabolism in neurons is often related to defects in the cellular cytoskeleton and phosphorylation state of NF-H, in particular, resulting in aberrant axonal transport of mitochondria (Jung et al., 2000; Shea and Chan, 2008). Furthermore, proteomic data contained dysregulated proteins pivotal for microtubular cytoskeleton stability and axon organization. Dysregulated proteins were also involved in anterograde and retrograde microtubule-based transport (Kif5c, Kif5b, Kif21a, Klc1, Klc2, and Kif3a; Dnm3, Dync1li1, Dync1h1, and Dynll2), in particular in "severe" phenotype, which may suggest that disruption of axonal transport contributes to increased severity of SCA3 symptoms. Among the microtubular proteins, Tau (Gao et al., 2018) was elevated in the cerebral cortex of symptomatic Ki91 mice, RhoG (Zinn et al., 2019), and dysregulated group of proteins that are also enriched in oligodendrocytes such as Cryab protein stabilizing cytoskeleton and previously proposed as a component of therapeutic strategy (Ghosh et al., 2007; Houck and Clark, 2010; Cox and Ecroyd, 2017; Zhu and Reiser, 2018). Dysregulation of Cryab, RhoG, Mbp, and Marcks indicates that oligodendrocytic processes and myelination contribute to axon dysfunction in SCA3 (Ishikawa et al., 2002; Guimarães et al., 2013; Zhang et al., 2017; Rezende et al., 2018). In addition, we previously identified altered levels of mRNA related to oligodendrocyte differentiation and function in older SCA3 mice (Wiatr et al., 2019). Interestingly, several oligodendrocytic marker proteins dysregulated in our proteomic studies, such as Plp, Qdpr, Mbp, and Mog were predicted to localize in extracellular vesicles (EVs). EVs are often released by oligodendrocytes and deliver trophic support for axons but may also transfer pathogenic triggers (Krämer-Albers et al., 2007; Porro et al., 2019).

The investigation of two candidate consensus processes related to vesicle transport and neuronal cytoskeleton required a targeted proteomic approach focused on axons. The proteins that were deficient in SCA3 axons were associated with vesicles, axonal transport, and mitochondria. Depleted proteins suggesting altered transport along the axon in Ki91 included proteins interacting or forming dynactin complex, required for mitochondria and endosome/lysosome and synaptic vesicles transport along the axons, such as Actr1a and Ank2 (Holleran et al., 1996; Moughamian et al., 2013; Lorenzo et al., 2014). Besides, there were also essential cytoskeletal proteins involved in regulating axonal transport and actin dynamics, Arf6 and its interactor RhoB, targeted by Arf6 to endosomes (Eva et al., 2017; Zaoui et al., 2019). Components of SNAREs responsible for vesicular trafficking were also depleted in SCA3 axons, such as Napa (a.k.a. α-SNAP), Vti1b, and Nsf. Lower levels of Napa, Nsf, and Actr1a were also identified by the "parallel" proteomic approach in the cerebellum of Ki91 mice. Of note, Nsf is the ATPase indispensable for membrane fusion and for regenerating active SNAREs. Nsf depletion results in the arrest of membrane trafficking and, consequently, neuronal damage and death (Stenbeck, 1998; Emperador-Melero et al., 2018; Yuan et al., 2018). In particular, disturbed axonal transport may affect delivery and proper localization of mitochondria since we detected several essential mitochondrial proteins with diminished levels in Ki91 axons.

In addition to defective energy metabolism, all of our proteomic approaches identified the vesicular processes and cytoskeletal structure and regulation processes in the SCA3 Ki91 brain. In addition to vesicular and cytoskeletal localization, most dysregulated proteins identified in proteomics were predicted to localize in axons. Therefore we designed two simple assays to detect functional fingerprints of vesicular and cytoskeletal phenotypes in neurons. We decided to load the neuronal vesicles with fluorescent Rab7 protein as the universal, external marker often occurring in a variety of vesicle species. We were able to detect the accumulation of vesicles in cell bodies and in the processes of SCA3 neurons. Moreover, the vesicles were enlarged in SCA3 neuronal processes. The second assay was based on immunostaining detection of axonal cytoskeleton phosphorylation to assess a putative pathogenic process related to the axonal cytoskeleton. We used the SMI-312 antibody, an axon-specific marker (phosphorylated NFs), and detected highly increased phosphorylation in the 12-month-old Ki91 cerebellum compared to WT cerebellum. Non-phosphorylated NFs (SMI-32; pan-neuronal staining) were also increased in the SCA3 KI91 cerebellum. Accumulation and aggregation of phosphorylated neurofilaments in axons is a biomarker indicating axonal damage, which may disturb the transport of vesicles and mitochondria. Moreover, in neurodegenerative disorders and SCA3, the NFs could serve as a biomarker (Li et al., 2019).

Lastly, axonal proteomics in Ki91 has also demonstrated highly enriched protein translation machinery represented by ribosomal proteins, various RNA-binding proteins, and translation initiation factors (**Supplementary Tables 5**, **7**). Protein synthetic machinery is intensively transported to the axons in response to cellular stress (Baleriola and Hengst, 2015). We detected the signs of cellular stress by identifying elevated Tpp1 and Tmem33 proteins, which play a role in unfolded protein response (UPR) (Sakabe et al., 2015; Mukherjee et al., 2019). Along this line, protein chaperons and proteasome subunits (Cct2 and Pmsd14) were highly enriched in SCA3 Ki91 axons. Moreover, ribosomal and RNA-binding proteins are also compounds of RNP granules (mRNPs, messenger ribonucleoproteins) or stress granules, both holding mRNAs translationally repressed (Sossin and DesGroseillers, 2006; El Fatimy et al., 2016). One of the crucial components of the granules is Fxr2 (Chyung et al., 2018), which is highly enriched in Ki91 cerebellar axons. Interestingly, vesicular platforms in axons were recently identified as carriers of translation machinery, mRNPs, and structure responsible for axonal mitochondria maintenance (Cioni et al., 2019). Furthermore, it was also demonstrated that protein inclusions specifically impair the transport of endosomes and autophagosomes (Volpicelli-Daley et al., 2014; Guo W. et al., 2020). Also, locally active translation machinery and local energy production are long known phenomena in axons since it provides critical substrates even to the most distal part of the neuronal terminals. However, in the case of accumulation of the polyQ proteins, such an organization of protein synthesis in long processes may accelerate neuronal dysfunction. In such a case, upregulated translation machinery may be a "vicious cycle" for the accumulation of polyQ proteins in axons, gradually aggravating the disease and leading to profound neuronal dysfunction.

CONCLUSION

Spinocerebellar ataxia type 3 molecular disease mechanism is insufficiently explored. Ataxin-3 is ubiquitin protease, but very little is known about the broader influence of mutant protein on other proteins in the SCA3 brain. The missing knowledge about the proteome may be one of the reasons for the incomplete understanding of the disease mechanism and lack of cure. Therefore, we present the first global model picture of SCA3 disease progression based on the alterations in protein levels in the brain and embryonic SCA3 axons, combined with an *in vivo* behavioral study and neuropathology. We propose the most relevant pathogenic processes in SCA3 involving disturbed energy metabolism, impairment of the vesicular system, cell and axon structure, and altered protein homeostasis. We demonstrate that the consensus processes identified in the SCA3 Ki91 brains show their functional signs in the primary pre-symptomatic neurons, and therefore may be the first steps of pathogenesis. Our data have demonstrated for the first time that one of the essential pathogenic aspects of SCA3 is the faulty localization of proteins between axons and soma. Further signs of affected SCA3 axons are vesicle accumulation and increased neurofilament phosphorylation. The important novel finding is the highly increased axonal localization of proteins involved in the translation machinery in SCA3. It is possible that local mutant protein production in axons may accelerate neuronal dysfunction; therefore, upregulated translation machinery in axons may aggravate the disease. Moreover, we identified a variety of molecular signatures related to mitochondria in the SCA3/MJD Ki91 model, and we show that the earliest global process which occurs already in the neonatal neurons is the OXPHOS and glycolysis deficits. For the first time, we demonstrate that the young developing SCA3 neurons fail to undergo the transition from glycolytic to OXPHOS phenotype typical for normal neurons. Summarizing, we revealed that the SCA3 disease mechanism is related to the broad influence of mutant ataxin-3 on the brain, neuronal and axonal proteome, and disruption of the proper localization of axonal and somatodendritic proteins and organelles such as vesicles, translation machinery, and mitochondria (**Figure 10**).

MATERIALS AND METHODS

Animals

Maintaining and breeding were performed at standard conditions with an 18/6-h light/dark cycle and water and food *ad libitum*. No differences in food or water intake between Ki91 and WT mice were observed. The animals were marked using numerical ear tags (National Band & Tag Company, Newport, RI, United States). The stress level of the animals was minimized throughout all procedures and animal handling. The animal experimentation and handling were approved and monitored by the Local Ethical Commission for Animal Experiments in Poznań. The animals were sacrificed according to AVMA Guidelines for the Euthanasia of Animals by placing them in the programmable CO_2 chamber (Rothacher Medical, Heitenried, Switzerland). Homozygous SCA3 Ki91 animals contained between 103 and 132 CAG repeats on a single mutant ataxin3 allele. SCA3 Ki91 mice (C57BL/6 background) and age-matched WT littermates bred in-house were used for behavioral tests (n = 36) and collecting brain tissues for proteomic analysis (n = 32, and n = 21, after behavioral tests), validation of proteomics (n = 32), MRI (n = 12) and immunostaining (n = 8, after behavioral tests and n = 6 from a separate cohort of 12-month-old animals). The cerebellum and cerebral cortex for proteomic analysis were collected from 4, 10, 12, 14, and 18 month-old animals, which corresponded to the timepoints of behavioral testing. An experimental group consisted of four mutant mice vs. four WT littermates (proteomics: 4, 10, 12, and 14-month-old and immunostaining), and 11 mutant mice vs. 10 WT littermates (proteomics: 18-month-old).

Behavioral Studies

Mice were trained and tested for motor deficits, starting from 4-month-old animals, and consequently every 2 months, until the age of 18-month-old in a cohort of 18 mutant mice vs. 18 WT littermates. Tests included accelerating rotarod (4–40 rpm in 9.5 min), elevated beam walk (diameter of rods: 35, 28, 21,

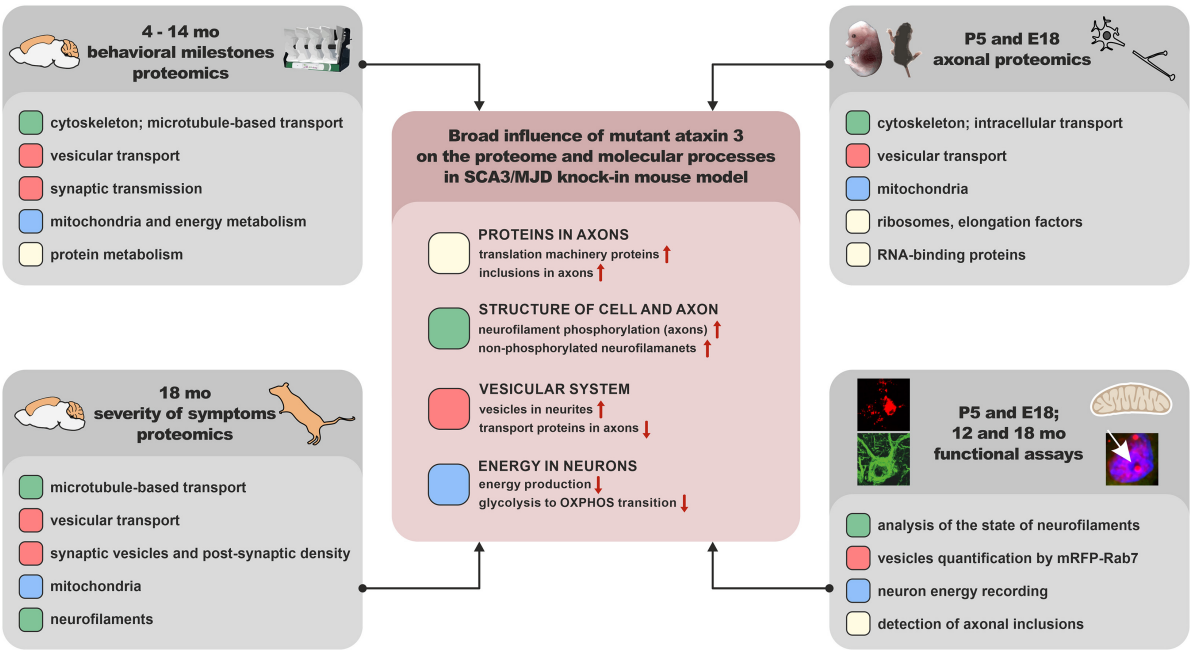

FIGURE 10 | The graphical summary of broad influence of mutant ataxin 3 on the proteome and molecular processes in SCA3/MJD knock-in mouse model.

17, and 9 mm) as previously described (Switonski et al., 2015), and additionally in 18-month-old animals open field test in which locomotor activity and zone preferences in the experimental cage (50 cm^2) were analyzed and measured during 10 min. Each test consisted of 1 training day (T) and 3 consecutive days of measurement. We also performed scoring tests designed for evaluation of the ataxia phenotype in mouse models (Guyenet et al., 2010), wire test for evaluating muscle strength, and footprint for gait ataxia. For gait analysis, the forelimbs of the mice were stained with black and hindlimbs with red non-toxic paint. Mice were placed on a sheet of paper inside a tunnel (80 × 10 cm). Only the middle part of a series of steps was measured for the distance between two steps (stride length), for- and hindlimb base, and overlapping between for- and hindlimb. All mice were weighed during each testing session. Graphing and statistics were performed on PrismVR software (San Diego, CA, United States), using ANOVA with Bonferroni *post hoc* test.

Magnetic Resonance Imaging and Image Analysis

After PFA perfusion of the mice, brains (n = 6 per genotype) were removed and stained by a one-week soaking in Gadolinium solution (Dotarem, Guerbet, France) in PBS at 2.5 mM. This protocol enhances the signal- and contrast-to-noise ratios on MR images of fixed brains (Dhenain et al., 2006). *Ex vivo* MRI experiments were performed on a horizontal 11.7 T Bruker scanner (Bruker, Ettlingen, Germany). A quadrature cryoprobe (Bruker, Ettlingen, Germany) was used for radiofrequency transmission and reception. Diffusion Tensor Imaging (DTI) data were acquired using Echo Planar Imaging sequence (Resolution = 100 × 100 × 200 μm3, TR = 3,000 ms, TE = 28 ms, 60 directions). To preserve their integrity and avoid deformations, brains were kept inside skulls for *ex vivo* MRI experiments. Anatomical images were co-registered in the same space to create a study template. Transformations to match the study template to an atlas composed of a high-resolution template and a map of region's labels adapted from the Allen mouse brain Atlas (Lein et al., 2007) were calculated. Finally, transformations to match the study template and labels to each anatomic image were calculated. The automated segmentation pipeline was performed using an in-house python library (Sammba-MRI[1]).

Protein Sample Preparation

Protein extraction was performed as previously described (Wiatr et al., 2019). Mouse brain tissues were homogenized with a Mixer Mill MM400 (Retch, Haan, Germany), followed by a threefold cycle of freezing and thawing and bath sonication (3 × 3-min). Protein concentration was estimated using Quant kit (GE Healthcare, Chicago, IL, United States). Ten-microgram aliquots of proteins were diluted with 15 μl of 50 mM NH4HCO3 and reduced with 5.6 mM DTT for 5 min at 95°C. Samples were then alkylated with 5 mM iodoacetamide for 20 min in the dark at RT. Subsequently, the proteins were digested with 0.2 μg of sequencing-grade trypsin (Promega, Madison, WI, United States) overnight at 37°C.

Liquid Chromatography Coupled to Tandem Mass Spectrometry

The analysis of the proteome was performed with the use of Dionex UltiMate 3000 RSLC nanoLC system connected to

[1]https://github.com/sammba-mri/sammba-mri

the Q Exactive Orbitrap mass spectrometer (Thermo Fisher Scientific, Waltham, MA, United States). Peptides derived from in-solution digestion were separated on a reverse-phase Acclaim PepMap RSLC nanoViper C18 column (75 μm × 25 cm, 2 μm granulation) using acetonitrile gradient (from 4 to 60%, in 0.1% formic acid) at 30°C and a flow rate of 300nL/min (for 230 min). The spectrometer was operated in data-dependent MS/MS mode with survey scans acquired at a resolution of 70,000 at m/z 200 in MS mode and 17,500 at m/z 200 in MS2 mode. Spectra were recorded in the scanning range of 300–2,000 m/z in the positive ion mode. Higher energy collisional dissociation (HCD) ion fragmentation was performed with normalized collision energies set to 25. Swiss-Prot mouse database was used for protein identification with a precision tolerance set to 10 ppm for peptide masses and 0.08 Da for fragment ion masses. Raw data obtained for each dataset were processed by MaxQuant 1.5.3.30 version for protein identification and quantification. Protein was considered as successfully identified if the Andromeda search engine found at least two peptides per protein, and a peptide score reached the significance threshold FDR = 0.01.

Obtained data were exported to Perseus software ver. 1.6.1.3 (part of MaxQuant package; Munich, Germany). Numeric data were transformed to a logarithmic scale, and each sample was annotated with its group affiliation. Proteins only identified by site, reverse database hits, and contaminants were removed from the results. Next, data were filtered based on valid values for proteins. Proteins that contained valid values in 75% of samples in at least one group were included as valid hits. Before statistical analysis, normalization of data was performed by subtracting the median from each value in a row. A two-sample *t*-test was performed on analyzed sample data with p-value < 0.05 was considered as significant, and differentiating proteins were normalized using the *Z*-score algorithm for the hierarchical clustering of data.

Bioinformatic Analysis of Proteomic Data

Proteins were grouped using the CPDB according to the pathways (pathway enrichment p-value cut-off < 0.01), GO term by molecular function (MF), biological process (BP), and cellular component (GO term B, MF level 5, CC level 4 and 5, p-value cut-off < 0.01). CPDB integrates data from 30 different resources, including such databases as Reactome, KEGG, and BioCarta (Kamburov et al., 2013). Next, common pathways and GO terms for four datasets separately in both tissues (4, 10, 12, and 14 months of age) containing the highest relative number of dysregulated proteins and p-values were selected. The relative number of dysregulated proteins was calculated as a number of dysregulated proteins involved in the pathway or GO term divided by the total number of dysregulated proteins in a given dataset (%). For each analysis, the names of genes corresponding to the names of dysregulated proteins were used. In the separate analysis, we performed identification of cell types in the brain, which are affected by pathogenesis with the use of the Dropviz tool (Saunders et al., 2018) for the cerebellum and cerebral cortex. Significantly dysregulated ($p < 0.05$) proteins identified from label-free proteomic and experiments were included together into two tissue groups based on origin from the cerebellum and cortex. Relative expression is presented in Dropviz as the number of transcripts per 100,000 in the cluster. The analysis of proteins displaying altered ratio between axon and soma in cerebellar and cortical neurons of Ki91 mice was performed using the String database[2] and clustering tool (MCL clustering, inflation parameter = 6).

Vacuum Dot Immunoblot

Before use in the dot blot assay, each antibody was validated with western blot assay (WB). WB was performed as previously described (Wiatr et al., 2019). Cerebellum and cortex samples were harvested from 16 homozygous Ki91 animals and 16 WT littermates; $n = 4$ mice per tested age (4, 10, 14, and 18 months of age) and per each genotype. The protein concentration was estimated using a Pierce BCA protein assay kit (Thermo Fisher Scientific, Waltham, MA, United States). The nitrocellulose membrane and Whatman filters (all GE Healthcare, Chicago, IL, United States) were washed two times with Milli-Q H_2O and two times with Tris-Buffered Saline (TBS) by vacuum filtration. A total of 2.5 μg of each protein sample in 50 μL of PB lysis buffer with PMSF cocktail inhibitor (Sigma-Aldrich, St. Louis, MO, United States) was spotted on nitrocellulose membrane and washed two times with TBS by vacuum filtration, and then allowed to air-dry. The blots were stained with Ponceau S solution and blocked with 5% non-fat milk in PBS/0.05% Tween-20 for 1 h at RT and subsequently incubated at 4°C overnight with the following primary antibodies: rabbit anti-MBP (1:1,000; Cell Signaling, Danvers, MA, United States), mouse anti-CRYAB (1:1,000; Developmental Studies Hybridoma Bank, Iowa City, IA, United States), mouse anti-GLUL (1:1,000; BioLegend, San Diego, CA, United States), rabbit anti-CA2 (1:2,000; ProteinTech, Rosemont, IL, United States), rabbit anti-QDPR (1:2,000; ProteinTech, Rosemont, IL, United States). The blots were probed with the respective HRP-conjugated secondary antibody (anti-rabbit or anti-mouse, 1:2,000; Jackson Immuno Research, Suffolk, United Kingdom). The immunoreaction was detected using the ECL substrate (Thermo Fisher Scientific, Waltham, MA, United States).

Primary Neuron Culture and Transfection

Primary neuron cultures were derived from Ki91 and C57 mice according to AVMA Guidelines for the Euthanasia of Animals. Cortices were dissected from E18 mouse embryos and cerebella from P5 pups. Cortical neurons were dissociated by trypsin (Merck, Darmstadt, Germany) diluted 10×, and cerebellar neurons were dissociated by trypsin diluted 5×. Cells were washed two times in a disassociation medium consisting of HBSS (Thermo Fisher Scientific, Waltham, MA, United States), supplemented with 0.1% glucose, 1× penicillin-streptomycin (Thermo Fisher Scientific, Waltham, MA, United States), then two times in a plating medium consisting of Dulbecco's modified Eagle medium (DMEM), 1× CTS GlutaMAX-I supplement, 1× penicillin-streptomycin (all Thermo Fisher Scientific, Waltham, MA, United States). Clumps of tissue debris were allowed to settle to the bottom of a 15 ml tube, and the supernatant containing

[2]https://string-db.org/

dissociated cells was centrifuged for 3 min at 1,300 rpm. Cells were seeded onto coverslips, tissue culture inserts (Greiner Bio-One GmbH, Kremsmünster, Austria), or Seahorse XFp Cell Culture Miniplates (Agilent Technologies, Santa Clara, CA, United States) coated with poly-D-lysine (Thermo Fisher Scientific, Waltham, MA, United States). Neurons were maintained in conditioned Neurobasal medium (Thermo Fisher Scientific, Waltham, MA, United States) supplemented with 2% B27 supplement, 1× CTS GlutaMAX-I supplement, 1× penicillin-streptomycin (all Thermo Fisher Scientific, Waltham, MA, United States), 1× apo-transferrin (Sigma-Aldrich, St. Louis, MO, United States), and N2 (0.005 mg/ml insulin, 0.0161 mg/ml putrescin, 30 nM Na-Selenite, 51 nM T3, 20 nM progesterone) in a humidified incubator with 5% O_2 and 5% CO_2 in air at 37°C. The maintenance medium was replenished with half-feed changes every 2–3 days. For transfection, cells were seeded at a density of 2×10^5 cells/well onto coverslips in 24-well culture plates. Neurons were transfected at DIV 3–4 with mRFP-Rab7 (Addgene plasmid # 14436[3]; dgene_14436) at a concentration of 0.8 μg DNA per well using Lipofectamine 2000 (Thermo Fisher Scientific, Waltham, MA, United States) followed by fixation (4% PFA, 15 min in RT) and confocal imaging at DIV 7–11 from three biological replicates and five independent transfections. An approximately 10–15% transfection efficiency was achieved.

Isolation of Axons

Dissociated neurons (cortical and cerebellar) were seeded at a density of 1×10^6 cells/well onto tissue culture inserts containing porous membrane (1 μm pores; Greiner Bio-One GmbH, Kremsmünster, Austria) in a 6-well cell culture plates. The bottom compartment medium was supplemented with 15 ng/ml of BDNF (PeproTech, London, United Kingdom) so that it could act as a chemoattractant for axons growing through the insert membrane. Axonal fraction and the fraction containing neuronal body with dendrites were isolated by carefully detaching the cellular contents from the inner and outer insert membrane surface with a cell scraper in TAEB buffer (Merck, Darmstadt, Germany) four times, alternating the direction by 90° each time. Axons were collected after 11 days in culture because, after DIV14, dendrites, which grow at a slower rate, are also detected on the other side of the porous membrane. Before isolation of the axon part, the inner membrane surface was scrubbed with a cotton-tipped applicator, and the membranes were cut out from the insert. To examine whether the separation of axons from the somatodendritic part was correctly performed, we also immunostained culture filters isolated from the Boyden chamber before and after scraping off the cell bodies, with immunofluorescence assay (β-III-tubulin, 1:500; Burlington, MA, United States) and nuclear dye Hoechst (**Supplementary Figures 5A,B**). The presence of axons on the outer site of the membrane was examined, and the purity of the obtained axonal fraction was evaluated with nuclear and axonal markers (**Supplementary Table 3**). The axon isolation procedures were adapted from Unsain et al. (2014).

[3]http://n2t.net/addgene:14436

Seahorse XFp Cell Energy Phenotype Test

Seahorse XFp Cell Energy Phenotype assays (Seahorse, Agilent Technologies, Santa Clara, CA, United States) were performed according to the manufacturer's instructions on an XFp instrument. Dissociated cerebellar neurons were seeded at a density of 5,300 or 12,500 cells/well onto culture mini plates with the protocol described in the section "Primary neuron culture and transfection." The assays were performed at DIV3, 11, 18, and 21. On the day of assay, the XF assay medium was supplemented with 25 mM glucose, 0.5 mM pyruvate, and 2 mM glutamine, and the pH adjusted to 7.4. After assay performance, cells were lysed with PB1× buffer, and protein concentration was measured, and the obtained values were used for data normalization. Data analysis was performed using the Seahorse XFe Wave software and the Seahorse XF Cell Energy Phenotype Test Report Generator. The baseline OCR/ECAR ratio was higher than 4 only in DIV3, which means that the stressed ECAR parameter, in this case, may include both glycolysis and mitochondrial activity.

Immunofluorescence Staining

The animals were deeply anesthetized and transcardially perfused using saline, followed by 4% PFA. The brains were removed, post-fixed in 4% PFA for 48 h, and cryopreserved with graded sucrose (10–20–30%) over 72 h. The 20 or 30-μm parasagittal mouse brain sections were cut using a cryostat at −20°C and collected on SuperFrost Plus slides (Thermo Fisher Scientific, Waltham, MA, United States). The sections were processed immediately. The HIER procedure was applied by incubation of the sections in citrate buffer (pH 9.0) for 30 min at 60°C. The sections were blocked via incubation in 4% normal goat serum in TBS for 1 h. For immunofluorescent staining, the sections were incubated overnight at 4°C with the primary mouse anti-ataxin-3 antibody 1H9 (1:200; kindly provided by Yvon Trottier), rabbit anti-ataxin-3 (1:200; ProteinTech, Rosemont, IL, United States), rabbit anti-ubiquitin (1:500; Z0458, Dako, Jena, Germany), mouse SMI-32 against non-phosphorylated heavy and medium neurofilament subunits (1:1,000) and mouse SMI-312 against phosphorylated heavy and medium neurofilaments (1:1,000) (Biolegends, San Diego, CA, United States), and subsequently with the anti-mouse or anti-rabbit antibody labeled by AlexaFluor488, Dylight594, or AlexaFluor647 (1:400; Jackson ImmunoResearch; Suffolk, United Kingdom). The sections were end-stained with Hoechst 33342 (Sigma) nuclear stain at 1:1,000 and embedded in Fluoroshield (Sigma) mounting medium.

Image Acquisition and Quantification

Confocal images were acquired using two microscope systems. The first system was Opera LX (PerkinElmer) using 40× water objective, 200 ms exposure time, and 50–70% laser power. For each picture, 25–50 confocal sections were collected, from which 10 sections were dissected for further analysis. The second system was TCS SP5 II (Leica Microsystems; Poland), using oil immersion 63× objective with a sequential acquisition setting. For fluorescent quantification, images were acquired using the

same settings at a resolution of 1024 × 1024 pixels and 100 Hz. Confocal sections (8–10) were acquired to a total Z-stack thickness of 0.13 μm. For each condition, we performed three independent cultures; and five independent transfections from which 46 pictures of Ki91 and 33 pictures of WT were collected and analyzed. For analyzing the state of mrFp-Rab7+ vesicles in fixed neurons, we selected axons, which were distinguished from dendrites based on known morphological characteristics: greater length and sparse branching (Banker and Cowan, 1979). For immunostaining of mouse brains, we used four slices, and randomly acquired from each slice, ≥5 fields were. Offline analysis of the image Z-stack was performed using the open-source image-processing package Fiji/ImageJ. Morphometric measurements were performed using Fiji/ImageJ. Measured data were imported into Excel software for analysis. The thresholds in all images were set to similar levels. Data were obtained from at least three independent experiments, and the number of cells or imaging sections used for quantification is indicated in the figures. All statistical analyses were performed using the Student's *t*-test and are presented as mean ± SEM.

Statistical Analysis

The data regarding behavioral experiments were subjected to a two-way ANOVA, followed by Bonferroni post-tests. *p*-values of less than 0.05 were considered significant. Identification of proteins on raw proteomic data was performed by the Andromeda search engine in Mascot using the following inclusion criteria: at least two different peptides per protein were identified per sample, and a total peptide score reached the significance threshold FDR = 0.01. Identified proteins matching the inclusion criteria were subjected to further statistical analysis with a two-sample *t*-test, and dysregulation of protein level reaching p-value < 0.05 was considered as significant. Kruskal–Wallis test was used to perform a score assessment in the 0–5 scale of mild, moderate, and severe phenotype in 18-month-old animals (p-value < 0.05).

DATA AVAILABILITY STATEMENT

The datasets presented in this study can be found in online repositories. The names of the repository/repositories and accession number(s) can be found below: PRIDE, PXD024945.

ETHICS STATEMENT

The animal study was reviewed and approved by the Local Ethical Committee for Animal Experiments in Poznań.

AUTHOR CONTRIBUTIONS

MF was responsible for the research concept and obtaining funding, conceived, designed, and supervised all experiments, and analyzed the data. KW and ŁM performed all proteomic experiments. KW analyzed the data, designed and performed all experiments except of MRI. EB, J-BP, and JF performed the MRI experiment and analyzed the data. MF and KW wrote the manuscript. All authors contributed to the article and approved the submitted version.

FUNDING

This work was supported by the grant from the National Science Centre (grant number 2013/10/E/NZ4/00621), the European Research Projects On Rare Diseases (JTC 2017) grant from the National Centre for Research and Development (grant numbers: ERA-NET-E-RARE-3/III/TreatPolyQ/08/2018 and ERA-NET-E-RARE-3/III/SCA-CYP/09/2018), and a grant of Polish Ministry of Science and Higher Education for young scientists GM_KW_ICHB.

ACKNOWLEDGMENTS

Proteomic mass spectrometry analyses were performed in the Laboratory of Mass Spectrometry (European Centre for Bioinformatics and Genomics; ECBiG; IBCH, PAS, Poznań, Poland). Confocal imaging was performed using the facilities in the Laboratory of Subcellular Structures Analysis and Laboratory of Molecular Assays (IBCh, PAS, Poland). Primary neuron cultures were maintained in the Cell and Tissue Culture Laboratory (IBCh, PAS, Poland). We thank Adam Plewinski for his help in maintaining the colonies of mice. We also thank Joanna Mieloch for help in maintaining the animals. We also thank Magdalena Surdyka and Łukasz Przybył for collecting tissues, which were sent for MRI. We also thank Yvon Trottier for kindly providing anti-ataxin-3 1H9 antibody and Ari Helenius for supplying mRFP-Rab7 plasmid via Addgene (#14437). We also thank Chengbiao Wu and Ruinan Shen for help with the analysis of Rab-7 transfection in Fiji. We also thank Krzysztof Sobczak for kindly providing a vacuum dot-blot apparatus.

SUPPLEMENTARY MATERIAL

The Supplementary Material for this article can be found online at: https://www.frontiersin.org/articles/10.3389/fnmol.2021.658339/full#supplementary-material

Supplementary Table 1 | MS/MS proteomic data for each tested age (4, 10, 12, and 14-month-old) in the parallel approach in the cerebellum.

Supplementary Table 2 | MS/MS proteomic data for each tested age (4, 10, 12, and 14-month-old) in the parallel approach in the cerebral cortex.

Supplementary Table 3 | MS/MS proteomic data for 18-month-old Ki91 cerebellum and cortex in the correlative approach.

Supplementary Table 4 | MS/MS proteomic data for the of protein levels in somatodendritic and axon compartment in cerebellar and cortical samples.

Supplementary Table 5 | Proteins depleted in Ki91 cerebellar axons.

Supplementary Table 6 | Proteins enriched in Ki91 cerebellar axons.

Supplementary Table 7 | Proteins depleted in Ki91 cortical axons.

Supplementary Table 8 | Proteins enriched in Ki91 cortical axons.

REFERENCES

Baleriola, J., and Hengst, U. (2015). Targeting axonal protein synthesis in neuroregeneration and degeneration. *Neurotherapeutics* 12, 57–65. doi: 10.1007/s13311-014-0308-8

Banker, G. A., and Cowan, W. M. (1979). Further observations on hippocampal neurons in dispersed cell culture. *J. Comp. Neurol.* 187, 469–493. doi: 10.1002/cne.901870302

Bettencourt, C., and Lima, M. (2011). Machado-Joseph disease: from first descriptions to new perspectives. *Orphanet J. Rare Dis.* 6:35. doi: 10.1186/1750-1172-6-35

Breuer, M., Guglielmi, L., Zielonka, M., Hemberger, V., Kölker, S., Okun, J. G., et al. (2019). QDPR homologues in Danio rerio regulate melanin synthesis, early gliogenesis, and glutamine homeostasis. *PLoS One* 14:e0215162. doi: 10.1371/journal.pone.0215162

Casella, C., Lipp, I., Rosser, A., Jones, D. K., and Metzler-Baddeley, C. (2020). A critical review of white matter changes in Huntington's disease. *Mov. Disord. Off. J. Mov. Disord. Soc.* 35, 1302–1311. doi: 10.1002/mds.28109

Chen, L., Stone, M. C., Tao, J., and Rolls, M. M. (2012). Axon injury and stress trigger a microtubule-based neuroprotective pathway. *Proc. Natl. Acad. Sci. U.S.A.* 109, 11842–11847. doi: 10.1073/pnas.1121180109

Chyung, E., LeBlanc, H. F., Fallon, J. R., and Akins, M. R. (2018). Fragile X granules are a family of axonal ribonucleoprotein particles with circuit-dependent protein composition and mRNA cargos. *J. Comp. Neurol.* 526, 96–108. doi: 10.1002/cne.24321

Cioni, J.-M., Lin, J. Q., Holtermann, A. V., Koppers, M., Jakobs, M. A. H., Azizi, A., et al. (2019). Late endosomes act as mRNA translation platforms and sustain mitochondria in axons. *Cell* 176, 56.e15–72.e15. doi: 10.1016/j.cell.2018.11.030

Coarelli, G., Brice, A., and Durr, A. (2018). Recent advances in understanding dominant spinocerebellar ataxias from clinical and genetic points of view. *F1000Research* 7:F1000FacultyRev–1781. doi: 10.12688/f1000research.15788.1

Coutinho, P., and Andrade, C. (1978). Autosomal dominant system degeneration in Portuguese families of the Azores Islands. A new genetic disorder involving cerebellar, pyramidal, extrapyramidal and spinal cord motor functions. *Neurology* 28, 703–709.

Cox, D., and Ecroyd, H. (2017). The small heat shock proteins αB-crystallin (HSPB5) and Hsp27 (HSPB1) inhibit the intracellular aggregation of α-synuclein. *Cell Stress Chaperones* 22, 589–600. doi: 10.1007/s12192-017-0785-x

Da Silva, J. D., Teixeira-Castro, A., and Maciel, P. (2019). From pathogenesis to novel therapeutics for spinocerebellar ataxia type 3: evading potholes on the way to translation. *Neurotherapeutics* 16, 1009–1031. doi: 10.1007/s13311-019-00798-1

D'Abreu, A., França, M., Appenzeller, S., Lopes-Cendes, I., and Cendes, F. (2009). Axonal dysfunction in the deep white matter in Machado-Joseph disease. *J. Neuroimaging Off. J. Am. Soc. Neuroimaging* 19, 9–12. doi: 10.1111/j.1552-6569.2008.00260.x

de Rezende, T. J. R., D'Abreu, A., Guimarães, R. P., Lopes, T. M., Lopes-Cendes, I., Cendes, F., et al. (2015). Cerebral cortex involvement in Machado-Joseph disease. *Eur. J. Neurol.* 22, e23–e24. doi: 10.1111/ene.12559

Dhenain, M., Delatour, B., Walczak, C., and Volk, A. (2006). Passive staining: a novel ex vivo MRI protocol to detect amyloid deposits in mouse models of Alzheimer's disease. *Magn. Reson. Med.* 55, 687–693. doi: 10.1002/mrm.20810

Diallo, A., Jacobi, H., Schmitz-Hübsch, T., Cook, A., Labrum, R., Durr, A., et al. (2017). Body mass index decline is related to spinocerebellar ataxia disease progression. *Mov. Disord. Clin. Pract.* 4, 689–697. doi: 10.1002/mdc3.12522

El Fatimy, R., Davidovic, L., Tremblay, S., Jaglin, X., Dury, A., Robert, C., et al. (2016). Tracking the fragile X mental retardation protein in a highly ordered neuronal ribonucleoparticles population: a link between stalled polyribosomes and RNA granules. *PLoS Genet.* 12:e1006192. doi: 10.1371/journal.pgen.1006192

Emperador-Melero, J., Huson, V., van Weering, J., Bollmann, C., Fischer, von Mollard, G., et al. (2018). Vti1a/b regulate synaptic vesicle and dense core vesicle secretion via protein sorting at the Golgi. *Nat. Commun.* 9:3421. doi: 10.1038/s41467-018-05699-z

Eva, R., Koseki, H., Kanamarlapudi, V., and Fawcett, J. W. (2017). EFA6 regulates selective polarised transport and axon regeneration from the axon initial segment. *J. Cell Sci.* 130, 3663–3675. doi: 10.1242/jcs.207423

Falck, J., Bruns, C., Hoffmann-Conaway, S., Straub, I., Plautz, E. J., Orlando, M., et al. (2020). Loss of piccolo function in rats induces cerebellar network dysfunction and pontocerebellar hypoplasia Type 3-like phenotypes. *J. Neurosci. Off. J. Soc. Neurosci.* 40, 2943–2959. doi: 10.1523/JNEUROSCI.2316-19.2020

Farrar, M. A., Vucic, S., Nicholson, G., and Kiernan, M. C. (2016). Motor cortical dysfunction develops in spinocerebellar ataxia type 3. *Clin. Neurophysiol. Off. J. Int. Fed. Clin. Neurophysiol.* 127, 3418–3424. doi: 10.1016/j.clinph.2016.09.005

Ferrari Bardile, C., Garcia-Miralles, M., Caron, N. S., Rayan, N. A., Langley, S. R., Harmston, N., et al. (2019). Intrinsic mutant HTT-mediated defects in oligodendroglia cause myelination deficits and behavioral abnormalities in Huntington disease. *Proc. Natl. Acad. Sci. U.S.A.* 116, 9622–9627. doi: 10.1073/pnas.1818042116

Gao, Y.-L., Wang, N., Sun, F.-R., Cao, X.-P., Zhang, W., and Yu, J.-T. (2018). Tau in neurodegenerative disease. *Ann. Transl. Med.* 6:175. doi: 10.21037/atm.2018.04.23

Ghosh, J. G., Houck, S. A., and Clark, J. I. (2007). Interactive sequences in the stress protein and molecular chaperone human alphaB crystallin recognize and modulate the assembly of filaments. *Int. J. Biochem. Cell Biol.* 39, 1804–1815. doi: 10.1016/j.biocel.2007.04.027

Graves, T. D., and Guiloff, R. J. (2011). SCA3 presenting as an isolated axonal polyneuropathy. *Arch. Neurol.* 68, 653–655. doi: 10.1001/archneurol.2011.86

Guimarães, R. P., D'Abreu, A., Yasuda, C. L., França, M. C., Silva, B. H. B., Cappabianco, F. A. M., et al. (2013). A multimodal evaluation of microstructural white matter damage in spinocerebellar ataxia type 3. *Mov. Disord. Off. J. Mov. Disord. Soc.* 28, 1125–1132. doi: 10.1002/mds.25451

Guo, J., Chen, H., Biswal, B. B., Guo, X., Zhang, H., Dai, L., et al. (2020). Gray matter atrophy patterns within the cerebellum-neostriatum-cortical network in SCA3. *Neurology* 95, e3036–e3044. doi: 10.1212/WNL.0000000000010986

Guo, W., Stoklund Dittlau, K., and Van Den Bosch, L. (2020). Axonal transport defects and neurodegeneration: molecular mechanisms and therapeutic implications. *Semin. Cell Dev. Biol.* 99, 133–150. doi: 10.1016/j.semcdb.2019.07.010

Guyenet, S. J., Furrer, S. A., Damian, V. M., Baughan, T. D., Spada, A. R. L., and Garden, G. A. (2010). A simple composite phenotype scoring system for evaluating mouse models of cerebellar ataxia. *JoVE J. Vis. Exp.* 39:e1787. doi: 10.3791/1787

Holleran, E. A., Tokito, M. K., Karki, S., and Holzbaur, E. L. (1996). Centractin (ARP1) associates with spectrin revealing a potential mechanism to link dynactin to intracellular organelles. *J. Cell Biol.* 135, 1815–1829. doi: 10.1083/jcb.135.6.1815

Houck, S. A., and Clark, J. I. (2010). Dynamic subunit exchange and the regulation of microtubule assembly by the stress response protein human alphaB crystallin. *PLoS One* 5:e11795. doi: 10.1371/journal.pone.0011795

Ishikawa, Y., Katoh, H., Nakamura, K., Mori, K., and Negishi, M. (2002). Developmental changes in expression of small GTPase RhoG mRNA in the rat brain. *Brain Res. Mol. Brain Res.* 106, 145–150. doi: 10.1016/s0169-328x(02)00413-8

Jacobi, H., du Montcel, S. T., Bauer, P., Giunti, P., Cook, A., Labrum, R., et al. (2015). Long-term disease progression in spinocerebellar ataxia types 1, 2, 3, and 6: a longitudinal cohort study. *Lancet Neurol.* 14, 1101–1108. doi: 10.1016/S1474-4422(15)00202-1

Jung, C., Yabe, J. T., Lee, S., and Shea, T. B. (2000). Hypophosphorylated neurofilament subunits undergo axonal transport more rapidly than more extensively phosphorylated subunits in situ. *Cell Motil. Cytoskeleton* 47, 120–129. doi: 10.1002/1097-0169(200010)47:2<120::AID-CM3<3.0.CO;2-6

Kamburov, A., Stelzl, U., Lehrach, H., and Herwig, R. (2013). The ConsensusPathDB interaction database: 2013 update. *Nucleic Acids Res.* 41, D793–D800. doi: 10.1093/nar/gks1055

Karus, C., Ziemens, D., and Rose, C. R. (2015). Lactate rescues neuronal sodium homeostasis during impaired energy metabolism. *Channels Austin Tex* 9, 200–208. doi: 10.1080/19336950.2015.1050163

Kevenaar, J. T., and Hoogenraad, C. C. (2015). The axonal cytoskeleton: from organization to function. *Front. Mol. Neurosci.* 8:44. doi: 10.3389/fnmol.2015.00044

Krämer-Albers, E.-M., Bretz, N., Tenzer, S., Winterstein, C., Möbius, W., Berger, H., et al. (2007). Oligodendrocytes secrete exosomes containing major myelin

and stress-protective proteins: Trophic support for axons? *Proteomics Clin. Appl.* 1, 1446–1461. doi: 10.1002/prca.200700522

Kurosaki, H., Yamaguchi, K., Man-Yoshi, K., Muramatsu, S.-I., Hara, S., and Ichinose, H. (2019). Administration of tetrahydrobiopterin restored the decline of dopamine in the striatum induced by an acute action of MPTP. *Neurochem. Int.* 125, 16–24. doi: 10.1016/j.neuint.2019.02.005

Lein, E. S., Hawrylycz, M. J., Ao, N., Ayres, M., Bensinger, A., Bernard, A., et al. (2007). Genome-wide atlas of gene expression in the adult mouse brain. *Nature* 445, 168–176. doi: 10.1038/nature05453

Li, Q.-F., Dong, Y., Yang, L., Xie, J.-J., Ma, Y., Du, Y.-C., et al. (2019). Neurofilament light chain is a promising serum biomarker in spinocerebellar ataxia type 3. *Mol. Neurodegener.* 14:39. doi: 10.1186/s13024-019-0338-0

Liao, Y., Tong, L., Tang, L., and Wu, S. (2017). The role of cold-inducible RNA binding protein in cell stress response. *Int. J. Cancer* 141, 2164–2173. doi: 10.1002/ijc.30833

Lorenzo, D. N., Badea, A., Davis, J., Hostettler, J., He, J., Zhong, G., et al. (2014). A PIK3C3-ankyrin-B-dynactin pathway promotes axonal growth and multiorganelle transport. *J. Cell Biol.* 207, 735–752. doi: 10.1083/jcb.201407063

Lu, M.-K., Chen, J.-C., Chen, C.-M., Duann, J.-R., Ziemann, U., and Tsai, C.-H. (2017). Impaired cerebellum to primary motor cortex associative plasticity in Parkinson's disease and spinocerebellar ataxia type 3. *Front. Neurol.* 8:445. doi: 10.3389/fneur.2017.00445

Lunnon, K., Keohane, A., Pidsley, R., Newhouse, S., Riddoch-Contreras, J., Thubron, E. B., et al. (2017). Mitochondrial genes are altered in blood early in Alzheimer's disease. *Neurobiol. Aging* 53, 36–47. doi: 10.1016/j.neurobiolaging.2016.12.029

Mazzucchelli, S., De Palma, A., Riva, M., D'Urzo, A., Pozzi, C., Pastori, V., et al. (2009). Proteomic and biochemical analyses unveil tight interaction of ataxin-3 with tubulin. *Int. J. Biochem. Cell Biol.* 41, 2485–2492. doi: 10.1016/j.biocel.2009.08.003

McLoughlin, H. S., Moore, L. R., and Paulson, H. L. (2020). Pathogenesis of SCA3 and implications for other polyglutamine diseases. *Neurobiol. Dis.* 134:104635. doi: 10.1016/j.nbd.2019.104635

Mendonça, C. F., Kuras, M., Nogueira, F. C. S., Plá, I., Hortobágyi, T., Csiba, L., et al. (2019). Proteomic signatures of brain regions affected by tau pathology in early and late stages of Alzheimer's disease. *Neurobiol. Dis.* 130:104509. doi: 10.1016/j.nbd.2019.104509

Moughamian, A. J., Osborn, G. E., Lazarus, J. E., Maday, S., and Holzbaur, E. L. F. (2013). Ordered recruitment of dynactin to the microtubule plus-end is required for efficient initiation of retrograde axonal transport. *J. Neurosci. Off. J. Soc. Neurosci.* 33, 13190–13203. doi: 10.1523/JNEUROSCI.0935-13.2013

Mukherjee, A. B., Appu, A. P., Sadhukhan, T., Casey, S., Mondal, A., Zhang, Z., et al. (2019). Emerging new roles of the lysosome and neuronal ceroid lipofuscinoses. *Mol. Neurodegener.* 14:4. doi: 10.1186/s13024-018-0300-6

Neves-Carvalho, A., Logarinho, E., Freitas, A., Duarte-Silva, S., Costa, M., do, C., et al. (2015). Dominant negative effect of polyglutamine expansion perturbs normal function of ataxin-3 in neuronal cells. *Hum. Mol. Genet.* 24, 100–117. doi: 10.1093/hmg/ddu422

Orr, H. T., and Zoghbi, H. Y. (2007). Trinucleotide repeat disorders. *Annu. Rev. Neurosci.* 30, 575–621. doi: 10.1146/annurev.neuro.29.051605.113042

Porro, C., Panaro, M. A., Lofrumento, D. D., Hasalla, E., and Trotta, T. (2019). The multiple roles of exosomes in Parkinson's disease: an overview. *Immunopharmacol. Immunotoxicol.* 41, 469–476. doi: 10.1080/08923973.2019.1650371

Pulido-Valdeolivas, I., Gómez-Andrés, D., Sanz-Gallego, I., Rausell, E., and Arpa, J. (2016). Patterns of motor signs in spinocerebellar ataxia type 3 at the start of follow-up in a reference unit. *Cerebellum Ataxias* 3:4. doi: 10.1186/s40673-016-0042-6

Rezende, T. J. R., Paiva, J. L. R., de Martinez, A. R. M., Lopes-Cendes, I., Pedroso, J. L., Barsottini, O. G. P., et al. (2018). Structural signature of SCA3: from presymptomatic to late disease stages. *Ann. Neurol.* 84, 401–408. doi: 10.1002/ana.25297

Sakabe, I., Hu, R., Jin, L., Clarke, R., and Kasid, U. N. (2015). TMEM33: a new stress-inducible endoplasmic reticulum transmembrane protein and modulator of the unfolded protein response signaling. *Breast Cancer Res. Treat.* 153, 285–297. doi: 10.1007/s10549-015-3536-7

Salpietro, V., Malintan, N. T., Llano-Rivas, I., Spaeth, C. G., Efthymiou, S., Striano, P., et al. (2019). Mutations in the neuronal vesicular SNARE VAMP2 affect synaptic membrane fusion and impair human neurodevelopment. *Am. J. Hum. Genet.* 104, 721–730. doi: 10.1016/j.ajhg.2019.02.016

Sánchez, I., Balagué, E., and Matilla-Dueñas, A. (2016). Ataxin-1 regulates the cerebellar bioenergetics proteome through the GSK3β-mTOR pathway which is altered in Spinocerebellar ataxia type 1 (SCA1). *Hum. Mol. Genet.* 25, 4021–4040. doi: 10.1093/hmg/ddw242

Sánchez-Valle, R., Monté, G. C., Sala-Llonch, R., Bosch, B., Fortea, J., Lladó, A., et al. (2016). White matter abnormalities track disease progression in PSEN1 autosomal dominant Alzheimer's disease. *J. Alzheimers Dis. JAD* 51, 827–835. doi: 10.3233/JAD-150899

Santos, T. C., Wierda, K., Broeke, J. H., Toonen, R. F., and Verhage, M. (2017). Early golgi abnormalities and neurodegeneration upon loss of presynaptic proteins Munc18-1, Syntaxin-1, or SNAP-25. *J. Neurosci. Off. J. Soc. Neurosci.* 37, 4525–4539. doi: 10.1523/JNEUROSCI.3352-16.2017

Saunders, A., Macosko, E. Z., Wysoker, A., Goldman, M., Krienen, F. M., Rivera, H., et al. (2018). Molecular diversity and specializations among the cells of the adult mouse brain. *Cell* 174, 1015.e16–1030.e16. doi: 10.1016/j.cell.2018.07.028

Schmidt, J., Mayer, A. K., Bakula, D., Freude, J., Weber, J. J., Weiss, A., et al. (2019). Vulnerability of frontal brain neurons for the toxicity of expanded ataxin-3. *Hum. Mol. Genet.* 28, 1463–1473. doi: 10.1093/hmg/ddy437

Seidel, K., den Dunnen, W. F. A., Schultz, C., Paulson, H., Frank, S., de Vos, R. A., et al. (2010). Axonal inclusions in spinocerebellar ataxia type 3. *Acta Neuropathol.* 120, 449–460. doi: 10.1007/s00401-010-0717-7

Shea, T. B., and Chan, W. K.-H. (2008). Regulation of neurofilament dynamics by phosphorylation. *Eur. J. Neurosci.* 27, 1893–1901. doi: 10.1111/j.1460-9568.2008.06165.x

Sittler, A., Muriel, M.-P., Marinello, M., Brice, A., den Dunnen, W., and Alves, S. (2018). Deregulation of autophagy in postmortem brains of Machado-Joseph disease patients. *Neuropathol. Off. J. Jpn. Soc. Neuropathol.* 38, 113–124. doi: 10.1111/neup.12433

Skotte, N. H., Andersen, J. V., Santos, A., Aldana, B. I., Willert, C. W., Nørremølle, A., et al. (2018). Integrative characterization of the R6/2 mouse model of Huntington's disease reveals dysfunctional astrocyte metabolism. *Cell Rep.* 23, 2211–2224. doi: 10.1016/j.celrep.2018.04.052

Sorolla, M. A., Reverter-Branchat, G., Tamarit, J., Ferrer, I., Ros, J., and Cabiscol, E. (2008). Proteomic and oxidative stress analysis in human brain samples of Huntington disease. *Free Radic. Biol. Med.* 45, 667–678. doi: 10.1016/j.freeradbiomed.2008.05.014

Sossin, W. S., and DesGroseillers, L. (2006). Intracellular trafficking of RNA in neurons. *Traffic* 7, 1581–1589. doi: 10.1111/j.1600-0854.2006.00500.x

Sowa, A. S., Martin, E., Martins, I. M., Schmidt, J., Depping, R., Weber, J. J., et al. (2018). Karyopherin α-3 is a key protein in the pathogenesis of spinocerebellar ataxia type 3 controlling the nuclear localization of ataxin-3. *Proc. Natl. Acad. Sci. U.S.A.* 115, E2624–E2633. doi: 10.1073/pnas.1716071115

Stenbeck, G. (1998). Soluble NSF-attachment proteins. *Int. J. Biochem. Cell Biol.* 30, 573–577. doi: 10.1016/s1357-2725(97)00064-2

Stridh, M. H., Alt, M. D., Wittmann, S., Heidtmann, H., Aggarwal, M., Riederer, B., et al. (2012). Lactate flux in astrocytes is enhanced by a non-catalytic action of carbonic anhydrase II. *J. Physiol.* 590, 2333–2351. doi: 10.1113/jphysiol.2011.220152

Switonski, P. M., Szlachcic, W. J., Krzyzosiak, W. J., and Figiel, M. (2015). A new humanized ataxin-3 knock-in mouse model combines the genetic features, pathogenesis of neurons and glia and late disease onset of SCA3/MJD. *Neurobiol. Dis.* 73, 174–188. doi: 10.1016/j.nbd.2014.09.020

Toonen, L. J. A., Overzier, M., Evers, M. M., Leon, L. G., van der Zeeuw, S. A. J., Mei, H., et al. (2018). Transcriptional profiling and biomarker identification reveal tissue specific effects of expanded ataxin-3 in a spinocerebellar ataxia type 3 mouse model. *Mol. Neurodegener.* 13:31. doi: 10.1186/s13024-018-0261-9

Unsain, N., Heard, K. N., Higgins, J. M., and Barker, P. A. (2014). Production and isolation of axons from sensory neurons for biochemical analysis using porous filters. *J. Vis. Exp. JoVE.* 89: 51795. doi: 10.3791/51795

Volpicelli-Daley, L. A., Gamble, K. L., Schultheiss, C. E., Riddle, D. M., West, A. B., and Lee, V. M.-Y. (2014). Formation of α-synuclein Lewy neurite-like

aggregates in axons impedes the transport of distinct endosomes. *Mol. Biol. Cell* 25, 4010–4023. doi: 10.1091/mbc.E14-02-0741

Wiatr, K., Piasecki, P., Marczak, Ł, Wojciechowski, P., Kurkowiak, M., Płoski, R., et al. (2019). Altered levels of proteins and phosphoproteins, in the absence of early causative transcriptional changes, shape the molecular pathogenesis in the brain of young presymptomatic Ki91 SCA3/MJD Mouse. *Mol. Neurobiol.* 56, 8168–8202. doi: 10.1007/s12035-019-01643-4

Yang, J.-S., Chen, P.-P., Lin, M.-T., Qian, M.-Z., Lin, H.-X., Chen, X.-P., et al. (2018). Association between body mass index and disease severity in chinese spinocerebellar ataxia type 3 patients. *Cerebellum Lond. Engl.* 17, 494–498. doi: 10.1007/s12311-018-0929-2

Yoo, B. C., Cairns, N., Fountoulakis, M., and Lubec, G. (2001). Synaptosomal proteins, beta-soluble N-ethylmaleimide-sensitive factor attachment protein (beta-SNAP), gamma-SNAP and synaptotagmin I in brain of patients with Down syndrome and Alzheimer's disease. *Dement. Geriatr. Cogn. Disord.* 12, 219–225. doi: 10.1159/000051261

Yuan, D., Liu, C., and Hu, B. (2018). Dysfunction of membrane trafficking leads to ischemia-reperfusion injury after transient cerebral ischemia. *Transl. Stroke Res.* 9, 215–222. doi: 10.1007/s12975-017-0572-0

Zaoui, K., Rajadurai, C. V., Duhamel, S., and Park, M. (2019). Arf6 regulates RhoB subcellular localization to control cancer cell invasion. *J. Cell Biol.* 218, 3812–3826. doi: 10.1083/jcb.201806111

Zeng, L., Zhang, D., McLoughlin, H. S., Zalon, A. J., Aravind, L., and Paulson, H. L. (2018). Loss of the Spinocerebellar Ataxia type 3 disease protein ATXN3 alters transcription of multiple signal transduction pathways. *PLoS One* 13:e0204438. doi: 10.1371/journal.pone.0204438

Zhang, Z.-H., Ma, F.-F., Zhang, H., and Xu, X.-H. (2017). MARCKS is necessary for oligodendrocyte precursor cell maturation. *Neurochem. Res.* 42, 2933–2939. doi: 10.1007/s11064-017-2324-7

Zhou, Y., Dhaher, R., Parent, M., Hu, Q.-X., Hassel, B., Yee, S.-P., et al. (2019). Selective deletion of glutamine synthetase in the mouse cerebral cortex induces glial dysfunction and vascular impairment that precede epilepsy and neurodegeneration. *Neurochem. Int.* 123, 22–33. doi: 10.1016/j.neuint.2018.07.009

Zhu, Z., and Reiser, G. (2018). The small heat shock proteins, especially HspB4 and HspB5 are promising protectants in neurodegenerative diseases. *Neurochem. Int.* 115, 69–79. doi: 10.1016/j.neuint.2018.02.006

Zinn, A., Goicoechea, S. M., Kreider-Letterman, G., Maity, D., Awadia, S., Cedeno-Rosario, L., et al. (2019). The small GTPase RhoG regulates microtubule-mediated focal adhesion disassembly. *Sci. Rep.* 9:5163. doi: 10.1038/s41598-019-41558-7

Conflict of Interest: The authors declare that the research was conducted in the absence of any commercial or financial relationships that could be construed as a potential conflict of interest.

Advantages of publishing in Frontiers

OPEN ACCESS
Articles are free to read for greatest visibility and readership

FAST PUBLICATION
Around 90 days from submission to decision

HIGH QUALITY PEER-REVIEW
Rigorous, collaborative, and constructive peer-review

TRANSPARENT PEER-REVIEW
Editors and reviewers acknowledged by name on published articles

Frontiers
Avenue du Tribunal-Fédéral 34
1005 Lausanne | Switzerland

Visit us: www.frontiersin.org
Contact us: frontiersin.org/about/contact

REPRODUCIBILITY OF RESEARCH
Support open data and methods to enhance research reproducibility

DIGITAL PUBLISHING
Articles designed for optimal readership across devices

FOLLOW US
@frontiersin

IMPACT METRICS
Advanced article metrics track visibility across digital media

EXTENSIVE PROMOTION
Marketing and promotion of impactful research

LOOP RESEARCH NETWORK
Our network increases your article's readership